



**A STUDY OF THE GROWTH AND
AGGREGATION OF CALCIUM OXALATE
MONOHYDRATE**

by

Allan Sidney Bramley, BE (Hons)

A thesis submitted for the degree of Doctor of Philosophy

in

The University of Adelaide

(Department of Chemical Engineering, Faculty of Engineering)

November, 1994

SUMMARY

This thesis reports an experimental investigation of the growth and aggregation of calcium oxalate mono-hydrate in metastable saline solutions using batch and continuous systems. There is much interest in the crystallisation of calcium oxalate hydrates for one reason – they are the principal inorganic constituent of most human kidney stones. Growth and aggregation have been identified as the important size enlargement mechanisms responsible for stone formation, and although both have been extensively studied the mechanism by which aggregation occurs is still poorly understood.

Firstly, states of saturation in the calcium oxalate system are studied, as supersaturation is a key variable in any precipitation reaction. A simple method of calculating supersaturation in metastable saline solutions, in terms of free ion concentrations from total ion concentrations is developed. This method is shown to be as accurate, but much easier to use than more complicated models that exist in the literature.

Seeded batch crystallisation experiments were conducted to investigate the effect of supersaturation and the agitation rate on the growth and aggregation of calcium oxalate mono-hydrate. A standard metastable solution of calcium (1.0 mM) and oxalate (0.2 mM) ions in a saline solution of ionic strength 0.158 M was used to investigate the effect of different rates of agitation. The supersaturation of the metastable solutions was increased by adding different quantities of oxalate. Metastable solutions with initial oxalate ion concentrations of 0.2 mM, 0.3 mM, 0.4 mM and 0.5 mM were used.

The data from the batch experiments were analysed using the program *Batch*, (Hounslow, 1990). This program extracts the growth and aggregation rates from changes in crystal size distributions with time. It is found the growth rate is size-independent. The growth rates from experiments at different agitation rates using solutions with different calcium to oxalate ratios are all described by a single equation with a second order dependence of the growth rate on relative supersaturation. These findings are consistent with those reported in many other studies available in the literature.

The aggregation rate is best described by a size-independent aggregation kernel. It is found that the aggregation rate constant decreases as the agitation rate increases. Of more interest is the finding that the aggregation rate constant in metastable solutions is dependent on the oxalate ion concentration only, rather than the activity product, or supersaturation.

A mechanism is developed for the aggregation of calcium oxalate crystals in saturated and supersaturated solutions. It is proposed that aggregation in supersaturated solutions proceeds as a two-stage process, the first being reversible and described by conventional electrical double-layer theory, the second irreversible and controlled by crystal growth. Further, it is proposed that in order for crystals to aggregate irreversibly solute must first diffuse to the point of contact and then deposit on the touching surfaces in order to “cement” the crystals together. It appears that diffusion to the cementing site is the rate determining step.

A novel tubular crystalliser is used to investigate calcium oxalate growth and aggregation in long, thin tubes, similar to the tubules of the kidney.

Both the solute and particle phase residence time distributions (RTDs) of the crystalliser were determined. A diffusion-advection model is used to explain the experimentally observed solute RTD. The particle RTD is best described by a model in which it is assumed the particles maintain a constant radial position in the tubes as they pass through them.

Continuous crystallisation experiments reveal that in addition to growth and aggregation, sticking and breakage also occur in the crystalliser. A moment form of the population balance is used to determine the rate constants for each mechanism from the experimental data. Sticking is found to be size-independent and inversely proportional to the shear rate in the crystalliser. Breakage is modelled by assuming that when an aggregate breaks, crystals of all sizes are equally likely to form. It is found that the breakage rate is directly proportional to the shear rate in the crystalliser.

The aggregation rates in the crystalliser are orders of magnitude lower than those from the batch experiments at the same relative supersaturation. It is found that the aggregation rate increases as the shear rate increases, and does not strongly depend on the oxalate ion concentration. These observations can be explained by the aggregation mechanism proposed and indicates the importance that hydrodynamics and particle shape may have on aggregation.

Mechanisms and the kinetics for the growth and aggregation of calcium oxalate monohydrate over a wide range of shear rates and supersaturation in both a batch system and a novel continuous tubular crystalliser have been determined in this study.

TABLE OF CONTENTS

Summary	ii
Table of Contents.....	iv
Acknowledgements.....	x
Declaration.....	xi

Chapter 1

INTRODUCTION.....	1
1.1 Introduction	1
1.2 Size enlargement mechanisms	2
1.3 Particle size distribution analysis	4
1.3.1 Phase space.....	4
1.3.2 Particle size distributions.....	5
1.3.3 Moments of a size distribution	5
1.4 Modelling particulate processes	6
1.4.1 The population balance	6
1.4.2 The moment form of the population balance.....	7
1.4.3 Growth and aggregation in the population balance.....	8
1.5 Solving the population balance	10
1.5.1 Analytical solutions.....	10
1.5.2 Numerical methods	11
1.5.3 The inverse problem.....	12
1.6 Modelling calcium oxalate crystallisation.....	12
1.6.1 Introduction	12
1.6.2 Empirical measures of growth and aggregation.....	12
1.6.3 Population balance models for growth and aggregation.....	13
1.7 Layout of this thesis.....	15

Chapter 2

PHYSICAL CHEMISTRY OF CALCIUM OXALATE IN AQUEOUS SOLUTIONS	17
2.1 Introduction	17
2.2 States of Saturation	17
2.3 Defining supersaturation	18
2.3.1 Physico-chemical considerations.....	19
2.3.2 Reversibility.....	19
2.3.3 The reaction of two ionic species	19
2.3.4 Dissociation	23
2.3.5 Concluding remarks on defining supersaturation.....	24
2.4 Calculating supersaturation	24

2.4.1	A simple method of calculating free ion concentrations.....	24
2.4.2	Saturated and supersaturated solutions	26
2.5	Parameter estimation	29
2.5.1	Literature values	32
2.5.2	Experimental value of the solubility product	32
2.6	Discussion.....	34
2.7	Conclusions	36

Chapter 3

BATCH CRYSTALLISATION: MATERIALS AND METHODS.....		37
3.1	Introduction	37
3.2	Analysis techniques	37
3.2.1	Crystal size distributions	38
3.2.2	Solution and solids concentrations	38
3.2.3	Other experimental techniques	39
3.3	Experimental	40
3.3.1	Background	40
3.3.2	Solutions.....	41
3.3.3	Method.....	45
3.4	Parameters investigated	46
3.4.1	Supersaturation	46
3.4.2	Agitation rate	47
3.5	Calculating the growth and aggregation rates	48
3.5.1	The program <i>Batch</i>	48
3.5.2	Determining the rates.....	48
3.5.3	Running <i>Batch</i>	50
3.6	Data analysis	51
3.7	Conclusions	54

Chapter 4

BATCH CRYSTALLISATION: RESULTS AND ANALYSIS.....		56
4.1	Introduction	56
4.2	The inverse problem.....	56
4.3	Preliminary results.....	59
4.4	The growth rate	66
4.4.1	Analysis of experimental data	66
4.4.2	Discussion.....	70
4.5	The aggregation rate.....	78
4.5.1	Analysis of experimental data	78
4.5.2	Discussion.....	83
4.6	Error analysis	89

4.6.1	Growth rate and relative supersaturation.....	90
4.6.2	Aggregation rate constant and oxalate ion concentration.....	90
4.7	Kidney stone formation.....	92
4.8	Conclusions	94

Chapter 5

THE AGGREGATION MECHANISM.....		95
5.1	Introduction	95
5.2	Aggregation mechanisms	96
5.2.1	DLVO theory.....	96
5.3	An experimental investigation.....	98
5.3.1	Materials and methods	98
5.3.2	Results	99
5.4	Discussion.....	114
5.5	Aggregation in supersaturated solutions	118
5.5.1	A cementing model.....	118
5.5.2	Results	121
5.5.3	Discussion.....	124
5.6	An improved cementing model	125
5.6.1	Derivation.....	125
5.6.2	Results	129
5.6.3	Discussion.....	129
5.7	Conclusions	135

Chapter 6

THE <i>IN VITRO</i> STUDY OF UROLITHIASIS		136
6.1	Introduction	136
6.2	<i>In vitro</i> experimental systems	136
6.2.1	Batch crystallisation	137
6.2.2	Constant composition methods	137
6.2.3	The M.S.M.P.R. crystalliser	138
6.2.4	The Couette agglomerator	138
6.2.5	Reverse osmosis.....	139
6.3	A new tubular crystalliser	140
6.3.1	The crystalliser.....	140
6.3.2	The seed suspension delivery system	143
6.3.3	Apparatus set-up.....	149
6.3.4	Modes of operation.....	151
6.3.5	Hydrodynamics in the crystalliser	152
6.4	Conclusions	153

Chapter 7

THE SOLUTE RESIDENCE TIME DISTRIBUTION IN THE TUBULAR

CRYSTALLISER 154

7.1 Introduction 154

7.2 The residence time distribution 154

 7.2.1 The *E* and *F* curves 154

 7.2.2 Experimental determination 155

7.3 Experimental investigation 156

 7.3.1 Method 156

 7.3.2 Calculating the RTD 157

 7.3.3 Results 157

7.4 Analysis 159

 7.4.1 The velocity field in the crystalliser 159

 7.4.2 Poiseuille flow 160

 7.4.3 Taylor dispersion 161

 7.4.4 A diffusion-advection model 163

 7.4.5 Moment transforms 167

 7.4.6 End effects 168

 7.4.7 Parameters in the model 170

7.5 Results from the diffusion-advection model 171

 7.5.1 Testing the model 171

 7.5.2 Moments of the experimental RTDs 174

 7.5.3 Solute diffusivity and jacket cross-sectional area 175

7.6 Discussion 182

7.7 Conclusions 183

Chapter 8

THE PARTICLE RESIDENCE TIME DISTRIBUTION IN THE

TUBULAR CRYSTALLISER 185

8.1 Introduction 185

8.2 Preliminary experiments 186

 8.2.1 Testing the particle suspension delivery system 186

 8.2.2 Step-change tests 188

 8.2.3 Particle mass balance 188

8.3 Residence time distribution experiments 191

 8.3.1 Materials 191

 8.3.2 Method 191

 8.3.3 Parameters investigated 193

 8.3.4 Calculating the RTDs 193

8.4 Experimental results 193

8.5 Analysis 200

8.5.1	Poiseuille flow	200
8.5.2	Streamline model	203
8.5.3	Constant radial position model.....	206
8.6	Discussion.....	210
8.6	Conclusions	211

Chapter 9

CRYSTALLISATION IN A CONTINUOUS SYSTEM.....		212
9.1	Introduction	212
9.2	Preliminary experiments	213
9.2.1	Method.....	213
9.2.2	Results	213
9.2.3	Discussion.....	214
9.2.4	Seed preparation	216
9.3	Experimental investigation.....	218
9.3.1	Materials	218
9.3.2	Method.....	218
9.3.3	Parameters investigated	219
9.4	Results	219
9.4.1	Size distributions	222
9.5	Analysis.....	222
9.5.1	Introduction	222
9.5.2	Sticking	225
9.5.3	Breakage.....	225
9.5.4	Simultaneous sticking and breakage	227
9.5.5	The effect of the particle residence time distribution	231
9.6	Saturated solutions	233
9.6.1	Independent variables	233
9.6.2	Experimental results.....	238
9.6.3	Discussion.....	240
9.7	Metastable solutions.....	240
9.7.1	Identifying breakage.....	243
9.7.2	Simultaneous growth, aggregation, sticking and breakage.....	245
9.7.3	Results	247
9.7.4	Discussion.....	247
9.8	The effect of inclination.....	253
9.9	Stone formation.....	257
9.10	Conclusions	259

Chapter 10

CONCLUSIONS AND RECOMMENDATIONS.....	262
10.1 The crystallisation of calcium oxalate	262
10.2 Work presented in this thesis.....	262
10.2.1 Supersaturation	262
10.2.2 Batch crystallisation	263
10.2.3 The aggregation mechanism.....	264
10.2.4 The tubular crystalliser.....	264
10.2.5 Continuous crystallisation	265
10.3 Recommendations for future work	266
10.3.1 Batch crystallisation	267
10.3.2 The aggregation mechanism.....	267
10.3.3 <i>In vitro</i> experimental systems	268
10.4 A concluding comment	268

Appendices

1 Nomenclature	270
2 Literature cited	278
3 Solubility product experimental data	290
4 Experimental analysis procedures	294
5 Seed suspension data	297
6 Conversion of size distributions to CSDs with a $\sqrt[3]{2}$ progression	299
7 Batch crystallisation experimental data.....	303
8 Error analysis for growth and aggregation rates	309
9 Continuous crystallisation experimental data.....	319

ACKNOWLEDGEMENTS

First, and foremost I would like to thank my supervisor Dr Michael Hounslow. Whether from an office just up or down a flight of stairs or from the other side of the planet he has always encouraged me and offered great insight into my work. It has been a pleasure to work with, and become friends with him and his family.

At The University of Adelaide I would like to thank Dr Dzuy Nguyen and Dr Brian O'Neill for supervising me when Dr Hounslow left for Cambridge University. Finally, Mr Bruce Ide was responsible for producing much of the experimental apparatus, his expertise and willingness to help at any time is much appreciated.

At Flinders Medical Centre, I must thank Dr R.L. Ryall and Professor V.R. Marshall for involving me in their project and allowing me to work in the Urology Laboratory at Flinders. My thanks also to the members of the Urology Laboratory for their friendship and for helping to keep me sane during the long hours in the lab. I would particularly like to thank Dr Kumar Grover for his help producing the SEM micrographs in this thesis.

At Cambridge University I would like to thank Dr W.R. Paterson for his help with the model for aggregation developed in Chapter 5. The members of the "Crystal Group": Denis Smit, John Gooch, Ed Wynn and Alan Collier, the inhabitants, past and present, of the "Foreign Office", particularly Hamish Drewry and Craig Jensen have made my time in Cambridge when writing up very enjoyable.

Financial support for this work has come from two sources, an Australian Postgraduate Research Award and a research grant from the Australian National Health and Medical Research Council. This support is gratefully acknowledged.

Two very special people deserve more thanks than I can offer them. Firstly, my mother who understood my pre-occupation with work at all times both good and bad. Many late dinners, even later nights and other countless disruptions were caused by my work, however my mother always supported and helped me. Finally, Sabina has always been there for me, despite my pre-occupation with work after we were apart for so long. I would like to thank her for proof reading this thesis, helping me in so many other ways, but most of all for her love.

DECLARATION

This work contains no material which has been accepted for the award of any other degree or diploma in any university or other tertiary institution and, to the best of my knowledge and belief, contains no material previously published or written by another person, except where due reference has been made in the text.

I give consent to this copy of my thesis, when deposited in the University Library, being available for loan and photocopying.

SIGNED:

DATE: 29/11/1994

Chapter 1:



INTRODUCTION

In this chapter an outline of the problem to be addressed is given; this consists of outlining the methods of modelling particulate systems, then reviewing the work that has been done on modelling the growth and aggregation of calcium oxalate.

1.1 INTRODUCTION

Although calcium oxalate crystals are responsible for the toxicity of various plants (Doaigey, 1991 and Perera *et al.*, 1990) and may be found in the human thyroid gland (Hackett and Khan, 1988) and breast (Gonzalez *et al.*, 1991), undoubtedly the principal reason for the interest in the crystallisation of calcium oxalates is that they are the major inorganic constituent of human kidney stones (Prien and Prien, 1968). Calcium oxalate exists in three states of hydration: the mono-hydrate (whewellite), di-hydrate (wheddellite) and tri-hydrate. The mono-hydrate, then the di-hydrate being most prevalent in stones (Blomen and Bijvoet, 1983).

Kidney stone disease (urolithiasis) is a significant health problem with approximately 10% of the male population likely to experience one stone episode in their lifetime (Sierakowski *et al.*, 1978). Therefore, not unexpectedly the cost to the community in both lost time and financial terms is enormous (Marshall and Ryall, 1981). For example, according to Shuster and Schaeffer (1984), the projected cost of stone treatment for adult males in the United States is \$315 million per annum. Thus an understanding of the underlying mechanisms of stone formation will provide valuable information in efforts to prevent the occurrence of this disease.

Although there are many detailed aspects to the theories of stone formation, it is commonly accepted that some form of nucleation lies at the origin and that two processes, crystal growth and aggregation are essential for the increase in size of the original crystals (Vermeulen and Lyon, 1968, Pak, 1978). Further, Robertson *et al.* (1969) propose that the formation of crystal aggregates is the critical phase of stone formation.

Human autopsy studies by Haggitt and Pitcock (1971) strongly implicate the kidney tubules as the initial site of stone formation, a finding which has been confirmed in animal models by Jordan *et al.* (1978) and Rushton *et al.* (1981). As urine passes through the tubules, water is removed leaving a progressively more concentrated solution of wastes behind. Among these wastes are both calcium and oxalate ions and it is possible to envisage a situation where the solubility of a sparingly soluble salt such as calcium oxalate is exceeded, in which case precipitation can occur.

Many complications such as the extremely complex chemical composition of urine, the difference between the urine of stone formers and normal subjects and the potential role of inhibitors and promoters of nucleation, growth and aggregation make research into the cause of stone disease very difficult.

However, it is essential to have a clear understanding of the mechanisms of the size enlargement processes, namely growth and aggregation. Thus, the main aim of this thesis is to study and model the simultaneous growth and aggregation of calcium oxalate in inorganic metastable solutions. Particular attention is paid to aggregation, as although nucleation and growth have been extensively studied, aggregation has been largely neglected (Finlayson, 1978). Before reviewing the literature on the growth and aggregation of calcium oxalate, the general mathematical framework for modelling particulate processes is introduced.

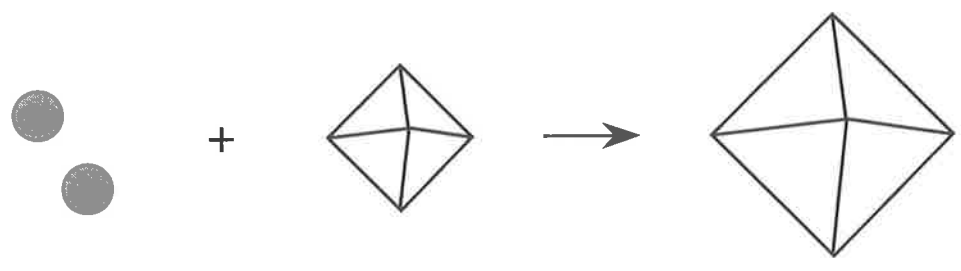
1.2 SIZE ENLARGEMENT MECHANISMS

The size enlargement mechanisms which are the focus of this thesis are growth and aggregation. Breakage is also considered briefly, but other mechanisms such as nucleation are not studied.

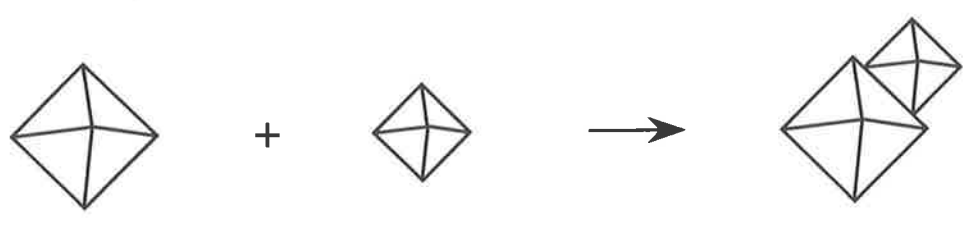
Growth occurs when non-particulate material is deposited, usually on the surface, of a particle. In solution crystallisation, such as that studied here, the non-particulate material is usually an ion diffusing to, and reacting on, the surface of a crystal. Growth results in an increase in particle size and the total volume of particulate material. However, growth has no effect on the number of particles in a system. Growth is shown schematically in Figure 1.1 (a).

Aggregation is the process where particles collide, adhere to one another and form a new, larger particle. Therefore aggregation not only acts to increase the size of particles, but also to decrease the total number of particles present in a system. Importantly, aggregation conserves the total mass of particulate material in a system, which is frequently taken to

(a) Growth



(b) Aggregation





Legend:		Non-particulate matter
		Particle

Figure 1.1 Schematic depiction of (a) growth and (b) aggregation.

mean the volume of particulate material is conserved. Aggregation is shown schematically in Figure 1.1 (b).

1.3 PARTICLE SIZE DISTRIBUTION ANALYSIS

1.3.1 Phase space

A particle may be characterised by a number of independent properties such as its size, shape, surface area or volume. These are its *internal coordinates*. The location of a particle in space is defined by its *external coordinates*. Together the internal and external coordinates locate a particle in *Phase Space*, a concept introduced to the analysis of particulate systems by Hulburt and Katz (1964).

This work by Hulburt and Katz implies that the exact theoretical characterisation of groups of particles would require a multi-dimensional description. However, for a whole group of particles the practical difficulties of measuring more than a few coordinates in phase space outweighs theoretical considerations. Frequently only one coordinate of phase space is measured, that being the size of the particles.

Randolph and Larson (1988) note that provided all particles have approximately the same shape, it is generally sufficient to use only a single coordinate of phase space: particle size. The usual way to characterise particle size is to use either volume, v , or length, L , (some linear dimension of the particle). As will be shown later, both have merits, depending on the size enlargement mechanisms that are present in a system. Particle length and volume are simply related by

$$v = k_v L^3 \tag{1.1}$$

where k_v is the volume shape factor. Finally, there are many different measures of particle length, such as Stoke's diameter, sieve diameter, volume equivalent diameter and many others. The measure of crystal size chosen usually depends on the method of measurement. Such is the case in the current work in which nearly all particle sizing was performed using a Coulter Counter, which gives the particle size as the diameter of a sphere of the same volume as the particle. In this case the shape factor in eq 1.1 is $\pi/6$. For a more comprehensive discussion of particle size measurement see Allen (1981).

1.3.2 Particle size distributions

There are many mathematical formulations available to present a particle size distribution (PSD). Perhaps the simplest conceptually are the cumulative size distributions. For example the cumulative number oversize distribution, $COSN(L)$, gives the fraction of particles larger than size L , and the cumulative number undersize distribution, $CUSN(L)$, gives the fraction of particles less than size L . As these distributions are normalised, they tend to a value of one regardless of the number of particles present.

Another means of describing PSDs is by the use of density functions. The number density function, $n(L)$, gives the differential number of particles, dN , in the size range L to $L + dL$

$$dN = n(L) dL \quad (1.2)$$

In eq 1.2, length is the internal coordinate, however a density function with volume as the internal coordinate can be written as

$$dN = n(v) dv \quad (1.3)$$

From the above equations it can be seen that the number density function is the local derivative of the cumulative distribution.

Similar to the density function is the histogram, which merely plots the amount of a measured quantity, either number or volume, that appears over each increment of the measured characteristic, normally particle size. Particle size analysers such as the Coulter Counter usually report PSDs in the form of a histogram, however these can be used to calculate density and cumulative distributions.

1.3.3 Moments of a size distribution

The moment of the number density function, $n(x)$, with respect to its internal coordinate, x , is defined as

$$m_j = \int_0^{\infty} x^j n(x) dx \quad (1.4)$$

If particle length is the internal coordinate the first four moments provide useful overall properties of the PSDs:

- The total number of particles per unit volume of suspension = m_0
- The total length of particles per unit volume of suspension = $k_l m_1$
- The total surface area of particles per unit volume of suspension = $k_a m_2$
- The total volume of particles per unit volume of suspension = $k_v m_3$

The standard statistical properties of the PSD may also be calculated directly from the moments.

$$\text{The mean size, } \bar{L} = \frac{m_1}{m_0} \quad (1.5)$$

$$\text{The variance, } \sigma^2 = \frac{m_2}{m_0} - \left(\frac{m_1}{m_0} \right)^2 \quad (1.6)$$

$$\text{The coefficient of variation, } CV = \frac{\sigma}{\bar{L}} = \sqrt{\frac{m_0 m_2}{m_1^2} - 1} \quad (1.7)$$

The advantage of representing a PSD in terms of its moments or statistical properties is that it can substantially reduce the complexity of modelling particulate systems, as will be illustrated in Chapter 10.

1.4 MODELLING PARTICULATE PROCESSES

The aim of modelling a particulate process is to describe how the size and number of particles change with time. The *Population Balance* is the mathematical description of this problem.

1.4.1 The population balance

Although population balances were developed by Smoluchowski (1916), and Muller (1928), Hulburt and Katz (1964) are generally credited with the first thorough description of the population balance. The population balance can be deduced by various methods: Hulburt and Katz proceed by analogy (with for example the conservation of mass in fluid flow), Randolph and Larson (1988) use a Lagrangian view and Hounslow (1990) an Eulerian approach. The outcome of any of these methods of analysis, in terms of the number density function, n , is:

$$\frac{\partial n}{\partial t} + \nabla \cdot (n\mathbf{u}) = B - D \quad (1.8)$$

where \mathbf{u} , is the velocity vector which gives the rate of change of position in phase space. Here $\mathbf{u} = \{\mathbf{u}_{int}, \mathbf{u}_{ext}\}$, where, \mathbf{u}_{int} and \mathbf{u}_{ext} are the internal and external velocity vectors. For the external coordinates the components of \mathbf{u}_{ext} are the conventional velocities in 3-D space, for the internal coordinates the components of \mathbf{u}_{int} are the rate of change of position along the internal coordinate axes. In many systems, such as the one studied here, the change in particle size, or the *growth rate*, G , is the only important internal coordinate velocity. The right hand side of eq 1.8 gives the birth and death rates of particles per unit volume of phase space due to mechanisms such as nucleation, aggregation and breakage.

Eq 1.8 is referred to by Randolph and Larson (1988) as the micro-distributed form of the population balance as it applies to a differential zone in phase space. Those authors then develop a macro-distributed form of the population balance that is of more use in practical applications. This form of the population balance assumes a well mixed control volume and therefore discards \mathbf{u}_{ext} . The macro-distributed population balance is

$$\frac{\partial n}{\partial t} + \nabla \cdot (n\mathbf{u}_{int}) + \frac{n}{V} \frac{dV}{dt} = -\frac{1}{V} \sum_{i=1}^k Q_i n_i + B - D \quad (1.9)$$

where V , is the volume of the vessel, k , the number of streams entering and leaving the vessel and Q_i and n_i are the flowrates and number density function in the streams entering and leaving the vessel.

The macro-distributed population balance has been widely used to model particulate processes in fields such as crystallisation (Hulburt and Katz, 1964 and Randolph and Larson, 1988), granulation and pelletisation (Sastry, 1975 and Ouchiyama and Tanaka, 1982), polymerisation (Stokmeyer, 1943) and aerosol coalescence (Schumann, 1940 and Friedlander, 1977). It has also been used to model the growth and aggregation of calcium oxalate by Hartel and Randolph (1986) and Hounslow *et al.* (1988a).

1.4.2 The moment form of the population balance

In most situations where growth and aggregation are active a complete solution to the population balance is not possible. In the absence of an analytical solution for $n(L)$, the moments of the PSD may be obtained from writing the population balance in terms of moments. Randolph and Larson (1988) develop micro- and macro-moment forms of the population balance, the more useful for this work being the latter which is:

$$\frac{dm_j}{dt} + \frac{m_j}{V} \frac{dV}{dt} = jGm_{j-1} - \frac{1}{V} \sum_{i=1}^k Q_i m_{j,i} + \bar{B}_j - \bar{D}_j \quad (1.10)$$

This equation applies only for a system with size as the only internal coordinate and with a size-independent growth rate. The birth and death terms on the right hand side of eq 1.10 are defined by

$$\bar{B}_j = \int_0^{\infty} L^j B(L) dL \quad (1.11)$$

$$\bar{D}_j = \int_0^{\infty} L^j D(L) dL \quad (1.12)$$

The moment forms of the population balance can be very powerful. Typically they reduce to a set of ordinary differential equations, which are often analytically tractable. This is illustrated in Chapter 10, when the growth and aggregation of calcium oxalate in a continuous system is modelled.

1.4.3 Growth and aggregation in the population balance

Growth. There is much discussion in the literature regarding the nature of the growth rate. For crystallisation from solution, McCabe (1929) suggested that the linear rate of crystal growth, $G = dL/dt$, is size-independent. The alternatives to this formulation are either a size-dependent linear growth rate (*e.g.* Branson, 1960, Canning and Randolph, 1967 and Abegg *et al.*, 1968) or growth rate dispersion (*e.g.* White and Wright, 1971, Larson *et al.*, 1982 and Human *et al.*, 1982).

For size-independent growth, a convenient form of the population balance is obtained with length as the only internal coordinate. The appropriate form of eq 1.9 is

$$\frac{\partial n}{\partial t} + G \frac{\partial n}{\partial L} = B - D \quad (1.13)$$

By contrast, if volume is used as the internal coordinate then the resulting form of the population balance is more complex. The growth rate may be written as

$$G_v = 3k_v^{1/3} G_v^{2/3} \quad (1.14)$$

Then eq 1.13 becomes

$$\frac{\partial n}{\partial t} + 3k_v^{1/3} G \frac{\partial(nv^{2/3})}{\partial v} = B - D \quad (1.15)$$

Comparing eq 1.13 with eq 1.15 it is clear that for size-independent growth the population balance is much simpler with length rather than volume as the internal coordinate.

Aggregation. A binary collision model for aggregation was included in the population balance formulated by Hulburt and Katz (1964), extending the analysis of Smoluchowski (1916) on particle coalescence. Aggregation results in the simultaneous birth and death of particles at different sizes. The birth of a particle of volume, v can occur when particles of volume $v - \varepsilon$ and ε aggregate. The birth rate for this event is calculated by summing over all the possible values of ε :

$$B(v) = \frac{1}{2} \int_0^v \beta(v - \varepsilon, \varepsilon) n(v - \varepsilon) n(\varepsilon) d\varepsilon \quad (1.16)$$

where $\beta(v, \varepsilon)$ is the aggregation rate constant called the *aggregation kernel*, as explained below, and the factor of 1/2 is included as the integral counts each collision twice.

A death occurs at a particle volume v when a particle of that volume aggregates with another particle of volume ε , summing over all possible values of ε gives the following death rate:

$$D(v) = n(v) \int_0^\infty \beta(v, \varepsilon) n(\varepsilon) d\varepsilon \quad (1.17)$$

The above expressions for the birth and death rate may also be written with length as the internal coordinate, they are according to Hounslow *et al.* (1988a)

$$B(L) = \frac{L^2}{2} \int_0^L \frac{\beta\left(\left(L^3 - \lambda^3\right)^{1/3}, \lambda\right) n\left(\left(L^3 - \lambda^3\right)^{1/3}\right) n(\lambda) d\lambda}{\left(L^3 - \lambda^3\right)^{2/3}} \quad (1.18)$$

$$D(L) = n(L) \int_0^\infty \beta(L, \lambda) n(\lambda) d\lambda \quad (1.19)$$

Clearly the formulation for the birth term is much more complex with length as the internal coordinate.

The above expressions have been developed assuming that particles are free to collide with any other particle in the system. This is known as a free-in-space system. Sastry and Fuerstenau (1970) suggest that in a system that is not free-in-space, the birth and death terms should be altered by dividing by the total number of particles, N_T . The systems studied in this work are considered to be free-in-space.

The aggregation kernel, $\beta(v, \varepsilon)$ measures the frequency with which particles of sizes v and ε collide and successfully form a stable aggregate. The aggregation kernel is often viewed as being a combination of two factors: one relating the frequency with which particle collisions occur, the other describing the effectiveness of collisions in forming an aggregate. Many different functional forms of the aggregation kernel, both theoretical and empirical, have been proposed for various aggregating systems. For aggregation in crystallising systems, Hartel *et al.* (1986) and Beckman and Farmer (1987) tabulate some of the relevant theoretical and empirical kernels.

1.5 SOLVING THE POPULATION BALANCE

Solving the population balance involves finding the PSD, $n(L)$, that satisfies the population balance for the system, subject to the appropriate initial and boundary conditions. A related problem is the inverse problem in which mechanisms are chosen to model experimental data.

In this section an overview of some of the useful analytical and numerical methods of solving the population balance that are relevant to the current work is given. For a more comprehensive review of methods of solving the population balance see, Ramkrishna (1985), Pulvermacher and Ruckenstein (1974) and Seigneur *et al.* (1986).

1.5.1 Analytical solutions

Analytical solutions to the population balance are notoriously difficult to obtain particularly when growth and aggregation occur simultaneously. As pointed out by Hounslow (1990) for systems that are analytically tractable integral transforms such as the Laplace transform are most frequently used.

The moment form of the population balance may also be used to obtain analytical solutions, for example for size-independent batch aggregation. Hulburt and Katz (1964), using volume as the internal coordinate, and Hounslow (1990), using length as the internal coordinate, show that the rate of change of the zeroth and third moments are given by:

$$\frac{dm_0}{dt} = -\frac{1}{2}\beta_0 m_0^2 \quad (1.20)$$

$$\frac{dm_3}{dt} = 0 \quad (1.21)$$

The last result simply states that the rate of change of the third moment must be zero if aggregation is to conserve total particle volume.

If a size-independent growth term is included, then eq 1.20 remains unchanged as growth does not affect the number of particles in a system, however from eq 1.10, the rate of change of the third moment becomes:

$$\frac{dm_3}{dt} = 3Gm_2 \quad (1.22)$$

The results given by eqs 1.20 to 1.22 are important and are used later in Chapter 10.

1.5.2 Numerical methods

The majority of the solutions to the population balance reported in the literature are obtained by numerical methods. Hounslow (1990) classifies these methods into three groups: classical numerical methods (such as finite elements), cubic spline methods and discretized population balances (DPBs). Of these a particularly useful method is the DPB, in which the size domain is discretized into intervals and it is assumed that the particle size distribution function is constant within each interval. The advantage of using a DPB is that it transforms the population balance equation into a set of ordinary differential equations, which drastically reduces the complexity of solving the population balance.

Many different DPBs have been developed and are reviewed by Hounslow (1990). He proposed that a DPB must imply a set of moments which are consistent with the continuous population balance. Stated formally, Hounslow's criterion is that:

The rates of change of moments implied by the DPB should be equal to the rates of change implied by the continuous population balance.

He showed that all the existing DPBs failed to satisfy this criterion and proceeded to develop a DPB which satisfies the criterion. It is this feature that distinguishes the DPB of Hounslow from others. In particular this DPB ensures the correct prediction of particle number and volume for the aggregation terms in the DPB and the correct prediction of the first three moments for the growth terms. This DPB has been applied in modelling

crystallisation, by Hounslow *et al.* (1988a), Ilievski (1991) and Hostomsky and Jones (1993), it is also used to model the batch experiments reported in the current work.

1.5.3 The inverse problem

The problem of choosing an appropriate aggregation kernel to model experimental data is called the inverse problem in aggregation (Muralidhar and Ramkrishna, 1986). This problem and methods of solving it has been recently investigated by Smit *et al.* (1993) and (1994). These authors show that under specific operating conditions some kernels may be rejected *a priori* as being unsuitable for modelling aggregation. One of the major aims of this work is to determine the form of the aggregation kernel that best describes the aggregation of calcium oxalate in batch and continuous systems.

1.6 MODELLING CALCIUM OXALATE CRYSTALLISATION

1.6.1 Introduction

As a result of the important role that growth and particularly aggregation may play in the formation of kidney stones, there are many studies of these phenomena in the literature. However, most research focuses on the prevention of stone formation. Consequently, great importance has been placed on the effect of many different inhibitors of both growth and aggregation and very little importance has been placed on understanding the mechanism and kinetics of growth and particularly aggregation. Studies of the growth and aggregation of calcium oxalate can be divided into two groups:

- Those that measure growth and aggregation in terms of some empirical parameter.
- Those that use a population balance analysis to propose a model for growth and aggregation.

1.6.2 Empirical measures of growth and aggregation

When particle size analysis, for example by Coulter Counter, of seeded systems was first applied to kidney stone research no attempt was made to distinguish between growth and aggregation. For example, Robertson and Peacock (1972) use the increase in the number of crystals larger than a certain critical diameter as a measure of growth and aggregation.

A similar technique is used by Robertson *et al.* (1973) to determine the effect of chemical inhibitors on growth and aggregation. A degree of inhibition is defined as

$$I = \frac{R_{cont} - R_{test}}{R_{cont}} \times 100\% \quad (1.23)$$

where R_{cont} and R_{test} are the experimental results under control and test conditions respectively. In this case the experimental results are the number of crystals greater than some critical size.

The shortcomings of the method outlined above have been stated by Ryall *et al.* (1981a) who recognise that the effects of growth and aggregation should be measured independently even though they occur simultaneously. They propose the use of two parameters, as defined in eq 1.23, one for growth and one for aggregation. For growth, the experimental result used is the change in crystal volume and for aggregation the experimental result is the change in crystal number. This approach is then used to show that the same value of the degree of inhibition, eq 1.23, can be obtained from different combinations of growth and aggregation inhibition.

This method is extended by Ryall *et al.* (1986) who produce a computer program to calculate the “extents” of growth and aggregation over some time interval. Here growth and aggregation are investigated using overall changes in crystal number and volume with time, given that growth conserves crystal number and aggregation conserves crystal volume. However, even though this method deals with simultaneous growth and aggregation, as its authors point out, it only calculates the extents of growth and aggregation and cannot be used to obtain rate equations for the mechanisms.

1.6.3 Population balance models for growth and aggregation

A population balance analysis has been extensively used to study the growth of calcium oxalate, particularly in a mixed suspension, mixed product removal crystalliser (MSMPR). The main advantage of using an MSMPR to study crystallisation is that an analytical solution to the population balance exists if only growth and nucleation occur, as shown by Randolph and Larson (1988). Consequently the MSMPR has been extensively used to study the nucleation and growth kinetics of calcium oxalate (Kavanagh, 1992). However, if aggregation occurs the analytical solution for nucleation and growth alone is not valid, and the rates calculated will be wrong. In the context of this study, in which simultaneous growth and aggregation are of interest, many of the studies in the literature, which ignore aggregation are not relevant.

The author is aware of only two studies that use a population balance analysis to model the simultaneous growth and aggregation of calcium oxalate, and these give rise to contradictory results.

Hartel and Randolph

Hartel and Randolph (1986) model growth and aggregation in a Couette-flow agglomerator in series with an MSMPR. They propose that in addition to growth and aggregation, two other mechanisms must be included, namely breakage and a source function. Breakage is modelled by using a two-body equal-volume breakage function (Randolph and Larson, 1988) in which it is assumed that one large particle breaks into two smaller fragments, each of half the original volume. A source function is used to account for a problem often encountered with particle size analysers, being that during the course of an experiment crystals can grow and aggregate into its field of view. A source function is defined, as the rate of appearance of crystals in the first interval of the size range covered by the particle size analyser.

A population balance is derived, with volume as the internal coordinate, and is solved numerically using the method of Gelbard and Seinfeld (1978). A size-independent growth rate is assumed and is calculated from the size distributions at the outlet of the MSMPR.

The inverse problem for aggregation is investigated and a best fit procedure is used to find values of the aggregation, breakage and source function rate constants that minimize the logarithmic sum of square errors difference between the experimental and predicted size distributions. The results of Hartel and Randolph will be discussed in more detail in relation to the findings of the current work, but in summary they find:

- A semi-empirical kernel for aggregation developed by Thompson (1968) best fits the experimental data.
- The size-independent part of the aggregation kernel and the breakage rate constant are both highly dependent on supersaturation and shear rate in the agglomerator.

Hounslow

Hounslow (1990) summarises the work of Hounslow *et al.* (1988a) and (1988b) on the seeded batch crystallisation of calcium oxalate. Hounslow assumes that growth is size-independent and uses a source function to account for growth of particles into the field of view of the particle size analyser. A computer program, *Batch*, is produced that solves the population balance using the DPB outlined in Section 1.5.2. The inverse problem in aggregation is investigated, using a sum of square errors to minimize the difference between

experimental and simulated size distributions. The findings of this work may be summarised as follows:

- Aggregation may be modelled using a size-independent aggregation kernel.
- Both the growth rate and the aggregation rate constant are directly proportional to supersaturation.

1.7 LAYOUT OF THIS THESIS

The objective of this thesis is to address the problem of the simultaneous growth and aggregation of calcium oxalate mono-hydrate, particularly to investigate the mechanism for each phenomenon and their dependence on supersaturation. To this end, in Chapter 2, the physical chemistry of calcium oxalate mono-hydrate in aqueous solutions is considered. This is a necessary preliminary as the growth and aggregation kinetics cannot be treated in isolation from their driving force.

In Chapter 3 the details of the experimental procedure used to investigate seeded batch crystallisation is given. In Chapter 4 the growth and aggregation kinetics obtained from the batch experiments are examined and discussed in relation to the results available in the literature.

The topic of Chapter 5 is an in-depth study of aggregation. A mechanism is proposed for aggregation in saturated and supersaturated solutions. Further, a diffusion-reaction model is developed to explain the observed behaviour of the aggregation rate in supersaturated solutions.

A review of the systems for the *in vitro* study of kidney stone formation is presented in Chapter 6. Significantly, it is found that one of the faults common to all systems is geometry. While the kidney has a vastly complicated geometry, at least part of it is, to a good approximation, made up of cylindrical tubes. A tubular crystalliser to be used as an *in vitro* system is described.

Chapters 7 and 8 report experimental studies and analysis of the solute and particulate residence time distributions in the tubular crystalliser. The solute residence time distribution is described by a diffusion-advection model. The particle residence time is described by a model in which it is assumed that the particles maintain a constant radial position as they pass through the tubes in the crystalliser.

In Chapter 9 seeded continuous crystallisation is studied in the tubular crystalliser. In addition to growth and aggregation, the crystals stick to the tubes in the crystalliser, and also undergo breakage. The aggregation rates obtained are compared to the results from the batch experiments.

Finally, Chapter 10 gives an overview of the main results of this thesis and recommendations for future work.

Chapter 2:

PHYSICAL CHEMISTRY OF CALCIUM OXALATE IN AQUEOUS SOLUTIONS

In this chapter existing definitions of supersaturation are discussed. It is found that several physico-chemical factors complicate the definition and calculation of supersaturation.

A simple method for calculating supersaturation is developed. This method produces results in excellent agreement with a more sophisticated method for both saturated and supersaturated solutions.

Various physical constants are used in the model, the most important of these is the solubility product. The value of the solubility product determined experimentally was found to be in good agreement with those in the literature.

2.1 INTRODUCTION

Söhnel and Garside (1992) identify supersaturation as a key variable in any precipitation reaction: the level of supersaturation inevitably governs the rate of the precipitation process. For calcium oxalate many workers have found that the growth rate is dependent on supersaturation. Hartel and Randolph (1986) and Hounslow *et al.* (1988a) find that for calcium oxalate the aggregation rate may also be correlated with supersaturation.

The objective of the work in this chapter is to study different definitions and methods of calculating supersaturation with respect to calcium oxalate in aqueous solutions.

2.2 STATES OF SATURATION

In solution, soluble calcium oxalate exists within well defined physico-chemical ranges as illustrated in Figure 2.1. In Figure 2.1 supersaturation is measured by the *activity product*, *AP*, which is the product of calcium and oxalate ion activities,

$$AP = a_{Ca^{2+}} a_{Ox^{2-}} \quad (2.1)$$

The activities are related to concentrations by an activity coefficient, γ_{\pm}

$$a_{Ca^{2+}} = \gamma_{\pm}[Ca^{2+}] \quad a_{Ox^{2-}} = \gamma_{\pm}[Ox^{2-}] \quad (2.2a \text{ and } b)$$

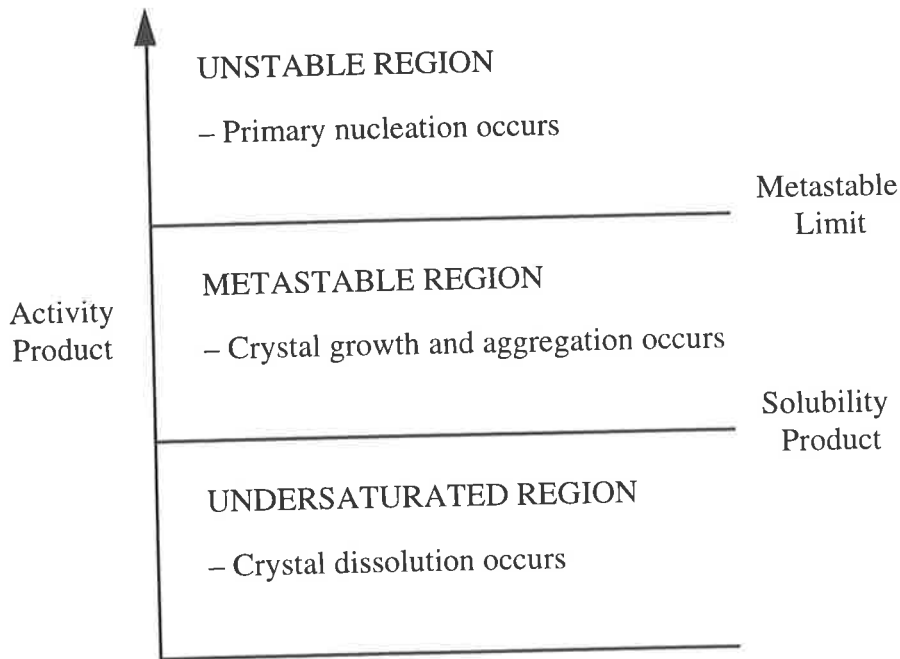


Figure 2.1 Regions of saturation of calcium oxalate in solution.

A solution is said to be *saturated* when soluble and solid calcium oxalate are in *equilibrium*, the value of the activity product at equilibrium is called the *solubility product*. If the activity product is less than the solubility product the solution is *undersaturated*. The addition of solid calcium oxalate to an undersaturated solution will result in dissolution. If the activity product is greater than the solubility product the solution is *supersaturated*. The supersaturated region is divided into two ranges. As the activity product increases a point is reached at which primary nucleation occurs, which is called the formation product, or metastable limit. Between the solubility product and the metastable limit is the *metastable range*. The addition of solid calcium oxalate to a metastable solution will result in crystal growth and aggregation. Above the metastable limit solutions are unstable as primary nucleation occurs.

2.3 DEFINING SUPERSATURATION

Hounslow (1990) observes that despite an extensive literature on the crystallisation of calcium oxalate there is no generally accepted definition of supersaturation. There are two reasons for the existence of many different definitions of supersaturation. Firstly, the apparatus and solutions used in crystallisation experiments differ considerably, as a result an

appropriate definition of supersaturation for one system might not be suitable for another. Secondly, and of greater importance, a definition of supersaturation must account for various physico-chemical complexities in the calcium oxalate system.

2.3.1 Physico-chemical considerations

There are three physico-chemical problems to consider:

- The characterisation of the reversibility of the precipitation reaction.
- The fact that two ionic species react to form a crystal.
- The formation of ion complexes.

These problems can be avoided if supersaturation is not calculated. As mentioned in Section 1.6.3, the mixed suspension, mixed product removal crystalliser (MSMPR) has been widely used, for example by Miller *et al.* (1977), Li *et al.* (1985) and Springman *et al.* (1986) in the study of the growth and nucleation of calcium oxalate. In this case the growth rate may be correlated with the nucleation rate without calculating the supersaturation, see for example Miller *et al.* (1977) and Rodgers and Garside (1981).

2.3.2 Reversibility

Reversibility is characterised by the solubility product, as explained in Section 2.2. At equilibrium

$$K_{sp} = a_{Ca^{2+}}^* a_{Ox^{2-}}^* = \gamma_{\pm}^2 [Ca^{2+}]_{eq} [Ox^{2-}]_{eq} \quad (2.3)$$

where K_{sp} is the solubility product and $a_{Ca^{2+}}^*$, $a_{Ox^{2-}}^*$, $[Ca^{2+}]_{eq}$ and $[Ox^{2-}]_{eq}$ are the calcium and oxalate ion activities and concentrations at equilibrium.

2.3.3 The reaction of two ionic species

Under certain conditions a single variable can describe the reaction of two ionic species. This is possible if the initial concentration of one ion is much higher than that of the other, or if both ions have the same initial concentration.

In the first case supersaturation may be defined in terms of the ion which is not in excess. For example Drach *et al.* (1978) use

$$s = C - C_s \quad (2.4)$$

where C is the mass of calcium oxalate equivalent to the solution oxalate concentration and C_s is the mass equivalent to the oxalate concentration at equilibrium. Similarly Hounslow *et al.* (1988a) use

$$\Delta C = [Ox^{2-}] - [Ox^{2-}]^* \quad (2.5)$$

where $[Ox^{2-}]^*$ is the oxalate concentration at equilibrium, which can be calculated from eq 2.3. Since calcium is in excess, $[Ca^{2+}]$ is almost constant.

In the second case the concentration of both ions is the same throughout an experiment. In this situation, Nancollas and Gardner (1974) define supersaturation in terms of concentrations as

$$N = [Ca^{2+}] - [Ca^{2+}]^* = [Ox^{2-}] - [Ox^{2-}]^* \quad (2.6)$$

whereas activities are used by Meyer and Smith (1975a and b)

$$N = a_{Ca^{2+}} - a_{Ca^{2+}}^* = a_{Ox^{2-}} - a_{Ox^{2-}}^* \quad (2.7)$$

In the current work neither of these methods can be applied. The metastable solutions used in the experiments reported in Chapters 3 and 10 neither reactant was in excess and the calcium and oxalate concentrations were not equal.

Two other approaches are available. One is to define supersaturation as a measure of the change in concentration required to reach equilibrium. Both Nancollas and Gardner (1974) and Meyer and Smith (1975a and b) define supersaturation as the amount of calcium oxalate that must be deposited from solution before equilibrium is reached. In terms of activities

$$K_{sp} = (a_{Ca^{2+}} - N)(a_{Ox^{2-}} - N) \quad (2.8)$$

from which it follows,

$$N = \frac{(a_{Ca^{2+}} + a_{Ox^{2-}}) - \sqrt{(a_{Ca^{2+}} + a_{Ox^{2-}})^2 - 4(a_{Ca^{2+}}a_{Ox^{2-}} - K_{sp})}}{2} \quad (2.9)$$

Alternatively a relative supersaturation may be defined as the ratio of an ion, or product of ions, to its value at equilibrium. DeLong and Briedis (1985) use the concentration of calcium oxalate

$$S = \frac{[CaOx]}{[CaOx]_{eq}} \quad (2.10)$$

Werness *et al.* (1985) use the activity product, defined in eq 2.1 giving

$$\sigma = \frac{AP}{K_{sp}} \quad (2.11)$$

There are many other similar definitions. Some are identical, but with different nomenclature. For example Gardner (1975) uses geometric mean concentrations

$$\sigma = \frac{\sqrt{[Ca^{2+}][Ox^{2-}]} - \sqrt{[Ca^{2+}]_{eq}[Ox^{2-}]_{eq}}}{\sqrt{[Ca^{2+}]_{eq}[Ox^{2-}]_{eq}}} \quad (2.12)$$

whereas Singh *et al.* (1987) use the activity product and K_{sp} giving

$$\sigma = \left(\frac{AP}{K_{sp}} \right)^{\frac{1}{2}} - 1 \quad (2.13)$$

Substituting eqs 2.1 and 2.3 into 2.13, it can be re-arranged to give eq 2.12.

Alternatively the same product of ions are compared but different functional forms are used to define the relative supersaturation. Hounslow (1990) defines

$$S^* = AP - K_{sp} \quad (2.14)$$

which may be divided by K_{sp} to give a relative supersaturation

$$\sigma = \frac{AP}{K_{sp}} - 1 \quad (2.15)$$

Brečević *et al.* (1986) define

$$\sigma = \ln \left(\frac{AP}{K_{sp}} \right) \quad (2.16)$$

Common to all these definitions are the activity product and the fact that at equilibrium the value of the activity product is K_{sp} . However, as the activity product increases the values calculated depend on the functional form of the definition of the relative supersaturation. This point is illustrated in Figure 2.2 in which the relative supersaturation defined by eqs

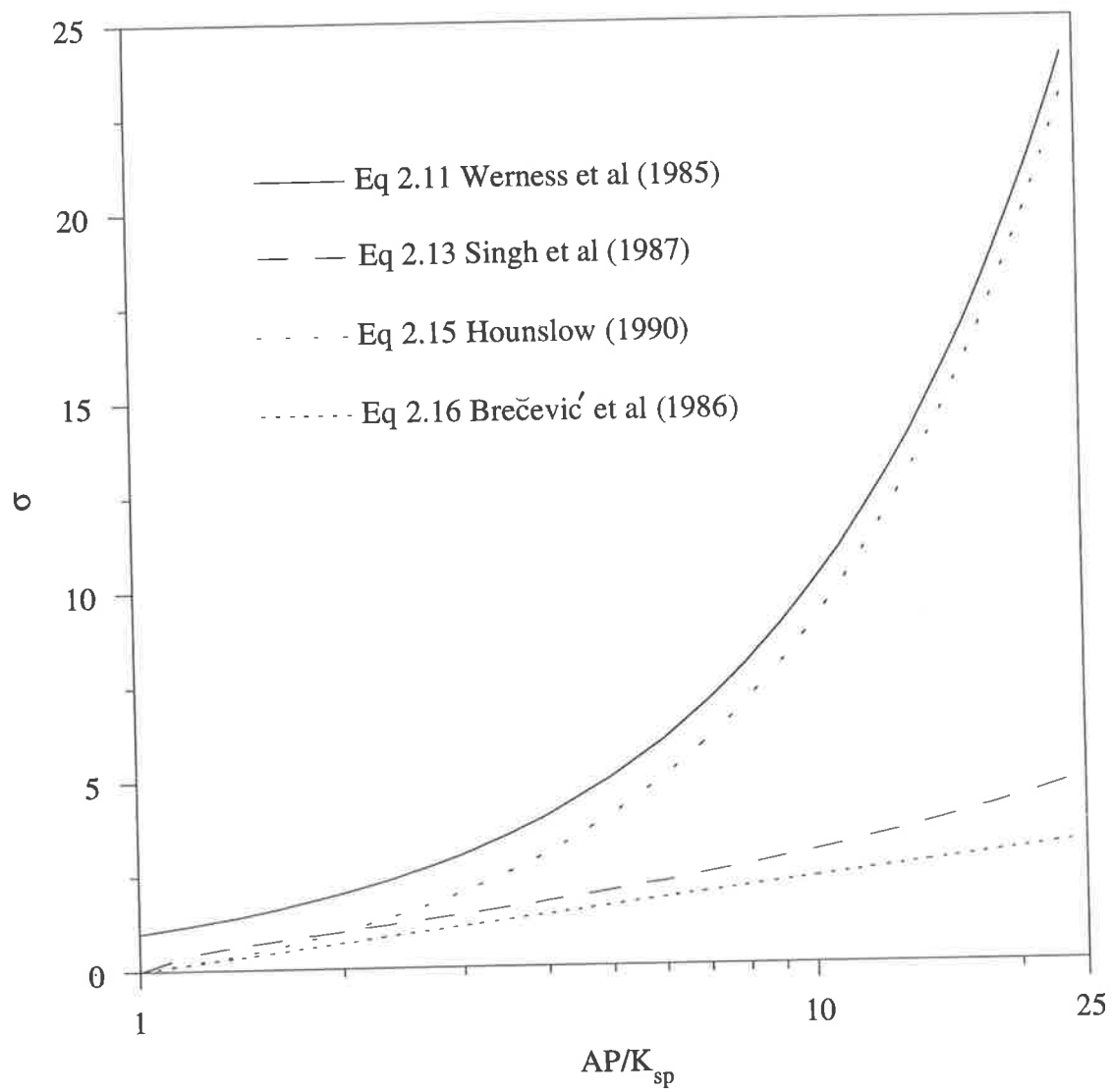


Figure 2.2 Comparison of different definitions of relative supersaturation.

2.11, 2.13, 2.15 and 2.16 are plotted against the ratio of the activity product to K_{sp} . At low values of the activity product all the definitions give approximately the same value of the relative supersaturation, as the value of the activity product increases the difference between the values of the relative supersaturation obtained from each definition increases.

From a thermodynamic point of view the functional form of the definition of supersaturation is not important, at a given temperature and pressure K_{sp} is constant, thus the value of the activity product in a system at equilibrium is constant. From a kinetic point of view the functional form is important, for the same value of the activity product, different values of the supersaturation are obtained from different definitions. The apparent reaction order for a process that varies with supersaturation must depend on how it is defined.

2.3.4 Dissociation

In solution, ions may exist in a free form, or as complexes in association with other ions. Only the free ions are available for precipitation, which implies free ion concentrations should be used to calculate supersaturation.

In experimental studies of the crystallisation of calcium oxalate the use of an artificial urine is common. In addition to calcium and oxalate these solutions contain other ions found in human urine such as phosphate, biphosphate, sulphate, citrate, magnesium and ammonium. As Rodgers and Garside (1981) observe, these ions form complexes in solution making evaluation of the free ion concentrations and supersaturation extremely difficult.

The mass action equation for the formation of a complex between two ions A^{2+} and B^{2-} is

$$K_{so} = \frac{a_{AB}}{a_{A^{2+}} a_{B^{2-}}} = \frac{[AB]}{\gamma_{\pm}^2 [A^{2+}] [B^{2-}]} \quad (2.17)$$

where K_{so} is the association constant. Eq 2.17 may be written as

$$K_{AB} [AB] = \gamma_{\pm}^2 [A^{2+}] [B^{2-}] \quad (2.18)$$

where K_{AB} is the dissociation constant which is simply the reciprocal of the association constant.

An equation such as eq 2.18 can be written for each complex that forms giving a system of simultaneous equations. This is investigated by Finlayson (1977), who produces a computer program, EQUIL, to determine the free ion concentrations. Subsequent updates of

this code, EQUIL2, Werness *et al.* (1985), and the latest version EQUIL89d (EQUIL89d Users manual) have increased its capability, for example by expanding the number of complexes available.

These programs use an iterative method to determine the free ion concentrations. It is assumed that the total concentration of each species is known and initial guesses are made for the free ion concentrations. The mass action equations for the formation of each complex and mass conservation equations for each ion are solved to generate new estimates of the free ion concentrations. This process is repeated until the values of the free ion concentrations have converged.

2.3.5 Concluding remarks on defining supersaturation

The physico-chemical problems associated with defining supersaturation are dealt with in the following ways in the current work:

- Reversibility is characterised by a solubility product.
- Supersaturation is measured by the activity product.
- Free rather than total ion concentrations are used to calculate the activity product.

2.4 CALCULATING SUPERSATURATION

To calculate the supersaturation the first step is to determine the free ion concentrations from the total concentrations. To do this the use of a program such as EQUIL is warranted for a solution such as an artificial urine. Solving a system of mass action equations for complex formation is a difficult task if more than a few complexes form. However, in some cases the iterative approach used by EQUIL may overcomplicate a problem to which there is a simpler solution.

2.4.1 A simple method of calculating free ion concentrations

The solutions used in the current work contain only Ca^{2+} , Ox^{2-} , Na^+ , and Cl^- ions. From these the formation of only two complexes, namely CaOx and NaOx^- , are likely to be important. The mass action equations for their formation are

$$K_{\text{CaOx}}[\text{CaOx}] = \gamma_{\pm}^2[\text{Ca}^{2+}][\text{Ox}^{2-}] \quad (2.19)$$

$$K_{\text{NaOx}^-}[\text{NaOx}^-] = \gamma_{\pm}[\text{Na}^+][\text{Ox}^{2-}] \quad (2.20)$$

Note that in eq 2.19, the activity coefficient for a zero charged ion is one and the activity coefficients for the singly charged ions cancel in eq 2.20.

A mass conservation equation can be written for each ion involved in complex formation,

$$T_{Ca^{2+}} = [Ca^{2+}] + [CaOx] \quad (2.21)$$

$$T_{Ox^{2-}} = [Ox^{2-}] + [CaOx] + [NaOx^-] \quad (2.22)$$

$$T_{Na^+} = [Na^+] + [NaOx^-] \quad (2.23)$$

where, for example, $T_{Ca^{2+}}$ and $[Ca^{2+}]$ are the total and free ion concentrations of calcium respectively.

Before solving these equations a simplification is possible. In the work reported in this thesis the ionic strength of the solutions is provided almost entirely by the sodium and chloride ions present. The total concentration of sodium is approximately 0.16 M, some 800 times that of the total oxalate concentration, 0.2 mM. As sodium only forms one complex, with oxalate, it can be assumed that the total and free ion concentrations are equal for this species. This makes eq 2.23 redundant and enables the use of the total sodium concentration in eq 2.20.

Expressions for the free and complex ion concentrations in terms of the total concentrations, the dissociation constants and activity coefficient can be obtained by solving eqs 2.19 to 2.22 analytically, which gives:

$$[Ca^{2+}] = \frac{1}{2} \left(\frac{-K_{CaOx}}{\gamma_{\pm}^2} - \frac{T_{Na^+} K_{CaOx}}{\gamma_{\pm} K_{NaOx^-}} + T_{Ca^{2+}} - T_{Ox^{2-}} + \frac{\sqrt{\Theta}}{\gamma_{\pm}^2 K_{NaOx^-}} \right) \quad (2.24)$$

$$[Ox^{2-}] = \frac{K_{NaOx^-} \left(-T_{Na^+} \gamma_{\pm} - K_{CaOx} - \gamma_{\pm}^2 (T_{Ca^{2+}} - T_{Ox^{2-}}) \right) + \sqrt{\Theta}}{2 \gamma_{\pm}^2 K_{NaOx^-} (T_{Na^+} \gamma_{\pm} + K_{NaOx^-})} \quad (2.25)$$

$$[CaOx] = \frac{1}{2} \left(\frac{K_{CaOx}}{\gamma_{\pm}^2} + \frac{T_{Na^+} K_{CaOx}}{\gamma_{\pm} K_{NaOx^-}} + T_{Ca^{2+}} + T_{Ox^{2-}} - \frac{\sqrt{\Theta}}{\gamma_{\pm}^2 K_{NaOx^-}} \right) \quad (2.26)$$

$$[NaOx^-] = \frac{T_{Na^+} \left(-K_{CaOx} (T_{Na^+} \gamma_{\pm} + K_{NaOx^-}) \right)}{2 \gamma_{\pm} K_{NaOx^-} (T_{Na^+} \gamma_{\pm} + K_{NaOx^-})} + \frac{T_{Na^+} \left(K_{NaOx^-} \gamma_{\pm}^2 (T_{Ox^{2-}} - T_{Ca^{2+}}) + \sqrt{\Theta} \right)}{2 \gamma_{\pm} K_{NaOx^-} (T_{Na^+} \gamma_{\pm} + K_{NaOx^-})} \quad (2.27)$$

where the parameter Θ is given by

$$\begin{aligned} \Theta = & K_{NaOx^-} \gamma_{\pm}^2 T_{Ox^{2-}} \left(2T_{Na^+} \gamma_{\pm} K_{CaOx} + K_{NaOx^-} \left(2K_{CaOx} + \gamma_{\pm}^2 (T_{Ox^{2-}} - 2T_{Ca^{2+}}) \right) \right) \\ & + K_{NaOx^-} \gamma_{\pm}^2 T_{Ca^{2+}} \left(2T_{Na^+} \gamma_{\pm} K_{CaOx} + 2K_{CaOx} K_{NaOx^-} + \gamma_{\pm}^2 K_{NaOx^-} T_{Ca^{2+}} \right) \\ & + K_{CaOx} \left(T_{Na^+}^2 \gamma_{\pm}^2 + 2T_{Na^+} \gamma_{\pm} K_{NaOx^-} + K_{NaOx^-}^2 \right) \end{aligned}$$

The other roots of the equations give negative values for the complex ion concentrations and values for the free ion concentrations that are greater than the total ion concentrations. Both of these are physically impossible.

While the above expressions are quite complicated, they are simple enough to be used in a standard spreadsheet. The computer application Microsoft Excel was used to produce a spreadsheet to calculate the free and complex ion concentrations from the total concentrations.

2.4.2 Saturated and supersaturated solutions

In addition to knowing the free ion concentrations a measure of supersaturation is required. One may be found by including the definition of relative supersaturation from eq 2.11 in the list of equations to be solved as

$$\sigma K_{sp} = AP = \gamma_{\pm}^2 [Ca^{2+}] [Ox^{2-}] \quad (2.28)$$

Eq 2.28 and eqs 2.19 to 2.22, provide a system of equations from which an expression for the relative supersaturation can be obtained in terms of total concentrations. Alternatively, the total concentrations can be written in terms of the relative supersaturation, dissociation constants, solubility product and activity coefficient. For example solving eqs 2.19 to 2.22 and 2.28, the expression for the total calcium concentration is

$$T_{Ca^{2+}} = \frac{K_{sp} \sigma}{K_{CaOx}} + \frac{K_{sp} K_{CaOx} \sigma (T_{Na^+} \gamma_{\pm} + K_{NaOx^-})}{\gamma_{\pm}^2 K_{NaOx^-} (K_{CaOx} T_{Ox^{2-}} - K_{sp} \sigma)} \quad (2.29)$$

The accuracy of this simplified method was assessed by comparing results from it with those from EQUIL89d.

Firstly, consider saturated solutions. Although $\sigma = 1$ for all these solutions they may have different total calcium and oxalate concentrations. Values of the total calcium and oxalate concentrations in different saturated solutions were obtained from EQUIL89d. The temperature used was 37°C and the solutions had an ionic strength of 0.1578 M supplied by sodium and chloride ions. These conditions are the same as those in the batch experiments reported in Chapter 3. The values of the dissociation constants, solubility product and activity coefficient used by EQUIL89d are given in Table 2.1

Table 2.1 Constants used by EQUIL89d.

Constant	Value
Activity coefficient, γ_{\pm}	0.314
Solubility product, K_{sp}	2.24×10^{-9}
Dissociation constant for CaOx, K_{CaOx}	3.64×10^{-4}
Dissociation constant for NaOx ⁻ , K_{NaOx^-}	7.52×10^{-2}

Using eq 2.29 with $\sigma = 1$ and the values of the constants in Table 2.1 the total calcium concentrations in saturated solutions, with different total oxalate concentrations can be calculated.

Eq 2.29 is plotted along with the results from EQUIL89d in Figure 2.3. The agreement between the two is excellent. The method, which only considers the formation of two complexes accurately describes solutions at equilibrium. EQUIL89d considers the formation of many other complexes, such as $CaOx_2^{2-}$, $CaHOx^+$ and HOx^- , however this only complicates the calculations without changing the results.

Now consider solutions that are supersaturated. Eq 2.29 can be re-arranged to give

$$a\sigma^2 + b\sigma + c = 0 \quad (2.30)$$

$$\text{where } a = -K_{NaOx^-} (\gamma_{\pm} K_{sp})^2 \quad (2.31a)$$

$$b = K_{sp} K_{CaOx} (K_{NaOx^-} \gamma_{\pm}^2 (T_{Ca^{2+}} + T_{Ox^{2-}}) + K_{CaOx} (T_{Na^+} \gamma_{\pm} + K_{NaOx^-})) \quad (2.31b)$$

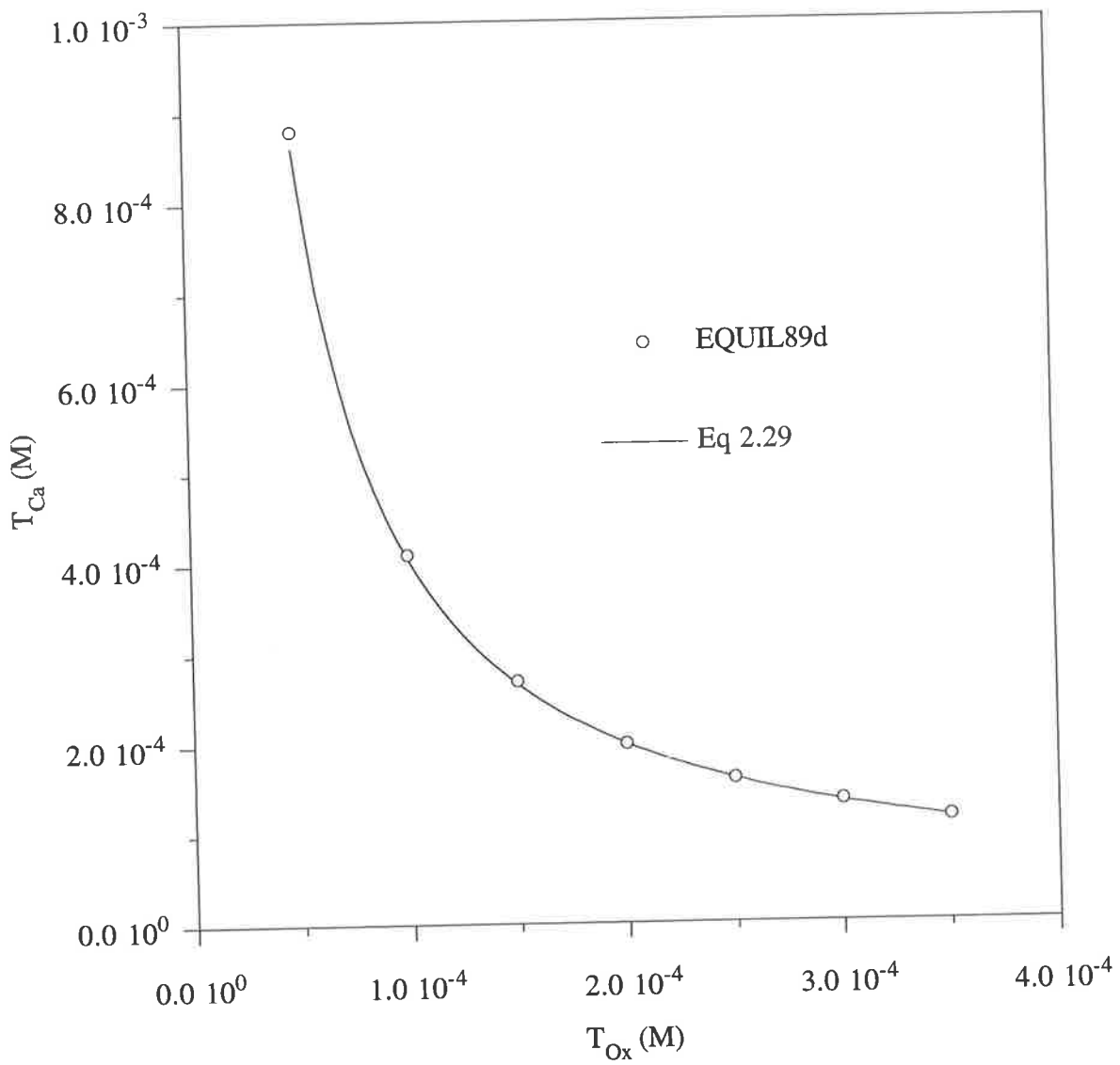


Figure 2.3 A comparison of total calcium ion concentrations calculated from eq 2.29 and by EQUIL89d for saturated solutions with different total oxalate ion concentrations.

$$\text{and } c = -K_{NaOx^-} (K_{CaOx} \gamma_{\pm})^2 T_{Ca^{2+}} T_{Ox^{2-}} \quad (2.31c)$$

The relative supersaturation can be calculated from the appropriate root of eq 2.30. Further simplification is possible by considering the magnitude of the coefficients in eq 2.30. Using the values of the constants in Table 2.1 and the total calcium and oxalate concentrations in a standard metastable solution described in Section 3.3.2, 1 mM and 0.2 mM respectively gives

$$a = -3.75 \times 10^{-20}, \quad b = 4.43 \times 10^{-17}, \quad c = -1.97 \times 10^{-16}$$

The constants b and c are three to four orders of magnitude greater than a , which suggests eq 2.30 may be written as

$$\sigma = \frac{-c}{b} = \frac{K_{NaOx^-} K_{CaOx} \gamma_{\pm}^2}{K_{sp} (K_{NaOx^-} \gamma_{\pm}^2 (T_{Ca^{2+}} + T_{Ox^{2-}}) + (T_{Na^+} \gamma_{\pm} + K_{NaOx^-}))} \quad (2.32)$$

Data from the batch experiments reported in Chapter 3 were used to compare the value of σ from EQUIL89d with those calculated from eqs 2.30 and 2.32. As an experiment proceeds crystals grow and aggregate in a solution of decreasing supersaturation. From data which are collected at regular time intervals the total calcium and oxalate concentrations can be calculated (see Section 3.5.2).

The values of the relative supersaturation calculated from eqs 2.30 and 2.32 are plotted along with the value from EQUIL89d, for the batch experiment 22/12a, in Figure 2.4. The agreement is excellent over the entire range of supersaturation. For the range of supersaturation used in the work in this thesis the relative supersaturation may be calculated from eq 2.32.

As the relative supersaturation is defined in terms of free ion concentrations, both the free and complex ion concentrations must also be accurately predicted. This is verified in Figures 2.5 (a) and (b), which are plots of the free and complex ion concentrations calculated from eqs 2.24 to 2.27 and those from EQUIL89d for the batch experiment 22/12a.

2.5 PARAMETER ESTIMATION

Having developed a method for calculating supersaturation there is another issue to consider: that of parameter estimation. So far the values of the dissociation constants, solubility product and activity coefficient from EQUIL89d have been used. It is worth considering

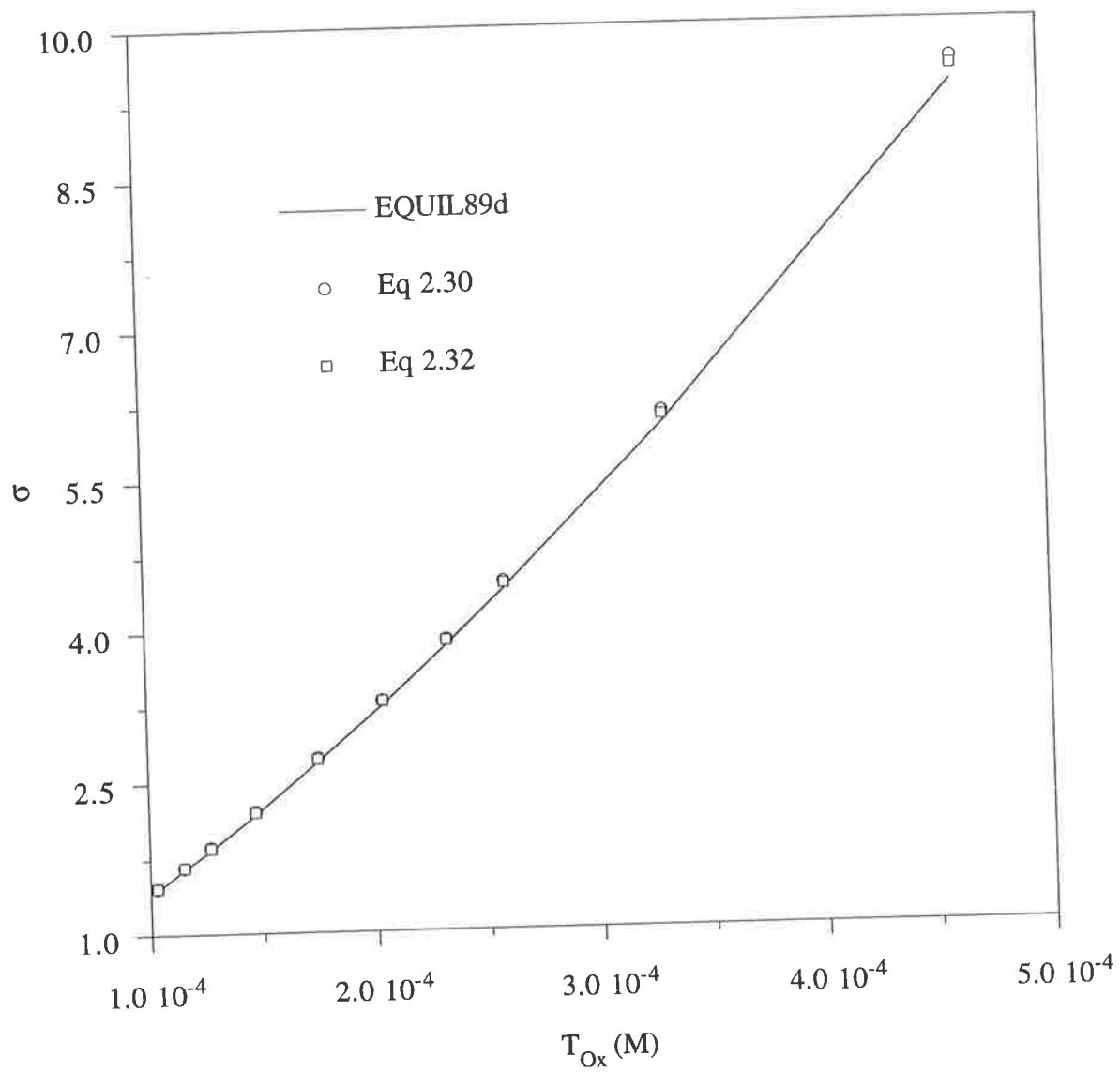
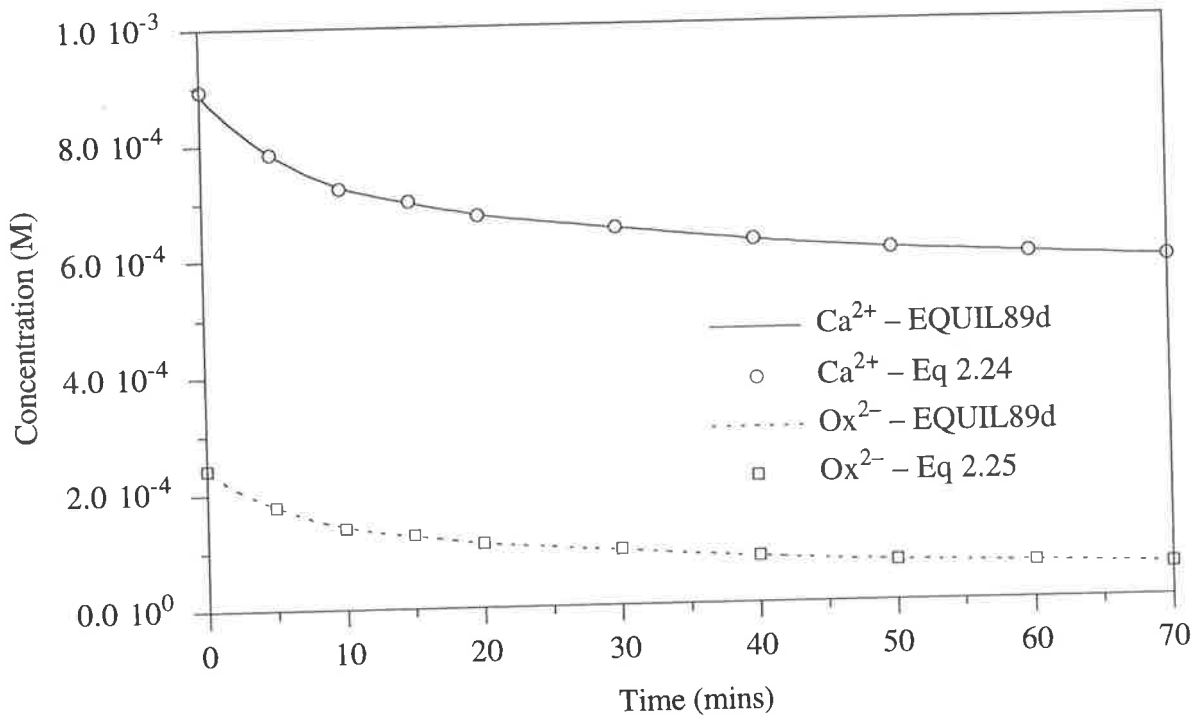
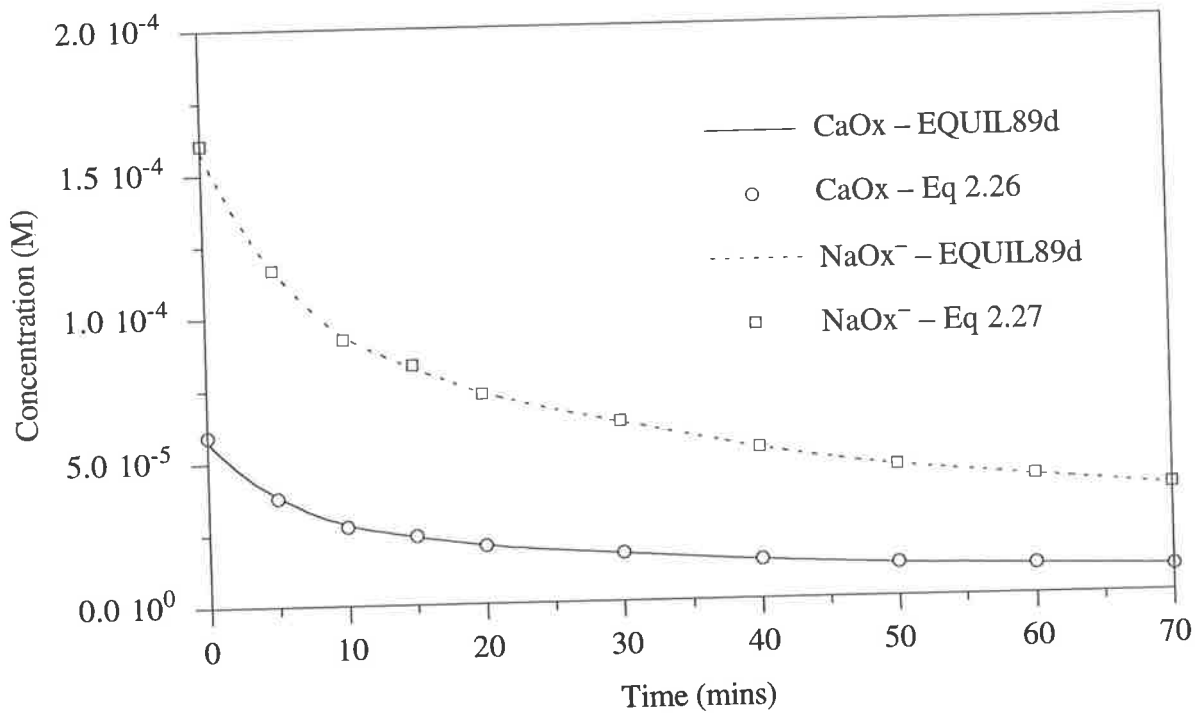


Figure 2.4 A comparison of the relative supersaturation calculated from eqs 2.30 and 2.32 and by EQUIL89d for a supersaturated solution.



(a)



(b)

Figure 2.5 A comparison of (a) free and (b) complex ion concentrations calculated from eqs 2.24 to 2.27 and by EQUIL89d for a supersaturated solution.

how these constants are obtained and comparing the values from EQUIL89d with others available in the literature.

2.5.1 Literature values

Finlayson (1977) outlines how the activity coefficient can be calculated from the Davies modification of the Debye-Hückel solution to the Poisson-Boltzmann equation. This method has been widely used in the literature, for example by Nancollas and Gardner (1974), Meyer and Smith (1975a), Brečević *et al.* (1986) and is also the method used by EQUIL89d.

The association constants for the formation of CaOx and NaOx⁻ are available in the literature. From these the dissociation constants can be calculated. For example from Finlayson (1977) the values are 3.65×10^{-4} and 7.46×10^{-2} , respectively, whereas from Tomažič and Nancollas (1979) the values are 5.35×10^{-4} and 7.58×10^{-4} . These are different from those used by EQUIL89d as given in Table 2.1, particularly for CaOx. However, as the value of the dissociation constant for CaOx is small compared to that for NaOx⁻, the concentration of CaOx is always much less than that of NaOx⁻, as shown in Figure 2.5 (b). Thus the variation in the dissociation constant for CaOx is not significant and the values for the dissociation constants from EQUIL89d can be used.

Blomen *et al.* (1983) tabulate values of the solubility product. There is considerable variation in the values they report, from a minimum of 2.2×10^{-9} (Koutsoukos *et al.*, 1980), to a maximum of 3.63×10^{-9} (Meyer and Smith, 1975a). These values vary by a factor of 1.65. Nancollas and Gardner (1974) report other literature values that range from 4.46×10^{-9} to 6.7×10^{-9} , however they point out these values may not allow for complex ion formation.

It appears that the most uncertainty exists in the value of the solubility product, which is perhaps the most important parameter as it defines equilibrium in a system. In view of this experiments were conducted to determine a value of the solubility product and compare it with values from the literature, particularly the one used by EQUIL89d.

2.5.2 Experimental value of the solubility product

Batch experiments using a standard metastable solution were performed as described in Section 3.3.3. No data were collected until 24 hours after the start of the experiment, when the system was at equilibrium.

At equilibrium, $\sigma=1$, re-arranging eq 2.29 the expression for the solubility product is

$$K_{sp} = \frac{\gamma_{\pm}^2 K_{CaOx} K_{NaOx^-} T_{Ca^{2+}} T_{Ox^{2-}}}{\gamma_{\pm}^2 K_{NaOx^-} (T_{Ca^{2+}} + T_{Ox^{2-}}) + K_{CaOx} (T_{Na^+} \gamma_{\pm} + K_{NaOx^-})} \quad (2.33)$$

Experimental values of the total calcium and oxalate concentrations at equilibrium can be calculated by a mass balance as the initial concentrations are known and the volume of particulate matter deposited can be determined from the crystal size distributions measured using the Multisizer.

Values of the total calcium and oxalate concentrations at equilibrium and the solubility product from the experiments, as well as the mean and standard deviation of each parameter are given in Table 2.2. The experimental data and calculations used to determine the results in Table 2.2 are presented in Appendix 3.

The mean experimental value of the solubility product was compared with that used by EQUIL89d. A two sided *t*-test, with the null hypothesis that both values are the same, against the alternative that they are different was used. At the 5% level, the null hypothesis was accepted. Based on this result the value of the solubility product from EQUIL89d, 2.24×10^{-9} is used in this work.

Table 2.2 Experimental values of the solubility product.

Experiment	$T_{Ca^{2+}}$ (M)	$T_{Ox^{2-}}$ (M)	K_{sp}
25/6	8.22×10^{-4}	3.72×10^{-5}	1.60×10^{-9}
28/6	8.38×10^{-4}	5.33×10^{-5}	2.32×10^{-9}
29/6	8.33×10^{-4}	4.85×10^{-5}	2.11×10^{-9}
30/6	8.32×10^{-4}	4.72×10^{-5}	2.05×10^{-9}
1/7	8.34×10^{-4}	4.94×10^{-5}	2.15×10^{-9}
11/7	8.27×10^{-4}	4.28×10^{-5}	1.85×10^{-9}
mean	8.31×10^{-4}	4.64×10^{-5}	2.01×10^{-9}
standard deviation	2.31×10^{-6}	2.31×10^{-6}	1.04×10^{-10}

2.6 DISCUSSION

It is worth noting at this point that the difficulty of calculating relative supersaturation and the free and complex ion concentrations has been significantly reduced. By assuming that the formation of only two complexes, CaOx and NaOx^- , is significant, the relative supersaturation, in terms of *free ion concentrations*, can be accurately calculated from a single linear equation, eq 2.32, in terms of the *total concentrations*. This is much simpler and faster than using EQUIL89d.

Calculation of the free and complex ion concentrations is somewhat more difficult as the expressions for them are quite complicated. However, the equations are simple enough that a spreadsheet package, such as Microsoft Excel, can be used to calculate the concentrations. This makes the analysis of experimental data very easy as the flexibility of a spreadsheet is utilised. Calculating the free ion concentrations for a new set of data is as simple as entering the new values of the total concentrations into the spreadsheet.

Compare the method just described to using EQUIL89d, in which a FORTRAN program performs the iterative calculation of the free and complex ion concentrations. For each set of data an input file must be created and output from the program is written to another file. The required data, for example the relative supersaturation, must then be extracted from the file containing the output. This is obviously more time consuming and much less flexible than using a spreadsheet.

However, the problem of complex formation should not be oversimplified. For a standard metastable solution as reported in Chapter 3, Hounslow (1990) only considered the formation of one complex, CaOx . He found that during an experiment the fractions of each ion present as a complex varied from 0.03 to 0.01 and 0.16 to 0.14 respectively for calcium and oxalate. As these fractions are approximately constant and relatively low, he assumed total concentrations may be used to calculate supersaturation.

These results can be compared with those from the method adopted in this work which considers the formation of two complexes. The concentrations of CaOx and NaOx^- for the batch experiment 22/12a are given in Figure 2.5 (b). The concentration of NaOx^- is always at least twice that of CaOx . This shows that the formation of NaOx^- cannot be disregarded, it is actually more important than the formation of CaOx .

When both complexes form, the fraction of each ion present as a complex during an experiment varies from 0.06 to 0.02, and 0.47 to 0.45, respectively, for calcium and

oxalate. While the variation in the fraction dissociated is not significant for either ion, the fraction of oxalate that is present as a complex is significant.

These results differ from those quoted by Hounslow (1990), as he did not consider the formation of NaOx^- . Consequently the fraction of oxalate bound up in complexes is underestimated in his work. Also, as the free ion concentration is only approximately half the total concentration it is wrong to calculate supersaturation using total concentrations. Therefore the supersaturation used by Hounslow is unreliable, as the method used to determine the free ion concentrations is not accurate.

Further, the correlations for the growth rate and aggregation rate constant with supersaturation must be questioned. The form of the correlation will be correct, but the constants in it will not be, because both the growth rate and the aggregation rate constant are directly proportional to supersaturation. The fraction of calcium and oxalate present as free ions is approximately constant, therefore by ignoring the formation of NaOx^- the amount by which the supersaturation is underestimated is approximately constant. For example, according to Hounslow, for growth

$$G \approx k_G S^* \quad (2.34)$$

where $S^* = [\text{Ca}^{2+}][\text{Ox}^{2-}] - K_{sp} \approx [\text{Ca}^{2+}][\text{Ox}^{2-}] \quad (2.35)$

Now, the actual free calcium and oxalate ion concentrations are a fraction of the values in eq 2.35 therefore

$$S^* \approx k[\text{Ca}^{2+}][\text{Ox}^{2-}] \quad (2.36)$$

where $k < 1$. Eq 2.34 then becomes

$$G \approx k_G k [\text{Ca}^{2+}][\text{Ox}^{2-}] = k'_G S^* \quad (2.37)$$

As explained above, when the free rather than total ion concentrations are used, the form of the correlation is unchanged, but the value of the constant of proportionality will be different. The same analysis can be performed for the aggregation rate constant.

2.7 CONCLUSIONS

In this chapter definitions and methods of calculating supersaturation for calcium oxalate in aqueous solutions have been investigated. Three physico-chemical factors were identified that complicate the definition and calculation of supersaturation, *viz.*

- The reversability of the precipitation reaction
- Two ionic species reacting to form a crystal
- The formation of ion complexes

In this work supersaturation is expressed in terms of the activity product, AP , calculated in terms of free ion concentrations. At times it will be convenient to determine a relative supersaturation, in which case the activity product is compared with its value at equilibrium, K_{sp} .

A simple method has been developed to calculate relative supersaturation in terms of free ion concentrations from total ion concentrations. It has been demonstrated that the relative supersaturation as well as the free and complex ion concentrations are all accurately predicted by this method.

Chapter 3:

BATCH CRYSTALLISATION: MATERIALS AND METHODS

This chapter describes an experimental investigation of the batch crystallisation of calcium oxalate. A detailed description of the materials, methods and analytical techniques used in the experiments is given. The experimental method used is based on the seeded technique of Ryall et al. (1981b).

Of particular interest is the dependence of the growth and aggregation rates on supersaturation and the agitation rate. The range of supersaturation is increased by varying the calcium and oxalate concentrations in the metastable solution, the agitation rate altered by changing the rate at which the flasks are shaken.

Batch, an interactive computer program written by Hounslow (1990), which is used to calculate growth and aggregation rates from the experimental crystal size distributions is described.

3.1 INTRODUCTION

Batch crystallisation has been widely used to study calcium oxalate crystal growth and aggregation. Two factors make batch crystallisation appealing; firstly there are well-established experimental protocols. Secondly, and of greater importance, numerical methods have been developed to determine growth and aggregation rates from experimental data. This is highly desirable given the complexity of the analysis of an experimental system in which there is simultaneous growth and aggregation. Further, Smit *et al.* (1994) describe the ambiguity in extracting aggregation rates from continuous systems.

In this chapter experiments to determine the dependence of growth and aggregation rates on supersaturation and agitation rate in a batch system are reported.

3.2 ANALYSIS TECHNIQUES

In many systems in which crystallisation is studied the most important data are the crystal size distributions (CSDs). In this study, the CSDs are used to calculate the growth and

aggregation kinetics and solution concentrations. This Section describes the equipment and methods used to measure and verify the accuracy of the CSDs, and outlines the other experimental techniques used.

3.2.1 Crystal Size Distributions

All CSDs were obtained using a Coulter Multisizer II. In common with all zone sensing devices the Multisizer records particle numbers classified by equivalent volume diameter (Multisizer II Users Manual, 1987).

A size range of 2 to 32 μm was wide enough to cover all the crystals considered in this work. This size range was easily spanned with a single 70 μm orifice. In addition to selecting the correct orifice it is necessary to use a suitable electrolyte together with a procedure for representative sampling to obtain reliable data. The sampling procedure used is shown to be representative in Section 3.2.2. The metastable solutions used in the experiments were effectively 0.15 M saline which were suitable for use as an electrolyte with the Multisizer. Further, the concentration of crystals was such that no dilution was necessary. Thus there was no need to store samples taken during an experiment – they were analysed directly as collected. A detailed description of the operation and configuration of the Multisizer used in this work is given in Appendix 4.

3.2.2 Solution and Solids Concentrations

Solution and solids concentrations were calculated from the CSDs obtained from the Multisizer. The mass of solid present in a sample can be estimated from the third moment of the CSD using

$$w = \rho_s \frac{\pi}{6} m_3 \quad (3.1)$$

It is important to determine whether this method is an accurate way to measure crystal mass. For example, in calculating mass from eq 3.1 no account is taken of possible voids in the crystals, such as may be present in aggregates.

Prior to the start of the batch crystallisation experimental program, experiments were performed to demonstrate that data from the Multisizer could be used to determine crystal mass. A 4 ml sample of a calcium oxalate seed suspension was added to 200 ml of a 0.15 M saline solution, saturated with respect to calcium oxalate, and samples analysed by the Multisizer. The solution was then filtered (0.22 μm), the filter paper thoroughly washed

with filtered, distilled water and dried at 37°C. The drying temperature was well below that necessary to cause any phase change or decomposition of the crystals. The dried filter paper with the crystals was then weighed and compared with the weight of the filter paper alone to determine the mass of crystals present.

Batch experiments as described in Section 3.3.3 were also performed and allowed to run to equilibrium. CSDs and solid samples were collected after 24 hours. No samples were taken prior to these.

The results from these experiments are presented in Table 3.1. The values of the solids content reported are the mean plus-or-minus one standard error in the mean. A two sided *t*-test was used to test the null hypothesis that the solids contents determined from the Multisizer data are the same as those from weighing the crystals, against the alternative that they are different. At the 5% level the null hypothesis was accepted for both sets of data.

Table 3.1 Assessment of the accuracy of Multisizer measurements of crystal mass.

Experiment Type	Solids content determined from samples analysed by Multisizer (grams/litre)	Solids content determined by drying and weighing crystals (grams/litre)
Seeds added to saline	$1.61 \times 10^{-2} \pm 4 \times 10^{-4}$	$1.59 \times 10^{-2} \pm 4 \times 10^{-4}$
Batch experiment	$3.94 \times 10^{-2} \pm 8 \times 10^{-4}$	$3.89 \times 10^{-2} \pm 7 \times 10^{-4}$

The results in Table 3.1 show that the Multisizer can be used to determine accurately the crystal mass in the batch experiments. Further, they demonstrate that the sampling procedure used in the experiments is representative. If the samples taken were not representative then it is most likely that larger crystals would not be collected. If this were the case then the solids content determined from the Multisizer data would be lower than that obtained from drying and weighing the crystals. However, the solids content determined by both methods are not statistically different indicating that the sampling procedure is representative.

3.2.3 Other experimental techniques

Scanning electron microscopy

In various experiments samples of the crystals produced were taken and examined by scanning electron microscope (SEM). The technique for preparing and viewing these samples is described in Appendix 4.

Atomic absorption spectroscopy

Calcium ion concentrations in the metastable solutions used were verified using atomic absorption spectroscopy (AA). The technique for preparing the samples for analysis by AA is reported in Appendix 4.

3.3 EXPERIMENTAL

3.3.1 Background

Robertson and Peacock

The seeded, batch crystallisation of calcium oxalate in inorganic solutions using the Coulter Counter to monitor the CSD, was first performed by Robertson and Peacock (1972). Their metastable solution initially contained calcium (1 mM), oxalate (0.2 mM), sodium chloride (0.15 M) and was buffered to pH 6 with sodium cacodylate (10 mM).

In an experiment 10 ml of a calcium oxalate seed suspension (containing 1 gram/litre calcium oxalate crystals) was added to 500 ml of the metastable solution. The Coulter Counter was used to measure variations in the CSD with time. No mention is made of how the solutions were agitated, or how samples were collected for Coulter Counter analysis.

Ryall *et al.*

A similar approach was used by Ryall *et al.* (1981b). They investigated, among other things, the choice of buffer. Two metastable solutions were used, one buffered with sodium cacodylate, the other with 2,N-morpholinoethane-sulphonic acid (MES). They found significantly better reproducibility of the CSDs in the absence of sodium cacodylate. These authors recommend the use of MES as a buffer.

The composition of the metastable solution used by Ryall *et al.* was 1 mM calcium chloride, 0.2 mM sodium oxalate and 0.15 M sodium chloride buffered to pH 6 with MES (10 mM). The seeds used were calcium oxalate mono-hydrate ground with a pestle in a mortar then suspended in distilled water, the final solids concentration being 1 gram/litre. The seed suspension was kept at room temperature and stirred with a magnetic stirrer.

In an experiment 7 ml of seed suspension was added to 350 ml of metastable solution. Aliquots of 40 ml were withdrawn for analysis by the Coulter Counter at appropriate times. Soda-glass flasks were used as Ryall *et al.* report that the crystals stick to borosilicate glass. The experiments were performed using a shaking water bath at 37°C, oscillating at 90 cycles per minute.

This protocol has been used by Ryall *et al.* (1981c) to investigate the effect of urine and various other inhibitors respectively on crystal growth and aggregation. Hounslow *et al.* (1988a) use the same protocol to obtain data to model growth and aggregation kinetics. It is also the protocol to be used in the experiments reported in this Chapter, but with some modifications, that will be described in Section 3.3.3.

3.3.2 Solutions

Chemicals

All chemicals used were analytical grade. Calcium and sodium chloride were obtained from Ajax Chemicals, Sydney, Australia. Calcium and sodium oxalate were obtained from BDH Laboratory Supplies, Poole, England. MES was obtained from Sigma Chemical Company, Saint Louis, USA.

Distilled water

Distilled water used in the preparation of all solutions was from a “Hi-Pure” model water purification system fitted with a 0.2 μm pore size filter, supplied by Permutit Australia, Sydney, Australia.

Stock Solutions

Stock solutions of distilled water, calcium chloride, sodium oxalate and sodium chloride were kept at 37°C. When the solutions were prepared they were filtered (0.22 μm) using GS Millipore filters.

The Standard Metastable Solution

For each batch experiment one litre of metastable solution was required. To avoid the risk of primary nucleation, the solution was prepared no more than one hour before use. The method used to prepare the solution is as follows.

MES (2.05g) was dissolved in 800 ml of distilled water. To this 105 ml of 1.5 M sodium chloride solution was added. Then 10.5 ml of 0.1 M calcium chloride solution followed by 10.5 ml of 0.02 M sodium oxalate solution were added. To avoid nucleation, these solutions were added dropwise using volumetric pipettes. The pH was adjusted to 6 by dropwise addition of a 5 M sodium hydroxide solution. The solution was made up to one litre by the addition of distilled water. The solution was magnetically stirred throughout. After filtration (0.22 μm) the solution was kept at 37°C until required. This solution is referred to as the *stock metastable solution* and has the composition given in Table 3.2 in Section 3.3.3.

Seed Suspension

Calcium oxalate mono-hydrate (1 gram) was added to a mortar and wet ground with a pestle in a 0.15 M saline solution. The wet ground crystals were added to a 0.15 M saline solution, the final volume of the seed suspension was one litre. The seed suspension was stored at room temperature and was stirred by a magnetic stirrer. This is similar to the seed suspension used by Ryall *et al.* (1981b), the difference being that the seeds were kept in 0.15 M saline rather than distilled water.

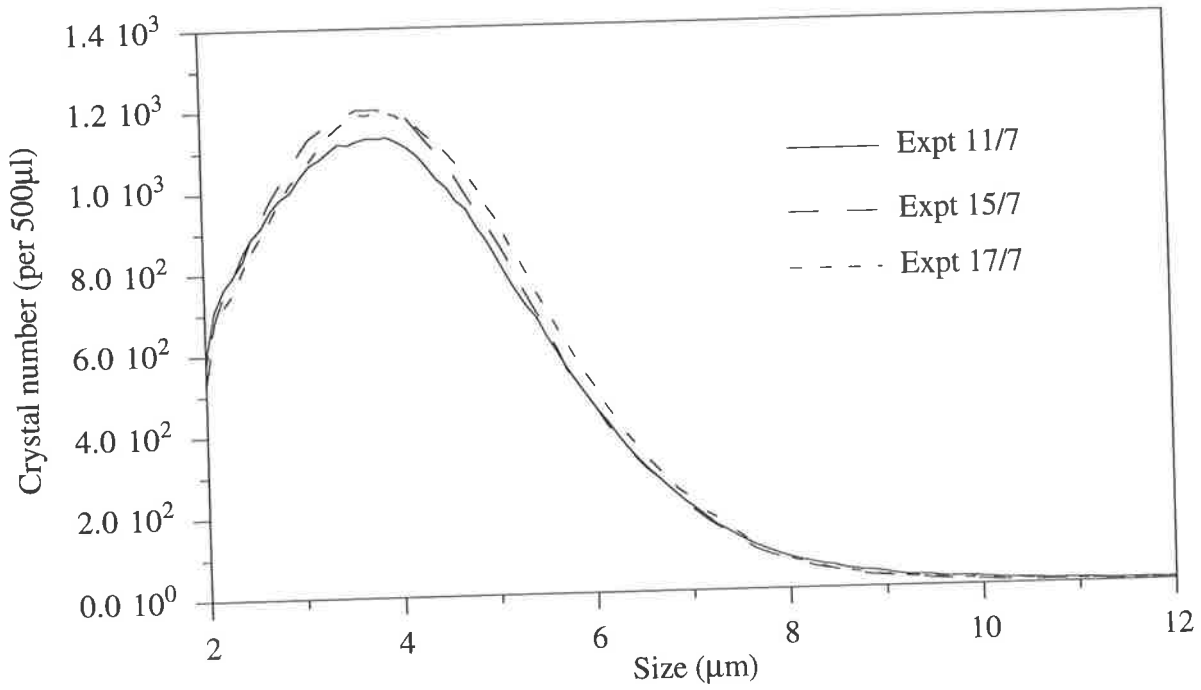
The CSDs and actual solids concentration of the seed suspension were determined using the Multisizer. Prior to commencing many of the batch experiments 4 ml of the seed suspension was added to 200 ml of a 0.15 M saline solution, saturated with respect to calcium oxalate. Samples were taken and analysed by the Multisizer, typical CSDs, by number and volume, of the seed suspension used in the batch experiments are displayed in Figures 3.1 (a) and (b).

The CSDs shown in Figures 3.1 (a) and (b) are histograms of the number and volume of crystals in each size interval or channel respectively, rather than density functions as defined in Section 1.3.2. The number and volume of crystals in each channel is plotted against the average size of the channel. The Multisizer divides the entire size range into channels with a geometric discretisation in which the ratio of the upper and lower sizes in each channel is $2^{1/50}$. More details on this and the operation of the Multisizer are given in Section 3.6 and Appendix 4. All the CSDs presented in this thesis will be of the same form as those in Figures 3.1 (a) and (b).

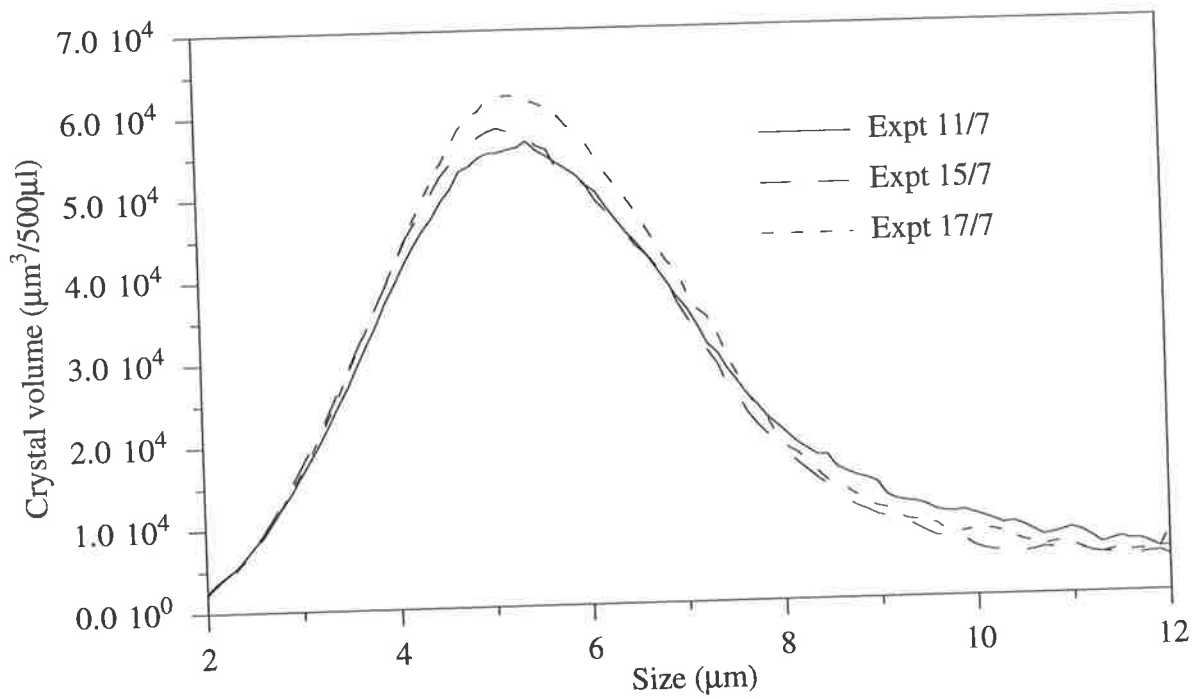
The actual solids concentration in the seed suspension was found to be 0.82 ± 0.01 grams/litre. The solids concentration was calculated from the third moment of the CSD using eq 3.1. The uncertainty indicated is plus-or-minus one standard error in the mean. The data and method used to calculate the solids concentration are given in Appendix 5.

Although the seeds were made by wet grinding one gram of calcium oxalate and adding it to one litre of 0.15 M saline the *actual* solids concentration is *less* than 1 gram/litre. There are two reasons for this: firstly, any very coarse calcium oxalate that remained after wet grinding was not added to the saline and secondly, some of the calcium oxalate will dissolve as the saline was not saturated with respect to calcium oxalate.

Samples of the seed suspension were also examined under SEM. Figure 3.2 is a SEM micrograph of the crystals in the seed suspension used in the batch experiments, it can be seen that the seeds are clearly not individual crystals but rather loose aggregates of crystals



(a)



(b)

Figure 3.1 Typical CSDs by (a) number and (b) volume for the seed suspension used in the batch experiments.

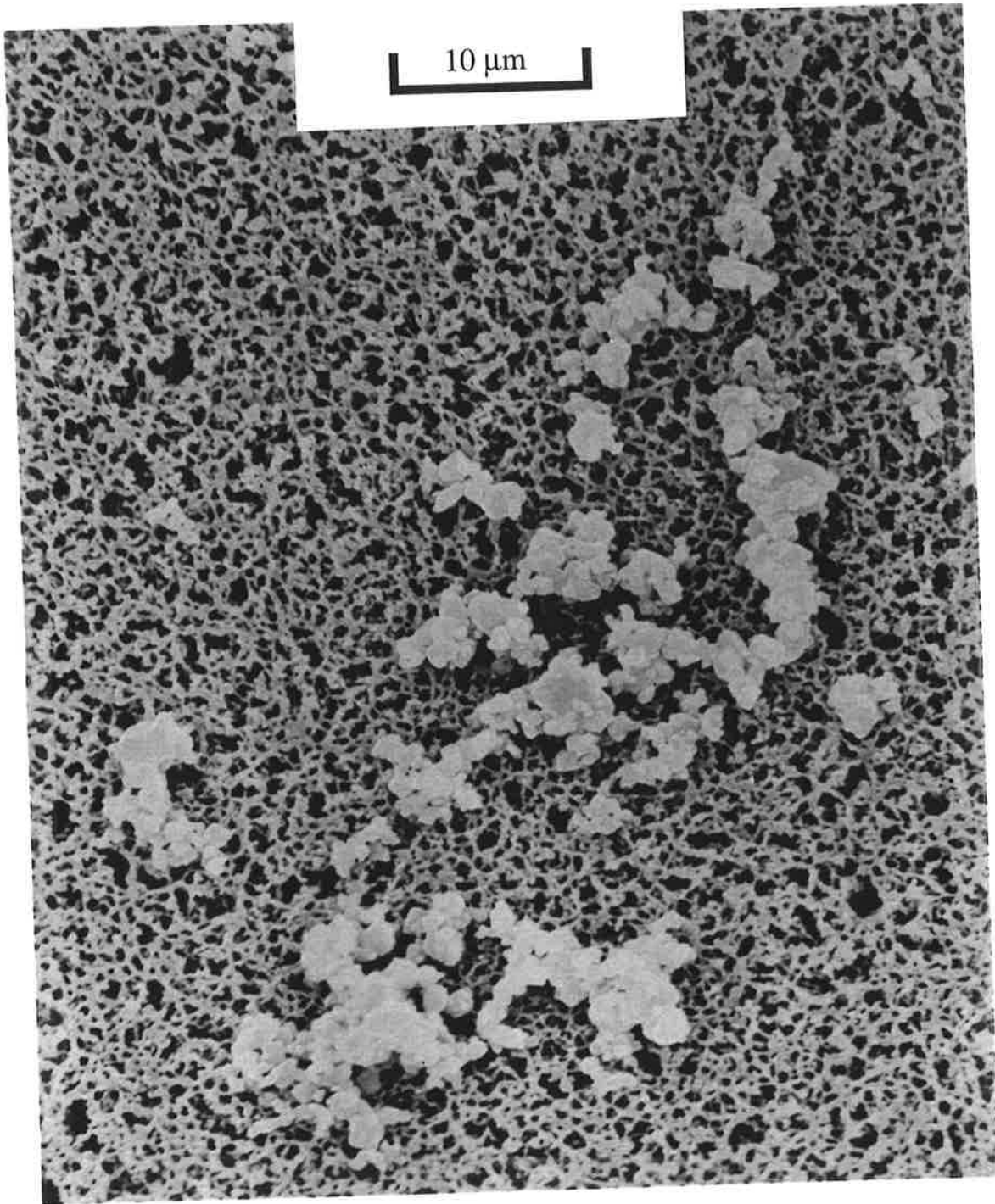


Figure 3.2 SEM micrograph of calcium oxalate crystals in the seed suspension used in the batch crystallisation experiments.

approximately 1-2 μm in size. This is consistent with the findings of other workers such as Nancollas and Gardner (1974) who observed the calcium oxalate mono-hydrate seed crystals used in their study of crystal growth appeared as aggregates when viewed under SEM.

3.3.3 Method

In each experiment four replicates were conducted. The vessels used were 1 litre EMIL or Exelo Permagold soda-glass volumetric flasks. Soda-glass flasks were used to avoid crystal sticking as described by Ryall *et al.* (1981b). Prior to each experiment the flasks were cleaned by rinsing at least three times with each of tap, de-ionised and distilled water. After each experiment the flasks were washed and stored, filled with dilute hydrochloric acid.

To each flask, 190 ml of stock metastable solution and 10 ml of a 0.15 M saline solution were added. The flasks were then placed in a reciprocating shaking water bath (Paton Industries Model RW1812) at 37°C. Before starting the experiment the temperature of the solution in each flask was measured to ensure it was 37°C. The absence of particulate matter was confirmed by analysis of a sample with the Multisizer.

Crystallisation was initiated by the addition, using a volumetric pipette, of 4 ml of seed suspension to each flask. At time intervals of 5 or 10 minutes, aliquots of approximately 10 ml were taken from each flask and analysed by the particle size analyser. After analysis each aliquot was returned to the flask from which it was taken. Samples were obtained by pouring the contents of the flask into a sample vial. As shown in Section 3.3.2 this method gave representative sampling without the problems of isokinetic sampling that may be introduced by withdrawing a sample with a pipette. Samples were collected for between 60 and 90 minutes depending on the experimental conditions. The primary experimental data consists of a series of timed CSDs recorded as the seed crystals grew and aggregated in a solution of decreasing supersaturation.

The composition of the metastable solution used in the batch experiments is different from that of the stock solution. Firstly, the stock metastable solution, 190 ml, is added to each flask, along with 10 ml of a 0.15 M saline solution, the resulting solution is referred to as the *pre-crystallisation solution*. Secondly, at the start of an experiment 4 ml of the seed suspension is added to each flask, giving the metastable solution referred to as the *crystallisation solution*. The composition of each of these solutions is given in Table 3.2.

Table 3.2 Metastable solution compositions.

Component	Stock metastable solution	Pre-crystallisation solution	Crystallisation solution
Ca ²⁺	1.05×10 ⁻³ M	1.0×10 ⁻³ M	9.81×10 ⁻⁴ M
Ox ²⁻	2.11×10 ⁻⁴ M	2.0×10 ⁻⁴ M	1.96×10 ⁻⁴ M
Na ⁺	1.584×10 ⁻¹ M	1.58×10 ⁻¹ M	1.578×10 ⁻¹ M
Cl ⁻	1.6×10 ⁻¹ M	1.596×10 ⁻¹ M	1.594×10 ⁻¹ M
MES	1.05×10 ⁻² M	9.98×10 ⁻³ M	9.78×10 ⁻³ M

3.4 PARAMETERS INVESTIGATED

There are a number of studies of the growth and aggregation of calcium oxalate in a batch system reported in the literature. Many have focused on chemical inhibitors of growth and aggregation rather than the kinetics of these processes. In this work the growth and aggregation kinetics are of more interest. In this respect the work of Hounslow *et al.* (1988a) is most relevant. They find, using experiments similar to those in this work that both the growth rate and the aggregation rate constant are directly proportional to supersaturation. However, their observations are restricted to a limited range of supersaturation. Only one initial solution composition was used. Also they did not explore the effect of different agitation rates on the growth and aggregation rates.

The aim of this work is to obtain growth and aggregation rates over a wider range of supersaturation than that considered by Hounslow *et al.* (1988a). Also the effect of the agitation rate, which has been largely ignored, will be investigated.

3.4.1 Supersaturation

Initially experiments were conducted using the standard stock metastable solution described in Section 3.3.2. The crystallisation solution prepared from this stock metastable solution has the same composition as that used by Hounslow *et al.* (1988a). The standard stock metastable solution was then modified by the addition of variable quantities of sodium oxalate. This allowed both the initial supersaturation and the calcium to oxalate ratio to be varied. Solutions were used in which the oxalate concentrations were 1.5, 2 and 2.5 times that of a standard stock metastable solution.

A further modification of the standard stock metastable solution was also considered. Solutions with the same initial supersaturation as a standard stock metastable solution, but different calcium to oxalate ratios were used. The oxalate concentration was increased by factors of 1.5 and 2. The calcium and oxalate concentrations in each of the metastable solutions used are given in Table 3.3. The concentrations are those in the crystallisation solution (containing 190 ml stock metastable solution, 10 ml 0.15 M saline and 4 ml of seed suspension) rather than the stock solutions.

In all these experiments an agitation rate of 90 oscillations per minute (OPM) was used.

Table 3.3 Calcium and oxalate concentrations in metastable crystallisation solutions with different initial supersaturations.

Solution Description	Calcium to Oxalate Ratio	Oxalate concentration (M)	Calcium concentration (M)	Initial Relative Supersaturation $\sigma = \frac{AP}{K_{sp}}$
Standard metastable	5	1.96×10^{-4}	9.81×10^{-4}	4.31
1.5×Std Oxalate, Std Calcium	3.33	2.94×10^{-4}	9.81×10^{-4}	6.39
2×Std Oxalate, Std Calcium	2.5	3.92×10^{-4}	9.81×10^{-4}	8.42
2.5×Std Oxalate, Std Calcium	2	4.90×10^{-4}	9.81×10^{-4}	10.41
1.5×Std Oxalate, Std Calcium/1.5	2.22	2.94×10^{-4}	6.54×10^{-4}	4.45
2×Std Oxalate, Std Calcium/2	1.25	3.92×10^{-4}	4.91×10^{-4}	4.49

3.4.2 Agitation rate

The effect of agitation rate was investigated by simply altering the speed at which the flasks were shaken in the water bath. The agitation rate was increased in increments of 10 OPM from 80 to 110 OPM. In all these experiments a standard metastable solution was used.

The slowest agitation rate used was 80 OPM, as at slower rates it was observed that during an experiment the crystals were settling. The fastest agitation rate used was 110 OPM, as at faster rates there was a change in the fluid motion in the flasks. Between 80 and 110 OPM the fluid was moved backwards and forwards in the flask; the fluid motion was lateral. At

rates faster than 110 OPM the fluid was swirled around the flask. To keep the fluid motion the same in all the experiments agitation rates above 110 OPM were not used.

3.5 CALCULATING THE GROWTH AND AGGREGATION RATES

The difficult problem of calculating the rates for simultaneous growth and aggregation has been studied for the batch system. Hounslow (1990) describes a computer program, *Batch*, written for the analysis of batch calcium oxalate crystallisation experiments. In this section details of the program, the method by which it calculates the rates and its use in this work are described.

3.5.1 The program *Batch*

Batch is a program written in FORTRAN for use on the Apple Macintosh brand of personal computer. It is capable of performing three main tasks; the extraction of kinetic coefficients from experimental data, fitting models to the coefficients and simulating changes in a crystal size distribution during an experiment. Its principle use in the current work was for extracting kinetic coefficients from experimental data.

3.5.2 Determining the rates

Method

Batch uses a differential technique to calculate the rates. From experimental data the rates of change of crystal number and volume are obtained, then the moment form of the population balance is used to calculate the growth rate and aggregation rate constant. Eqs 1.20 and 1.22 can be re-arranged to give

$$\beta_0 = \frac{-2\dot{m}_0}{m_0^2} \quad (3.2)$$

$$G = \frac{\dot{m}_3}{3m_2} \quad (3.3)$$

A problem often encountered with particle size analysers, such as the Multisizer, is that during the course of an experiment a number of crystals grow into its field of view. This has been observed for calcium oxalate by Ryall *et al.* (1986) and Hartel and Randolph (1986). Hartel and Randolph suggest that growth into the field of view be accounted for by a source function, B_u , which is the rate of appearance of crystals in the first interval of the size range covered by the particle size analyser.

The differential method must be modified to allow for this extra mechanism. In *Batch* another time derivative is introduced, the rate of change of the crystal number in the first size interval, \dot{N}_1 . As Hounslow (1990) points out the source function has a bigger influence on the number of crystals than any other measured parameter. Four new parameters are defined: the rate of change of the first moment and the rate of change of the number of crystals in the first size interval, for aggregation and growth occurring alone. For aggregation only,

$$\Phi_0 = \frac{\dot{m}_0|_{agg}}{\beta_0} \quad (3.4)$$

$$\Phi_1 = \frac{\dot{N}_1|_{agg}}{\beta_0} \quad (3.5)$$

For growth only,

$$\Phi_2 = \frac{\dot{N}_1|_g}{G} \quad (3.6)$$

$$\Phi_3 = \frac{\dot{m}_3|_g}{G} \quad (3.7)$$

Eqs 3.2 to 3.7 may be written as three equations in terms of the three unknown rate constants.

$$\dot{m}_0 = \beta_0 \Phi_0 + B_u \quad (3.8)$$

$$\dot{m}_3 = G \Phi_3 + B_u \bar{L}_1^3 \quad (3.9)$$

$$\dot{N}_1 = G \Phi_2 + \beta_0 \Phi_1 + B_u \quad (3.10)$$

The values of \dot{m}_0 , \dot{m}_3 , \dot{N}_1 , Φ_0 , Φ_1 , Φ_2 and Φ_3 can all be calculated from the experimental CSDs. The above equations can then be solved to obtain the rate constants.

Calculating the parameters and kinetic coefficients

The rates of change of the first and third moments and the number of crystals in the first size interval are calculated from the experimental CSDs supplied to *Batch*. These time derivatives are calculated using a three point difference scheme adapted from the Turbo Pascal toolbox.

The parameters in eqs 3.4 to 3.7 are calculated using the discretized population balance of Hounslow *et al.* (1988a). Those authors develop equations for the rate of change of crystal number in each size interval for aggregation alone, and growth alone. The parameter Φ_1 is calculated from the equation for aggregation alone for the first size interval only, the parameter Φ_0 by summing the change in crystal number for each size interval. Similarly Φ_2 is obtained from the equation for growth alone by considering only the first size interval, the parameter Φ_3 by summing the product of the change in crystal numbers and the average size cubed for each size interval.

Eqs 3.8 to 3.10, a set of linear equations, are solved for the kinetic coefficients using a routine developed from Carnahan *et al.* (1969) which calculates the solution to an augmented matrix.

Calcium and oxalate concentrations

The other useful data reported by *Batch* are the total calcium and oxalate concentrations. These are calculated by a mass balance. If w_0 is the initial concentration of seeds, in mass per unit volume, at time, t , the number of moles of calcium oxalate deposited, per unit volume, Δn , is given by

$$\Delta n = \frac{w_t - w_0}{Mr} \quad (3.11)$$

where Mr is the molecular weight of calcium oxalate, 146.1 gmol^{-1} , and w_t is the solids concentration, in mass per unit volume, at time, t , which can be calculated from eq 3.1. The concentrations at time t , are

$$T_{Ca^{2+}} = T_{Ca^{2+}}^0 - \Delta n \quad \text{and} \quad T_{Ox^{2-}} = T_{Ox^{2-}}^0 - \Delta n \quad (3.12a \text{ and } b)$$

3.5.3 Running *Batch*

Input

To run *Batch*, the user must supply: experimental data, the experimental set-up and finally which mechanisms of nucleation, growth, aggregation and source function are active. Using this information *Batch* returns the moments of the experimental CSDs, the total calcium and oxalate concentrations, supersaturation, and the rate constants for each active mechanism at each time interval.

The experimental data are entered as CSDs in a tabular form, one row per time interval, with the time at which each sample was taken in the first column. This is convenient as data from

a spreadsheet package, such as Microsoft Excel, can be copied directly into *Batch* in the correct format. An example of this format is given in Figure 3.3 (a).

The set-up used in the experiments must also be entered before *Batch* can be run and the experimental CSDs analysed. The following data are required: the initial seed concentration, the initial total calcium and oxalate ion concentrations and the ionic strength of the crystallisation solution. The set-up of the Coulter Counter must be entered as well, giving the number of size intervals, the lower limit of the first size interval and the volume of the samples analysed to obtain the experimental CSDs.

In addition to choosing which mechanisms are active, it is possible to select different functional forms of the aggregation kernel. This allows the inverse problem, that of the selection of an appropriate aggregation kernel to model the experimental data, to be investigated.

Output

The output from *Batch* is conveniently displayed in separate windows, one for the rate constants of the active mechanisms, another for the moments of the CSDs and total calcium and oxalate concentrations in the crystallisation solution. Both are in tabular form, one row per time interval, as shown in Figures 3.3 (b) and (c). This is very convenient as the output can be copied directly into a spreadsheet for further analysis.

3.6 DATA ANALYSIS

Perhaps the only restricting feature of the program *Batch* is that it uses a geometric discretisation for the particle size domain with a $\sqrt[3]{2}$ progression. This means that the lower limits of consecutive size intervals are related by

$$\frac{L_{i+1}}{L_i} = \sqrt[3]{2} \quad (3.13)$$

This is restricting as many particle size analysers, such as the Multisizer used in this work, do not use a geometric discretisation for the size domain with a $\sqrt[3]{2}$ progression. The Multisizer divides the size domain into 256, 128, 64 or 32 intervals or channels. When 256 channels are used the geometric progression is such that the size doubles every 50 channels, (Multisizer II Users Manual, 1987). That is the ratio of the upper limits in adjacent channels is

Experimental CSDs for batch experiment 16/7

0	11794	15673	18270	17406	12070	5027	1035	181	50	15	2	1	0
5	9135	11655	13698	14571	12589	7500	2217	352	68	17	2	2	0
10	7993	10079	12183	13644	12753	8501	2895	462	88	19	4	4	0
20	7432	9179	11199	12901	12942	9384	3658	645	96	22	6	2	0
30	6781	8355	10250	11990	12566	9765	4107	768	107	23	5	2	0
40	6218	7833	9607	11575	12437	10027	4489	861	131	24	6	2	0
50	5912	7444	9291	11197	12397	10401	4810	966	134	28	6	3	0
60	5592	7078	8876	10885	12186	10604	5104	1081	152	25	7	3	0
70	5237	6572	8482	10652	12033	10639	5251	1144	158	34	7	2	0
80	4874	6391	8203	10417	12089	10582	5448	1225	163	29	4	4	0
90	4653	6122	8122	10312	11913	10739	5525	1267	171	34	8	6	0

(a) An example of the experimental data window from *Batch*.

Growth rates, aggregation rate constants and source functions for the batch experiment 16/7

Experimental Results for						
t	S*	Sm	Bo or Bu	G	f ₀	
.0000	1.3304E-08	1.3304E-08	5.319	7.6686E-02	7.9096E-04	
5.000	1.0457E-08	1.0457E-08	2.264	4.9921E-02	4.6968E-04	
10.00	8.7719E-09	8.7719E-09	1.096	3.1030E-02	2.1467E-04	
20.00	7.0212E-09	7.0212E-09	.4427	1.3287E-02	9.1535E-05	
30.00	6.2921E-09	6.2921E-09	.2303	8.2161E-03	7.8295E-05	
40.00	5.5141E-09	5.5141E-09	.2038	8.6120E-03	5.2163E-05	
50.00	4.7137E-09	4.7137E-09	.1797	7.7173E-03	4.3572E-05	
60.00	4.0880E-09	4.0880E-09	9.9421E-02	4.8347E-03	4.4445E-05	
70.00	3.8189E-09	3.8189E-09	3.7436E-02	3.1956E-03	3.5008E-05	
80.00	3.5058E-09	3.5058E-09	4.7846E-02	3.9248E-03	2.5730E-05	
90.00	3.1038E-09	3.1038E-09	8.8760E-02	4.8670E-03	2.5630E-05	

(b) Output window from *Batch* showing values of the growth rate, aggregation rate constant and source function calculated for the data from the experimental window.

Total calcium and oxalate concentrations and moments of the CSDs for batch experiment 16/7

Experimental Results for						
t	Cox	Cca	m0	m1	m2	m3
.000	1.743E-04	9.593E-04	163.0	665.6	3107.	1.6700E+04
5.00	1.486E-04	9.336E-04	143.6	639.5	3317.	1.9954E+04
10.0	1.328E-04	9.178E-04	137.2	638.0	3471.	2.1955E+04
20.0	1.160E-04	9.010E-04	134.9	649.7	3674.	2.4097E+04
30.0	1.087E-04	8.937E-04	129.4	639.4	3717.	2.5011E+04
40.0	1.010E-04	8.860E-04	126.4	637.6	3786.	2.6000E+04
50.0	9.284E-05	8.778E-04	125.2	641.7	3874.	2.7035E+04
60.0	8.637E-05	8.713E-04	123.2	641.3	3933.	2.7855E+04
70.0	8.356E-05	8.685E-04	120.4	635.1	3942.	2.8211E+04
80.0	8.027E-05	8.652E-04	118.9	633.5	3969.	2.8628E+04
90.0	7.601E-05	8.610E-04	117.7	632.8	3998.	2.9168E+04

(c) Output window from *Batch* showing total calcium and oxalate concentrations and moments calculated for the data from the experimental window.

Figure 3.3 (a) Input and (b) and (c) output windows from the program *Batch*.

$$\frac{L_{i+1}}{L_i} = 2^{1/50} \quad (3.14)$$

When less than 256 channels are used the upper limit of any channel, L_X can be calculated from

$$L_X = L_{256} i^U \quad (3.15)$$

where L_{256} is the upper limit of the last channel, i is the log step ratio defined in eq 3.13 and U is given by

$$U = 256 \left(\frac{X}{J} - 1 \right) \quad (3.16)$$

where J is the total number of channels, i.e. 256, 128, 64, or 32.

From eqs 3.15 and 3.16 it follows that the ratio of the upper limit in adjacent channels is given by

$$\frac{L_{i+1}}{L_i} = 2^{256/50J} \quad (3.17)$$

For each possible value of J , the ratio of the upper limits in adjacent channels are calculated by eq 3.17 as

$$\frac{L_{i+1}}{L_i} = 2^{1/50} \quad J = 256$$

$$\frac{L_{i+1}}{L_i} = 2^{1/25} \quad J = 128$$

$$\frac{L_{i+1}}{L_i} = 2^{2/25} \quad J = 64$$

$$\frac{L_{i+1}}{L_i} = 2^{4/25} \quad J = 32$$

Therefore it is not possible to get an exact $\sqrt[3]{2}$ progression in size from the Multisizer. However the CSDs must be in a $\sqrt[3]{2}$ progression in size if they are to be used as input for the program *Batch*. Further, the CSDs must be number rather than volume distributions.

The CSDs obtained from the Multisizer were converted so they have a $\sqrt[3]{2}$ progression in size. Over the size domain used in this work, 2 to 32 μm , the channels in which the size

corresponding to an exact value of a $\sqrt[3]{2}$ progression were identified. The data from all the channels between those containing the exact sizes were summed. In the channels that contained an exact value, linear interpolation was used to distribute the counts in these channels between adjacent channels in the $\sqrt[3]{2}$ progression.

The Multisizer reports CSDs by number and volume, the volume distribution being calculated from the number distribution as the average size for each channel is known. The CSDs from the Multisizer have a much finer discretization than a $\sqrt[3]{2}$ progression. The conversion of a number CSD from the Multisizer format to a $\sqrt[3]{2}$ progression conserves the total number crystals. However, a discretization error is incurred in properties, such as crystal volume, calculated from the converted CSDs, as crystals from a large number of small intervals, each with an average size, are allocated to one larger interval with one average size.

Two different approaches are available: the first is to convert the Multisizer number distribution into a CSD with a $\sqrt[3]{2}$ progression and from it calculate the corresponding volume distribution with a $\sqrt[3]{2}$ progression. The second to convert the Multisizer volume distribution into a CSD with a $\sqrt[3]{2}$ progression and from it calculate the corresponding number distribution. In the first case the discretization error is in the volume distribution with a $\sqrt[3]{2}$ progression, in the second the error is in the number distribution with a $\sqrt[3]{2}$ progression.

It was found that if the number CSDs were converted the implied volume in each channel was overestimated and the total volume was in error by approximately 9%, compared to the volume distribution from the Multisizer. If the volume CSDs were converted the implied number in each channel was underestimated and the total number of crystals was in error by approximately 4%, compared to the number distribution from the Multisizer.

As the total crystal volume is used to calculate solution concentrations, and supersaturation, it is important that the error in the crystal volume be as small as possible. For this reason the volume distributions from the Multisizer were converted to CSDs with a $\sqrt[3]{2}$ progression. An example of the conversion of the CSDs from the format reported by the Multisizer to a $\sqrt[3]{2}$ progression is given in Appendix 6.

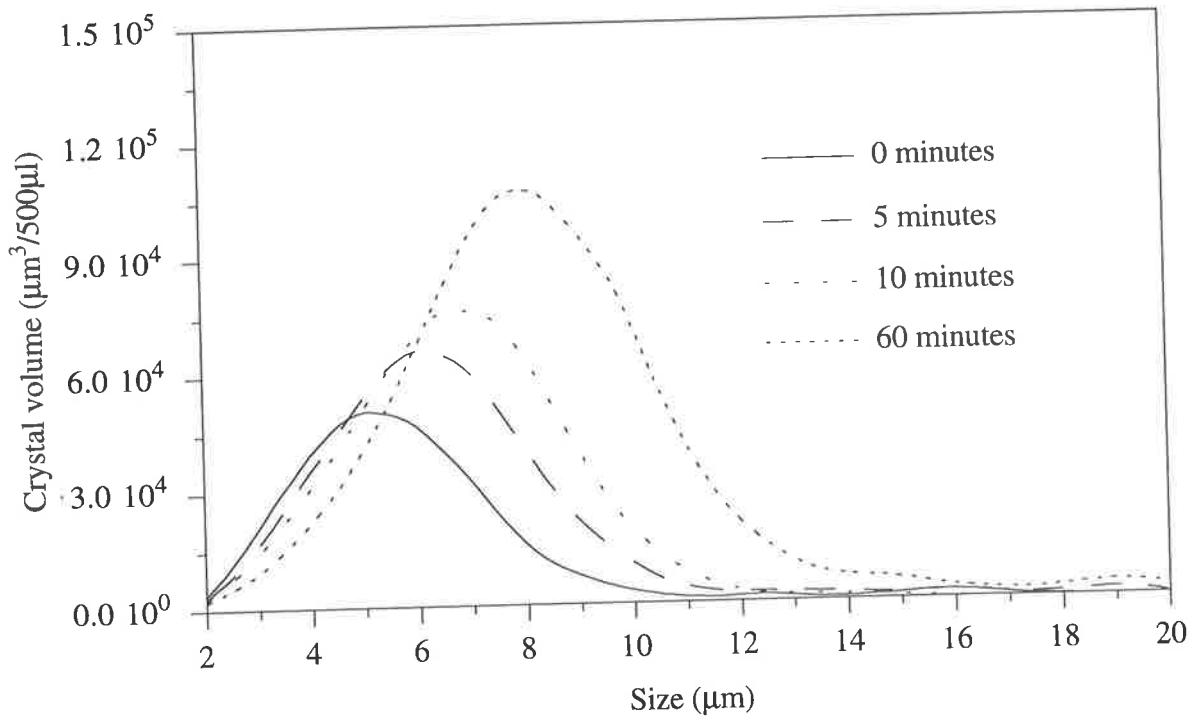
3.7 CONCLUSIONS

The experimental materials, methods and analysis techniques used to study the batch crystallisation of calcium oxalate have been described. The reasons for conducting batch

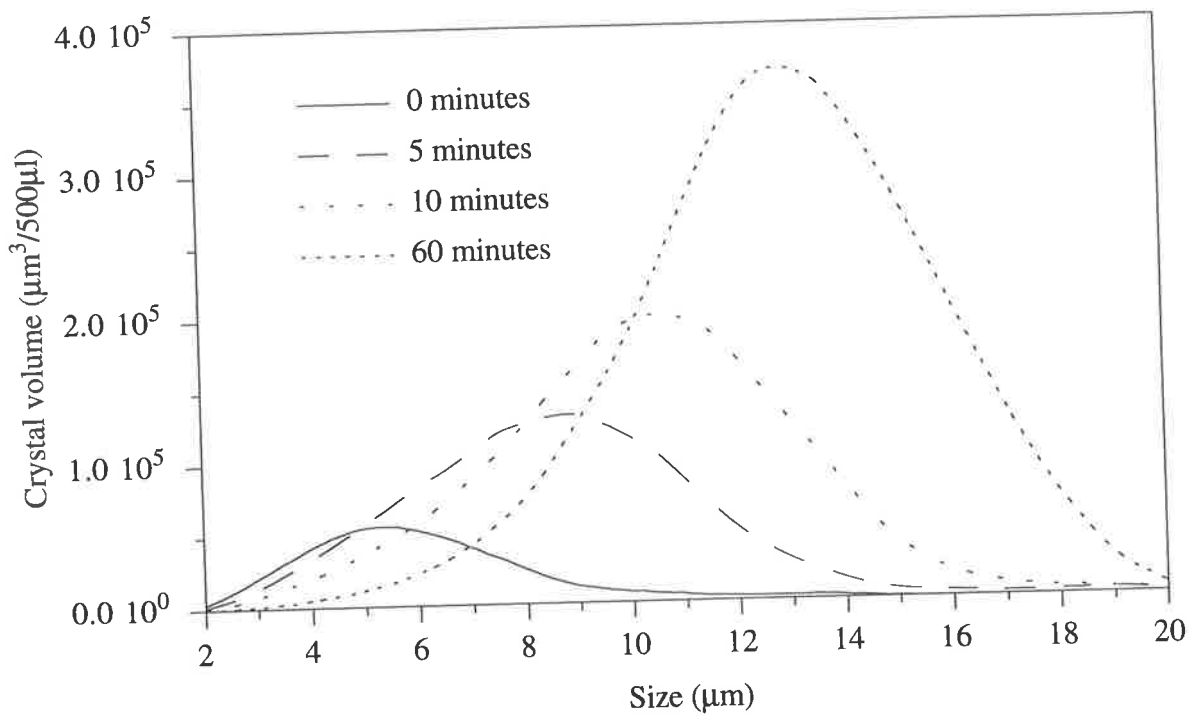
experiments are that well established experimental protocols exist, as does a computer program that calculates the growth and aggregation rates from experimental data.

The effect of supersaturation and agitation rate on the growth and aggregation rates was investigated. The supersaturation was varied by changing the calcium and oxalate concentrations in the metastable solution. The agitation rate was varied by changing the shaking rate in the water bath.

The computer program *Batch*, which allows growth and aggregation rates to be determined from experimental data, has been described. *Batch* was used to analyse the data from the experiments reported in this chapter. The dependence of the growth and aggregation rates on supersaturation and agitation rate is investigated in the next chapter.

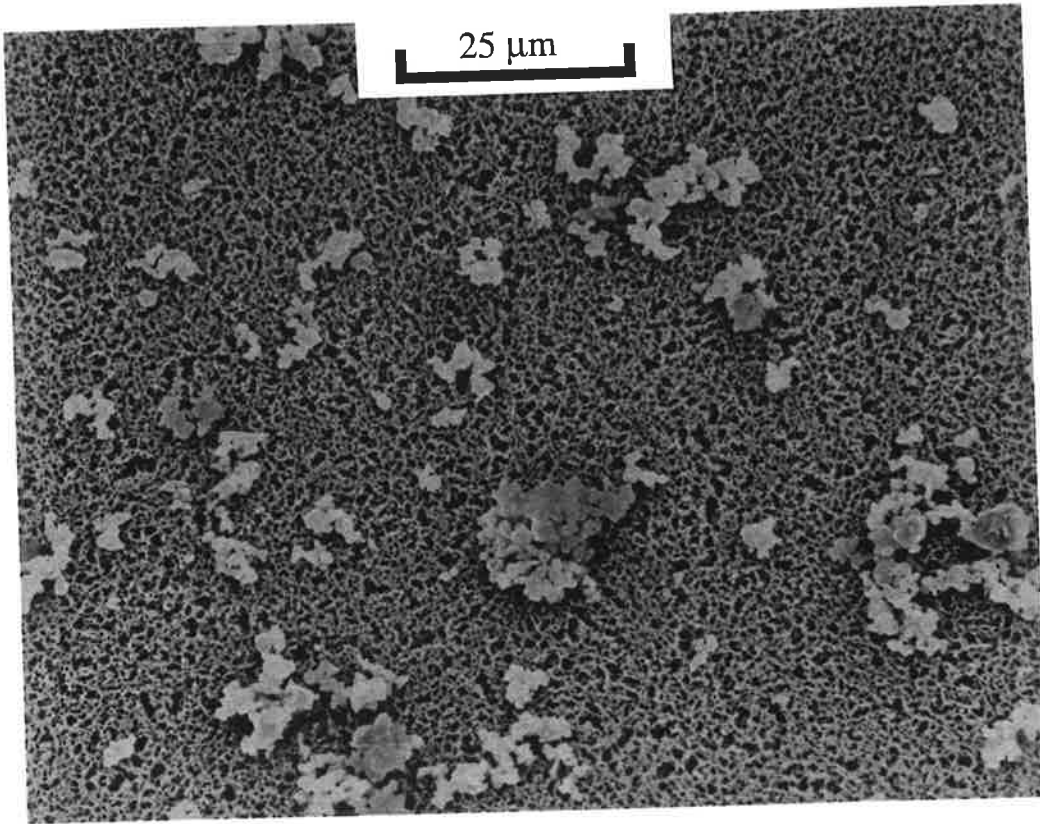


(a)

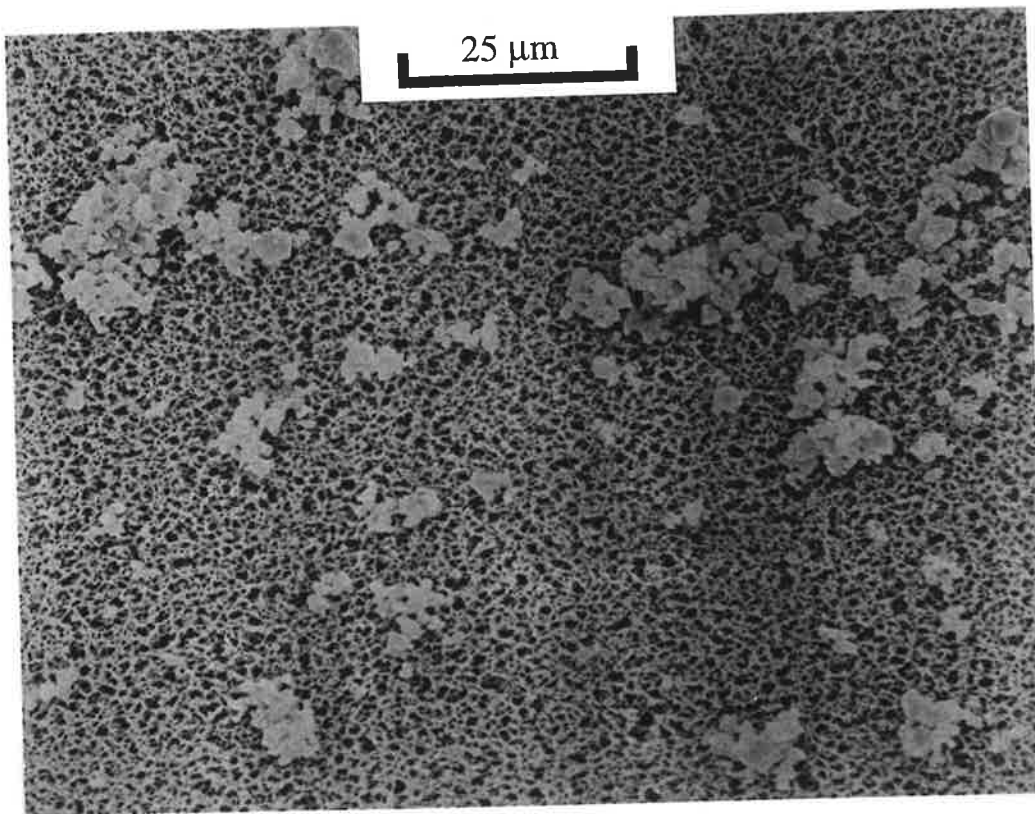


(b)

Figure 4.2 CSDs by volume at different time intervals from batch experiments with (a) a standard metastable solution (Ca:Ox = 5:1) and (b) a metastable solution with 2.5 times the standard oxalate concentration (Ca:Ox = 2:1).

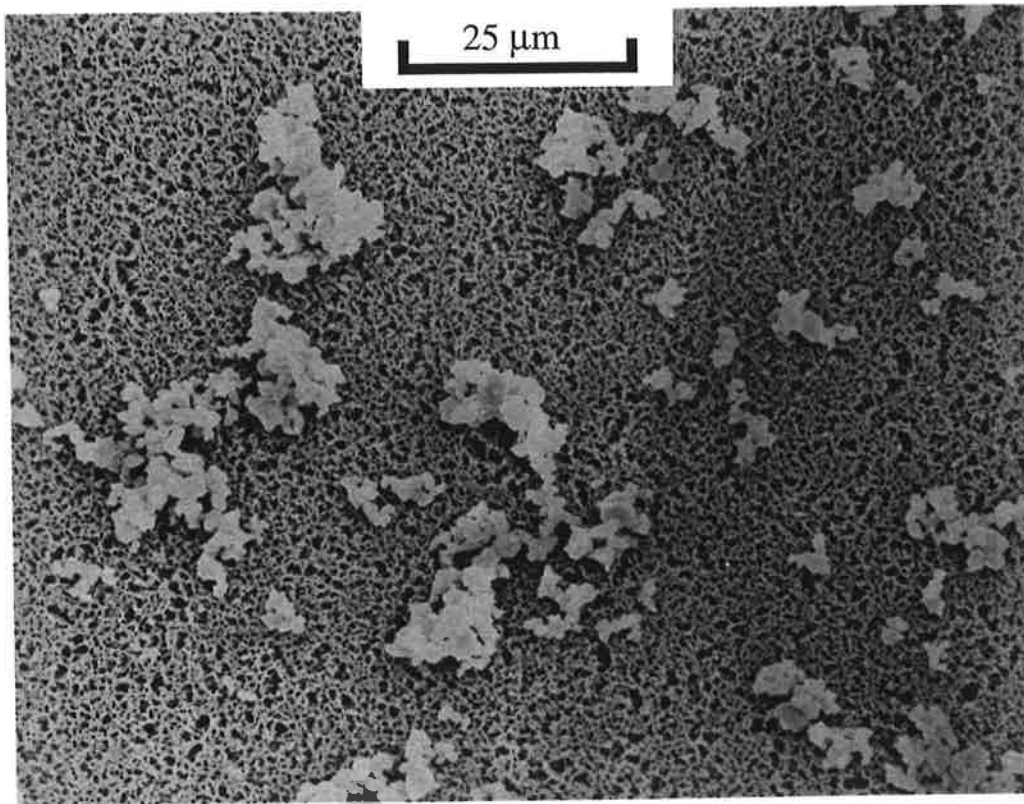


(i) Standard metastable solution (Ca:Ox = 5:1).

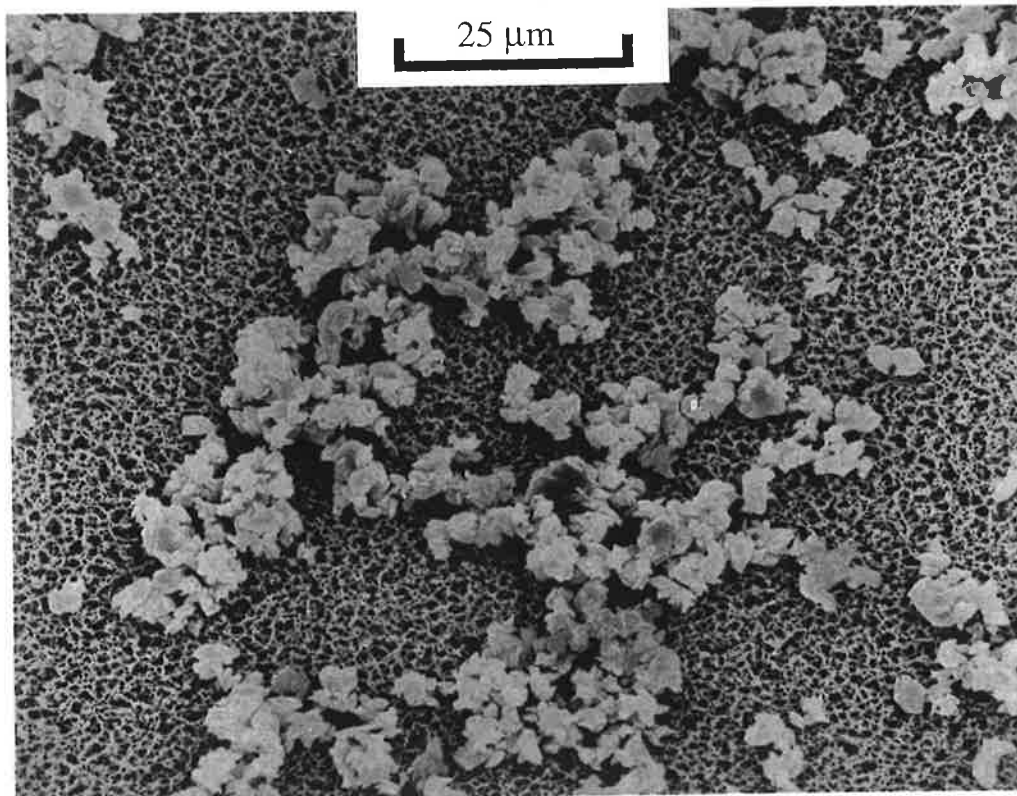


(ii) Metastable solution with 2.5 times the standard oxalate concentration (Ca:Ox = 2:1).

Figure 4.3 (a) SEM micrographs of calcium oxalate crystals from different batch experiments at $t = 0$ minutes.

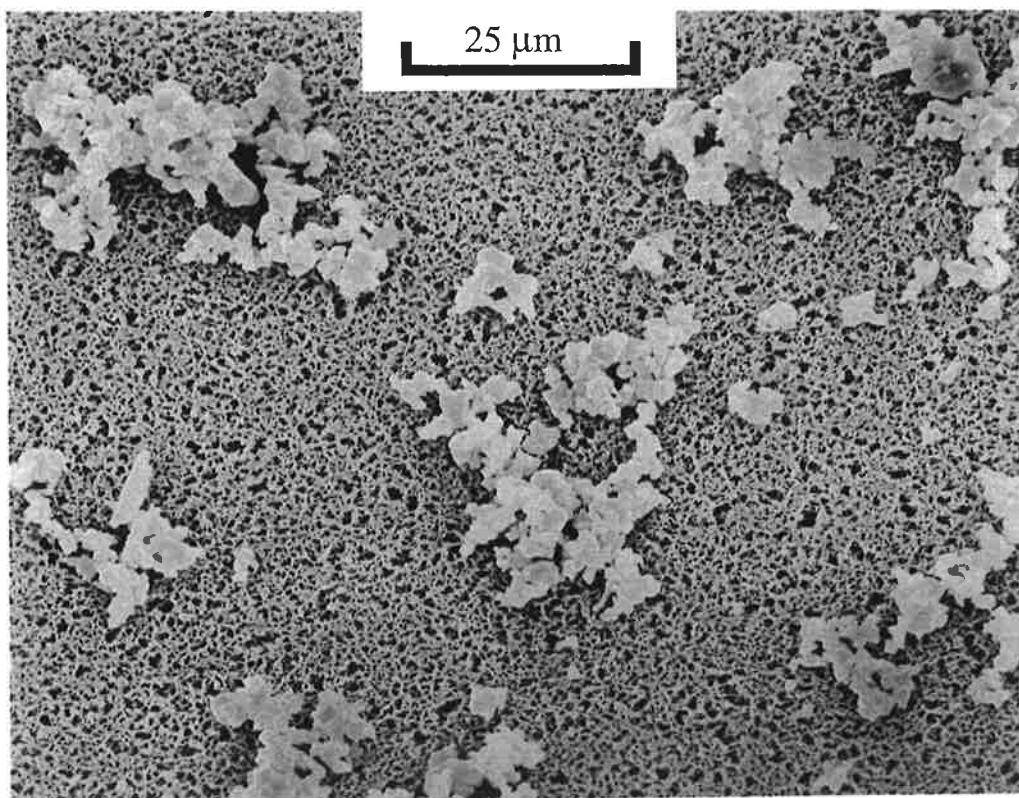


(i) Standard metastable solution (Ca:Ox = 5:1).

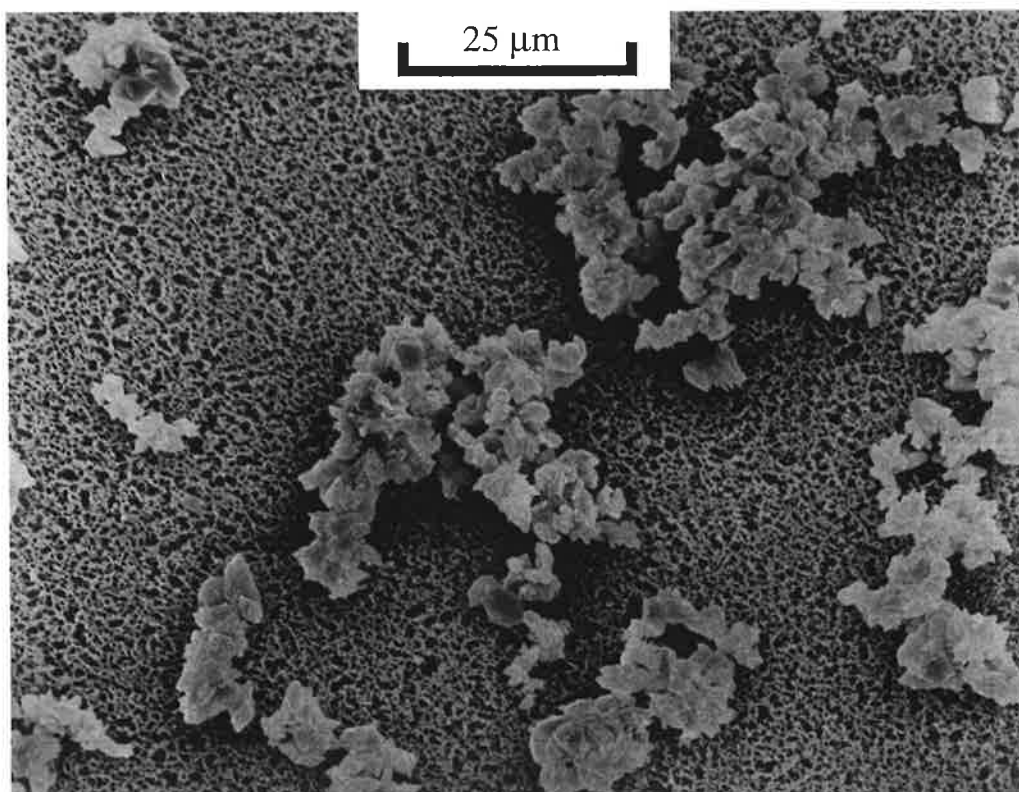


(ii) Metastable solution with 2.5 times the standard oxalate concentration (Ca:Ox = 2:1).

Figure 4.3 (b) SEM micrographs of calcium oxalate crystals from different batch experiments at $t = 5$ minutes.

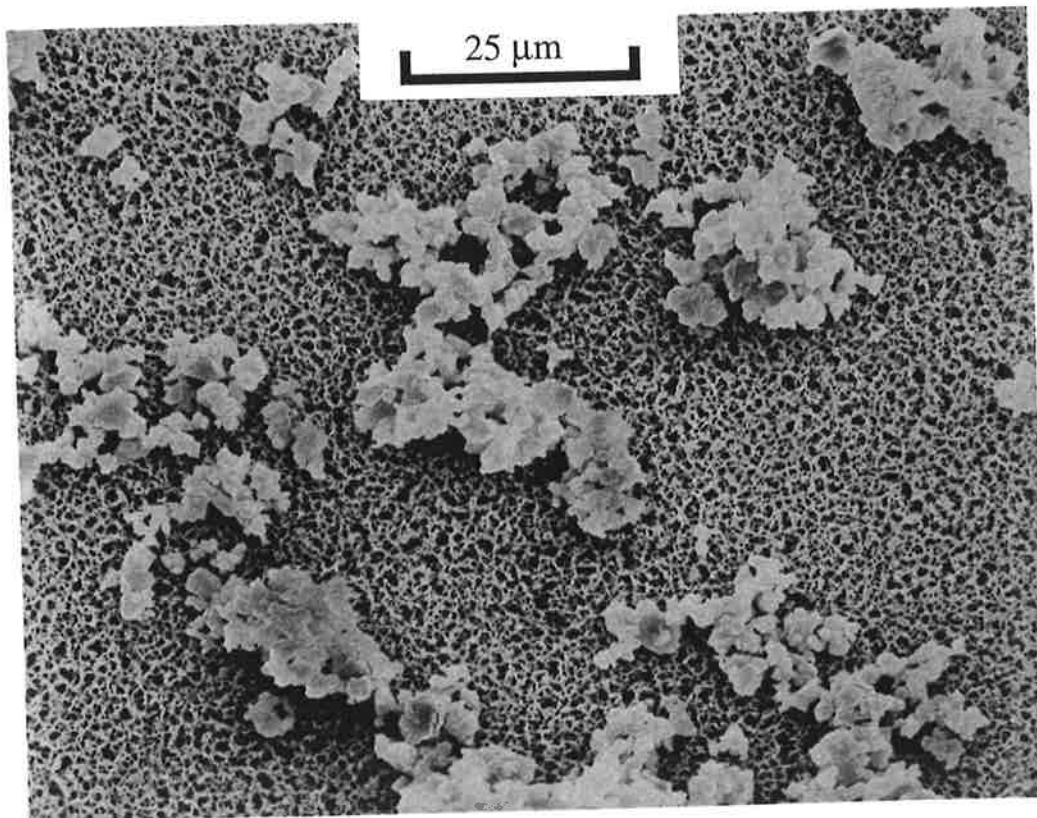


(i) Standard metastable solution (Ca:Ox = 5:1).

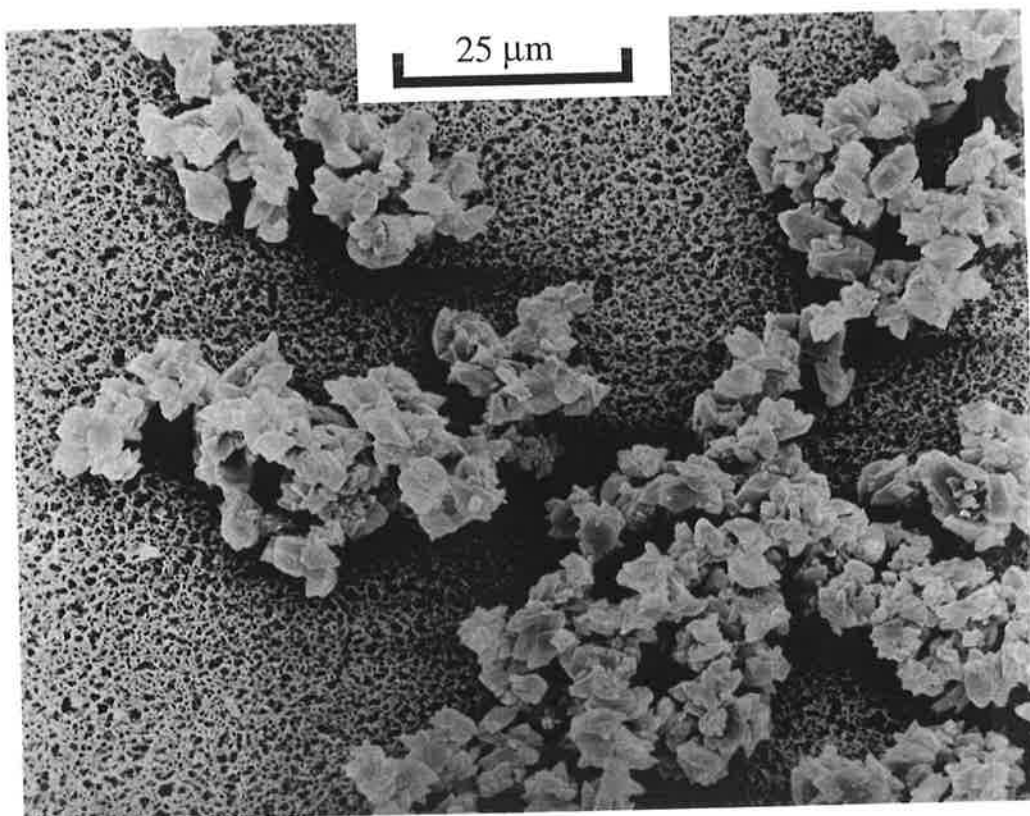


(ii) Metastable solution with 2.5 times the standard oxalate concentration (Ca:Ox = 2:1).

Figure 4.3 (c) SEM micrographs of calcium oxalate crystals from different batch experiments at $t = 10$ minutes.



(i) Standard metastable solution (Ca:Ox = 5:1).



(ii) Metastable solution with 2.5 times the standard oxalate concentration (Ca:Ox = 2:1).

Figure 4.3 (d) SEM micrographs of calcium oxalate crystals from different batch experiments at $t = 60$ minutes.

the higher oxalate concentration. From the SEM micrographs displayed in Figures 4.3 (b) to (d) it can be seen that at each time interval the crystals in the samples taken from the solution with the higher oxalate concentration are much larger and more aggregated than those from the standard solution.

4.4 THE GROWTH RATE

Mullin (1993) points out there are many mechanisms proposed for crystal growth and many reviews of the historical development of these theories. Nielsen and Toft (1984) observe that the growth rate may be controlled by transport of ions through the solution by convection and diffusion, by various processes on the crystal surface or a combination of the two. Nielsen (1984) states that for sparingly soluble salts, such as calcium oxalate, the growth rate is normally surface controlled in which case the following rate expressions

$$G = k_1 (S - 1) \quad (4.2)$$

$$G = k_2 (S - 1)^2 \quad (4.3)$$

$$G = k_e S^{7/6} (S - 1)^{2/3} (\ln S)^{1/6} \exp(-K_e / (\ln S)) \quad (4.4)$$

are appropriate for the following rate determining mechanisms respectively: ion transport or adsorption, surface spiral growth and surface polynucleation. In the above expressions, S is a relative supersaturation, which for calcium oxalate is given by

$$S = \left(\frac{AP}{K_{sp}} \right)^{1/2} \quad (4.5)$$

A detailed discussion of the mathematical analysis used to obtain the rate expressions for the various growth mechanisms is given for example by, Söhnel and Garside (1992).

4.4.1 Analysis of experimental data

In this section the data from the experiments described in Chapter 3 are studied with the aim of determining which of the growth rate mechanisms outlined above is appropriate for the batch crystallisation of calcium oxalate.

The details of the conditions for each of the batch experiments are given in Table 4.3. The CSDs measured by the Multisizer were converted to CSDs with a $\sqrt[3]{2}$ progression as described in Section 3.6 and were analysed using the program *Batch* as described in Section

Table 4.3 Initial experimental conditions for the batch experiments.

Run	Agitation Rate (OPM)	Solution Description	Ca:Ox ratio	Calcium ion concentration (M)	Oxalate ion concentration (M)	$\sigma = \frac{AP}{K_{sp}}$
11/7	90	Std Ox	5	9.81×10^{-4}	1.96×10^{-4}	4.31
13/7	90	Std Ox	5	9.81×10^{-4}	1.96×10^{-4}	4.31
14/7	90	Std Ox	5	9.81×10^{-4}	1.96×10^{-4}	4.31
16/7	90	Std Ox	5	9.81×10^{-4}	1.96×10^{-4}	4.31
17/7	90	Std Ox	5	9.81×10^{-4}	1.96×10^{-4}	4.31
20/7	90	Std Ox	5	9.81×10^{-4}	1.96×10^{-4}	4.31
23/7a	90	Std Ox	5	9.81×10^{-4}	1.96×10^{-4}	4.31
23/7b	90	Std Ox	5	9.81×10^{-4}	1.96×10^{-4}	4.31
18/11	90	Std Ox	5	9.81×10^{-4}	1.96×10^{-4}	4.31
19/11	90	Std Ox	5	9.81×10^{-4}	1.96×10^{-4}	4.31
3/8a	90	1.5×Std Ox	3.33	9.81×10^{-4}	2.94×10^{-4}	6.39
3/8b	90	1.5×Std Ox	3.33	9.81×10^{-4}	2.94×10^{-4}	6.39
4/8a	90	1.5×Std Ox	3.33	9.81×10^{-4}	2.94×10^{-4}	6.39
4/8b	90	1.5×Std Ox	3.33	9.81×10^{-4}	2.94×10^{-4}	6.39
10/12	90	2×Std Ox	2.5	9.81×10^{-4}	3.92×10^{-4}	8.42
11/12	90	2×Std Ox	2.5	9.81×10^{-4}	3.92×10^{-4}	8.42
12/12	90	2×Std Ox	2.5	9.81×10^{-4}	3.92×10^{-4}	8.42
13/12	90	2×Std Ox	2.5	9.81×10^{-4}	3.92×10^{-4}	8.42
22/12a	90	2.5×Std Ox	2	9.81×10^{-4}	4.90×10^{-4}	10.41
22/12b	90	2.5×Std Ox	2	9.81×10^{-4}	4.90×10^{-4}	10.41
23/12	90	2.5×Std Ox	2	9.81×10^{-4}	4.90×10^{-4}	10.41
24/12	90	2.5×Std Ox	2	9.81×10^{-4}	4.90×10^{-4}	10.41
25/7	90	1.5×Ox, Ca/1.5	2.22	6.54×10^{-4}	2.94×10^{-4}	4.45
26/7	90	2×Ox, Ca/2	1.25	4.91×10^{-4}	3.92×10^{-4}	4.49
29/7	80	Std Ox	5	9.81×10^{-4}	1.96×10^{-4}	4.31
30/7	80	Std Ox	5	9.81×10^{-4}	1.96×10^{-4}	4.31
24/11a	80	Std Ox	5	9.81×10^{-4}	1.96×10^{-4}	4.31
24/11b	80	Std Ox	5	9.81×10^{-4}	1.96×10^{-4}	4.31
25/11	80	Std Ox	5	9.81×10^{-4}	1.96×10^{-4}	4.31
31/7	100	Std Ox	5	9.81×10^{-4}	1.96×10^{-4}	4.31
22/11a	100	Std Ox	5	9.81×10^{-4}	1.96×10^{-4}	4.31
22/11b	100	Std Ox	5	9.81×10^{-4}	1.96×10^{-4}	4.31
22/11c	110	Std Ox	5	9.81×10^{-4}	1.96×10^{-4}	4.31
23/11a	110	Std Ox	5	9.81×10^{-4}	1.96×10^{-4}	4.31
23/11b	110	Std Ox	5	9.81×10^{-4}	1.96×10^{-4}	4.31

3.5. The values of the growth rate and the relative supersaturation for each experiment are given in Appendix 7. The activity product was calculated, in terms of free ion concentrations, using the method described in Section 2.4, the relative supersaturation was calculated from eq 4.5 and the value of K_{sp} used was 2.24×10^{-9} .

Figure 4.4 shows the square root of the growth rates from all the batch experiments plotted against the relative supersaturation. All the data from experiments using solutions with different initial supersaturations, solutions with different calcium to oxalate ratios and agitation rates collapse onto a straight line. The line fitted to the data is

$$\sqrt{G} = 0.277(S - 1) \quad (4.6)$$

where the growth rate is measured in units of $\mu\text{m}/\text{min}$, the error in the constant of proportionality is 2.1×10^{-3} and the regression coefficient is 0.968.

There are over 350 growth rates plotted in Figure 4.4 from some 35 different experiments with a wide range of experimental conditions, yet a parabolic rate law, appropriate for surface spiral growth, accurately describes all the data. The results also support the equilibrium calculation, in that they show the growth rate tends to zero when $S = 1$.

There is some scatter in the values of the growth rates, particularly at high supersaturation. An error analysis is presented in Section 4.6, but the errors calculated are not large enough to account for this scatter. However, there is another point to consider, Hounslow (1990) also found some scatter in the growth rates and aggregation rate constants determined from the program *Batch*. He observed that:

“Values of the growth and aggregation rate are deduced from estimates of rates of change, a process which must induce error.”

The error introduced will be greatest at high growth and aggregation rates which would account, to some extent, for the scatter in the data, particularly the data at a relative supersaturation of approximately 3.2.

Errors in the relative supersaturation are presented later when the errors in the kinetic rate constants are discussed in Section 4.6. The values of the concentrations used to calculate the activity product are inferred from the total crystal volume and initial seed mass. Any error in calculating the activity product and hence relative supersaturation will be systematic and lead

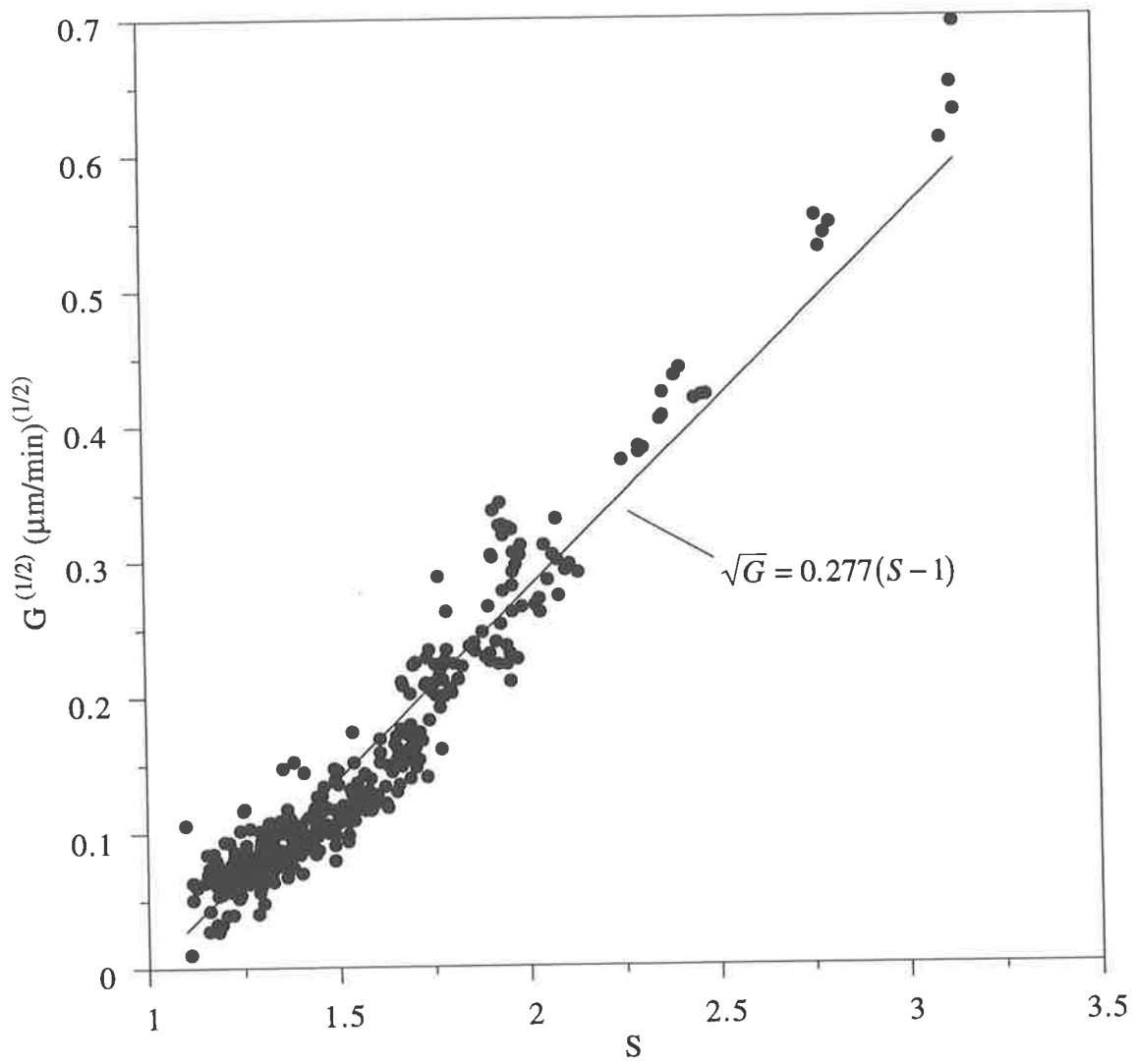


Figure 4.4 The dependence of the growth rate on relative supersaturation for all the batch experiments.

to a translation of the data points along the abscissa. In Section 3.2.2 it was shown that the Multisizer can accurately measure crystal volume, consequently any random errors in the value of the relative supersaturation will be small.

From the results presented the growth rate can be accurately calculated by eq 4.6 over a wide range of supersaturation from the relative supersaturation, regardless of the calcium to oxalate ratio in the metastable solution, or the agitation rate. Using the method described in Section 2.4 the activity product, in terms of free ion concentrations, can be determined from total concentrations. The fact that all the growth rates are described by eq 4.6 will be very useful in Chapter 9 in which the growth and aggregation of calcium oxalate in a tubular crystalliser is investigated. Rather than having to use experimental data to determine the growth rate, it can be calculated from eq 4.6 provided the solution composition is known.

4.4.2 Discussion

While the growth rates are well described by eq 4.6 for all the experimental conditions investigated it is important to compare the results from the current work with those available in the literature.

The dependence of the growth rate on the agitation rate

The experimental results indicate that the growth rate does not depend on the agitation rate. This is consistent with the findings of Brečević *et al.* (1986) who observe no difference between growth rates in magnetically stirred and unstirred batch experiments. Meyer and Smith (1975a) also find that the growth rate is not influenced by the hydrodynamics of the experimental system.

Nielsen and Toft (1984), state that for crystals larger than 5 μm the following criterion may be used: if the growth rate depends on the stirring rate, growth is transport controlled, whereas if the growth rate is insensitive to stirring rate, then growth is surface controlled. The results presented in Section 4.4.1 are consistent with this statement as the growth rate is not dependent on the shaking rate and is best described by a surface controlled mechanism. A similar observation is made by Nancollas and Gardner (1974) who find the growth rate in a batch system does not depend on the mode of stirring and conclude that this rules out bulk diffusion of ions to the crystal surface as the rate controlling step and suggests a surface controlled mechanism.

The dependence of the growth rate on supersaturation

The growth rates determined from many studies of the growth of calcium oxalate cannot be compared with those of this work for two main reasons. Firstly, in many cases the

supersaturation at which the growth rates were obtained is not reported. This is common in studies using an MSMR, in which the growth rate is correlated with the nucleation rate as both are dependent on the supersaturation in the crystalliser. Rather than calculating the supersaturation, the composition of the feed solutions is given. For example results are presented in this manner by Randolph and Drach (1981), Rodgers and Garside (1981) and Miller *et al.* (1977). Often it is the effect of an inhibitor on the growth rate that is of primary interest in which case the growth rates are plotted against the inhibitor concentration, for example, Springman *et al.* (1986) and Robertson and Scurr (1986).

Secondly, in some studies the true growth rate is not calculated but rather some empirical parameter in terms of the change in crystal volume, or ion concentrations is defined to represent the growth rate. These parameters do not take into account the effect that other factors such as aggregation have on crystal enlargement. Examples of workers who have used this approach are Robertson and Peacock (1972), Ryall *et al.* (1981b) (crystal volume), Ligabue *et al.* (1979) and Fellström *et al.* (1982) (ion concentration).

There are also many studies in which a parabolic dependence of the growth rate on some measure of supersaturation has been found to follow a second order rate law such as eq 4.6.

Nancollas and Gardner

Nancollas and Gardner (1974) study the precipitation reaction by measuring properties of the fluid rather than the particulate phase. They follow the rate of growth using solution conductivity measurements to determine the decrease in ion concentrations. They find the relationship between the depletion of the ion concentration and supersaturation, if the initial calcium and oxalate concentrations are equal, is

$$-\frac{d[Ca^{2+}]}{dt} = k([Ca^{2+}] - [Ca^{2+}]_0)^2 \quad (4.7)$$

where the subscript, 0, refers to equilibrium conditions. If the initial calcium and oxalate concentrations are different then,

$$-\frac{dN}{dt} = k' N^2 \quad (4.8)$$

where the supersaturation, N , is the number of moles of calcium oxalate that must be deposited to reach equilibrium and is calculated from

$$K_{sp} = ([Ca^{2+}] - N)([Ox^{2-}] - N) \quad (4.9)$$

The depletion of the ion concentration and the growth rate are related by

$$-\frac{d[Ca^{2+}]}{dt} \propto A_T G \quad (4.10)$$

where A_T is the total crystal surface area per unit volume. Clearly for solutions with equal calcium and oxalate concentrations, $[Ca^{2+}] \propto \sqrt{AP}$, thus eq 4.7 is of the same form as eq 4.6. Also the number of moles of calcium oxalate that must be precipitated to reach equilibrium will be related to the relative supersaturation, thus eq 4.8 is also consistent with eq 4.6.

To calculate the growth rate from measurements of the change in ion concentration the total crystal surface area must be known. It is difficult to determine the total crystal surface area and also it increases as the crystals grow. As experimental measurements of the total crystal surface area are not reported by Nancollas and Gardner, actual growth rates cannot be calculated from their data and compared with those of the current work.

In contrast with the findings of this work, in which the calcium to oxalate ratio had no effect on the growth rate, Nancollas and Gardner observe the rate constant in eq 4.8 is appreciably higher in experiments using a solution in which calcium is in excess. This difference can be accounted for by considering the effect of aggregation, which is ignored in the analysis of Nancollas and Gardner. In Section 4.5 it is shown that the aggregation rate is dependent on the oxalate ion concentration. For metastable solutions with a fixed activity product, the higher the calcium concentration, the lower the oxalate concentration will be. Consequently, in a solution in which calcium is in excess, the oxalate concentration will be lower and the aggregation rate will also be lower. A lower aggregation rate, will lead to greater total crystal surface area and from eq 4.10 the observed rate of depletion of the calcium ion concentration will be higher.

Meyer and Smith

Meyer and Smith (1975a) determine crystal growth rates from measurements of the change in the calcium concentration in solution. Their results are consistent with those of Nancollas and Gardner (1974) and may be described by eqs 4.7 and 4.8. Therefore the results of Meyer and Smith are consistent with eq 4.6 and the findings of this work.

There are also many other studies in which the kinetics for the growth of calcium oxalate are found to be of the form of eq 4.6, these include: Gardner (1975) for stirred batch experiments with equal calcium and oxalate ion concentrations, Singh *et al.* (1987) using

conditions of constant composition over a range of supersaturation, Nielsen and Toft (1984) for batch crystallisation and Sheehan and Nancollas (1980) using a constant composition method.

Kavanagh (1992) notes that for restricted ranges of conditions, eq 4.6 may be simplified to the form of eq 4.7, involving calcium concentrations (Ito and Coe, 1977) or oxalate concentrations (Libague *et al.*, 1979) to describe the growth of calcium oxalate. Further, Kavanagh shows that more complex expressions such as those used by Blomen *et al.* (1983), who describe growth in terms of the uptake of a radioactive tracer from solution, which is fitted by an orthogonal hyperbola, are also consistent with eq 4.6.

There are also a number of studies in which the growth rate correlation is not the same as eq 4.6, however it can be shown the results are still consistent with eq 4.6.

Nielsen

Nielsen (1960) shows the relationship between the growth rate and the activity product is given by

$$G \propto AP^2 - K_{sp}^2 \quad (4.11)$$

Which implies the growth rate is fourth order rather than second order. Data are reported in which the growth rate, dl/dt , where l is the length of a cube of the same volume as one of the growing crystals, is proportional to the 3.3rd power of the concentration of the complex ion, CaOx. From the association equation for the complex formation, eq 2.17, the activity product and the relative supersaturation can be calculated.

Figure 4.5 shows the data of Nielsen plotted against the relative supersaturation, it can be seen that the data are well described by an equation of the form of eq 4.6. While these data show the same dependence of the growth rate on the relative supersaturation as the data from the current work, the range of the relative supersaturation and growth rate are different. However, it is difficult to assess the accuracy of the relative supersaturation calculated from Nielsen's data, as neither the value for the solubility product, or the temperature at which the experiments were conducted is given. Also there are no details of other ions that might have been present in the solutions, for example sodium. As discussed in Section 2.6, the formation of the complex NaOx^- , has a significant effect on the free oxalate ion concentration, consequently, the values of the relative supersaturation calculated from Nielsen's data must remain uncertain.

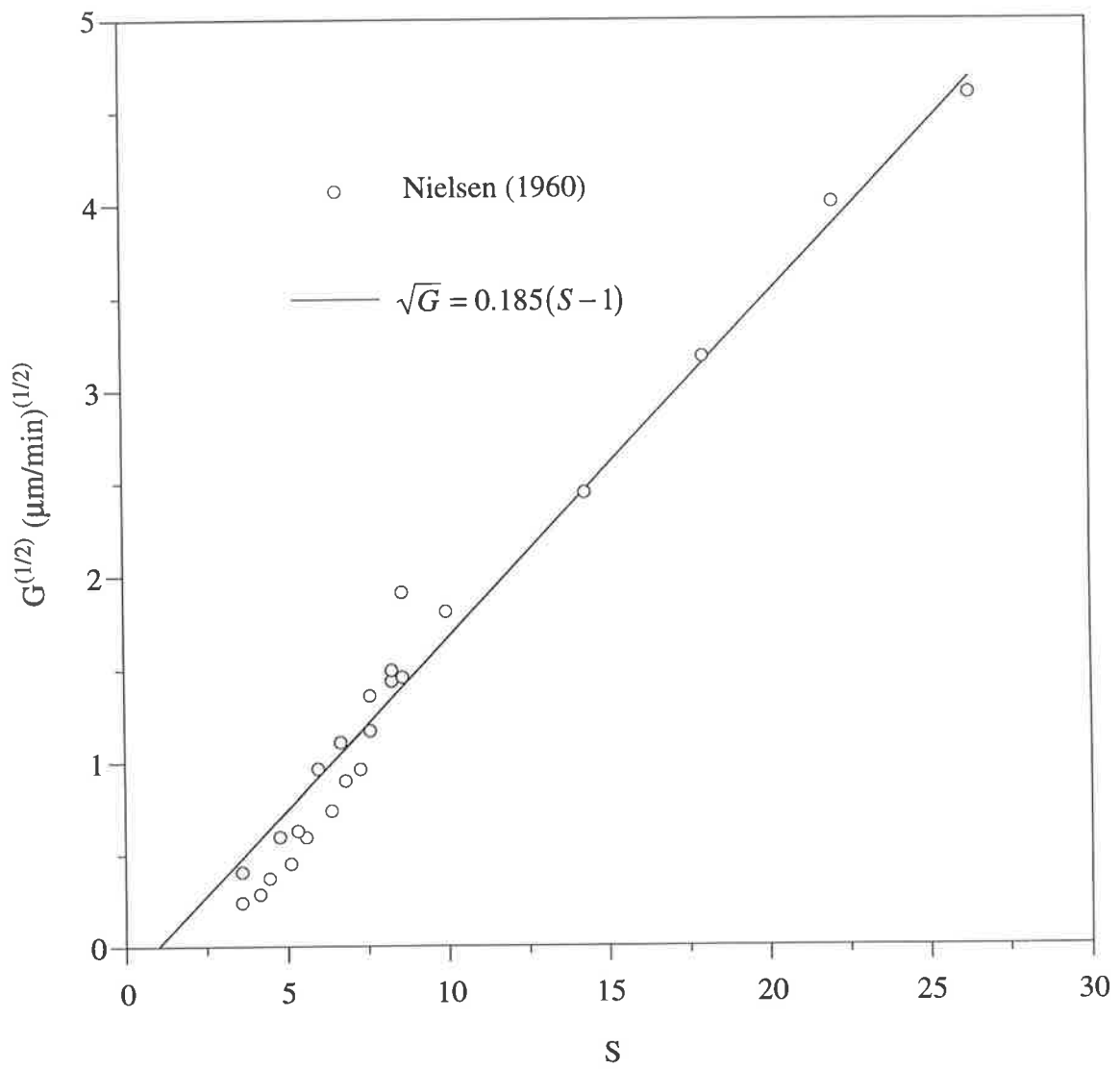


Figure 4.5 Growth rates from the data of Nielsen (1960) plotted against relative supersaturation

Hounslow

Hounslow (1990), summarises the results presented in two earlier papers on the growth and aggregation of calcium oxalate by Hounslow *et al.* (1988a) and (1988b). Data from experiments using the seeded batch technique of Ryall *et al.* (1981b) are analysed by the program *Batch*. If supersaturation is defined by

$$S^* = AP - K_{sp} \quad (4.12)$$

the growth rate is found to be directly proportional to supersaturation,

$$G = k_G (AP - K_{sp}) \quad (4.13)$$

The batch experiments described in Chapter 3 are based on the protocol of Ryall *et al.* (1981b) and the growth rates were determined using the program *Batch*. Despite the similarities in the experimental protocol and method of data analysis, the findings of Hounslow seem to differ with those of this work, however it can be shown that this is not the case.

As already discussed in Section 2.6 Hounslow used total rather than free ion concentrations to calculate the activity product, as a consequence the values of the activity product will be incorrect. But it is also shown in Section 2.6 that this will only change the value of the constant in eq 4.13, not the relationship between the growth rate and supersaturation.

The dependence of the growth rate on supersaturation will be different if there is an error in the growth rate. In the current work and that of Hounslow the growth rates were determined using *Batch*, however the CSDs were measured with different Coulter Counters. The experiments in this work and those reported by Hounslow were conducted in the same laboratory, in the Department of Surgery at Flinders Medical Centre. The CSDs used by Hounslow were measured with a Coulter TAI, whereas the CSDs in the current work were measured with a Coulter Multisizer. A batch experiment was conducted in which the same samples were analysed by both counters and it was found that the crystal volume measured by the TAI was always greater than that measured by the Multisizer. When the CSDs from the two counters were analysed by *Batch* different growth and aggregation rates were obtained for the same experiment.

The CSDs reported by Hounslow were corrected to allow for the error introduced by the TAI counter and analysed by *Batch*, and the correct value of the activity product was calculated using the method in Section 2.4. Figure 4.6 shows the growth rates calculated

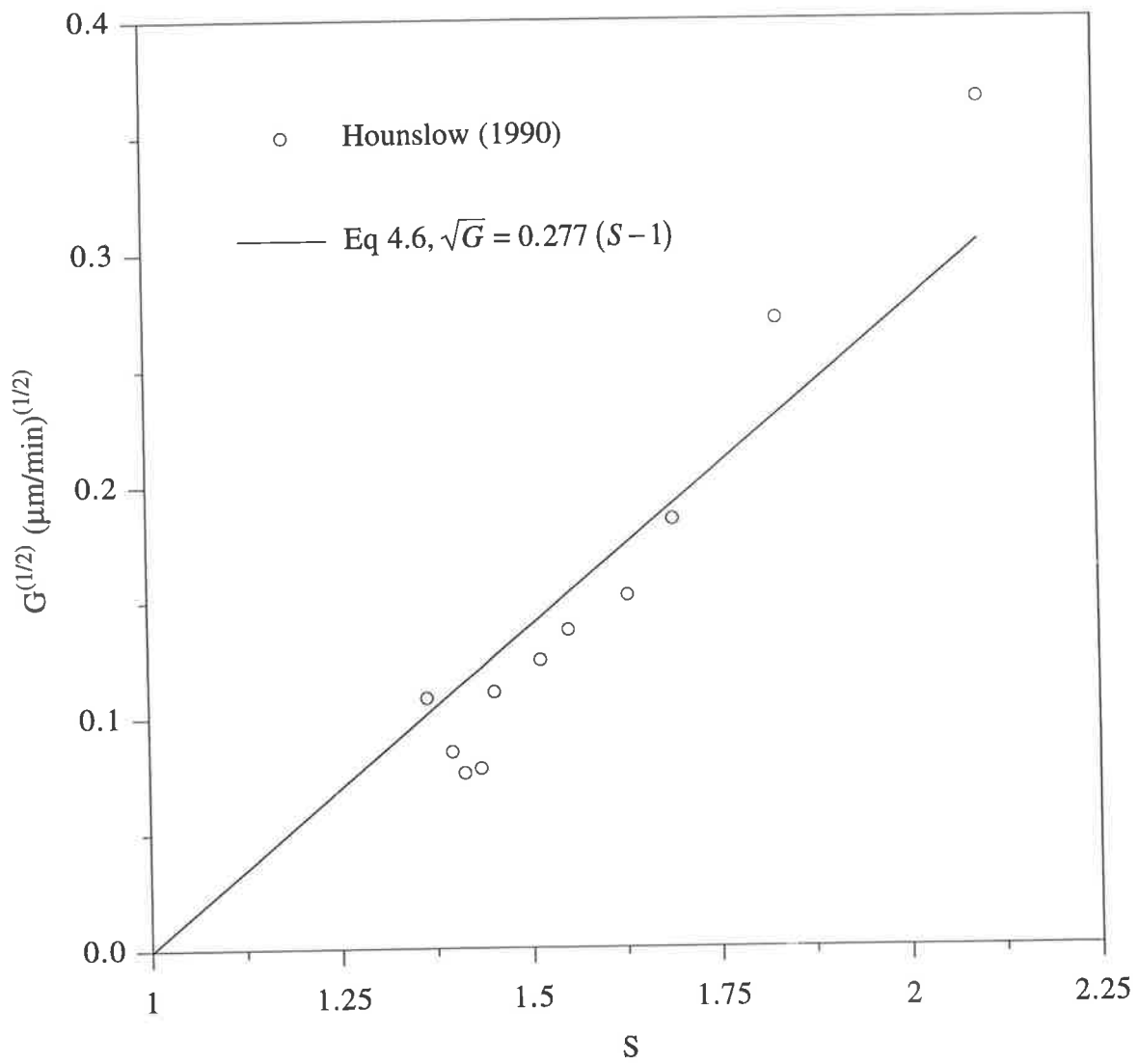


Figure 4.6 Growth rates from the modified data of Hounslow (1990) plotted against relative supersaturation, together with eq 4.6.

from the corrected data, it can be seen that they are well described by eq 4.6, and the values of the growth rates are similar to those obtained in this work.

Finally, there are some studies which find the growth kinetics of calcium oxalate are not second order but rather fourth order in supersaturation. Two such studies are those of Škrtić *et al.* (1984) and Marković and Füredi-Milhofer (1988). Both these authors model growth using the following equation

$$\frac{d\alpha}{dt} \alpha^{-2/3} = K N_t^{1/3} (C - C_s)^g \quad (4.14)$$

where N_t is the total number of crystals, C and C_s are the calcium concentrations in the solution and at equilibrium and α is the degree of reaction defined as $\alpha = V_t/V_{max}$, where V_t is the volume of material deposited at time, t and V_{max} is the maximum possible precipitate volume.

Škrtić *et al.* (1984) find the value of g in eq 4.14 is 3.6 ± 0.3 , Marković and Füredi-Milhofer (1988) find $g = 3.9 \pm 0.1$. The experimental protocol used by both authors is to nucleate crystals, then observe them grow and aggregate. The experiments are divided into sections in which each mechanism is dominant. The results quoted above are for the period in which growth dominates and it is claimed that the total number of crystals is constant. However, the data of Škrtić *et al.* (1984) reveal that over the time in which the growth rate is calculated the total number of crystals halves. From the data of Marković and Füredi-Milhofer (1988), when the growth rate is calculated the total number of crystals decreases by approximately one third. The significant decrease in the number of crystals is characteristic of aggregation, which is ignored in the calculation of the growth rates, which must make the values of g reported questionable.

A concluding remark on growth rates

All the data studied from other investigations of the growth of calcium oxalate are consistent with the results of the current work, which may be summarised as:

Regardless of the solution composition and agitation rate the growth rate, in $\mu\text{m}/\text{min}$, may be related to the relative supersaturation by:

$$G = (0.0767 \pm 0.0012)(S - 1)^2$$

4.5 THE AGGREGATION RATE

In contrast to crystal growth, there are few theories and investigations into the dependence of the aggregation rate on supersaturation. In a batch system Hounslow (1990) finds the aggregation rate constant is directly proportional to supersaturation defined in eq 4.12, giving

$$\beta_0 = k_{agg} (AP - K_{sp}) \quad (4.15)$$

In a continuous Couette agglomerator Hartel and Randolph (1986b) find that the aggregation constant is highly dependent on the oxalate concentration. They use the oxalate concentration to measure supersaturation as the calcium concentration was not known.

4.5.1 Analysis of experimental data

In this section the data from the batch experiments are studied with the aim of determining the dependence of the aggregation rate constant on supersaturation and agitation rate.

The aggregation rate constants and activity product were calculated from the same experimental data using the same method of analysis as the growth rates presented in the previous section. The aggregation rate constants calculated from *Batch* are given in Appendix 7. The conditions in each of the experiments are given in Table 4.3.

The dependence of the aggregation rate constant on supersaturation

As the experiments reported in Chapter 3 are similar to those of Hounslow (1990), the supersaturation is measured by using the activity product. Figure 4.7 shows the aggregation rate constant plotted against the activity product for the batch experiments conducted using a standard metastable solution. The data from these experiments are well described by the following equation:

$$\beta_0 = 3.74 \times 10^{25} AP^{3.55} \quad (4.16)$$

with the errors in the constant of proportionality and the exponent being 7.03×10^{24} and 0.10, and the regression coefficient for the fit is 0.979.

Next the data from the other experiments in which the initial supersaturation was increased by the addition of variable amounts of oxalate to the metastable solution are considered. However, rather than plotting the aggregation rate constants from every experiment, the data obtained from experiments with the same initial supersaturation were averaged. A total of 10

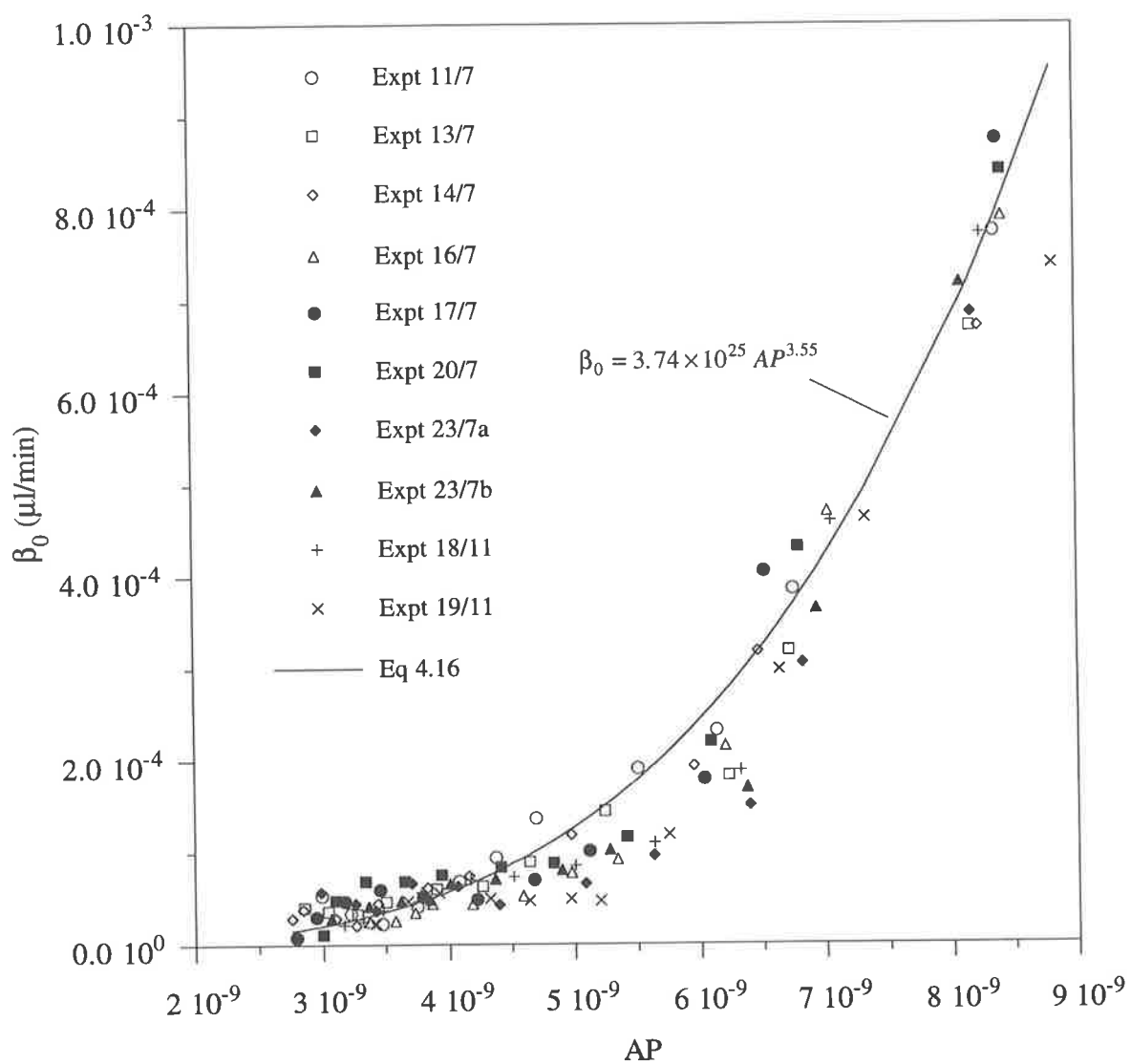


Figure 4.7 The dependence of the aggregation rate constant on the activity product for experiments using a standard metastable solution (Ca:Ox =5:1).

experiments were conducted using the standard metastable solution and 4 experiments with each of the other initial oxalate concentrations.

The aggregation rate constant is plotted against the activity product for the experiments conducted using solutions with different initial oxalate concentrations in Figure 4.8. The errors shown are plus-or-minus one standard error in the mean. It can be seen that over the complete range of supersaturation studied the aggregation rate constant does not correlate with the activity product. There is substantial scatter in the data, that cannot be attributed to either averaging the data from each experiment, or the errors calculated in Section 4.6. For a given value of the activity product the higher the oxalate concentration the greater the value of the aggregation rate constant.

The dependence of the aggregation rate constant on oxalate ion concentration

All the metastable solutions used in the experiments had the same initial calcium concentration, the supersaturation was increased by increasing the oxalate concentration. As no other parameters were altered this suggests that the aggregation rate may be dependent on the oxalate concentration rather than the activity product or supersaturation.

The free oxalate ion concentration can be calculated from the total calcium and oxalate concentrations using the method described in Section 2.4. In Figure 4.9 the aggregation rate constant is plotted against the oxalate concentration, as in Figure 4.8 the data from each series of experiments were averaged and the mean, plus-or-minus one standard error is plotted.

The aggregation rate constants correlate well with the oxalate ion concentration with the exception of the data at the highest oxalate concentrations. As mentioned in Section 4.4.2 there are errors associated with the method used by *Batch* to determine the aggregation rate constant. Even though this error will be greatest at high aggregation rates, it is probably not enough to account for the deviation observed. However, the correlation between the aggregation rate constant and the oxalate concentration is much better than that with the activity product. Therefore to investigate the dependence of the aggregation rate on the agitation rate the oxalate concentration will be used as the independent variable, even though the experiments with different agitation rates used a standard metastable solution.

The dependence of the aggregation rate constant on the agitation rate

As with the experiments used to investigate the effect of supersaturation, a number of runs were conducted at each agitation rate. The data from each series of experiments were

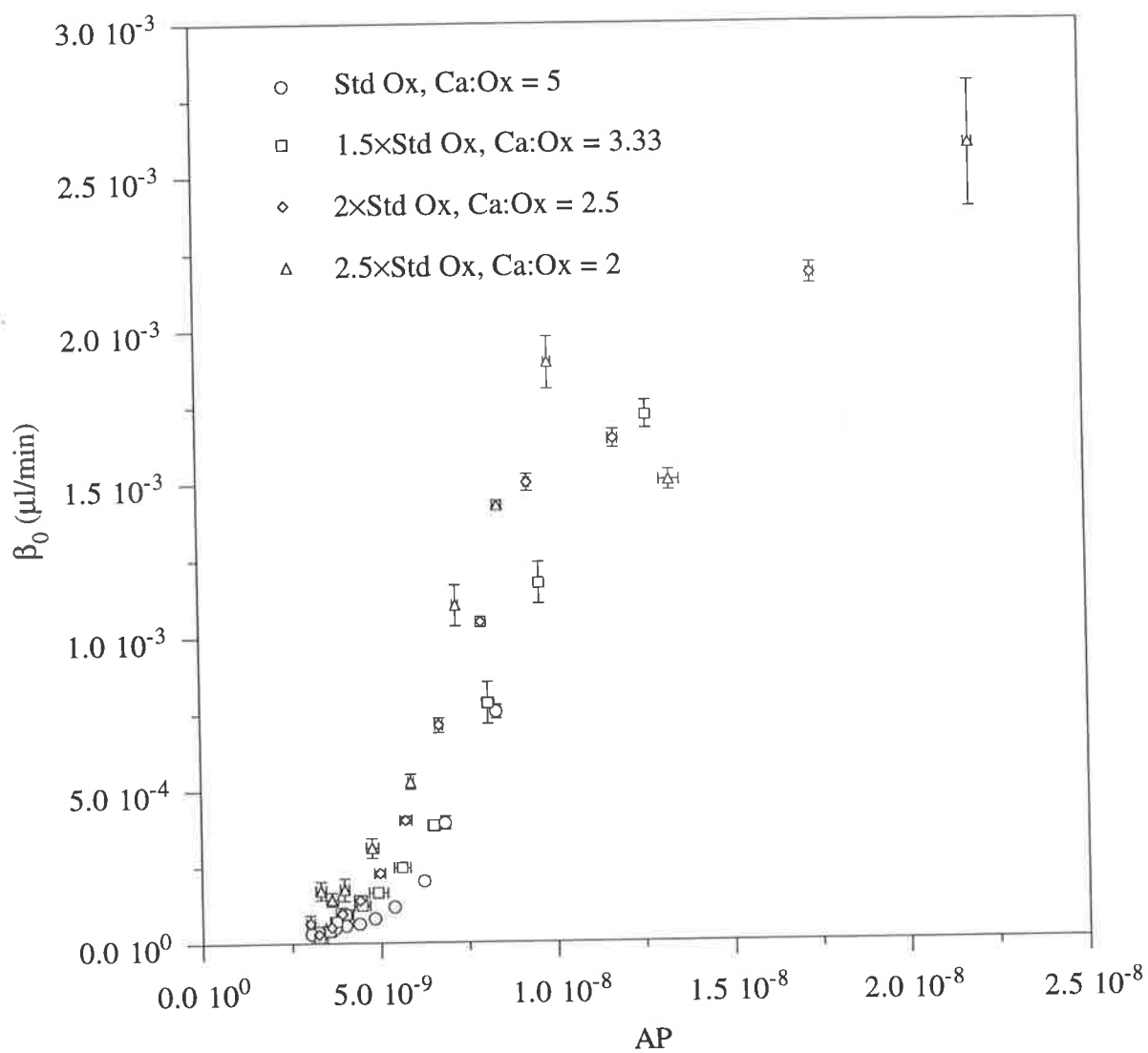


Figure 4.8 The dependence of the aggregation rate constant on the activity product for metastable solutions with different initial supersaturation and calcium to oxalate ratios.

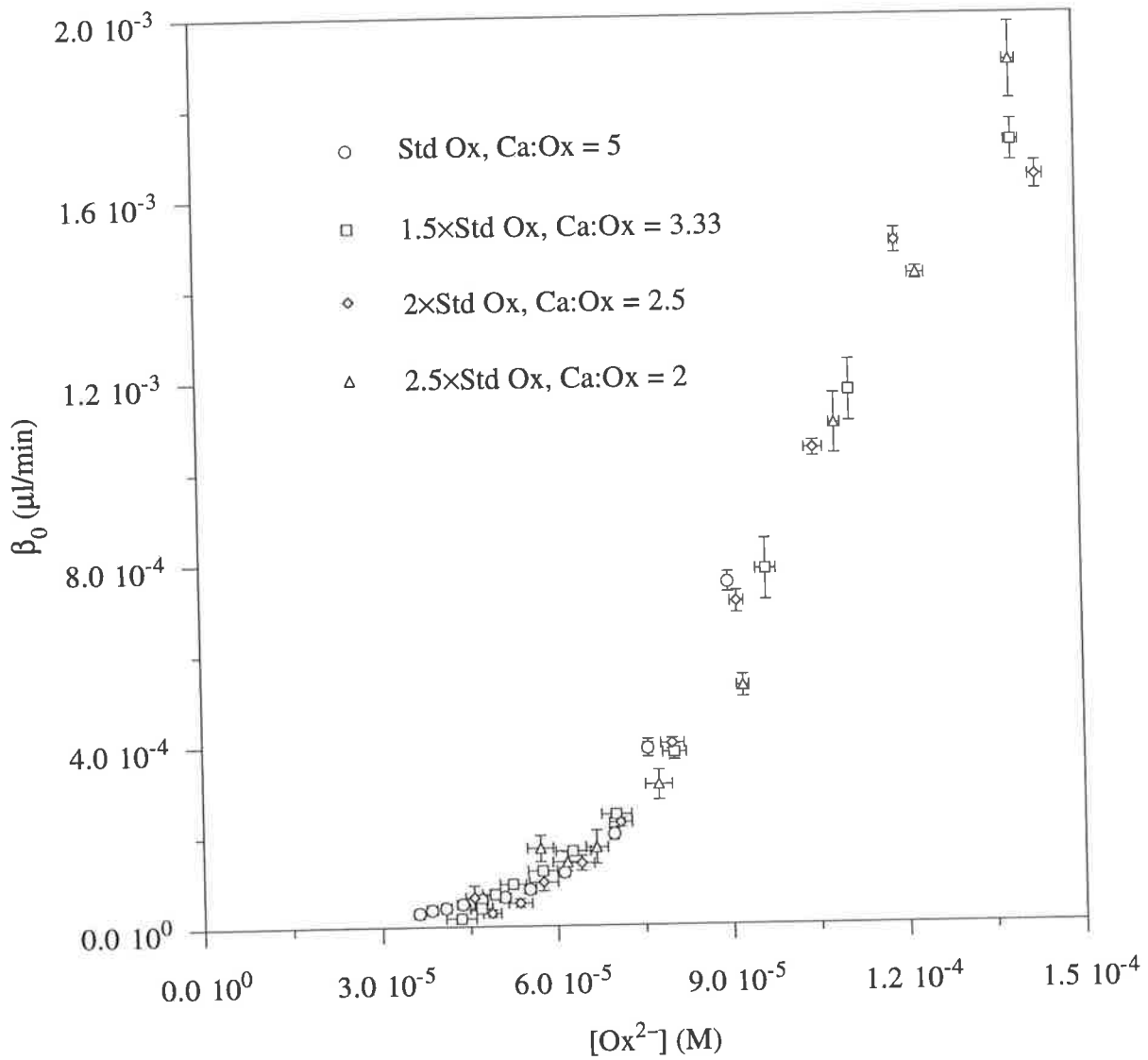


Figure 4.9 The dependence of the aggregation rate constant on the oxalate ion concentration for metastable solutions with different initial supersaturation and calcium to oxalate ratios.

averaged and it is the mean plus-or-minus one standard error that is used to display the results.

In Figure 4.10 the aggregation rate constants from the experiments using different agitation rates are plotted against the oxalate concentration. It can be seen that at each agitation rate the dependence of the aggregation rate on the oxalate concentration is of the same form, but the aggregation rate constant is also dependent on the agitation rate. For a given oxalate concentration the aggregation rate constant increases as the agitation rate decreases, over the entire range of oxalate concentrations the aggregation rate constant at the lowest agitation rate is some three times that at the fastest agitation rate.

The dependence of the aggregation rate constant on the agitation rate is further investigated in Figures 4.11 (a) and (b) in which the aggregation rate constants, from the same time interval but different experiments are plotted against the reciprocal of the agitation rate. The reason for plotting data from the same time interval together is that as an experiment proceeds the oxalate concentration decreases as a result of crystal growth. As a standard metastable solution was used in all the experiments, then data obtained at a given time corresponds approximately to a given oxalate concentration, and growth rate. Therefore the data from each time interval corresponds to data at a constant growth rate.

The aggregation rate constants plotted in Figure 4.11 (a) come from the samples analysed in the first 20 minutes of the experiment. It can be seen that at each time interval the aggregation rate constant varies linearly with N^{-1} .

In Figure 4.11 (b) the aggregation rate constants corresponding to the data collected from 30 to 60 minutes are plotted against the reciprocal of the agitation rate. It can be seen that the aggregation rate constant no longer varies linearly with N^{-1} . As the experiment proceeds and the growth rate decreases, the variation in the aggregation rate with the agitation rate is less well defined.

4.5.2 Discussion

In order to understand the factors that might affect the aggregation rate it is important to have some concept of how aggregation occurs in solution. For a stable aggregate to form from individual crystals, the crystals have to come into contact, or collide, and then remain together. The aggregation kernel must take these two events into account: it must describe the frequency and also the effectiveness of collisions. In solution, the frequency of

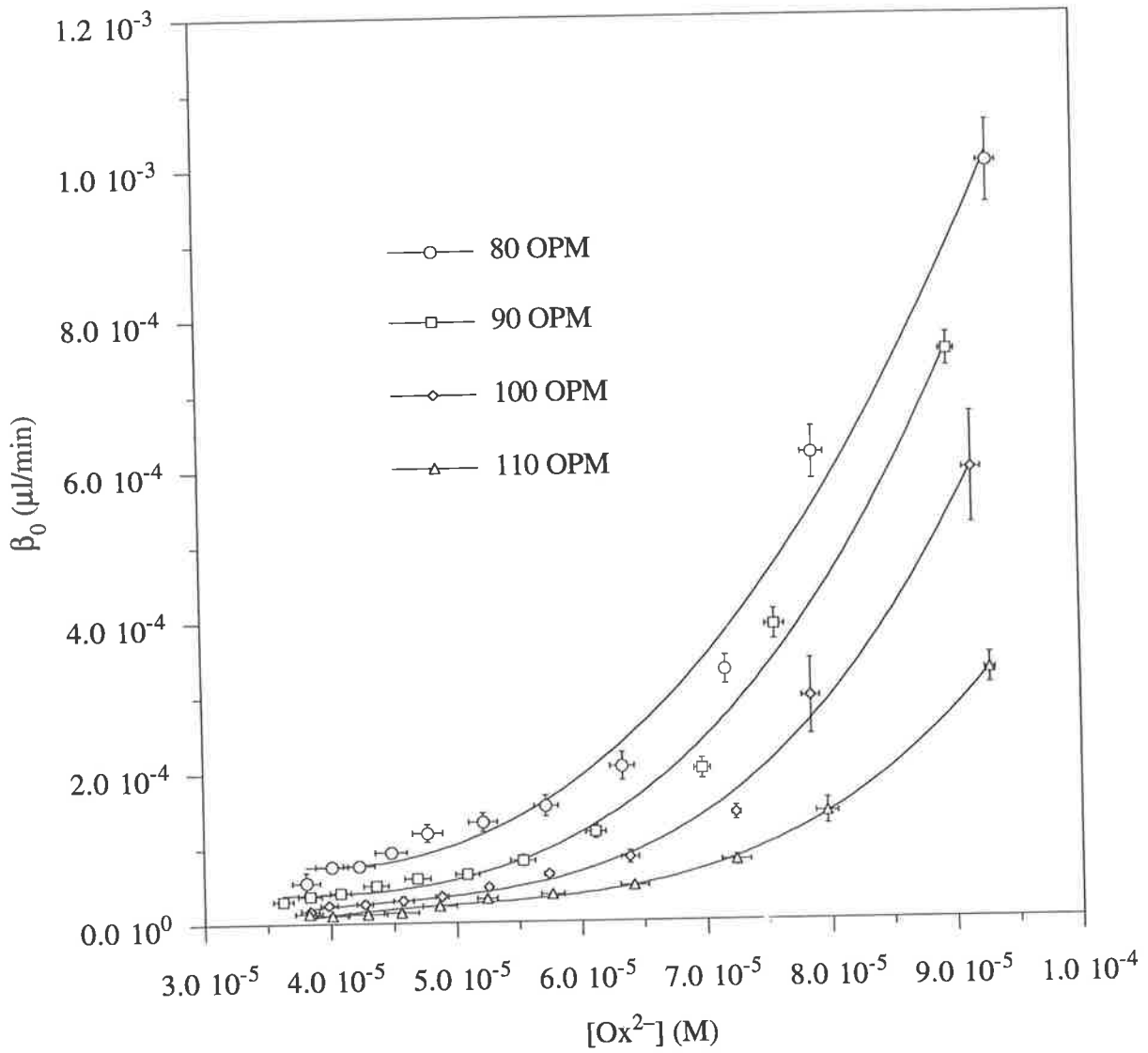
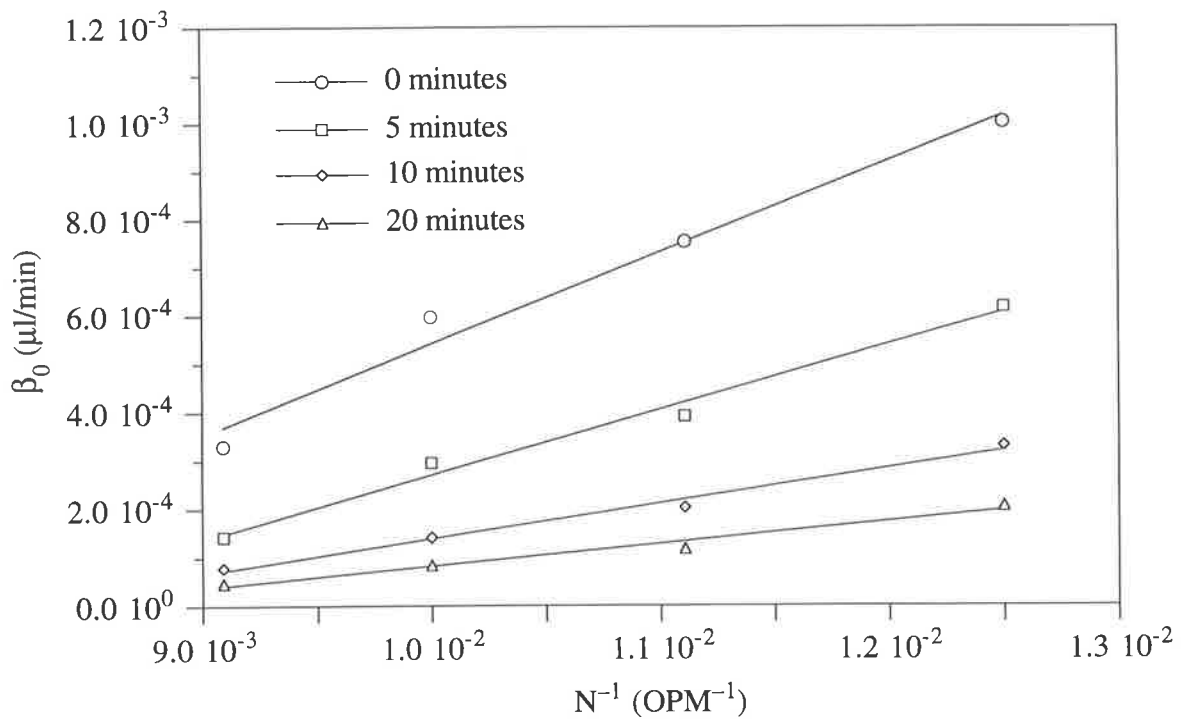
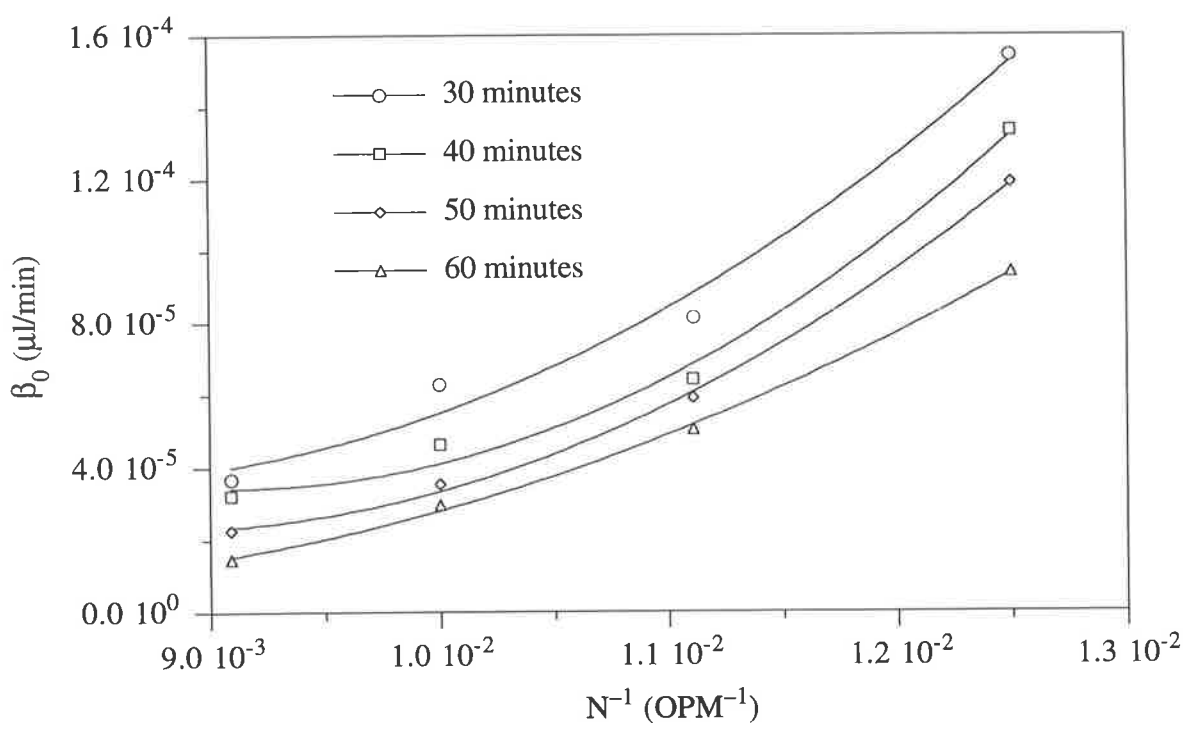


Figure 4.10 The dependence of the aggregation rate constant on the agitation rate for standard metastable solutions (Ca:Ox = 5).



(a)



(b)

Figure 4.11 The dependence of the aggregation rate constant on the reciprocal of the agitation rate in batch experiment for (a) the first 20 minutes and (b) from 30 to 60 minutes.

collisions will be determined by the hydrodynamics, and it is to be expected that the growth rate, and therefore supersaturation, will play a role in the effectiveness of collisions.

It has been observed that the aggregation rate decreases as the agitation rate increases and correlates with the oxalate concentration rather than with supersaturation. The first experimental observation can be explained by the brief outline of the aggregation mechanism given above, however the second cannot. The aggregation mechanism must be considered in greater detail to find an explanation for the experimentally observed behaviour of the aggregation rate. This will be the focus of the Chapter 5, in this section the aggregation rate constants are compared with results from other studies in the literature.

The mathematical complexity associated with solving the population balance for simultaneous growth and aggregation has meant that there are very few studies in which *true* growth and aggregation rates are reported. Often the effect of an inhibitor on aggregation has been studied, and an empirical parameter involving the change in the total number of crystals is used as a measure of the aggregation rate, for example Robertson *et al.* (1973), and Ryall *et al.* (1981c).

There are, to the knowledge of the author, only two studies that report aggregation rates rather than an empirical parameter: those of Hartel and Randolph (1986) and Hounslow (1990).

Hartel and Randolph

Hartel and Randolph use a Couette agglomerator to study the aggregation of calcium oxalate crystals generated in an MSMPR. As mentioned in Section 4.2 they find that the kernel of Thompson (1968) best fits their data, which contradicts the findings of this work and of Hounslow (1990) in which a size-independent kernel is most appropriate. It is also at odds with Smit *et al.* (1993) who find that the Thompson kernel is an instantly gelling kernel in a continuous system. Smit *et al.* reflect on how a gelling kernel might be used to describe a non-gelling system. Hartel and Randolph include in their model a breakage function. Smit *et al.* point out that this approach is open to some criticism as the breakage rate calculated may be artificially large in order to stop the occurrence of mathematical gelation when modelling the experimental CSDs. Consequently the values of the aggregation rate constants calculated by Hartel and Randolph must be questionable, for this reason the values are not compared with those from this work. However, a comparison of the qualitative behaviour of the aggregation rate constant can be made.

Hartel and Randolph find that the aggregation rate constant is highly dependent on the oxalate concentration and the dependence is non-linear, which is consistent with the findings of this work. Also Hartel and Randolph find that at the same oxalate concentration the aggregation rate constant depends on the rate of rotation of the Couette agglomerator. This observation is consistent with the finding of the current work that the aggregation rate is dependent on the agitation rate. Both the rate of rotation in the Couette agglomerator and the agitation rate must inevitably be related to the shear rate in the fluid.

Hounslow

Hounslow (1990) finds that the aggregation rate constant is directly proportional to the supersaturation, as given by eq 4.12. The range of supersaturation for which eq 4.12 is valid is lower than that considered in this work. However, the composition of the standard metastable solution described in Section 3.3.2 is the same as that used by Hounslow. The results from the experiments using a standard metastable solution can be compared to those of Hounslow, provided the data are modified, as described in Section 4.4.2.

In Figure 4.12 the aggregation rate constants obtained from the modified data of Hounslow are compared with those from this work for the experiments using a standard metastable solution and different agitation rates. The values of the aggregation rate constant from the data of Hounslow are higher than those from this work. There is no reason to believe the modification of the data is responsible for the difference in the values of the aggregation rate constant, as the same procedure produced growth rates in good agreement with those from this work. An agitation rate of 90 OPM was used in the experiments reported by Hounslow, an agitation rate less than 80 OPM would be required for the aggregation rate constants to be consistent with the results from this work.

It is possible that the state of aggregation of the seed crystals used in the experiments may be responsible for the observed difference in the aggregation rate constants. The mechanisms active in the aggregation of colloidal particles in ionic solutions can be described in a semi-quantitative way by the theory of Derjaguin, Landau, Verwey and Overbeek (DLVO), as presented, for example by Hiemenz (1986). This theory predicts that increasing the ionic strength of a solution is favourable for the formation of aggregates. There is a substantial difference between the ionic strength of the seed suspensions from this work and those of Hounslow. The seed crystals used in this work were suspended in 0.15 M saline and as shown in Figure 3.2 were aggregates of crystals approximately 1-2 μm in size. The seed crystals used in the work of Hounslow were suspended in distilled water. It is likely that the number of very small crystals less than 2 μm in size in these seeds is much higher than in the seeds used in this work.

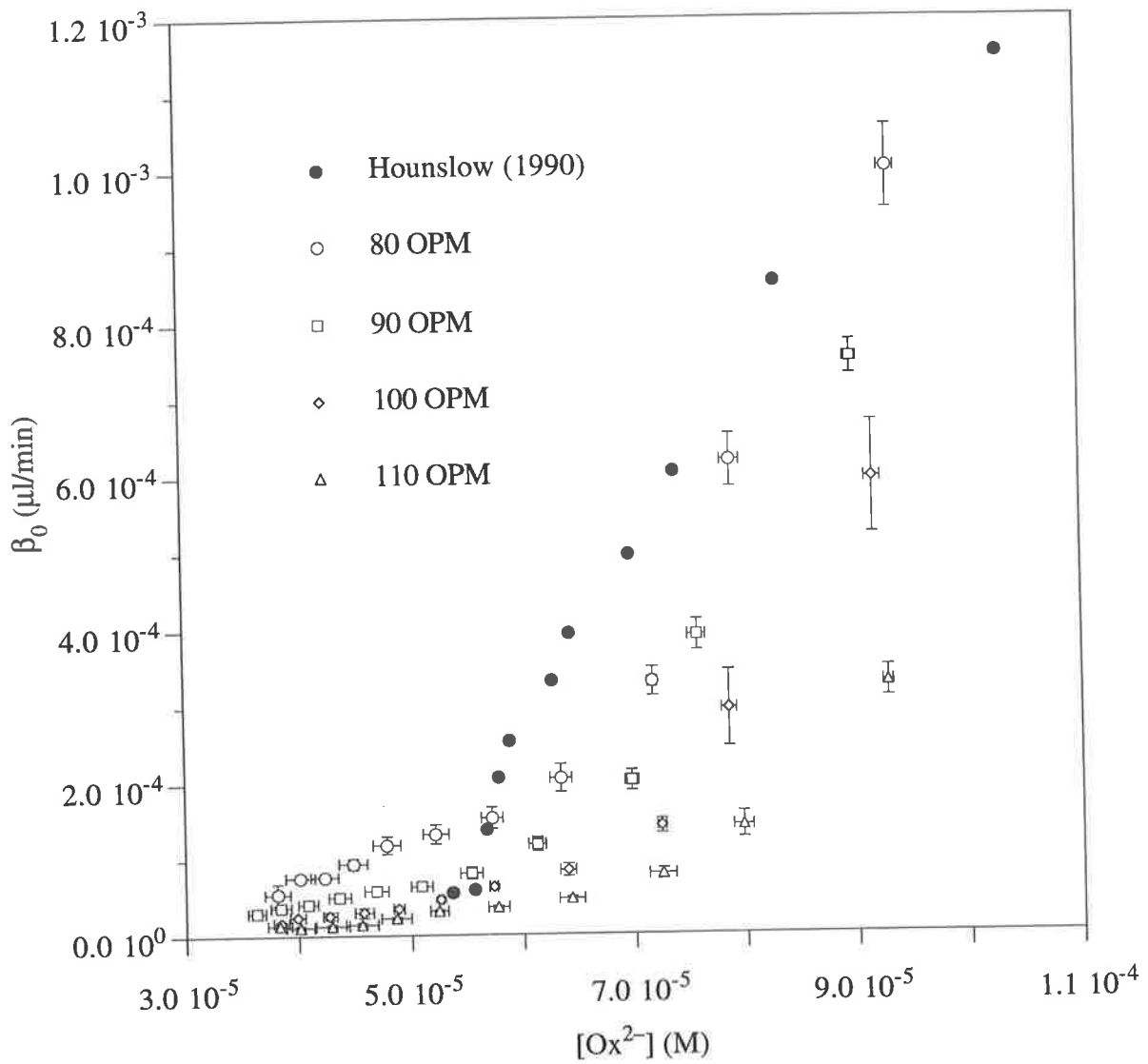


Figure 4.12 A comparison of the aggregation rate constants using a standard metastable solution (Ca:Ox = 5) and different agitation rates with those from the modified data of Hounslow (1990).

If a very large number of small crystals are present in the seed suspension added to the metastable solution in a batch experiment then as these crystals grow a large number of them will appear in the field of view of the particle size analyser. Consequently the value of the source function used in *Batch* to model the appearance of crystals in the field of view will be large. As the growth and aggregation rates are calculated from equations involving the source function, the magnitude of the source function must affect the values of the growth and aggregation rates. The source function will have a much more significant effect on the number of crystals, and hence the aggregation rate, than on the crystal volume and hence the growth rate. Crystals of a very small size contribute very little to the total volume, but significantly to the total number of crystals. The source function used in *Batch* is only an approximate correction for growth into the field of view of the particle size analyser and thus if the value of the source function is high results from *Batch* will be less reliable.

The source functions from this work and that of Hounslow were compared and it was found the values of the source function from the data of Hounslow were at least double those of the source function from this work. As the other experimental conditions are the same, a higher value of the source function will give a higher aggregation rate.

A concluding remark on the aggregation rates

It has been shown that the behaviour of the aggregation rate for the experimental conditions investigated is much more complex than the growth rate. The dependence of the aggregation rate on the oxalate ion concentration and agitation rate must inevitably be related to the aggregation mechanism. A mechanism for the aggregation of calcium oxalate in saturated and supersaturated solutions to explain the experimental observations is developed in Chapter 5.

4.6 ERROR ANALYSIS

As described in Section 3.3.3 CSDs were obtained from the four replicates of an experiment at regular time intervals. At each time interval the CSDs from the replicates were averaged, and the growth rate and aggregation rate constant were determined from the average CSD. In Appendix 8 an analysis of the errors associated with the growth rate and aggregation rate constant is presented. The propagation of error equation, together with some useful results from mathematical statistics, allow the error in a parameter, which is a function of different variables, to be estimated. Full details of the mathematical analysis and a sample calculation of the errors are given in Appendix 8.

4.6.1 Growth rate and relative supersaturation

The growth rates determined using *Batch*, from the experiments conducted to determine the effect of supersaturation on the growth and aggregation rates were used to investigate the magnitude of the errors in the growth rate and relative supersaturation.

Figure 4.13 is a semi-log plot of the growth rate against the relative supersaturation for experiments using metastable solutions with different initial supersaturations. The growth rate is plotted on a logarithmic scale so the magnitude of the error can be assessed as the growth rate decreases. The errors shown are plus-or-minus one standard error, as calculated in Appendix 8 from eq A8.16 for growth and A8.34 for relative supersaturation.

It can be seen that the magnitude of the error in the growth rate is quite small over the entire range of supersaturation used in the experimental investigation. The absolute value of the error is almost constant during an experiment, and therefore the percentage error is greater at lower growth rates. This can be explained by considering the form of the expression for the standard error in the growth rate, from eq A8.16

$$\sigma_{\bar{G}} \propto \bar{G} \sqrt{\left(\frac{\sigma_{m_2}}{\bar{m}_2}\right)^2 + \left(\frac{\bar{m}_3}{\bar{m}_2 \bar{G}}\right)^2} \quad (4.17)$$

The following observations were made from the experimental data: firstly, the ratio of the standard deviation in the second moment to the second moment was approximately constant throughout an experiment. This implies the first term on the right hand side of eq 4.17 is approximately constant. Secondly, \bar{m}_2 increased by a factor of approximately 1.5 in each of the experiments, whereas \bar{m}_3 increased by factors of 1.5 to 4 depending on the initial supersaturation of the metastable solution. As an experiment proceeds, the increase in \bar{m}_3 is greater than that in \bar{m}_2 , and the growth rate decreases, thus from the second term on the right hand side of eq 4.17 the standard deviation as a percentage of the growth rate will increase.

It can also be seen that the error in the activity product is approximately constant, and relatively small, over the range of supersaturation studied in the experiments.

4.6.2 Aggregation rate constant and oxalate ion concentration

The error analysis already described was also used to determine the error associated with the aggregation rate constant and the oxalate ion concentration. The expressions for the error in

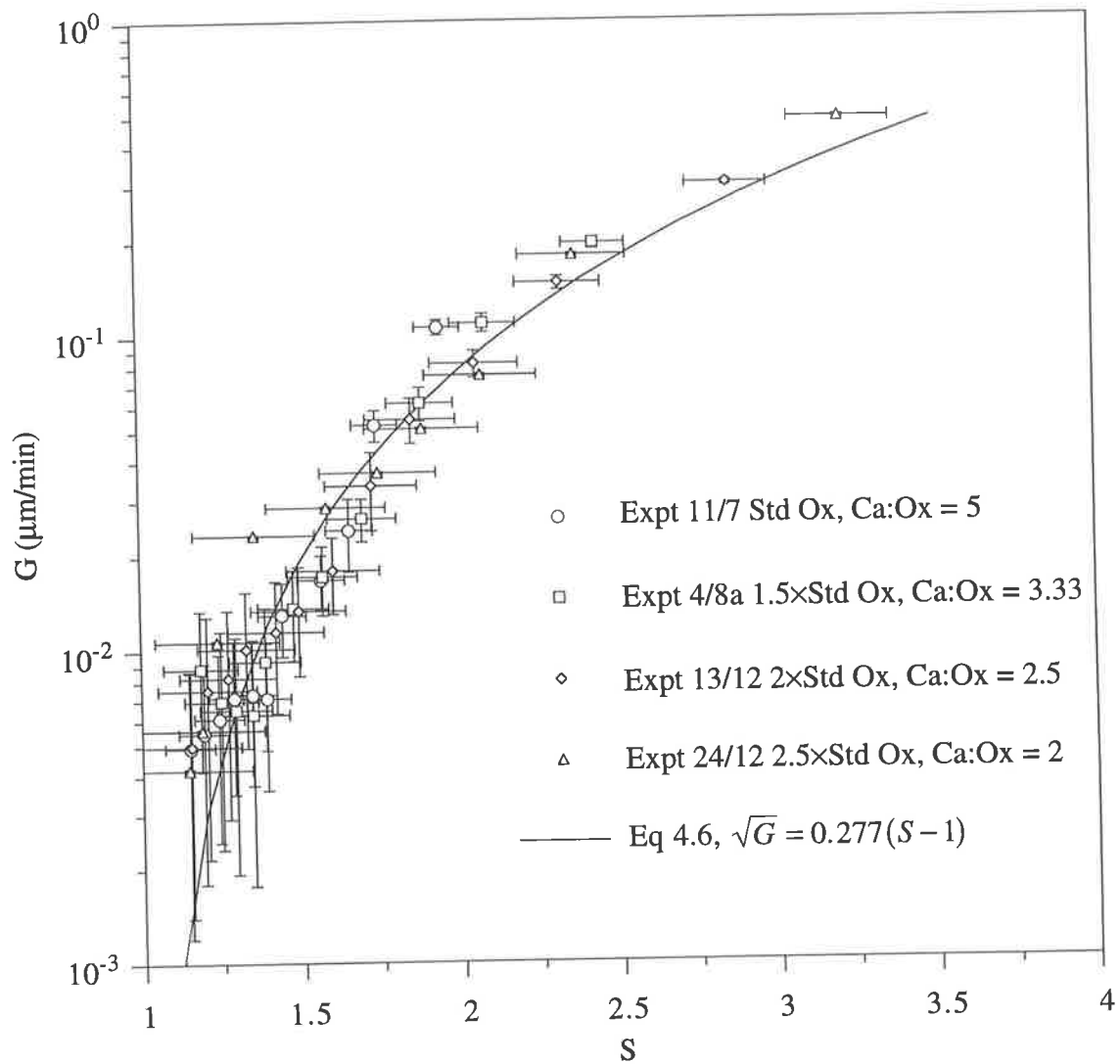


Figure 4.13 The errors in the growth rate and relative supersaturation for experiments using metastable solutions with different initial supersaturations.

the aggregation rate constant and oxalate ion concentrations are derived and a sample calculation of the errors is given in Appendix 8.

Figure 4.14 shows the aggregation rate constant plotted against the oxalate ion concentration for the same experiments used to illustrate the error in the growth rate and the activity product. It can be seen that for each experiment the errors in the aggregation rate constant are very small. The errors are typically less than 2% of the value of the aggregation rate constant. The errors are smaller than those for the growth rate as the expression for the error in the aggregation rate constant, given by eq A8.22, is only dependent on the total number of crystals, and the aggregation rate. Both these parameters decrease during an experiment, in contrast to the crystal volume which increases.

As with the relative supersaturation, the error in the oxalate ion concentration is approximately constant and relatively small over the entire range of conditions considered. The errors shown are for the total oxalate ion concentration rather than the free ion concentration. However, as shown in Section 2.4, over the concentration range used in the experiments the fraction of oxalate present as the free ion is approximately constant, thus the percentage error in the total and free oxalate ion concentrations will be the same.

4.7 KIDNEY STONE FORMATION

It is generally accepted that human urine is ordinarily supersaturated with respect to calcium oxalate (Andrews *et al.*, 1955 and Miller *et al.*, 1958). As Robertson and Nordin (1976) observe the two main factors affecting the saturation of urine with calcium oxalate are the urinary concentrations of calcium and oxalate. The underlying processes involved in stone formation are also well understood as crystal nucleation, and enlargement by growth and aggregation (Finlayson, 1978 and Ryall, 1989). Both hypercalciuria, increased urinary calcium concentration, and hyperoxaluria, increased urinary oxalate concentration, have been recognised as risk factors for stone disease (Robertson *et al.*, 1976).

The findings of this chapter raises an important question in the pathogenesis of kidney stones as well as the assessment of risk factors for stone formation. If the primary crystal enlargement mechanism is growth, then the traditional characterisation of risk by assessing the supersaturation of urine is appropriate. However, if the primary enlargement mechanism is aggregation, supersaturation is not the appropriate measure. Rather, judgement should be based on the urinary oxalate concentration.

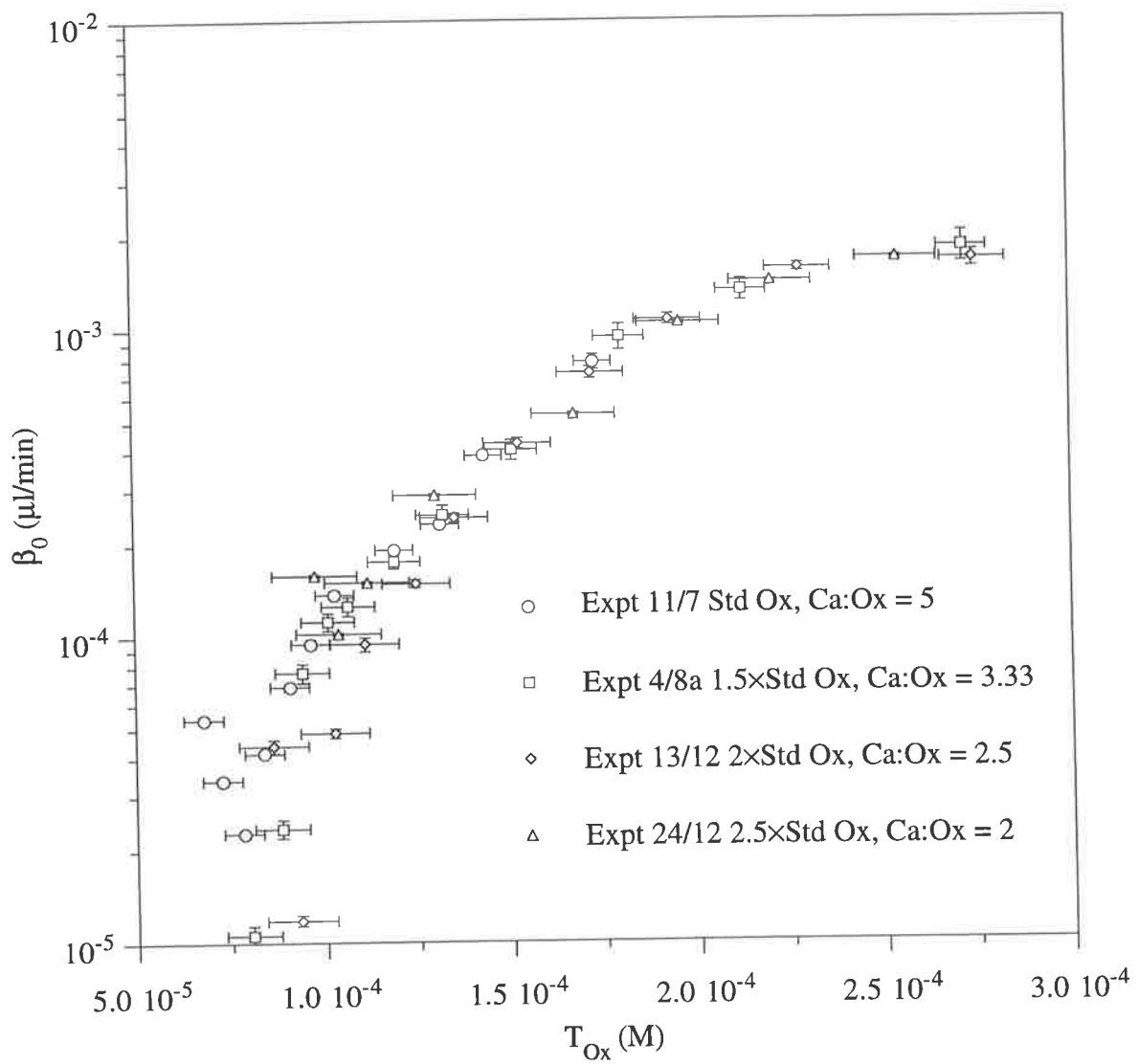


Figure 4.14 The errors in the aggregation rate constant and oxalate concentration for experiments using metastable solutions with different initial supersaturations.

4.8 CONCLUSIONS

Data from the experimental investigation of growth and aggregation of calcium oxalate in a batch system has been analysed using the program *Batch* to determine the dependence of both phenomena on the agitation rate and supersaturation:

- The experimental data are well described by McCabe's ΔL law for growth and a size-independent aggregation kernel.
- Regardless of the solution composition and the agitation rate the growth rate, in $\mu\text{m}/\text{min}$, in metastable solutions is described by an equation that is second order in relative supersaturation, *viz.*

$$G = (0.0767 \pm 0.0012)(S - 1)^2$$

These results imply the growth rate is controlled by surface spiral growth. The findings of many other studies on the growth of calcium oxalate are consistent with the results presented in this chapter.

- The observed behaviour of the aggregation rate is more complex: it is found to depend on the agitation rate and also the oxalate ion concentration, rather than some measure of supersaturation. The aggregation mechanism is investigated in more detail, with the aim of explaining the observed experimental behaviour in Chapter 5.

Chapter 5:

THE AGGREGATION MECHANISM

In this chapter an aggregation mechanism is developed to explain the dependence observed in Chapter 4 of aggregation rates on both solute concentration and agitation rate.

Seeded batch crystallisation experiments in supersaturated and saturated solutions with various rates and types of agitation reveal that aggregation proceeds irreversibly in supersaturated solutions, but reversibly in saturated solutions. In both cases aggregation depends on the agitation rate.

It is proposed that aggregation in supersaturated solutions proceeds as a two stage process, the first is reversible, the second irreversible and controlled by crystal growth. Further, a model is developed to explain the dependence of the aggregation rate on the oxalate ion concentration rather than on supersaturation. It is proposed that in order for particles to aggregate irreversibly solute must first diffuse to the point of contact and then deposit on the touching surfaces in order to "cement" the particles together. It appears that diffusion to the cementing site is the rate determining step.

5.1 INTRODUCTION

The mechanism by which aggregation occurs is now considered, in particular how the dependence of the aggregation rate on the oxalate concentration and agitation rate may be explained.

It has been possible for many years to describe in a semi-quantitative way the mechanisms active in the aggregation of colloidal particles in ionic solutions. These mechanisms are summarised by the theory of Derjaguin, Landau, Verwey and Overbeek (DLVO) who initially brought the diverse elements of the theory together.

However, DLVO theory takes no account of the effects of supersaturation during the aggregation process, so while aggregation in saturated or undersaturated solutions may be accounted for in this way, the more immediately relevant issue of how crystals aggregate while they are growing, is not addressed.

5.2 AGGREGATION MECHANISMS

Finlayson (1978) has proposed that DLVO theory may be used to describe the factors affecting the aggregation of calcium oxalate crystals. Finlayson *et al.* (1984) and Nancollas (1990) also suggest that the stability of aggregates of crystalluria in urine can be described by DLVO theory. Both authors claim that in urine repulsive electrostatic forces are reduced because of elevated ionic strength and the effect on the surface zeta potential of urinary constituents. The reduction of these repulsive forces is favourable for aggregation.

5.2.1 DLVO theory

DLVO theory treats the stability of aggregates in terms of the energy changes which occur when particles approach one another. The theory involves estimations of the energy of attraction by London and Van der Waals forces and repulsion from overlapping electrical double layers.

Van der Waals forces. These weak attractive forces between un-charged molecules originate from electrical interactions of which there are three types:

1. Dipole-dipole interactions: molecules with permanent dipoles mutually orientate in such a way that an average attraction results.
2. Dipole induced dipole interactions: a molecule with a permanent dipole may induce dipoles in other molecules resulting in attraction.
3. Attractive forces may also be induced in non-polar molecules. These are known as dispersion or London forces and are caused by the fluctuations in the charge distribution of a molecule inducing polarisation in another. Nearly all Van der Waals forces are London dispersion forces except in the case of highly polar molecules.

The electrical double layer. Most substances acquire a surface electric charge when they are immersed in a polar solvent, which arises from effects such as ionisation, ion adsorption and dissolution. The surface charge influences the distribution of ions in the solvent near the surface. Ions of the opposite charge to that at the surface are attracted which leads to an electrical double layer consisting of two regions, the surface region of adsorbed ions and a diffuse region where ions of the opposite charge are distributed according to the influence of electrical forces and thermal motion. When two particles come together to form

an aggregate their double layers must overlap, which produces a repulsive force as the two diffuse regions of the double layer of like charge come together.

Mathematical expressions for the changes in potential energy that occur when two particles near each other as a result of Van der Waals and electrostatic forces can be derived. As shown by Shaw (1980) for Van der Waals forces

$$V_A = -\frac{A}{12} \frac{r}{h} \quad (5.1)$$

where A is the Hamaker constant, r the radius of the particles and h the separation between the particles. For double layer interactions

$$V_R = 2 \pi \epsilon \Psi_0^2 \exp(-\kappa h) \quad (5.2)$$

where ϵ is the di-electric constant, Ψ_0 is the surface potential and the quantity, κ , which is related to the size of the double layer, is given by

$$\kappa = \left(\frac{2e^2 N_A I}{\epsilon k T} \right)^{1/2} \quad (5.3)$$

where N_A is the Avogadro number, e the charge of an electron, k the Boltzmann constant, T the temperature and I the ionic strength of the solution. The quantity $1/\kappa$ has units of length and is termed the Debye length.

DLVO theory explains the effect of ionic strength as follows: an increase in the ionic strength leads to a decrease in the size of the electrical double layer, as seen from eqs 5.2 and 5.3, so the repulsive force associated with the double layer acts over a smaller distance, while the attractive Van der Waals forces are unchanged. Thus the potential barrier to particle interaction decreases.

It should be noted that hydrodynamic shear forces may be able to bring together particles with sufficient energy to overcome the repulsive energy barrier and lead to aggregation, or break up aggregates held together by Van der Waals forces.

DLVO theory predicts that calcium oxalate crystals will aggregate rapidly in urine-like systems as a consequence of the effect of elevated ionic strength on the electrical double layer of each crystal. In agreement with this prediction are the experimental results of Sarig *et al.* (1989) and Hess *et al.* (1989), who both observe aggregation in urine-like solutions in the absence of supersaturation. However, in contrast, Hounslow (1990) reports that in a

batch system aggregation does not occur in saturated solutions, only supersaturated solutions.

DLVO theory takes no account of the effects of supersaturation on the aggregation process, so the influence of growth is not accounted for. The results from Chapter 4 show that in supersaturated solutions the aggregation rate is dependent on the oxalate ion concentration.

Hounslow (1990) finds that the aggregation of calcium oxalate is dependent on supersaturation and shows DLVO theory cannot account for the dependence based on the following argument. In the experiments reported by him, and those in Chapter 4, the ionic strength is held virtually constant by the substantial concentration of Na^+ and Cl^- ions, yet the aggregation rate decreases by as much as two orders of magnitude. It is clear that DLVO theory cannot account for the observed dependence of the aggregation rate on the oxalate ion concentration in supersaturated solutions.

5.3 AN EXPERIMENTAL INVESTIGATION

An experimental investigation was undertaken to explore the apparent contradiction between the two sets of results presented in the previous Section. Conventional DLVO theory – and some experimental observations (Hess *et al.*, 1989 and Sarig *et al.*, 1989) – indicate that aggregation should proceed rapidly in saturated solutions. Whereas, Hounslow (1990) has observed that no aggregation takes place in saturated solutions but that it does occur in supersaturated solutions, at a rate proportional to the supersaturation. The findings of Chapter 4 and those of Hartel and Randolph (1986), suggest that aggregation is dependent on the oxalate ion concentration and also the rate of agitation, or shear rate.

5.3.1 Materials and methods

Two stock solutions were prepared: a standard metastable (supersaturated) solution according to the protocol described in Section 3.3.2 and a saline solution saturated with respect to calcium oxalate. The saturated solution was prepared from a 0.15 M sodium chloride solution by the addition of *ca* 5 grams/litre of calcium oxalate mono-hydrate crystals. The crystal-saline slurry was allowed to equilibrate for a minimum of 24 hours, at the temperature of intended use. Immediately before each experiment, the crystals were removed by filtration (0.22 μm).

Each of the experiments reported entails the addition of 4 ml of a 1 gram/litre seed suspension, prepared as described in Section 3.3.2, to 200 ml of either the saturated or supersaturated solution. At various times during each experiment the CSD, the total number

and the total volume of crystals per unit volume of suspension were determined by a PDI Elzone 280PC. Experiments were either conducted at room temperature ($17.5\pm 2.5^\circ\text{C}$) or in a Grant Instruments SS40-D shaking water bath at $37\pm 0.5^\circ\text{C}$. The experiments described above were performed in the Department of Chemical Engineering at the University of Cambridge, which is why some of the equipment used, notably the particle size analyser, is different from that described in Chapter 3.

5.3.2 Results

Four types of experiment were conducted using either the supersaturated or saturated solutions described above, with agitation either by the propeller-stirrer supplied with the Elzone 280PC or by the Grant water bath. The presentation of results is divided, according to the method of agitation.

Preliminary studies – stirred vessel

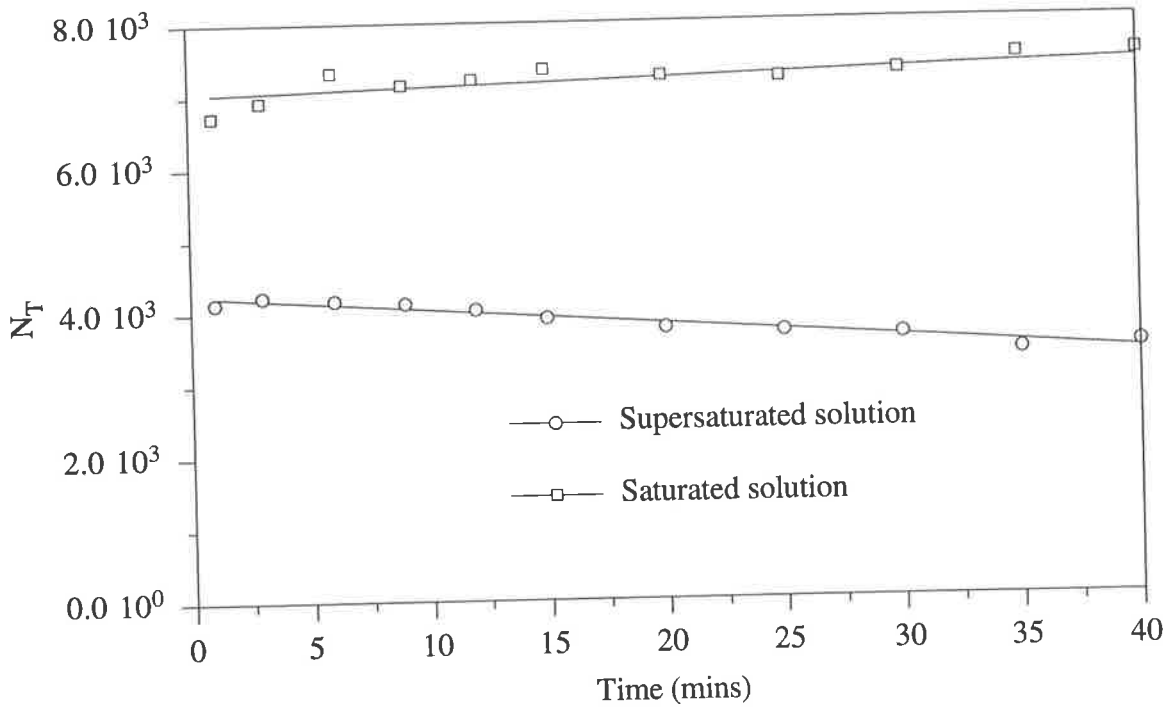
The standard result. As described in Section 5.3, the results of Chapter 4 and those of Hounslow (1990) and Hartel and Randolph (1986) suggest that in the presence of supersaturation, calcium oxalate seed crystals will grow and aggregate. Further, in the absence of supersaturation the seed crystals may aggregate or dis-aggregate, depending on the rate of agitation.

Figures 5.1 and 5.2 present the results of a pair of parallel experiments conducted in saturated or supersaturated solutions. From Figures 5.1 (a) and (b) it may be seen that in the supersaturated solution the total volume, V_T , of crystals rises, clearly identifying the presence of growth, and the total number, N_T , of crystals falls, identifying aggregation. Conversely, in the saturated solution, the volume of crystalline matter remains constant and the numbers slowly rise.

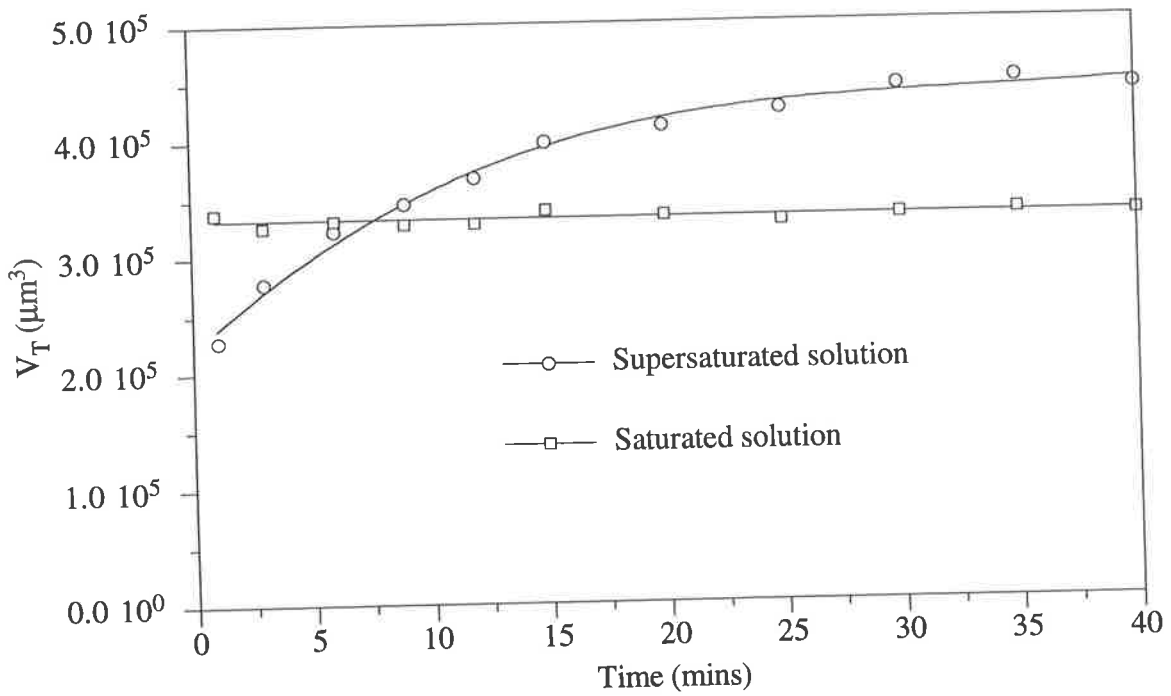
Figure 5.2 shows the CSDs for the same experiments. In Figure 5.2 (a), in the supersaturated solution the effects of growth and aggregation are clearly visible: the mean size increases and the CSD broadens. In Figure 5.2 (b), in the saturated solution the CSD remains static, with some dis-aggregation possibly identified by the gradual narrowing of the peak.

Figures 5.1 and 5.2 show that under circumstances where aggregation does not occur in saturated solution, it does occur in the presence of supersaturation.

Saturated solutions – effect of agitation. The results from Section 4.5.1 suggest that in supersaturated solutions aggregation is dependent on the agitation rate. The agitation

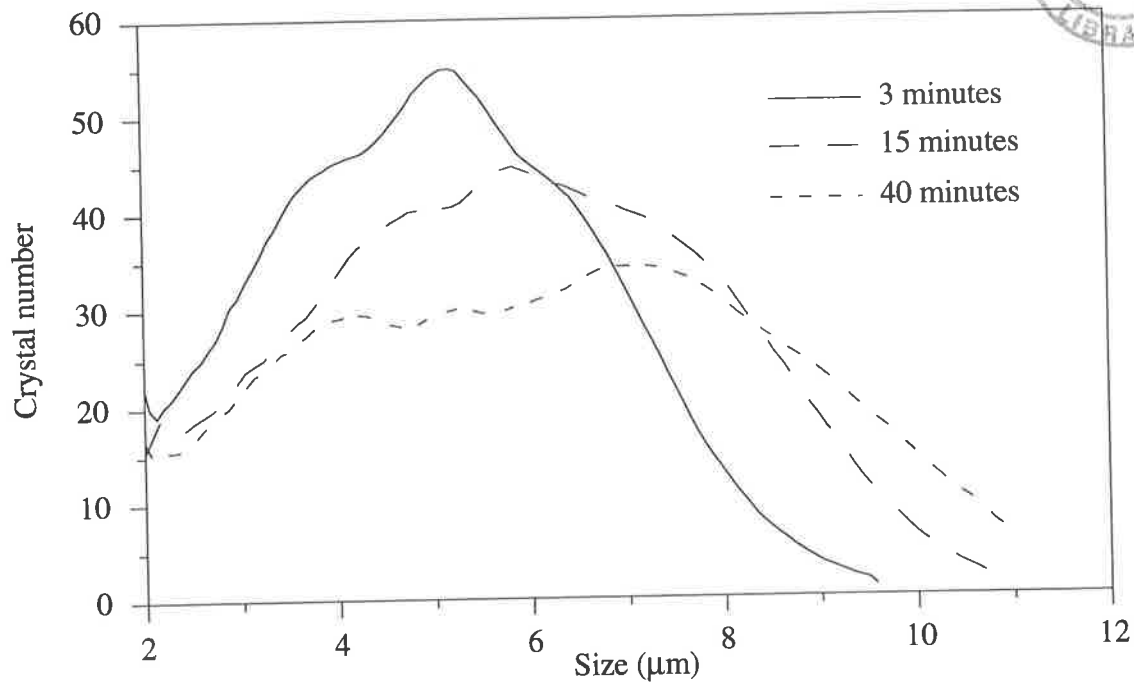


(a)

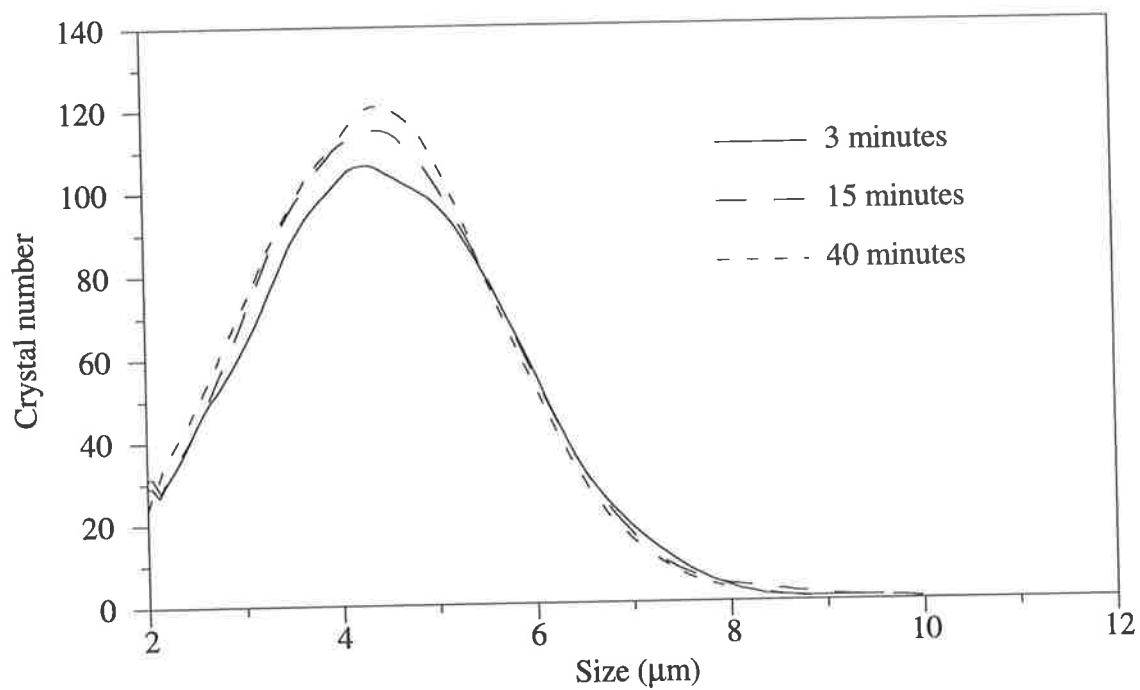


(b)

Figure 5.1 Variation in (a) total number and (b) total volume of crystals in supersaturated and saturated solutions: agitation by stirring.

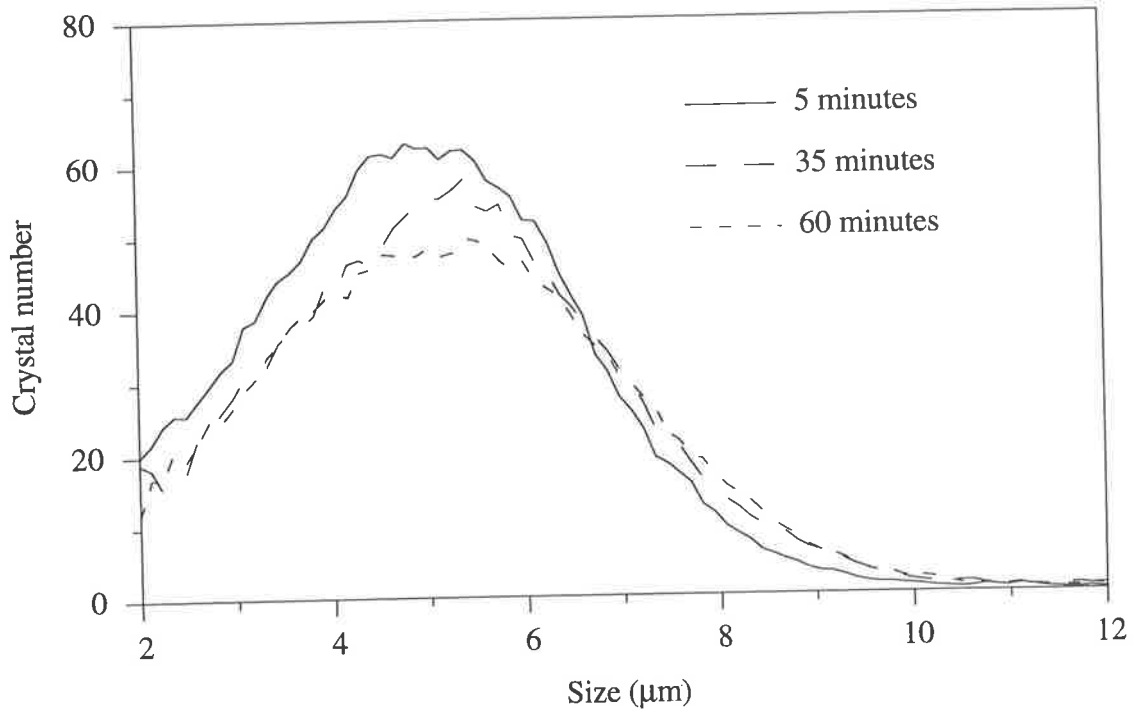


(a)

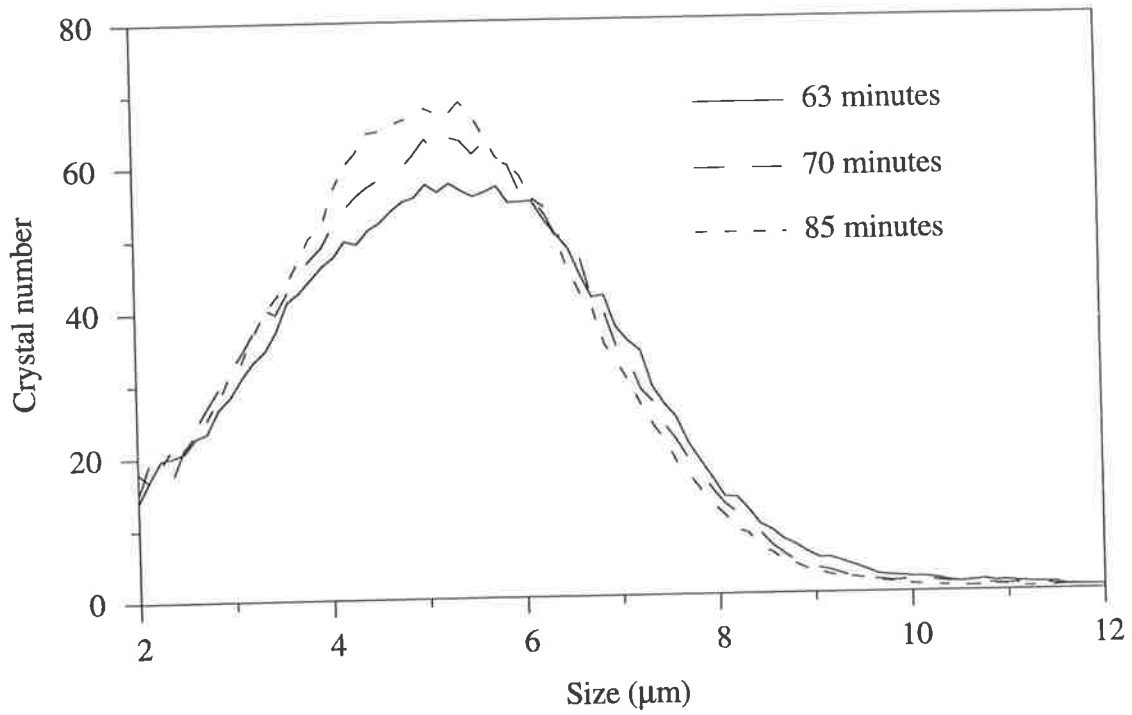


(b)

Figure 5.2 Variation in CSDs by number in (a) supersaturated and (b) saturated solutions: agitation by stirring.

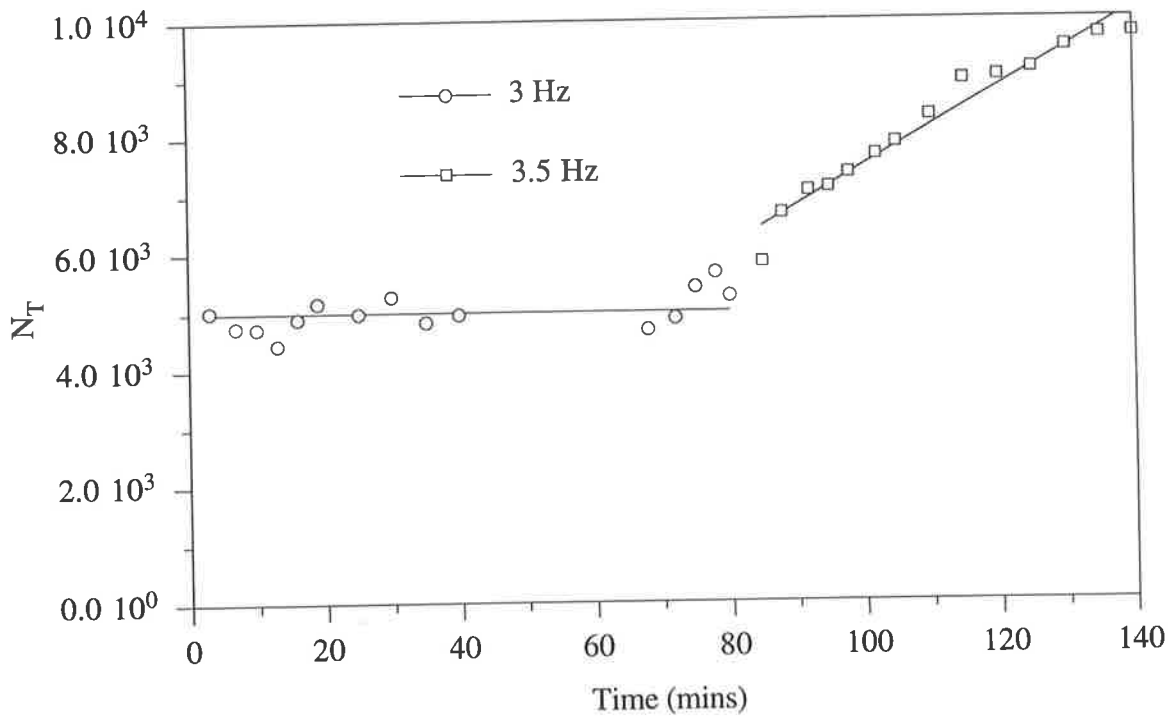


(a)

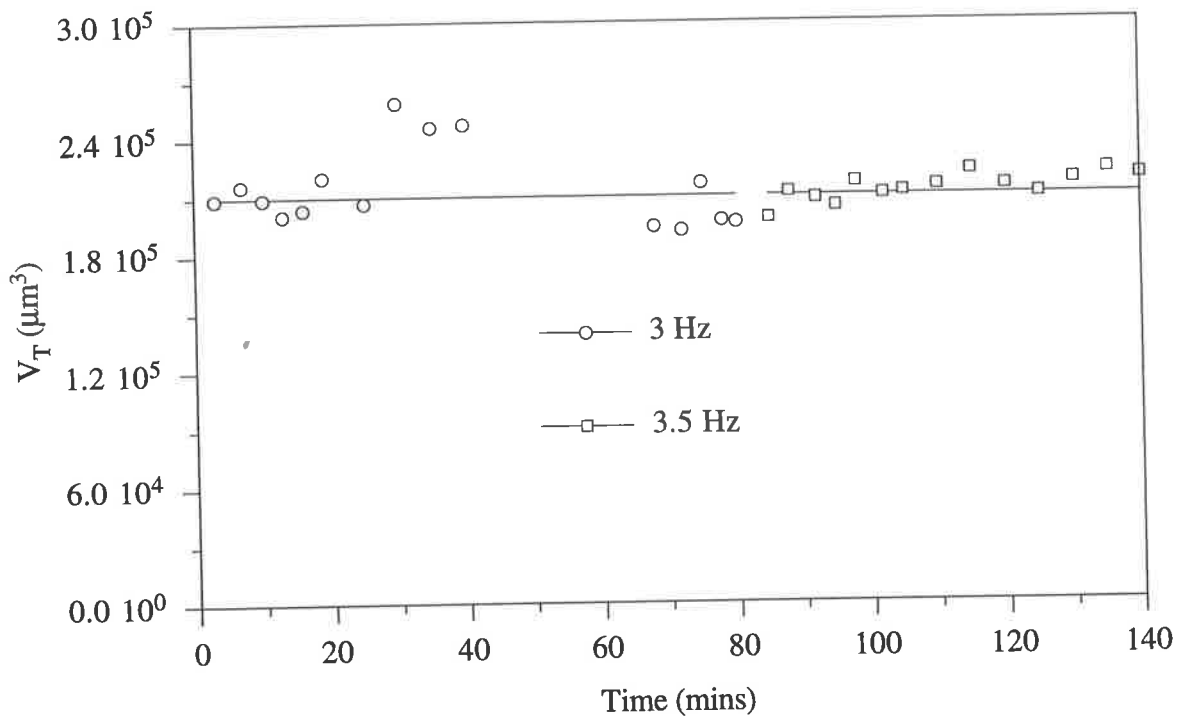


(b)

Figure 5.4 Variation in CSDs by number for (a) medium stirrer speed and (b) fast stirrer speed in a saturated solution.

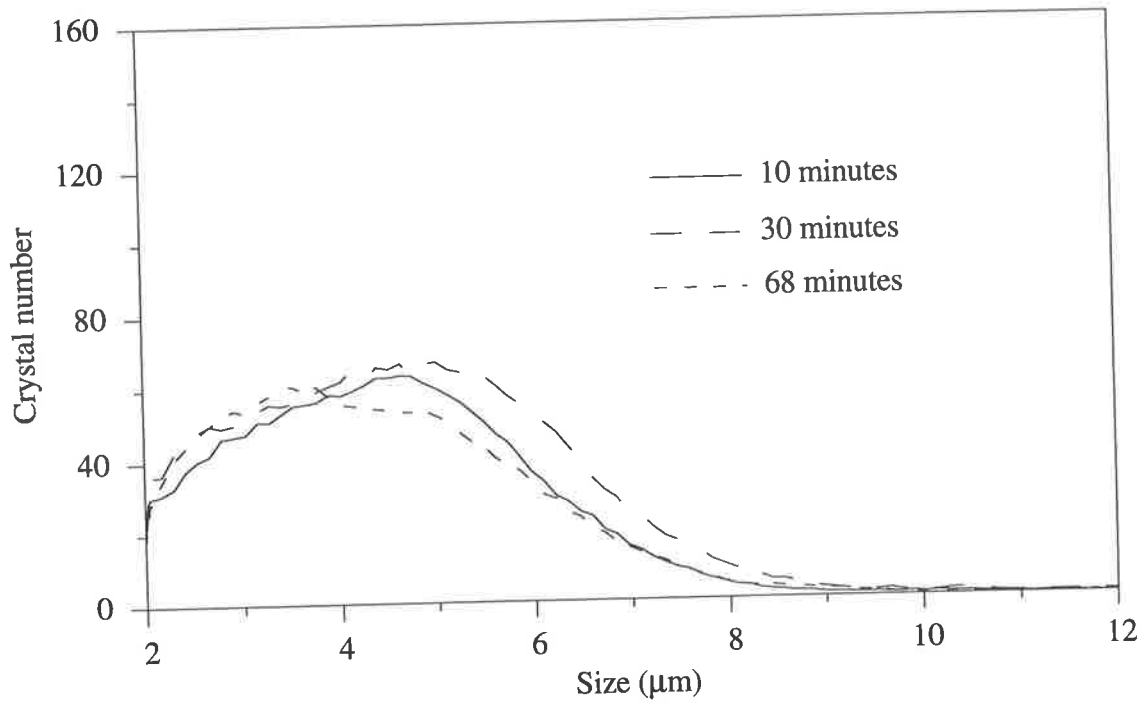


(a)

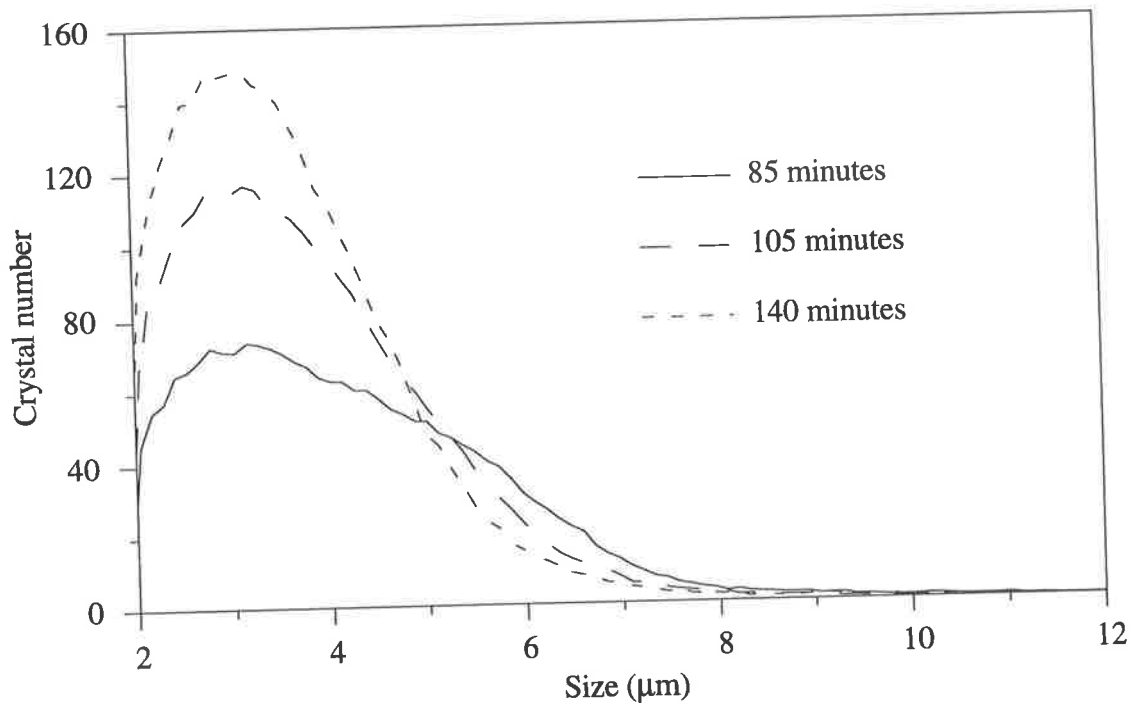


(b)

Figure 5.5 Variation in (a) total number and (b) total volume of crystals in a saturated solution: effect of agitation rate.



(a)



(b)

Figure 5.6 Variation in CSDs by number in a saturated solution at (a) 3 Hz and (b) 3.5 Hz: the effect of agitation rate.

Figure 5.7 shows the CSDs from an experiment in which the agitation rate for the first 24 hours was 110 OPM¹. The agitation rate was then decreased to 90 OPM, inducing aggregation, indicated by the decrease in number and the shift of the CSD towards larger sizes. The agitation rate was then increased to 110 OPM, causing dis-aggregation, indicated by the shift of the CSD back towards the CSD obtained after 24 hours.

Figure 5.7 confirms the observation from the preliminary experiments, that crystals may aggregate or dis-aggregate in saturated solutions, depending on the agitation rate.

Supersaturated solutions – effect of agitation. In Section 4.5.1 results are presented that suggest the aggregation rate is dependent on the agitation rate in supersaturated solutions. A series of experiments was conducted using different agitation rates to investigate further the effect of agitation. Seeds were added to a supersaturated solution, samples were taken just after the seeds were added and then again after 24 hours when the solution was saturated.

Figure 5.8 shows the effect of the agitation rate on the total crystal number and volume after 24 hours. It can be seen from Figure 5.8 (a), that as the agitation rate increases, the total number of crystals increases, indicating a decrease in aggregation. Figure 5.8 (b) shows that the agitation rate has no effect on the total crystal volume. This is consistent with the results from Chapter 4: the agitation rate affects aggregation and has no effect on growth. The total number and volume of crystals at the start of the experiment are also shown in Figure 5.8. It can be seen that in each experiment the total number and volume of seeds added was approximately constant. Therefore it is not the initial condition of the seeds that is responsible for the results observed but the effect of agitation on aggregation.

The CSDs after 24 hours are presented in Figure 5.9. The effect of the agitation rate on the CSDs can clearly be seen, as the agitation rate decreases the mean size increases and the CSD broadens.

Finally, Figures 5.10 (a) to (c) show SEM micrographs of samples taken at the beginning and after 24 hours for experiments with agitation rates of 75, 90 and 110 OPM. The seeds added are clearly aggregates and similar in number and size at the beginning of each experiment. After 24 hours the effect of the rate of agitation on aggregation can be seen by the difference in the number and size of the crystals.

¹ This experiment was conducted using the water bath described in Section 3.3.3, thus the shaking rate is in OPM rather than Hz.

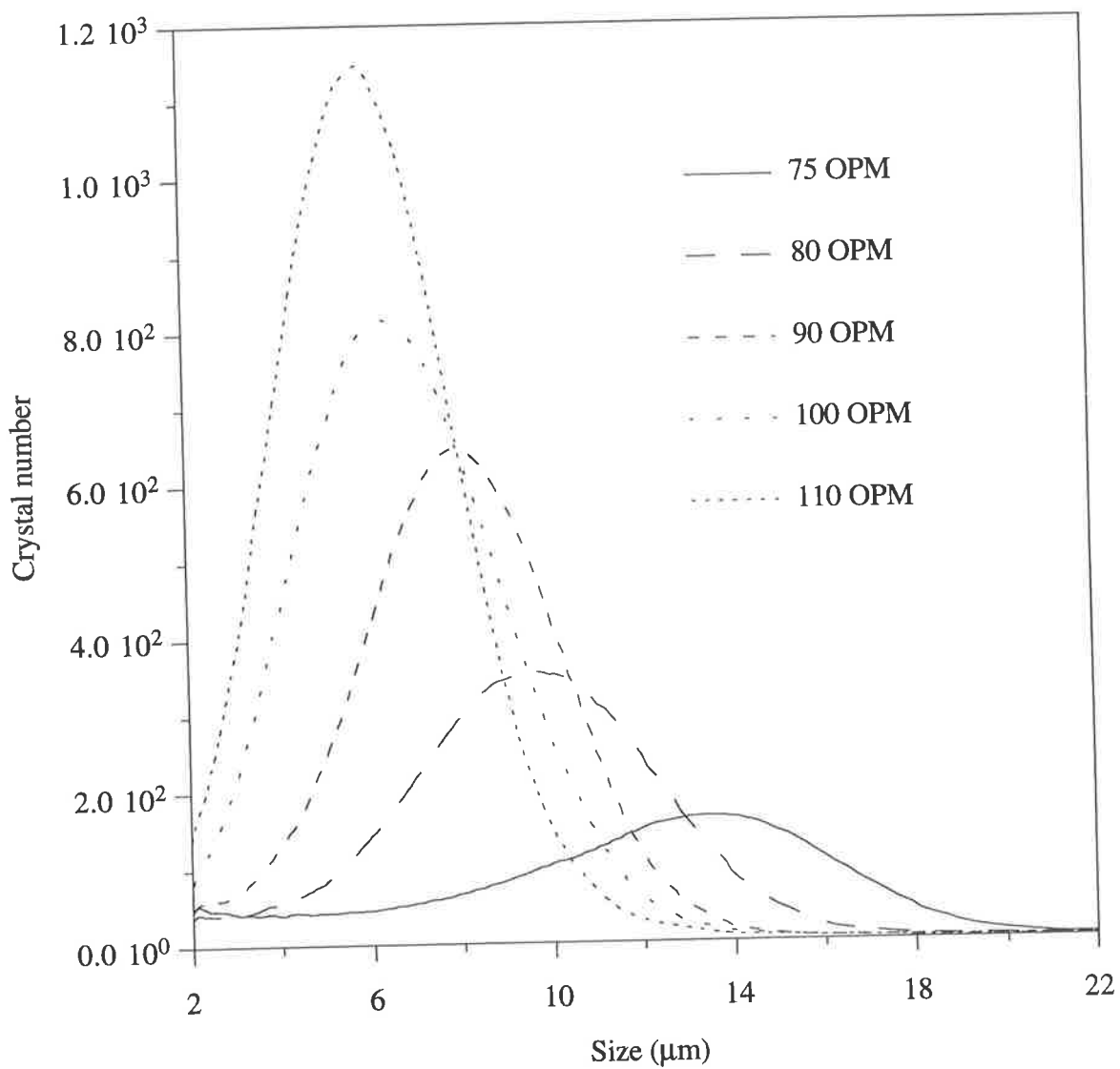
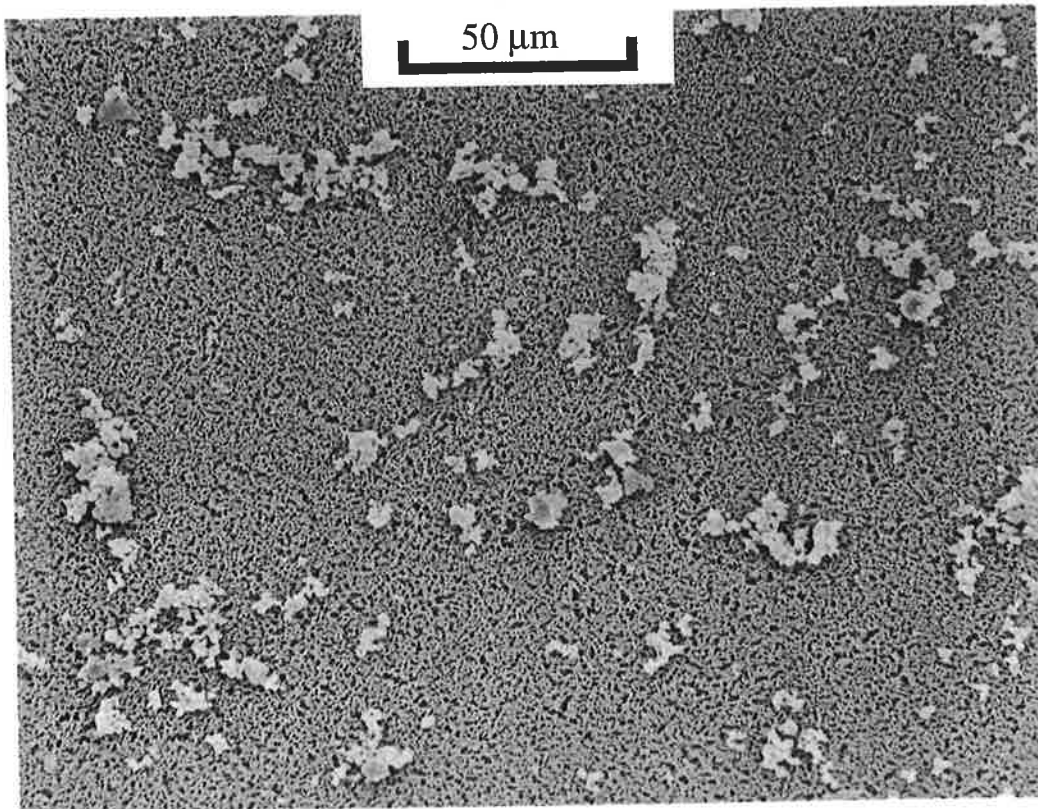
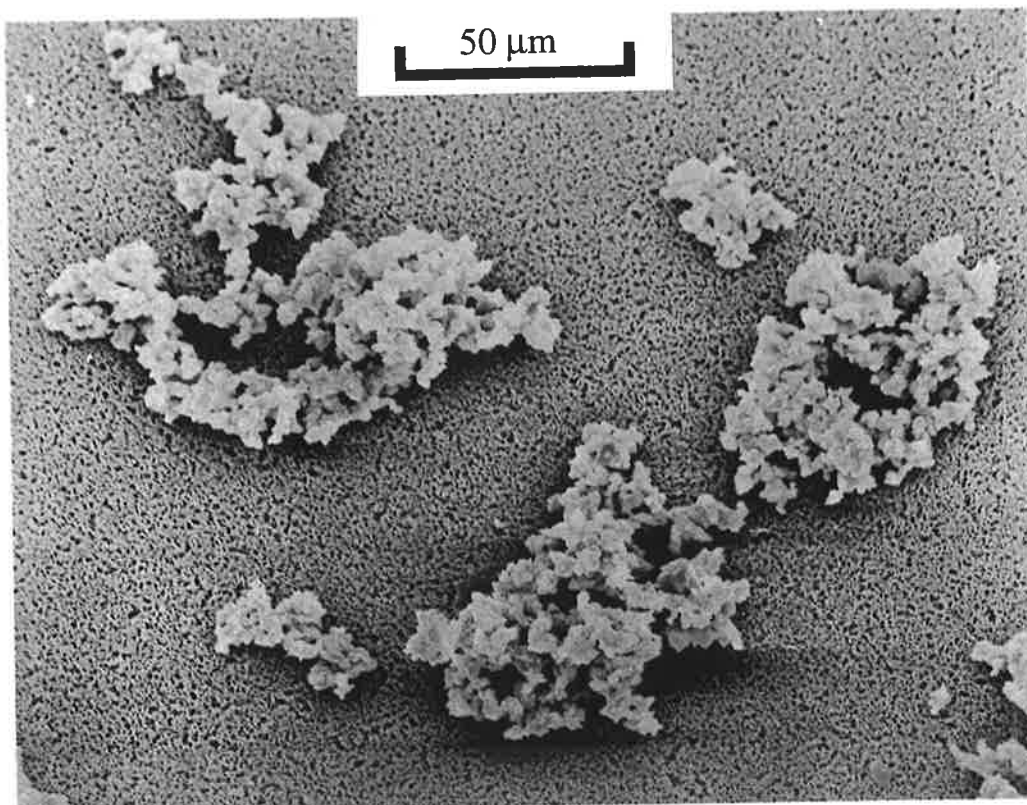


Figure 5.9 CSDs by number in a supersaturated solution at different agitation rates: the effect of agitation.

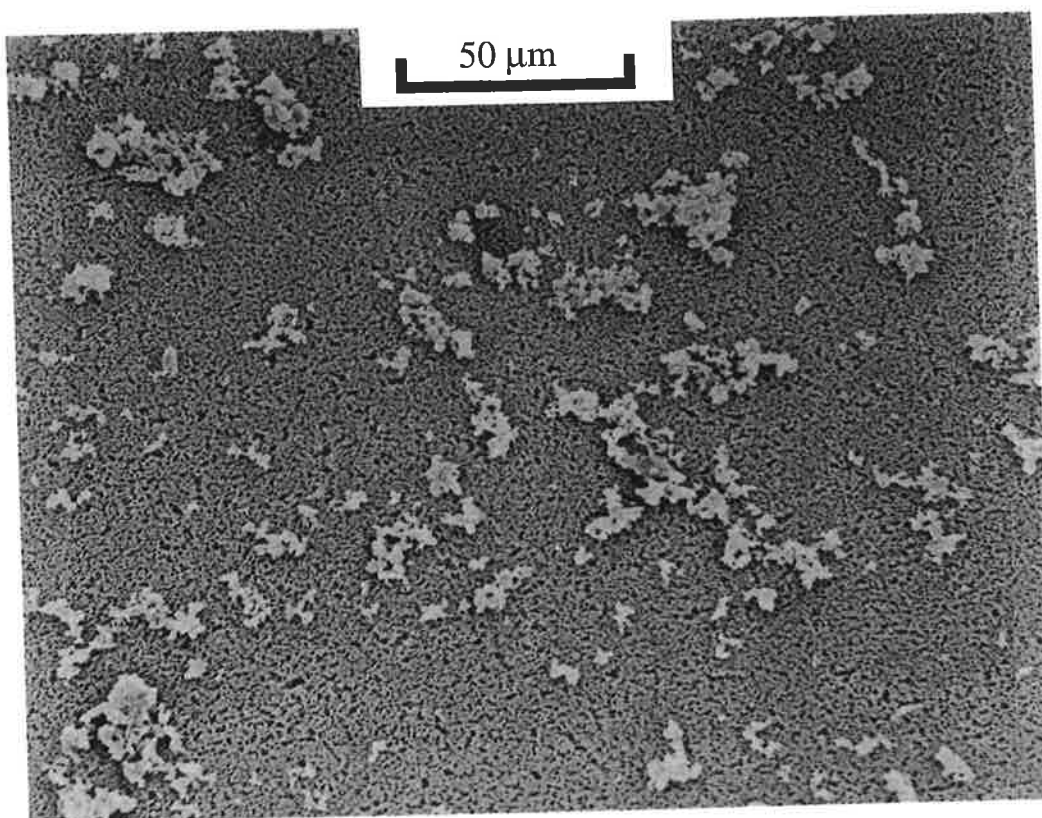


(i) Time, $t = 0$ minutes.

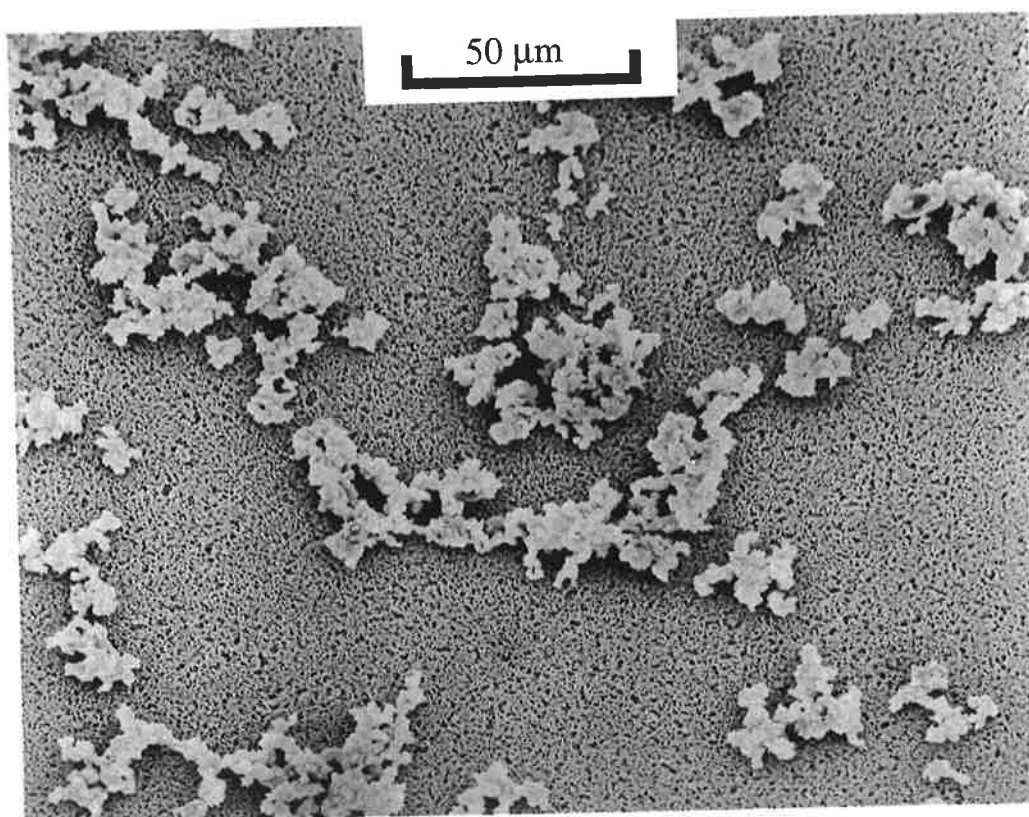


(ii) Time, $t = 24$ hours.

Figure 5.10 (a) SEM micrographs of calcium oxalate crystals at different times for a batch experiment using an agitation rate of 75 OPM.

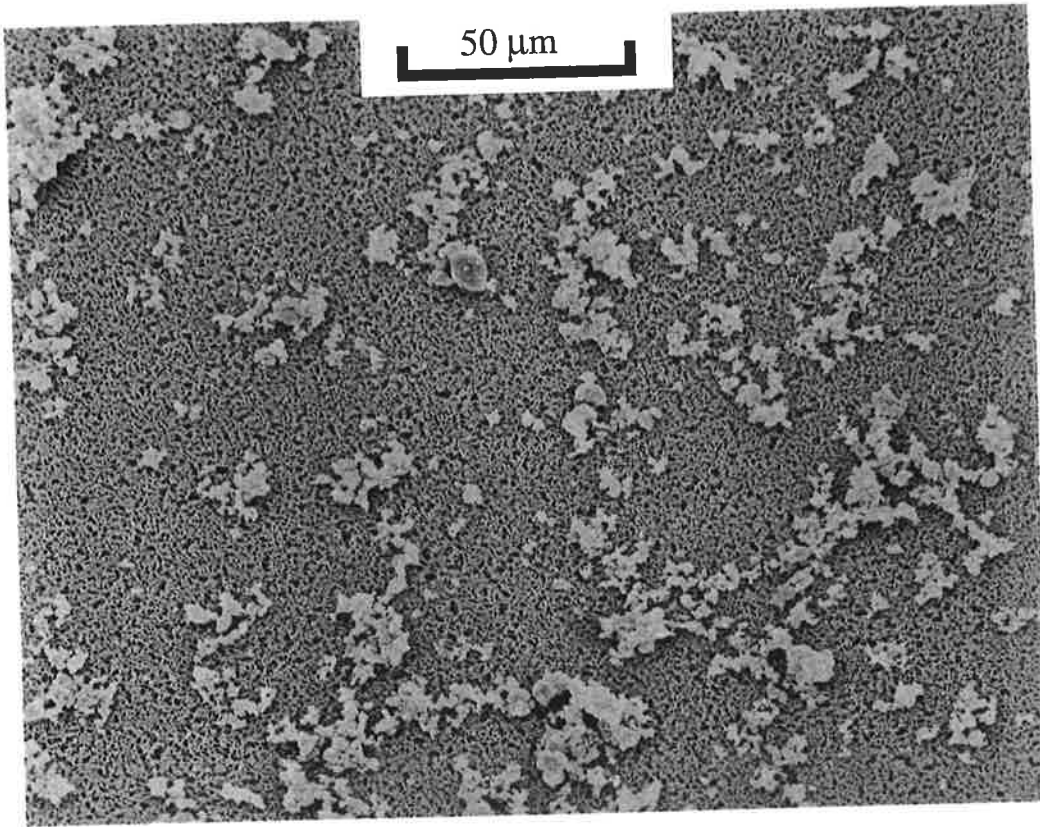


(i) Time, $t = 0$ minutes.

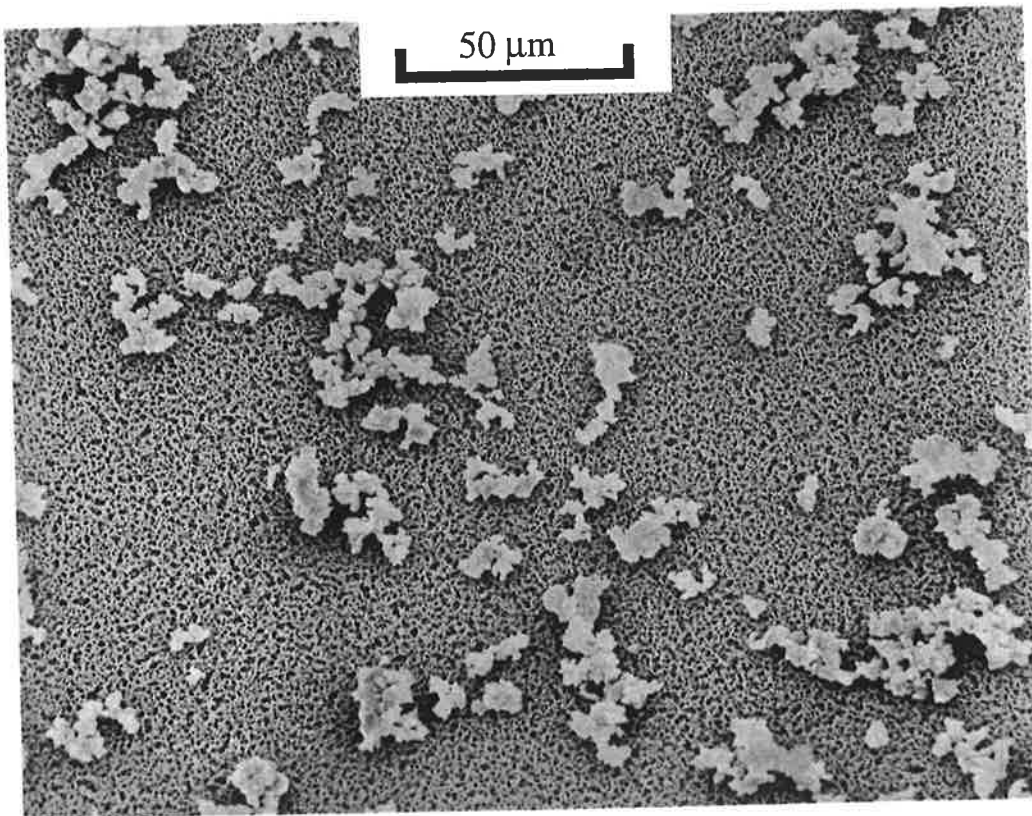


(ii) Time, $t = 24$ hours.

Figure 5.10 (b) SEM micrographs of calcium oxalate crystals at different times for a batch experiment using an agitation rate of 90 OPM.



(i) Time, $t = 0$ minutes.



(ii) Time, $t = 24$ hours.

Figure 5.10 (c) SEM micrographs of calcium oxalate crystals at different times for a batch experiment using an agitation rate of 110 OPM.

Supersaturated solutions – reversibility. A two-stage experiment using a supersaturated solution was conducted over 80 minutes with the agitation rate being increased from 3 Hz to 3.5 Hz at 60 minutes.

Figures 5.11 (a) and (b) show that at the 3 Hz agitation rate the crystals grow and aggregate as expected. In Figure 5.11 (a) during this phase the total numbers decrease and from Figure 5.11 (b) the volume increases. In Figure 5.12 (a) the CSDs show the characteristic effects of growth and aggregation, the mean size increases and the distribution broadens. However, when the agitation rate is increased to 3.5 Hz, *no dis-aggregation is observed*, in Figure 5.11 (a), the total number of crystals remains constant and in Figure 5.12 (b), the CSDs are approximately static. This behaviour is in marked contrast to the results shown in Figures 5.5 and 5.6.

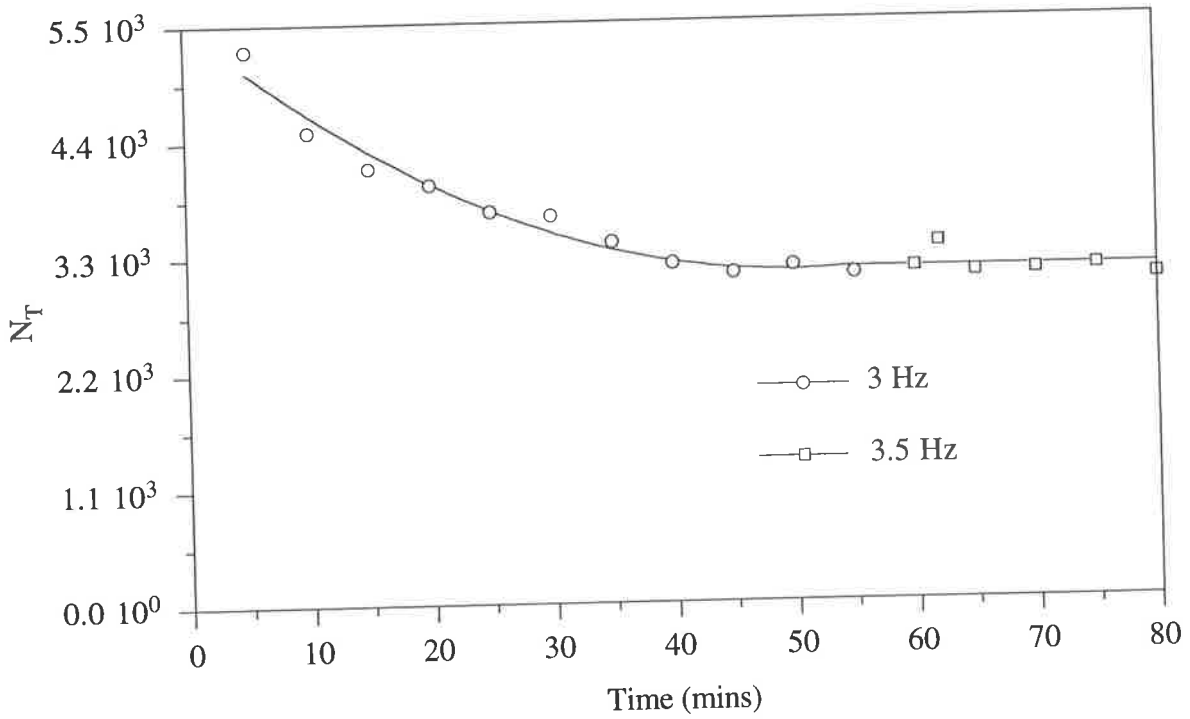
These observations show that in the presence of supersaturation, aggregation is irreversible.

5.4 DISCUSSION

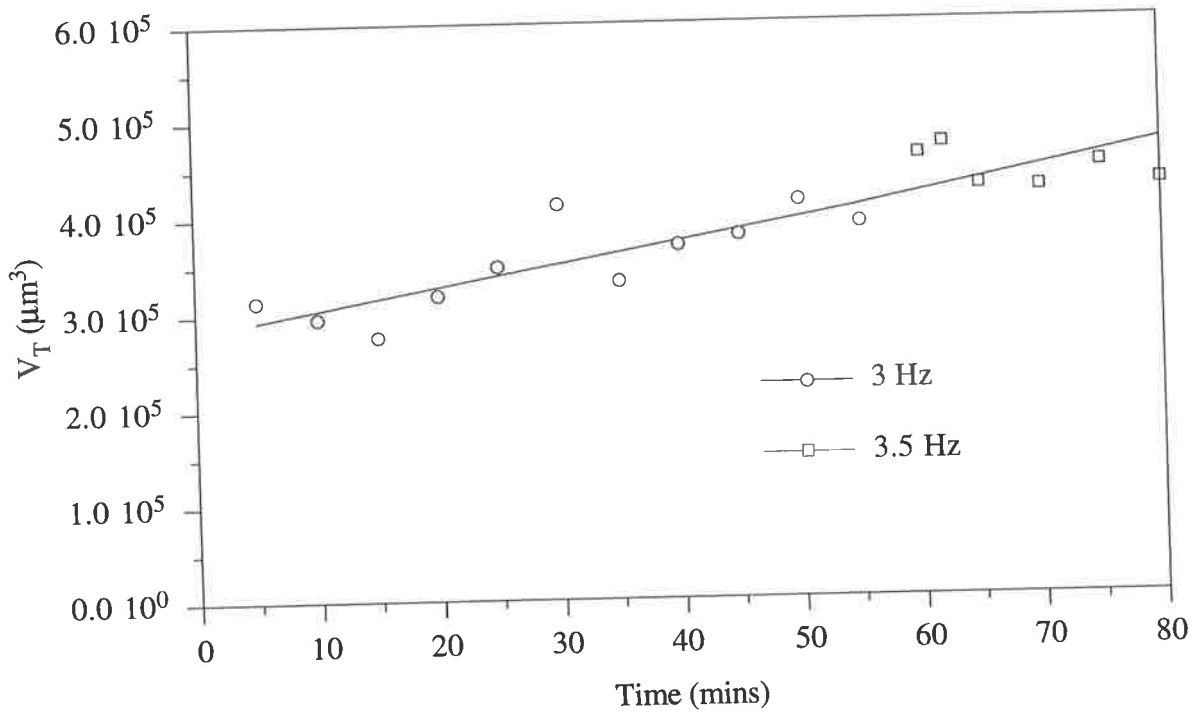
The results presented in the previous section may be summarised as follows:

- In supersaturated solutions, crystals grow and aggregate.
- In saturated solutions crystals do not grow, however they may aggregate or dis-aggregate.
- In saturated solution crystals can aggregate and dis-aggregate reversibly.
- In supersaturated solutions aggregation is irreversible.
- Aggregation rates in both saturated and supersaturated solutions depend on the agitation rate.

A two-stage mechanism is proposed to account for these observations: in the first, reversible, stage, crystals collide and form weak aggregates held together by the forces described by DLVO theory. In the second, irreversible, stage, the loose aggregates are cemented together by the deposition of new material. The second stage can only occur in supersaturated solutions, while the first can occur in any solution. This mechanism is shown schematically in Figure 5.13.

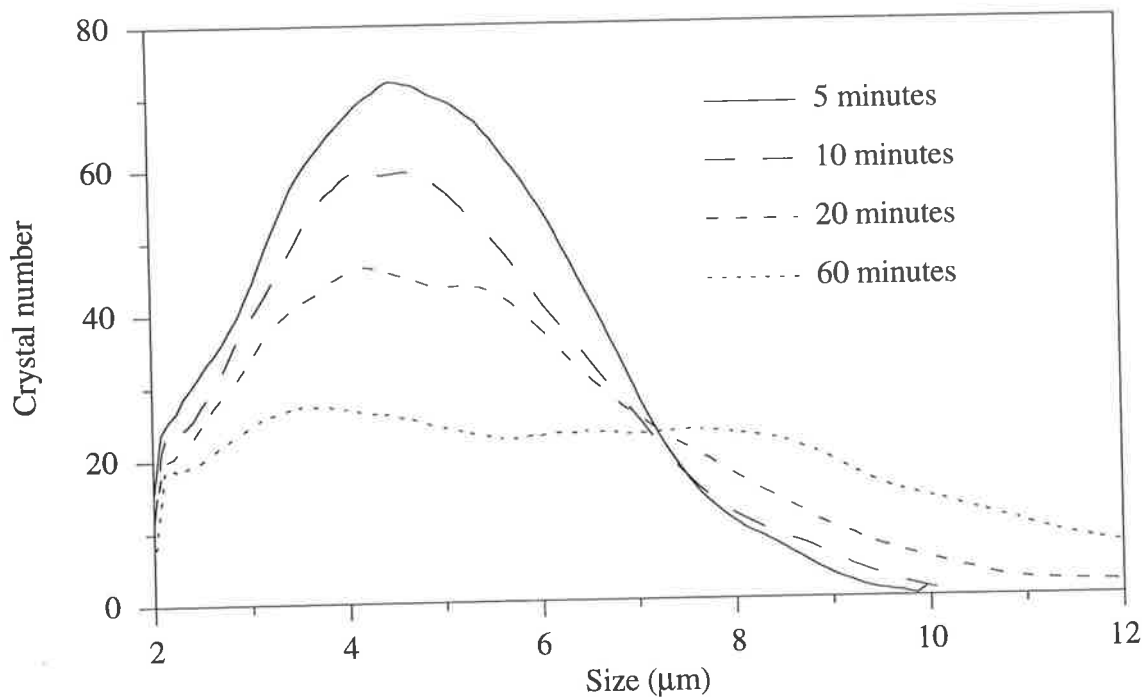


(a)

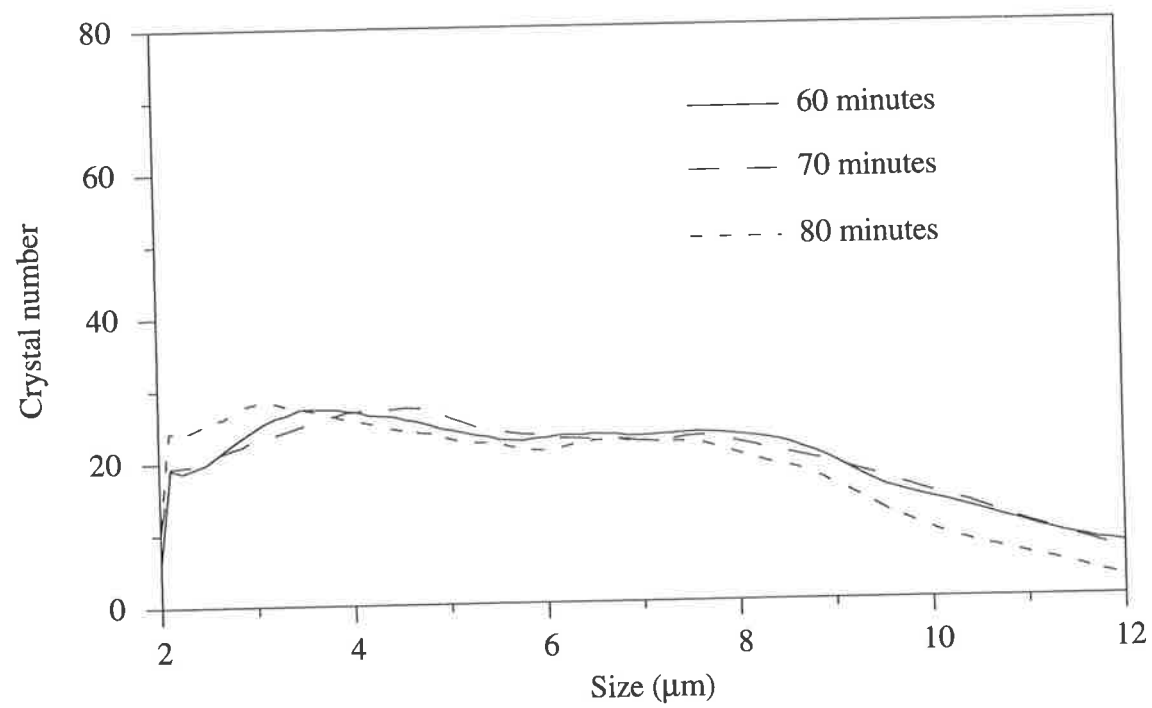


(b)

Figure 5.11 Variation in (a) the total number and (b) the total volume of crystals in supersaturated solutions: the effect of increasing the rate of agitation.



(a)



(b)

Figure 5.12 Variation in CSDs by number in a supersaturated solution at (a) 3 Hz and (b) 3.5 Hz: the effect of increasing the rate of agitation.

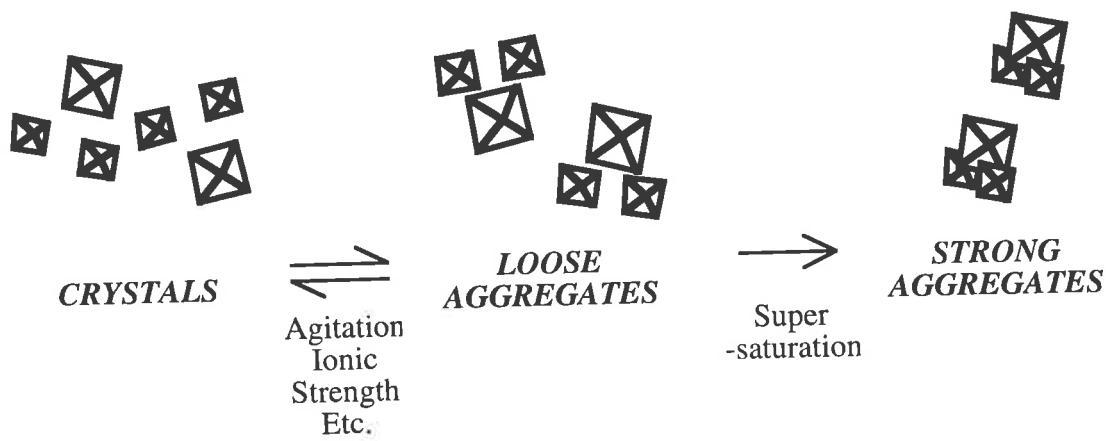


Figure 5.13 A general mechanism for the aggregation of calcium oxalate crystals in saturated and supersaturated solutions.

The combination of DLVO theory and the cementing of weak aggregates by growth has been used before to describe aggregation. Low (1975) has proposed, and found experimental evidence, for a similar mechanism to explain the aggregation of $\text{Al}(\text{OH})_3$ in caustic aluminate solutions. Hartel *et al.* (1986) also suggest that the aggregation of calcium oxalate involves the formation of weak aggregates which can either be cemented by growth to form stable aggregates, or disrupted by hydrodynamic conditions.

By means of the proposed mechanism it is possible to explain the apparently contradictory observations of Sarig *et al.* (1989), Hess *et al.* (1989) and Hounslow (1990) – for saturated solutions – and the dependence of aggregation on supersaturation reported by Hounslow. Clearly Sarig *et al.* and Hess *et al.*, who find that aggregation occurs reversibly, were observing the first stage of the mechanism, while the second stage was not active. Conversely, results reported by Hounslow were at operating conditions, such as a high agitation rate, that moved the “equilibrium” position of the first stage far to the left, causing no aggregation to be observed at zero supersaturation. Only in the presence of supersaturation was it possible for short-lived loose aggregates to be cemented together to form stable aggregates.

The dependence of both stages of the aggregation mechanism on the agitation rate is also readily explained. In saturated solutions only weak aggregates form and shear forces caused by agitation will have a strong effect on the efficiency of collisions between crystals and therefore the rate of aggregation. In supersaturated solutions aggregation is controlled by growth, however the efficiency with which particles are cemented together will still depend on the agitation rate.

5.5 AGGREGATION IN SUPERSATURATED SOLUTIONS

One observation that remains unexplained by the mechanism proposed is that the aggregation rate depends on the oxalate ion concentration. If the second part of the aggregation mechanism is controlled by growth, then the aggregation rate should correlate with the growth rate, or the activity product. However, from Figure 4.11 this is clearly not the case.

In this section a model is developed for the aggregation of crystals in supersaturated solutions. As with aggregation in saturated solutions, the first step is the collision of crystals, but in supersaturated solutions crystal growth cements the crystals together. It is this cementing process that is explained now.

5.5.1 A cementing model

Suppose that when two crystals come into contact with each other a pore is formed, and regardless of how complicated the actual shape of the pore might be, it can be approximated as a right cylinder of length, L_p , with the cementing taking place at a right disc with area, A_p , at the end of the pore. This is shown schematically in Figure 5.14.

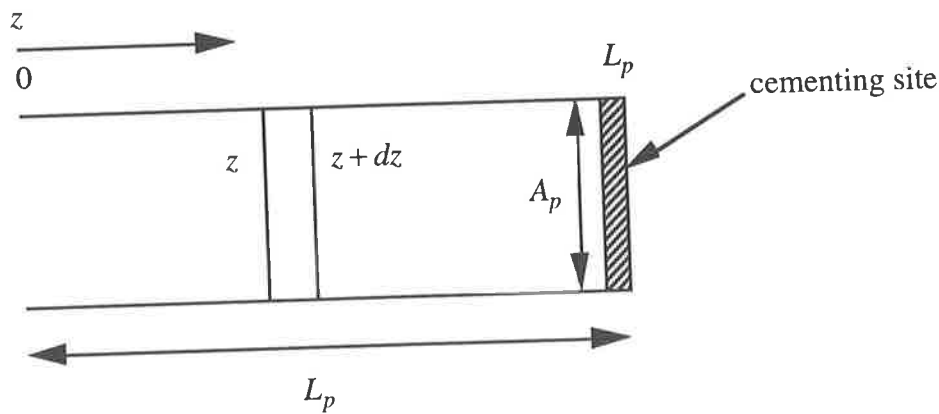


Figure 5.14. Pore formed when two crystals come in contact

The cementing at the end of the pore will occur as a result of crystal growth according to the reaction,



Suppose the rate law for the cementing reaction is first order in both reactants, then

$$r = k a b \quad (5.5)$$

where a and b are the concentrations of A and B .

By analogy with crystal growth in which ions must diffuse from the bulk to the crystal surface before precipitation occurs, the ions must diffuse along the pore before cementing occurs. A pseudo-steady state analysis is performed considering the diffusion of the ions along the pore and the cementing reaction at the end of the pore. In making the pseudo-steady state assumption, factors such as growth of the cementing site towards the pore mouth are neglected.

The general material balance for mass transfer of the reactant A by diffusion, without reaction, given for example by Westerterp *et al.* (1984) is

$$\mathcal{D}_A \frac{d^2 a}{dz^2} = 0 \quad (5.6)$$

Where the boundary conditions are that the concentration of A at the entrance to the pore is equal to the bulk concentration, a_0 , *i.e.* $a = a_0$ at $z = 0$ and the concentration of A at the end of the pore is a_L , *i.e.* $a = a_L$ at $z = L_p$. The solution to eq 5.6 subject to these conditions is

$$\mathcal{D}_A \frac{da}{dz} = \text{constant} = -\mathcal{D}_A \frac{a_0 - a_L}{L_p} \quad (5.7)$$

The flux of A may be calculated as

$$J_A = -\mathcal{D}_A A_p \frac{da}{dx} = -\mathcal{D}_A A_p \frac{a_0 - a_L}{L_p} \quad (5.8)$$

At the end of the pore the transfer of the reactants A and B by diffusion is balanced by the cementing reaction; a mass balance for this process yields

$$\mathcal{D}_A A_p \frac{a_0 - a_L}{L_p} = \mathcal{D}_B A_p \frac{b_0 - b_L}{L_p} = A_p r \quad (5.9)$$

Assuming the diffusivities of A and B are approximately equal, substituting the expression for the cementing rate, eq 5.5 and simplifying implies

$$a_0 - a_L = b_0 - b_L = \frac{k L_p}{\mathcal{D}} a_L b_L \quad (5.10)$$

Now, the cementing rate, r , is the rate per unit surface area. It follows that

$$\phi = \frac{k L_p a_0}{\mathcal{D}} \quad (5.11)$$

is dimensionless. In reaction engineering terminology, ϕ is a modulus relating the rate of the cementing reaction to the rate of transfer by diffusion.

If the reactant B is in excess, then the concentration of reactant A is limiting, and the ratio of the reactants in the bulk is given by

$$\zeta = \frac{b_0}{a_0} \quad \therefore \zeta \geq 1 \quad (5.12)$$

Further, dimensionless reactant concentrations may be defined by dividing by the bulk concentrations:

$$x = \frac{a_L}{a_0} \quad \therefore 0 \leq x \leq 1 \quad (5.13)$$

$$y = \frac{b_L}{b_0} \quad \therefore 0 \leq y \leq 1 \quad (5.14)$$

Dividing eq 5.10 by a_0 and writing the resulting expression in terms of the dimensionless variables gives,

$$(1 - x) = \zeta(1 - y) = \zeta \phi x y \quad (5.15)$$

The following dimensionless cementing rate at the end of the pore may also be defined:

$$\hat{r} = \frac{r}{\mathcal{D} A_p a_0 / L_p} = (1 - x) \quad \therefore 0 \leq \hat{r} \leq 1 \quad (5.16)$$

Equating eqs 5.15 and 5.16 gives

$$\hat{r} = (1 - x) = \zeta(1 - y) = \zeta \phi x y \quad (5.17)$$

Eliminating the dimensionless concentrations, x and y from eq 5.17 and simplifying gives the following equation involving the dimensionless cementing rate

$$\phi \hat{r}^2 - (1 + \phi + \zeta \phi) \hat{r} + \zeta \phi = 0 \quad (5.18)$$

As $\hat{r} \leq 1$ the appropriate solution for the dimensionless cementing rate from eq 5.18 is,

$$\hat{r} = \frac{1 + \phi + \zeta \phi - \sqrt{1 + 2\phi + 2\zeta\phi + \phi^2 - 2\zeta\phi^2 + \zeta^2\phi^2}}{2\phi} \quad (5.19)$$

Figure 5.15 is a plot of the dimensionless cementing rate calculated from eq 5.19 for various values of the reactant ratio, ζ . It can be seen that for large values of the modulus, ϕ , the value of the dimensionless cementing rate is approximately constant. This corresponds to the cementing rate being limited by diffusion. For small enough values of the modulus, the cementing rate is proportional to the modulus and the process is reaction limited.

The dependence of the cementing rate on solution composition is now explored. The group $\hat{c} = \mathcal{D}/kL_p$ has the units of concentration. The reactant of interest is the oxalate ion, which is equivalent to reactant A in the model, as in the experimental work the oxalate ion was the limiting reactant. The expression for the dimensionless oxalate ion concentration is

$$\phi_1 = \phi = \frac{a_0}{(\mathcal{D}/kL_p)} = \frac{a_0}{\hat{c}} \quad (5.20)$$

The dimensionless activity product, a product of the concentrations of the two reactants is

$$\phi_2 = \zeta \phi^2 = \frac{a_0 b_0}{(\mathcal{D}/kL_p)^2} = \frac{a_0 b_0}{\hat{c}^2} \quad (5.21)$$

A dimensionless cementing rate may also be written in terms of \hat{c} as

$$\hat{r}^* = \hat{r} \phi = \frac{r}{k A_p (\mathcal{D}/kL_p)^2} = \frac{r}{k A_p \hat{c}^2} \quad (5.22)$$

5.5.2 Results

Figure 5.16 shows the dependence of the dimensionless cementing rate, \hat{r}^* on the dimensionless concentration, ϕ_1 and the dimensionless activity product, ϕ_2 for various values of the reactant ratio, ζ . From Figure 5.16 (a) it can be seen that for values of the concentration greater than approximately 1.0, the cementing rate is independent of the reactant ratio and further the cementing rate is equal to the concentration. From Figure 5.16 (b) it can be seen for values of the activity product less than approximately 0.1, the cementing rate is independent of the reactant ratio and further the cementing rate is equal to the activity product.

The limits observed in Figures 5.16 (a) and (b) can be verified from eq 5.18, which in terms of the dimensionless variables defined in eqs 5.20 to 5.22, is

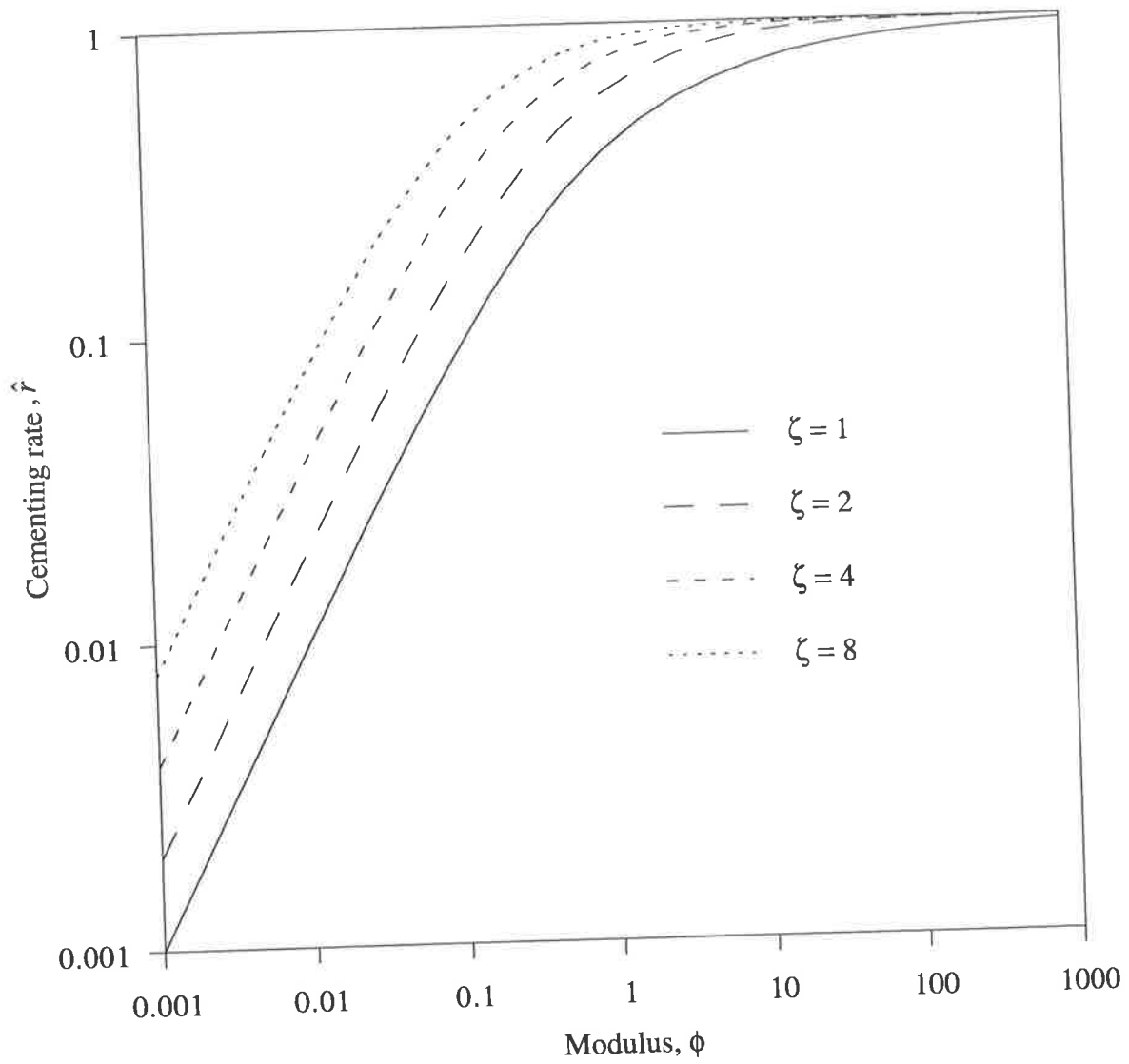
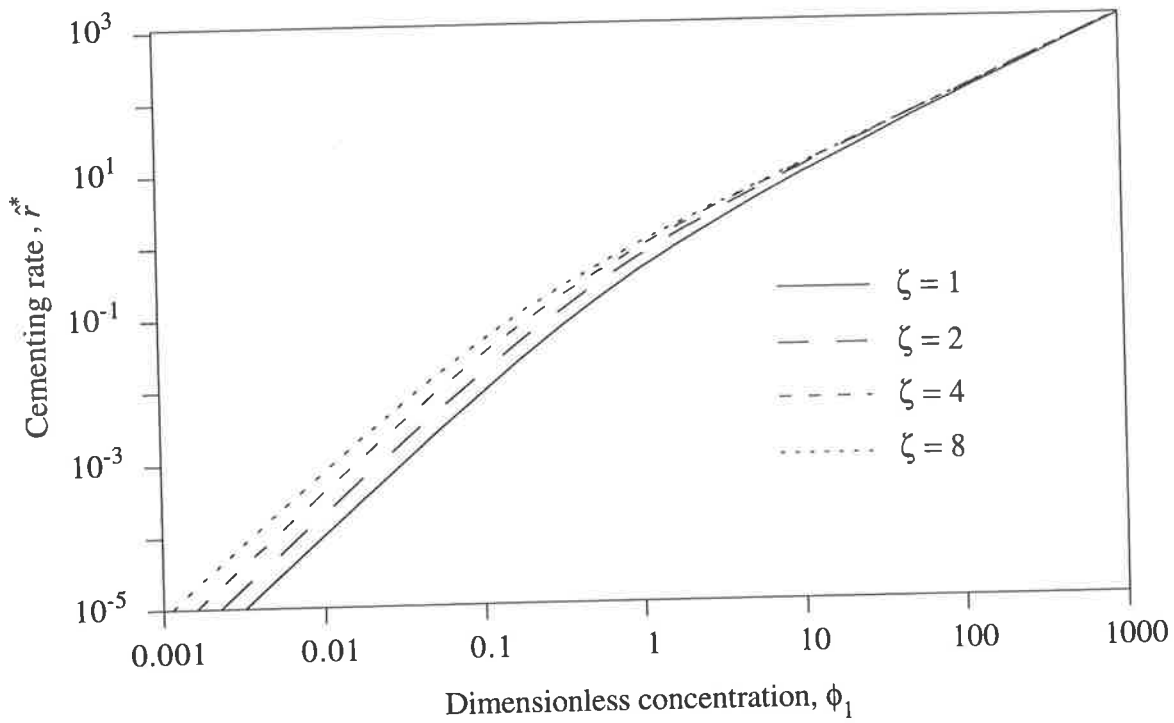
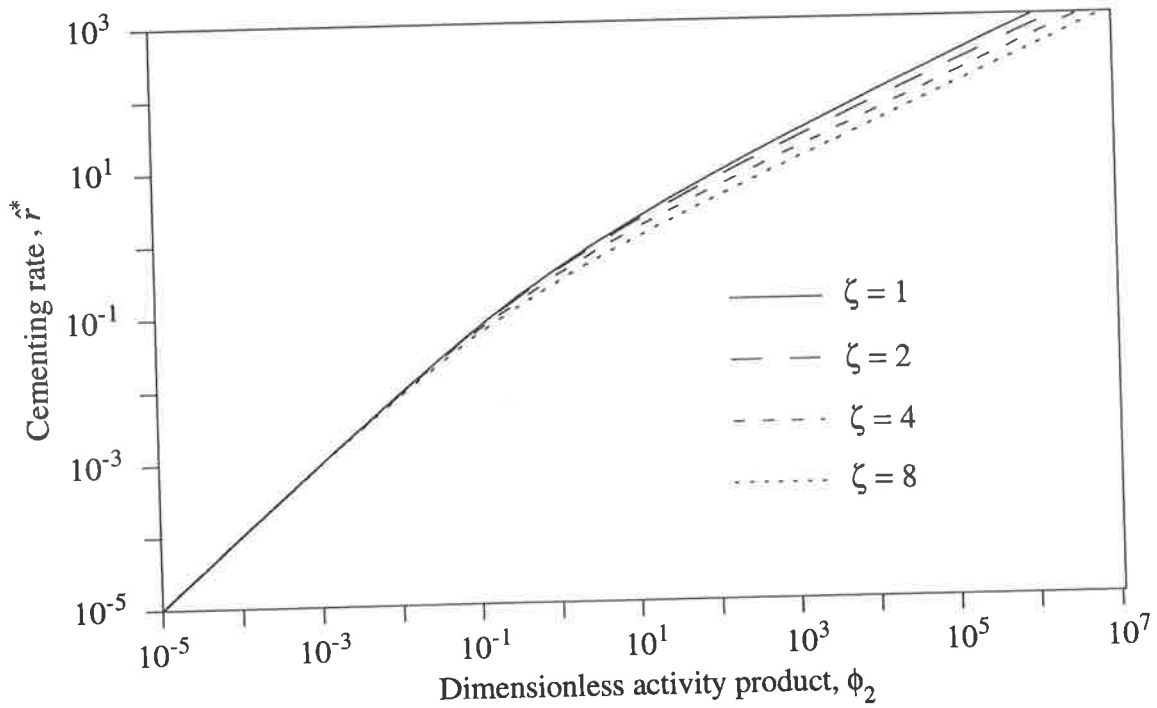


Figure 5.15 The dependence of the cementing rate on the modulus for various values of the reactant ratio, ζ .



(a)



(b)

Figure 5.16 The dependence of the dimensionless cementing rate on (a) the dimensionless concentration and (b) the dimensionless activity product for various values of the reactant ratio, ζ .

$$\hat{r}^{*2} - \hat{r}^*(1 + \phi_1(1 + \zeta)) + \phi_2 = 0 \quad (5.23)$$

If the cementing reaction rate is low, the rate constant, k is small, then from eq 5.20 the value of the concentration, ϕ_1 is small. In which case $\phi_1(1 + \zeta) \ll 1$ and from eqs 5.21 and 5.22, $\hat{r}^{*2} \ll \phi_2$ then using eq 5.23 implies $\hat{r}^* = \phi_2$.

When the rate of reaction is fast, $\hat{r}^{*2} \gg \hat{r}^*$ and eq 5.23 may be written in the form

$$\hat{r}^{*2} - \hat{r}^*(1 + \zeta)\phi_1 + \zeta\phi_1^2 = 0 \quad (5.24)$$

The solutions to eq 5.24 are: $\hat{r}^* = \phi_1$ and $\hat{r}^* = \zeta\phi_1$.

The second root can be ignored because $\hat{r}^* \leq 1$ but as $\zeta \geq 1$, if $\phi_1 = 1$ then $\hat{r}^* = \zeta \geq 1$. Thus the limits observed in Figures 5.16 (a) and (b) have been verified.

5.5.3 Discussion

The model proposed for aggregation in supersaturated solutions involves two steps, the diffusion of the reactant ions along a pore and a cementing reaction which takes place at the end of the pore. Either of these steps may be limiting, if the cementing reaction is very fast, the reactants will be rapidly precipitated at the end of the pore and the diffusion of reactants along the pore will be limiting. Conversely, if the cementing reaction is slow, this will be the limiting step in the process.

Figures 5.16 (a) and (b) show that for solutions of different composition if cementing is diffusion limited then the cementing rate depends only on the limiting reactant concentration, ϕ_1 , and not on the ratio of the reactants, ζ . If the process is reaction limited the cementing rate depends on the activity product of the reactants.

In Chapter 4 the aggregation rate constant in supersaturated solutions of different compositions is seen to depend only on the oxalate ion concentration, which was the limiting reactant. Tentatively, this suggests that the aggregation of calcium oxalate in supersaturated solutions is controlled by the rate of diffusion of oxalate ions to the cementing sites when crystals collide.

The agreement between the basic model for aggregation and the experimental results are qualitative, in order to investigate whether a more quantitative agreement can be obtained the basic model must be modified. The model must incorporate the actual growth kinetics

determined in Chapter 4 *viz.* the precipitation reaction is second order in relative supersaturation and is reversible.

5.6 AN IMPROVED CEMENTING MODEL

The model proposed in the previous section to explain aggregation in the presence of growth is re-worked with the experimental kinetics for crystal growth determined in Section 4.4.1.

5.6.1 Derivation

From eq 4.6 the growth rate may be described by the following equation

$$G \propto \left(\sqrt{\frac{AP}{K_{sp}}} - 1 \right)^2 \quad (5.25)$$

For these kinetics the cementing reaction rate at the end of the pore is

$$r = k \left(\sqrt{\frac{a_L b_L}{K_{sp}}} - 1 \right)^2 \quad (5.26)$$

where a_L and b_L are the oxalate and calcium ion concentrations at the end of the pore. Using the same definitions for the dimensionless concentrations and cementing rate, given by eqs 5.13, 5.14 and 5.16, the expression equivalent to eq 5.17 using the new equation for the cementing reaction rate is

$$\hat{r} = \frac{\mathcal{D} a_L}{L_p} (1-x) = \frac{\mathcal{D} a_L}{L_p} (1-y) = k \left(\sqrt{\frac{a_0 b_0 x y}{K_{sp}}} - 1 \right)^2 \quad (5.27)$$

The variables of interest are the activity product and the oxalate ion concentration, accordingly the following useful dimensionless groups are formed: a dimensionless activity product,

$$AP^* = \frac{a_0 b_0}{K_{sp}} \quad (5.28)$$

a dimensionless oxalate ion concentration,

$$a^* = \frac{a_0}{\sqrt{K_{sp}}} \quad (5.29)$$

and a dimensionless calcium ion concentration,

$$b^* = \frac{b_0}{\sqrt{K_{sp}}} \quad (5.30)$$

Eq 5.27 may be re-arranged to give

$$\hat{r}^* = a^*(1-x) = b^*(1-y) = k^* \left(\sqrt{a^* b^* x y} - 1 \right)^2 \quad (5.31)$$

where \hat{r}^* and k^* are the dimensionless cementing reaction rate and a dimensionless rate constant. The expressions for these parameters are

$$\hat{r}^* = \frac{\hat{r} L_p}{\mathcal{D} \sqrt{K_{sp}}} \quad (5.32)$$

and
$$k^* = \frac{k L_p K_{sp}^{3/2}}{\mathcal{D}} \quad (5.33)$$

Eliminating the dimensionless concentrations, x and y from eq 5.31 gives the following equation involving the dimensionless cementing rate

$$\begin{aligned} & k^{*2} \hat{r}^{*4} - 2k^{*2} (a^* + b^*) \hat{r}^{*3} \\ & + \left[-1 + k^{*2} (-2 + a^{*2} + 4a^* b^* + b^{*2}) \right] \hat{r}^{*2} \\ & + \left[2(a^* + b^*) + k^{*2} (2(1 - a^* b^*) (a^* + b^*)) \right] \hat{r}^* \\ & - 2(1 + a^* b^*) + k^{*2} (1 - a^* b^* (2 - a^* b^*)) = 0 \end{aligned} \quad (5.34)$$

Eq 5.34 is a quartic and is much more difficult to solve than the same expression from the simple model, eq 5.18. Rather than solving eq 5.34, which produces truly horrific equations for the cementing rate, a different approach is taken. It can be seen that eq 5.34 is a quadratic in a^* and the appropriate root is

$$a^* = \frac{\hat{r}^* + k^* (1 - b^* \hat{r}^* - \hat{r}^{*2}) + 2\sqrt{k^* \hat{r}^*}}{k^* (b^* - \hat{r}^*)} \quad (5.35)$$

During an experiment the decrease in the bulk concentration of the calcium and oxalate ions, as a result of growth, is the same for both species. If the initial bulk calcium and oxalate ion concentrations are b_i and a_i , it follows that

$$a_i^* - a^* = b_i^* - b^* \quad (5.36)$$

Using the expression for b^* from eq 5.36 in eq 5.35 the appropriate solution is

$$a^* = \hat{r}^* + \frac{a_i^* - b_i^*}{2} + \sqrt{\left(\frac{a_i^* - b_i^*}{2}\right)^2 + \left(1 + \sqrt{\frac{\hat{r}^*}{k^*}}\right)^2} \quad (5.37)$$

It is convenient to use eq 5.37 as it relates the dimensionless oxalate concentration to two unknowns, the dimensionless cementing rate and the dimensionless rate constant, k^* . For the experiments conducted the initial calcium and oxalate concentrations are known.

The procedure adopted to investigate the dependence of the cementing rate on the activity product and oxalate ion concentration is as follows. To consider the different regimes, from reaction rate to diffusion limited, a range of values of the rate constant were chosen. By varying the value of the cementing rate, eq 5.37 can be used to calculate the oxalate concentration, because the initial oxalate and calcium concentrations are known. Then the calcium concentration and activity product can be determined from eqs 5.36 and 5.28.

In the model for aggregation the formation of complex ions has been ignored, in particular for diffusion total concentrations were used. In Chapter 2 it was shown that the formation of complex ions reduces the free calcium and oxalate ion concentrations in the solutions used in the experiments reported in Chapter 3. Consider the diffusion of an ion, c , along a pore, together with the formation of a complex ion, d . If the rate of complex formation is, $r_{c \rightarrow d}$ and the reverse rate is $r_{d \rightarrow c}$, then at equilibrium the rates are equal, which implies $r_{d \rightarrow c} = -r_{c \rightarrow d}$. From eq 5.6, and including the complex formation reaction

$$\mathcal{D} \frac{d^2 c}{dz^2} = r_{c \rightarrow d} \quad \text{and} \quad \mathcal{D} \frac{d^2 d}{dz^2} = -r_{c \rightarrow d} \quad (5.38a \text{ and } b)$$

Combining eqs 5.38a and b it follows that

$$\frac{d(c+d)}{dz} = \text{constant} \quad (5.39)$$

Eq 5.39 implies that from the point of view of mass transfer by diffusion the total and free ion concentrations are the same, and thus total ion concentrations can be used to calculate the cementing rate.

Now if total concentrations are used rather than activities the value of the solubility product will be different. In Section 2.6 it was found that over the range of concentrations used in

the experiments reported in Chapter 4, the fractions of calcium and oxalate present as free ions are approximately constant.

As the fractions of calcium and oxalate ions present as free ions are approximately constant the free ion concentrations may be written in terms of the total ion concentrations as

$$[Ca^{2+}] = f_{Ca} T_{Ca^{2+}} \quad [Ox^{2-}] = f_{Ox} T_{Ox^{2-}} \quad (5.40a \text{ and } b)$$

where f_{Ca} and f_{Ox} are the fractions of calcium and oxalate present as the free ion and have values of 0.98 and 0.53 respectively. The activity product is defined by eq 2.1, replacing the free ion concentrations with eqs 5.40a and b, the activity product in terms of total concentrations is

$$K'_{sp} = T_{Ca^{2+}} T_{Ox^{2-}} = \frac{K_{sp}}{\gamma_{\pm}^2 f_{Ca} f_{Ox}} \quad (5.41)$$

The values of K_{sp} and γ_{\pm} are 2.24×10^{-9} and 0.315 respectively, which implies the value of K'_{sp} is $4.38 \times 10^{-9} \text{ M}^2$.

Finally, the model has been developed to describe aggregation in supersaturated solutions, in the presence of growth. In saturated solutions in which there is no growth, the model is not valid as cementing cannot take place. As such the values of the dependent variables should be measured relative to their values in a saturated solution. For the activity product this presents no problem as the modified solubility product defined in eq 5.41 can be used. The value of the oxalate concentration at equilibrium, a_{eq}^* , can be determined from eq 5.37, as at equilibrium the cementing rate, $\hat{r}^* = 0$, which implies

$$a_{eq}^* = \frac{a_i^* - b_i^*}{2} + \sqrt{\left(\frac{a_i^* - b_i^*}{2}\right)^2 + 1} \quad (5.42)$$

The values of the oxalate concentration at equilibrium for the experimental data were calculated using the method developed in Section 2.4.1. The system of equations (2.19 to 2.22 and 2.28) that represent the mass action equations for complex ion formation, the mass conservation equations and the expression for the solubility product were solved numerically together with eq 5.36, written in terms of total concentrations. The values of a_{eq}^* were then calculated from eq 5.29.

5.6.2 Results

In Figures 5.17 (a) to (c) the experimental values of the aggregation rate constant, β_0 , are plotted against AP^* , a^* and $a^* - a_{eq}^*$. In Figures 5.18 and 5.19 the dimensionless cementing rate is plotted against AP^* , a^* and $a^* - a_{eq}^*$ for values of the rate constant, k^* equal to 0.01 and 100. The values of the rate constant were chosen to give reaction rate limited and diffusion limited regimes. The range of each of the independent variables in these Figures is the same as the experimental range. The four curves plotted in each Figure have values of a_i^* and b_i^* corresponding to those in the four metastable solutions reported in Section 3.4.1.

From Figure 5.19 (b) when the value of the rate constant is large, the cementing rate is a linear function of the dimensionless oxalate ion concentration. This observation can be explained by considering eq 5.37. If the rate constant is large, then the cementing reaction will be fast and the value of \hat{r}^* will be large as well and $\hat{r}^*/k^* \approx 1$, consequently from eq 5.37,

$$a^* = \hat{r}^* + \frac{a_i^* - b_i^*}{2} + \sqrt{\left(\frac{a_i^* - b_i^*}{2}\right)^2 + 4} \quad (5.43)$$

Similarly if the rate constant is small, in which case the cementing rate is slow, and the value of \hat{r}^* will be small. If $\hat{r}^* \rightarrow 0$ in eq 5.36 it can be shown that

$$\hat{r}^* \approx 4k^*(a^*b^* - 1)^2 \quad (5.44)$$

The product of the reactant concentrations is equivalent to the dimensionless activity product, so eq 5.44 predicts second order dependence of the cementing rate on both the dimensionless activity product and dimensionless oxalate concentration. These predictions are confirmed in Figures 5.18 (a) and (b).

5.6.3 Discussion

In Figures 5.18 and 5.19 the relationship between the independent variable and the cementing rate is determined by whether the cementing reaction rate or reactant transfer by diffusion is limiting. While there is no expectation that the cementing rate, \hat{r}^* and the aggregation rate constant, β_0 will be identical, instead the patterns of behaviour of these parameters are investigated to determine whether they are similar.

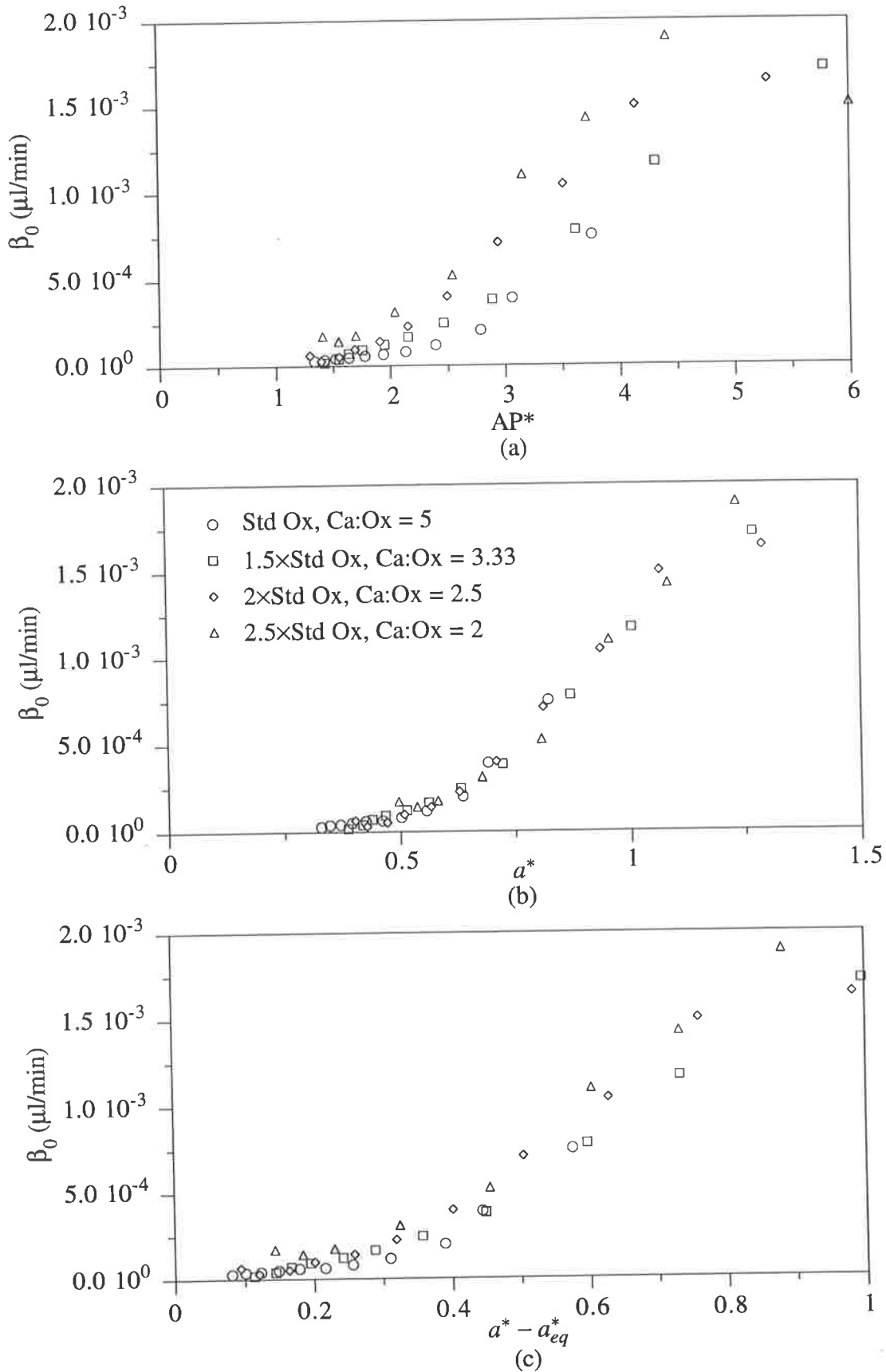


Figure 5.17 The dependence of the experimental aggregation rate constant on (a) the dimensionless activity product, (b) the dimensionless oxalate ion concentration and (c) $a^* - a_{eq}^*$ for metastable solutions with different initial supersaturations.

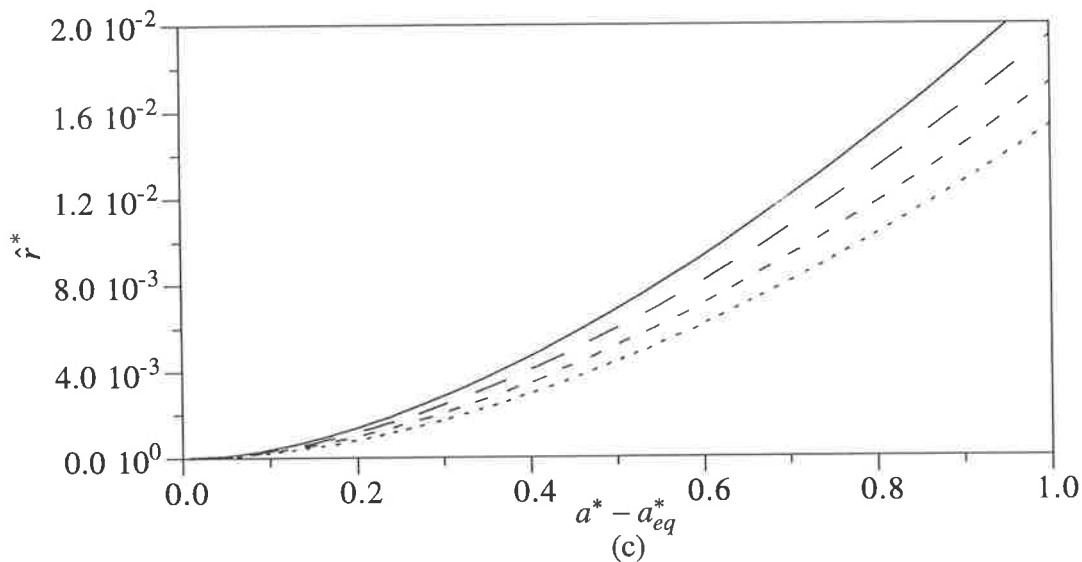
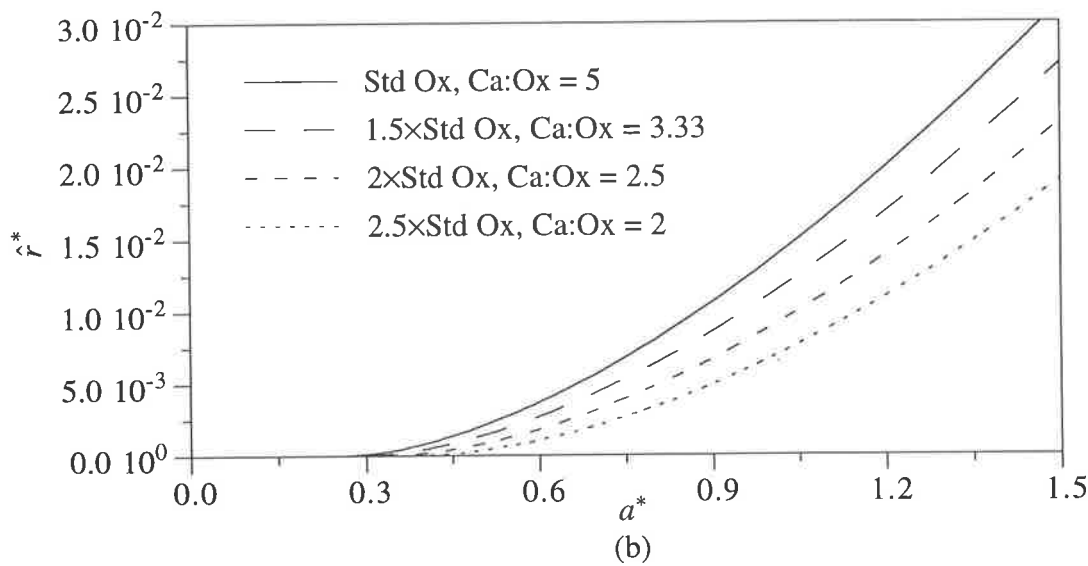
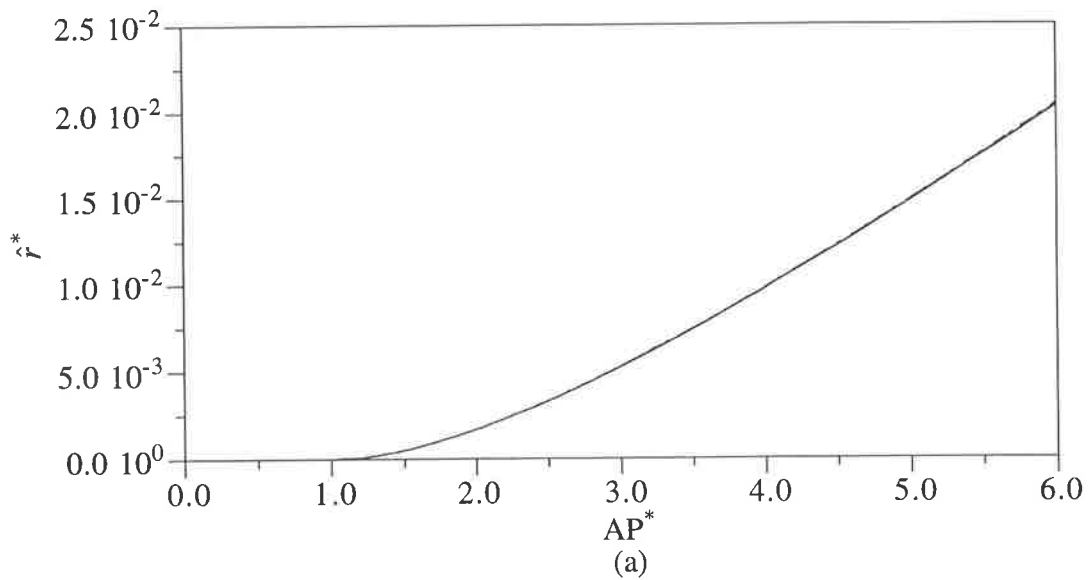


Figure 5.18 Model predictions for reaction rate limited aggregation. The dependence of the cementing rate on (a) the dimensionless activity product, (b) the dimensionless oxalate ion concentration and (c) $a^* - a_{eq}^*$ with $k^* = 0.01$ and for reactant ratios the same as those for the metastable solutions used in the batch experiments.

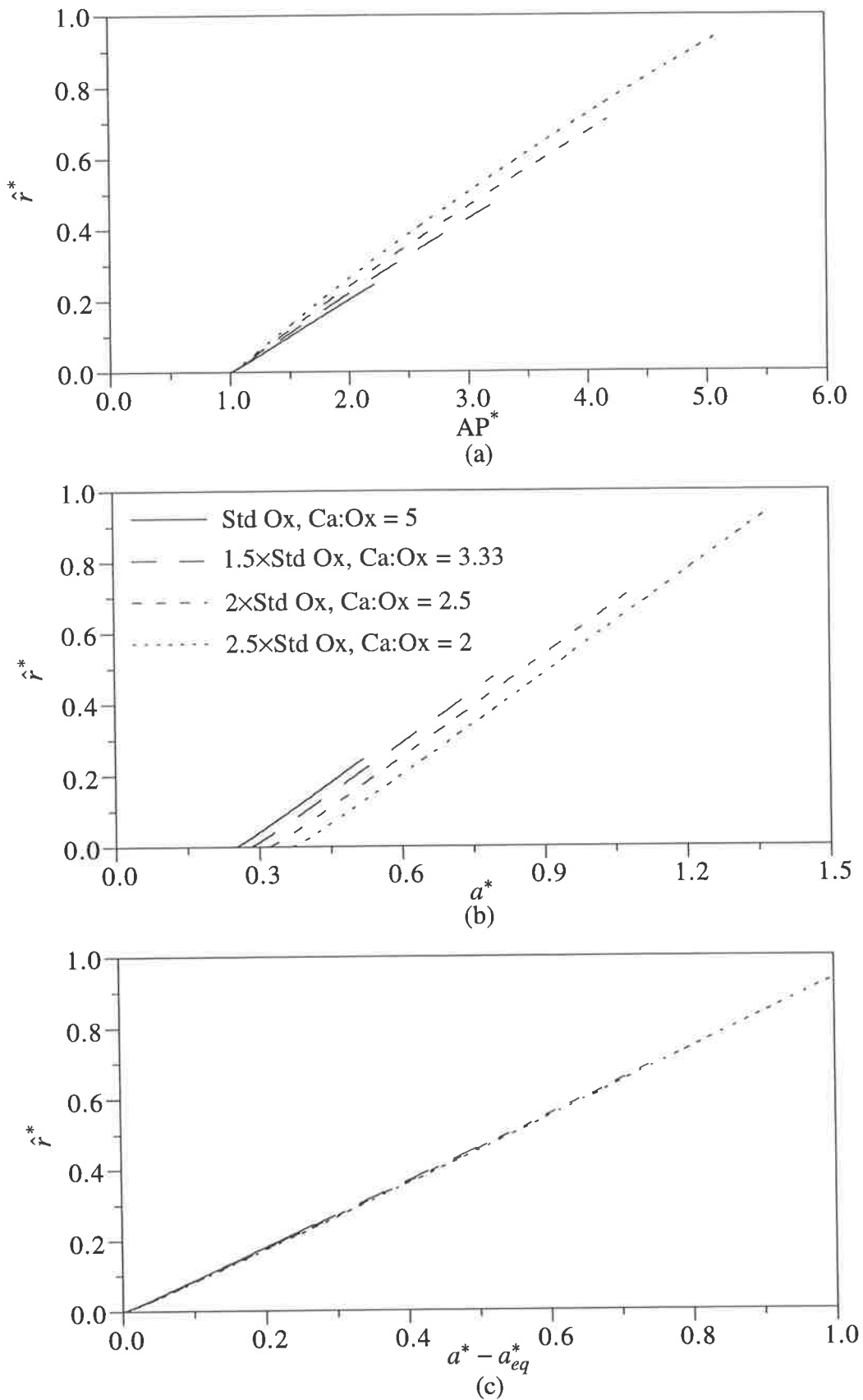


Figure 5.19 Model predictions for diffusion limited aggregation. The dependence of the cementing rate on (a) the dimensionless activity product, (b) the dimensionless oxalate ion concentration and (c) $a^* - a_{eq}^*$ with $k^* = 100$ and for reactant ratios the same as those for the metastable solutions used in the batch experiments.

5.19 (a), with $k^* = 100$ have the same appearance as the experimental data in Figure 5.17 (a). Different values of the cementing rate, or aggregation rate are obtained at the same value of the activity product, for different calcium to oxalate ratios.

For the same value of the rate constant there is correspondence between the plots of the oxalate concentration and $a^* - a_{eq}^*$, from the model and the experimental data. As shown in Figures 5.19 (b) and 5.17 (b) for the oxalate concentration and Figures 5.19 (c) and 5.17 (c) for $a^* - a_{eq}^*$. The experimental aggregation rates show more scatter when plotted against $a^* - a_{eq}^*$ than against the oxalate concentration, the opposite is true for the results from the model.

The cementing model would better describe the experimental data if the value of the dimensionless oxalate concentration at equilibrium, a_{eq}^* were smaller than that expected. Consider an analogy with capillary condensation, for calcium and oxalate ions dissolved in solution the chemical potential, μ , is given by

$$\mu = G_d^0 + RT \ln a_{Ca^{2+}} a_{Ox^{2-}} \quad (5.45)$$

where G_d^0 is the Gibbs free energy in the standard state. On a flat surface the chemical potential is given by the Gibbs free energy in the standard state, G_s^0 . At equilibrium, the Gibbs free energy of the ions in solution and the surface are equal and the value of the activity product is K_{sp} . A flat surface may be thought of as a cylindrical pore of infinite radius, thus

$$\Delta G = G_s^0 - G_d^0 = RT \ln K_{sp} (r = \infty) \quad (5.46)$$

In a cylindrical pore, if one mole of calcium oxalate precipitates, the surface area is reduced by, $a = 2\pi r L$. But the volume occupied by the precipitated material is

$$\pi r^2 L = 1/\rho_M \quad (5.47)$$

where ρ_M is the molar density. Hence, using eq 5.47 in the above expression for the change in surface area, implies

$$a = 2/\rho_M r \quad (5.48)$$

The overall change in Gibbs free energy is

$$\Delta G = G_s^0 - G_d^0 - \frac{2\gamma}{\rho_M r} \quad (5.49)$$

Eq 5.46 can be applied to the left hand side of eq 5.49, but with a finite radius, as well as to the right hand side, which gives

$$\frac{K_{sp}(r)}{K_{sp}(r = \infty)} = \exp\left(\frac{-2\gamma}{\rho_M RT r}\right) \quad (5.50)$$

Eq 5.50 implies that for small values of r , the apparent solubility product in the pore is very much lower than the actual solubility product. From Söhnel and Garside (1992), for calcium oxalate the value of the surface energy is $120 \times 10^{-3} \text{ J/m}^2$ and the molar density is 15.75 kmol/m^3 , so at 37°C the value of the constant in eq 5.50 is $5.91 \times 10^{-9} \text{ m}$. Since r is probably in the order of 10^{-9} m , then from eq 5.50 $K_{sp}(r) \approx 0.027 K_{sp}$. This implies the deposition of material at the cementing site is energetically highly favourable. Combining eq 5.41 for the solubility product with the definition of a_{eq}^* , implies at equilibrium

$$a_{eq}^* = \sqrt{K_{sp}/T} \text{Ca}^{2+} \quad (5.51)$$

Thus as the apparent solubility product in the pore is lower than that in solution, the value of a_{eq}^* will also be lower than that calculated.

If the dimensionless oxalate concentration at equilibrium is very small, then the results for the different calcium to oxalate ratios in Figure 5.19 (b) for a diffusion limited process, will collapse onto one curve which compares reasonably well with the experimental data in Figure 5.18 (c).

5.7 CONCLUSIONS

In this chapter the mechanism for the aggregation of calcium oxalate crystals in both saturated and supersaturated solutions has been investigated.

A two-stage mechanism is proposed to account for experimental observations of the dependence of aggregation on the agitation rate and supersaturation:

- In the first stage, which is reversible, crystals collide and form weak aggregates held together by the forces described by DLVO theory.
- In the second irreversible stage, the loose aggregates are cemented together by the deposition of new material.

The second stage can only occur in supersaturated solutions, while the first can occur in any solution. By means of this mechanism the experimental observations reported in Chapter 4, as well as those of other investigations in the literature can all be explained.

A model is proposed to explain the cementing in the second stage of the aggregation mechanism. It is assumed that in order for cementing to take place, ions must diffuse to a cementing site and then precipitate. In the model it is proposed that the diffusion resistance is that of a long thin pore. It is found that this model at least qualitatively predicts the experimentally observed dependence of the aggregation rate on the activity product and oxalate concentration and that the transport process is limited by diffusion.

Chapter 6:

THE *IN VITRO* STUDY OF UROLITHIASIS

In this chapter a review of the in vitro experimental systems that have been used to study the crystallisation of calcium oxalate is presented. It is found that virtually all the experimental systems ignore the geometry of the tubules in the kidney and the effect that this might have on important factors in stone formation such as crystal retention and aggregation.

A novel tubular crystalliser is described that will be used to investigate calcium oxalate crystallisation in long, thin tubes, similar to the tubules of the kidney.

6.1 INTRODUCTION

Without doubt the major reason for the interest in the crystallisation of calcium oxalate is that the major inorganic constituent of most human kidney stones are crystals of calcium oxalate (Prien and Prien, 1968).

Because of the difficulty involved in observing crystal growth *in vivo* (in the kidney itself) an *in vitro* experimental system is highly desirable. In this way the mechanisms thought to be responsible for stone formation and stone disease (urolithiasis) can be studied in great detail.

One of the most difficult tasks in the investigation of stone formation is the development of an *in vitro* experimental system that has all the attributes of an organ as complex as the kidney. The objective of this chapter is to review the existing *in vitro* experimental systems, and describe the tubular crystalliser to be used in the current work.

6.2 *IN VITRO* EXPERIMENTAL SYSTEMS

Various *in vitro* experimental systems have been used to study the processes thought to be important in stone formation, namely crystal nucleation, growth and aggregation; some differ in technical detail and others at a more fundamental level. By using alternative techniques each phenomena can be investigated. However, the comparison of results may be difficult. Different experimental systems have specific features that make them suitable for investigating one or more of the factors affecting stone formation. Nonetheless inherent

in each, and perhaps every experimental system, are several critical conditions which prevent an analogy with the kidney being as close as might be desirable.

6.2.1 Batch crystallisation

Seeded batch crystallisation has been one of the most widely used techniques for studying factors affecting the growth and aggregation of calcium oxalate. It has been used to study growth: Nancollas and Gardner (1974), and Meyer and Smith (1975a), growth and aggregation: Hounslow *et al.* (1988a) and (1988b) and Will *et al.* (1983), inhibition of growth and aggregation: Robertson *et al.* (1973), Ryall *et al.* (1981c) and Kok *et al.* (1990) and factors affecting precipitation: Škrtić *et al.* (1984), Brečević *et al.* (1989) and Babić - Ivančić *et al.* (1985). This is only a short list of the many different investigations that have used seeded batch crystallisation.

As batch experiments have been widely used to study such a range of phenomena, there are, not surprisingly, many different methods of monitoring the crystallisation process. The purpose of this discussion is to point out the advantages and disadvantages of the different *in vitro* experimental systems rather than giving a detailed description of each. An excellent review of batch crystallisation methodology is given by Kavanagh (1992).

The principal virtues of batch crystallisation are the well established experimental protocols that exist and the ease with which experiments can be conducted. Also as described in Chapter 3 a computer program has been developed that can calculate the *true* growth and aggregation rates from batch experimental data.

However, the main problem with batch experiments is that an agitated vessel on a bench is a poor representation of the kidney. According to Sheehan and Nancollas (1980) the supersaturation with respect to calcium oxalate *in vivo* is relatively constant, whereas in a batch experiment the supersaturation decreases as a consequence of crystal growth. Also the flow of urine through the kidney is a continuous rather than a batch process.

6.2.2 Constant composition methods

The problem of supersaturation decreasing during a batch experiment has been addressed by Sheehan and Nancollas (1980), who use the constant composition method of Tomson and Nancollas (1978). Constant calcium and oxalate ion concentrations are maintained by the simultaneous addition of solutions containing these ions, controlled by measurements of the calcium ion concentration by a calcium ion specific electrode. This method is well suited for

measuring the growth rate, particularly at low supersaturations, but does not account for aggregation and is still a batch, rather than a continuous process.

6.2.3 The M.S.M.P.R. crystalliser

The concept of the urinary tract as a biological analogue of a sequence of continuous crystallisers was first proposed by Finlayson (1972), based on the observation that any vessel continuously receiving a stream of supersaturated fluid and continuously ejecting a stream of fluid and suspended crystals is a crystalliser. The renal pelvis continuously receives urine and suspended crystals from the ducts of Bellini. Therefore the ducts of Bellini and the renal pelvis may be viewed as a sequence of two MSMPRs.

The main advantage of using an MSMPR to study crystallisation is that an analytical solution to the population balance exists if only nucleation and growth occur, as shown by Randolph and Larson (1988). Consequently the MSMPR has been extensively used to study nucleation and growth kinetics and to examine the effects of various urinary constituents and other compounds on these processes. For example see Miller *et al.* (1977), Rodgers and Garside (1981), Drach *et al.* (1981), Li *et al.* (1985) and Kohri *et al.* (1988) and (1989).

However, there are problems associated with the operation of an MSMPR. Rodgers and Garside (1981) note that the supersaturation at steady state is often very low and difficult to measure. Also, more importantly, if aggregation occurs the analytical solution for nucleation and growth alone is not valid, and the rates calculated will be wrong. Garside *et al.* (1982), Robertson and Scurr (1986) and Kohri *et al.* (1988) all observe the effects of aggregation in either the CSDs or SEM micrographs of the product crystals from an MSMPR.

The MSMPR is perhaps a more realistic representation of the kidney, it operates at constant supersaturation at steady state, and is a continuous device. However, it cannot easily be used to study the most important mechanism in stone formation, crystal aggregation. Also it does not have the tubular geometry of the kidney, thus the fluid velocity profile and residence time distributions of the fluid and crystals in an MSMPR will be different from those in the kidney.

6.2.4 The Couette agglomerator

The addition of a Couette agglomerator in series with an MSMPR – the agglomerator being fed with fresh seed generated continuously in the MSMPR, has been used to study the aggregation of calcium oxalate by Springman *et al.* (1986) and Hartel *et al.* (1986).

The problem of simultaneous growth and aggregation is not solved by this modification. The solutions fed to the agglomerator are still supersaturated, so to determine the effect of aggregation the growth rate in the agglomerator must be known. Springman *et al.* and Hartel *et al.* both assume the growth rate in the agglomerator is the same as that in the MSMPR. While this might be acceptable when the output of the MSMPR is fed directly to the agglomerator, Hartel *et al.* add more oxalate to the solution before it enters the agglomerator, which must increase the supersaturation and therefore the growth rate.

A further problem with the agglomerator, acknowledged by both authors, is that the shear rates in the device are much higher than might be expected in the tubules of the kidney. Finally, as with the MSMPR alone, the fluid velocity profile and residence time distribution in the Couette agglomerator will be different from those in the kidney.

6.2.5 Reverse osmosis

Azoury *et al.* (1986) and (1987) use reverse osmosis (RO), or hyperfiltration, to generate and maintain supersaturation. The RO unit, may be visualised as a shell and tube exchanger, in which a large number of porous hollow fibres are the tubes. A metastable solution is fed to the shell, water is driven through the walls of the porous tubes by high pressure then flows along the tubes. This process produces a concentrated flow that leaves the shell side. The operation of this device is shown schematically in Figure 6.1.

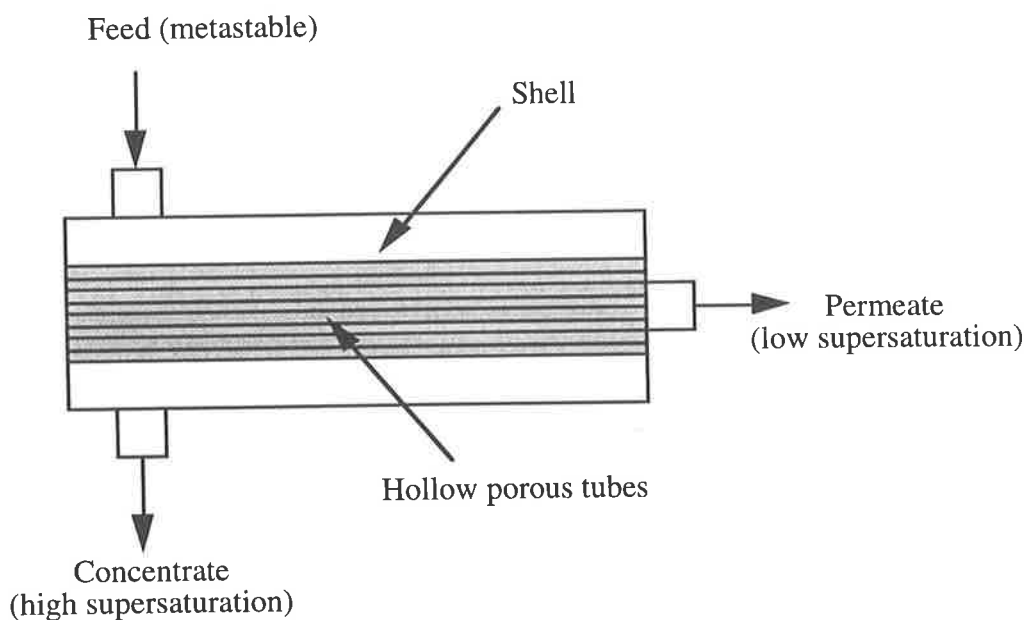


Figure 6.1. Reverse osmosis unit (After Azoury *et al.* (1986))

Azoury *et al.* (1986) operate a RO unit with a pressure difference of 8 bar across the hollow tubes and feed flow rates of 0.5 litre/min and 1.5 litre/min. These conditions give mean residence times of 3 and 1 minute respectively. Under these conditions the concentrate supersaturation is sufficient to bring about nucleation, and the mean residence time long enough for subsequent growth and aggregation of the nucleated crystals to occur.

The RO unit is an attractive *in vitro* experimental system as it possesses many of the features of the kidney. It may be operated at constant supersaturation, is a continuous device, and like none of the other experimental systems discussed has a tubular geometry. However, some aspects of the operation of this device by Azoury *et al.* (1986) are not representative of the conditions in the kidney. An extremely high pressure difference between the shell and the porous tubes was used, together with fluid flowrates high enough to give plug flow. Finlayson and Reid (1978) state that the flow in the tubules of the kidney will be laminar and that approximately 1440 ml of urine is produced per day. Schulz (1987) in a study of the influence of the fluid flow field on the formation of urinary stones using scale models of the renal pelvis also finds that the fluid flow is in the laminar regime.

6.3 A NEW TUBULAR CRYSTALLISER

Despite the attractive features of the *in vitro* experimental system described in the previous section, it has not been used to further investigate the growth and aggregation of crystals in a tubular geometry similar to that of the kidney. One of the aims of this work is to consider the effect that the geometry of the tubules in the kidney has on factors influencing stone formation, such as aggregation and crystal retention. For this reason a crystalliser similar to the one used by Azoury *et al.* (1986) was developed.

6.3.1 The crystalliser

The tubular crystalliser is shown in Figure 6.2. It consists of 262 Amicon H1P10-20 hollow porous fibre tubes each of internal diameter 410 μm , and length 45.5 cm contained as a bundle in a perspex tube of internal diameter 2.0 cm. The porous fibre tubes are constructed from a polysulfone material and are used for hemodialysis, desalination of salt water by reverse osmosis and the concentration of proteins by ultrafiltration (Baum *et al.*, 1976). The fibres are robust, resistant to acid, alkali and detergents, simple to clean and may be used repeatedly for long periods (Amicon, 1986). A SEM micrograph of the porous structure of the tubes is shown in Figure 6.3.

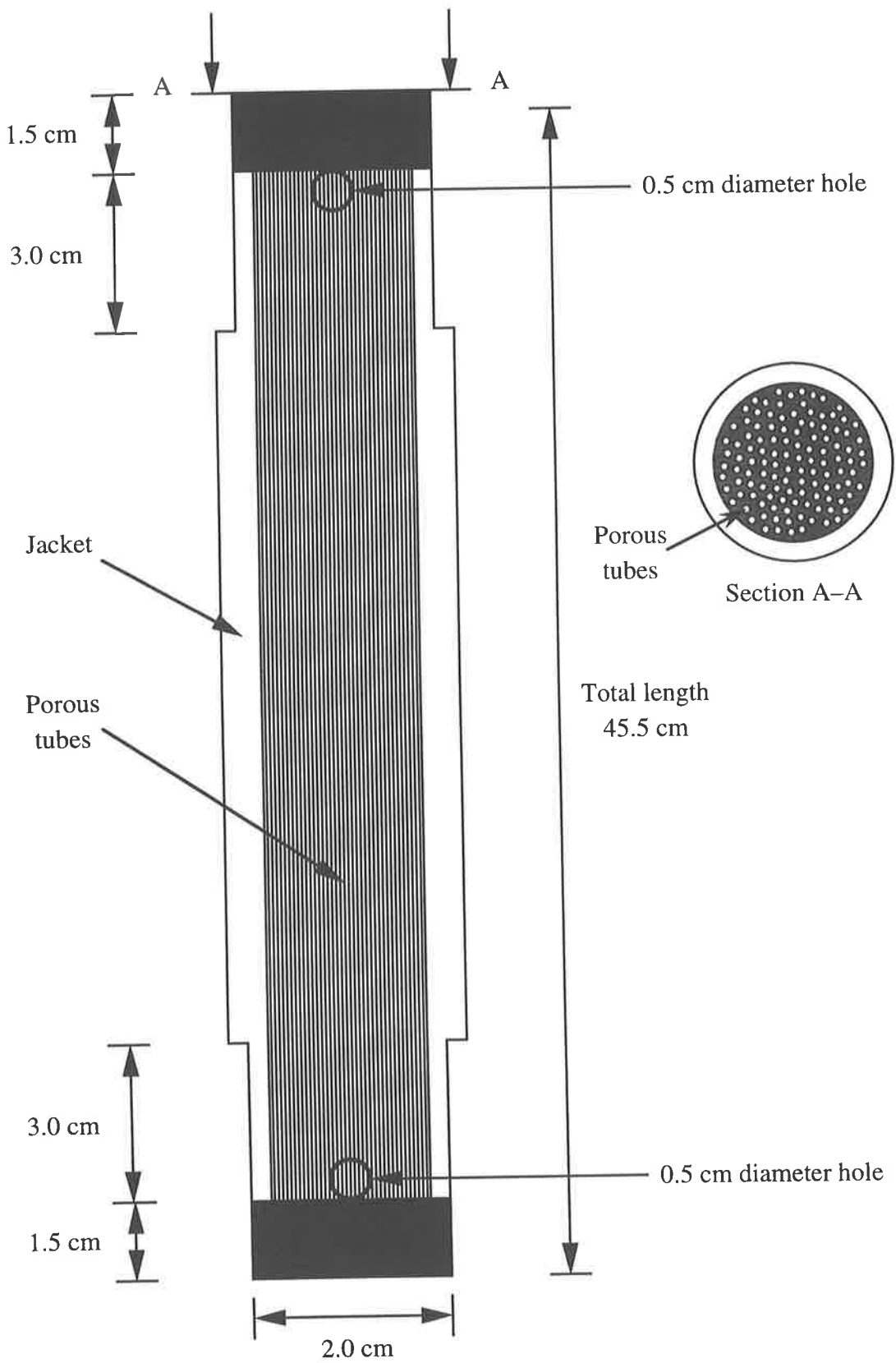


Figure 6.2 A schematic diagram of the tubular crystalliser.

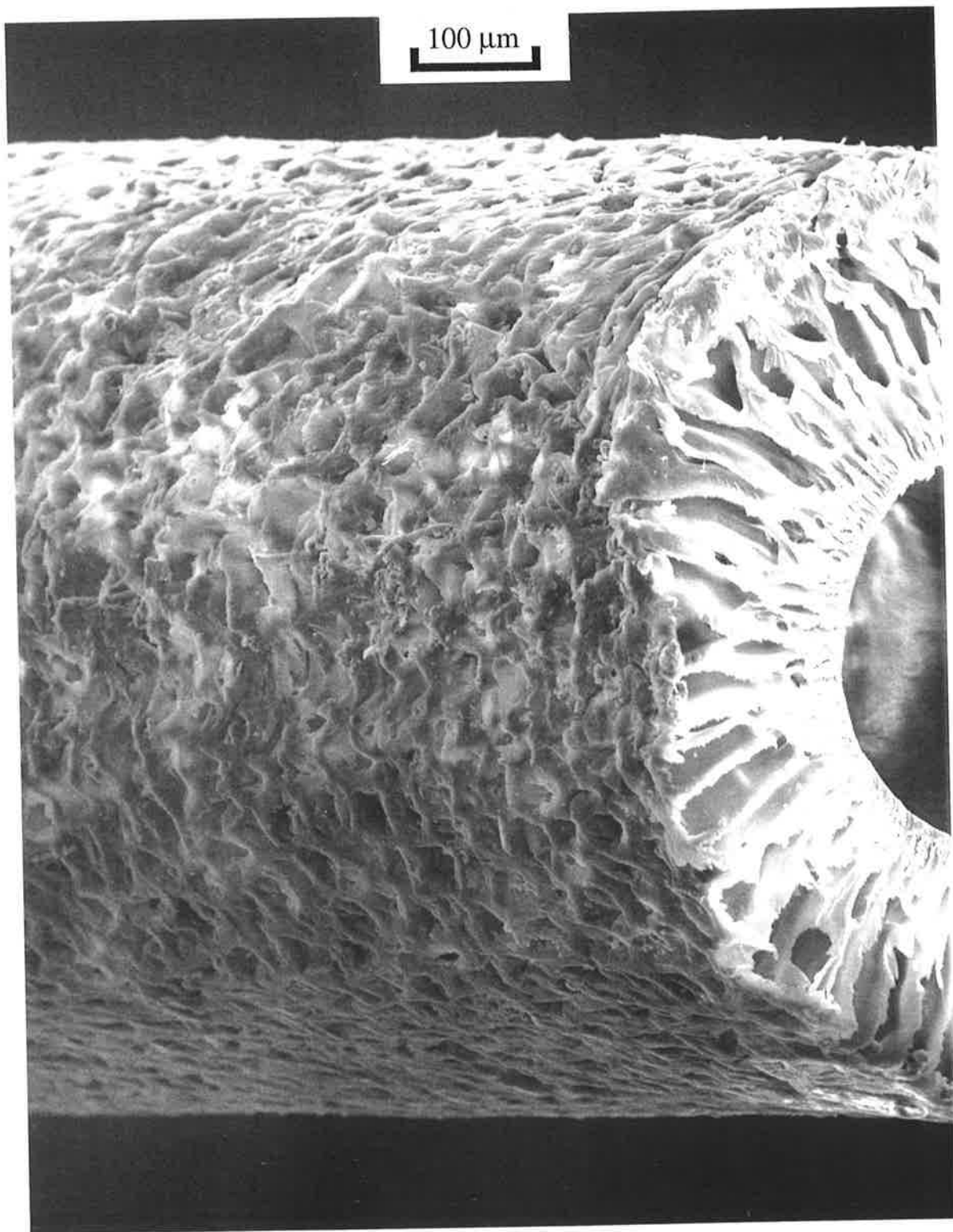


Figure 6.3 A SEM micrograph of the Amicon H1P10-20 hollow porous fibre tubes in the tubular crystalliser.

The tubular crystalliser has two compartments:

- The hollow porous fibre tubes, which will be referred to as the **lumen**.
- The region surrounding the lumen in the perspex tube which will be referred to as the **jacket**.

The fibres are held in place at both ends of the perspex tube by epoxy resin for a length of 1.5 cm. At each end of the perspex tube are four holes, 0.5 cm in diameter, through which fluid can enter and leave the jacket.

Manifolds are fitted to both ends of the crystalliser to allow fluid to be fed to the hollow sections of the lumen and the jacket. The manifolds are shown in Figures 6.4 (a) and (b). The crystalliser fits into the manifolds as shown in Figure 6.5. The crystalliser is held in place and sealed, so fluid will not leak from it, by two O-rings in both the inlet and outlet manifolds. However, the crystalliser does not fit flush with the manifolds, there is a dead volume at both ends, as indicated in Figure 6.5 by the regions A and B.

Devices similar to the tubular crystalliser, known as hollow fibre cartridges (Amicon, 1986), have been used extensively as artificial kidneys and for various processes such as ultrafiltration. The fluid flow distribution in hollow fibre cartridges has been investigated by Park and Chang (1986) and they suggest that the geometry and size of the dead volume in each manifold will affect the fluid flow distribution in the lumen. Under certain conditions it is possible for fluid to preferentially flow through the lumen in the centre of the cartridge and leave stagnant regions near the edge. Based on numerical simulations of the fluid flow in the cartridge, Park and Chang (1986) recommend that for uniform flow distribution, the manifolds should be shaped such that the dead volumes at the inlet and outlet are cylindrical and conical respectively. Accordingly implants were made to fit into the manifolds to reduce the size of the dead volumes and alter their geometry. The implants, and their positioning in the manifolds are shown in Figures 6.6 (a) and (b).

6.3.2 The seed suspension delivery system

In the continuous crystallisation experiments reported in Chapter 9, a calcium oxalate seed suspension was mixed with the fluid fed to the lumen just before it enters the crystalliser. Thus another important part of the apparatus is the seed suspension delivery system, which is shown in Figure 6.7.

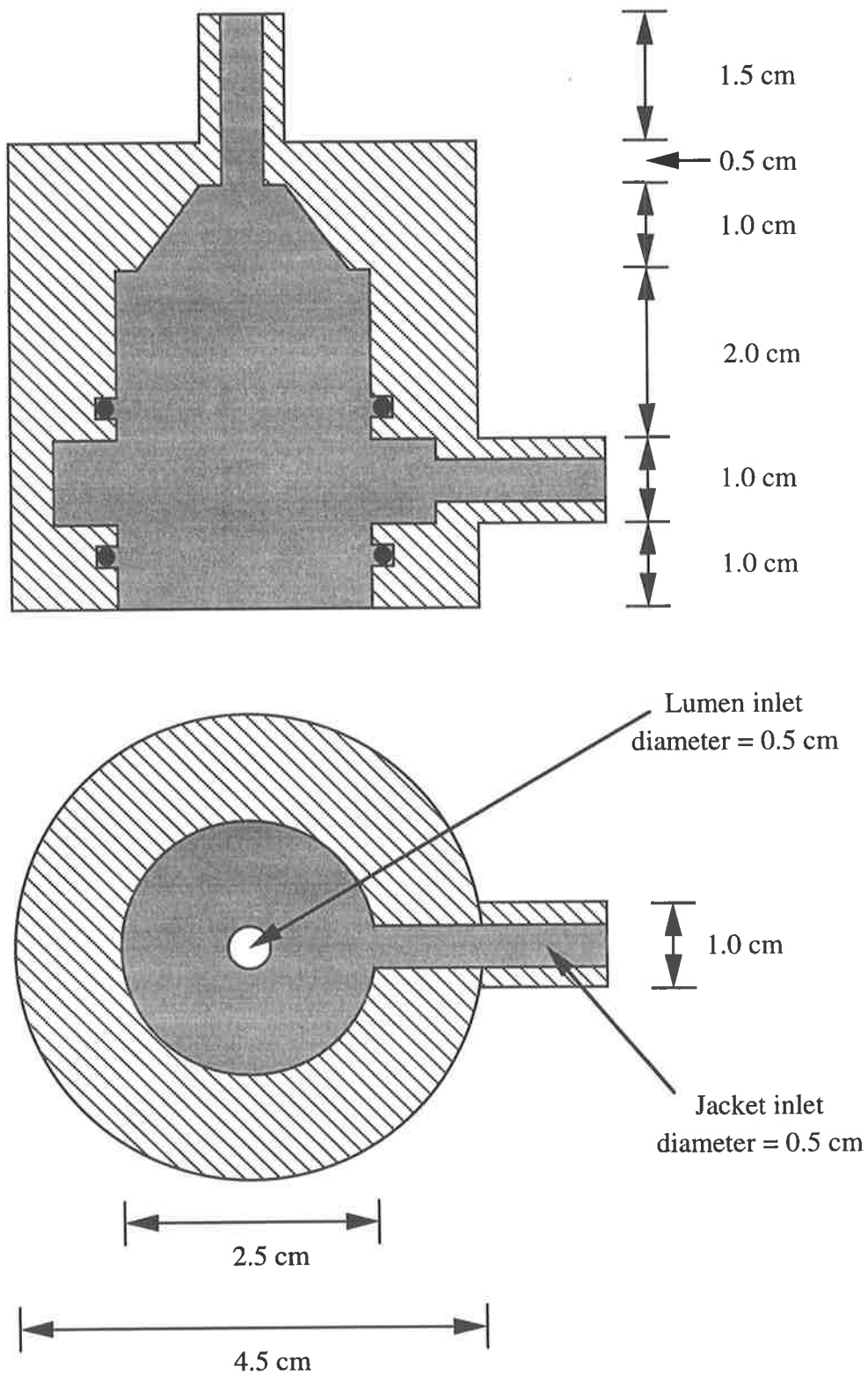


Figure 6.4 (a) The manifold at the inlet of the tubular crystalliser.

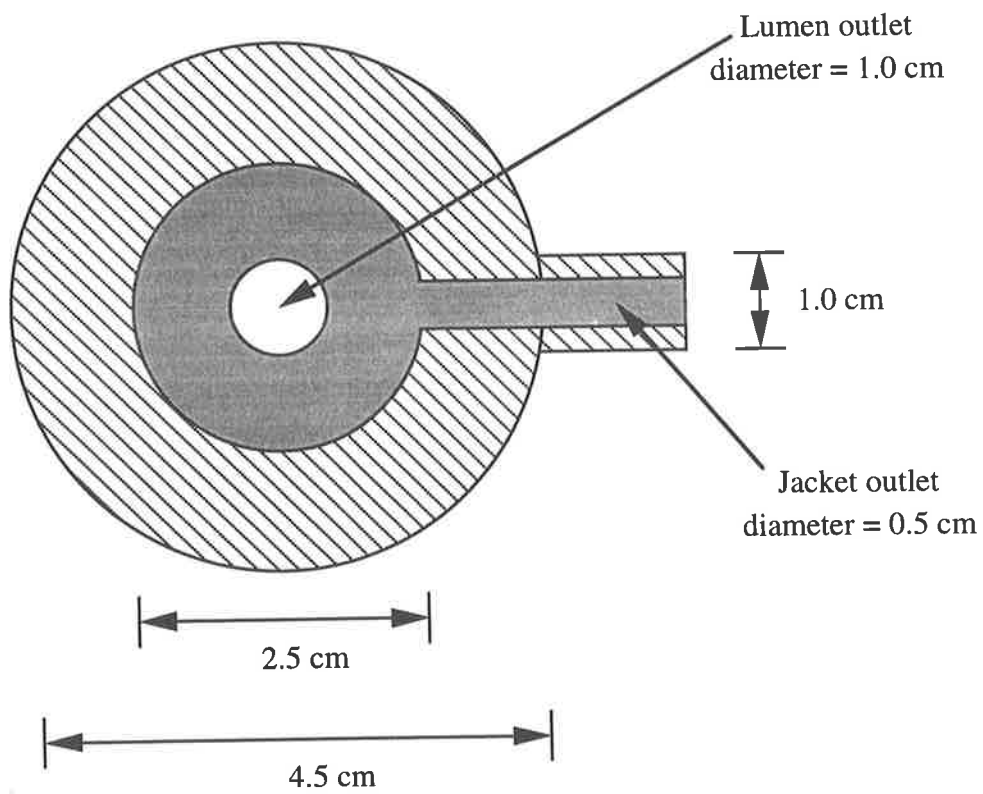
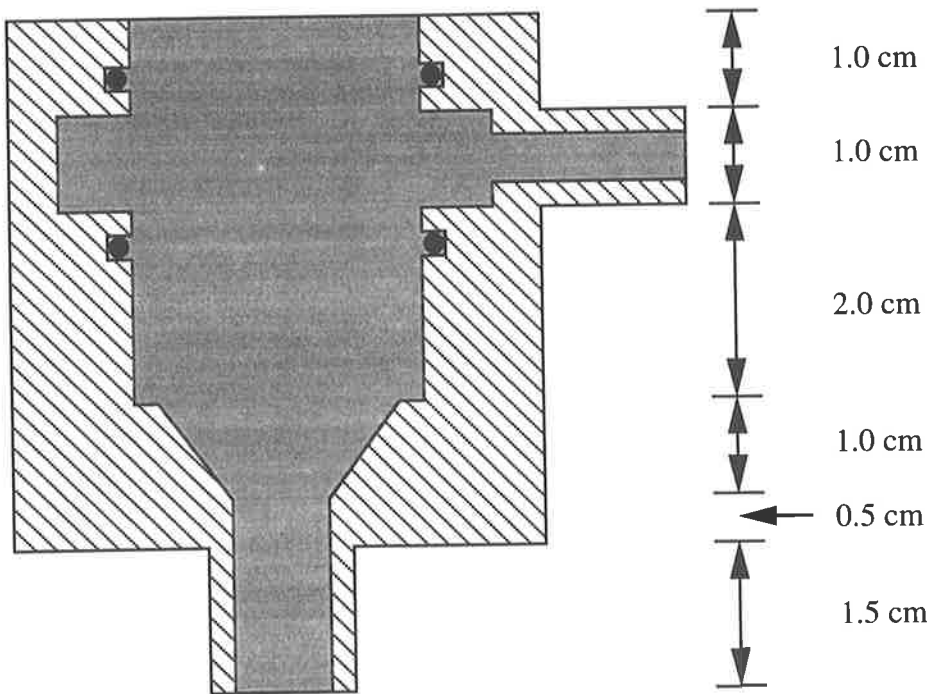


Figure 6.4 (b) The manifold at the outlet of the tubular crystalliser.

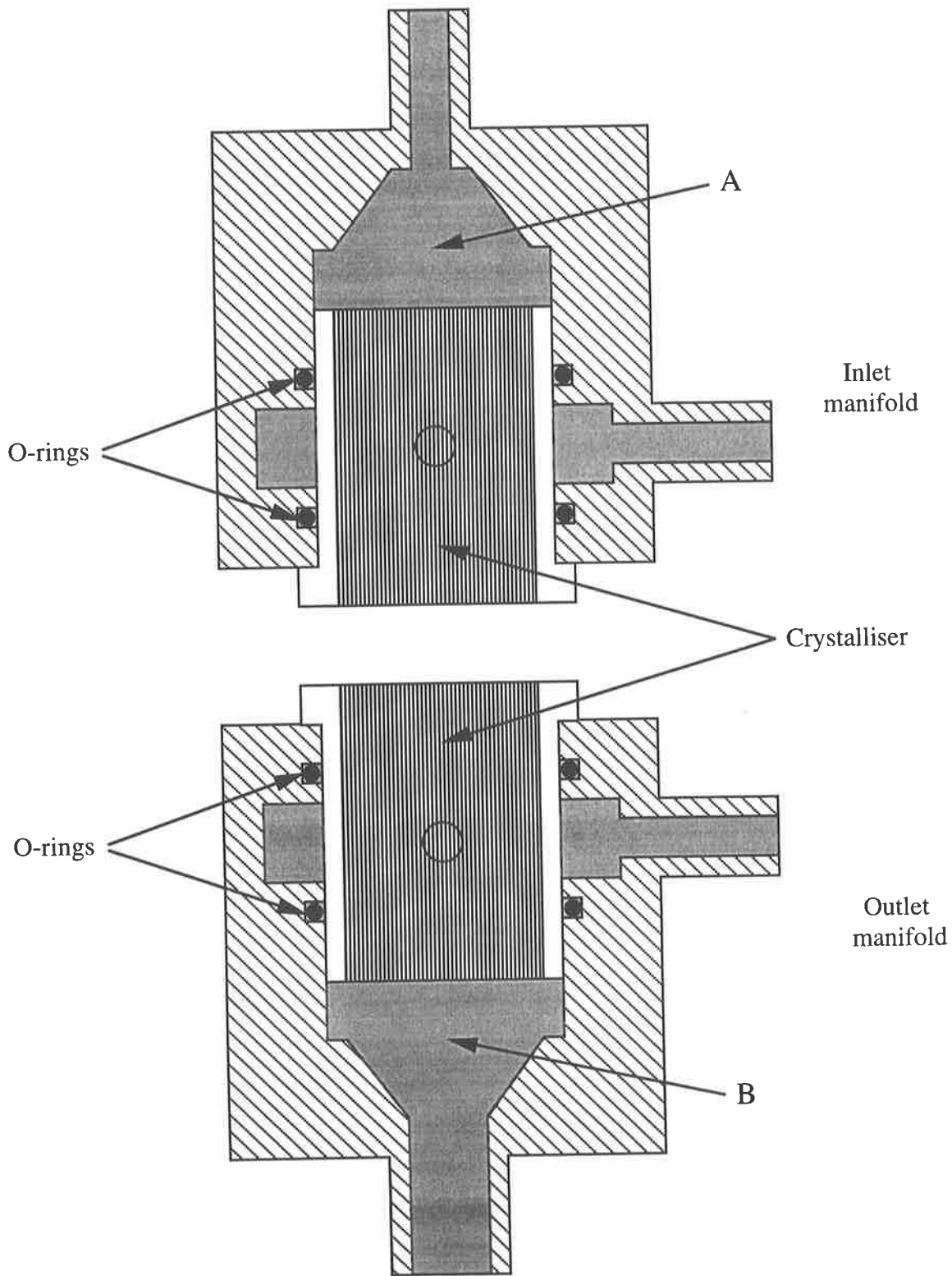
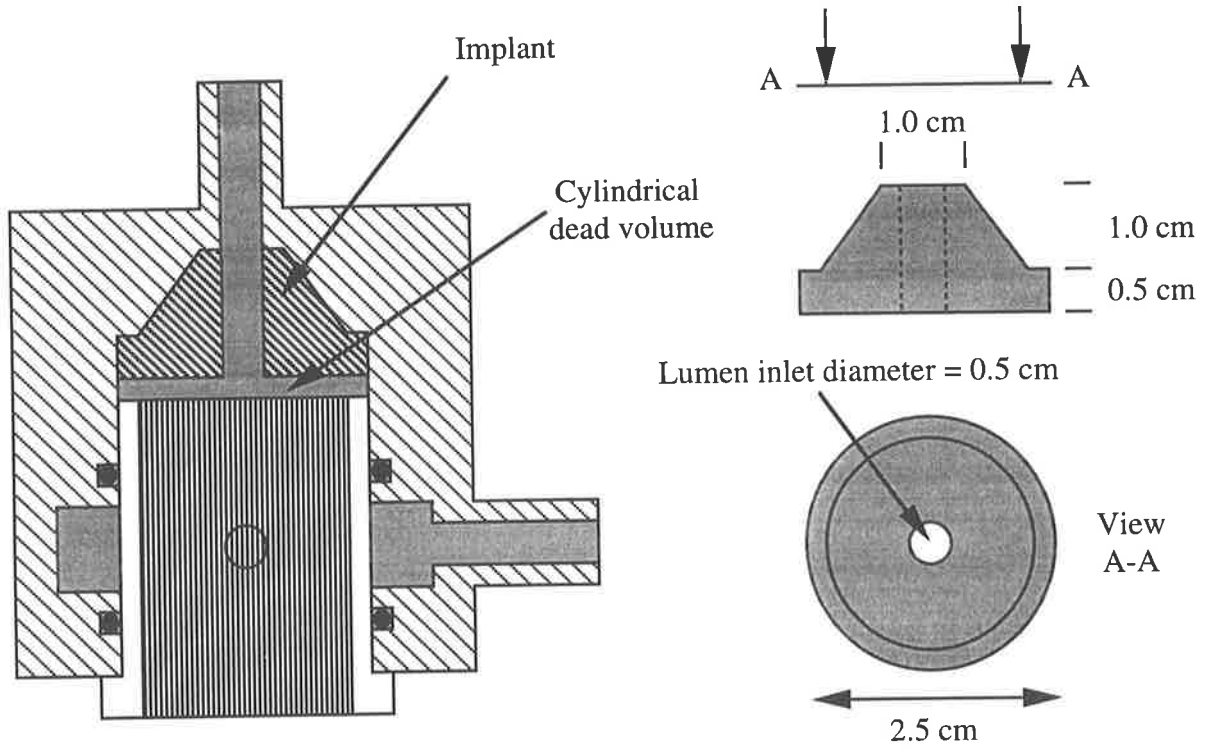
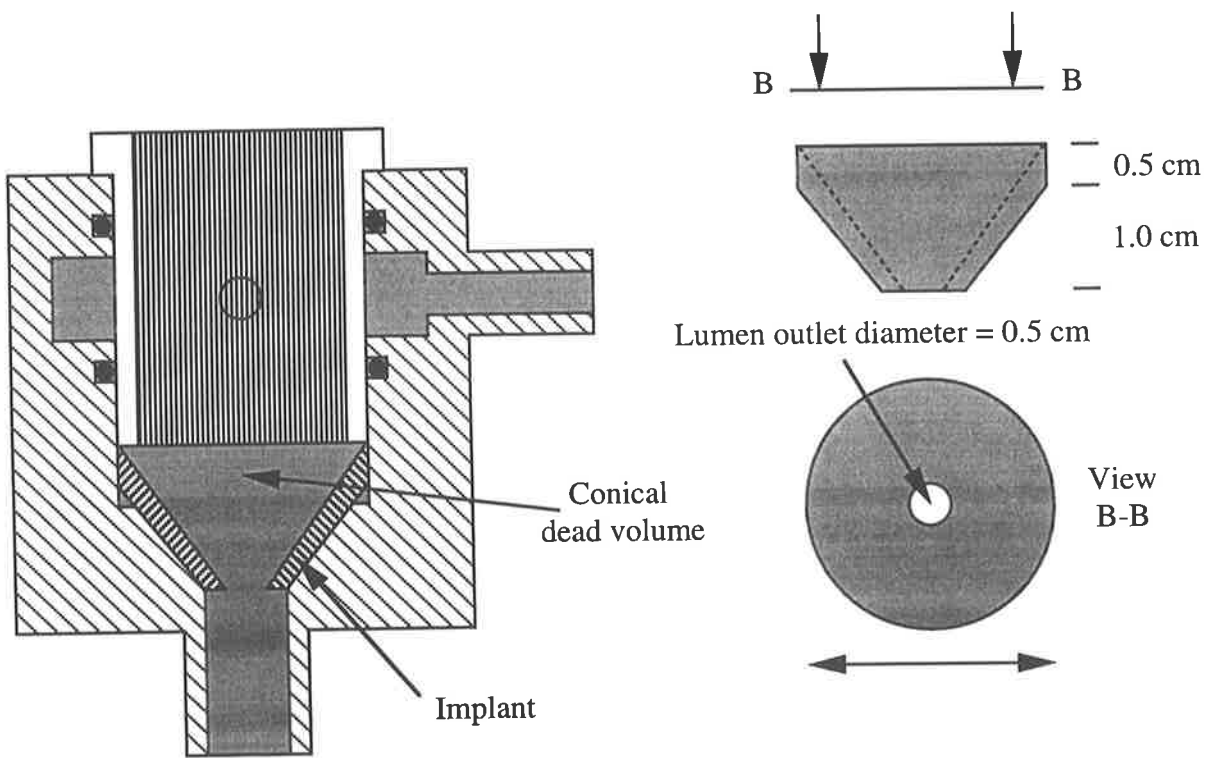


Figure 6.5 A schematic diagram showing how the crystalliser fits into the manifolds at the inlet and outlet and the dead volumes at both ends.



(a)



(b)

Figure 6.6 A schematic diagram of the implants and their positioning in (a) the inlet manifold and (b) the outlet manifold.

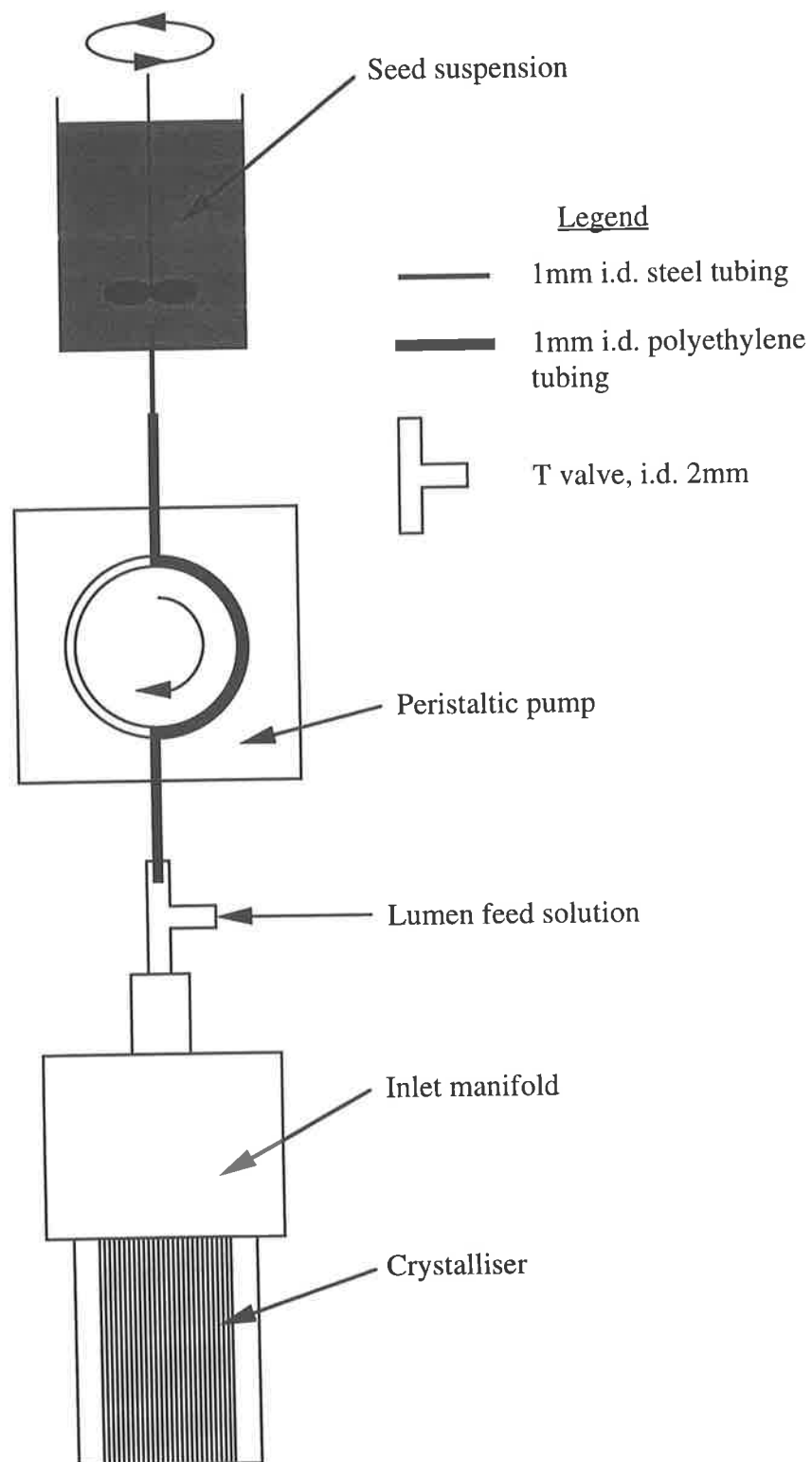


Figure 6.7 A schematic diagram of the seed suspension delivery system.

The seed suspension was stored in a perspex tank with a capacity of 400 ml, in which the seeds were suspended by the propeller-stirrer supplied with the Multisizer II. The seed suspension was fed to the crystalliser, *via* 5 cm of steel tubing of internal diameter 1 mm, and 20 cm of polyethylene tubing of internal diameter 1 mm. A peristaltic pump, Pharmacia Fine Chemicals, model P-1 (Pharmacia Fine Chemicals, Upsala, Sweden) was used to supply the seed suspension to the crystalliser at flowrates between 0.12 ml/min and 0.55 ml/min. The seed suspension mixes with the fluid fed to the lumen in a three way T-valve, then enters the crystalliser.

Experiments were conducted to investigate the performance of the seed suspension delivery system, of particular interest was any variation in the number of crystals and volume of particulate material fed to the crystalliser. The results of the experiments are presented in Chapter 8, but briefly they showed the delivery system was capable of supplying a seed suspension of constant composition.

6.3.3 Apparatus set-up

The crystalliser is of course the most important part of the apparatus, but it cannot be operated without other equipment to supply fluid to it. Fluid was supplied to the lumen and jacket by centrifugal pumps, *via* head tanks and rotameters, thus ensuring constant flowrates in both sections of the apparatus during operation. The set-up of the experimental apparatus is shown schematically in Figure 6.8.

The pumps used were both Iwaki MD-10 magnetic drive centrifugal pumps (All Pumps Supplies, Adelaide, Australia).

The lumen flowrate was metered by a KDG Flowmeters Series 1100 rotameter, with a DD ISO tube and DS float, (Bell Automation, Adelaide, Australia) capable of measuring between 1 and 9 ml/min of water at 20°C. The jacket flowrate was metered by a KDG Flowmeters Series 1100 rotameter, with a EC ISO tube and ES float, (Bell Automation, Adelaide, Australia) capable of measuring between 2 and 40 ml/min of water at 20°C.

The head tanks were manufactured from perspex and have a capacity of approximately 200 ml. All tubing used to feed solutions to the crystalliser was made of polyethylene, with internal diameters of either 1.0, 0.5 or 0.25 cm.

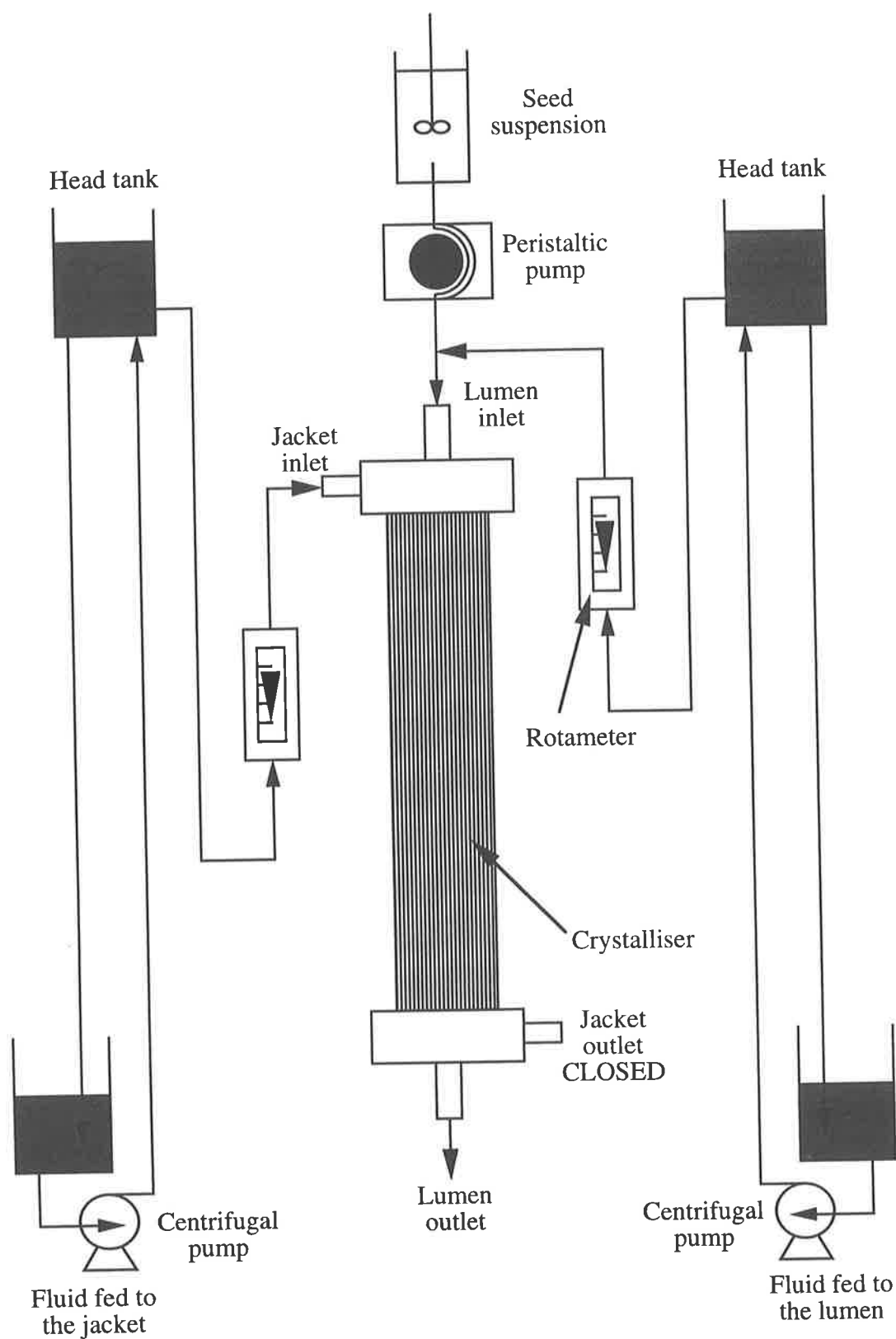


Figure 6.8 Schematic diagram of the experimental apparatus set-up.

6.3.4 Modes of operation

Fluid can enter and leave the lumen and jacket via the inlets and outlets in the manifolds fitted to the ends of the crystalliser. The crystalliser can be operated with any of the inlets and outlets open or closed and consequently a number of different operating configurations are available. In this work only one configuration was used, which was with both the lumen and jacket inlets open, the lumen outlet open and the jacket outlet closed. As the jacket outlet was closed, the fluid fed to the jacket passes through the walls of the porous tubes to mix with the fluid in the lumen and leaves the crystalliser via the lumen outlet. This configuration is shown schematically in Figure 6.9.

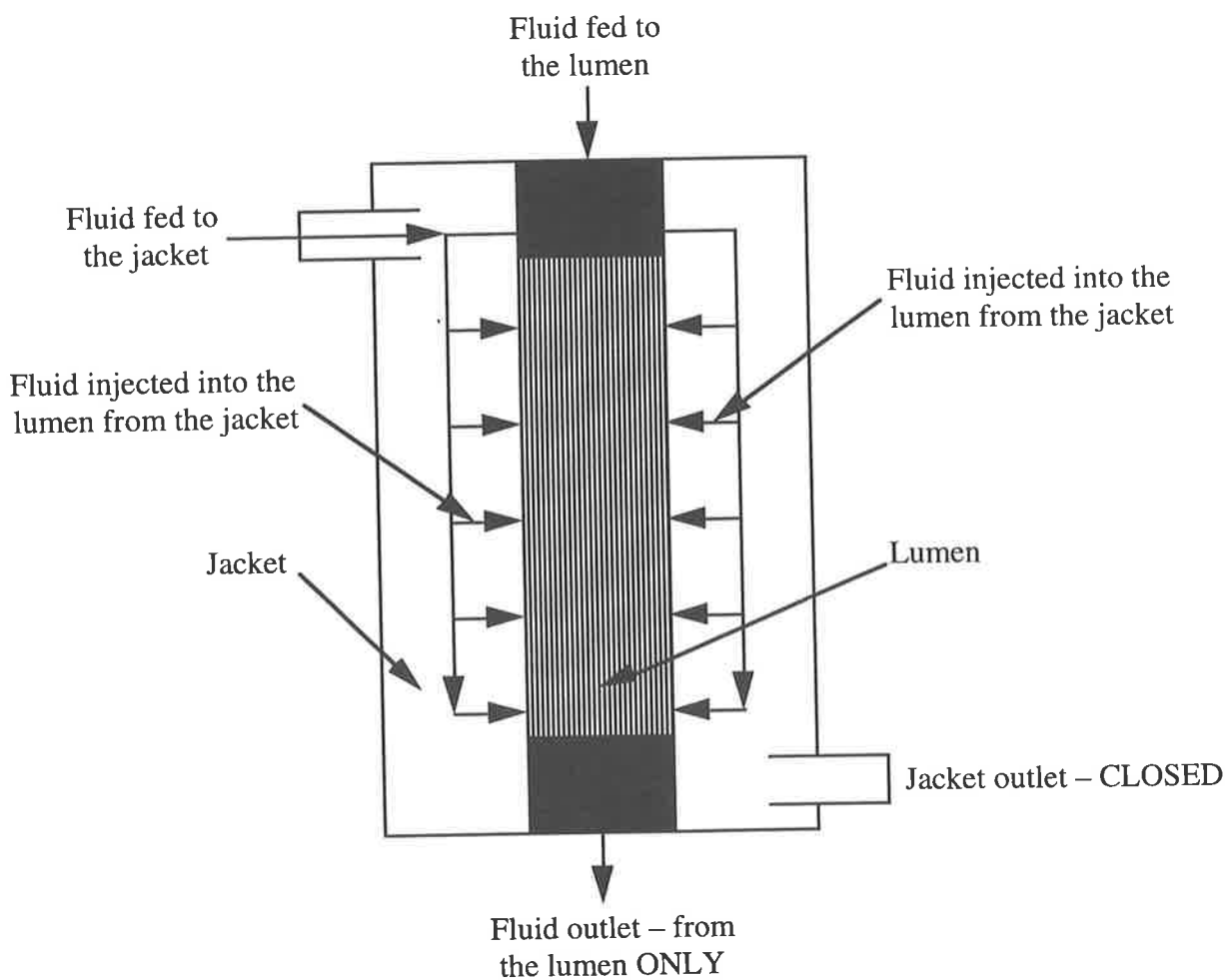


Figure 6.9 Schematic diagram of fluid flow in the tubular crystalliser.

The mode of operation just described has two important characteristics of the flow of urine in the kidney. Firstly, the fluid flow in the lumen is two-dimensional, as a result of the fluid that passes through the porous walls of the tubes from the jacket to the lumen, there will be flow in both the axial and a radial directions. Water is continually removed from urine as it passes through the tubules in the kidney, a process that will also give rise to radial and axial

fluid flow. Secondly, the fluid passing from the jacket to the lumen provides a method of maintaining supersaturation in the lumen. In the crystallisation experiments reported in Chapter 9, seed crystals were fed to the lumen, in a metastable solution, as the crystals pass through the crystalliser, growth occurs which will lead to a decrease in supersaturation. However, if the fluid passing from the jacket to the lumen is supersaturated, then the supersaturation in the lumen will be almost constant, similar to the conditions in the kidney (Sheehan and Nancollas, 1980).

Although the crystalliser can be operated at constant supersaturation, the method of generating supersaturation differs from that found in the kidney. In the crystalliser supersaturation is maintained in the lumen by the addition of supersaturated fluid, thus increasing the total flowrate, whereas in the kidney urine supersaturation is generated by the removal of water through the walls of the tubules, which decreases the overall flowrate. From an operational point of view, it is much easier to maintain supersaturation in the crystalliser by the addition rather than the removal of fluid from the lumen.

6.3.5 Hydrodynamics in the crystalliser

As discussed in the previous section, the fluid flow in the lumen is two-dimensional, having both axial and radial components. In the crystallisation experiments the crystals pass through the lumen, so it is important to understand the flow field in the lumen.

The operation of the crystalliser is characterised by the amount of fluid that is injected from the jacket through the walls of the porous tubes into the lumen. The fluid injection is characterised by a parameter known as the *dilution factor*, α , defined as the ratio of the total flowrate of fluid leaving the lumen, to the fluid flowrate fed to the lumen, or

$$\alpha = \frac{Q_L + Q_J}{Q_L} \quad (6.1)$$

where Q_L and Q_J are the fluid flowrates supplied to the lumen and jacket.

The lumen flowrates used in all the experiments were between 2 and 10 ml/min and the jacket flowrate was chosen according to the value of the dilution factor required. The values of the dilution factor used did not exceed six in any of the experiments conducted. For a lumen flowrate of 10 ml/min and a value of the dilution factor of six, that is a flowrate of fluid fed to the jacket of 50 ml/min, the maximum average fluid velocity in the lumen can be calculated, as the maximum flowrate will be 60 ml/min. Hence the Reynolds number can be determined, and the flow regime in the lumen identified.

The maximum average velocity in a single porous tube is:

$$\bar{u} = \frac{Q_L}{262 A_t} \quad (6.2)$$

where A_t is the cross-sectional area of the single porous tube, and the factor of 262 is included as it is assumed the fluid fed to the lumen is uniformly distributed between all 262 porous tubes in the crystalliser. The Reynolds number is calculated from

$$\text{Re} = \frac{\rho \bar{u} d_t}{\eta} \quad (6.3)$$

As the tube diameter is 410 μm and using values for the density and viscosity of water at 20°C, a value for the Reynolds number of 11.9 is obtained for a flowrate of 60 ml/min. Thus the fluid flow in the lumen is in the laminar regime for all the experiments described in this work.

To determine the solute and particle residence time distributions in the crystalliser the velocity field in the lumen, both in the radial and axial directions, must be known. Expressions for the axial and radial velocities are derived in Chapter 7.

6.4 CONCLUSIONS

A review of *in vitro* experimental systems used to study calcium oxalate crystallisation and the factors influencing stone formation and disease (urolithiasis) has been given. Although each of the experimental systems have advantages and disadvantages for studying stone formation, none take into account the tubular geometry in the kidney and the effect it might have on factors that influence stone formation such as aggregation and retention time.

A tubular crystalliser has been described that will be used to study the growth and aggregation of calcium oxalate, in a tubular geometry, with continuous fluid flow at almost constant supersaturation, under well defined hydrodynamic conditions.

Chapter 7:

THE SOLUTE RESIDENCE TIME DISTRIBUTION IN THE TUBULAR CRYSTALLISER

In this chapter the residence time distribution of the dissolved solute in the tubular crystalliser is investigated. The experimental fluid residence time distributions were determined using a step-change tracer response technique.

A diffusion-advection model is proposed to explain the observed experimental residence time distributions. This analysis produces a system of coupled partial differential equations, which are transformed into ordinary differential equations using the method of moments. The mean and standard deviation of the residence time distribution are used to compare the experimental results with those from the diffusion-advection model.

It is found that the mean and standard deviation of the residence time distribution depend on the solute diffusivity and jacket area. Acceptable values of both these parameters give a mean residence time and standard deviation in agreement with the experimental values.

7.1 INTRODUCTION

The residence time is defined as the time it takes for a molecule, or particle, to pass through the apparatus being considered, which might for example be a reactor, or a length of tube. The residence time distribution (RTD) is often used to characterise deviations from ideality, and is largely dependent on the apparatus. Since the initial work of Danckwerts (1953a, b and 1958) and Zwietering (1959) much work has been done on this topic in the field of reaction engineering; *e.g.* see Levenspiel (1972), Westerterp *et al.* (1984) and Shinnar (1987).

7.2 THE RESIDENCE TIME DISTRIBUTION

7.2.1 The *E* and *F* curves

The RTD is usually represented in one of two different ways, the first is as a frequency function, often used in statistics and called the *E curve* when describing RTDs. The value of

the E curve at time, t represents the differential fraction of material that entered the vessel at $t = 0$ and leaves the vessel between t and $t + dt$. The E curve is usually normalised, and in a continuous form is given by

$$\int_0^{\infty} E(t) dt = 1 \quad (7.1)$$

Alternatively the RTD may be represented by a cumulative function called the F curve. The F curve at time t represents the fraction of the material that has a residence time less than t . The E and F curves are related by

$$F(t) = \int_0^t E(t) dt \quad (7.2)$$

7.2.2 Experimental determination

The RTD may be obtained from response type experiments, in which some property of the material entering the vessel is changed, and the response to this change is measured at the outlet. For solute RTDs usually the concentration of some inert tracer is changed. There are two main types of response experiments in which different input changes are used. The first is a pulse response test in which a sharp pulse of the tracer is injected into the inlet material in the shortest possible time. The second is a step-change response test, in which the concentration of the tracer in the inlet material is changed from one value, usually zero to another.

Both of these input changes can be represented mathematically, and the RTD determined from a mass balance over the vessel. Smith (1970) shows that for a pulse response the E curve is given by

$$E(t) = C(t) \quad (7.3)$$

where $C(t)$ is the solute concentration at the outlet at time, t and the expression for the F curve is

$$F(t) = \int_0^t C(t) dt \quad (7.4)$$

For a step-change of magnitude, C_0 Smith also shows the F curve is

$$F(t) = \frac{C(t)}{C_0} \quad (7.5)$$

The results given by eqs 7.3 and 7.5 will be used to determine the RTDs in this work. For a more complete review of RTD theory, see for example Levenspiel (1972).

7.3 EXPERIMENTAL INVESTIGATION

7.3.1 Method

The solute RTD was determined by a step-change tracer response technique. The crystalliser was operated as described in Section 6.3.4; that is with the jacket outlet closed and with fluid fed to both the lumen and jacket. Initially, distilled water was fed to the jacket and no fluid fed to the lumen. At time $t = 0$, a saline solution was introduced to the lumen, and the response of the saline concentration in the fluid leaving the crystalliser was recorded until a steady state was achieved. The saline concentration in the fluid was inferred from its conductivity, which was measured by a purpose built flow-through conductivity cell, cylindrical in shape, with a volume of approximately 0.07 ml and equipped with a platinum electrode. The conductivity cell was connected to a Townson and Mercer conductivity meter Model No. 2101, and chart recorder.

The solute RTD was determined for different values of the dilution factor, α , defined in Section 6.3.5 as

$$\alpha = \frac{Q_L + Q_J}{Q_L} \quad (6.1)$$

where Q_L and Q_J are the fluid flowrates fed to the lumen and jacket. Values of the dilution factor from 1 to 5 were studied. The same lumen flowrate was not used in all the experiments, rather for each value of the dilution factor a particular lumen flowrate was chosen. The flowrates used in the RTD experiments are displayed in Table 7.1.

In the experiments the concentration of the saline solution fed to the lumen was such that the outlet concentration at steady state had a maximum value of 0.15 M. For example, in an experiment in which the value of the dilution factor was 3, the saline fed to the lumen is diluted by distilled water from the jacket by a factor of 3, consequently a 0.45 M saline solution was fed to the lumen.

Table 7.1. Flowrates used in the solute RTD experiments.

Dilution factor, α	Lumen flowrate, Q_L (ml/min)	Jacket Flowrate, Q_J (ml/min)
1	16	0
2	8	8
3	4	8
4	4	12
5	2	8

7.3.2 Calculating the RTD

As step-change tests were conducted the RTD is most conveniently presented as an F curve and may be calculated directly from eq 7.5. A step-change in the saline concentration was used in the experiments, however the response was detected by measuring the solution conductivity. The solution conductivity is a function of the saline concentration, thus the RTD calculated from eq 7.5 using values of either the concentration or conductivity will be the same.

7.3.3 Results

The experimental RTDs are shown in Figure 7.1. As different lumen flowrates were used for each value of the dilution factor, a plot of the F curve with time as the independent variable is mis-leading, as any effect the dilution factor has on the RTD will be masked by the effect of the different lumen flowrates. Rather than using time as the independent variable the following dimensionless time is defined:

$$\theta = \frac{t u_0}{L} \quad (7.6)$$

where u_0 is the centre-line fluid velocity in the lumen at the inlet of the crystalliser and L is the length of the crystalliser, 45.5 cm.

The RTD plotted for each value of the dilution factor is the average of four experiments, the errors shown are plus-or-minus one standard error. It can be seen that the RTDs are highly dependent on the value of the dilution factor, because the injection of fluid from the jacket

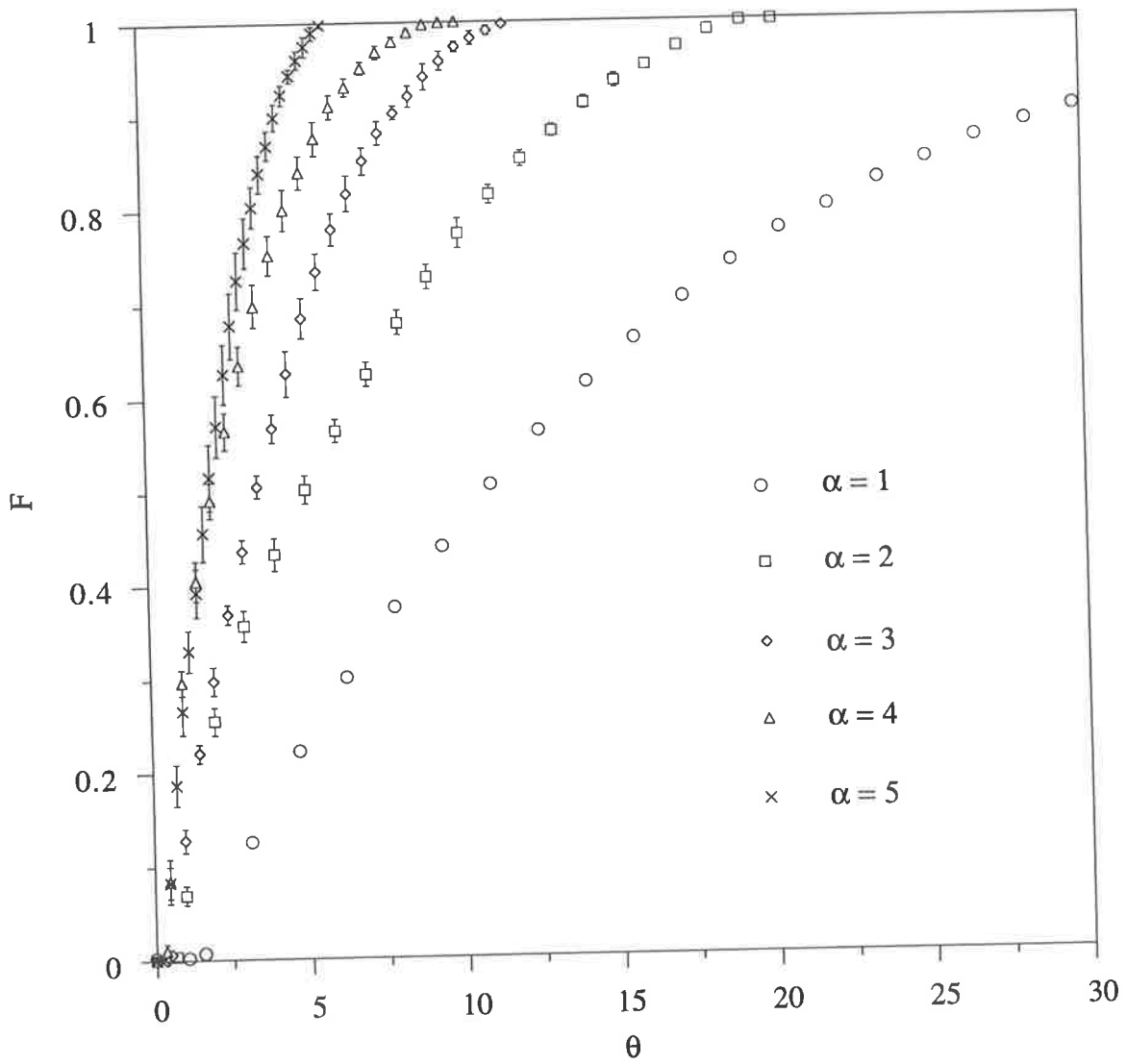


Figure 7.1 Experimental solute RTDs for different values of the dilution factor.

will increase the flowrate in the lumen and consequently decrease the time it takes for the fluid to pass through the crystalliser. Qualitatively it appears that the shape of the RTD is also dependent on the value of the dilution factor, with the RTDs for low values of the dilution factor being more like an RTD for plug flow than those at higher values of the dilution factor.

7.4 ANALYSIS

7.4.1 The velocity field in the crystalliser

Before proceeding with an analysis of the RTDs the expressions for the axial and radial velocities in the lumen of the crystalliser are developed. Without expressions for these velocities theoretical RTDs cannot be determined.

If no fluid is fed to the jacket of the crystalliser, there will be no fluid injection into the lumen and the value of the dilution factor will be one, in which case the flow in the lumen is equivalent to Poiseuille flow. If the dilution factor is greater than one, the velocity field in the lumen is more complicated as there is fluid flow in the axial and radial directions. The effect of fluid injection at the wall on the two-dimensional steady-state laminar flow of fluid in a porous tube has been analysed by Yuan and Finkelstein (1956). They find that for constant fluid injection along the length of the porous tube, the axial and radial velocities are given by

$$u = u_0 \left(1 + \frac{v_0 x}{u_0 R} \right) \left(1 - \left(\frac{r}{R} \right)^2 \right) \quad (7.7)$$

and

$$v = -2v_0 \left(\frac{r}{R} \right) \left(1 - \frac{1}{2} \left(\frac{r}{R} \right)^2 \right) \quad (7.8)$$

where u_0 and v_0 are the maximum axial and radial velocities, r , is the radial position, which varies from 0 at the centre of the tube to R at the wall, and x is the axial position. The velocities may be written in terms of the dilution factor by considering the expressions for the fluid flowrate in the lumen and jacket, which are

$$Q_L = \frac{1}{2} u_0 \pi R^2 \quad (7.9)$$

and

$$Q_J = v_0 2 \pi R L \quad (7.10)$$

Substituting eqs 7.9 and 7.10 into the expression for the dilution factor, eq 6.1, and rearranging gives,

$$\frac{v_0}{u_0} = (\alpha - 1) \frac{R}{4L} \quad (7.11)$$

which implies the axial and radial velocities may be written in terms of the dilution factor as

$$u = u_0 \left(1 + (\alpha - 1) \frac{x}{L} \right) \left(1 - \left(\frac{r}{R} \right)^2 \right) \quad (7.12)$$

and

$$v = \frac{-u_0 (\alpha - 1) r}{2L} \left(1 - \frac{1}{2} \left(\frac{r}{R} \right)^2 \right) \quad (7.13)$$

It can be seen from eq 7.12 that the axial velocity increases linearly along the length of the tube, also as $r/R < 1$, the radial velocity increases almost linearly with the radial distance from the centre of the tube, except near the wall of the tube. Note that the negative sign associated with the radial velocity is a result of the convention that the radial position is measured from the centre of the tube to the wall. As fluid is injected from the wall and travels towards the centre of the tube, by convention, it is moving in a negative direction.

The laminar flow of fluid in a porous tube and shell module similar to the tubular crystalliser has been measured using magnetic resonance imaging by Pangrle *et al.* (1992). They find that the axial velocity has a parabolic radial profile and the magnitude of the axial velocity is dependent on the axial position, as predicted by eq 7.12 from the results of Yuan and Finkelstein (1956). The velocity field determined by Yuan and Finkelstein (1956) has also been used by Abbas and Tyagi (1987) in their analysis of a hollow fibre artificial kidney performing simultaneous dialysis and ultrafiltration.

7.4.2 Poiseuille flow

The well known RTD for Poiseuille flow is derived, for example, by Smith (1970). In terms of the dimensionless time, θ , the F curve is

$$F(\theta) = \begin{cases} 0 & \theta \leq \bar{\theta}/2 \\ 1 - \frac{1}{4} \left(\frac{\bar{\theta}}{\theta} \right)^2 & \theta > \bar{\theta}/2 \end{cases} \quad (7.14)$$

where $\bar{\theta}$ is the mean residence time, which in this case is the time taken for fluid travelling at the flow average velocity to pass through the crystalliser.

In Figure 7.2 the experimental RTD for $\alpha = 1$ is plotted together with eq 7.14. It is clear that eq 7.14 does not describe the experimental RTD. Although the break-through time, the time when the first solute leaves the crystalliser, is approximately correct, the experimental RTD does not have the characteristic parabolic profile of the RTD for Poiseuille flow. The RTD is elongated and the fluid is taking longer to pass through the crystalliser than might be expected for Poiseuille flow.

7.4.3 Taylor dispersion

Taylor (1953) studied the dispersion of a soluble tracer flowing through a tube at low velocity. By considering convection across a plane moving at the flow average velocity, Taylor showed that, in the limiting case, the solute is dispersed relative to this plane as though it were being diffused by a process which obeys the same law as molecular diffusion, but with an axial diffusion coefficient, \hat{k} , where

$$\hat{k} = \frac{R^2 u_0^2}{192 \mathcal{D}} \quad (7.15)$$

The equation governing the axial dispersion is

$$\hat{k} \frac{\partial^2 C}{\partial x_1^2} = \frac{\partial C}{\partial t} \quad (7.16)$$

where $x_1 = x - \frac{1}{2} u_0 t$

For a step change in the solute concentration of magnitude, C_0 , at a point $x = 0$ from time $t = 0$, eq 7.16 can be solved analytically and as shown by Taylor, the solution is

$$\frac{C(t)}{C_0} = \begin{cases} \frac{1}{2} \left(1 + \operatorname{erf} \left(\frac{x_1}{2\sqrt{\hat{k}t}} \right) \right) & x_1 < 0 \\ \frac{1}{2} \left(1 - \operatorname{erf} \left(\frac{x_1}{2\sqrt{\hat{k}t}} \right) \right) & x_1 > 0 \end{cases} \quad (7.17)$$

where $\operatorname{erf}(z) = \frac{2}{\sqrt{\pi}} \int_0^z e^{-z^2} dz$

However, the preceding analysis is for flow in impervious rather than porous tubes and assumes that the axial velocity is constant. For fluid flow in the lumen, the axial velocity is

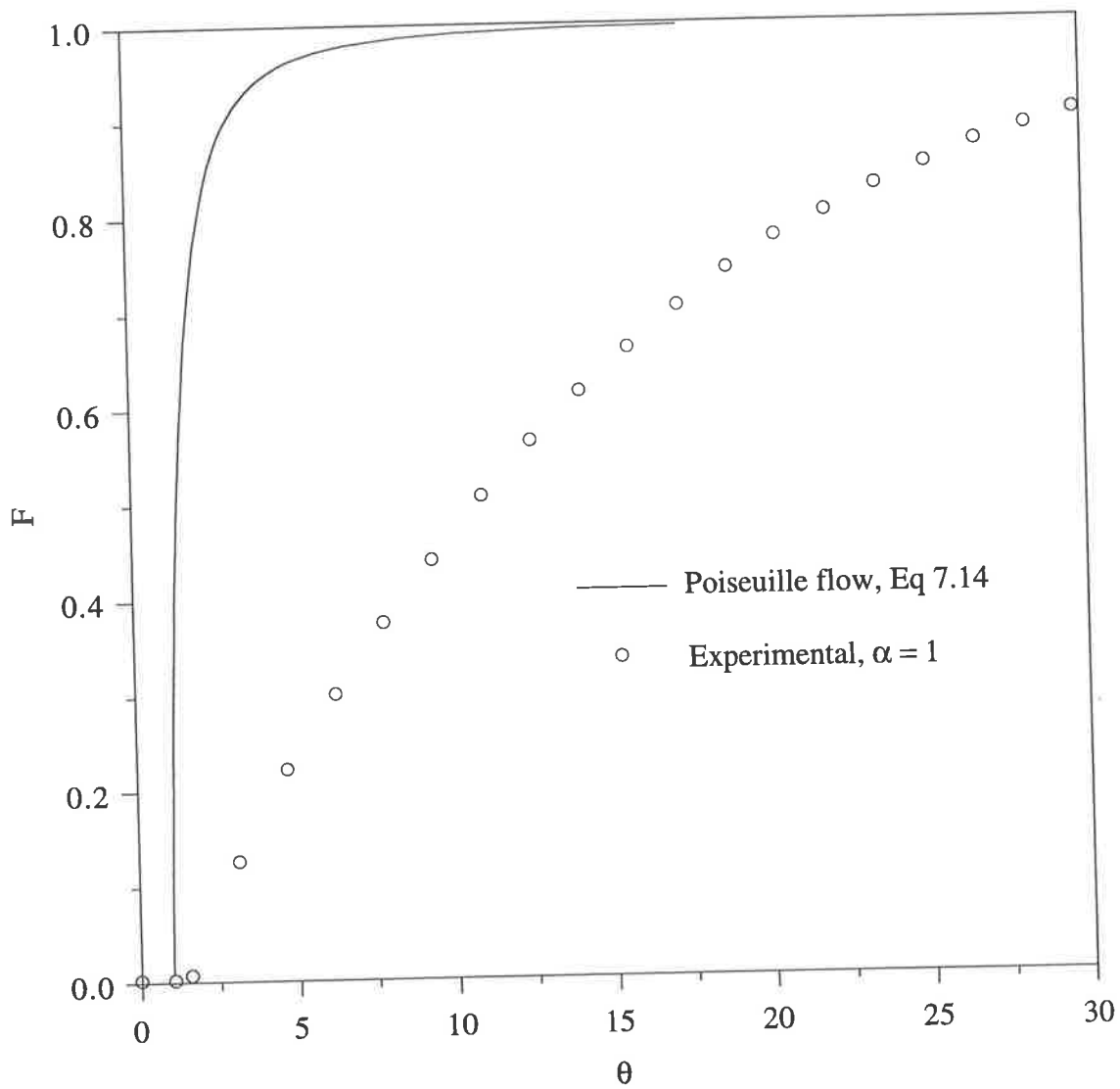


Figure 7.2 Comparison of the RTD for Poiseuille flow, eq 7.14 with the experimental RTD for $\alpha = 1$.

a linear function of the axial position, as shown in eq 7.12. As the axial diffusion coefficient is dependent on the axial velocity, it will also be a function of the axial position. Under these circumstances, it can be shown that eq 7.16 becomes

$$\hat{k}' \frac{\partial^2 C}{\partial x^2} + \left(\left(2\hat{k} \frac{(\alpha-1)}{L} - \frac{u_0}{2} \right) \left(1 + (\alpha-1) \frac{x}{L} \right) \right) \frac{\partial C}{\partial x} - \frac{u_0(\alpha-1)}{2L} C = \frac{\partial C}{\partial t} \quad (7.18)$$

where
$$\hat{k}' = \hat{k} \left(1 + (\alpha-1) \frac{x}{L} \right)^2$$

Eq 7.18 does not have an analytical solution for a step change in the solute concentration, and must be solved numerically. However, if the value of the dilution factor is one eq 7.17 can be used. In Figure 7.3 the experimental RTD for $\alpha = 1$ is plotted together with eq 7.17, at an axial position, $x = 45.5$ which corresponds to the outlet of the crystalliser. It can be seen that eq 7.17 does not fit the experimental data, the fluid is taking much longer to pass through the crystalliser than predicted. As the fit is so poor it is unlikely that this model will be more accurate for other values of the dilution factor. Since eq 7.18 must be solved numerically, and Taylor dispersion does not describe the experimental RTD for $\alpha = 1$ an alternative model is proposed.

7.4.4 A diffusion-advection model

In the preceding analysis the possibility that the solute may diffuse from the lumen, where the concentration is high, to the jacket, where the concentration is low, was not taken into account. The lumen and jacket can be considered as two compartments separated by a porous membrane, as shown in Figure 7.4.

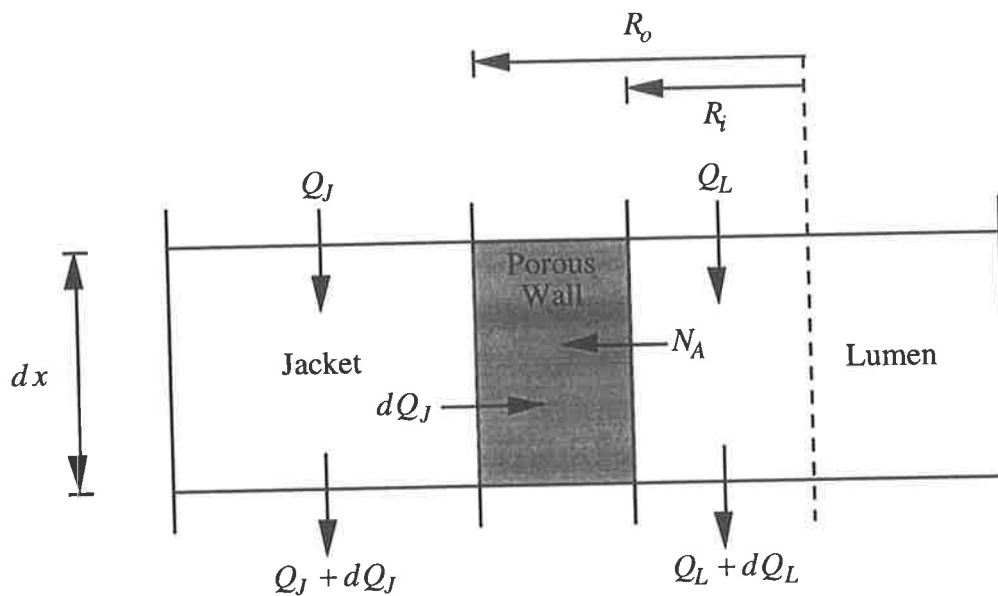


Figure 7.4 Compartment model for the tubular crystalliser

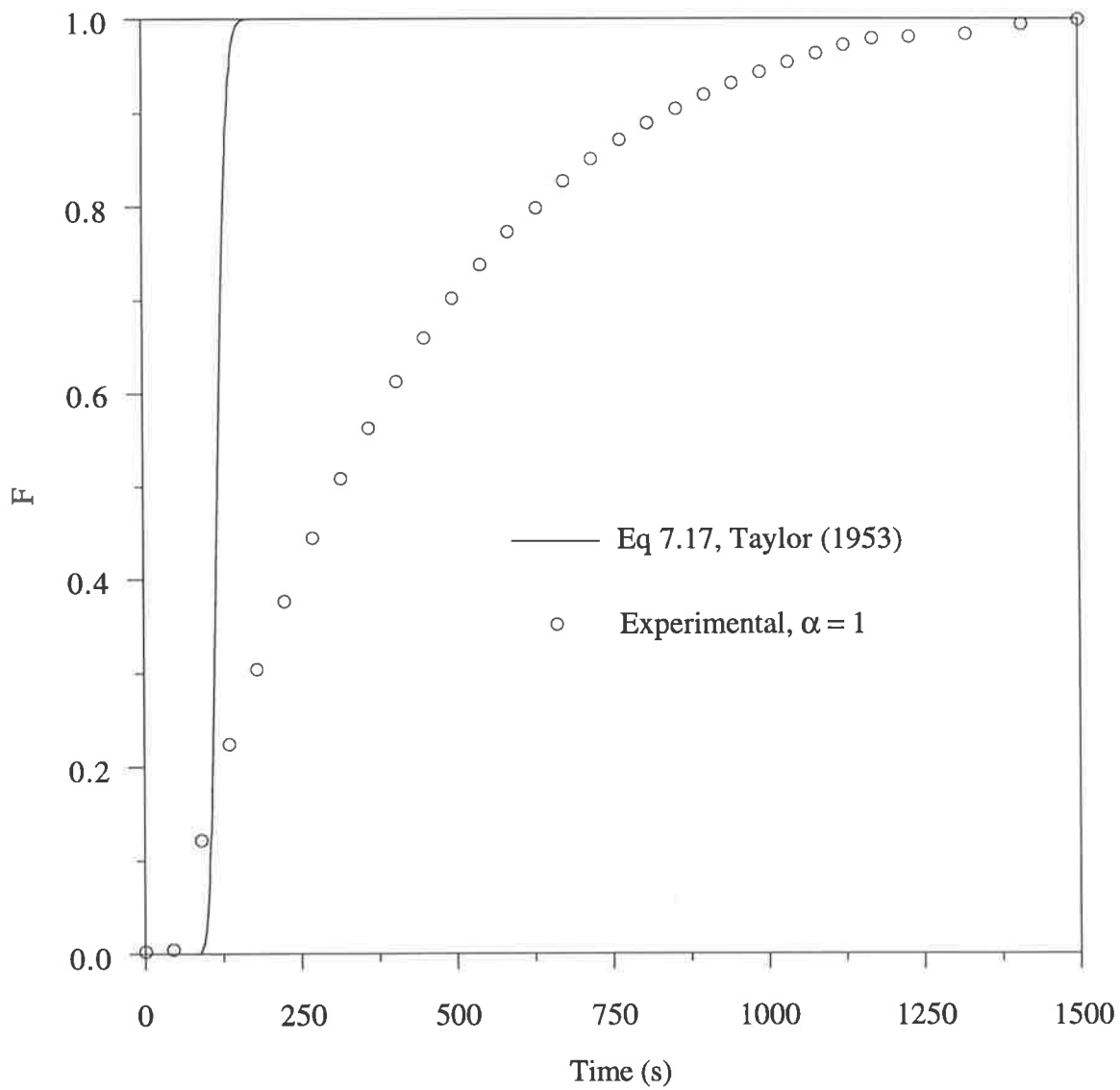


Figure 7.3 Comparison of the RTD for Taylor dispersion, eq 7.17, with the experimental RTD for $\alpha = 1$.

The solute concentration in both compartments is determined by the flux in the axial and radial directions. Assuming perfect radial mixing in both compartments, mass balances over the lumen and the jacket give:

$$-\frac{\partial(Q_L C_L)}{\partial x} - 2\pi r N_A = A_L \frac{\partial C_L}{\partial t} \quad (7.19)$$

$$-\frac{\partial(Q_J C_J)}{\partial x} + 2\pi r N_T N_A = A_J \frac{\partial C_J}{\partial t} \quad (7.20)$$

where Q , is the flowrate, C , the solute concentration, A , the cross-sectional area, N_A is the solute flux through the tube wall and the subscripts L and J refer to the lumen and jacket. Finally, N_T is the number of tubes, this term is included in the mass balance for the jacket as the mass balance over the lumen is for a single tube, and the flux from all the tubes enters the jacket.

Both the lumen and jacket flowrates are functions of axial position. By considering a mass balance over the crystalliser and using the definition of the dilution factor given by eq 6.1, it can be shown that the flowrates in the jacket and the lumen are

$$Q_J = Q_L^i N_T (\alpha - 1) \left(1 - \frac{x}{L}\right) \quad (7.21)$$

$$Q_L = Q_L^i \left(1 + (\alpha - 1) \frac{x}{L}\right) \quad (7.22)$$

where Q_L^i is the flowrate fed to each tube in the crystalliser, that is the flowrate in a single tube at the inlet of the crystalliser. The expression for the flowrate in the jacket includes N_T as the mass balance over the lumen is for a single tube.

Substituting 7.21 and 7.22 into 7.19 and 7.20 and simplifying gives

$$(\alpha - 1) Q_L^i N_T \left(\frac{C_L}{L} - \left(1 - \frac{x}{L}\right) \frac{\partial C_J}{\partial x} \right) + 2\pi r N_T N_A = A_J \frac{\partial C_J}{\partial t} \quad (7.23)$$

$$-\frac{(\alpha - 1) Q_L^i}{L} C_L - \left(1 + (\alpha - 1) \frac{x}{L}\right) Q_L^i \frac{\partial C_L}{\partial x} - 2\pi r N_A = A_L \frac{\partial C_L}{\partial t} \quad (7.24)$$

An expression for the flux through the porous wall may be derived by considering the transfer by convection and diffusion between the jacket and the lumen as shown schematically in Figure 7.5.

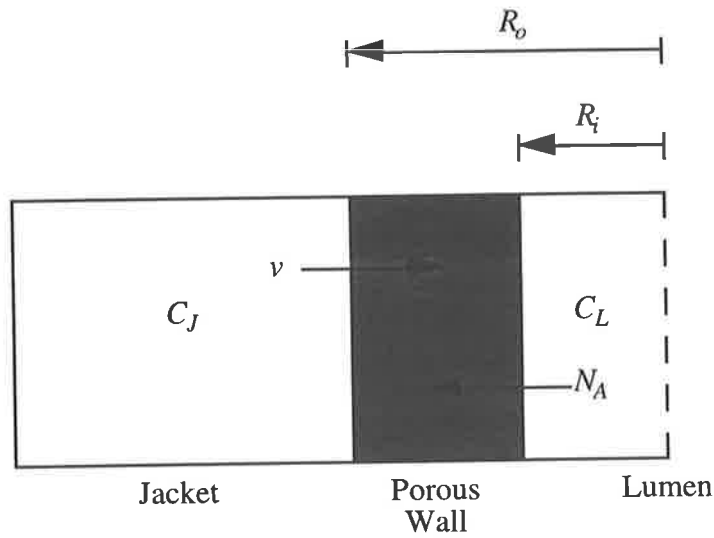


Figure 7.5 Solute transfer by convection and diffusion between the jacket and lumen.

Bird *et al.* (1960) show that the flux of component A in a binary system of A and B is

$$N_A = x_A(N_A + N_B) - C\mathcal{D}\nabla x_A \quad (7.25)$$

where A is the solute, B the solvent, x the mole fraction and C the concentration of component A. In cylindrical coordinates and only considering the radial direction, eq 7.25 may be written as

$$N_A r = Cvr - \mathcal{D}\frac{\partial C}{\partial r} \quad (7.26)$$

Applying the appropriate form of the continuity equation it can be shown that at steady state both $N_A r$ and vr must be constant if there is no axial advection or diffusion in the porous wall, see for example Bird *et al.* (1960). The solution to eq 7.26, subject to the boundary conditions, $C = C_L$ at $r = R_i$ and $C = C_J$ at $r = R_o$ is

$$N_A r = \frac{vr(C_J R_i^{vr/\mathcal{D}} - C_L R_o^{vr/\mathcal{D}})}{R_i^{vr/\mathcal{D}} - R_o^{vr/\mathcal{D}}} \quad (7.27)$$

To evaluate $N_A r$ an expression for vr is required. Assuming fluid from the jacket is injected uniformly over the entire length of the porous tubes a mass balance over the lumen implies

$$Q_L|_{x=L} - Q_L^i = 2\pi vrL$$

Using eq 7.22 to evaluate the lumen flowrate at $x = L$ it follows that

$$vr = \frac{(\alpha - 1)Q_L^i}{2\pi L} \quad (7.28)$$

Eqs 7.27 and 7.28 can be substituted into eqs 7.23 and 7.24, which are two coupled partial differential equations that describe changes in the solute concentration in the lumen and jacket with axial position and time. However, these equations do not have an analytical solution, and must be solved numerically. To obtain the RTDs the axial concentration profiles in the lumen and jacket must be calculated over a very long period of time.

7.4.5 Moment transforms

When modelling processes involving variables that are distributed, for example particulate processes in which the size distribution is of interest, the use of short-cut techniques to reduce the computational intensity has been investigated by Hounslow and Wynn (1993). These authors show that the use of moment transforms give accurate results with much less computational effort than techniques such as discretized population balances. A similar approach is adopted here where the moments of the RTDs are calculated rather than solving eqs 7.24 and 7.25 repeatedly to obtain the RTD. If the following moments are defined:

$$m_{j,J} = \int_0^{\infty} t^j C_J(x,t) dt \quad (7.29)$$

$$m_{j,L} = \int_0^{\infty} t^j C_L(x,t) dt \quad (7.30)$$

Applying eqs 7.29 and 7.30 to eqs 7.23 and 7.24, and considering a pulse-input of tracer, the following equations in terms of moments are obtained

$$\frac{dm_{j,J}}{dx} = \frac{A_J j m_{j-1,J} + (\omega_1 + \omega_2) N_T m_{j,J} - \omega_3 N_T m_{j,L}}{(\alpha - 1) Q_L^i N_T \left(1 - \frac{x}{L}\right)} \quad (7.31)$$

and

$$\frac{dm_{j,L}}{dt} = \frac{\omega_2 m_{j,J} - A_L j m_{j-1,L} - (\omega_3 - \omega_1) m_{j,L}}{Q_L^i \left(1 + (\alpha - 1) \frac{x}{L}\right)} \quad (7.32)$$

where, $\omega_1 = (\alpha - 1) Q_L^i / L$, $\omega_2 = \frac{2\pi vr R_i^{vr/D}}{R_i^{vr/D} - R_o^{vr/D}}$ and $\omega_3 = \frac{2\pi vr R_o^{vr/D}}{R_i^{vr/D} - R_o^{vr/D}}$

Eqs 7.31 and 7.32 are a coupled pair of ordinary, rather than partial, differential equations and therefore it is much easier to solve these equations numerically. Rather than obtaining the RTD, the solution of these equations gives the moments of the RTD. Statistical parameters of the RTD, such as the mean, and standard deviation can easily be calculated from the moments, as shown in Section 1.3.3.

To investigate whether the diffusion-advection model can be used to describe the experimental RTDs, the mean and standard deviation obtained from the model must be compared with those from the experimental RTDs. However, firstly some differences between the proposed model and the experiments should be considered.

For mathematical convenience a pulse input rather than a step-change at the lumen inlet was used to derive the differential equations given by eqs 7.31 and 7.32. However, the experimental RTDs were determined using a step-change response technique. In Section 7.5.2 it is shown how the experimental RTDs may be converted so that the moments and statistics calculated from them can be compared with those from the model.

7.4.6 End effects

The statistics calculated from the solution to eqs 7.31 and 7.32 are for the region in which fluid is injected from the jacket to the lumen. As described in Chapter 6 there are also sections at both ends of the crystalliser in which there is no fluid injection. Thus, the crystalliser can be divided into three sections in series and the RTD of each section must be considered. In the field of reaction engineering, the RTD of a cascade of reactors may be calculated by the use of convolution integrals, however as Westerterp *et al.* (1984) point out, this method is only applicable to flow regions that are statistically independent. If open boundaries exist between the regions, then this procedure cannot be adopted. As there are open boundaries between the regions in the lumen, the method of convolution integrals cannot be used to obtain the RTD of the crystalliser. As an alternative, the regions at both ends of the lumen were characterised by a dead time defined as

$$t_d = L/\bar{u} \quad (7.33)$$

where \bar{u} is the average fluid velocity, which can be calculated from eq 7.12, and L is the axial length of the region. The three regions in the crystalliser are shown schematically in Figure 7.6.

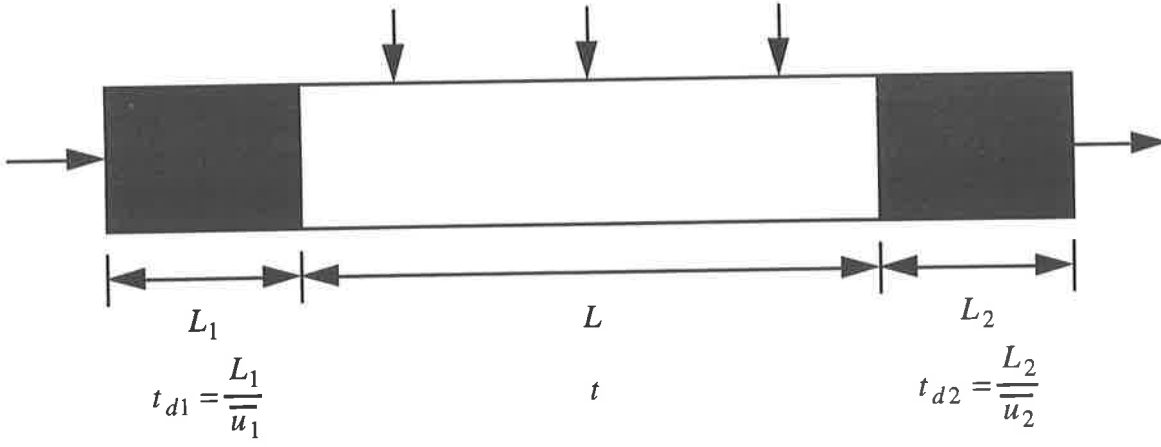


Figure 7.6 The three regions in the crystalliser

The E curve at the outlet of the crystalliser is given by

$$E(t) = E(t - t_{d1} - t_{d2}) \quad (7.34)$$

For a pulse input, from eq 7.3, $E(t) = C(t)$ and the moments may be written as

$$m_j = \int_0^{\infty} t^j E(t - t_{d1} - t_{d2}) dt = \int_0^{\infty} (t + t_{d1} + t_{d2})^j E(t) dt \quad (7.35)$$

where $E(t)$ is the E curve for the section with fluid injection. As the pulse is added to the fluid in the lumen, the moments calculated are for the lumen, therefore from eq 7.35, using the notation of eq 7.30,

$$m_0 = m_{0,L} \quad (7.36a)$$

$$m_1 = m_{1,L} + (t_{d1} + t_{d2}) m_{0,L} \quad (7.36b)$$

$$\text{and} \quad m_2 = m_{2,L} + 2(t_{d1} + t_{d2}) m_{1,L} + (t_{d1} + t_{d2})^2 m_{0,L} \quad (7.36c)$$

$$\text{or} \quad m_j = \sum_{k=0}^j \binom{j}{k} (t_{d1} + t_{d2})^{j-k} m_{k,L} \quad (7.36d)$$

where $\binom{j}{k}$ is the binomial coefficient.

As the RTDs are normalised, the value of m_0 is one and it can be seen from eq 1.5 that the mean residence time for the crystalliser will be the mean residence time for the section with fluid injection plus the two dead times. Also it can be shown using eq 1.6, that the standard deviation of the RTD for the crystalliser is the same as the standard deviation of the RTD for the section with fluid injection. Both these results are expected, a time delay will not affect the shape of the RTD, only the time taken for the fluid to pass through the crystalliser.

7.4.7 Parameters in the model

The values of the parameters in the model, namely the internal and external radii of the lumen, the jacket cross-sectional area, and the solute diffusivity must be determined. The internal and external radii of the lumen were evaluated from measurements taken from SEM micrographs of the lumen. The internal radius and wall thickness of the lumen were found to be approximately 205 μm and 235 μm respectively, which implies the external radius is 440 μm .

Values of the solution diffusivity of saline solutions are widely reported, for example Mullin (1993), and over the concentration range used in the experiments, 0.75 to 0.15 M, the solution diffusivity is $1.48 \times 10^{-9} \text{ m}^2/\text{s}$. However, Karel and Robertson (1989) find that in a hollow-fibre reactor, the effective diffusivity in the fibre membrane, \mathcal{D}_M is related to the solution diffusivity by

$$\mathcal{D}_M = \delta_M \mathcal{D} \quad (7.37)$$

where δ_M is approximately 0.3. Thus the diffusivity in the walls of the lumen is lower than the solution diffusivity, and it is possible that the value of δ_M will depend on the pore structure.

A lower limit for the cross-sectional area of the jacket can be calculated as the number and the dimensions of the lumen are known as well as the diameter of the perspex tube in which they are contained. The cross-sectional area of the lumen can be calculated and subtracted from the cross-sectional area of the perspex tube to give an estimate of the jacket cross-sectional area. The external radius of one of the porous tubes is 440 μm , and as described in Chapter 6 there are 262 of them in a perspex tube 2.0 cm in diameter. Based on these dimensions, the minimum jacket cross-sectional area is 1.55 cm^2 . However, it is possible that the solute concentration within the porous walls of the tubes will approach that in the jacket, thus decreasing the apparent wall thickness and increasing the apparent jacket cross-sectional area. Therefore the upper limit for the jacket cross-sectional area is that of the

perspex tube, 3.14 cm^2 less the cross-sectional area of the 262 porous tubes with internal radius $205 \mu\text{m}$, giving a value of 2.79 cm^2 .

The exact values of the solute diffusivity in the porous walls of the tubes, and the jacket cross-sectional area are not known, however bounds on their values have been established.

7.5 RESULTS FROM THE DIFFUSION-ADVECTION MODEL

A computer program was written in FORTRAN to solve eqs 7.30 and 7.31 for values of j from 0 to 2. The program used the numerical routine, DIVPAG, from the IMSL numerical library (IMSL Users Manual, 1987), which solves an initial value problem for a system of ordinary differential equations using Gear's method. The moments over the crystalliser, allowing for the sections at each end without fluid injection, were calculated using eq 7.36d. The mean and standard deviation were calculated from the moments using eqs 1.5 and 1.6. The values of the mean and standard deviation calculated from the solution to eqs 7.30 and 7.31 must depend on the values of the solute diffusivity and the jacket cross-sectional area. The dependence of the statistics of the RTD on these parameters is investigated in Section 7.5.3.

7.5.1 Testing the model

The accuracy of the computer program was tested by considering a set of conditions for which there is an analytical solution for the RTD in the crystalliser. If the diffusivity of the solute is very low, then the diffusive flux is negligible and the solute concentration in the jacket will be very low. For a step-change of solute concentration of magnitude, C_0 , at the lumen inlet, a mass balance from the inlet to an axial position x , gives

$$C_0 \bar{u}_L A_L \Big|_{x=0} = C \bar{u}_L A_L \Big|_{x=x} \quad (7.38)$$

The average axial velocity in the lumen may be calculated from eq 7.22 by dividing by the lumen cross-sectional area as

$$\bar{u}_L = \bar{u}_L^i \left(1 + (\alpha - 1) \frac{x}{L} \right) \quad (7.39)$$

where \bar{u}_L^i is the average axial velocity at the inlet of the lumen, *i.e.* $x = 0$. Substituting eq 7.39 into eq 7.38 it follows that

$$C(x) = \frac{C_0}{1 + (\alpha - 1) \frac{x}{L}} \quad (7.40)$$

Eq 7.40 implies that the solute passes through the tube as a step-change of decreasing magnitude, as a result of the fluid injection from the jacket. At an axial position, x , the concentration will be zero until a time, t^* , at which time the concentration increases to the value given by eq 7.40, and then remains constant. The concentration may be written as a function of axial position and time as a Heaviside step function,

$$C(x,t) = \frac{C_0}{1 + (\alpha - 1) \frac{x}{L}} U(t - t^*) \quad (7.41)$$

The time taken for the concentration step-change to reach an axial position, x , using eq 7.39 for the axial velocity is:

$$t^* = \int_0^x \frac{dx}{\bar{u}_L} = \frac{L}{\bar{u}_L^i (\alpha - 1)} \ln \left(1 + (\alpha - 1) \frac{x}{L} \right) \quad (7.42)$$

The preceding analysis is for a step-change in concentration, thus $C(x,t)$ represents the F curve, however the diffusion-advection model was formulated for a pulse-input. From eq 7.2, $E = dF/dt$ and therefore the moments of the RTD are given by

$$m_j = \int_0^\infty t^j E dt = \int_0^\infty t^j \frac{dC(x,t)}{dt} dt \quad (7.43)$$

Using Laplace transforms, it can be shown that

$$m_j = (-1)^j \left. \frac{d^{(j)} \bar{E}(s)}{ds^j} \right|_{s=0} \quad (7.44)$$

where $\bar{E}(s)$ is the Laplace transform of $E(t)$ with respect to t . Further,

$$\bar{E}(s) = \mathcal{L} E(t) = \mathcal{L} \frac{dC(x,t)}{dt} = s \bar{C}(s) + C(x,0) \quad (7.45)$$

and from Abramowitz and Stegun (1960),

$$\bar{C}(s) = \frac{C_0}{1 + (\alpha - 1) \frac{x}{L}} \frac{e^{-t^* s}}{s} \quad (7.46)$$

Substituting eq 7.46 into 7.45 the moments can be calculated from eq 7.42 and the mean residence time and standard deviation determined. At the outlet of the crystalliser, $x = L$, and $C(L,0) = 0$, thus

$$m_0 = \frac{C_0}{\alpha} \quad (7.47a)$$

$$m_1 = \frac{C_0 t^*}{\alpha} \quad (7.47b)$$

and
$$m_2 = \frac{C_0 t^{*2}}{\alpha} \quad (7.47c)$$

From which it follows that

$$\bar{t} = \frac{m_1}{m_0} = t^* = \frac{L}{\bar{u}_L^i (\alpha - 1)} \ln \alpha \quad (7.48)$$

and
$$\sigma^2 = \frac{m_2}{m_0} - \bar{t}^2 = t^{*2} - t^{*2} = 0 \quad (7.49)$$

The preceding analysis is only valid when the dilution factor is not equal to one. In Table 7.2 the values of the mean and standard deviation calculated from the moments generated by the computer program used to solve the equations from the model are shown as well as the values calculated from eqs 7.48 and 7.49. The value of the diffusivity given is the one used in the computer program, and the value of \bar{u}_L^i is calculated from the lumen flowrates given in Table 7.1. The cross-sectional area used to calculate the \bar{u}_L^i from the lumen flowrate is 0.347 cm^2 , based on 262 tubes each with an internal radius of $205 \mu\text{m}$.

Table 7.2 Comparison of the mean residence time and standard deviations.

α	\bar{u}_L^i (cm/s)	\mathcal{D} (cm^2/s)	Computer Program		Eqs 7.48 and 7.49	
			\bar{t} (s)	σ (s)	\bar{t} (s)	σ (s)
2	0.38	1×10^{-7}	82.5	0.58	82.1	0
3	0.19	1×10^{-7}	131.2	0.66	130.1	0
4	0.19	1×10^{-7}	111.9	0.2	109.4	0
5	0.095	1×10^{-7}	196.4	0.71	190.6	0

It can be seen that the computer program correctly predicts the mean residence time and the standard deviation over the range of experimental conditions. For $\alpha = 1$, the program calculates the mean residence time exactly (correct to 2 significant figures). The standard deviation for Poiseuille flow is undefined and cannot be computed.

7.5.2 Moments of the experimental RTDs

To determine the mean residence time and the standard deviation of the experimental RTDs the moments must be calculated. The experimental RTDs were determined using a step-change and are in the form of F curves, whereas the moments and statistics determined by the computer program used to solve the equations for the diffusion-advection model are for a pulse-input which gives the RTD in the form of an E curve. However, as the E and F curves are related, the moments of the E curve can be calculated from the experimentally determined F curves. From eq 7.2, $E = dF/dt$, substituting into the definition of the moment for the lumen, eq 7.30, and integrating by parts for a finite time over which experimental data was collected, t_{\max} rather than an infinite time, gives

$$m_j = \int_0^{\infty} t^j dF(t) = t^j F(t) \Big|_{t=t_{\max}} - \int_0^{t_{\max}} j t^{j-1} F(t) dt \quad (7.50)$$

Eq 7.50 must be evaluated numerically as the experimental data are values of the F curve at discrete time intervals. Simpson's method was used to evaluate the integral in eq 7.50, as noted by Kreyszig (1993), this method is sufficiently accurate for most practical purposes. The step size used for the integration was the time interval at which data were recorded in the experiments, which was typically either 15 or 20 seconds. The step size is small compared to the total time for which data was collected, over 1000 seconds for all the experiments.

The numerical method used to evaluate the moments, given by eq 7.50, was tested using the RTD for Poiseuille flow, with a mean residence time of 400 seconds. Values of the F curve for Poiseuille flow were calculated using eq 7.14, with a step size of 15 seconds and a maximum time, t_{\max} of 1500 seconds. The mean residence time determined using eq 7.50 with the integral evaluated using Simpson's method was 368 seconds, a relative error of approximately 8%. An error of this magnitude is acceptable given the uncertainty associated with the experimental RTDs.

Table 7.3 shows the values of the mean residence time and standard deviation of the experimental RTDs for each value of the dilution factor. The RTDs from all the experiments

conducted at each value of the dilution factor were analysed, the results reported are the mean plus-or-minus one standard error.

Table 7.3. Mean residence times and standard deviations of the experimental RTDs.

Dilution factor, α	Mean residence time, \bar{t} (s)	Standard deviation, σ (s)
1	379±4	285±5
2	371±9	286±5
3	474±12	320±10
4	319±12	253±10
5	515±31	333±7

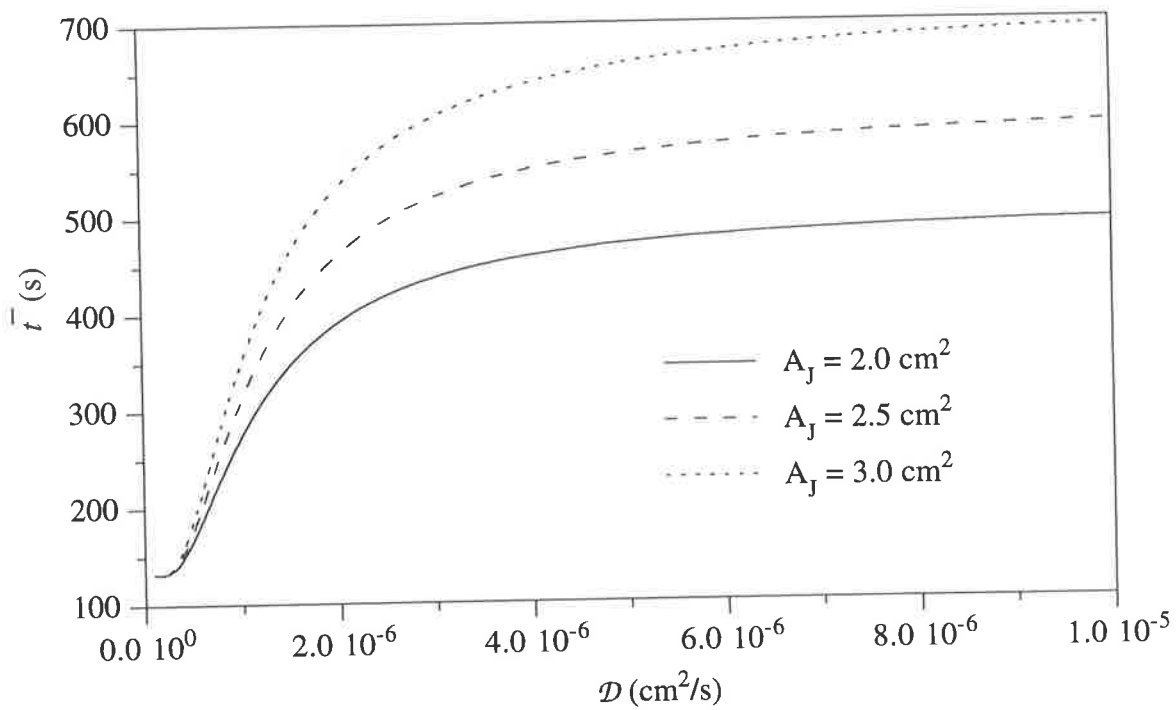
7.5.3 Solute diffusivity and jacket cross-sectional area

The values of the statistics of the RTDs obtained from the diffusion-advection model proposed are now compared with the experimental values given in Table 7.3. The procedure adopted is to investigate the effect that the jacket cross-sectional area and the solute diffusivity have on the statistics calculated using the model. If the diffusion-advection model describes the processes governing the fluid RTD, plausible values of the jacket cross-sectional area and solute diffusivity will give statistics in agreement with the experimental values.

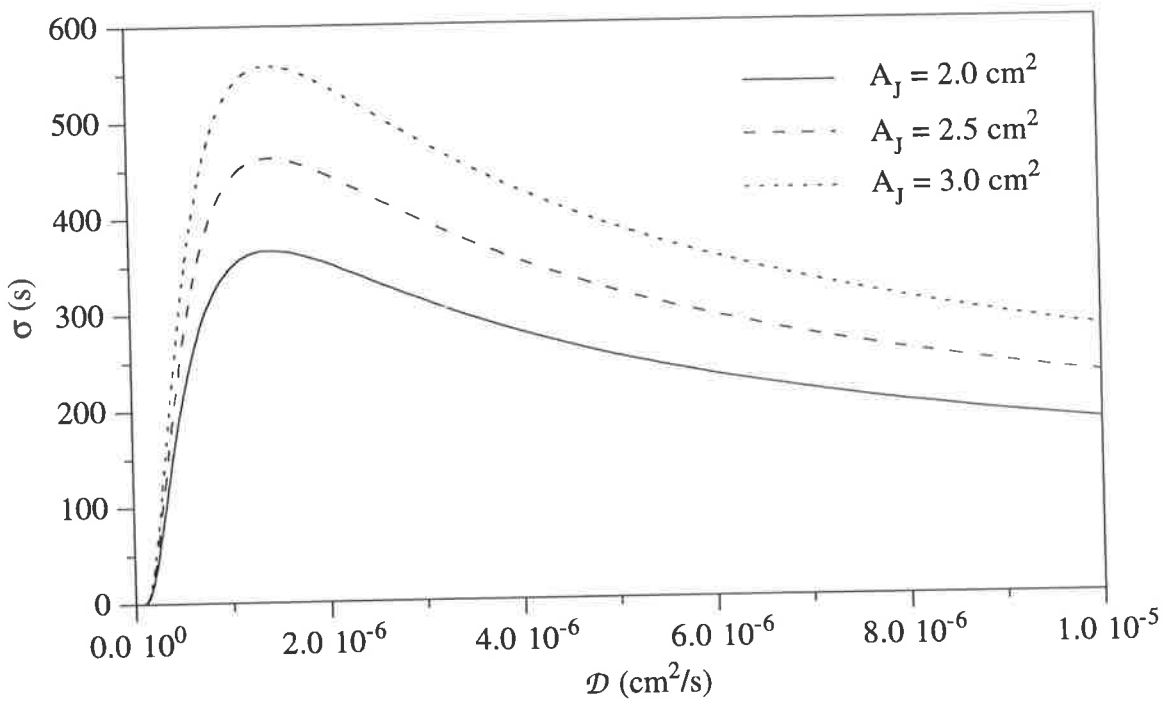
To generate data from the model at each value of the dilution factor, the jacket cross-sectional area was varied, and for each cross-sectional area a range of solute diffusivities were considered. Jacket cross-sectional areas from 1.75 cm² to 3.0 cm² were used, and the diffusivity was varied from 1×10⁻⁷ cm²/s to 1×10⁻⁵ cm²/s.

Figures 7.7 (a) and (b) show the sensitivity of the mean residence time and standard deviation of the RTD to the jacket cross-sectional area and solute diffusivity, for a value of the dilution factor of three. The dependence of both the mean residence time and the standard deviation on the jacket cross-sectional area and solute diffusivity can be explained by considering the effect these parameters have on the convective and diffusive fluxes.

From Figure 7.7 (a) it can be seen that if the jacket cross-sectional area is constant, the mean residence time increases as the solute diffusivity increases. This increase is a consequence



(a)



(b)

Figure 7.7 Sensitivity of (a) the mean residence time and (b) the standard deviation of the RTD to the value of the jacket cross-sectional area and solute diffusivity for $\alpha = 3$.

of the increase in the diffusive flux from the lumen to the jacket as the solute diffusivity increases. The solute concentration in the lumen will decrease as the solute diffusivity increases and it will take solute that diffuses into the jacket longer to pass through the crystalliser than solute that remains in the lumen.

It can also be seen in Figure 7.7 (a) that if the solute diffusivity is constant the mean residence time increases as the jacket cross-sectional area increases. The dependence of the mean residence time on the jacket cross-sectional area can be explained by considering the effect on the fluid velocity in the jacket. For example, consider solute that diffuses from the lumen to the jacket, once in the jacket it travels at the local fluid velocity until it is injected back into the lumen. As the jacket cross-sectional area increases the fluid velocity in the jacket decreases and the residence time must increase.

From Figure 7.7 (b) it can be seen that if the jacket cross-sectional area is constant, the standard deviation of the RTD is nearly zero for low values of the solute diffusivity, rapidly increases as the diffusivity increases, then decreases as the diffusivity becomes large. This behaviour can be explained by recalling that the standard deviation is a measure of the spread of a distribution. At very low diffusivities, the solute does not diffuse into the jacket, and travels as a sharp pulse through the lumen, does not spread axially, and thus the RTD has a very small standard deviation. As the diffusivity increases, the diffusive flux increases and solute enters the jacket where the axial velocity of the fluid is lower than in the lumen. As the solute is returned to the lumen with the fluid injected from the jacket, the pulse is spread out in the axial direction and the standard deviation of the RTD will increase. As the diffusivity becomes large the solute concentration in the jacket will approach the lumen concentration. Thus as the solute passes through the lumen it does not spread out as much in the axial direction, and the standard deviation of the RTD decreases.

It can also be seen in Figure 7.7 (b) that if the solute diffusivity is constant as the jacket cross-sectional area increases the standard deviation of the RTD increases, which can be explained by the effect the jacket cross-sectional area has on the fluid velocity in the jacket. Increasing the jacket cross-sectional area will decrease the fluid velocity in the jacket, thus solute that diffuses into the jacket will travel more slowly than solute in the lumen. Consequently the solute is spread out in the axial direction and the standard deviation of the RTD increases.

From plots such as those in Figures 7.7 (a) and (b) the mean residence time and the standard deviation of the RTD obtained from the model can be compared with the experimental values for different values of the solute diffusivity and jacket cross-sectional area. For a given

value of the jacket cross-sectional area, the values of the solute diffusivity that give a mean residence time and standard deviation equal to the values from the experimental RTDs can be determined.

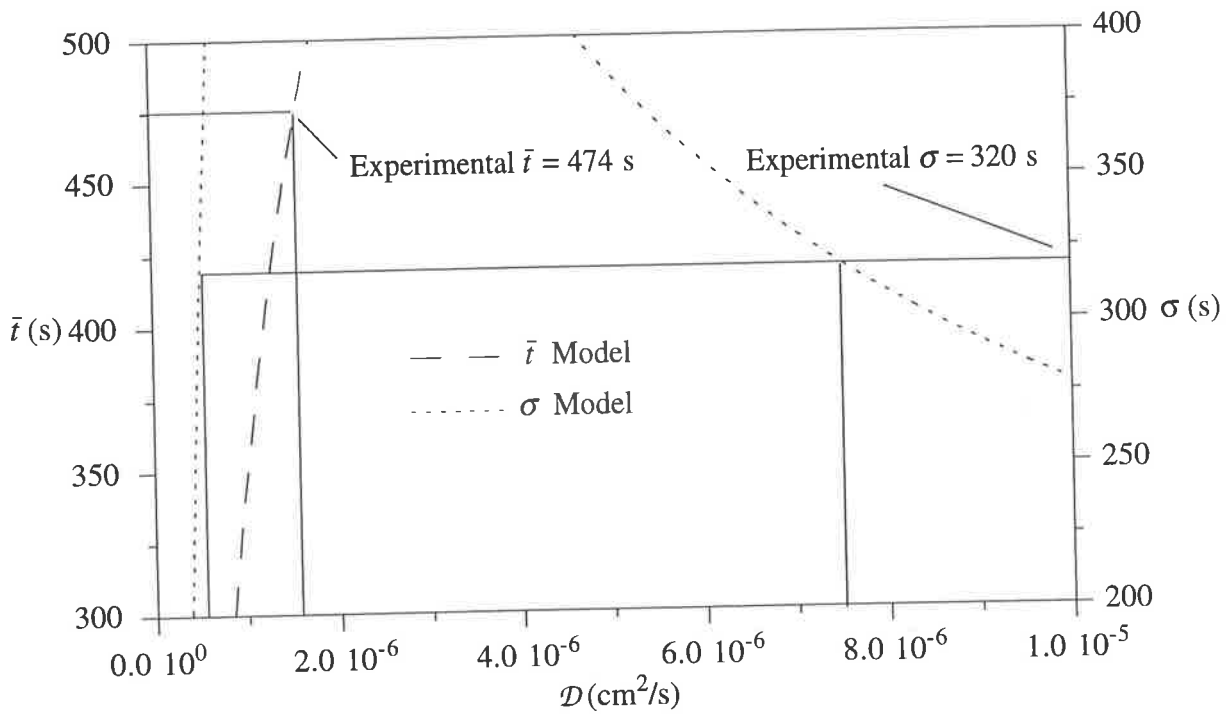
In Figure 7.8 (a), a jacket cross-sectional area of 3.0 cm^2 is used and the value of the dilution factor is three. From Table 7.3 the mean residence time and standard deviation of the experimental RTDs are 474 and 320 seconds respectively. It can be seen that there is one value of the solute diffusivity that gives the correct mean residence time and two values of the solute diffusivity that give the correct standard deviation. However, *different* values of the solute diffusivity give the correct mean residence time and the correct standard deviation. What is required is the value of the jacket cross-sectional area at which the *same* value of the solute diffusivity gives the correct value of both the mean residence time and the standard deviation. A jacket cross-sectional area of 2.17 cm^2 satisfies this criterion as shown in Figure 7.8 (b).

For a value of the dilution factor of three, if the jacket cross-sectional area is 2.17 cm^2 and the solute diffusivity is $3.55 \times 10^{-6} \text{ cm}^2/\text{s}$, then the diffusion-advection model predicts an RTD with the same mean residence time and standard deviation as the experimental RTD.

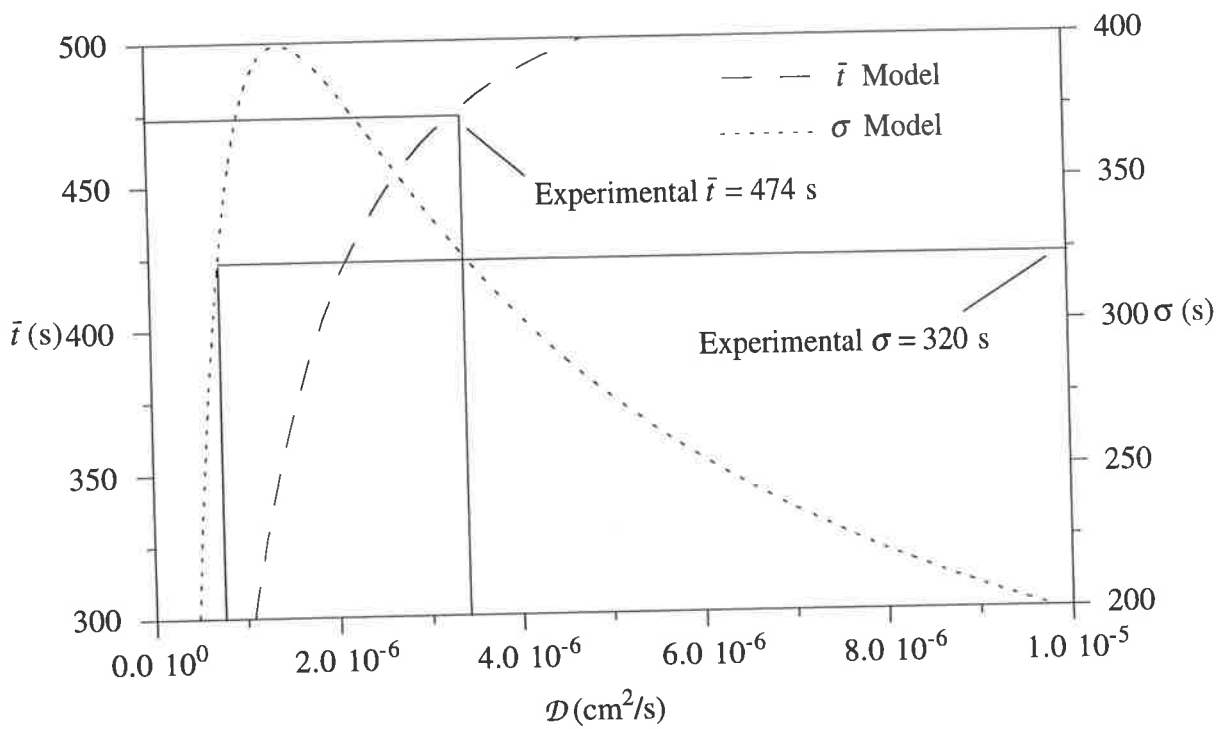
In Figures 7.9 (a) and (b) two curves involving the jacket cross-sectional area and the solute diffusivity are plotted for values of the dilution factor of two and four. Firstly, for each value of the jacket cross-sectional area used in the diffusion-advection model the value of the solute diffusivity that gives a mean residence time which is the same as the experimental value is plotted. Secondly, for each value of the jacket cross-sectional area used in the model the values of the solute diffusivity that predicts a standard deviation of the RTD which is the same as the experimental value is plotted. It can be seen from Figures 7.7 (a) and (b) that there are two values of the solute diffusivity that give the same standard deviation as the experimental RTD, hence the two curves plotted in Figures 7.9 (a) and (b).

In Figures 7.9 (a) and (b) it can be seen that for each value of the dilution factor there is *only one* value of the solute diffusivity and jacket cross-sectional area which give values of both the mean residence time and standard deviation of the RTD that are consistent with the experimental values.

Figures 7.10 (a) and (b) are plots of the solute diffusivity and jacket cross-sectional area that give a mean residence time and standard deviation in agreement with the experimental values for each value of the dilution factor. The values of the jacket cross-sectional area and solute diffusivity were determined from plots such as those shown in Figures 7.9 (a) and (b). It

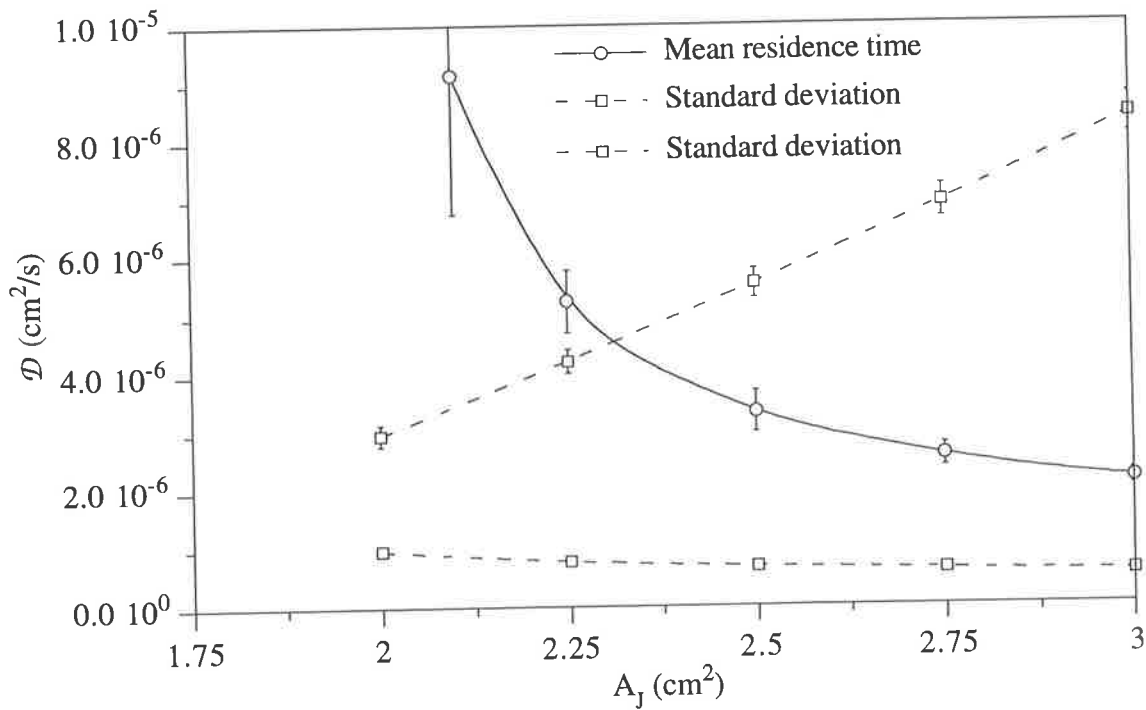


(a)

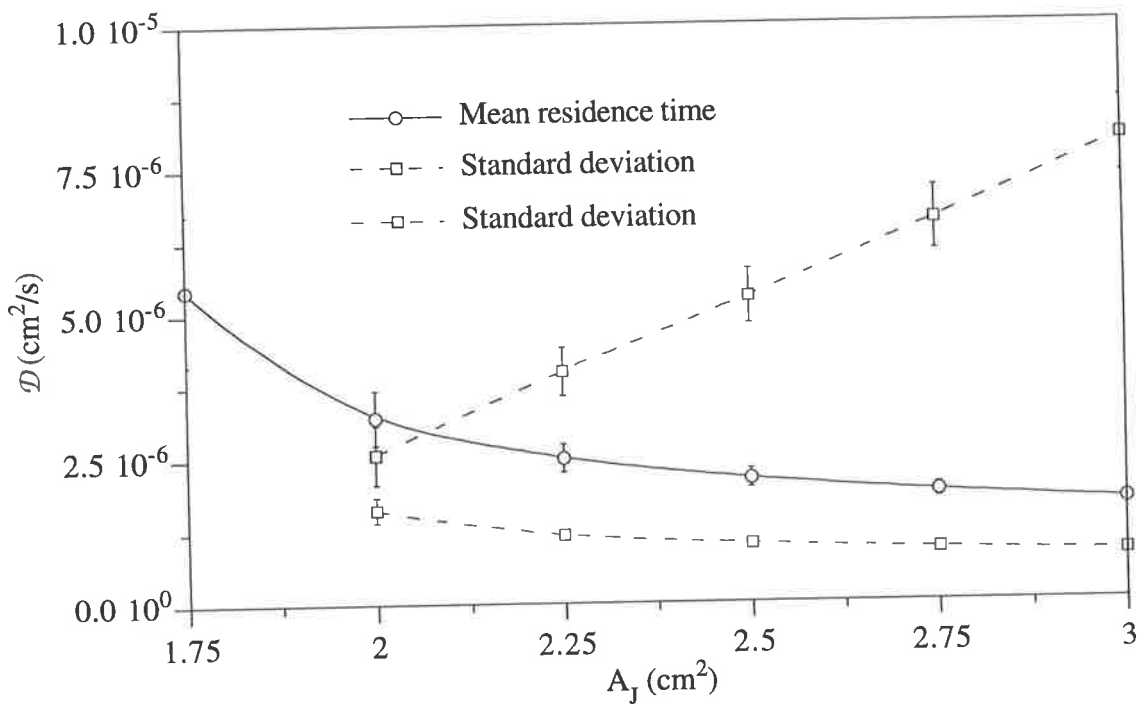


(b)

Figure 7.8 Plots of the mean residence time and standard deviation against the solute diffusivity for values of A_J of (a) 3.0 cm² and (b) 2.17 cm² for $\alpha = 3$.

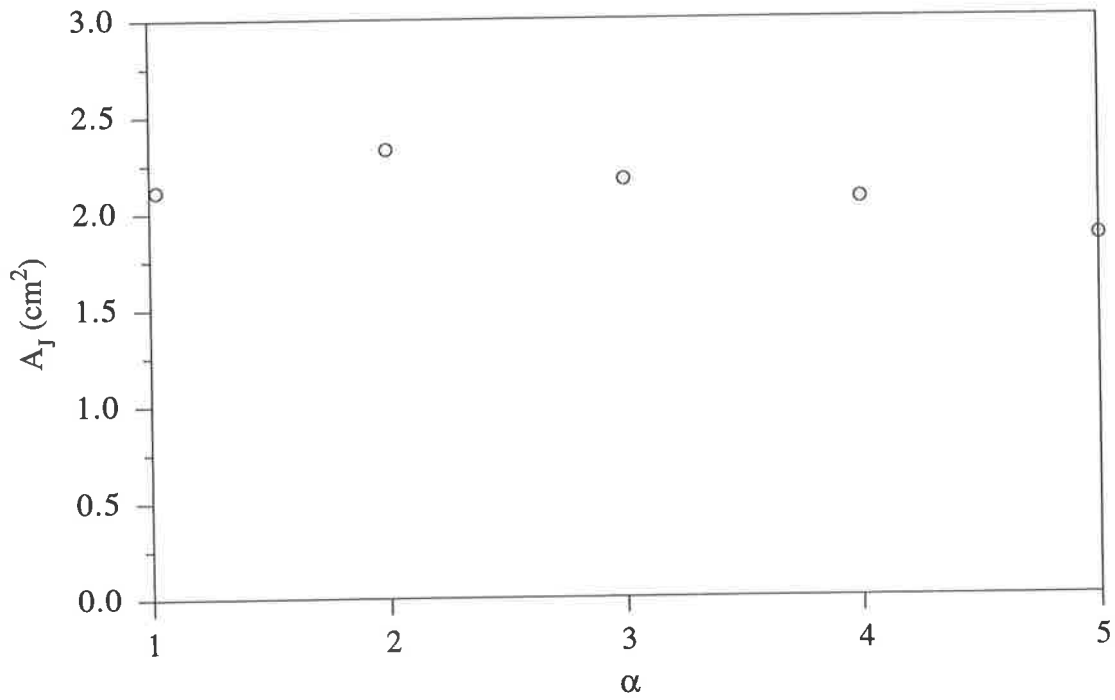


(a)

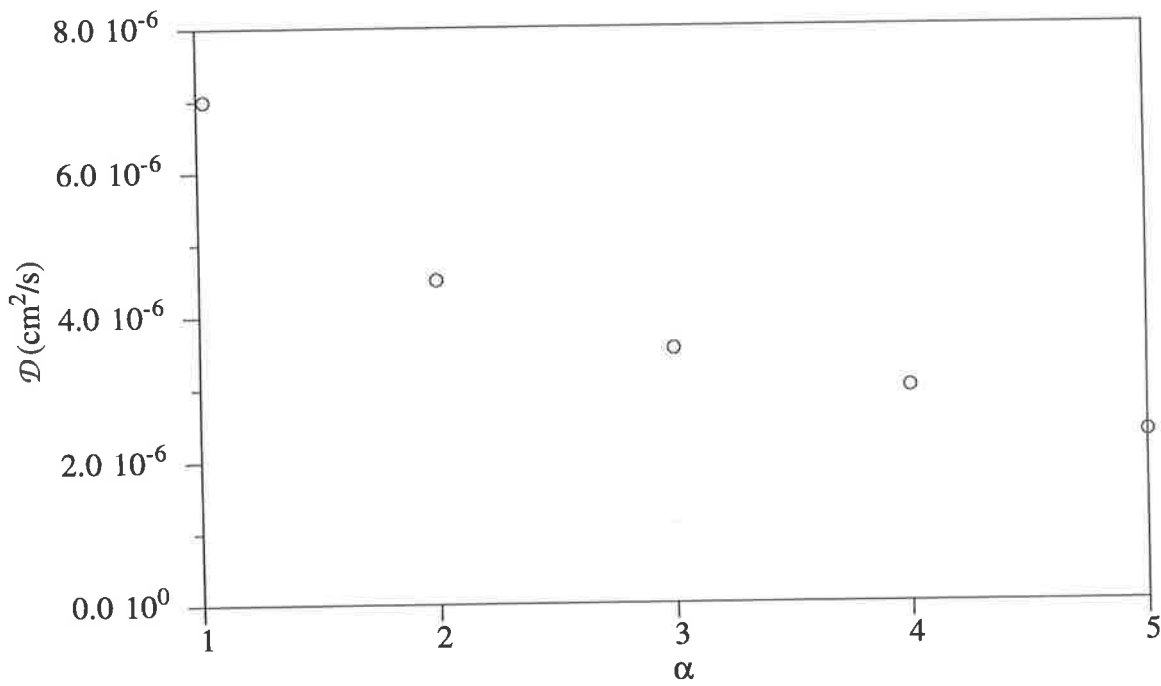


(b)

Figure 7.9 Plots of the values of the solute diffusivity and jacket cross-sectional area obtained from the diffusion-advection model that give an RTD with the same mean residence time and standard deviation as the experimental RTD for (a) $\alpha = 2$ and (b) $\alpha = 4$.



(a)



(b)

Figure 7.10 The dependence on the dilution factor of values of (a) the jacket cross-sectional area and (b) the solute diffusivity determined from the diffusion-advection model.

can be seen that both the jacket cross-sectional area and particularly the solute diffusivity are not constant but depend on the value of the dilution factor. However, the value of the jacket cross-sectional area is approximately constant, whereas the solute diffusivity increases as the dilution factor decreases.

7.6 DISCUSSION

The dependence of the calculated solute diffusivity and jacket cross-sectional area obtained from the diffusion-advection model on the value of the dilution factor highlights some of the limitations of the model. Both the jacket cross-sectional area and the solute diffusivity should be effectively constant, yet the values of these parameters are found to depend on the value of the dilution factor. It is possible to identify some shortcomings of the model that are responsible for the results that do not have physical meaning.

It can be seen from Figures 7.5 (a) and (b) that for values of the solute diffusivity greater than approximately $4.0 \times 10^{-6} \text{ cm}^2/\text{s}$, the mean residence time and the standard deviation of the RTD are insensitive to the value of the diffusivity. At these values of the diffusivity the mass transfer resistance across the lumen is very small and the lumen and jacket concentrations will be approximately equal. In this region, a large increase in the solute diffusivity produces a small change in the mean residence time and standard deviation. For low values of the dilution factor which require a high value of the solute diffusivity to be used if the model is to correctly predict the mean residence time and standard deviation of the RTD, if a lower value is used the error in the mean residence time and standard deviation of the RTD will be small. Consequently, the variation in the solute diffusivity may not be as large as that shown in Figure 7.10 (b).

Another assumption in the model proposed is that the lumen and jacket are both perfectly mixed and thus there is no radial concentration profile. If there is a radial concentration profile then the value of the solute concentration, particularly in the jacket will be different to that used in the present model. This is most likely to be the reason for the observed variation in the values of the jacket cross-sectional area and solute diffusivity which is physically implausible. By ignoring the radial concentration the problem has been over-simplified, however, radial variations in concentration significantly increases the complexity of the diffusion-advection model.

The effect of solute diffusivity and the jacket area must be related, and to fully explain whether the observed dependence of the jacket cross-sectional area and the solute diffusivity on the dilution factor is a consequence of the assumptions of the present model a full

mathematical analysis would be required. However, the values of the jacket cross-sectional area and solute diffusivity used in the diffusion-advection model to give statistics of the RTDs that are consistent with the experimental results can still be compared with the expected range of values given in Section 7.4.5.

The value of the solute diffusivity ranges from $2.35 \times 10^{-6} \text{ cm}^2/\text{s}$ to $7.0 \times 10^{-6} \text{ cm}^2/\text{s}$ for values of the dilution factor of five and one. Using eq 7.37 and the value of the solution diffusivity for the saline solutions used in the experiments, $1.48 \times 10^{-5} \text{ cm}^2/\text{s}$, the values of δ_M range from 0.16 to 0.47. The mean diffusivity for all values of the dilution factor is $4.1 \times 10^{-6} \text{ cm}^2/\text{s}$, which implies the value of δ_M is 0.28, which is in good agreement with the value of 0.3 quoted by Karel and Robertson (1989).

The variation in the jacket cross-sectional area is small, the mean for all the values of the dilution factor is 2.11 cm^2 , which is well within the range of plausible values based on the dimensions of the porous tubes and the perspex tube they are contained in given in Section 7.4.5.

The diffusion-advection model proposed can be used to describe the solute RTD as provided appropriate values of the solute diffusivity and the jacket cross-sectional area are used, it correctly predicts the mean residence time and standard deviation.

To validate fully the model the complete RTD, rather than the statistics, should be calculated and more importantly the effect of radial variations in concentration should be considered. However, the computational effort required to solve the partial differential equations that arise from the model is too demanding. The mechanisms governing the solute transport through the crystalliser have been identified, and it is more important to consider the RTD of the crystals. It is the time that the crystals take to pass through the crystalliser that will determine how long they have to grow and aggregate, which is of much more interest in this work.

7.7 CONCLUSIONS

In this chapter the RTD of the dissolved solute in the crystalliser has been investigated. The theory used to describe RTDs and experimental methods of determining the RTD have been discussed. Step-change tracer response experiments were conducted to determine the effect of the dilution factor on the solute RTD.

It was found that the solute RTDs may be described by a diffusion-advection model, in which the crystalliser can be considered as two compartments separated by a porous

membrane. Solute is transported from the lumen to the jacket by diffusion, and from the jacket to the lumen by the fluid injected from the jacket. Also it is assumed that there is no radial variation in solute concentration in both the lumen and jacket. The model correctly predicts the mean residence time and standard deviation of the experimental RTDs, however the complete RTDs were not obtained.

The mechanisms governing the fluid transport in the crystalliser have been identified, which is sufficient, as the crystal RTD is much more important than the solute RTD for studying crystal growth and aggregation.

Chapter 8:

THE PARTICLE RESIDENCE TIME DISTRIBUTION IN THE TUBULAR CRYSTALLISER

In this chapter the particle residence time distribution in the tubular crystalliser is investigated. Experimental particle residence time distributions were determined using both step-change and pulse-input tracer response techniques. A mass balance over the crystalliser using results from the step-change tests revealed particle mass was not conserved, which may be explained by the particles sticking to the walls of the lumen.

An extensive experimental program investigated the effect of particle size, lumen flowrate and the dilution factor on the particle residence time distribution. A second crystalliser with lumen of different diameter and length was also used.

It was found that the residence time distributions are well described by a model in which it is assumed that the particles maintain a constant radial position in the lumen, rather than following the fluid streamlines.

8.1 INTRODUCTION

A background to the theory and methods of representing RTDs was given in Chapter 7 in which the solute RTD was studied. In this chapter similar experimental techniques and analyses are used to investigate the particle RTD in the tubular crystalliser. The particle RTD is more important than the fluid RTD, and as shown by Brucati *et al.* (1992), even in a device such as a stirred tank the particle and fluid residence times can be different. In his review, Tavaré (1986) tabulates what little work there is on the effects of mixing and RTDs in the field of crystallisation. Studies on the effect of various non-ideal RTDs on continuous crystallisers, for example Becker and Larson (1969) and Abegg and Balakrishnan (1971) consider the fluid phase rather than the particulate phase. Smit *et al.* (1994) consider the effect of the state of mixing, including various RTDs, on aggregation and gelation in batch and continuous modes of operation. They show that the particle RTD can affect crystal

aggregation, which highlights the importance of the particle residence time for the crystalliser.

8.2 PRELIMINARY EXPERIMENTS

8.2.1 Testing the particle suspension delivery system

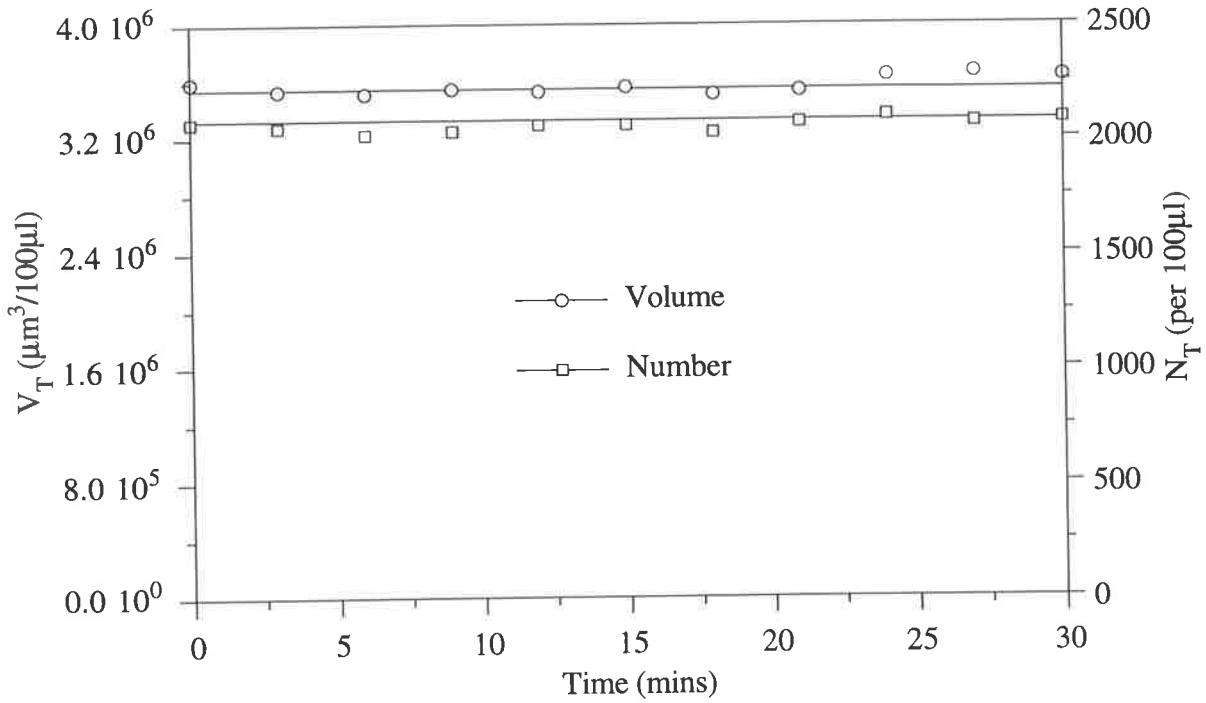
The particle suspension delivery system is described in Section 6.3.2. Before conducting the experiments to determine the particle RTDs it was important to test the performance of the particle suspension delivery system. Of particular interest was the ability to supply a particle suspension with a constant number of particles and volume of particulate material.

A suspension of calibration standard latex rather than a calcium oxalate seed suspension was used to test the performance of the delivery system. The reason for using latex particles is that unlike calcium oxalate seeds they will not aggregate or dis-aggregate. Thus, if the number and volume of particles in the suspension that is fed to the crystalliser is not constant it is because of problems with the delivery system.

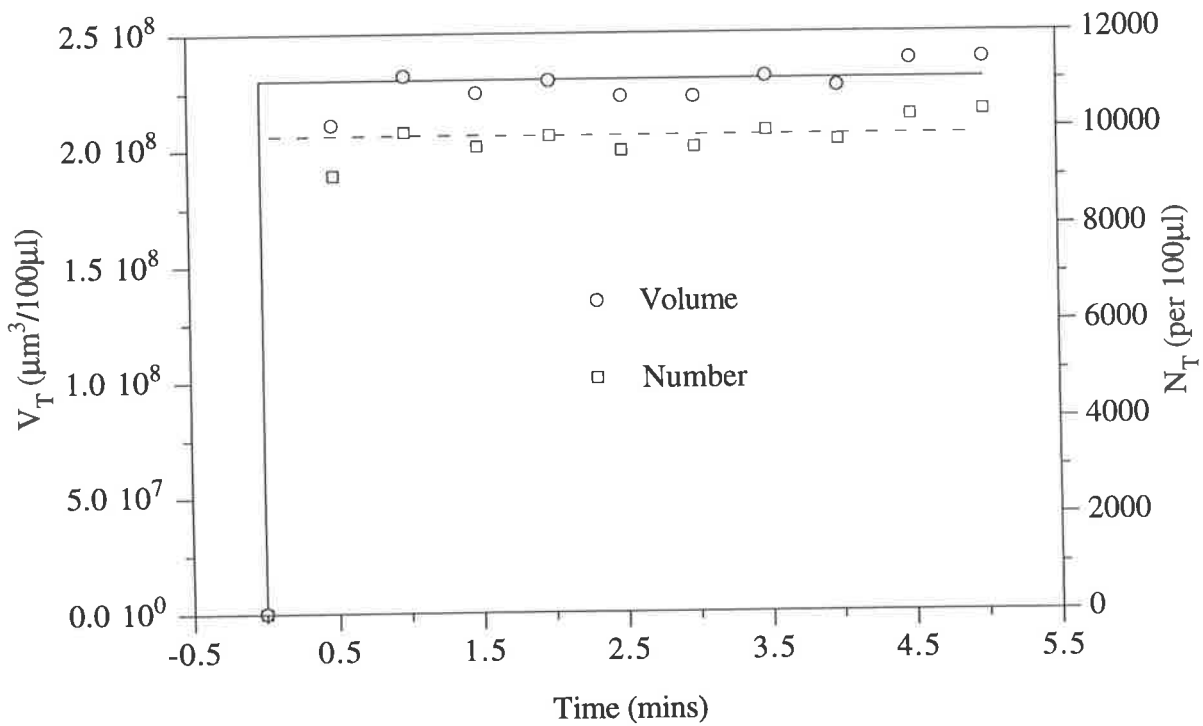
To test the delivery system, samples of the particle suspension, after it had mixed with the lumen feed solution, were collected every 3 minutes for a period of 30 minutes. The total number and volume of the particles in each sample was determined using the Multisizer. Figures 8.1 (a) shows the variation in the total number, N_T and volume, V_T of particles in the samples. Clearly both the total number and volume of particles are constant over a time period much longer than that required to conduct an experiment to determine the particle RTD.

A second test was conducted to determine whether the delivery system could produce a step-change. Of particular interest was the time taken for the particle number and volume to reach a constant value, if this time was too long then rather than a step-change a “ramp” input is obtained which will affect the RTD. In the test the lumen feed solution was supplied to the T-valve, and at time, $t = 0$, the flow of the particle suspension was started and samples of the fluid leaving the T-valve collected at 30 second intervals.

Figure 8.1 (b) shows the variation in the total number and volume of particles with time. It can be seen that both the total number and volume are approximately constant after 30 seconds. Thus, there is no time lag between starting the flow of the particle suspension and a constant number and volume of particles being supplied to the fluid entering the lumen.



(a)



(b)

Figure 8.1 The variation in total particle number and volume supplied to the crystalliser for (a) long times and (b) at start-up.

8.2.2 Step-change tests

Prior to conducting each step-change test, samples of the fluid fed to the lumen were collected and analysed by the Multisizer. The total number and volume of particles per unit volume represent the particle concentration by number and volume in the fluid fed to the crystalliser.

For the step-change tracer response tests the crystalliser was operated as described in Section 6.3.4, that is with the jacket outlet closed and with fluid fed to both the lumen and jacket. Initially, a filtered (0.22 μm), 0.15 M saline solution was fed to the lumen and the jacket, at time, $t = 0$, the flow of the latex particle suspension was started, and all the fluid leaving the crystalliser was collected in separate samples. The total number and volume of particles per unit volume in each sample was determined with the Multisizer. As the volume of fluid collected in each sample was relatively small, approximately 4 ml, when the samples were analysed rather than taking a single 500 μl count at least four separate 100 μl counts were taken. The advantage of this method was that if the orifice became blocked during a count, it could be cleared and another count taken. If a 500 μl count was taken and the orifice blocked towards the end of the count there would not be enough fluid in the sample for another count to be taken. Consequently, the number of particles in that sample would not be known, and the RTD could not be determined.

8.2.3 Particle mass balance

The expressions for the E and F curves given in Section 7.2.2 are derived on the basis of a mass balance. For a step-change, from eq 7.5 the expression for the F curve is $F(t) = C(t)/C_0$. For the particulate phase the concentration, C_0 may be written in terms of the total number, $N_{T,0}$ or volume, $V_{T,0}$ of particles per unit volume in the fluid fed to the crystalliser, thus

$$F(t) = \frac{N_T(t)}{N_{T,0}} = \frac{V_T(t)}{V_{T,0}} \quad (8.1)$$

With the crystalliser operating at steady state the number and volume of particles in the fluid at the outlet were compared with those in the fluid at the inlet. However, the number and volume of particles measured by the Multisizer must be corrected, to account for the effect of the fluid injected from the jacket to the lumen. Firstly, the dilution factor defined in Section 6.3.5 must be modified to take into account the flowrate of the particle suspension. The modified dilution factor, α' is defined as

$$\alpha' = \frac{Q_S + Q_L + Q_J}{Q_S + Q_L} \quad (8.2)$$

where Q_S is the seed suspension flowrate. A mass balance over the crystalliser gives

$$N_T(t) = \alpha' N_{T,M}(t) \quad \text{and} \quad V_T(t) = \alpha' V_{T,M}(t) \quad (8.3a \text{ and } b)$$

where $N_{T,M}(t)$ and $V_{T,M}(t)$ are the total number and volume of particles in the samples analysed by the Multisizer at time, t .

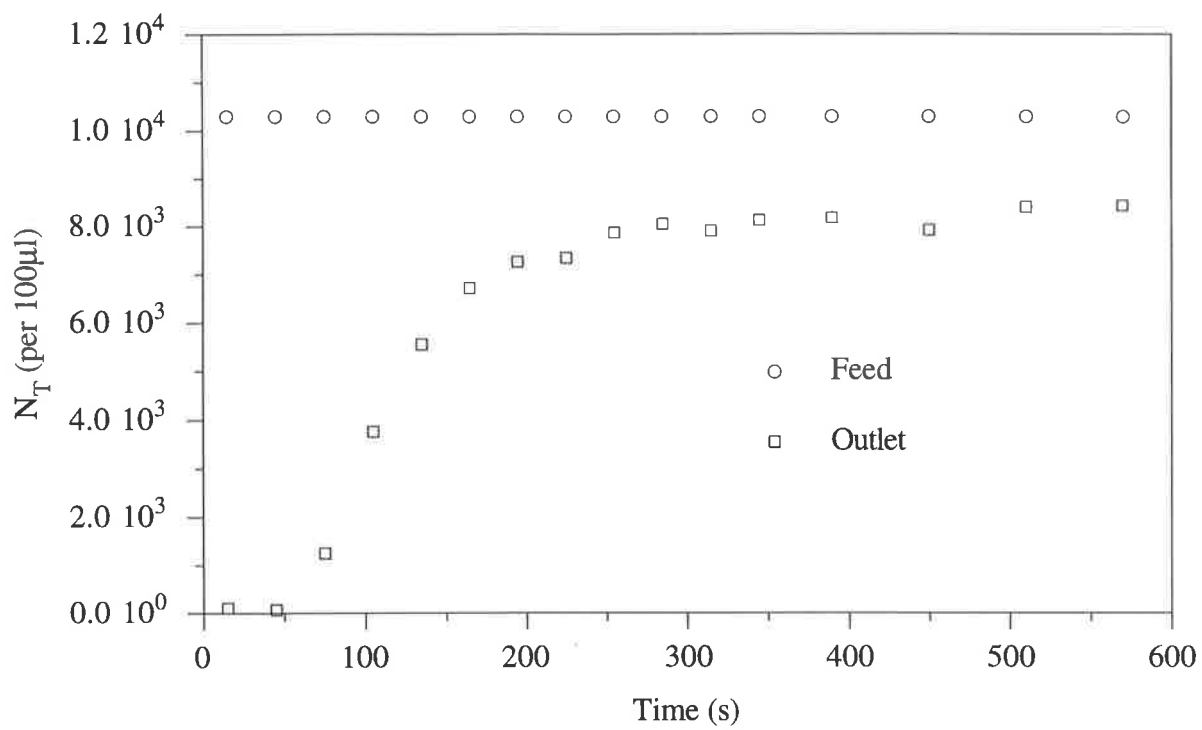
Figures 8.2 (a) and (b) show the total number and volume of particles fed to the crystalliser and the response at the outlet to the step change for a value of the dilution factor of one. After approximately 300 seconds the total number and volume of particles in the fluid at the outlet is constant, indicating a steady state has been reached. However, the steady state values of the total number and volume of particles at the outlet are *lower* than the values at the inlet.

The apparent loss of particle mass in the crystalliser can be explained if the particles are sticking to the walls of the lumen. Most of the particles pass through the crystalliser, however a small, but significant fraction stick to the walls of the lumen. The dilution factor affects the fraction of particles that stick to the walls of the lumen, as shown by the data in Table 8.1 in which the total number of particles in the fluid at the inlet and outlet of the crystalliser are compared for values of the dilution factor of one and two.

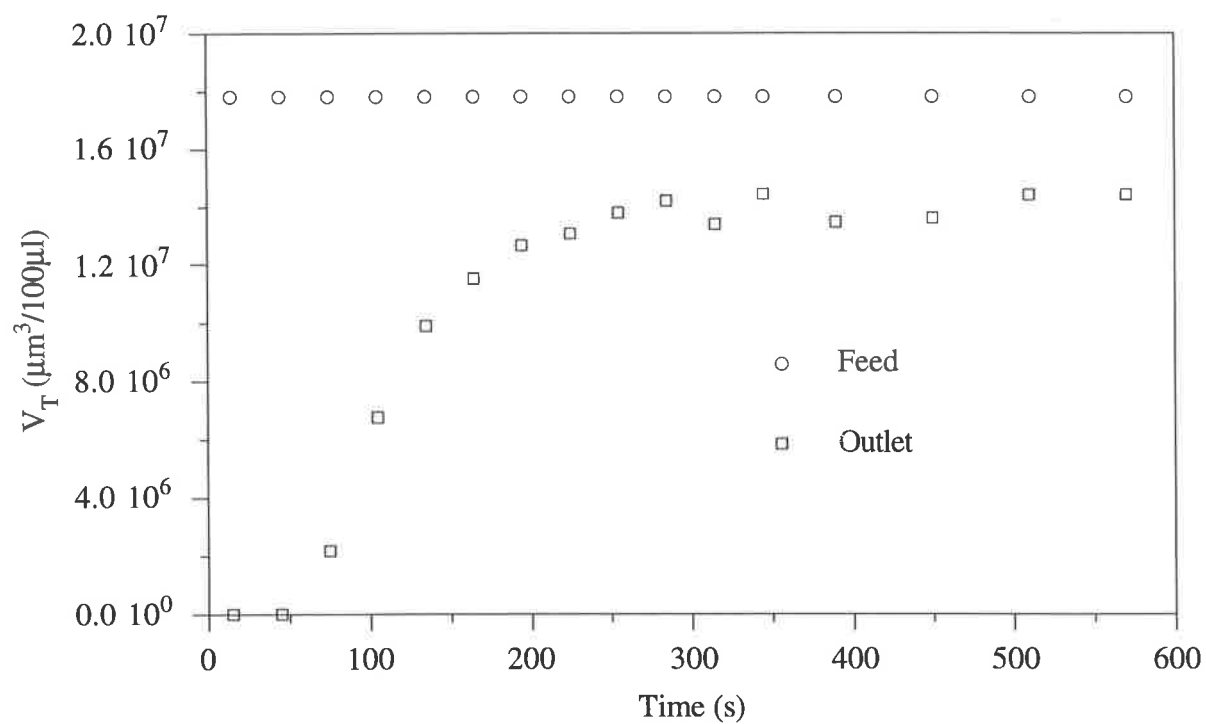
Table 8.1. The effect of the dilution factor on particle sticking.

Dilution factor, α	$N_{T,0}$ (per 100 μ l)	$N_T(t_{\max})$ (per 100 μ l)	$N_T(t_{\max})/N_{T,0}$ (%)
1	2057 \pm 51	1690 \pm 53	82 \pm 3
1	2123 \pm 50	1825 \pm 15	86 \pm 2
2	4409 \pm 92	4026 \pm 94	91 \pm 3
2	4409 \pm 92	3934 \pm 62	89 \pm 2

The sticking process will be investigated in Chapter 9, here the particle RTD is of interest. Before proceeding to investigate the RTDs there is one further point to consider. By equating the expressions for the F curve, eq 8.1, in terms of particle number and volume, it is assumed that both give the same F curve. As the latex particles are effectively mono-



(a)



(b)

Figure 8.2 The variation in total particle (a) number and (b) volume fed to the crystalliser and the response at the outlet to a step change for $\alpha = 1$.

disperse this should be a reasonable assumption.

Figure 8.3 shows the F curve calculated using both the particle number and volume for the data used in Figure 8.2. The F curves are in good agreement, suggesting that for the latex particles used in the RTD experiments either number or volume can be used to calculate the RTDs. It is convenient to calculate the RTD from the number data, as it is easier to obtain from the Multisizer than the volume data.

8.3 RESIDENCE TIME DISTRIBUTION EXPERIMENTS

The factors affecting the particle RTDs were investigated using pulse-input tests. The main reason for using pulse-input tests was that it is much easier to inject a pulse of particles into the fluid entering the crystalliser than it is to continuously supply a suspension of particles, of constant composition, to the crystalliser.

8.3.1 Materials

In all the experiments the solution fed to both the lumen and jacket was filtered (0.22 μm) 0.15 M saline. The particles used were calibration standard polystyrene divinyl benzene (PDVB) latex, (Coulter Electronics Ltd., England). Three different size particles were used with number modes of 5.9 μm , 8.8 μm and 13.7 μm .

In addition to the crystalliser described in Chapter 6, a second tubular crystalliser, similar in design to that shown in Figure 6.2, was used in some of the RTD experiments. This crystalliser consists of 50 Amicon H1MP01-43 hollow porous fibre tubes of internal diameter 1100 μm , and length 20 cm contained as a bundle in a perspex tube 2.0 cm in diameter. The porous tubes are held in place at each end of the perspex tube by epoxy resin for a length of 2.0 cm.

8.3.2 Method

The crystalliser was operated as described in Section 6.3.2, that is with the jacket outlet closed, and fluid fed to both the lumen and jacket. A 0.15 M saline solution was fed to both the lumen and the jacket, and at time, $t = 0$, a 50 μl pulse of the particle suspension was added to the fluid entering the lumen. After the addition of the pulse all the fluid leaving the crystalliser was collected in separate samples. In all the experiments the volume of each sample collected was approximately 4 ml. The total number of particles per unit volume in each sample was determined using the Multisizer. As in the step-change tests when the samples were analysed, several 100 μl counts were taken rather than a single 500 μl count.

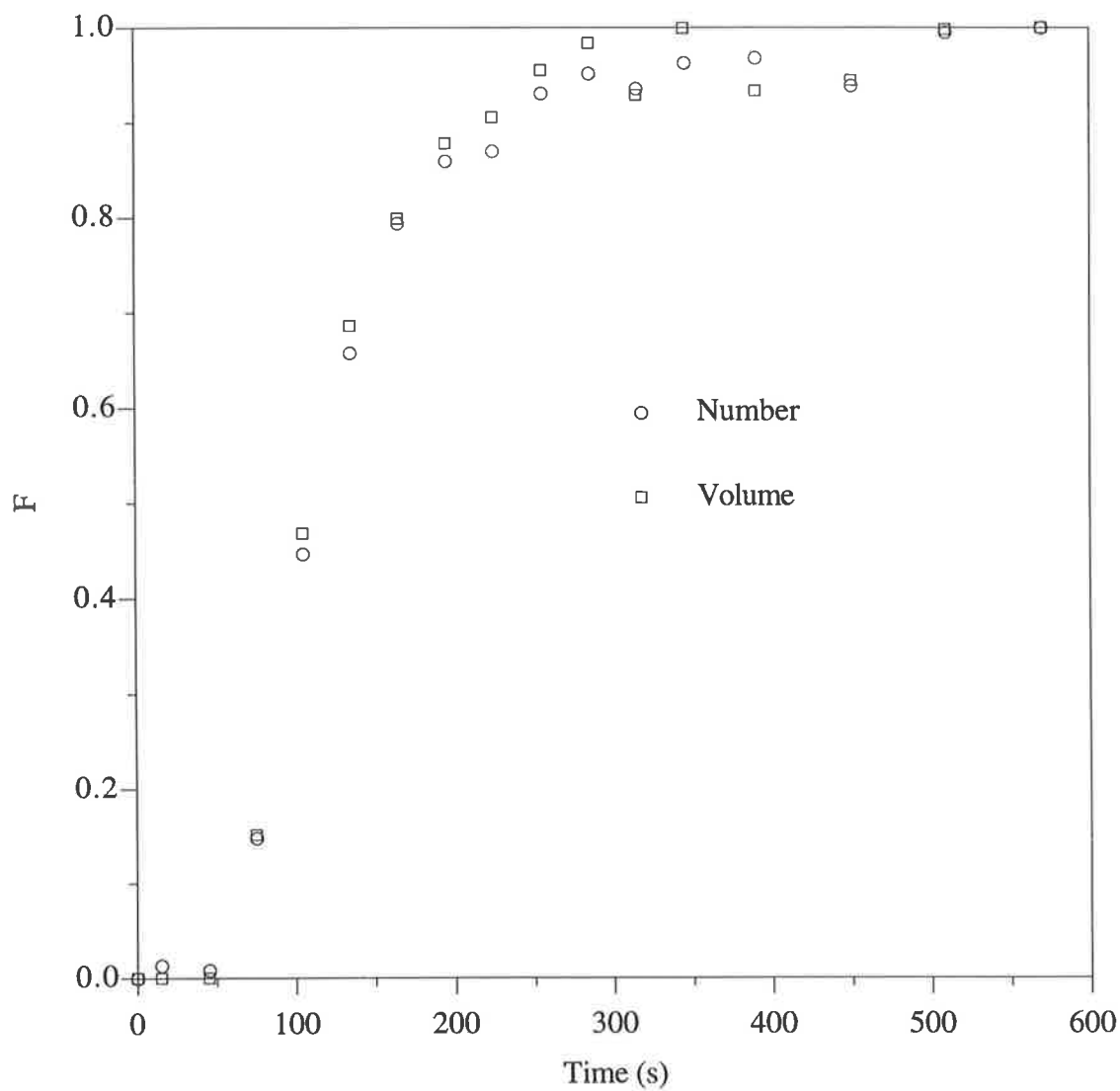


Figure 8.3 Comparison of particle RTDs calculated from measurements of particle number and volume.

8.3.3 Parameters investigated

The effect of the following parameters on the particle RTD was investigated:

- *Dilution factor*: this parameter was varied from 1 to 5 for both the crystallisers.
- *Lumen flowrate*: two lumen flowrates were used at each value of the dilution factor.
- *Particle size*: latex with sizes of 5.9 μm , 8.8 μm and 13.7 μm were used.
- *Crystalliser geometry*: a second crystalliser with lumen of different diameter, pore structure, and length was used.

8.3.4 Calculating the RTDs

The particles in a sample collected from time, t to $t + \Delta t$ are the fraction that have a residence time between t and $t + \Delta t$ and hence represent the E curve. The F curve can be calculated from the E curve using the discrete form of eq 7.2, which is

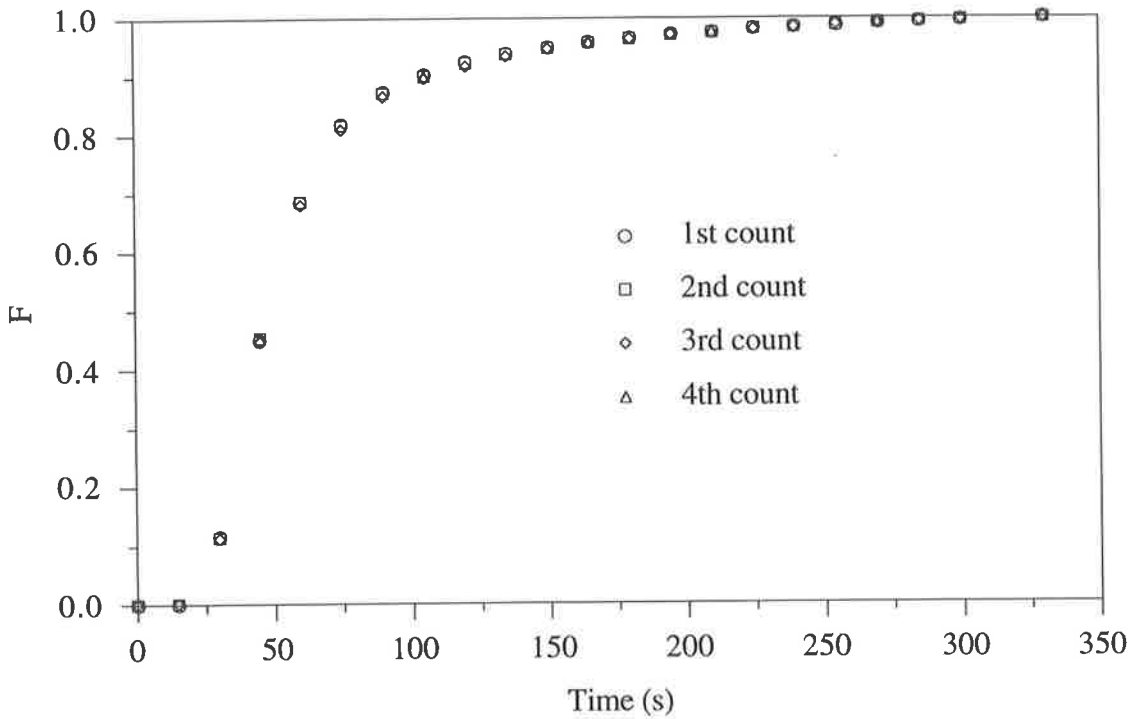
$$F(t_k) = \frac{\sum_{i=1}^k N_i}{N_T} \quad (8.4)$$

where t_k is the time at the end of the k^{th} sample, and N_T is the total number of particles in all the samples collected. As mentioned in the previous section when the samples were analysed several 100 μl counts were taken. In Figures 8.4 (a) and (b) the RTDs calculated from the separate counts taken are shown for values of the dilution factor of one and five. It can be seen that the RTDs calculated from the separate counts are virtually identical, thus averaging the counts reduces the error associated with calculating the RTD. The RTDs presented in the next section are calculated from the average of the counts taken from each sample.

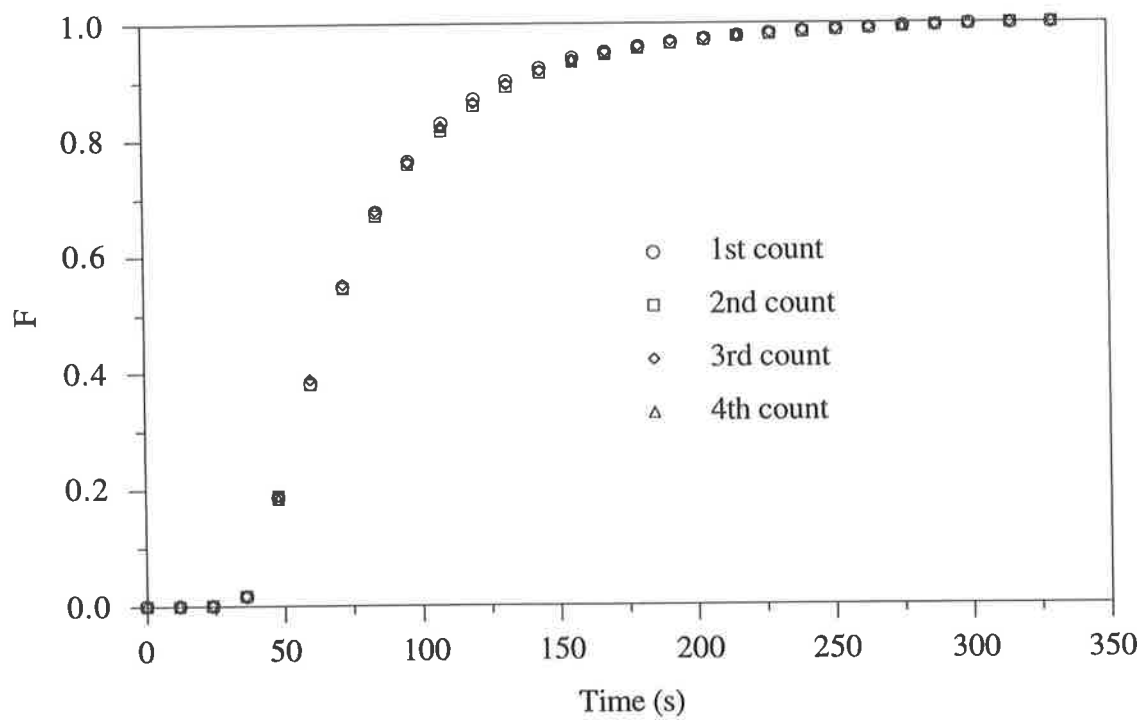
8.4 EXPERIMENTAL RESULTS

As different lumen flowrates were used to investigate the effect of the parameters listed in Section 8.3.3, a dimensionless time, the same as that used for the solute RTDs is used as the independent variable in the results presented, *i.e.*

$$\theta = \frac{tu_0}{L} \quad (8.5)$$



(a)



(b)

Figure 8.4 Comparison of RTDs calculated from separate counts taken from the same samples for (a) $\alpha = 1$ and (b) $\alpha = 5$.

where u_0 is the centre-line fluid velocity based on the fluid flowrate at the inlet of the lumen, and L is the length of the crystalliser.

For each value of the parameters being investigated, a number of experiments were conducted, the RTDs plotted are the average of all the experiments. The uncertainty associated with averaging the data from the experiments is expressed as a standard error, the errors shown in all the plots of the RTDs are plus-or-minus one standard error.

Firstly, the results from the pulse-input tests are compared with those from the step-change tests. In Figure 8.5 the RTDs determined from step-change and pulse-input experiments are presented for values of the dilution factor of one and two. The agreement between the RTDs is good for both values of the dilution factor. The uncertainty for the step-change experiments is larger than those for a pulse-input as fewer step-change experiments were conducted.

Dilution factor

Figure 8.6 shows the effect of the dilution factor on the RTD. It can be seen that as the dilution factor increases, the time taken for the particles to pass through the crystalliser decreases as a result of the increase in the fluid flowrate in the lumen.

Particle size

The effect of the particle size on the RTDs is shown in Figures 8.7 (a) and (b). It can be seen that for the three different sizes used, the RTD is independent of the particle diameter for all the values of the dilution factor. The latex particles are almost neutrally buoyant, having a specific gravity relative to water of 1.05, which implies that the single particle settling velocity for the largest particle used, 14 μm , is 5.34×10^{-6} m/s. The settling velocity may be compared to the fluid velocity in the lumen, at the lowest flowrate used, 2 ml/min, the average axial velocity is 9.6×10^{-4} m/s, which is two orders of magnitude greater than the settling velocity. Considering the difference between the particle settling velocity and fluid velocity there is no reason for the RTD to be size dependent.

Lumen flowrate

Figures 8.8 (a) and (b) show the effect of the lumen flowrate on the RTD for different values of the dilution factor. It can be seen that when plotted against the dimensionless time, that if the dilution factor is constant, the RTD does not depend on the lumen flowrate, except perhaps for values of the dilution factor of one and two. For both these values of the dilution factor it can be seen that the time taken for the particles to pass through the crystalliser increases as the lumen flowrate increases. As a dimensionless time is used the RTD should not depend on the lumen flowrate. Further, if the RTD were to depend on the

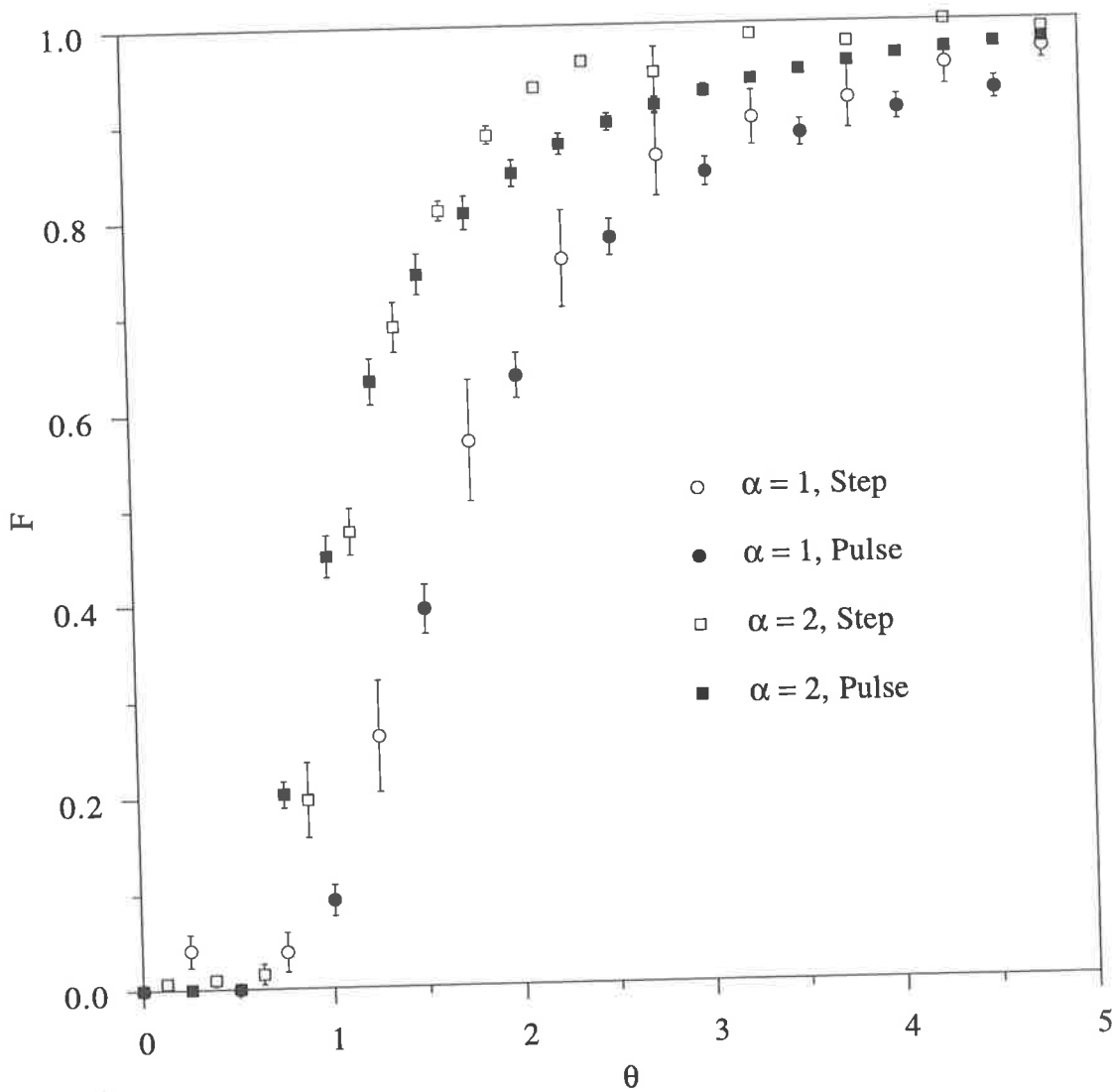


Figure 8.5 Comparison of particle RTDs calculated from step-change and pulse-input tests for $\alpha = 1$ and $\alpha = 2$.

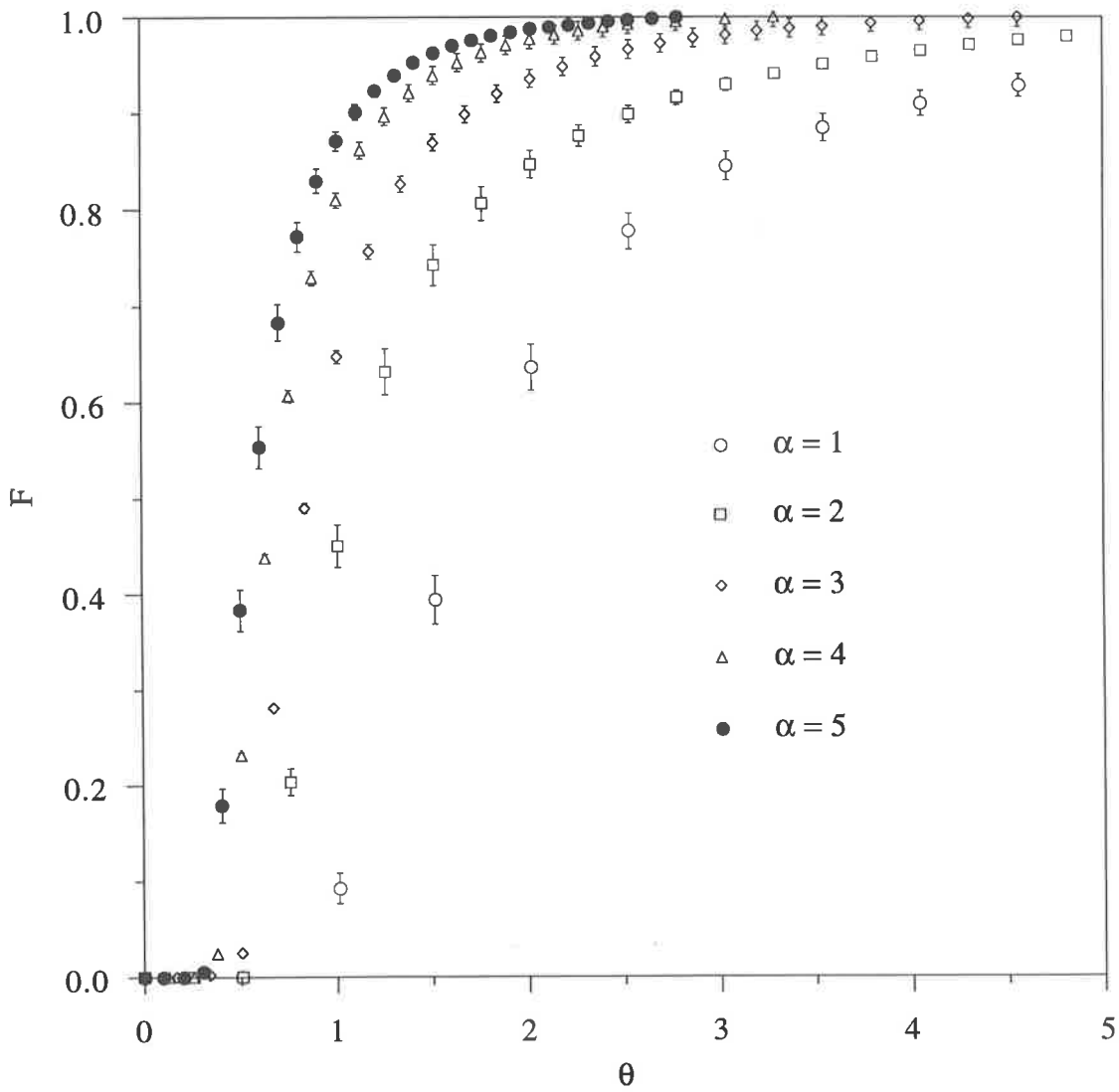
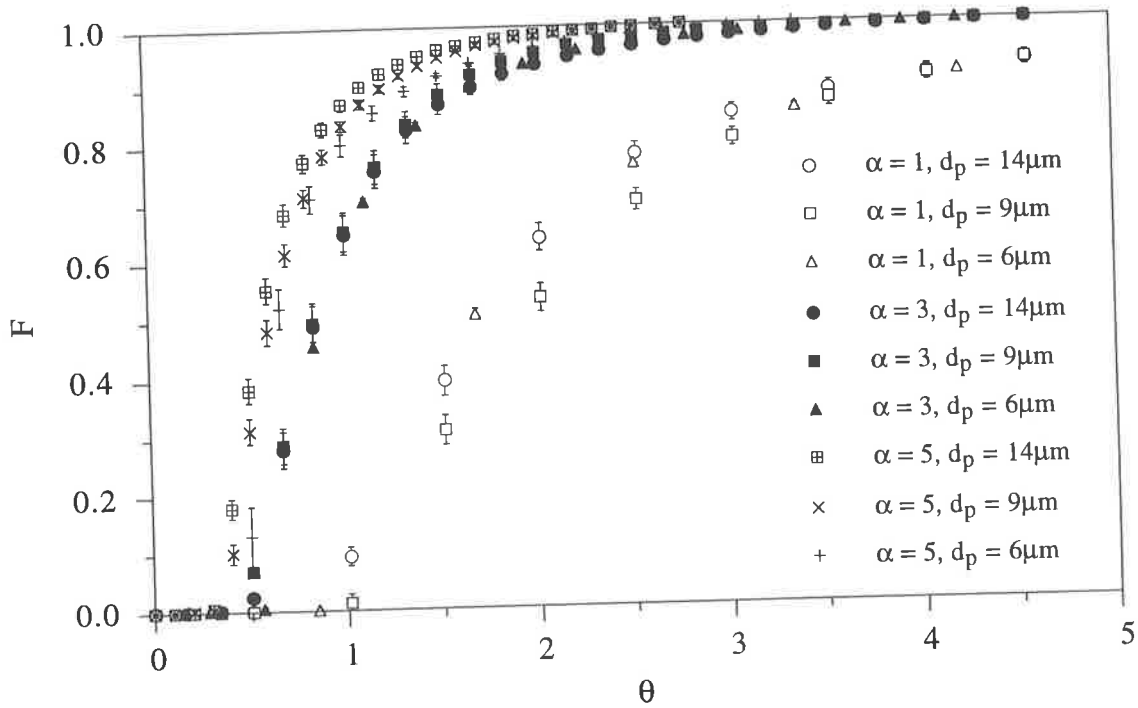
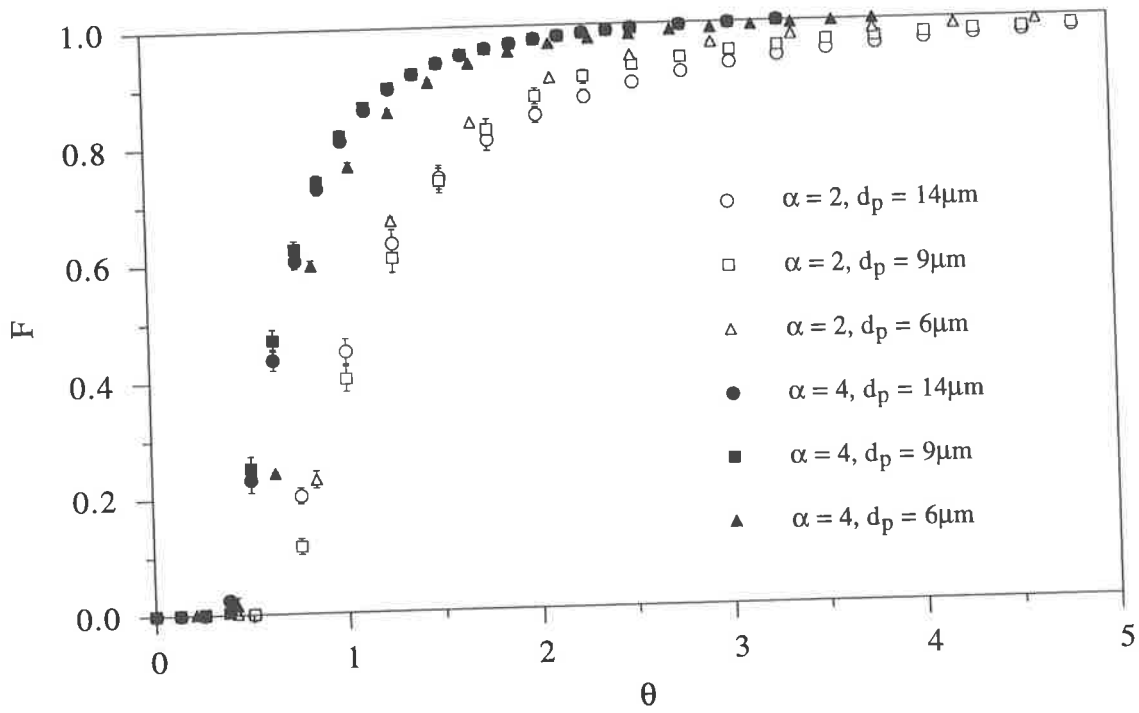


Figure 8.6 The effect of the dilution factor on the particle RTD.

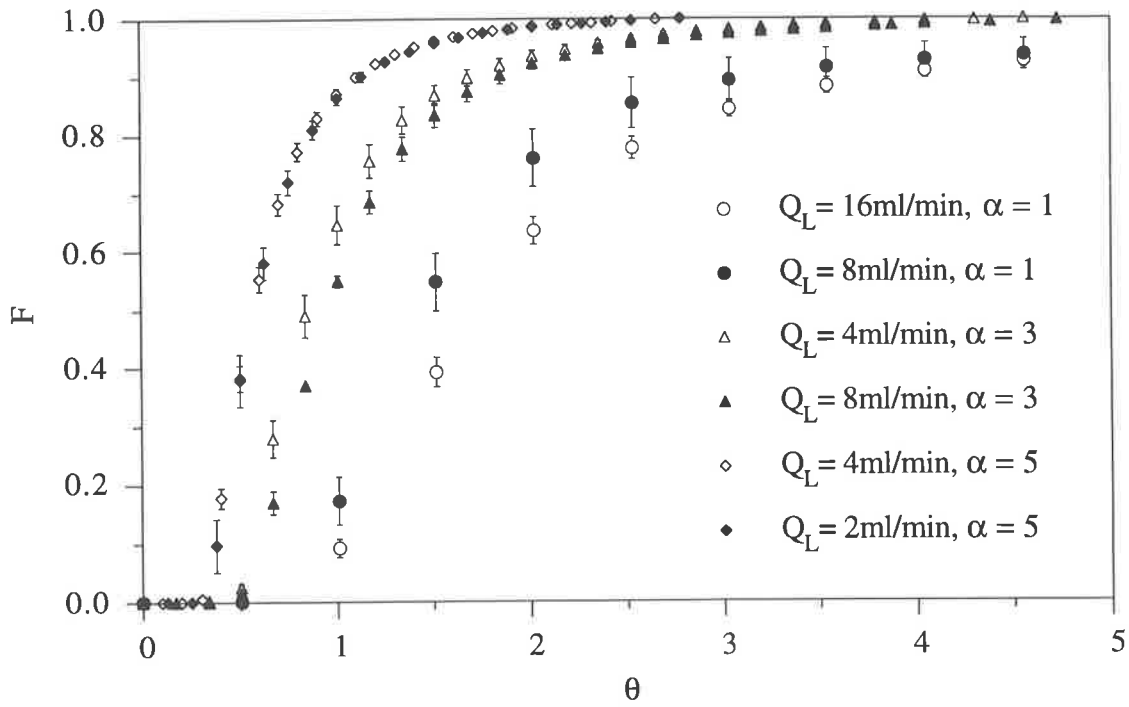


(a)

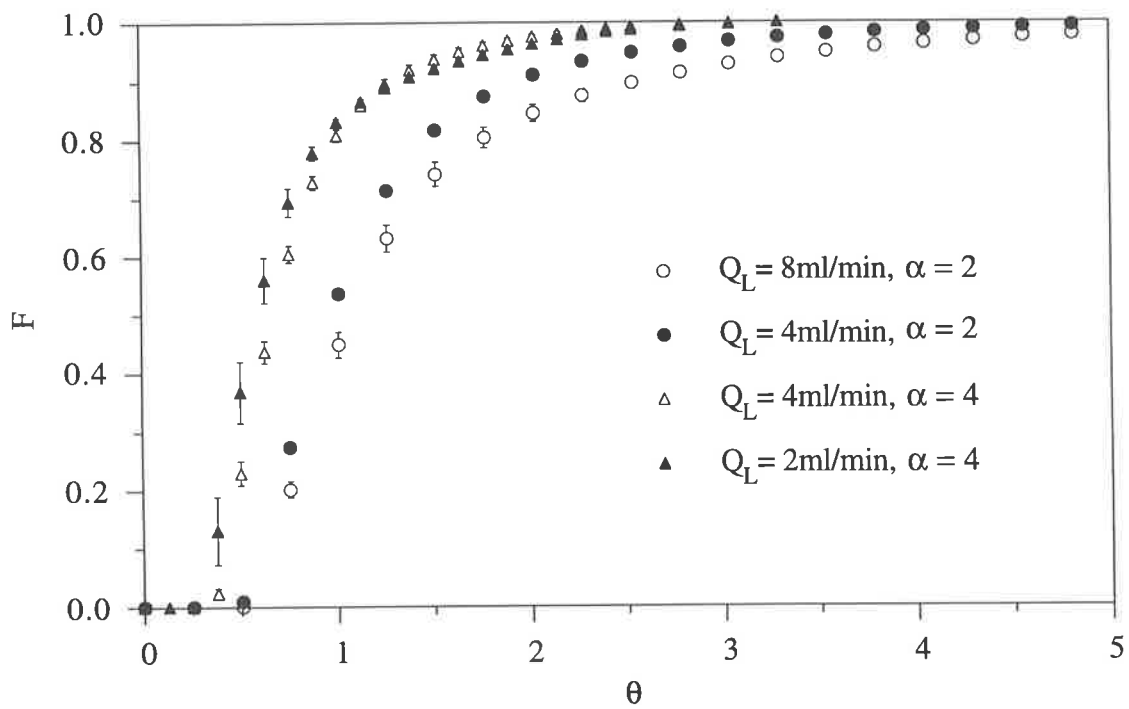


(b)

Figure 8.7 The effect of particle size on the RTD for (a) $\alpha = 1, 3$ and 5 and (b) $\alpha = 2$ and 4 .



(a)



(b)

Figure 8.8 The effect of the lumen flowrate on the particle RTD for (a) $\alpha = 1, 3$ and 5 and (b) $\alpha = 2$ and 4 .

lumen flowrate, increasing the lumen flowrate should decrease the residence time, which is not supported by the experimental results.

The experimental observations may be explained by considering the effect the lumen flowrate has on particles sticking to the walls of the lumen. As the lumen flowrate decreases it is possible that more particles stick to the walls of the lumen, particularly those nearer to the walls where the fluid velocity is lower. In this situation, most particles that pass through the crystalliser would be nearer to the centre of the lumen, where the fluid velocities are higher. Consequently the particles that pass through the crystalliser appear to have a shorter residence time.

Crystalliser geometry

Figures 8.9 (a) and (b) show the effect of the crystalliser geometry on the RTDs. In both Figures the abbreviation, “Std.”, refers to the standard crystalliser used in all the other experiments and “Short”, refers the crystalliser described in Section 8.3.1. The RTDs for the two crystallisers are in good agreement, except for when the dilution factor is five. A possible explanation for the difference when $\alpha = 5$ is that for the “shorter” crystalliser as a result of the high flowrates few data points were collected around the break-through time. Over half the particles counted appeared in the first two samples after break-through. Any error in these samples will significantly affect the RTD calculated from the experimental data.

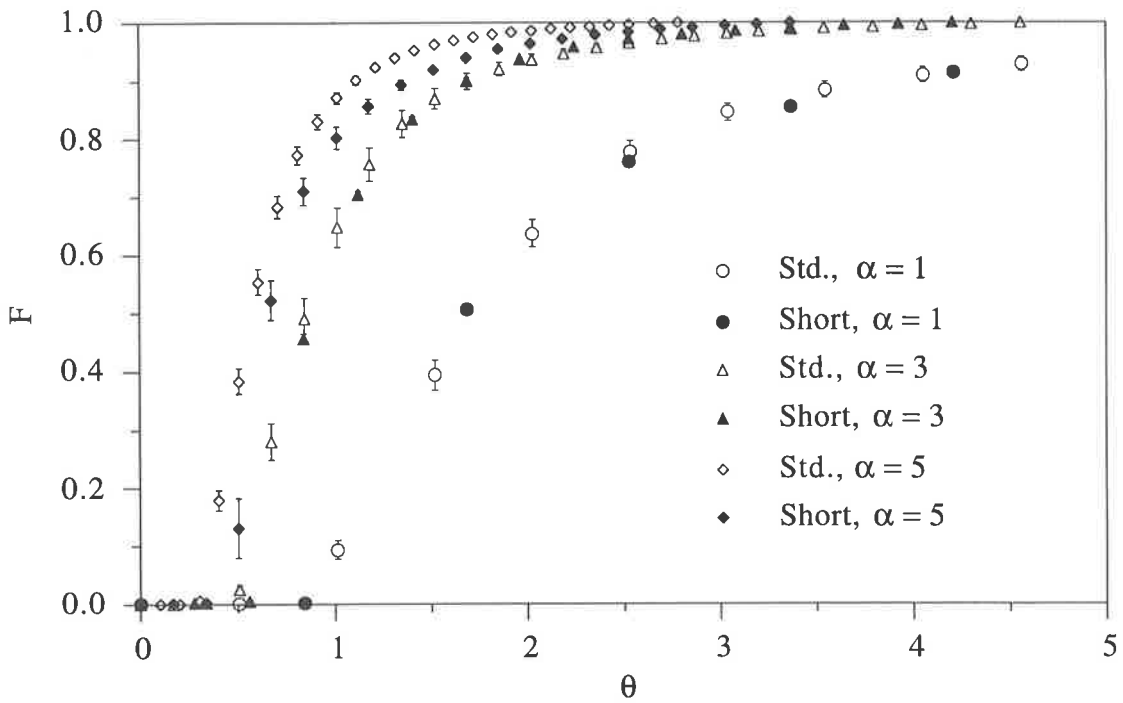
The results presented in Figures 8.6 to 8.9, clearly show that the particle RTDs are reproducible and relatively insensitive to the effects of particle size, lumen flowrate and crystalliser geometry, but dependent on the value of the dilution factor.

8.5 ANALYSIS

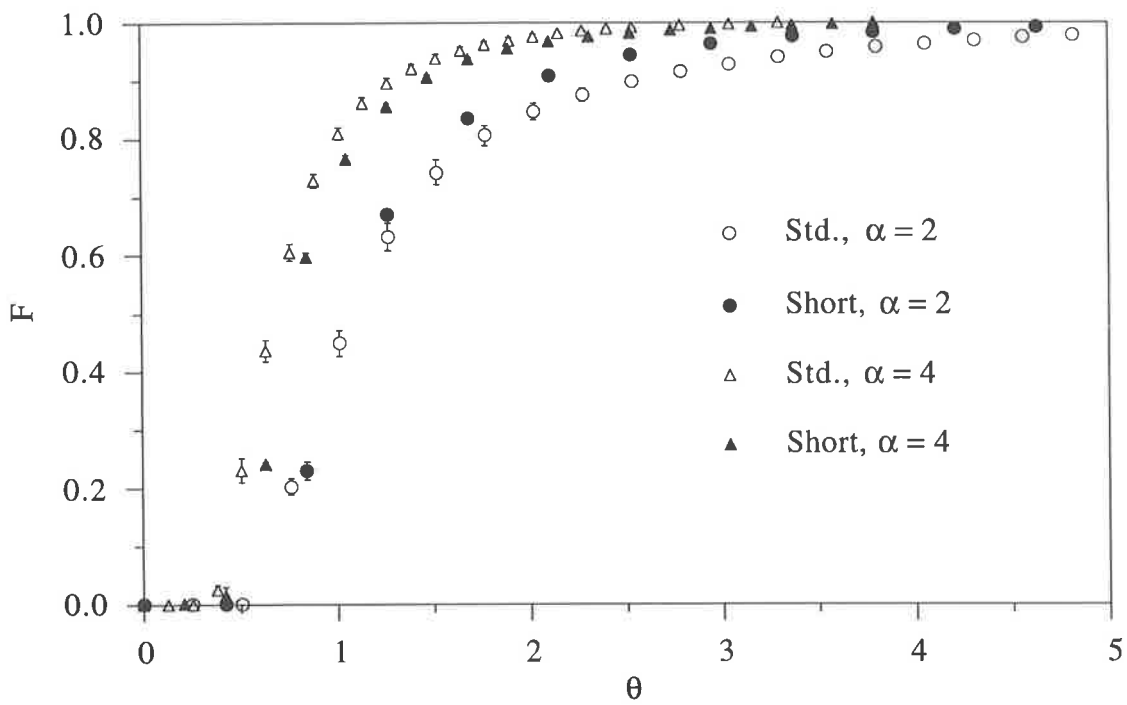
To determine a theoretical expression for the particle RTD the velocity profile of the particles must be known. As the latex particles are almost neutrally buoyant it is reasonable to assume that they travel at the local fluid velocity. If there is no fluid injection through the walls of the lumen, the dilution factor is one and the velocity field is described by the usual results for Poiseuille flow. For other values of the dilution factor, the fluid flow is two-dimensional having both axial and radial components, in which case the velocities in both directions are given by eqs 7.12 and 7.13.

8.5.1 Poiseuille flow

The RTD for Poiseuille flow is given by eq 7.14. Figure 8.10 shows the RTD calculated from eq 7.14 and the RTDs from the experiments in which the value of the dilution factor



(a)



(b)

Figure 8.9 The effect of crystalliser geometry on the particle RTD for (a) $\alpha = 1, 3$ and 5 and (b) $\alpha = 2$ and 4 .

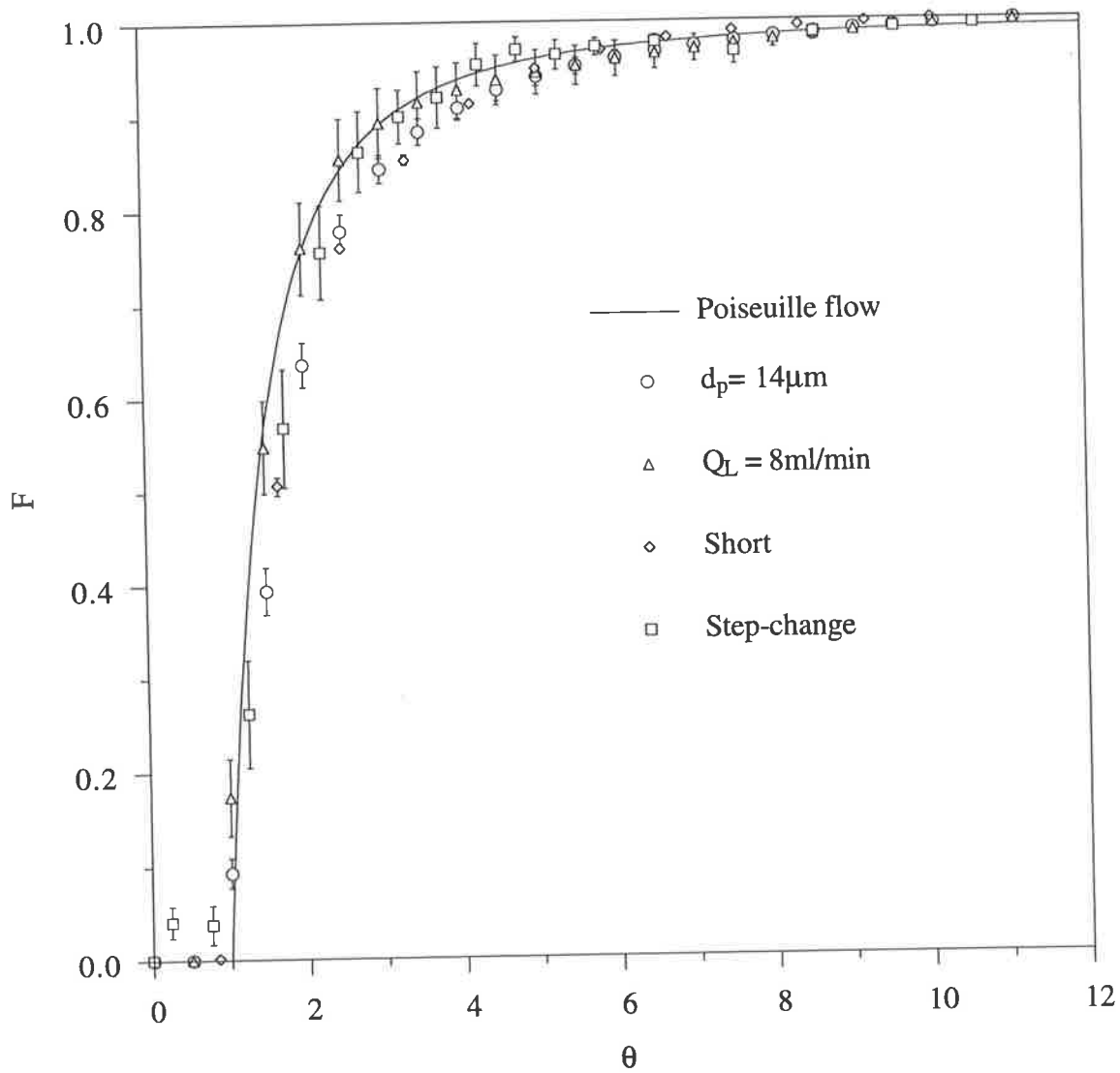


Figure 8.10 Comparison of experimental particle RTDs for $\alpha = 1$, with the RTD for Poiseuille flow.

was one. It can be seen that the experimental RTDs are well described by the RTD for Poiseuille flow. Both the break-through time, *i.e.* the time at which the first particles leave the crystalliser and the shape of the RTD are correct.

8.5.2 Streamline model

In this model it is assumed that the particles follow the fluid streamlines and travel at the local fluid velocity in both the axial and directions. Consequently, as the particles pass through the lumen they are swept towards the middle of the lumen by the fluid which is injected from the jacket. According to Yuan and Finkelstein (1956) for constant fluid injection through the porous wall of a tube the stream function for steady laminar flow in the tube is

$$\Psi = \frac{R^2}{2} \left(u_0 + 4v_0 \frac{x}{R} \right) \left(\eta - \frac{\eta^2}{2} \right) \quad (8.6)$$

where $\eta = (r/R)^2$ and v_0 is the radial velocity through the porous wall. At $x = 0$ and $\eta = 1$, the stream function is

$$\Psi = \frac{u_0 R^2}{4} \quad (8.7)$$

Dividing eq 8.6 by eq 8.7, substituting eq 7.11 for the ratio of the radial and axial velocities and simplifying, a dimensionless stream function, $\hat{\Psi}$ is defined as:

$$\hat{\Psi} = \left(1 + (\alpha - 1) \frac{x}{L_i} \right) (2\eta - \eta^2) \quad (8.8)$$

Where L_i is the length in the axial direction over which fluid is injected. The fraction of material between $\hat{\Psi}$ and $\hat{\Psi} + d\hat{\Psi}$ is equivalent to the fraction of material between r and $r + dr$, thus the stream function gives the F curve as a function of radial position, therefore

$$F = \hat{\Psi} = \left(1 + (\alpha - 1) \frac{x}{L_i} \right) (2\eta - \eta^2) \quad (8.9)$$

However, the F curve is required as a function of time rather than radial position. Eq 8.9 may be transformed to a function in time by considering the velocity along a streamline. Eq 7.12, gives the axial velocity along a streamline, and the time taken to travel an axial distance, dx , is

$$dt = \frac{dx}{u} = \frac{dx}{u_0 \left(1 + (\alpha - 1) \frac{x}{L_i}\right) (1 - \eta)} \quad (8.10)$$

From the appropriate solution to eq 8.9, η may be written in terms of the F curve, substituting this expression into eq 8.10 yields

$$dt = \frac{dx}{u_0 \left(1 + (\alpha - 1) \frac{x}{L_i}\right) \sqrt{1 - \frac{F}{1 + (\alpha - 1) \frac{x}{L_i}}}} \quad (8.11)$$

If the following parameter is defined,

$$Y = \frac{1}{F} \left(1 + (\alpha - 1) \frac{x}{L_i}\right) \quad \text{then} \quad dY = \frac{\alpha - 1}{F L_i} dx \quad (8.12 \text{ a and b})$$

Substituting into eq 8.11 yields

$$dt = \frac{L_i}{(\alpha - 1)u_0} \frac{dY}{\sqrt{Y^2 - Y}} \quad (8.13)$$

Integrating eq 8.13 the time, t , taken for a particle to travel the axial distance from $x = 0$ to $x = L_i$ (which is equivalent to the parameter Y varying from $Y = 1/F$ to $Y = \alpha/F$) is

$$t = \frac{L_i}{(\alpha - 1)u_0} \ln \left[\frac{2\alpha - F + 2\sqrt{\alpha^2 - \alpha F}}{2 - F + 2\sqrt{1 - F}} \right] \quad (8.14)$$

From eq 8.14 the F curve can be calculated as a function of time. If the dilution factor is one, eq 8.14 should give the RTD for Poiseuille flow. If $\alpha = 1$, the right hand side of eq 8.14 is of the form, $0/0$, in which case L'Hôspitals rule can be used to evaluate the fraction. Applying L'Hôspital's rule it can be shown that

$$t = \frac{L_i}{u_0 \sqrt{1 - F}} \quad (8.15)$$

As the flow average velocity is half the centre-line velocity, the mean residence time is

$$\bar{t} = \frac{2L_i}{u_0} \quad (8.16)$$

Substituting eq 8.16 into eq 8.15 and re-arranging gives the following result as required.

$$F = 1 - \frac{1}{4} \left(\frac{\bar{t}}{t} \right)^2 \quad (8.17)$$

The crystalliser can be divided into three separate regions: one at each end in which there is no fluid injection through the walls of the lumen, and a region in which there is fluid injection. The RTD for the region at the entrance of the crystalliser is given by eq 7.14 for Poiseuille flow, and the RTD for the section in the middle by eq 8.17. The RTD in the final region of the crystalliser can be determined by the same approach used for the region with fluid injection. At the end of the region in which fluid is injected, the integrated form of eq 8.11 with $x = L_i$ is

$$t_2 = \frac{L_2}{u_0 \sqrt{\alpha^2 - \alpha F}} \quad (8.18)$$

where L_2 is the length of the region at the end of the crystalliser. As with eq 8.17, using L'Hôpital's rule, it can be shown that eq 8.18 gives the correct RTD for Poiseuille flow if the value of the dilution factor is one.

The RTD for the crystalliser can now be determined for the streamline model. A schematic diagram of the crystalliser is shown in Figure 8.11.

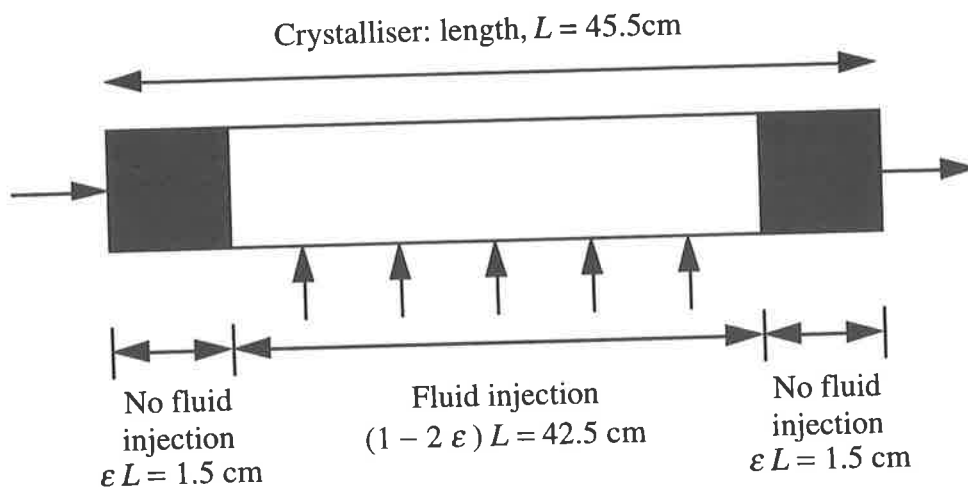


Figure 8.11. Schematic diagram of the crystalliser.

The regions in the crystalliser in which there is no fluid injection are characterised by a parameter, ϵ where $\epsilon = 1.5/45.5 = 0.03297$. The reason for defining the length of each region in terms of the total length of the crystalliser is that the dimensionless time used as the independent variable is defined in terms of total length of the crystalliser. In terms of the parameter, ϵ the lengths of each region in the crystalliser are:

$$L_1 = L_2 = \varepsilon L \quad \text{and} \quad L_i = (1 - 2\varepsilon)L \quad (8.19a \text{ and } b)$$

Substituting these lengths into the appropriate expressions for the RTD in each region, eqs 8.17, 8.14 and 8.18, and writing in terms of dimensionless time,

$$\theta = \frac{\varepsilon}{\sqrt{1-F}} + \frac{(1-2\varepsilon)}{(\alpha-1)} \ln \left[\frac{2\alpha - F + 2\sqrt{\alpha^2 - \alpha F}}{2 - F + 2\sqrt{1-F}} \right] + \frac{\varepsilon}{\sqrt{\alpha^2 - \alpha F}} \quad (8.20)$$

Figure 8.12 shows the RTD for the streamline model as well as the experimental RTDs for values of the dilution factor of two and five. It can be seen that the streamline model does not describe the experimental data at all well. The break-through time is correctly predicted, but a significant fraction of particles take much longer to pass through the crystalliser than predicted by the model. It seems likely that the streamline model cannot describe the RTDs as some particles stick to the walls of the lumen and therefore, do not follow the fluid streamlines.

8.5.3 Constant radial position model

In this model it is assumed that the particles maintain a constant radial position in the lumen as they pass through the crystalliser. That is the fluid being injected through the walls of the lumen does not cause the particles to move in the radial direction.

The fraction of material at the inlet of the crystalliser between a radial position r and $r + dr$ is

$$dF = \frac{u|_{x=0} 2\pi r dr}{Q} \quad (8.21)$$

where Q is the fluid flowrate. Using the usual expression for the fluid flowrate, evaluating the axial velocity from eq 7.12 and integrating, the F curve in terms of η is

$$F = 2\eta - \eta^2 \quad (8.22)$$

The time taken for a particle to traverse the length over which fluid is injected is obtained from the integrated form of eq 8.11, using eq 7.12 for the axial velocity and the appropriate root of eq 8.22 for η as

$$t = \frac{L_i}{u_0 \sqrt{1-F}} \frac{\ln \alpha}{(\alpha-1)} \quad (8.23)$$

If the dilution factor is one, eq 8.23 should give the RTD for Poiseuille flow. Using

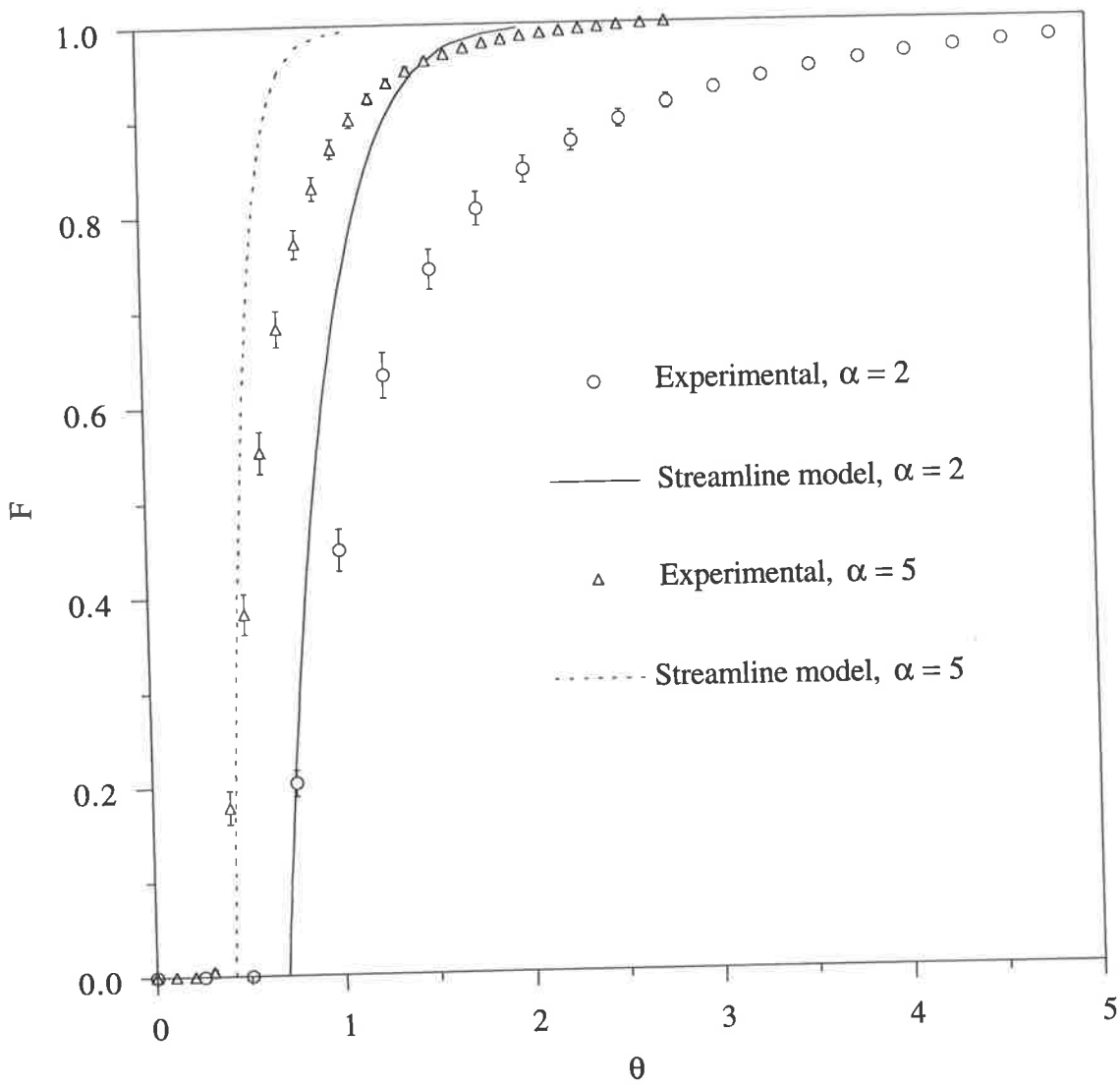


Figure 8.12 Comparison of experimental particle RTDs for $\alpha = 2$ and 5, with the RTD predicted by the streamline model, eq 8.20.

L'Hôspitals rule it can be shown that for $\alpha = 1$ eq 8.23 is equivalent to eq 7.14 for Poiseuille flow.

At the ends of the crystalliser, where there is no fluid injection, the RTD is given by eq 7.14 for Poiseuille flow. However, after fluid injection the axial velocity in the lumen is α times the axial velocity at the inlet. Using the appropriate lengths for each region, given by eqs 8.19a and b, the dimensionless time taken for a particle to travel through the crystalliser in terms of the F curve is

$$\theta = \left(\varepsilon + (1 - 2\varepsilon) \frac{\ln \alpha}{(\alpha - 1)} + \frac{\varepsilon}{\alpha} \right) \frac{1}{\sqrt{1 - F}} \quad (8.24)$$

The following dimensionless group may be defined:

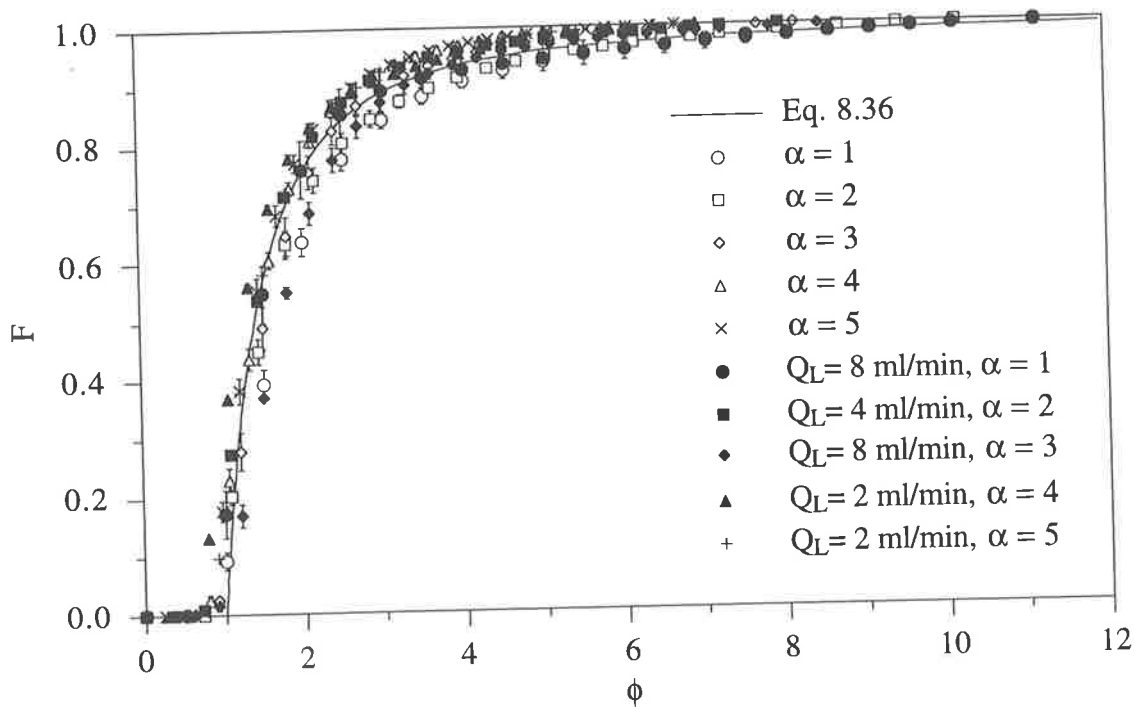
$$\phi = \frac{\theta}{\left(\varepsilon + (1 - 2\varepsilon) \frac{\ln \alpha}{(\alpha - 1)} + \frac{\varepsilon}{\alpha} \right)} \quad (8.25)$$

From eq 8.24 it follows that for the constant radial position model:

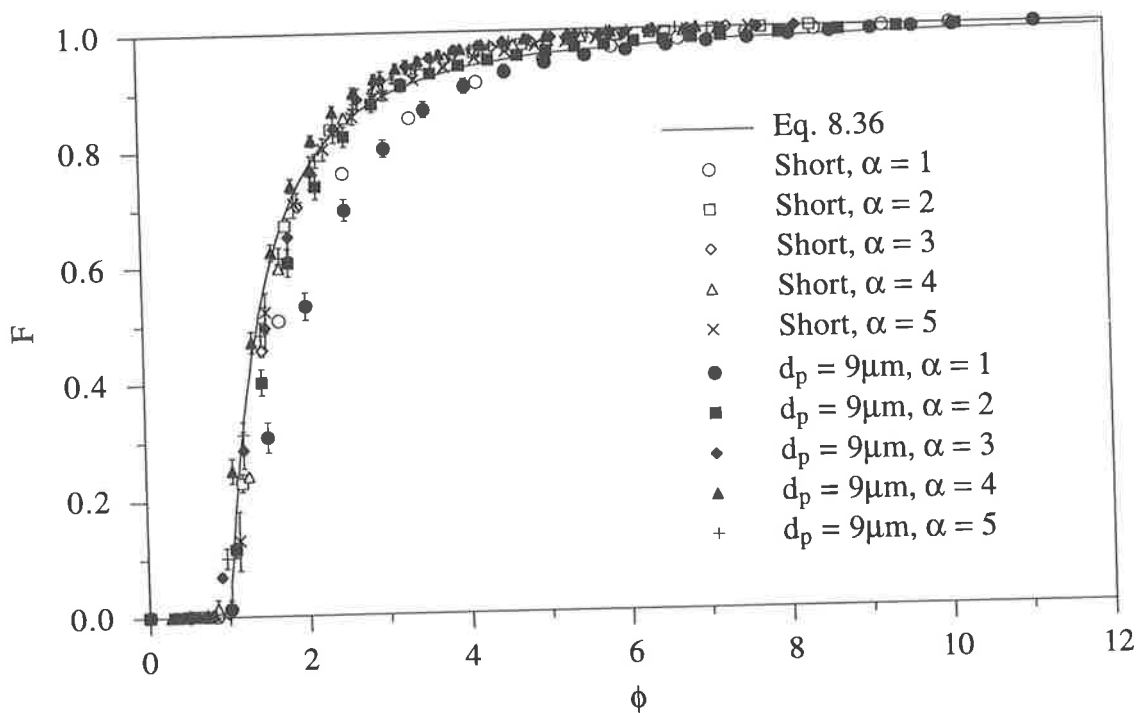
$$F = 1 - \frac{1}{\phi^2} \quad (8.26)$$

Eq 8.26 gives a unique relationship between the parameter, ϕ and the F curve, for all values of the dilution factor. Figure 8.13 (a) shows the experimental F curves from the experiments conducted with different values of the dilution factor, and different lumen flowrates, plotted against the parameter, ϕ together with eq 8.26. All the experimental data collapse onto one curve, and are well described by eq 8.26. Figure 8.13 (b) shows the F curves for the experiments conducted using 9 μm latex particles and those from the short crystalliser plotted against the parameter, ϕ together with eq 8.26. The data are described by a single curve in good agreement with eq 8.26. There is some scatter, particularly for the experiments in which the value of the dilution factor was one, but the experimental data are generally well described by the model.

It seems unlikely that the particles actually maintain a constant radial position as they pass through the crystalliser and do not acquire some radial velocity as a result of the fluid injected through the walls of the lumen. However, the RTD predicted by the constant radial position model is the one that best fits the experimental data. In this case it is better to use a model, that while physically implausible, accurately represents the experimental data, rather than one that is physically plausible but inaccurate. Also the fact that the particles stick to the



(a)



(b)

Figure 8.13 Comparison of the experimental particle RTDs for (a) different values of α and different lumen flowrates and (b) different particle sizes and crystalliser geometry with the RTD for the constant radial position model, eq 8.26.

walls of the lumen may explain why the constant radial position model can be used to describe the experimental RTDs.

8.6 DISCUSSION

The findings of the experimental investigation into the particle RTD in the crystalliser are important for two reasons: firstly, the RTD will be used in the analysis of the crystallisation experiments to be reported in Chapter 9 and secondly, they have implications for understanding the mechanism by which kidney stone formation occurs.

In most *in vitro* experimental systems used to study the factors affecting stone formation, the tubular geometry of the kidney has largely been ignored, despite both human autopsy, (Haggitt and Pitcock, 1971) and animal models, (Jordan *et al.*, 1978 and Khan *et al.*, 1979) indicating that the kidney tubules are the initial site of stone formation.

The results of the particle RTD experiments show that a tubular geometry has a significant effect on the residence time of the crystals. The implications of this cannot be overlooked: the ultimate size that a crystal attains must depend on the length of time that it remains in the tubules of the kidney. The author is aware of only one other study that addresses the influence of the residence time on the formation of kidney stones.

Finlayson and Reid (1978) consider two mechanisms for stone formation that of free and fixed particles. The free particle mechanism assumes that crystals do not become attached to the tubules of the kidney whereas the fixed particle mechanism allows for sticking. Finlayson and Reid state that there is insufficient time for free crystals to grow to a size large enough to obstruct flow in the tubules. This conclusion is based on the assumption that crystals travel under plug flow conditions, that is all crystals travel at the flow average velocity, and therefore all spend the same length of time in a tubule. From the results of the RTD experiments the assumption that all crystals travel at the flow average velocity is clearly not true. A small fraction of crystals take very much longer than the mean residence time to pass through the crystalliser, which must call into question the conclusion of Finlayson and Reid that a free particle mechanism cannot be responsible for stone disease in the renal tubules.

Further evidence that the flow in the kidney is laminar is provided by Schulz and Schneider (1981). Based on hydrodynamic studies, they find the Reynolds number in the tubules of the kidney is less than 500. A study using scale models of the renal pelvis by Schulz (1987), finds that the flow is mainly laminar, but that vortices and dead-zones can also

appear, depending on the fluid flowrate. These two studies both provide evidence that suggest the findings of Finlayson and Reid (1978), based on plug flow in the kidney, are unreliable. They also suggest that the hydrodynamics in the kidney must be considered when studying the factors affecting stone formation, which is in agreement with the findings presented in the current work.

8.6 CONCLUSIONS

Step-change and pulse-input tracer response tests have been used to investigate the particle RTD in the tubular crystalliser. A mass balance over the crystalliser, using the data from the step-change tests, suggested that some of the particles were sticking to the walls of the lumen. An extensive investigation of the factors affecting the particle RTDs revealed the following:

1. The same RTD is obtained from step-change and pulse-input tests.
2. If a dimensionless time scale is used, the RTD is independent of:
 - Particle size
 - Crystalliser geometry
 - Lumen flowrate
3. The RTD is dependent on the value of the dilution factor, because the flow field in the crystalliser is dependent on the dilution factor.

A model that assumes the particles follow the fluid streamlines does not describe the experimental RTDs. However, all the experimental RTDs are well described by a model in which it is assumed that the particles maintain a constant radial position. Although physically implausible, this model provides a mathematical expression that accurately predicts the RTDs.

The effect of the particle RTD in kidney stone formation has largely been ignored in the past. Finlayson and Reid (1978) have assumed that all crystals have the same residence time in the kidney, as they travel at the flow average velocity. The findings of the current work show that a small but significant number of particles have a residence time very much longer than the average. Thus, the particle RTD may be an important factor in stone formation, as the ultimate size that a crystal attains depends on the time it remains in the tubules of the kidney.

Chapter 9:

CRYSTALLISATION IN A CONTINUOUS SYSTEM

This chapter describes an experimental investigation and the modelling of the seeded crystallisation of calcium oxalate in the tubular crystalliser. It is found that in addition to growth and aggregation, two other phenomena, sticking and breakage occur.

Using a population balance, it is shown that sticking is size-independent and irreversible and that breakage can be modelled by assuming that crystals of all sizes are equally likely to form. Both phenomena are found to depend on the fluid shear rate in the crystalliser.

A similar analysis is used to model simultaneous, aggregation, growth, sticking and breakage in metastable solutions. It is found that the aggregation rate is dependent on both the shear rate and the supersaturation. The aggregation rate in supersaturated solutions is orders of magnitude lower than in the batch experiments reported in Chapter 4.

9.1 INTRODUCTION

As described in Chapter 6, the MSMPR crystalliser has been widely used to study the crystallisation of calcium oxalate in a continuous system. However, normally only nucleation and growth are considered in this device and aggregation is ignored. The findings of the batch crystallisation study reported in Chapter 4 reveal important and interesting aspects of the aggregation of calcium oxalate crystals in supersaturated solutions which should not be ignored. The purpose of this chapter is to study the aggregation of calcium oxalate crystals in a continuous system, and in particular to investigate the dependence on supersaturation and shear rate in laminar flow using the tubular crystalliser.

9.2 PRELIMINARY EXPERIMENTS

Prior to commencing the experimental program, preliminary experiments were conducted to determine whether calcium oxalate seed crystals stick to the walls of the lumen. As outlined in Section 8.2.3 the latex used in the RTD experiments stuck to the walls of the lumen.

9.2.1 Method

A calcium oxalate seed suspension was fed to the crystalliser using the particle suspension delivery system described in Section 6.3.2. The fluid fed to both the lumen and jacket of the crystalliser was a filtered (0.22 μm), 0.15 M saline solution, saturated with respect to calcium oxalate. The seed suspension was prepared by the method in Section 3.3.2.

At the beginning of each experiment samples of the seed suspension fed to the lumen of the crystalliser were collected and analysed by the Multisizer. The crystalliser was then operated as described in Section 6.3.4, that is with the jacket outlet closed and with fluid fed to both the lumen and jacket. Initially, the saturated saline solution was fed to both the lumen and the jacket, at time $t = 0$, the flow of the seed suspension was started. When the crystalliser was at steady state, after approximately five mean residence times, samples of the fluid leaving the crystalliser were collected and analysed by the Multisizer.

A lumen flowrate of 8 ml/min was used and values of the dilution factor from 1 to 4 were considered. In each run the maximum value of the dilution factor was considered first, then by decreasing the jacket flowrate, while keeping the lumen flowrate constant, lower values of the dilution factor were obtained. For all values of the dilution factor, samples of the fluid leaving the crystalliser were not collected until the crystalliser was operating at steady state.

9.2.2 Results

A mass balance over the crystalliser, using the number and volume of crystals in the fluid at the inlet and outlet of the crystalliser, was performed. As described in Section 8.2.3, the number and volume of crystals in the fluid leaving the crystalliser must be corrected to allow for the fluid injected from the jacket to the lumen. A mass balance gives

$$V_T = \alpha' V_{T,M} \tag{9.1}$$

where α' is the modified dilution factor, defined in eq 8.2, and $V_{T,M}$ is the total crystal volume in the samples analysed by the Multisizer.

Any change in the total number or volume of crystals can be quantified by calculating the ratio of the total number or volume of crystals in the fluid at the outlet to that at the inlet. These ratios, denoted f_N and f_V , are:

$$f_N = \frac{N_T}{N_{T,inlet}} \quad \text{and} \quad f_V = \frac{V_T}{V_{T,inlet}} \quad (9.2a \text{ and } b)$$

Figure 9.1 (a) shows the variation in f_N and f_V for one of the preliminary experiments. For all values of the dilution factor the calcium oxalate crystals are sticking to the walls of the lumen as f_V is always less than one. Also for all values of the dilution factor f_N is greater than f_V and at higher values of the dilution factor, there are more crystals leaving the crystalliser than were fed to it, as f_N is greater than one. As the saline solution used in the experiments was saturated with respect to calcium oxalate, the only mechanism that can explain the observed increase in crystal number is breakage.

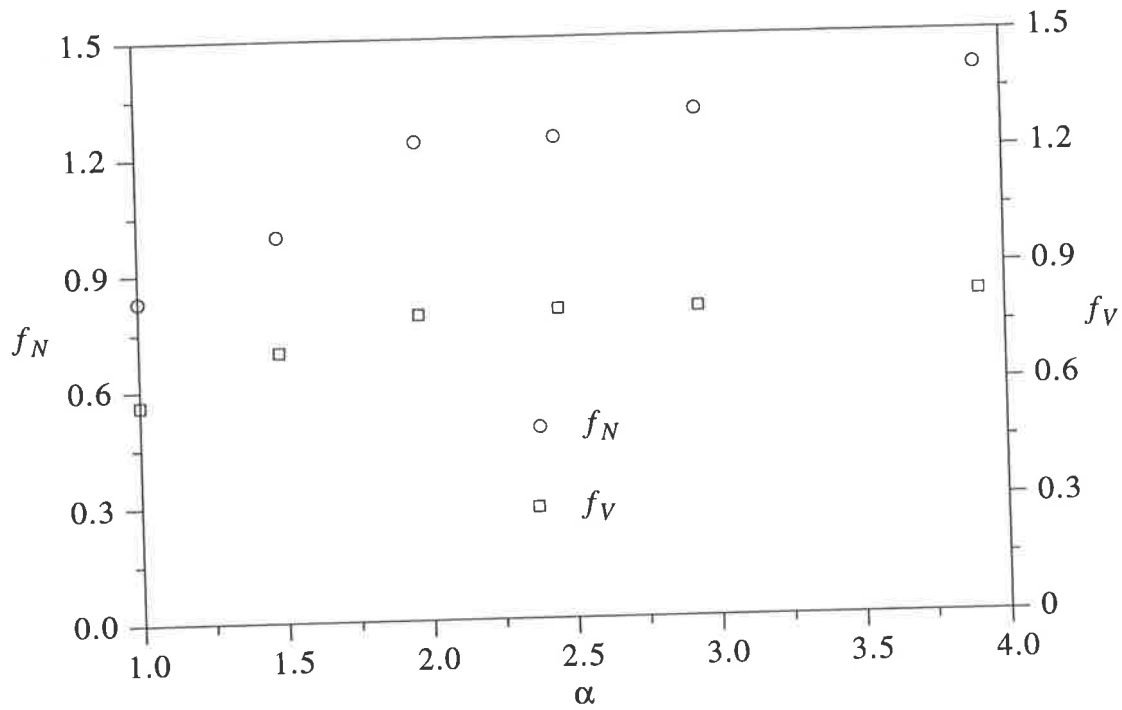
Further evidence of breakage is obtained from the CSDs, by number, at the inlet and outlet in Figure 9.1 (b). It can clearly be seen that the CSDs at the outlet are shifted towards smaller sizes as a result of breakage.

9.2.3 Discussion

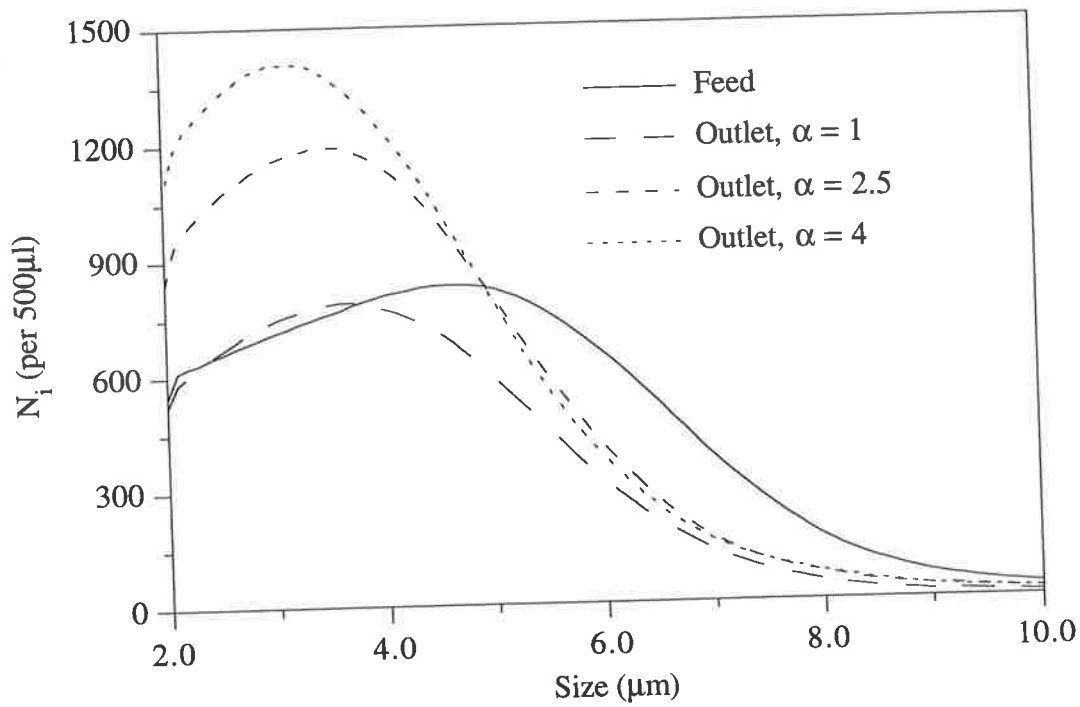
The tendency of calcium oxalate crystals to stick to surfaces during crystallisation experiments has been documented for other experimental systems. For example, Ryall *et al.* (1981b) observed that calcium oxalate crystals stuck to boro-silicate glass flasks in batch experiments and Randolph and Drach (1981) found fouling on the walls of an MSMPR crystalliser to be a major problem. Finally, Hartel *et al.* (1986) observe a loss of crystal mass in a Couette agglomerator due to fouling of the agglomerator walls at high supersaturations.

Hartel *et al.* (1986) also observe the breakage of aggregates of calcium oxalate crystals in their system. Those authors propose an aggregation mechanism for calcium oxalate similar to that developed in Chapter 5 and suggest that under certain operating conditions the aggregates are weakly bonded together and are subject to disruption, particularly at high shear rates and low supersaturation.

From the SEM micrograph of the seeds used in the current work shown in Figure 3.2, they are clearly aggregates composed of primary crystals approximately 1 μm in size. In a saline solution with an ionic strength of 0.15 M, the crystals will be loosely held together by DLVO type forces as explained in Section 5.2. In the crystalliser it is possible shear forces



(a)



(b)

Figure 9.1 Preliminary experimental results: (a) The dependence of the parameters f_N and f_V on the dilution factor and (b) CSDs by number of the seeds at the inlet and outlet of the crystalliser for various values of the dilution factor.

in the fluid will exceed the DLVO forces and consequently breakage will occur. Breakage is highly undesirable as it is another mechanism which must be included in a model of the crystallisation experiments.

9.2.4 Seed preparation

An alternative method of preparing the seeds was devised with the aim of stopping or at least decreasing breakage. The seeds were prepared by wet grinding calcium oxalate monohydrate (1 gram) in 10 ml of a 0.15 M saline solution. The wet ground crystals were then added to a stock metastable solution as described in Section 3.3.2, except the final volume of the seed suspension was 950 ml. Calcium ions are in excess in the metastable solution, to consume these ions, 42 ml of a 0.05 M sodium oxalate solution was added. The sodium oxalate was added in two aliquots, the first 6 and the second 12 hours after the crystals were added to the metastable solution. Throughout the process the seed suspension was stored at room temperature and stirred by a magnetic stirrer.

The seed suspension contains calcium oxalate crystals that have undergone three stages of growth and aggregation. The final solution is effectively a 0.15 M saline solution, saturated with respect to calcium oxalate, as equal quantities of calcium and oxalate were added during preparation. The stages of growth and aggregation will produce aggregates in which the primary crystals are cemented rather than weakly bound together and thus should be more stable under the influence of fluid shear in the crystalliser.

An experiment the same as that reported in Section 9.2.1 was conducted with these new pre-grown seeds. Figure 9.2 (a) shows the variation in the parameters f_N and f_V . The pre-grown seeds stick to the walls of the lumen as f_V is less than one for all values of the dilution factor. Comparison with Figure 9.1 (a) reveals that a similar fraction of both the standard and pre-grown seeds stick to the walls of the lumen.

It can also be seen that for all values of the dilution factor f_N is greater than f_V indicating that breakage is still occurring, or that it is size-dependent. However, the amount of breakage has been significantly reduced, for example at the highest value of the dilution factor, f_N has been reduced from 1.39 to 1.08. The CSDs, by number, for various values of the dilution factor, shown in Figure 9.2 (b) also indicate breakage has decreased. Although the CSDs are shifted towards smaller sizes the effect is not as pronounced as it is in Figure 9.1 (b).

9.3 EXPERIMENTAL INVESTIGATION

9.3.1 Materials

The batch crystallisation experiments reported in Chapter 3 were conducted at 37°C. To compare the results from the batch experiments with those using the crystalliser it must be operated isothermally at 37°C. The crystalliser was modified to the form of a simple double pipe heat exchanger. These devices are essentially two concentric pipes with one fluid flowing through the centre pipe while the other fluid moves cocurrently in the annular space. Here the centre pipe is the tubular crystalliser.

The crystalliser was enclosed in a perspex tube, 4.5 cm in diameter and 41 cm in length, which was sealed at each end by O-rings fitted to the top and bottom manifolds. Hot water was pumped through the perspex tube *via* inlets at the top and bottom using an Iwaki MD-10 magnetic drive centrifugal pump (All Pumps Supplies, Adelaide, Australia).

During operation the solutions were fed to the lumen and jacket of the crystalliser *via* tubing, head tanks and rotameters, which were not insulated. As the fluid flowrates used were quite low considerable cooling may take place during this process. Tests were conducted to determine an appropriate temperature at which to store the solutions. It was found that if the initial temperature of the solutions being fed to the crystalliser and the water used to heat the crystalliser were 45°C, then over the entire range of operating conditions, the temperature of the solutions leaving the crystalliser was 37°C. The solutions were stored at 45°C in a water bath (Paton Industries, Model RW 1812).

9.3.2 Method

The experiments may be divided into three stages. The first two were the same as those for the preliminary experiments described in Section 9.2.1, namely to analyse samples of the solution fed to the crystalliser and conduct a run with saturated saline at different values of the dilution factor. After completing the run with saturated saline, the crystalliser was rinsed with a 0.15 M saturated saline to remove the crystals stuck to the walls of the lumen. A peristaltic pump was used to supply saturated saline to the crystalliser at flowrates of up to 80 ml/min.

Finally, a metastable solution was fed to both the lumen and jacket, with the values of the dilution factor considered being the same as those for the saturated saline. At the end of the run using the metastable solution the crystalliser was again rinsed with saturated saline.

9.3.3 Parameters investigated

The two parameters of most interest were the supersaturation of the metastable solution and the shear rate in the crystalliser. Also the effect of the angle of inclination of the crystalliser was considered.

Supersaturation. Solutions of different supersaturation were prepared by changing the calcium to oxalate ratio in the metastable solution. As the same metastable solution was fed to both the lumen and jacket, the crystalliser operates at very nearly constant supersaturation. This was verified by measuring the calcium ion concentration in samples of the fluid at the inlet and outlet of the crystalliser with an Atomic Absorption spectrophotometer, using the method described in Appendix 4.

The total calcium and oxalate ion concentrations and the relative supersaturation, calculated from free ion concentrations using the method described in Chapter 2, for the different metastable solutions used are given in Table 9.1. The range of supersaturation covered is lower than that in the batch experiments for two reasons. Firstly, solutions with a high relative supersaturation were found to nucleate during an experiment, possibly because of secondary nucleation caused by a build up of background particles with time. Secondly, as the crystalliser operated at constant supersaturation and samples were only collected when the system was at steady state, the time required to prepare metastable solutions of different supersaturations and then perform the experiments was prohibitive. Consequently, several metastable solutions with different supersaturations were used in only one experiment, experiment 18/7, and only two values of the dilution factor were considered.

Shear rate. The shear rate was varied by using different lumen flowrates. For each lumen flowrate the same jacket flowrates were used, giving different values of the dilution factor in each experiment. The lumen flowrate was varied from 4 to 10 ml/min, and jacket flowrates of 0 to 20 ml/min were used. Complete details of the combinations of flowrates and the corresponding dilution factors for all the experiments are given in Table 9.2.

Angle of inclination. Experiments were conducted in which the crystalliser was inclined at a small angle to the vertical, mainly to investigate the effect on sticking. The crystalliser was inclined at angles of 2.5° and 5°, the flowrates and solutions used in these experiments were the same as those for the experiment 18/7.

9.4 RESULTS

The results from the experiments outlined in the previous section are given in Appendix 9.

Table 9.1 Details of the metastable solutions used to investigate the effect of supersaturation on aggregation.

Experiment	Calcium ion concentration, $T_{Ca^{2+}}$ (M)	Oxalate ion concentration, $T_{Ox^{2-}}$ (M)	Relative supersaturation $\sigma = \frac{AP}{K_{sp}}$	Values of dilution factor, α
18/7	5.27×10^{-4}	2.1×10^{-4}	2.62	All
	5.27×10^{-4}	1.05×10^{-4}	1.48	2 and 3.5
	5.27×10^{-4}	3.16×10^{-4}	3.74	2 and 3.5
	2.1×10^{-3}	1.05×10^{-4}	4.79	2 and 3.5
	5.27×10^{-4}	4.2×10^{-4}	4.82	2 and 3.5
	1.05×10^{-3}	2.1×10^{-4}	4.87	2 and 3.5
20/7	5.27×10^{-4}	2.1×10^{-4}	2.62	All
21/7	5.27×10^{-4}	2.1×10^{-4}	2.62	All
22/7	5.27×10^{-4}	2.1×10^{-4}	2.62	All

Table 9.2 Details of fluid flowrates and dilution factors used to investigate the effect of shear rate on aggregation.

Experiment	Lumen flowrate, Q_L (ml/min)	Jacket flowrate, Q_J (ml/min)	Seed flowrate, Q_S (ml/min)	Dilution factor, α
20/7	4	0	0.19	1
	4	4	0.19	2
	4	8	0.19	3
	4	12	0.19	4
	4	16	0.19	5
	4	20	0.19	6
21/7	6	0	0.19	1
	6	4	0.19	1.67
	6	8	0.19	2.33
	6	12	0.19	3
	6	16	0.19	3.67
	6	20	0.19	4.33
18/7	8	0	0.25	1
	8	4	0.25	1.5
	8	8	0.25	2
	8	12	0.25	2.5
	8	16	0.25	3
	8	20	0.25	3.5
22/7	10	0	0.25	1
	10	4	0.25	1.4
	10	8	0.25	1.8
	10	12	0.25	2.2
	10	16	0.25	2.6
	10	20	0.25	3

The analysis described in Section 9.5 uses the moment form of the population balance, consequently, the moments of the CSDs rather than the CSDs for the different operating conditions in each experiment are reported in Appendix 9.

9.4.1 Size distributions

Figures 9.3 (a) and (b) show product CSDs by number and volume for the experiment 18/7, for one value of the dilution factor, $\alpha = 2$, and different metastable solutions. In Figure 9.3 (a) as the supersaturation increases the CSDs clearly broaden, which is characteristic of aggregation. Figure 9.3 (b) shows translation of the CSDs towards larger sizes, which is characteristic of growth. In addition these Figures suggest both growth and aggregation are dependent on supersaturation.

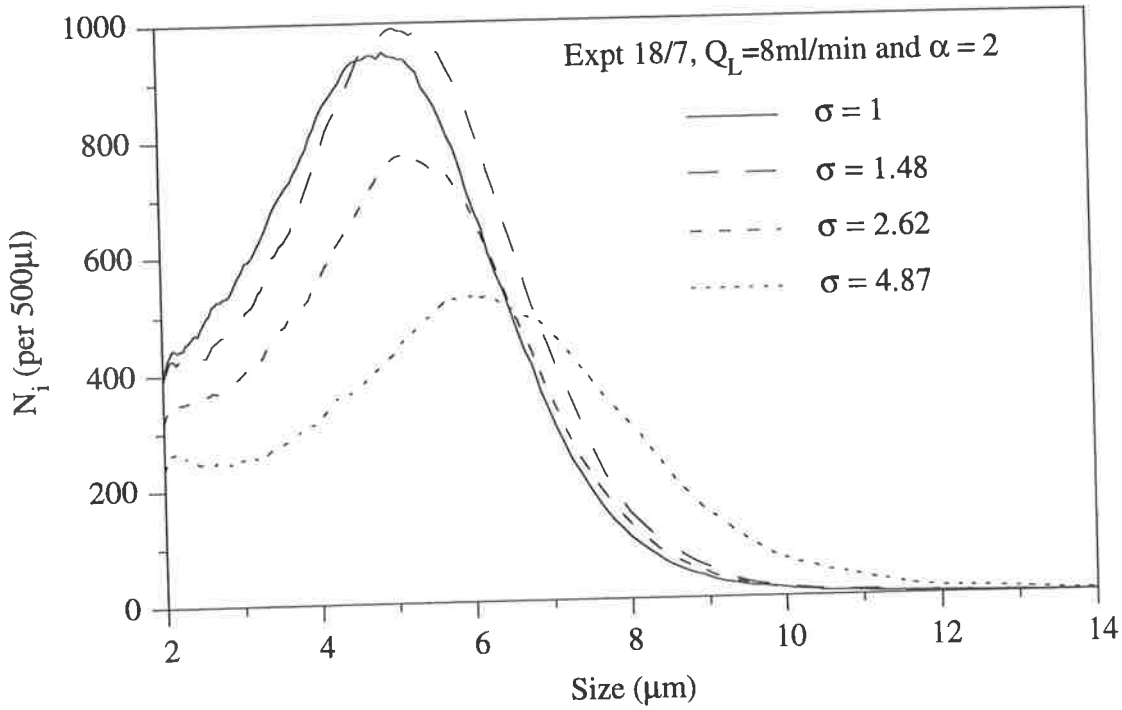
The effect of the shear rate on both mechanisms is revealed in Figures 9.4 (a) and (b) which show the variation in the parameters, f_N and f_V for different metastable solutions in experiment 18/7. For all operating conditions aggregation occurs in metastable solutions as the values of f_N are lower than those for saturated saline ($\sigma = 1$). The spread in the values of f_N increases as the total flowrate increases, suggesting the mechanisms that affect crystal number, namely aggregation and breakage, are dependent on the shear rate in the crystalliser. Figure 9.4 (b) indicates that growth occurs for all operating conditions as for metastable solutions the values of f_V are greater than those for saturated saline. However, there seems to be less dependence of the growth rate on shear rate as the spread in the data is approximately the same for all flowrates. Finally, for all solutions and all values of the dilution factor f_V is less than one, indicating sticking occurs at all operating conditions. To assess whether breakage occurs in metastable solutions the parameters f_N and f_V , cannot be used, a more rigorous analysis, such as a population balance model, is required.

9.5 ANALYSIS

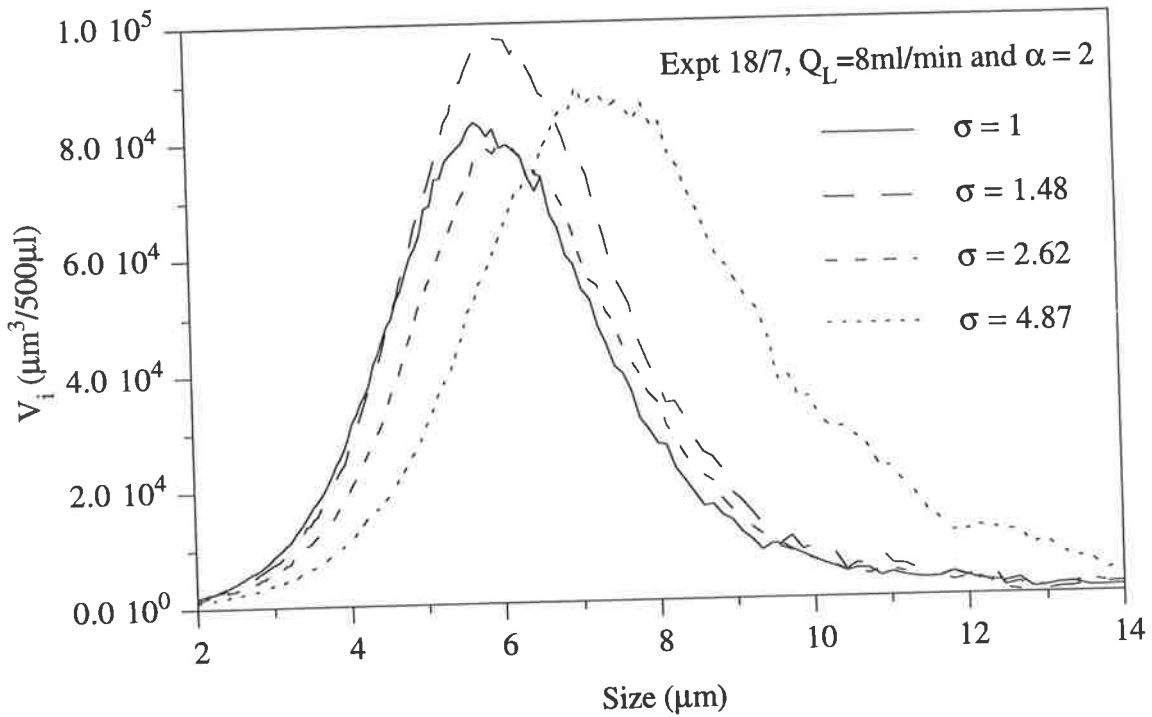
9.5.1 Introduction

As noted in Chapter 4 the most difficult task in the modelling of a process with simultaneous growth and aggregation is the identification of mathematical formulation for each. The presence of two additional mechanisms, sticking and breakage, further complicates this problem as a mathematical formulation for each of these must also be developed.

The problem here is simplified by the results of the batch crystallisation experiments reported in Chapter 4. In those experiments it was found that the growth of calcium oxalate was well

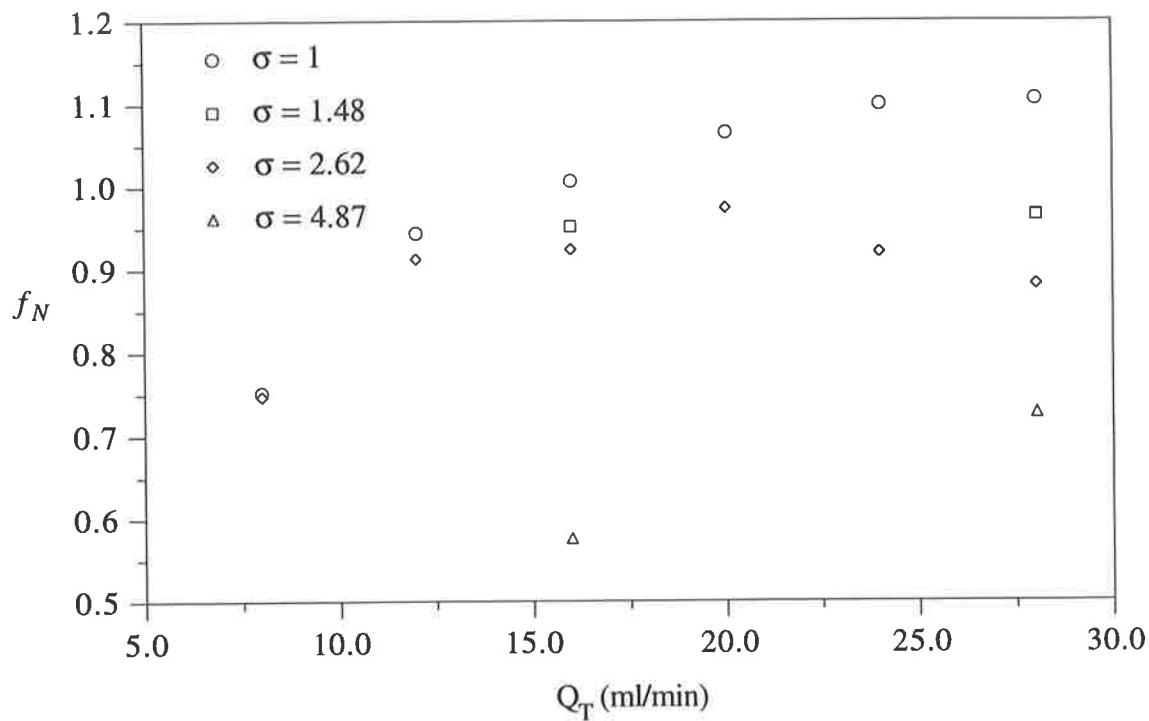


(a)

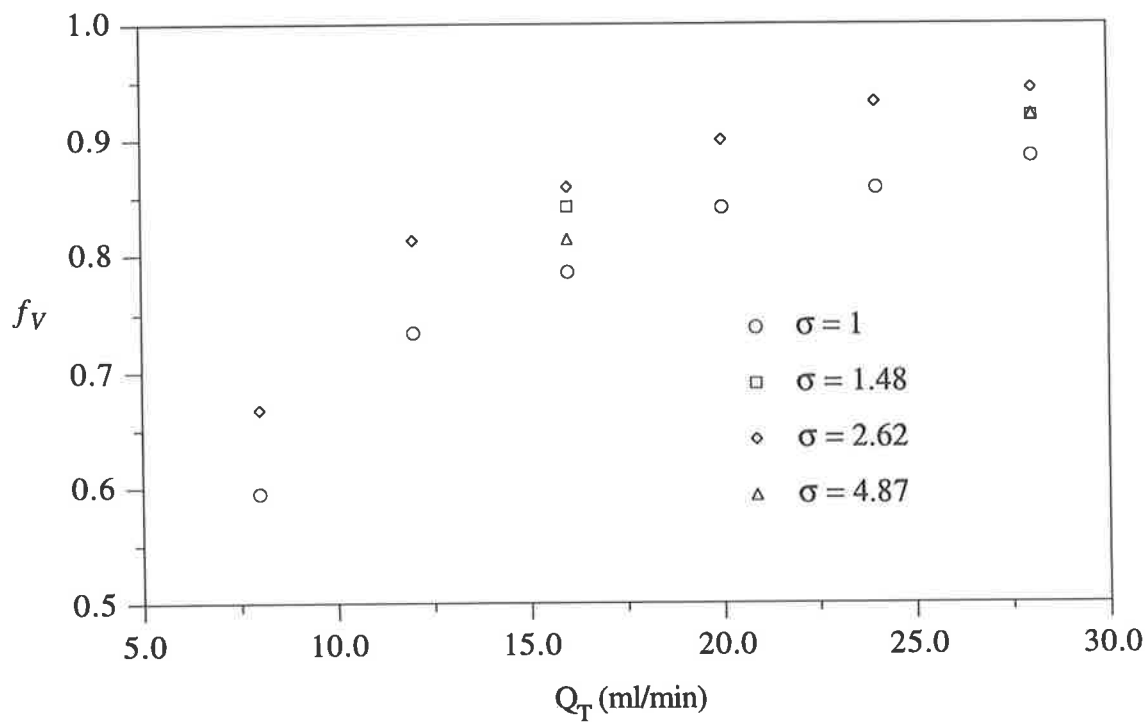


(b)

Figure 9.3 The effect of relative supersaturation on CSDs at the outlet of the crystalliser by (a) number and (b) volume for experiment 18/7 with $\alpha = 2$.



(a)



(b)

Figure 9.4 Variation in the parameters (a) f_N and (b) f_V with the total fluid flowrate for metastable solutions of different relative supersaturation for experiment 18/7.

described by a size-independent formulation and further the dependence of the growth rate on relative supersaturation is given by eq 4.6.

The results of the runs using saturated saline, are used to identify mathematical formulations for sticking and breakage, as it is assumed that growth and aggregation do not occur under the conditions in these experiments. Then as a correlation has been produced to calculate the growth rate in metastable solutions, the results from the experiments using metastable solutions are used to determine the aggregation rates.

The analysis is further simplified by firstly considering a batch process, then later incorporating the particle RTD to obtain an analysis appropriate for a continuous device operating at steady state.

9.5.2 Sticking

Although a number of other workers have observed sticking when studying the crystallisation of calcium oxalate, none have tried to model it. The approach adopted here is to postulate that sticking may be either size-independent or size-dependent. The simpler of these is a size-independent formulation, in which a crystal sticking to the walls of the lumen is a random event. Assuming that sticking is an irreversible, first-order process with a rate constant, k_S , then for sticking alone, from eq 1.9, the batch form of the population balance is

$$\frac{dn}{dt} = -k_S n \quad (9.3)$$

The moment form of the population balance is obtained by applying eq 1.4 to eq 9.3.

9.5.3 Breakage

Breakage has been widely studied in the literature, particularly in the area of modelling comminution processes. Randolph and Larson (1988) note that the population balance approach has been productive in modelling crystallisation and comminution processes as well as areas where these overlap such as modelling a CSD in a crystalliser with significant crystal breakage.

Breakage, in a similar fashion to aggregation, results in simultaneous birth and death events at different crystal sizes. From eq 1.9 the batch form of the population balance for breakage alone, with volume as the internal coordinate, is:

$$\frac{dn}{dt} = B_B(v) - D_B(v) \quad (9.4)$$

where $B_B(v)$ and $D_B(v)$ are the birth and death rates. There are various different mathematical formulations for breakage, the one most commonly used assumes that when a crystal breaks two crystals of equal-volume are formed, and further that the breakage rate has a power law dependence on size. This formulation has been used to model breakage in soy bean precipitation by Grabenbauer and Glatz (1981), flocculation formation by Chen *et al.* (1990), and significantly calcium oxalate crystallisation by Hartel and Randolph (1986).

In view of the structure of the seed crystals used in the experiments in the current work a different approach is adopted. From SEM micrographs of the seeds it is clear that they are aggregates composed of primary particles approximately 1 μm in size. It seems unlikely that when an aggregate breaks *only* crystals of the same volume will form, instead it is proposed that the aggregate can break at a random point and thus crystals of *any* size may form.

The birth and death rates for this formulation can easily be derived. A birth event at volume v occurs when:

1. A crystal of volume ε breaks into crystals of volume v and $\varepsilon - v$.
2. A crystal of volume ε breaks into crystals of volume $\varepsilon - v$ and v .

The probability of a crystal of volume ε breaking to form a crystal of volume v is given by the breakage probability density function, $p(\varepsilon, v)$. Assuming an equal probability for both events mentioned above, *i.e.* the breakage probability density function is symmetrical, and summing over all possible values of ε , the expression for the birth rate is:

$$B_B(v) = \int_v^\infty p(\varepsilon, v) D_B(\varepsilon) d\varepsilon + \int_v^\infty p(\varepsilon, \varepsilon - v) D_B(\varepsilon) d\varepsilon = 2 \int_v^\infty p(\varepsilon, v) D_B(\varepsilon) d\varepsilon \quad (9.5)$$

When breakage at all sizes is equally likely, then the breakage probability density function is independent of v . As the breakage probability density function is normalised then,

$$\int_0^\varepsilon p(\varepsilon) dv = 1 \quad (9.6)$$

from which it follows that $p(\varepsilon) = 1/\varepsilon$. Further, assuming the breakage of crystals is proportional to their population, the death rate is given by

$$D_B(\varepsilon) = k_B n(\varepsilon) \quad (9.7)$$

Substituting eq 9.7 into eq 9.5 the birth rate is,

$$B_B(v) = 2 \int_v^{\infty} \frac{k_B n(\varepsilon)}{\varepsilon} d\varepsilon \quad (9.8)$$

Applying eq 1.4 to eqs 9.7 and 9.8, the moment forms of the birth and death rates can be determined.

9.5.4 Simultaneous sticking and breakage

As demonstrated in Section 7.5, moment transforms give accurate results with much less computational effort than techniques which determine all the values of a distributed variable. The moment transforms of eqs 9.3 and 9.4 are used to determine whether the formulations proposed for sticking and breakage can be used to model the experimental results. However, the moments, as defined by eq 1.4, cannot be calculated from the experimental data. The CSDs obtained from the Multisizer have a size threshold of 2 μm , crystals smaller than this size are not counted. Consequently, the moments calculated from the experimental CSDs are only partial moments. The partial moment of a CSD, \tilde{m}_j , with volume as the internal coordinate, is defined as:

$$\tilde{m}_j = \int_{v_0}^{\infty} v^j n(v) dv \quad (9.9)$$

where v_0 is the size of the smallest particle counted by the Multisizer cubed, which is 8 μm^3 .

Considering breakage first, applying eq 9.9 to eq 9.8 gives

$$\bar{B}_{B,j} = \int_{v_0}^{\infty} v^j 2 \int_v^{\infty} \frac{k_B n(\varepsilon)}{\varepsilon} d\varepsilon dv \quad (9.10)$$

Reversing the order of integration and noting that $v_0 \leq v \leq \varepsilon$ eq 9.10 may be integrated and simplified to give

$$\bar{B}_{B,j} = \frac{2k_B}{j+1} (\tilde{m}_j - v_0^{j+1} \tilde{m}_{-1}) \quad (9.11)$$

Similarly applying eq 9.9 to eq 9.7 gives

$$\bar{D}_{B,j} = \int_{v_0}^{\infty} \varepsilon^j k_B n(\varepsilon) d\varepsilon = k_B \tilde{m}_j \quad (9.12)$$

Applying eq 9.9 to eq 9.3 for sticking, combining with eqs 9.11 and 9.12, and simplifying, the moment form of the population balance for simultaneous sticking and breakage in a batch system is:

$$\frac{d\tilde{m}_j}{dt} = \left(-k_S + \left(\frac{1-j}{1+j} \right) k_B \right) \tilde{m}_j - \frac{2k_B v_0^{j+1}}{j+1} \tilde{m}_{-1} \quad (9.13)$$

The analytical solution. Eq 9.13 forms a system of differential equations for different values of j . For $j = -1$ the right hand side of eq 9.13 is of the form, $0/0$, in which case L'Hôspital's rule can be used to show

$$\frac{d\tilde{m}_{-1}}{dt} = -(k_S + k_B(1 + 2 \ln v_0)) \tilde{m}_{-1} \quad (9.14)$$

The solution to eq 9.14 is

$$\tilde{m}_{-1} = \tilde{m}_{-1}^{\phi} \exp(-(k_S + k_B + 2k_B \ln v_0)t) \quad (9.15)$$

where the superscript, ϕ , represents the feed. Substituting eq 9.15 into 9.13 and solving, the expression for \tilde{m}_j is

$$\begin{aligned} \tilde{m}_j = & \frac{\tilde{m}_{-1}^{\phi} v_0^{j+1}}{1 + (1+j) \ln v_0} \exp(-(k_S + k_B + 2k_B \ln v_0)t) \\ & + \left(\tilde{m}_j^{\phi} + \frac{\tilde{m}_{-1}^{\phi}}{1 + (1+j) \ln v_0} \right) \exp\left(\frac{k_B(1-j) - k_S(1+j)}{(1+j)} t \right) \end{aligned} \quad (9.16)$$

A best fit procedure could be used to determine the values of the sticking and breakage rate constants that give partial moments in agreement with those from the experimental CSDs at the outlet of the crystalliser. However, Acton (1970) states that a series of exponential functions can be extremely ill conditioned, as there may be many combinations of the parameters that fit the experimental data quite well. Rather than using the analytical solution, an approximate method for determining the values of the rate parameters can be developed.

An approximate method. Dividing eq 9.13 by \tilde{m}_j and re-arranging implies:

$$\frac{d \ln \tilde{m}_j}{dt} = -k_S + k_B \left(\frac{1-j}{1+j} - \frac{2}{j+1} v_0^{j+1} \frac{\tilde{m}_{-1}}{\tilde{m}_j} \right) \quad (9.17)$$

which may be integrated to give

$$\frac{\ln \tilde{m}_j - \ln \tilde{m}_j^\phi}{\bar{t}} = -k_S + k_B \left(\frac{1-j}{1+j} - \frac{2}{j+1} v_0^{j+1} \frac{\tilde{m}_{-1}}{\tilde{m}_j} \right) \quad (9.18)$$

where the ratio $\frac{\tilde{m}_{-1}}{\tilde{m}_j}$ is assumed constant and is given by $\frac{\tilde{m}_{-1}}{\tilde{m}_j} = \frac{1}{2} \left(\frac{\tilde{m}_{-1}^\phi}{\tilde{m}_j^\phi} + \frac{\tilde{m}_{-1}}{\tilde{m}_j} \right)$.

The time chosen is the mean residence time, \bar{t} , which may be calculated as

$$\bar{t} = m_1 = \int_{t_b}^{\infty} t E(t) dt \quad (9.19)$$

where, t_b is the break-through time, the time at which the first crystals leave the crystalliser. The E curve can be calculated from eq 8.24 for the F curve of the particle RTD using eq 7.2. The break-through time is determined from eq 8.24 by setting $F = 0$.

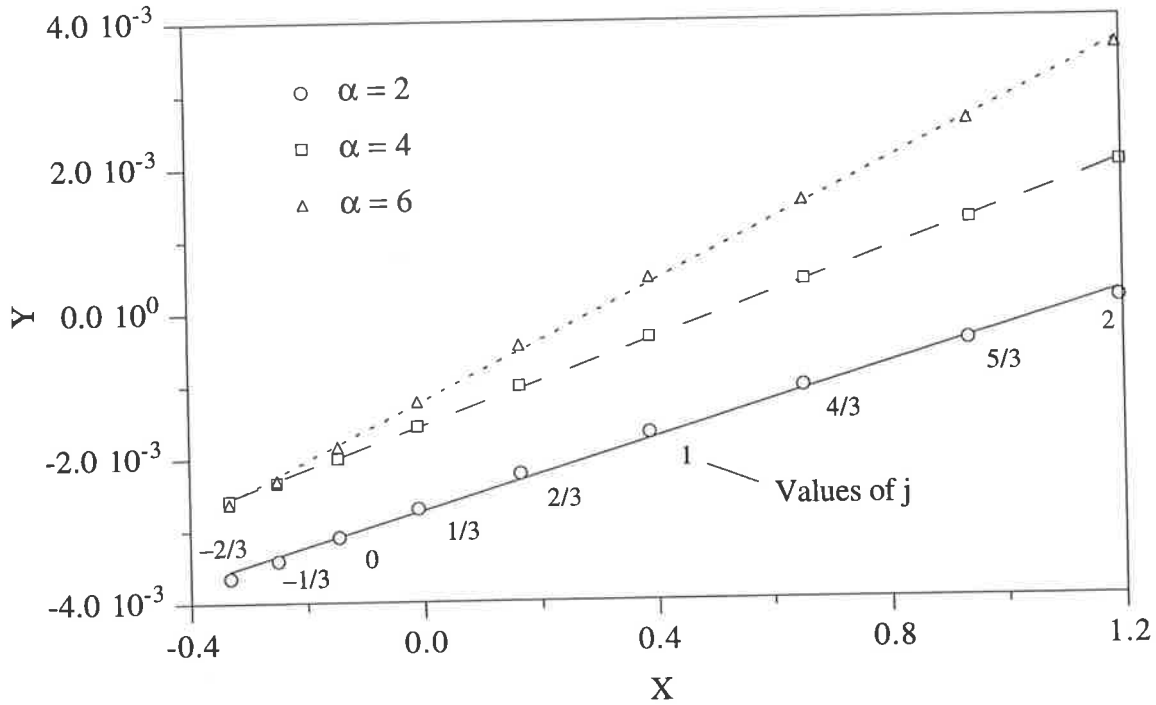
This analysis suggests a plot of the left hand side of eq 9.18, denoted, Y , against the parameter on the right hand side, denoted X , involving the partial moments, should be a straight line of slope, k_B and intercept $-k_S$. Figures 9.5 (a) and (b) show the data from experiments 20/7 and 22/7 for various values of the dilution factor, plotted in the manner of eq 9.18. The experimental moments were calculated for values of j from $-2/3$ to 2 in steps of $1/3$. It can be seen that all the data are well described by straight lines as predicted by the preceding analysis.

The partial moments of the experimental CSDs were calculated using the following formula

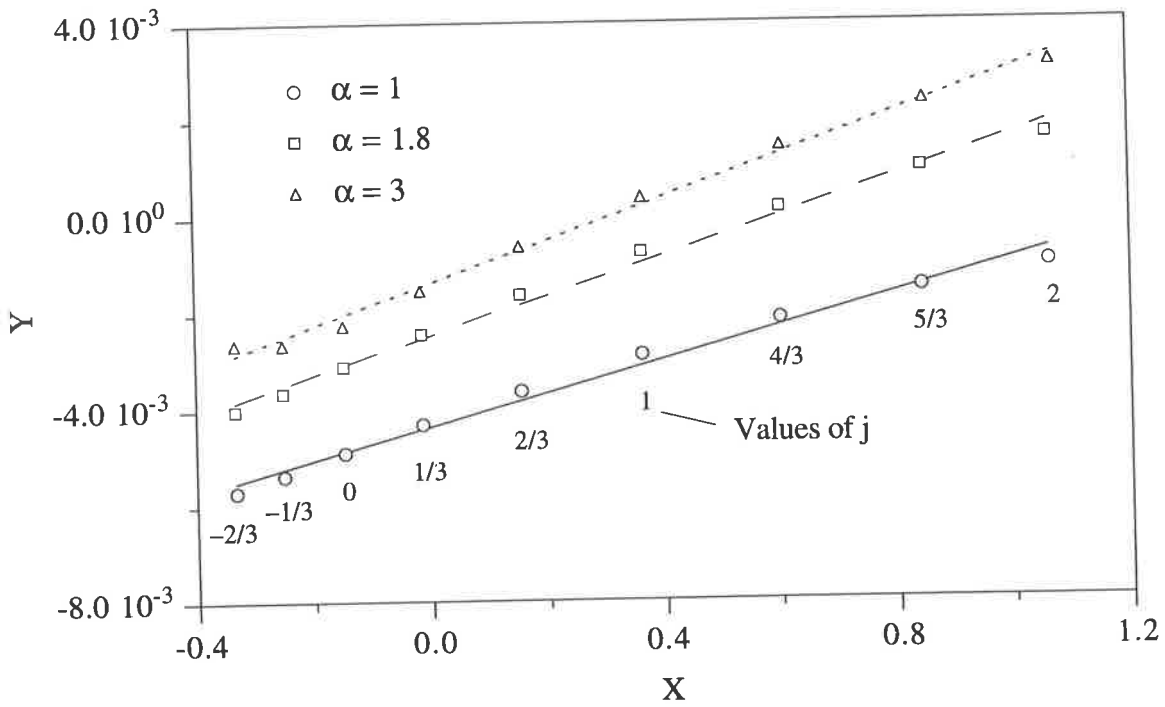
$$\tilde{m}_j = \sum_i \bar{L}_i^j N_i \quad (9.20)$$

where \bar{L}_i is the arithmetic average of the upper and lower sizes of channel i and N_i is the number of crystals in channel i .

Accuracy of the approximate method. The accuracy of the values of the sticking and breakage rate constants determined from the approximate analysis can be investigated by



(a)



(b)

Figure 9.5 Experimental data plotted in the manner of eq 9.18 for (a) experiment 20/7 and (b) experiment 22/7. Also shown are linear fits used to determine the sticking and breakage rate constants.

using these values to calculate the partial moments from the analytical solution, eq 9.16. These values can then be compared with the partial moments of the experimental CSDs.

Figures 9.6 (a) and (b) show the partial moments calculated from eq 9.16, plotted against the experimental partial moments for the experiments 18/7 and 21/7. It can be seen that apart from when $j = -2/3$ the experimental and analytical moments are virtually identical. Thus, only a small error is introduced by using the approximate analysis to evaluate the sticking and breakage rate constants.

9.5.5 The effect of the particle residence time distribution

Smit *et al.* (1994) show that for aggregation alone the state of mixing, ranging from completely segregated to maximum mixedness, has little effect on aggregation. However, those authors also show that departures from ideal RTDs affect aggregation. In the preceding analysis plug flow has been assumed, with all the crystals travelling through the crystalliser at the flow average velocity, the effect of the particle RTD is now considered.

By analogy with reaction engineering, for a device operating at steady state with an arbitrary RTD, the moments of the product CSD are given by

$$m_j^{cont} = \int_0^{\infty} m_j^{batch} E(t) dt \quad (9.21)$$

Here $E(t)$ is valid for $t \geq t_b$, and m_j^{batch} is given by eq 9.16, which is derived from the batch form of the population balance. From eq 8.24, the expression for $E(t)$ is

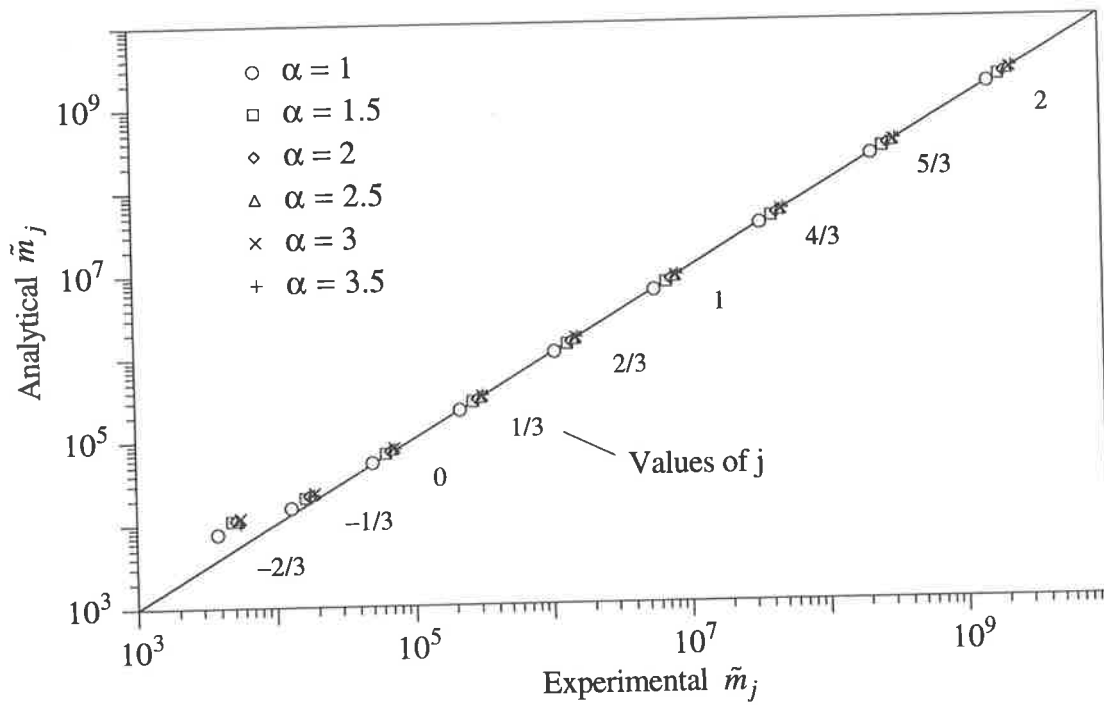
$$E(t) = \frac{dF}{dt} = \frac{2L^2}{u_0^2 t^3} \left(\varepsilon + (1-2\varepsilon) \frac{\ln \alpha}{\alpha-1} + \frac{\varepsilon}{\alpha} \right)^2 \quad (9.22)$$

Also from eq 8.24, with $F = 0$ the break-through time is

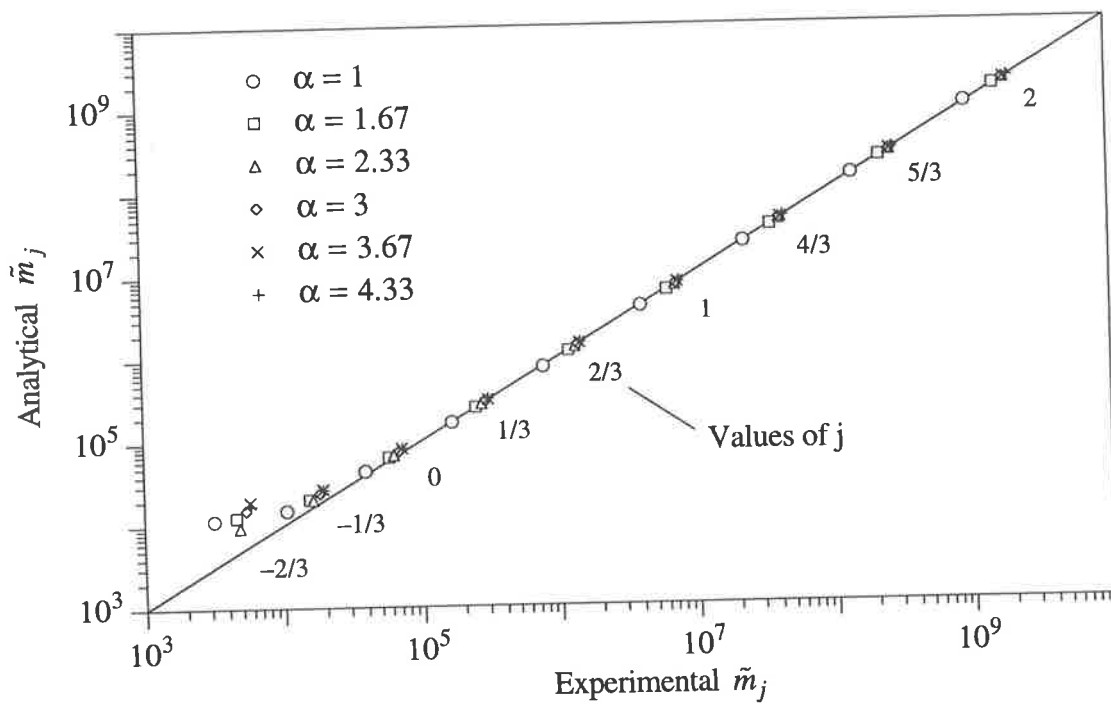
$$t_b = \frac{L}{u_0} \left(\varepsilon + (1-2\varepsilon) \frac{\ln \alpha}{\alpha-1} + \frac{\varepsilon}{\alpha} \right) \quad (9.23)$$

Substituting eqs 9.16, 9.22 and 9.23 into 9.21 and re-arranging gives

$$\tilde{m}_j^{cont}(t) = \int_{t_b}^{\infty} \frac{2t_b^2}{t^3} (A \exp(-at) + B \exp(-bt)) dt \quad (9.24)$$



(a)



(b)

Figure 9.6 Comparison of the experimental partial moments with those calculated from the analytical solution, eq 9.16, using the sticking and breakage rate constants determined from the approximate analysis for (a) experiment 18/7 and (b) experiment 21/7.

where A , B , a and b are constants that can be determined from eq 9.16. Making the following substitutions, $x_1 = at$ and $x_2 = bt$, eq 9.24 may be written as

$$\tilde{m}_j^{cont} = 2t_b^2 \left(A a^2 \int_{at_b}^{\infty} \frac{\exp(-x_1)}{x_1^3} dx_1 + B b^2 \int_{bt_b}^{\infty} \frac{\exp(-x_2)}{x_2^3} dx_2 \right) \quad (9.25)$$

Further, it can be shown that

$$I(a) = \int_a^{\infty} \frac{\exp(-at)}{t^3} dt = \frac{\exp(-a)}{2a} \left(\frac{1}{a} - 1 \right) - \frac{Ei(-a)}{2} \quad (9.26)$$

where $Ei(a)$ is the exponential integral. It follows that

$$\tilde{m}_j^{cont}(t) = 2t_b^2 \left(A a^2 I(at_b) + B b^2 I(bt_b) \right) \quad (9.27)$$

Figure 9.7 shows the partial moments calculated from eq 9.27 plotted against the experimental partial moments for experiments 18/7 and 21/7. It can be seen that the values of the partial moments calculated when the RTD is taken into account are in good agreement with the experimental partial moments. The results presented in Figure 9.6 suggest the partial moments calculated from the analytical solution are consistent with the experimental moments. Both these findings imply that the plug flow simplification is satisfactory.

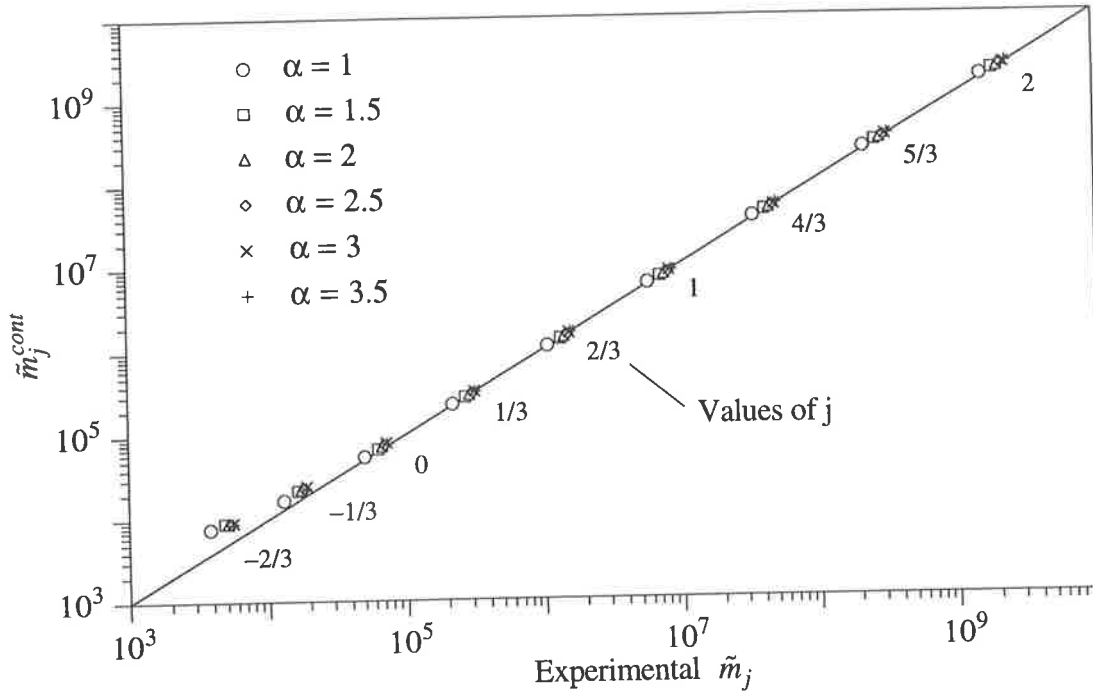
9.6 SATURATED SOLUTIONS

The runs from the experiments with saturated saline solution are now examined using the analysis developed in the previous section to investigate the dependence of sticking and breakage on the operating conditions in the crystalliser.

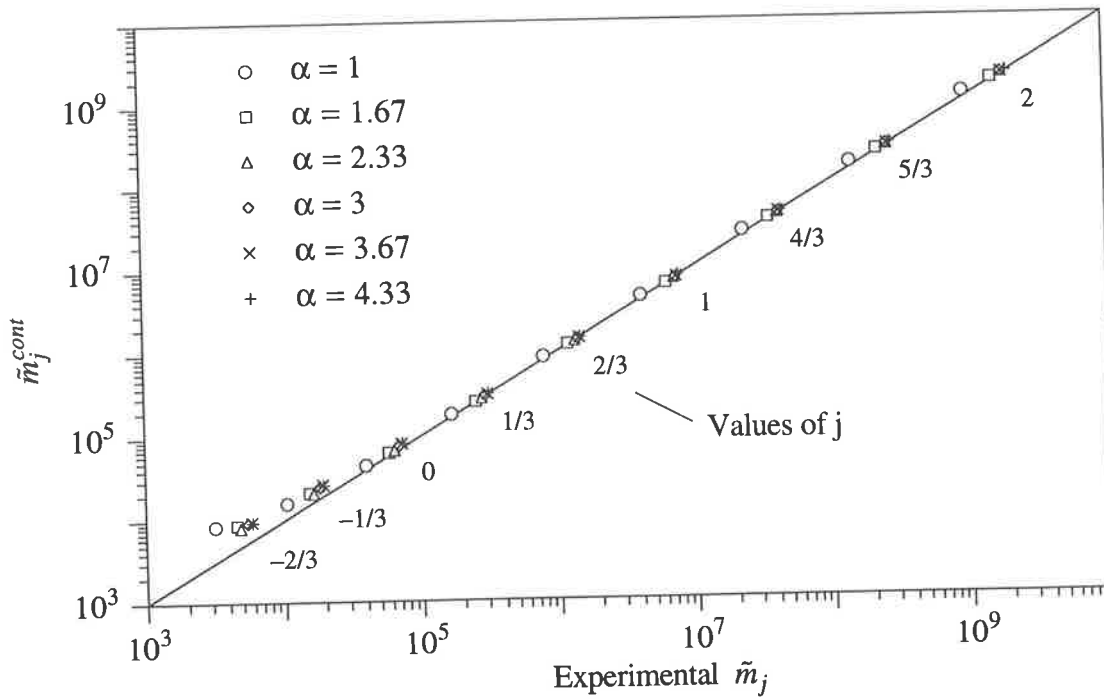
9.6.1 Independent variables

The sticking and breakage rate constants may be related to the jacket or lumen flowrates or some combination of these. However, it seems likely that both mechanisms will depend on the shear induced by fluid flow in the lumen.

Sticking. Assuming the sticking rate is inversely proportional to the shear rate and hence fluid flowrate then from eq 9.3,



(a)



(b)

Figure 9.7 Comparison of the experimental partial moments with those calculated allowing for the RTD, eq 9.27 using the sticking and breakage rate constants determined from the approximate analysis for (a) experiment 18/7 and (b) experiment 21/7.

$$\frac{dn}{n} \propto \frac{dt}{\gamma_s} \quad (9.28)$$

As the axial fluid velocity varies with axial position because of fluid injection from the jacket to the lumen, an average shear rate must be calculated. An average shear rate, $\overline{\gamma_s}$, is defined such that

$$\overline{\gamma_s} \int_0^L \frac{dx}{\bar{u}} = \int_0^L \frac{\gamma_s dx}{\bar{u}} \quad (9.29)$$

To determine an expression for the average shear rate the correct formulation of the shear rate is required. A crystal stuck to the walls of the lumen will experience forces due to the following: wall shear stress, axial and radial drag. The force due to the wall shear stress is given by

$$F_w = \tau_w A = -\mu \left. \frac{du(x,r)}{dr} \right|_{r=R} \frac{\pi}{4} d^2 = \frac{-\mu u_0(x) \pi d^2}{2R} \quad (9.30)$$

where the axial velocity, $u(x,r)$ is obtained from eq 7.12.

Bird *et al.* (1960) provide the following equation for the drag force on a sphere of diameter, d , in a fluid of viscosity, μ , flowing at velocity, u ,

$$F_D = 3\pi\mu du \quad (9.31)$$

To evaluate the radial drag force, the radial velocity given by eq 7.13 is used with $r = R$. For the axial drag force, eq 7.12 is used to determine the axial velocity at the centre of the crystal, one radius from the edge of the lumen, that is at $r = R - 0.5d$.

Figure 9.8 shows the variation in the three forces acting on a particle 6 μm in diameter for a lumen flowrate of 8ml/min and a dilution factor of 4. It can be seen that the forces due to axial drag and the wall shear stress are much greater than the force due to radial drag, consequently it is to be expected that sticking will be dominated by axial shear. The expression for the axial shear is given by

$$\gamma_s = \left. \frac{du(x,r)}{dr} \right|_{r=R} = \frac{2u(x)}{R} \quad (9.32)$$

Using eq 7.12 for the axial velocity, it can be shown the right hand side of eq 9.29 is

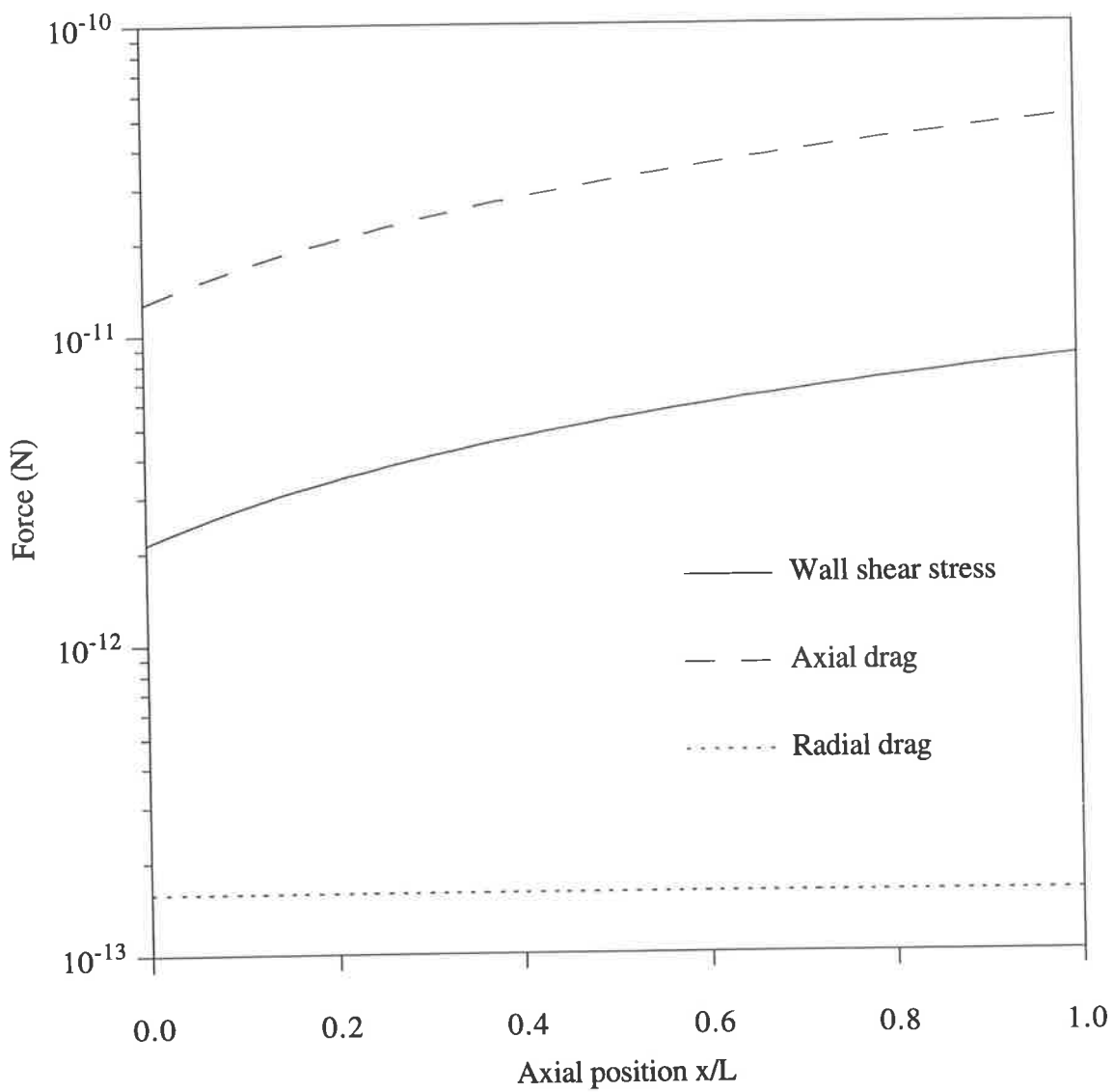


Figure 9.8 Variation with axial position of the forces acting on a $6 \mu\text{m}$ particle in the crystalliser for a lumen flowrate of 8 ml/min and $\alpha = 4$.

$$\bar{\gamma}_S \int_0^L \frac{dx}{\frac{u_0}{2} \left(1 + (\alpha - 1) \frac{x}{L}\right)} = \frac{\bar{\gamma}_S 2 \ln \alpha}{u_0 (\alpha - 1)}$$

and the left hand side is

$$\int_0^L \frac{\gamma_S dx}{\bar{u}(x)} = \int_0^L \frac{2u_0(x)}{R} \frac{2 dx}{u_0(x)} = \frac{4L}{R}$$

from which it follows that

$$\bar{\gamma}_S = \frac{2u_0 \ln \alpha}{R(\alpha - 1)} \quad (9.33)$$

Breakage. As with sticking, breakage will depend on axial shear in the fluid. However, for breakage the radial as well as the axial variation in the shear rate must be considered in the definition of an appropriate average shear rate. Assuming a constant radial position, r , at that radial position, the following average shear rate may be defined such that

$$\bar{\gamma}_B(r) \int_0^L \frac{dx}{u(r,x)} = \int_0^L \frac{\gamma_B(r,x) dx}{u(r,x)} \quad (9.34)$$

Using eq 7.12 for the axial velocity the left hand side of eq 9.34 is

$$\bar{\gamma}_B(r) \int_0^L \frac{dx}{\frac{u_0}{2} \left(1 + (\alpha - 1) \frac{x}{L}\right) \left(1 - \left(\frac{r}{R}\right)^2\right)} = \frac{2L \ln \alpha}{(\alpha - 1) u_0 \left(1 - \left(\frac{r}{R}\right)^2\right)}$$

The shear rate is

$$\gamma_B(r,x) = \frac{du(r,x)}{dr} = u_0 \left(1 - (\alpha - 1) \frac{x}{L}\right) \frac{2r}{R^2} \quad (9.35)$$

and therefore the right hand side of eq 9.34 is

$$\int_0^L \frac{u_0 \left(1 + (\alpha - 1) \frac{x}{L}\right) \frac{2r}{R^2}}{u_0 \left(1 + (\alpha - 1) \frac{x}{L}\right) \left(1 - \left(\frac{r}{R}\right)^2\right)} dx = \frac{2rL}{R^2 \left(1 - \left(\frac{r}{R}\right)^2\right)}$$

from which it follows that

$$\bar{\gamma}_B(r) = \frac{2ru_0(\alpha-1)}{R^2 \ln \alpha} \quad (9.36)$$

Similarly in the radial direction, an average shear rate may be defined such that

$$Q\bar{\bar{\gamma}}_B = \int_0^R \bar{\gamma}_B(r)u(r,0)dA \quad (9.37)$$

substituting for the flowrate and area, in terms of the fluid velocity and lumen radius, as well as the above expression for $\bar{\gamma}_B(r)$, integrating and simplifying yields

$$\bar{\bar{\gamma}}_B = \frac{16u_0(\alpha-1)}{15R \ln \alpha} \quad (9.38)$$

9.6.2 Experimental results

In Figure 9.9 the sticking rate constant, k_S , is plotted against the average shear rate calculated from eq 9.33 for all the experiments conducted; also shown are curves fitted assuming k_S is inversely proportional to the shear rate (as proposed in Section 9.6.1). It can be seen that the data from each of the experiments are well described by the fitted curves. In Table 9.3, the details of the curves fitted to the experimental data are presented.

Table 9.3. Details of the curves fitted to the experimental data in Figure 9.9.

Experiment	Lumen flowrate, Q_L (ml/min)	Constant of proportionality	Error in constant of proportionality	Regression coefficient, R
20/7	4	0.141	0.005	0.979
21/7	6	0.234	0.019	0.903
18/7	8	0.322	0.007	0.983
22/7	10	0.345	0.023	0.897

A plot of the constant of proportionality against the lumen flowrate reveals that they are directly proportional to each other. The preceding observations may be written as

$$k_S = \frac{KQ_L}{\bar{\gamma}_S} \quad (9.39)$$

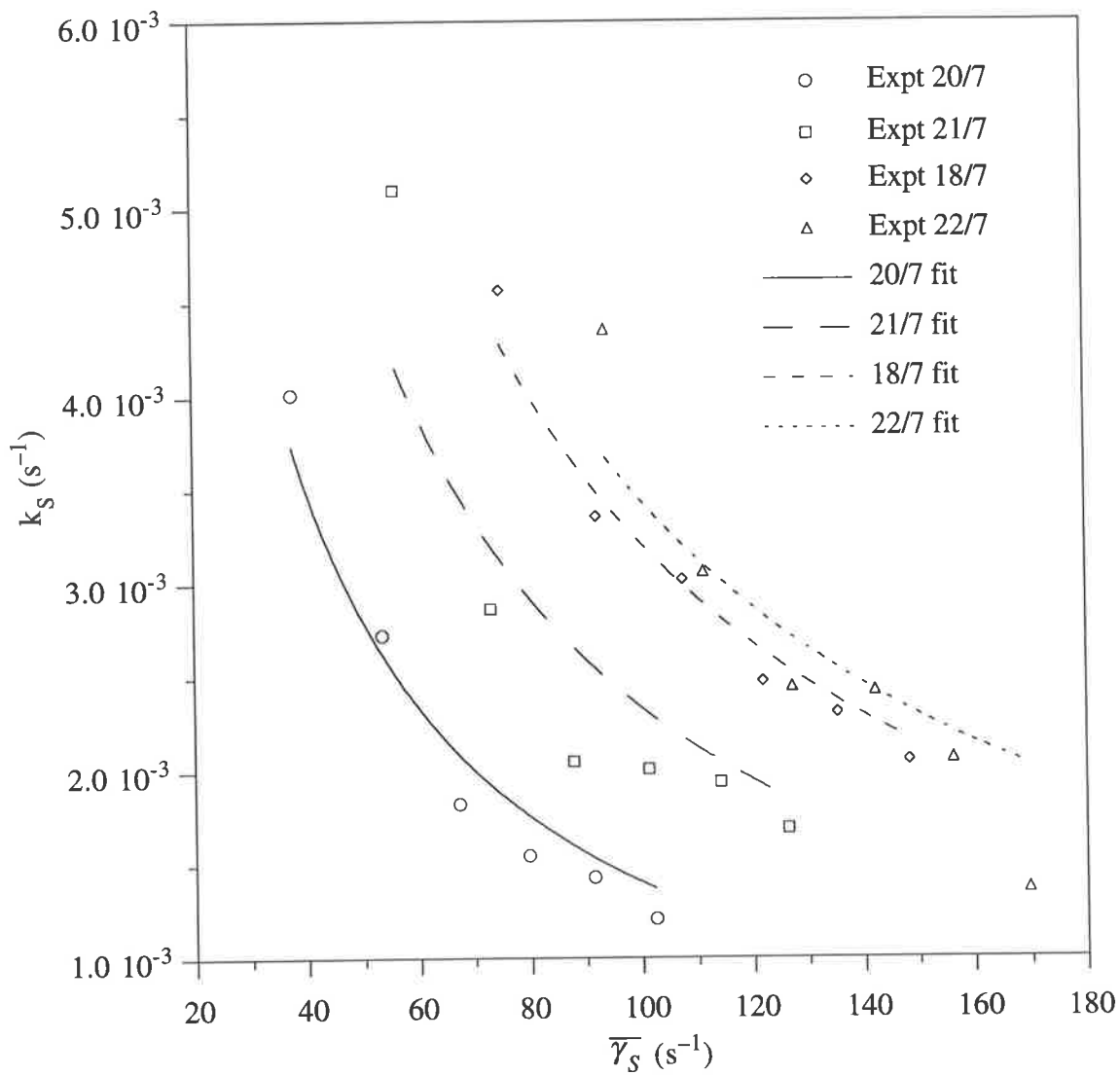


Figure 9.9 The dependence of the experimental sticking rate constants in saturated solutions on the shear rate in the tubular crystalliser. Also displayed are curves fitted to the data assuming the sticking rate constant is inversely proportional to the shear rate.

where K is a constant. Substituting the expression for the lumen flowrate, in terms of the axial fluid velocity and lumen cross-sectional area, and eq 9.33 for the shear rate and simplifying gives

$$k_S = \frac{K \pi R^3}{4} \frac{\ln \alpha}{\alpha - 1} \quad (9.40)$$

Eq 9.40 implies that for all the experiments k_S should be proportional to the group $\ln \alpha / (\alpha - 1)$, which is confirmed in Figure 9.10. No particular physical significance can be assigned to the dependence of k_S on the dilution factor, however it is more convenient to calculate the sticking rate using only one parameter, the dilution factor, rather than having to use a different equation for each experiment. The result of physical significance is that the sticking rate decreases as the shear rate in the crystalliser increases.

The dependence of the breakage rate constant, k_B , on the shear rate calculated from eq 9.38 is displayed in Figure 9.11. It can be seen that the data are reasonably well described by a curve which assumes k_B is directly proportional to the shear rate. The uncertainty in the constant of proportionality of the curve fitted to the data is 3.03×10^{-6} and the regression coefficient is 0.77.

9.6.3 Discussion

The results presented in Figure 9.6 show that the sticking and breakage rate constants determined from the experimental data can be used to calculate partial moments that are in excellent agreement the experimental partial moments. The results presented in the previous section provide physically meaningful evidence that the formulations for sticking and breakage proposed in Section 9.5 can be used to model these phenomena in the tubular crystalliser. As the shear rate in the crystalliser increases, the forces acting to remove crystals stuck to the walls of the lumen and those acting to break crystal aggregates that are loosely bound together both increase. Consequently, as the shear rate increases the sticking rate will decrease and the breakage rate will increase. These trends are consistent with those observed experimentally.

9.7 METASTABLE SOLUTIONS

As with the runs using saturated saline, those with metastable solutions are modelled using the moment form of the population balance. In Section 9.4 evidence that growth, aggregation and sticking occur in metastable solutions was presented, the question that remains unanswered, is whether breakage also occurs.

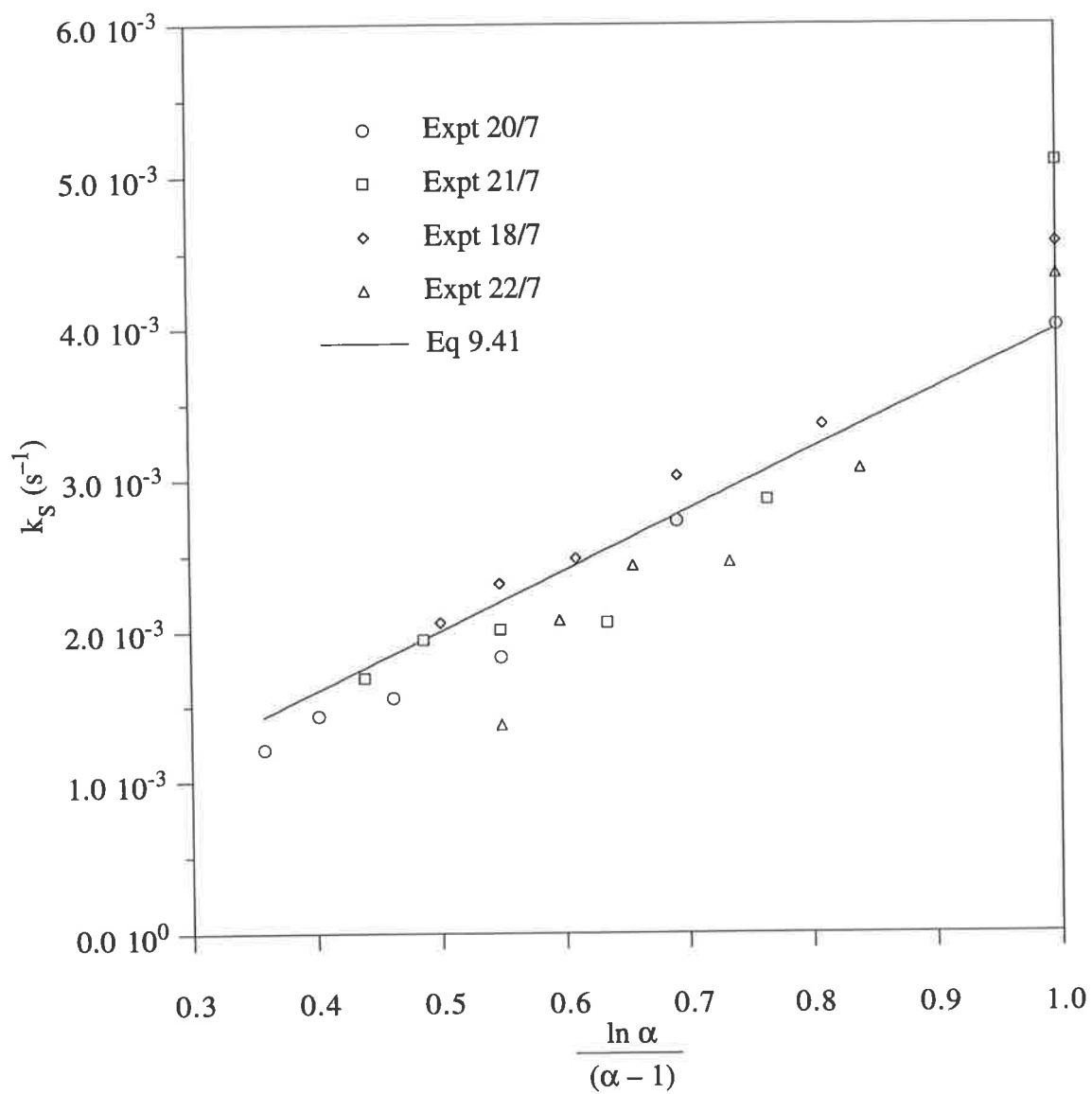


Figure 9.10 The dependence of the experimental sticking rate constants in saturated solutions on the parameter $\ln \alpha / (\alpha - 1)$.

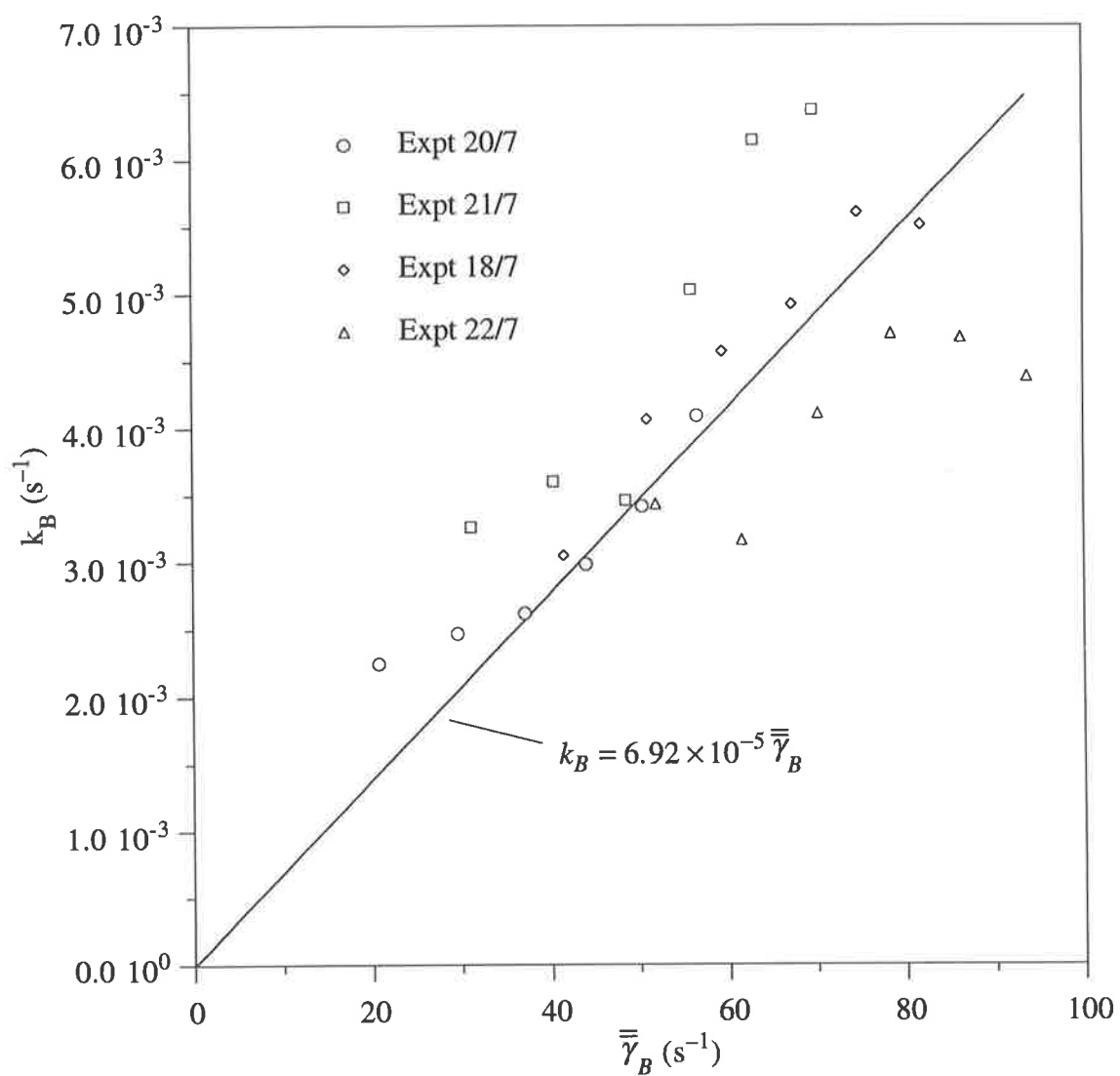


Figure 9.11 The dependence of the experimental breakage rate constants in saturated solutions on the shear rate in the crystalliser.

9.7.1 Identifying breakage

The moment form of the population balance for simultaneous growth and sticking in a batch system is now developed. Sticking, is described by the formulation proposed in Section 9.5.2. For growth alone, eq 1.22 cannot be used directly as growth into the field of view of the Multisizer must be included. With volume as the internal coordinate, eq 1.9 is

$$\frac{\partial n}{\partial t} + \frac{\partial(G_v n)}{\partial v} = 0 \quad (9.41)$$

where the definition of G_v is

$$G_v = \frac{d(L^3)}{dt} = 3L^2 \frac{dL}{dt} = 3v^{2/3} G \quad (9.42)$$

Substituting eq 9.42 into eq 9.41 and applying eq 9.9

$$\frac{d\tilde{m}_j}{dt} = - \int_{v_0}^{\infty} v^j d(3v^{2/3} G n)$$

Integrating by parts and simplifying yields

$$\frac{d\tilde{m}_j}{dt} = 3G(v_0^{j+2/3} n(v_0) + j\tilde{m}_{j-1/3}) \quad (9.43)$$

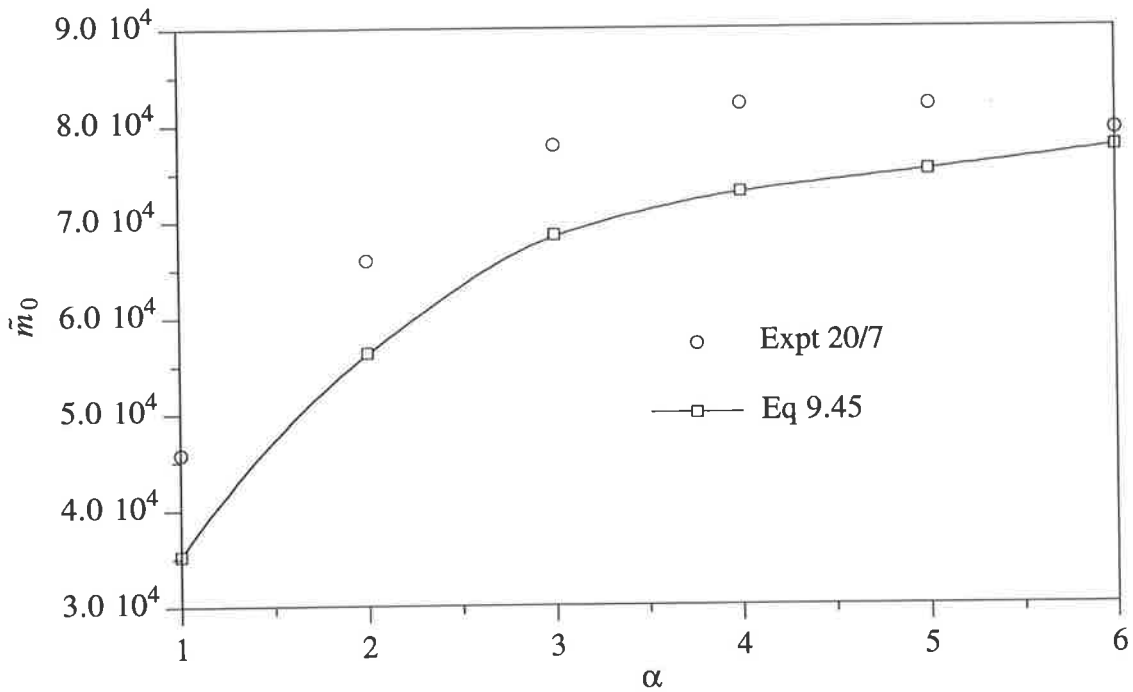
where $n(v_0)$ is the value of the number density function with volume as the internal coordinate, at the size threshold. Now, consider the moment form of the population balance for $j = 0$ which gives the rate of change of the total number of particles. For sticking and growth, the moment form of eq 9.3 and eq 9.43 give

$$\frac{d\tilde{m}_0}{dt} = -k_S \tilde{m}_0 + 3G v_0^{2/3} n(v_0) \quad (9.44)$$

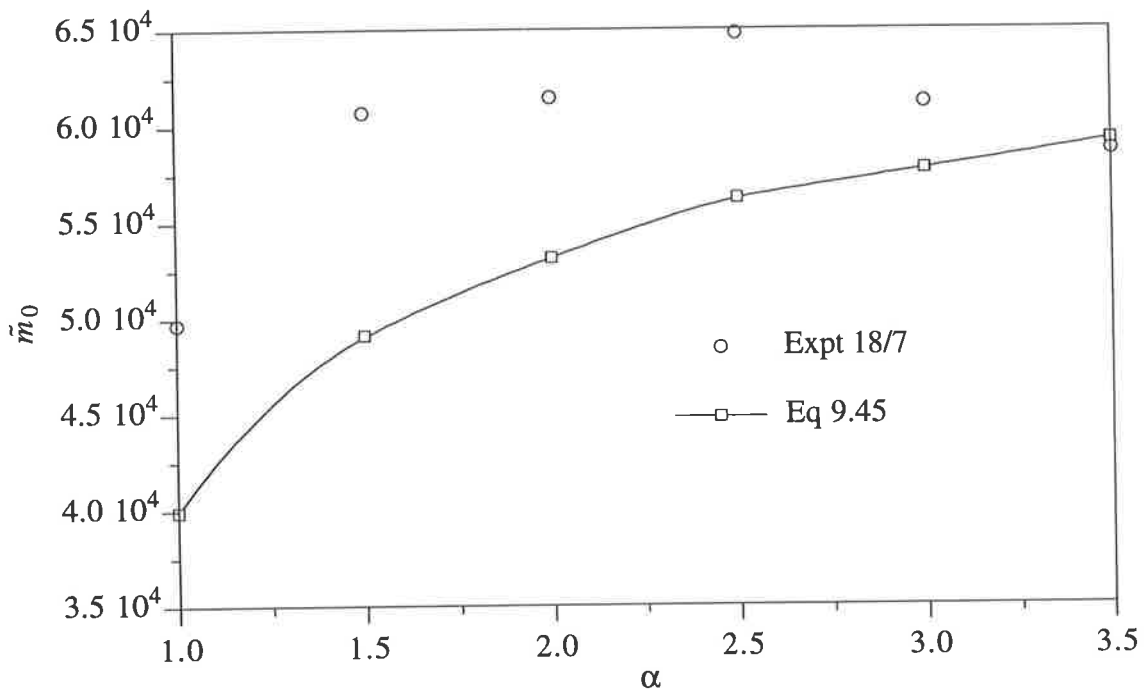
If the value of \tilde{m}_0 in the feed is denoted, \tilde{m}_0^ϕ , the solution to eq 9.44 is

$$\tilde{m}_0(\bar{t}) = \left(\tilde{m}_0^\phi k_S + 3G v_0^{2/3} n(v_0) (\exp(k_S \bar{t}) - 1) \right) k_S^{-1} \exp(-k_S \bar{t}) \quad (9.45)$$

In Figure 9.12, experimental values of \tilde{m}_0 are compared with those calculated from eq 9.45 for the experiments 20/7 and 18/7 using a metastable solution with a relative supersaturation, $\sigma = 2.62$. The values of the sticking rate constant were determined from the run with



(a)



(b)

Figure 9.12 Comparison of the experimental values of \tilde{m}_0 with a metastable solution of relative supersaturation, $\sigma = 2.62$ and those calculated from the model assuming no aggregation occurs, eq 9.45, for (a) experiment 20/7 and (b) experiment 18/7.

saturated saline, values of $n(v_0)$ were obtained from the experimental CSDs, the growth rate was calculated using eq 4.6 and the time used was the mean residence time.

Almost all the values of \bar{m}_0 calculated from eq 9.45, which does not include aggregation, are less than the experimental values. Aggregation causes the total number of crystals to decrease, so these results show that breakage must occur in metastable as well as saturated solutions. It is possible the breakage rate will depend on supersaturation, as in the presence of growth, crystals will be cemented rather than loosely bound together. However, the experimental data from the runs with saturated saline only give the dependence of the breakage rate constant on the shear rate. Therefore in the following analysis, it is assumed the breakage rates in saturated solutions are the same as those in saturated solutions for the same shear rate.

9.7.2 Simultaneous growth, aggregation, sticking and breakage

Assuming a size-independent aggregation kernel, the moment forms of the population balance for the total number and volume of crystals are given by eqs 1.20 and 1.21. Considering volume, $j=1$, eq 1.21 together with the appropriate equations for the other mechanisms gives

$$\frac{d\bar{m}_1}{dt} = 0 - k_S \bar{m}_1 - k_B v_0^2 \bar{m}_{-1} + 3G \left(v_0^{5/3} n(v_0) + \bar{m}_{2/3} \right) \quad (9.46)$$

which can be integrated and re-arranged to give

$$k_S = \frac{\ln(\bar{m}_0^\phi / \bar{m}_0)}{\bar{t}} - k_B v_0^2 \frac{\bar{m}_{-1}}{\bar{m}_1} + 3G \left(v_0^{5/3} \frac{n(v_0)}{\bar{m}_1} + \frac{\bar{m}_{2/3}}{\bar{m}_1} \right) \quad (9.47)$$

where for example, $\frac{\bar{m}_{-1}}{\bar{m}_1} = \frac{1}{2} \left(\frac{\bar{m}_{-1}^\phi}{\bar{m}_1^\phi} + \frac{\bar{m}_{-1}}{\bar{m}_1} \right)$ and the superscript ϕ denotes the feed.

Eq 9.47 is used to determine values of the sticking rate constant, k_S for metastable solutions, in which growth occurs. It was found that the values of k_S in saturated and metastable solutions were approximately equal for most operating conditions in the crystalliser. This observation is illustrated in Figure 9.13 in which values of k_S from the runs with a metastable solution, $\sigma = 2.62$, are plotted against the values of k_S from the runs with a saturated solution for experiments 20/7 and 21/7.

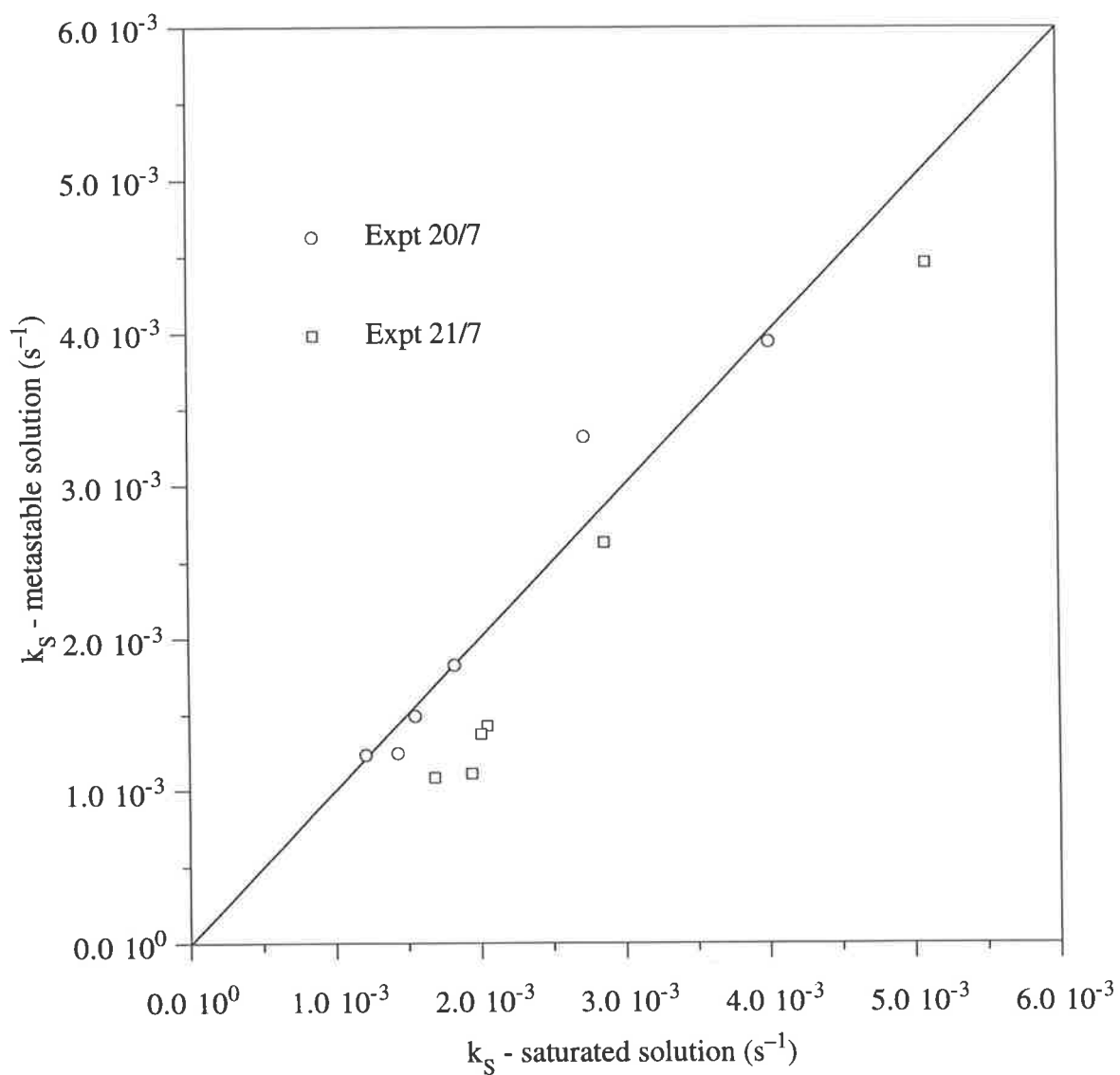


Figure 9.13 Comparison of the sticking rate constants in a metastable solution, $\sigma = 2.62$, with those in a saturated solution for the experiments 20/7 and 21/7.

For crystal number, $j = 0$, eq 1.20 together with the appropriate equations for the other mechanisms gives

$$\frac{d\tilde{m}_0}{dt} = -\frac{1}{2}\beta_0 \tilde{m}_0^2 + (k_B - k_S)\tilde{m}_0 - 2k_B v_0 \tilde{m}_{-1} + 3G v_0^{2/3} n(v_0) \quad (9.48)$$

Integrating and simplifying

$$\bar{t} = 2 \left[\tan^{-1} \left(\frac{(k_S - k_B + \beta_0 \tilde{m}_0^\phi)}{\Lambda} \right) - \tan^{-1} \left(\frac{(k_S - k_B + \beta_0 \tilde{m}_0)}{\Lambda} \right) \right] / \Lambda \quad (9.49)$$

where, $\Lambda = \sqrt{-(k_S - k_B)^2 - 6\beta_0 G n(v_0) v_0^{2/3} + 4\beta_0 k_B \tilde{m}_{-1} v_0}$

Eq 9.49 was solved numerically to find the value of the aggregation rate constant, subject to the values of the rate constants for the other mechanisms and using the experimental partial moments for the operating conditions in the crystalliser.

9.7.3 Results

Figure 9.14 shows the aggregation rate constant plotted against the shear rate in the crystalliser. The appropriate shear rate is that used for breakage given by eq 9.39, as both radial and axial variations in the shear rate will affect aggregation. It can be seen that the aggregation rate constant is dependent on the shear rate, but does not otherwise appear to depend on the lumen flowrate; the data from experiments with different lumen flow rates are described by a single curve.

Figure 9.15 shows the dependence of the aggregation rate constant on the oxalate ion concentration for values of the dilution factor of 2 and 3.5 from the experiment 18/7. Also plotted are the data from the batch experiments reported in Chapter 4. The values of the aggregation rate constants from the continuous experiments are at least two orders of magnitude lower than those from the batch experiments at the same oxalate ion concentration. Also the aggregation rate constants for the continuous experiments do not appear to correlate with the oxalate ion concentration.

9.7.4 Discussion

Two clear results emerge from the experiments using metastable solutions: firstly, the aggregation rate constant increases as the shear rate increases, and secondly the aggregation rate constant does not seem to depend on the oxalate ion concentration. Both of these results differ from those obtained from the batch experiments reported in Chapter 4.

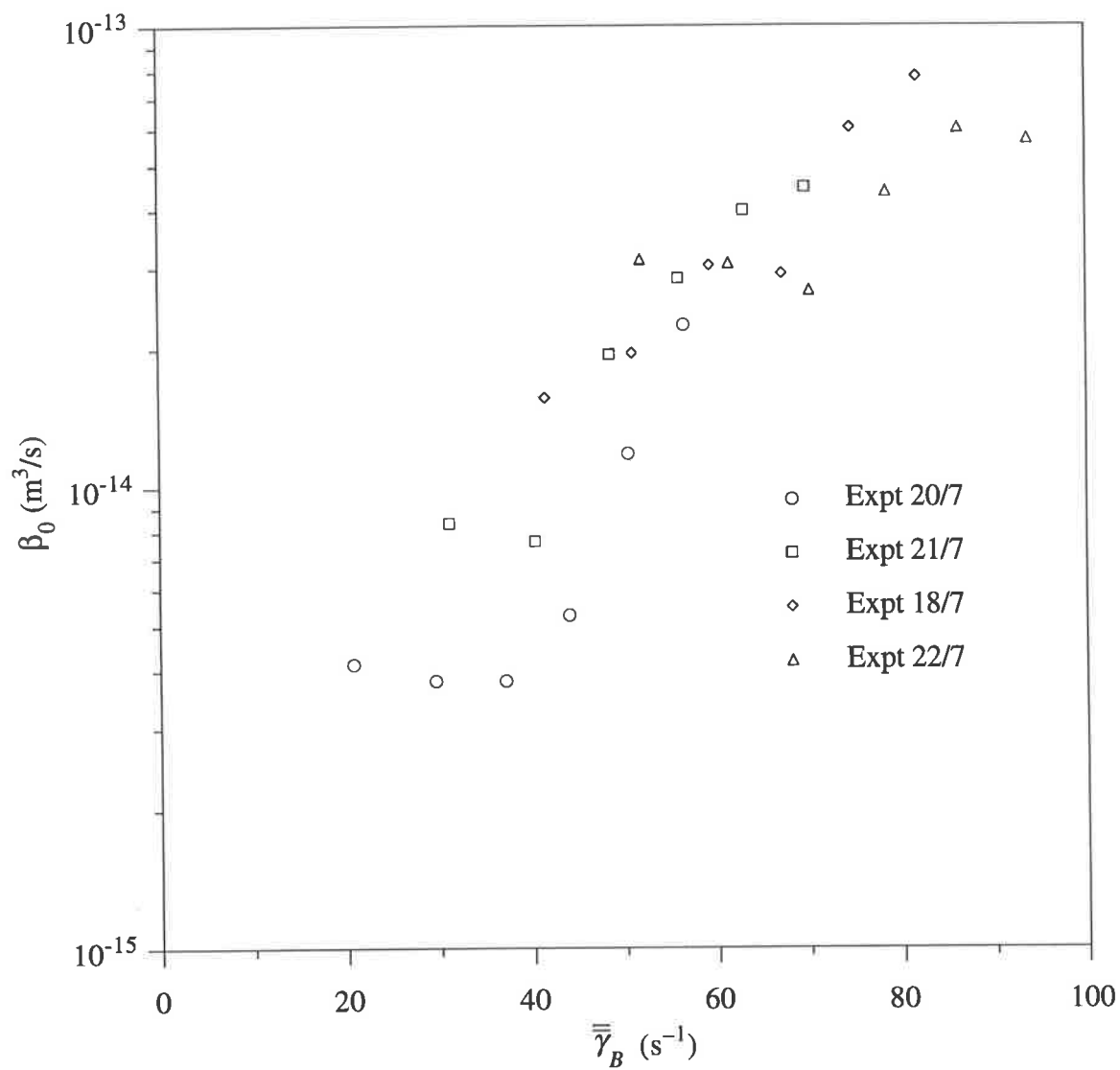


Figure 9.14 The dependence of the experimental aggregation rate constants in a metastable solution, $\sigma = 2.62$, on the shear rate in the crystalliser.

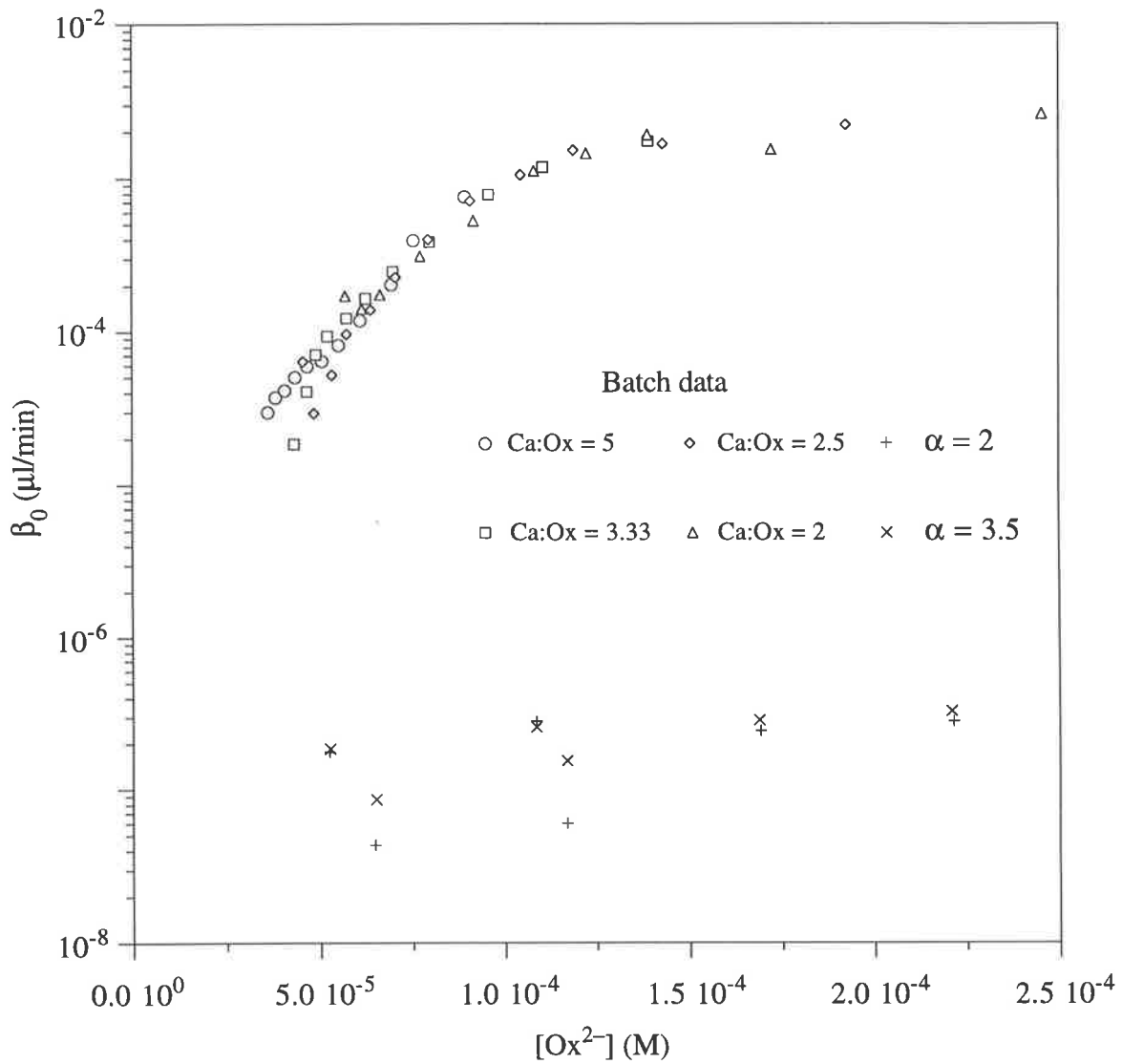


Figure 9.15 The dependence of the aggregation rate constants in metastable solutions on the oxalate ion concentration in the crystalliser for experiment 18/7. Also plotted are the aggregation rate constants from the batch experiments reported in Chapter 4.

The dependence of the aggregation rate on shear rate

The aggregation rate constants reported in the previous section were obtained assuming a size-independent aggregation kernel. As shown in Table 4.1, a kernel has been derived for aggregation in laminar flow, however, the shear kernel is size-dependent. The analysis presented in Section 9.7.2 cannot be re-worked for the shear kernel as the population balance is not amenable to the moment transformation, however an alternative approach is available. The aggregation rates obtained from the preceding analysis can be compared with the aggregation rate for the shear kernel by defining an apparent size-independent aggregation rate constant, $\beta_{0,A}$ such that:

$$\dot{m}_0|_{shear} = -\frac{1}{2}\beta_{0,A} m_0^2 \quad (9.50)$$

That is the rate of change of crystal number by aggregation for the shear kernel at any instant is given by an aggregation rate constant which is size-independent. This approximation may be used for the experimental data as from the CSDs in Figure 9.3 it can be seen the increase in crystal size in the crystalliser is reasonably small.

It is possible to define an average diameter, the shear diameter, by

$$\beta_{0,A} = K \bar{d}^3 \quad (9.51)$$

This mean diameter is chosen so that the apparent size-independent aggregation rate constant can be determined from Smoluchowski's result, in which the appropriate shear rate is, $\bar{\gamma}_B$, which implies:

$$\beta_{0,A} = \frac{\bar{\gamma}_B}{6} \bar{d}^3 \quad (9.52)$$

Combining eqs 9.50 and 9.51 and re-arranging gives

$$\bar{d} = \sqrt[3]{\frac{-2\dot{m}_0|_{shear}}{K m_0^2}} \quad (9.53)$$

The program *Batch* was used to simulate data from which \bar{d} was calculated. The CSD of the feed for experiment 18/7, in which m_0 is $135.6 \mu\text{l}^{-1}$, was used in the simulations. For this CSD, $\dot{m}_0|_{shear}/K$ was found to be $-89.8 \times 10^5 \text{ s}^{-1}$. Using these values in eq 9.53 implies the value of the shear diameter is $9.92 \mu\text{m}$. This value can be compared with the mean size, $\bar{L}_{3,0}$, of the crystals from the experimental CSD which is $5.27 \mu\text{m}$. These

results suggest that if the shear kernel is used to model aggregation in laminar flow in the crystalliser, the mean size of the crystals must be almost double the observed value.

At his point it is worth considering the assumptions made in deriving the expression for the shear kernel. In the context of the results of the current work the most important assumptions are that the crystals are spheres and that micro-lubrication and inter-particle force effects can be neglected (van de Ven and Mason, 1977). From SEM micrographs of the aggregates it is clear that they are not spherical. If the crystals are not spherical then the collision diameter, that diameter which measures whether two crystals will collide or not, may be underestimated.

Preliminary investigations into different methods of sizing calcium oxalate aggregates provide some insight into this problem. A sample of a seed suspension, prepared using the protocol in Section 9.2.3, was sized in three different ways. Firstly, using an Elzone 280 PC (which operates on the same principle as the Multisizer and reports volume equivalent diameters) and secondly using a Galai CIS-1. The Galai is able to size particles by two different methods, either by a laser scattering technique or by video monitoring, in which video images are analysed by computer and crystals sized from the video images. The diameter determined from the video image is the Feret's diameter. The mean size, $\bar{L}_{3,0}$, for the same sample of calcium oxalate seeds obtained from each method were as follows:

- Elzone 280 PC: 4.47 μm
- Galai CIS-1 (laser): 6.29 μm
- Galai CIS-1 (video): 9.93 μm

Assuming each of these mean sizes is the shear diameter, an apparent size-independent aggregation rate constant can be calculated from eq 9.52.

Figure 9.16 shows the experimental aggregation rate constants together with the aggregation rates constants calculated from eq 9.52 using the $\bar{L}_{3,0}$ mean sizes determined by the Elzone 280 PC and Galai CIS-1. It can be seen that the experimental aggregation rate constants lie between the aggregation rate constants calculated using the volume equivalent mean size obtained from the Elzone 280 PC and the mean Feret's diameter obtained from the Galai CIS-1. This finding highlights the importance that crystal shape may have on aggregation. The shape of the crystals will influence the size of the collision diameter as well as the fluid hydrodynamics in the region surrounding the crystal, both of which will in turn affect the aggregation rate.

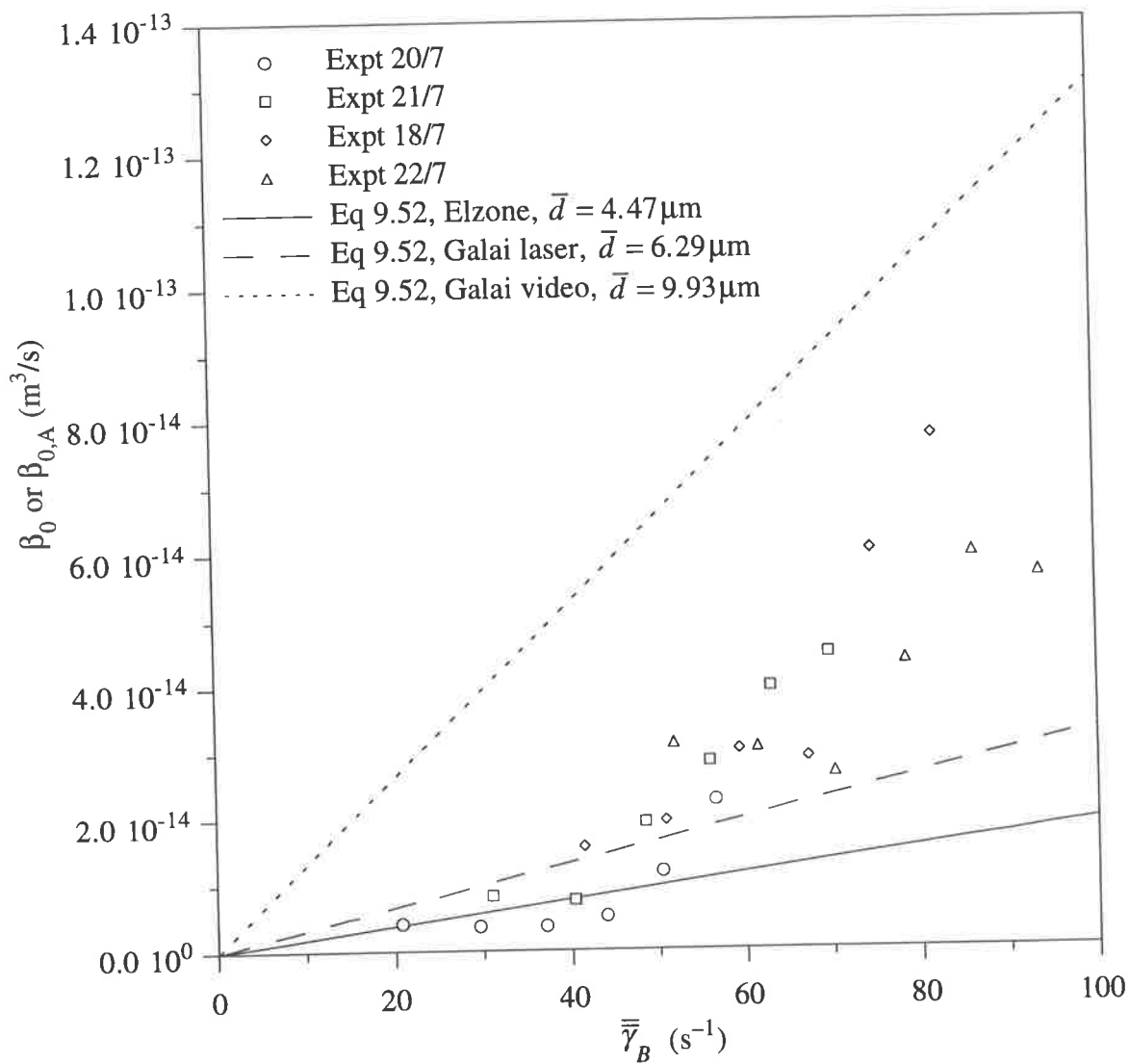


Figure 9.16 Aggregation rates constants calculated using eq 9.52, with mean sizes determined by different particle size analysers together with the experimental aggregation rate constants.

The dependence of aggregation on supersaturation

The results from the continuous experiments are at odds with those of the batch experiments. The aggregation rates in the tubular crystalliser are at least two orders of magnitude lower than those in the batch experiments and do not appear to correlate with the oxalate concentration. However, these observations can be explained by comparing the conditions in the crystalliser with those in the batch experiments.

While it is difficult to calculate the fluid shear rates in the batch experiments, they are likely to be much higher than those in the tubular crystalliser. The difference in the magnitude of the fluid shear rates can be used to explain the behaviour of the aggregation rate constant. Fluid shear affects aggregation in two ways; firstly, as the shear rate increases the number of collisions between crystals increases which promotes aggregation. Secondly, as the shear rate increases, the forces acting to disrupt aggregates prior to cementing, increase, which might decrease the aggregation rate.

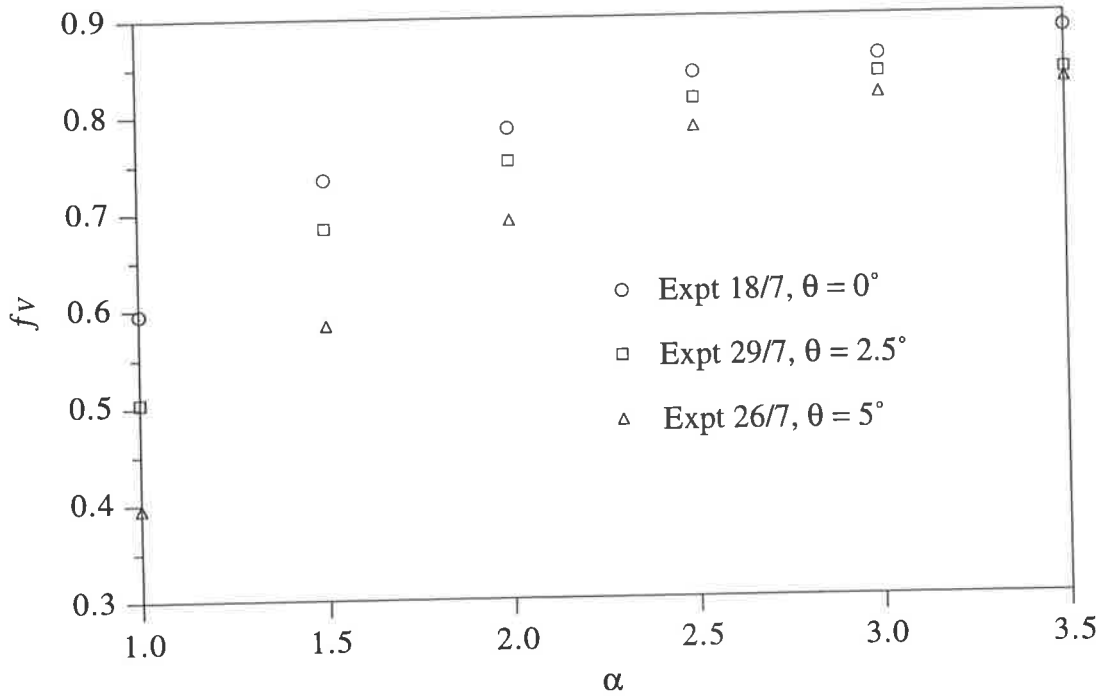
At low shear rates the effect on the aggregation rate of the increase in the frequency of collisions will be greater than that of the increase in the forces acting to disrupt aggregates. Particularly in supersaturated solutions where crystal growth acts to “cement” crystals together. As the shear rate in the tubular crystalliser is lower than in the batch system, the collision frequency and hence the aggregation rate will also be lower. Also as the shear rate in the crystalliser increases the collision frequency and aggregation rate will also increase, which is consistent with the experimental results shown in Figure 9.14.

The analysis presented in Chapter 5 suggests the aggregation rate depends on the oxalate ion concentration as a consequence of the mechanism for aggregation. Once two crystals collide, if a stable aggregate is to form, they must be in contact long enough for ions to diffuse to and react at the point of contact. Further, the results in Chapter 5 suggest diffusion to the point of contact is limiting in this process.

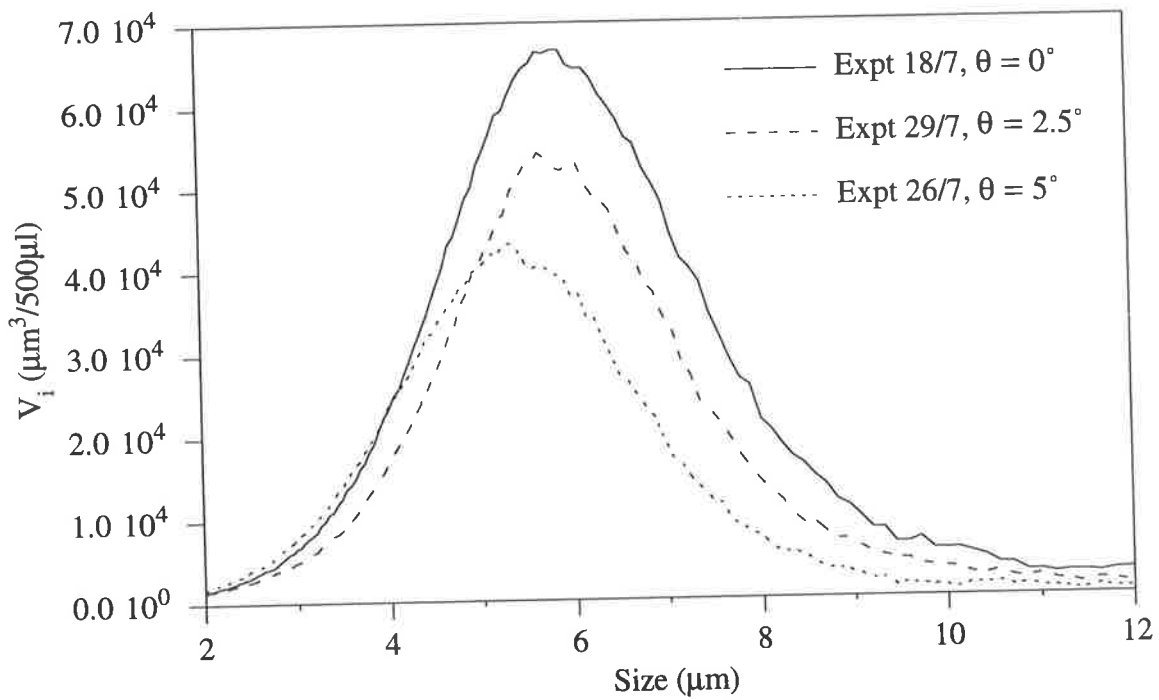
By contrast in the crystalliser collisions are nearly always successful in forming an aggregate. The shear forces are not strong enough to disrupt the aggregates during the cementing process.

9.8 THE EFFECT OF INCLINATION

The effect of the angle of inclination of the crystalliser can be seen from Figure 9.17 (a) which shows the variation of the parameter f_V for experiments 18/7, 29/7 and 26/7 in which the crystalliser was inclined by 0° , 2.5° and 5° respectively. It can be seen that as the



(a)



(b)

Figure 9.17 The effect of inclination of the crystalliser from vertical on (a) the parameter f_V and (b) the CSDs by volume at the outlet of the crystalliser for $\alpha = 1$ with a saturated saline solution.

angle of inclination increases the fraction of crystalline material sticking to the lumen increases for all operating conditions. This observation is confirmed by the CSDs, by volume, for the same experiments with $\alpha = 1$, shown in Figure 9.17 (b). It can be seen that as the angle of inclination increases a higher fraction of the larger crystals is retained in the crystalliser. Also it can be seen in Figure 9.17 (b) that as the angle of inclination increases the fraction of larger crystals lost increases, suggesting that sticking may be size-dependent under these conditions.

The increase in the loss of crystal mass can be explained by considering the effects of settling. With the crystalliser inclined from the vertical the lateral component of the settling velocity will carry crystals towards the walls of the lumen. The importance of the angle of inclination can be investigated by considering the analysis of gravitational settling in a horizontal pipe with laminar flow of Pich (1972). This author derives an expression for the fraction of material lost by considering the appropriate form of the particle continuity equation. For a horizontal tube of length, L , and radius, R , with fluid flowing at an average velocity, \bar{u} , containing particles with a Stoke's settling velocity, v_s , the fraction of material lost, η , is:

$$\eta = \frac{2}{\pi} \left[2S(1 - S^{2/3})^{1/2} - S^{1/3}(1 - S^{2/3})^{1/2} + \sin^{-1}(S^{1/3}) \right] \quad (9.54)$$

where
$$S = \frac{3v_s L}{8\bar{u} R}$$

Here two modifications must be made to the expression for the parameter, S . Firstly, the crystalliser is inclined to the vertical, not horizontal, and secondly the average fluid velocity in the lumen is dependent on the axial position due to fluid injection from the jacket. With the appropriate component of the settling velocity and using eq 7.12 for the fluid velocity, the expression for S is:

$$S = \int_0^L \frac{3v_s \sin \theta dx}{8R\bar{u}(1 + (\alpha - 1)x/L)} = \frac{3v_s L \sin \theta}{8R\bar{u}} \frac{\ln \alpha}{(\alpha - 1)} \quad (9.55)$$

Figure 9.18 shows the experimental values of the parameter f_V together with those predicted by eq 9.54 (f_V is equivalent to $1 - \eta$). In calculating the value of f_V from eq 9.54, the $\bar{L}_{3,0}$ mean size was used to calculate the Stoke's settling velocity. It can be seen that the data from the experiments fall between the two theoretical curves. An explanation for this might be that only the inclination of the crystalliser as a whole can be measured.

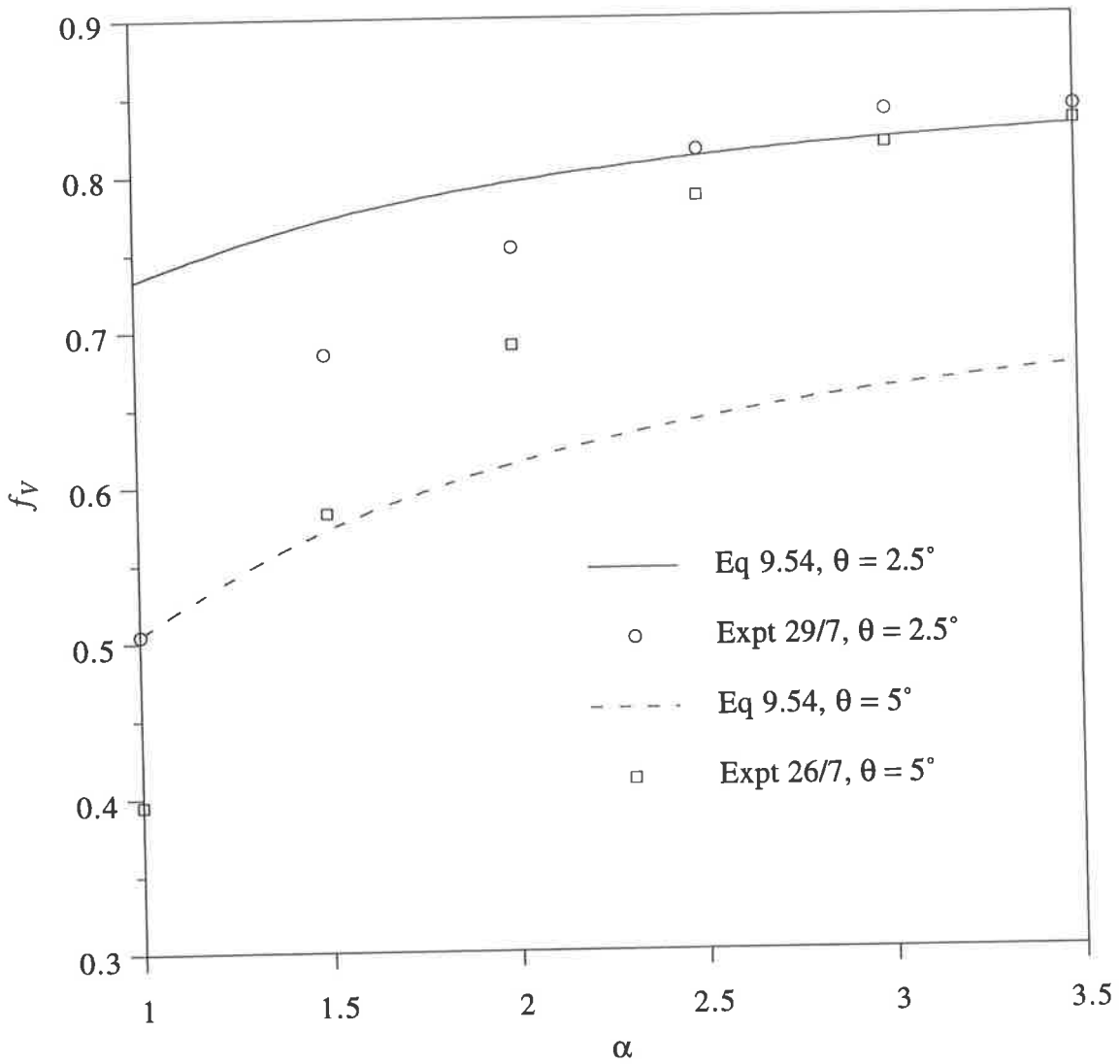


Figure 9.18 Experimental values of the parameter f_V and those calculated from the analysis of Pich (1972), eq 9.54, for different crystalliser inclinations.

Close examination reveals that each of the fibres follows a slightly “kinked” path and so will have sections that are not quite aligned with the axis of the jacket. It is not possible to estimate the angle of inclination of all parts of the fibres and so the amount of material lost is underestimated by eq 9.54.

The size dependence of sticking can also be investigated. Rather than using the ratio of the *total* volume of crystals in the fluid at the outlet to that at the inlet, the volume of crystals in *each* size interval of the CSD, $f_{V,i}$, is considered. The parameter, S is proportional to the mean crystal size squared, as the crystals in each size interval have a different Stoke’s settling velocity. In Figure 9.19 (a) the parameter $f_{V,i}$ is plotted against S for the CSD for $\alpha = 1$ from the experiment 26/7 in which the crystalliser inclination was 5° . The effects of breakage can be seen at small values of S , and therefore small crystal sizes, as the value of $f_{V,i}$ is greater than 1. At larger values of S there is reasonable agreement between the values of $f_{V,i}$ calculated from eq 9.54 and the experimental values. However in general eq 9.54 does not describe the size dependence of the sticking. This is confirmed in Figure 9.19 (b) in which the data for $\alpha = 3$ from the same experiment are considered. Again the effects of breakage can be seen at small crystal sizes, and at larger sizes eq 9.54 does not describe the size dependence of sticking.

As the sticking mechanism is size-dependent, but cannot be described by eq 9.54, no further attempt is made to determine the sticking, breakage and aggregation rates using the analysis in Section 9.7.2. However, the CSDs for the runs with metastable solution exhibit the same behaviour as the runs with saturated solution displayed in Figure 9.17 (b), suggesting that even small deviations from the vertical have a significant effect on the retention of large crystals in the crystalliser.

9.9 STONE FORMATION

The findings of the experiments using the tubular crystalliser have important implications for stone formation. Above all they underline the importance of the geometry of the kidney and the effect it has on fluid hydrodynamics.

The results of Figures 9.14 and 9.15 show that under conditions of constant supersaturation, as might be found in the kidney (Sheehan and Nancollas, 1980), the shear rate may be as, or more important as a risk factor than supersaturation. Further the results of Figure 9.15 suggest that aggregation rates determined using *in vitro* models such as batch systems are likely to be much higher than those found in the kidney. A tubular crystalliser

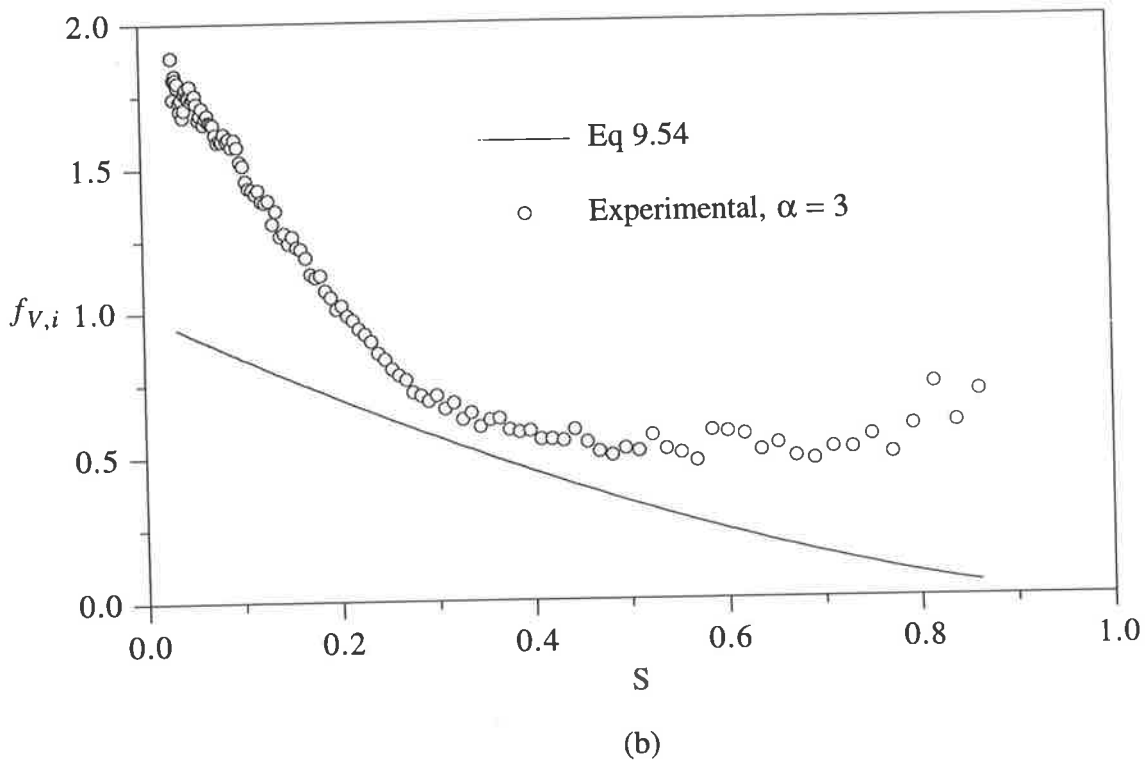
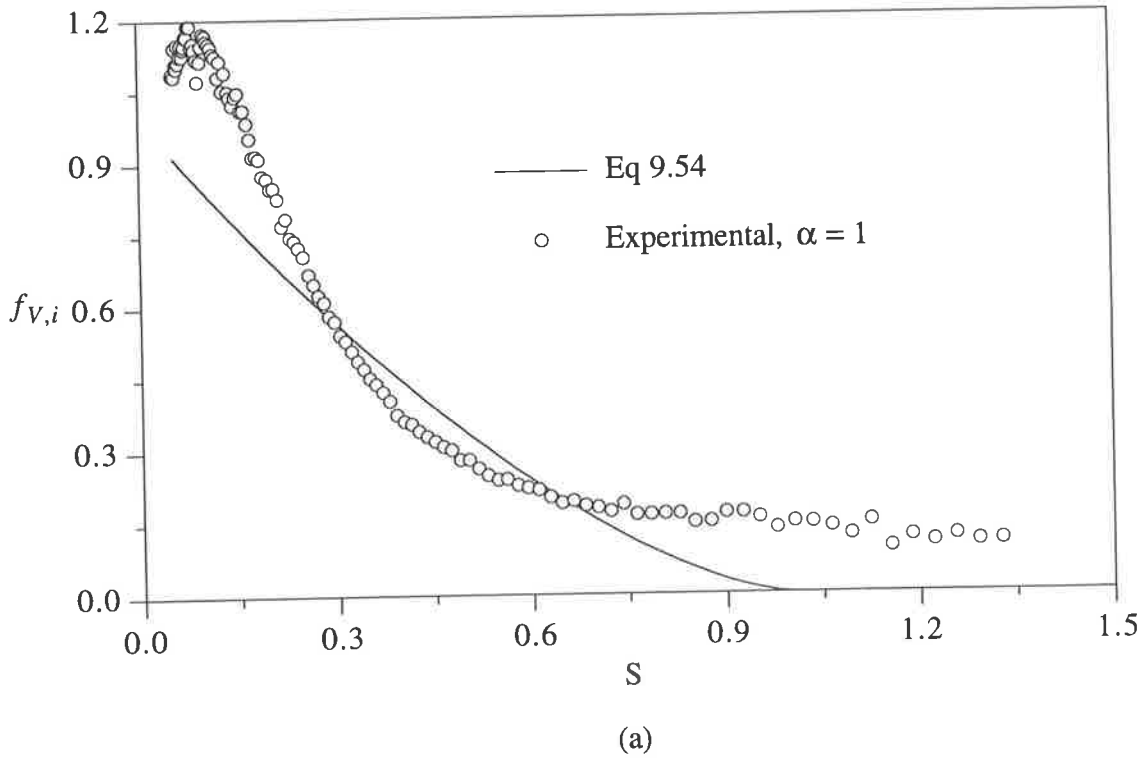


Figure 9.19 Comparison of the parameter, $f_{v,i}$, calculated from the analysis of Pich (1972), eq 9.54, with the experimental values for experiment 26/7 for (a) $\alpha = 1$ and (b) $\alpha = 3$.

such as that used in the current work may provide more relevant information about aggregation in hydrodynamic conditions similar to those in the kidney.

Finally, the results of Section 9.8 suggest that in the kidney tubules calculii must spend nearly all their time in contact with the tube walls and not free in the stream of flowing liquid. Thus, while possibly for the wrong reasons, the conclusions of Finlayson and Reid (1978), which were called into question in Chapter 8 are correct, it may be a fixed rather than a free particle mechanism that leads to stone formation.

The importance of crystals becoming attached to the walls of the lumen is illustrated in Figure 9.20, which is an SEM micrograph of a crystal aggregate rinsed from the crystalliser after a run using metastable solution as described in Section 9.3.2. The crystal shown is highly aggregated and much larger than the crystals fed to the crystalliser, in fact it is approximately one quarter of the diameter of the lumen. It is possible to envisage a situation where if the crystalliser was run for a long period of time, such a crystal could block the lumen; an *in vitro* stone formation event.

9.10 CONCLUSIONS

In this chapter the aggregation of calcium oxalate in a continuous system, the tubular crystalliser described in Chapter 6 has been studied.

In addition to growth and aggregation, sticking and breakage also occur in the crystalliser in both saturated and supersaturated solutions. The results of experiments conducted using solutions saturated with respect to calcium oxalate suggest:

- Sticking is irreversible, size-independent, and the sticking rate is inversely proportional to the fluid shear rate in the crystalliser.
- When breakage occurs crystals of any size may be formed, and the breakage rate is directly proportional to the shear rate in the crystalliser.

Using these formulations for sticking and breakage and eq 4.6 to describe the growth rate, the dependence of the aggregation rate on supersaturation and shear rate in the crystalliser were investigated. It was found that:

- The aggregation rates in the crystalliser were much lower than those in the batch experiments at the same relative supersaturation.

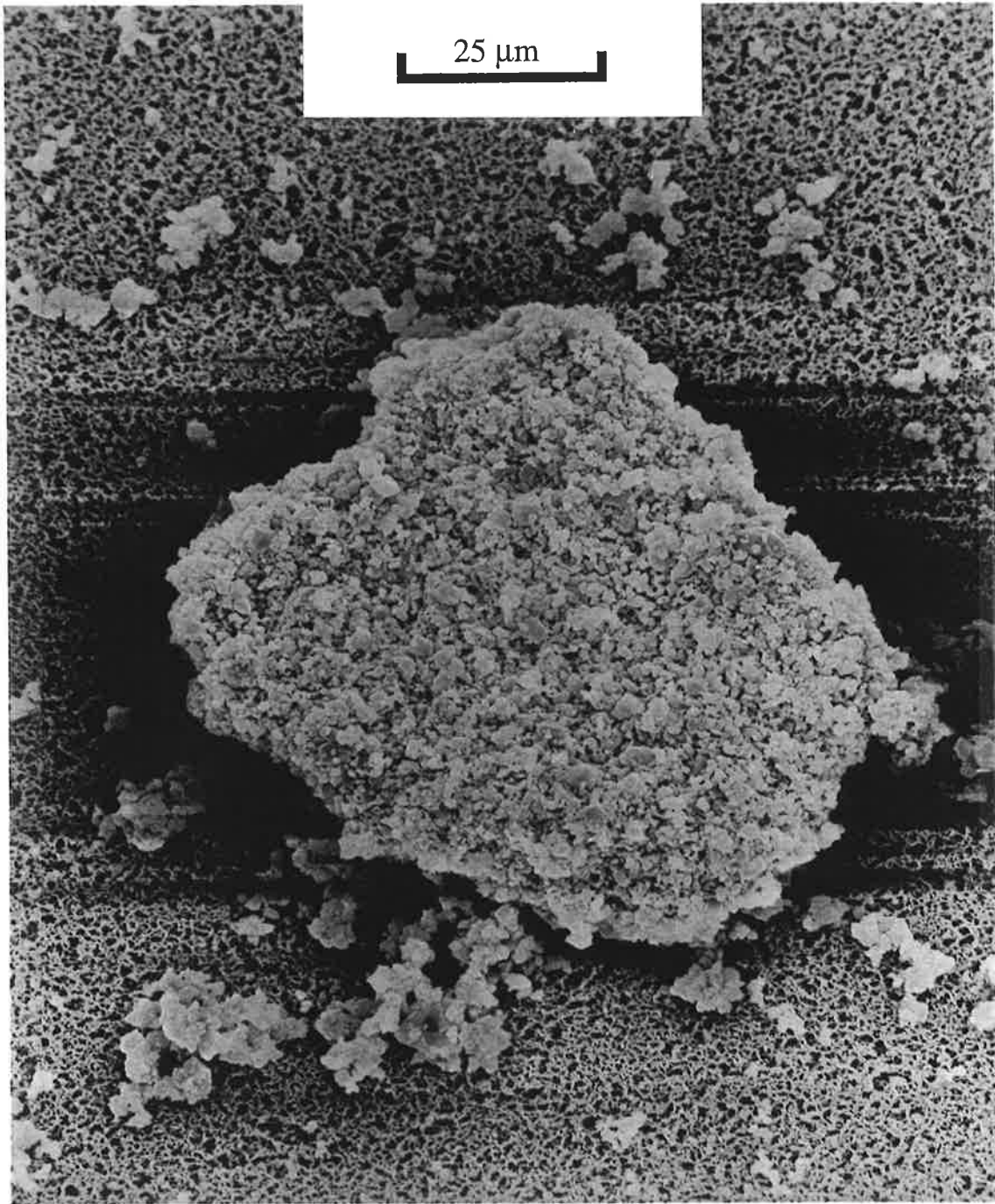


Figure 9.20 SEM micrograph of a calcium oxalate aggregate rinsed from the tubes of the crystalliser after a run using a metastable solution.

- The aggregation rate increases as the shear rate in the crystalliser increases and is relatively insensitive to the oxalate ion concentration.

These two observations, which are in contrast to the behaviour of the aggregation rate in a batch system, can be explained by the difference in the shear rate between the two systems.

Finally, it is shown that even small inclinations of the crystalliser from the vertical increases the fraction of crystalline material that sticks to the lumen in the crystalliser.

The findings of this chapter suggest that the tubular crystalliser may be a useful *in vitro* experimental system for studying factors that affect calcium oxalate aggregation under hydrodynamic conditions similar to those found in the kidney.

Chapter 10:

CONCLUSIONS AND RECOMMENDATIONS

In this chapter an overview of the findings of this thesis are given, as well as some recommendations for future work.

10.1 THE CRYSTALLISATION OF CALCIUM OXALATE

This thesis has focused on the simultaneous growth and aggregation of calcium oxalate mono-hydrate in metastable saline solutions. The mechanism and kinetics of growth and particularly aggregation have been investigated in batch and continuous systems. The main reason for interest in the crystallisation of calcium oxalate is that it is the principal inorganic constituent of human kidney stones. More importance is placed on aggregation as despite being the only mechanism that can cause crystals to increase in size rapidly enough to block the tubules of the kidney it is probably the least well understood.

10.2 WORK PRESENTED IN THIS THESIS

The work in this thesis may be divided into four parts: (i) an investigation of states of supersaturation of calcium oxalate in aqueous solutions (Chapter 2), (ii) batch crystallisation experiments and analysis (Chapters 3 and 4), (iii) an investigation of the aggregation mechanism for calcium oxalate (Chapter 5) and (iv) the development and characterisation of a novel *in vitro* experimental system, and the continuous crystallisation of calcium oxalate in this system (Chapters 6 to 9).

10.2.1 Supersaturation

Supersaturation is a key variable in any precipitation reaction and despite an extensive literature on the crystallisation of calcium oxalate there is no generally accepted definition of supersaturation. Three physico-chemical factors complicate the definition and calculation of supersaturation, namely, the reversibility of the precipitation process, two ionic species reacting to form a crystal and the formation of ion complexes.

In Chapter 2, a simple method is developed for calculating relative supersaturation in terms of free ion concentrations from total ion concentrations. This method solves the mass action

equations for complex ion formation together with mass conservation equations for each ion in solution. It is demonstrated that this simple method, is as accurate, but much easier to use than other more complicated models that exist in the literature, such as EQUIL89d.

10.2.2 Batch crystallisation

Two factors make batch crystallisation appealing; firstly there are well established experimental protocols and secondly a numerical method has been developed to determine growth and aggregation rates from experimental data.

A seeded technique, based on the protocol of Ryall *et al.* (1981b), was used to investigate the effect of agitation and supersaturation on growth and aggregation. A wide range of supersaturation was considered by increasing the oxalate ion concentration while keeping the calcium ion concentration constant. The full details of the metastable solutions used are given in Table 3.3.

The program *Batch*, which uses the discretised population balance of Hounslow (1990), to extract the growth and aggregation rates from changes in crystal size distributions with time was used to analyse the experimental data. It was found that:

- The growth rate is well described by McCabe's ΔL law, in which growth is size-independent.
- The data from some 35 experiments, over 350 different growth rates, conducted at different agitation rates and using metastable solutions with different calcium to oxalate ion ratios are all described by the following equation:

$$G = (0.0767 \pm 0.0012)(S - 1)^2$$

where the growth rate is measured in $\mu\text{m}/\text{min}$ and the relative supersaturation, S is given by $S = \sqrt{AP/K_{sp}}$.

- Aggregation is well described by a size-independent aggregation kernel.
- The aggregation rate constant is dependent on the agitation rate; the aggregation rate decreases as the agitation rate increases.
- The aggregation rate is found to correlate with the oxalate ion concentration rather than supersaturation.

The most interesting of these points concern the description of aggregation. Firstly, the decrease in the rate of aggregation as supersaturation decreases is much greater than conventional electrical double-layer (DLVO) theory would predict, and secondly the dependence on the oxalate ion concentration is surprising.

10.2.3 The aggregation mechanism

In Chapter 5, the experimental results of an investigation conducted with saturated and supersaturated solutions and different types and rates of agitation are used to develop a mechanism for calcium oxalate aggregation.

A two-stage mechanism is proposed to account for the experimental observations: in the first, reversible stage, crystals collide and form weak aggregates held together by the forces described by DLVO theory. In the second, irreversible stage, the loose aggregates are cemented together by the deposition of new material. The second stage can only occur in supersaturated solutions, while the first may occur in any solution.

Further, a model is developed for aggregation in supersaturated solutions. It is proposed that in order for crystals to aggregate irreversibly, solute must first diffuse to the point where the crystals are in contact, and then deposit on the touching surfaces in order to “cement” the crystals together. A basic analysis of the diffusion-cementing process suggests that the experimentally observed dependence of the aggregation rate constant on the oxalate ion concentration and activity product reported in Chapter 4, are predicted by the model. This analysis suggests that diffusion of the solute ions to the cementing site is the rate determining step.

10.2.4 The tubular crystalliser

In Chapter 6 a review of *in vitro* experimental systems for studying kidney stone formation is presented. It is observed that none of the commonly used experimental systems take into account the tubular geometry of the kidney and the effect it might have on aggregation.

A novel tubular crystalliser is described as is its use in a study of the growth and aggregation of calcium oxalate in laminar flow in long, thin tubes, similar to the tubules in the kidney.

The solute residence time distribution.

Chapter 7 reports an investigation into the solute residence time distribution (RTD) in the crystalliser. A diffusion-advection model is proposed to explain the solute RTD which is not described by the RTD for Poiseuille flow. A moment transform analysis is used to evaluate

the mean and standard deviation of the RTD. It was found that provided appropriate values of the solute diffusivity and crystalliser cross-sectional area are used the results from the model are in agreement with those from the experiments.

The particle residence time distribution

The effect of the dilution factor (defined in Section 6.3.5), the lumen flowrate, particle size and crystalliser geometry on the particle RTD was investigated using pulse-input response tests reported in Chapter 8. It was found that the RTD is independent of the particle size, lumen flowrate and the geometry of the crystalliser, but depends on the dilution factor. The RTDs are well described by a model in which it is assumed that the particles maintain a constant radial position in the tubes as they pass through the crystalliser.

Step-change tests conducted imply that mass of particles that leave the crystalliser is *less* than that fed to it. This apparent loss of mass can be explained if the particles are sticking to the walls of the lumen. It also explains how the RTD may be described by a model which is physically implausible.

10.2.5 Continuous crystallisation

In Chapter 9 the growth and aggregation of calcium oxalate in a continuous system, the tubular crystalliser, is investigated. Calcium oxalate seeds were fed to the crystalliser together with either a saline solution, saturated with respect to calcium oxalate, or a metastable solution. The shear rate in the crystalliser was varied by using different lumen and jacket flowrates. Solutions with different calcium to oxalate ion ratios were used to study the effect of supersaturation. Full details of the conditions in each of the experiments are given in Tables 9.1 and 9.2.

Preliminary experiments revealed that the calcium oxalate crystals were sticking to the walls of the lumen in the crystalliser, and that breakage was also occurring. The experiments using saturated saline were used to investigate sticking and breakage. A moment form of the population balance was used to determine the sticking and breakage rates. It was found that:

- Sticking is well described by a size-independent formulation, and is a first order, irreversible process.
- The sticking rate constant is inversely proportional to the fluid shear rate in the crystalliser.

- Breakage is modelled by assuming that when breakage occurs crystals of any size may be formed.
- The breakage rate constant is directly proportional to the shear rate in the crystalliser.

The simultaneous growth, aggregation, sticking and breakage of calcium oxalate in the crystalliser was also analysed using a moment form of the population balance. The growth rate law determined in Chapter 4 was used to describe growth and the formulations mentioned above were used for sticking and breakage. Assuming a size-independent aggregation kernel it was found that:

- The aggregation rates in the crystalliser were at least two orders of magnitude lower than those in the batch system at the same supersaturation.
- The aggregation rate increased as the shear rate in the crystalliser increased.
- The aggregation rate did not depend strongly on the oxalate ion concentration.

These observations, which contrast with the results from the batch experiments reported in Chapter 4, can be explained by the aggregation mechanism proposed in Chapter 5. These findings highlight the effect of hydrodynamic conditions on aggregation. An analysis of the results using an aggregation kernel of the form of the shear kernel suggests that crystal shape may also have a significant effect on aggregation.

Finally, it is shown that even small inclinations of the crystalliser from the vertical increases the fraction of crystals that stick to the walls of the lumen in the crystalliser. This is significant for stone formation as it implies that in the kidney most crystals must spend nearly all their time in contact with the walls of the tubules.

These findings show that the tubular crystalliser may be a useful *in vitro* experimental system for studying the factors that affect calcium oxalate aggregation under conditions similar to those in the kidney.

10.3 RECOMMENDATIONS FOR FUTURE WORK

There are a number of opportunities for future work that arise from the findings of this thesis, in the areas of batch crystallisation, the aggregation mechanism and developing *in vitro* experimental systems for studying stone formation.

10.3.1 Batch crystallisation

Most studies of growth and aggregation in a batch system in the literature use some empirical parameter to measure growth and aggregation, rather than obtaining the rates of both mechanisms. This has led to some confusion in the literature as it is often difficult to compare these parameters. If the *true rates* of growth and aggregation are obtained then it is much easier to compare results from different experimental systems. The program *Batch* is a useful tool for extracting growth and aggregation rates from experimental data.

The batch experimental technique described in Chapter 3 could be used to further investigate the growth and aggregation of calcium oxalate. For example, all the experiments in this thesis used metastable solutions in which calcium was in excess. Similar experiments could be done with metastable solutions in which oxalate is in excess.

In the current work it was found that the aggregation rate was dependent on the oxalate ion concentration, is this simply because it is the limiting reactant or is there some other reason? Experiments such as those described above could answer this question, if the aggregation rate is dependent on the limiting reactant it will now depend on the calcium ion concentration.

Generally, while the results from this work expand the region of supersaturation over which growth and aggregation rates have been studied the use of solutions with different ratios of reactants and supersaturation remain an avenue for future work.

10.3.2 The aggregation mechanism

A model has been proposed for the aggregation of calcium oxalate in supersaturated solutions which assumes that for crystals to aggregate, firstly solute must diffuse to the point of contact and then deposit on the touching surface to cement the crystals together. A number of assumptions were made in this model, for example that the pore formed when the crystals are in contact is a right cylinder and also the effect of precipitation on the size of the pore was neglected.

The effect of a different geometry could be examined, for example the pore formed when crystals are in contact could be described as a cone. Also the effect of precipitation on the size of the pore could be studied. This will decrease the length and width of the pore, and will make the mathematical analysis of the diffusion and reaction processes more complicated, but will make the model more realistic.

Finally, the preliminary experiments mentioned in Chapter 9 using different particle size analysers to size aggregates of calcium oxalate crystals suggest that crystal shape may be an important factor in aggregation. It was shown in Chapter 9 that by “pre-growing” seed crystals it is possible to alter the size and presumably the shape of the aggregates. Seed crystals of different sizes could be used to investigate the effect of shape on aggregation.

10.3.3 *In vitro* experimental systems

The results from the experiments reported in Chapter 9 highlight the difference between *in vitro* experimental models. Using metastable solutions with the same relative supersaturation, the aggregation rate in the tubular crystalliser is some two orders of magnitude lower than that in the batch experiments. The tubular crystalliser is attractive as an *in vitro* experimental system as it has a tubular geometry, hydrodynamics similar to those in the kidney (and thus similar shear rates and RTDs), and can be operated at almost constant supersaturation.

Experiments similar to those described in Chapter 9, but over an extended range of shear rates and supersaturation could be conducted. This would lead to a more complete understanding of the dependence of aggregation on these parameters under conditions similar to those in the kidney.

Finally, other mechanisms and phenomena thought to be important in stone formation could be studied. For example, crystals could be nucleated in the crystalliser, the effect of different inhibitors could be quantified, and the crystalliser could also be operated with an “artificial” urine, an inorganic solution with many of the ions present in urine, or with human urine.

10.4 A CONCLUDING COMMENT

I conclude this thesis by describing how this work proceeded and why it is useful.

The work commenced as a study of the growth and aggregation of calcium oxalate in a new *in vitro* experimental system, the tubular crystalliser. Before commencing the crystallisation experiments in the crystalliser the batch experiments were conducted with the aim of generating data to compare with those to be obtained from the crystalliser. However, the initial batch experiments revealed the very interesting aggregation behaviour of calcium oxalate crystals documented in this thesis. Based on the success of these experiments a more comprehensive experimental program was performed with the aim of investigating the mechanism by which aggregation occurs. The final crystallisation experiments in the

crystalliser were complicated by the presence of sticking and breakage. However, these experiments still produce interesting and useful results, which can be compared with those from the batch system.

As mentioned elsewhere in this thesis, the size enlargement of calcium oxalate crystals by growth and aggregation has been widely studied as an important factor in human kidney stone formation. However, scant attention has been paid to understanding the *mechanisms* of growth and particularly aggregation. Similarly few studies have reported the *kinetics* of these mechanisms.

The main virtue of this study is that it investigates the *mechanisms* and reports the *kinetics* of the growth and aggregation of calcium oxalate in metastable saline solutions over a wide range of supersaturation and shear rates.

Appendix 1:

NOMENCLATURE

ROMAN

a	Surface area
a_{eq}^*	Dimensionless oxalate ion concentration at equilibrium
$a_{Ca^{2+}}, a_{Ox^{2-}}$	Activities of calcium and oxalate ions
A	Hamaker constant
A	Cross-sectional area
A_p	Surface area of cementing site
A_t	Tube cross-sectional area
A_T	Total crystal surface area
AP	Activity product
AP^*	Dimensionless activity product, eq 5.28
a, b, c	Constants in eq 2.30
a, b	Reactant concentrations, eq 5.5
a_i, b_i	Initial bulk oxalate and calcium concentrations
a_L, b_L	Reactant concentrations at the cementing site, eq 5.9
a^*, b^*	Dimensionless oxalate and calcium concentrations, eqs 5.29 and 5.30
B	Birth rate
\bar{B}	Moment form of the birth rate, eq 1.11
B_u	Source function
\hat{c}	Dimensionless concentration
C	Mass concentration of Drach <i>et al.</i> (1978), eq 2.4
C	Solute concentration, eq 7.25
C	Calcium ion concentration, eq 4.14
C_s	Mass concentration at equilibrium of Drach <i>et al.</i> (1978), eq 2.4

C_s	Calcium ion concentration at equilibrium, eq 4.14
$C(t)$	Solute concentration as a function of time
CV	Coefficient of variation
d	Diameter
\bar{d}	Shear diameter, eq 9.52
d_t	Tube diameter
D	Death rate
\bar{D}	Moment form of the death rate
\mathcal{D}	Diffusivity
\mathcal{D}_M	Effective diffusivity, eq 7.37
e	Charge of an electron
$E, E(t)$	Normalised differential residence time distribution curve
$f_{Ca^{2+}}, f_{Ox^{2-}}$	Fractions of total calcium and oxalate concentrations present as free ions
f_N, f_V	Fraction of crystals by number or volume that pass through the crystalliser
$F, F(t)$	Cumulative residence time distribution curve
F_D	Drag force
F_w	Force due to wall shear stress
g	Exponent of growth rate law, eq 4.14
G	Growth rate, frequently the linear rate of growth
G	Gibb's free energy, eq 5.45
G_v	Volume rate of growth
h	Separation between particles, eq 5.1
i	Ratio of the upper limit of adjacent size intervals
I	Degree of inhibition, eq 1.23
I	Ionic strength
J	Total number of size intervals, eq 3.16
J	Flux of reactant
k	Integer eq 1.9
k	Boltzmann's constant
k	A constant

k_B	Breakage rate constant
k_S	Sticking rate constant
k^*	Dimensionless cementing rate constant, eq 5.33
K_{CaOx}	Association constant for the complex ion, CaOx
K_{NaOx^-}	Association constant for the complex ion, NaOx ⁻
K_{so}	Association constant
K_{sp}	Solubility product
K'_{sp}	Solubility product in terms of total concentrations, eq 5.41
k_l, k_a, k_v	Shape factors
k, k', \hat{k}, \hat{k}'	Constants
k_{agg}, k_e, k_1, k_2	Constants
k_G, k_N, k'_G	Constants
K, K_e	Constants
L	Particle size
L	Axial length
\mathcal{L}	Laplace transform
L_p	Pore length
L_X	Upper size limit of channel X
L_{256}	Upper size limit of last channel in a size range
m_j	j^{th} moment
\dot{m}_j	Rate of change of the j^{th} moment
\tilde{m}_j	Partial j^{th} moment, eq 9.9
Mr	Molecular weight
M_T	Solids concentration
n	Population number density function
N	Number of particles
N	Supersaturation of Meyer and Smith (1975 a and b) and Nancollas and Gardner (1974), eqs 2.6, 2.7 and 2.9
N	Agitation rate
N	Flux of material, eq 7.25

N_i	Number of particles in the i^{th} size interval
N_t	Total number of particles, eq 4.14
N_A	Avogadro's number
N_T	Total number of particles
N_T	Number of lumen, eq 7.20
$N_{T,M}$	Total number of particles in a sample analysed by the Multisizer, eq 8.3
\dot{N}_1	Rate of change of particle number in the first size interval
$p(\epsilon, \nu)$	Breakage probability density function
Q	Volumetric flowrate
Q_S	Volumetric flowrate of the seed suspension
Q_L^i	Volumetric flowrate per lumen at the inlet of the tubular crystalliser, eq 7.21
r	Radial position
r	Particle radius
r	Cementing rate
\hat{r}, \hat{r}^*	Dimensionless cementing rates, eqs 5.16 and 5.22
$r_{c \rightarrow d}$	Rate of complex ion formation, eq 5.38
R	Tube radius
R	Experimental result, eq 1.23
Re	Reynolds number
R_i	Internal tube radius, eq 7.27
R_o	External tube radius, eq 7.27
s	Supersaturation of Drach <i>et al.</i> (1978), eq 2.4
s	Laplace domain variable
S	Supersaturation of DeLong and Briedis (1985), eq 2.10
S	Relative supersaturation, defined in eq 4.5
S	Parameter, eq 9.54
S^*	Supersaturation of Hounslow (1990), eq 2.14
SSE	Sum of square error, as defined in eq 4.1
t	Time

\bar{t}	Mean residence time
t^*	Critical time, 7.41
t_b	Break-through time, eq 9.23
t_{d1}, t_{d2}	Time delays, eq 7.34
t_k	Time at the end of the k^{th} sample, eq 8.4
T	Temperature
$T_{Ca^{2+}}, T_{Ox^{2-}}$	Total concentration of calcium and oxalate ions
\mathbf{u}	Velocity vectors of phase space, eq 1.8
u	Axial velocity
u_0	Centre-line (maximum) axial velocity
\bar{u}_L^i	Average axial velocity per lumen at the inlet of the tubular crystalliser, eq 7.39
U	Parameter, eq 3.16
v	Particle volume
v	Radial velocity
v_0	Maximum radial velocity
v_0	Volume of smallest particle counted by the Multisizer
v_s	Stoke's settling velocity
V	Volume
V_A	Attractive potential energy, eq 5.1
V_R	Repulsive potential energy, eq 5.2
V_T	Total particle volume
$V_{T,M}$	Total particle volume in a sample analysed by the Multisizer
w	Solids concentration
x	Size
x	Axial position
x	Dimensionless reactant concentration, eq 5.13
x	Mole fraction, eq 7.25
\bar{x}	Mean of a variable x
X	Channel number for the Multisizer size channels

X	Parameter, eq A8.26
y	Dimensionless reactant concentration, eq 5.14
Y	Parameter, defined in eq 8.12
z	Length

GREEK LETTERS

α	Degree of reaction, eq 4.14
α	Dilution factor, defined in eq 6.1
α'	Modified dilution factor, defined in eq 8.2
β	Aggregation kernel
β_0	Size-independent part of the aggregation kernel
$\beta_{0,A}$	Apparent size-independent aggregation rate constant, eq 9.52
γ	Surface energy
γ_{\pm}	Activity coefficient
$\overline{\gamma}_B$	Average shear rate for breakage, eq 9.34
$\overline{\overline{\gamma}}_B$	Average shear rate for breakage, eq 9.38
$\overline{\gamma}_S$	Average shear rate for sticking, eq 9.33
δ_M	Constant, eq 7.37
ΔC	Supersaturation of Hounslow <i>et al.</i> (1988)
ΔG	Change in Gibb's free energy
Δn	Number of moles deposited
ε	Particle volume
ε	Di-electric constant
ε	Fraction of length at the ends of the tubular crystalliser, eq 8.19
ε	Uncertainty in a variable, eq A3.3
ζ	Reactant ratio, eq 5.12
η	Fluid viscosity
η	Dimensionless radial position, eq 8.6
η	Fraction of material lost, eq 9.54
θ	Dimensionless time, defined in eq 7.6
$\overline{\theta}$	Dimensionless mean residence time

Θ	Parameter, eqs 2.24 to 2.27
κ	Parameter, eq 5.3
λ	Particle length
Λ	Parameter, eq 9.50
μ	Chemical potential
μ	Fluid viscosity
ρ	Density
ρ_s	Solids density
ρ_M	Molar density
σ	Relative supersaturation
σ_x	Population standard deviation of a variable x
$\sigma_{\bar{x}}$	Standard deviation in estimates of the mean of a variable x
τ_w	Wall shear stress
ϕ	Dimensionless modulus, defined in eq 5.11
ϕ	Dimensionless time, eq 8.25
ϕ_1	Dimensionless oxalate concentration, eq 5.20
ϕ_2	Dimensionless activity product, eq 5.21
$\Phi_0, \Phi_1, \Phi_2, \Phi_3$	Parameters, eqs 3.4 to 3.7
Ψ	Stream function, eq 8.6
Ψ_0	Surface Potential
Ψ_{m_3}, Ψ_{m_0}	Constant, eqs A8.15 and A8.21
$\hat{\psi}$	Dimensionless stream function, eq 8.8
$\omega_1, \omega_2, \omega_3$	Constants, eqs 7.31 and 7.32

SUPERSCRIPTS AND SUBSCRIPTS

agg	Aggregation
A	Component A
B	Component B
Ca^{2+}	Calcium ion
$CaOx$	Calcium oxalate complex ion

<i>cont</i>	Control conditions, eq 1.23
<i>cont</i>	Continuous operation, eq 9.21
<i>eq</i>	Equilibrium conditions
<i>expt</i>	Experimental values
<i>ext</i>	External coordinates of phase space
<i>g</i>	Growth
<i>i</i>	Size interval
<i>int</i>	Internal coordinates of phase space
<i>j</i>	An integer, for example j^{th} moment, or j^{th} derivative
<i>J</i>	Jacket
<i>L</i>	Lumen
<i>max</i>	Maximum
NaOx^-	Sodium oxalate complex ion
Ox^{2-}	Oxalate ion
<i>pred</i>	Predicted values
<i>t</i>	Time, t
<i>test</i>	Test conditions
0	Initial or inlet conditions
ϕ	Relating to the feed

Appendix 2:

LITERATURE CITED

- Abbas, M. and Tyagi, V.P., "Analysis of a hollow-fibre artificial kidney performing simultaneous dialysis and ultrafiltration", *Chem. Eng. Sci.*, **42**, No. 1, 113, (1987)
- Abegg, C.F., Stevens, J.D. and Larson, M.A., "Crystallization size distributions in continuous crystallizers when growth rate is size dependent", *A.I.Ch.E. J.*, **14**, No. 1, 118, (1968)
- Abegg, C.F. and Balakrishnan, N.S., "The tanks-in-series concept as a model for imperfectly mixed crystallisers", *Chem. Eng. Prog. Symp. Ser.*, **67**, No. 110, 88, (1971)
- Abramowitz, M. and Stegun, I.E., *Handbook of Mathematical Functions*, 9th printing, Dover Publications Inc., New York, 1960
- Acton, F.S., *Numerical Methods that Work*, Harper and Row, New York, 1970
- Allen, T., *Particle Size Measurement*, 3rd ed., Chapman and Hall, London, 1981
- Amicon Corporation, *Diaflo[®] Hollow Fiber Cartridges*, Publication No. I-116D, Amicon Corporation, 1986
- Andrews, J.C., Yarbrow, C.L., Golby, R.L. and Shell, I.T., "Studies on the mechanism of formation of renal calculi. I", *J. Urol.*, **73**, 930, (1955)
- Azoury, R., Garside, J. and Robertson, W.G., "Calcium oxalate precipitation in a flow system: an attempt to simulate the early stages of stone formation in the renal tubules", *J. Urol.*, **136**, 150, (1986)
- Azoury, R., Robertson, W.G., and Garside, J., "Generation of supersaturation using reverse osmosis", *Chem. Eng. Res. Des.*, **65**, 342, (1987)
- Babić - Ivančić, V., Füredi-Milhofer, H., Purgarić, B., Brnicević, N. and Despotović, Z., "Precipitation of calcium oxalates from high ionic strength solutions. III. The influence

- of reactant concentrations on the properties of the precipitates”, *J. Cryst. Growth*, **71**, 655, (1985)
- Baum, B., Holley, W. and White, R.A., “Hollow fibers, reverse osmosis, dialysis and ultrafiltration”, in: *Membrane Separation Processes*, Meares, P. (ed), 187, Elsevier, New York, 1976
- Becker, G.W. Jr. and Larson, M.A., “Mixing effects in continuous crystallisation”, *Chem. Eng. Prog. Symp. Ser.*, **65**, No. 95, 14, (1969)
- Beckman, J.R. and Farmer, R.W., “Bimodal CSD Barite due to agglomeration in an MSMR crystallizer”, *A.I.Ch.E. Symp. Ser.*, **83**, No. 253, 83, (1987)
- Berry, E.X., “Cloud droplet growth by collection”, *J. Atmos. Sci.*, **24**, 688, (1967)
- Bird, R.B., Stewart, W.E. and Lightfoot, E.N., *Transport Phenomena*, Wiley International Edition, John Wiley and Sons Inc., New York, 1960
- Blomen, L.J.M.J and Bijvoet, O.L.M, “Physicochemical considerations in relation to urinary stone formation”, *World J. Urol.*, **1**, 119, (1983)
- Blomen, L.J.M.J, Will, E.J., Bijvoet, O.L.M. and Van Der Linden, H., “Growth kinetics of calcium oxalate monohydrate. II. The variation of seed concentration”, *J. Cryst. Growth*, **64**, 306, (1983)
- Branson, S.H., “Factors in the design of continuous crystallisers”, *Brit. Chem. Eng*, **5**, 838, (1960)
- Brečević, Lj., Škrčić, D. and Garside, J., “Transformation of calcium oxalate hydrates”, *J. Cryst. Growth*, **74**, 399, (1986)
- Brečević, Lj., Kralj, D. and Garside, J., “Factors influencing the distribution of hydrates in calcium oxalate precipitation”, *J. Cryst. Growth*, **97**, 460, (1989)
- Brucati, A., Brucati, V. and Rizzuti, L., “Residence time distribution of solid particles in stirred vessels”, *Chem. Eng. Comm.*, **115**, 161, (1992)
- Canning, T.F. and Randolph, A.D., “Some aspects of crystallization theory: Systems that violate McCabe’s delta L law”, *A.I.Ch.E. J.*, **13**, No. 1, 5, (1967)

- Carnahan, B., Luther, H.A. and Wilkes, J.O., *Applied Numerical Methods*, Wiley, New York, 290, 1969
- Chen, W., Fisher, R.R. and Berg, J.C., "Particle flocculation", *Chem. Eng. Sci.*, **45**, 3003, (1990)
- Danckwerts, P.V., 1953a, "Continuous flow systems. Distribution of residence times", *Chem. Eng. Sci.*, **2**, No. 1, 1, (1953)
- Danckwerts, P.V., 1953b, "Theory of mixtures and mixing", *Research*, **6**, 355, (1953)
- Danckwerts, P.V., "The effect of incomplete mixing on homogeneous reactions", *Chem. Eng. Sci.*, **8**, Nos 1-2, 93, (1958)
- DeLong, J.D. and Briedis, D., "A technique for the study of growth rates of single crystals of sparingly soluble salts", *J. Cryst. Growth*, **71**, 689, (1985)
- Doaigey, A.R., "Occurrence, type and location of calcium oxalate crystals in leaves and stems of 16 species of poisonous plants", *Am. J. Bot.*, **78**, No.12, 1608, (1991)
- Drake, R.L., "A general mathematical survey of the coagulation equation", *Top. Curr. Aerosol Res.*, Part 2, No. 3, 201, Hidy, G.M. and Brock, J.R., (eds), Pergamon, New York, 1972
- Drach, G.W., Randolph, A.D. and Miller, J.D., "Inhibition of calcium oxalate dihydrate crystallization by chemical modifiers: I. Pyrophosphate and methylene blue", *J. Urol.*, **119**, 99, (1978)
- Drach, G.W., Kraljevich, Z. and Randolph, A.D., "Effects of high molecular weight urinary macromolecules on crystallization of calcium oxalate dihydrate", *J. Urol.*, **127**, 805, (1981)
- EQUIL89d Users Manual, Center for the Study of Lithiasis and Pathological Calcification, J.H Miller Health Centre, Gainesville, Florida, 1989
- Fellström B., Backman, U., Danielson, B.G., Holmgren K., Ljunghall S. and Wikström B., "Inhibitory activity of human urine on calcium oxalate crystal growth : effect of sodium urate and uric acid", *Clin. Sci.*, **62**, 509-514, (1982)
- Finlayson, B., "The concept of a continuous crystallizer. Its theory and application to in vivo and in vitro urinary tract models", *Invest. Urol.*, **9**, 258, (1972)

- Finlayson, B., "Calcium stones: some physical and clinical aspects", in: *Calcium Metabolism in Renal Failure and Nephrolithiasis*, David, D.S. (ed), John Wiley and Sons, New York, 1977
- Finlayson, B., "Physicochemical aspects of urolithiasis", *Kidney Int.*, **13**, 344, (1978)
- Finlayson, B., Khan, S.R. and Hackett, R.L., "Mechanisms of stone formation – An overview", *Scan. Electron Microsc.*, **3**, 1419, (1984)
- Finlayson, B. and Reid, F., "The expectation of free and fixed particles in urinary stone disease", *Invest. Urol.*, **15**, 442, (1978)
- Friedlander, S.K., *Smoke, Dust and Haze*, John Wiley and Sons, New York, 1977
- Gardner, G.L., "Nucleation and crystal growth of calcium oxalate trihydrate", *J. Cryst. Growth*, **30**, 158, (1975)
- Garside, J., Brečević, Lj. and Mullin, J.W., "The effect of temperature on the precipitation of calcium oxalate", *J. Cryst. Growth*, **57**, 233, (1982)
- Gelbard, F. and Seinfeld, J.W., "Numerical solutions of the dynamic equation for particulate systems", *J. Comput. Phys.*, **28**, 357, (1978)
- Gonzalez, J.E.G., Caldwell, R.G. and Valaitis, J., "Calcium oxalate crystals in the breast – Pathology and significance", *Am. J. Surg. Pathol.*, **15**, No. 6, 586, (1991)
- Grabenbauer, G.C. and Glatz, C.E., "Protein precipitation–analysis of particle size distribution and kinetics", *Chem. Eng. Comm.*, **12**, 203-219, (1981)
- Hackett, R.L. and Khan, S.R., "Presence of calcium oxalate crystals in the mammalian thyroid gland", *Scan. Microsc.*, **2**, No. 1, 241, (1988)
- Haggitt, R.C. and Pitcock, J.A., "Renal medullary calcifications: A light and electron microscopic study", *J. Urol.*, **106**, 342, (1971)
- Hartel, R.W., Gottung, B.E., Randolph, A.D. and Drach, G.W., "Mechanisms and kinetic modeling of calcium oxalate crystal aggregation in a urinelike liquor. Part I: Mechanisms", *A.I.Ch.E. J.*, **32**, No. 7, 1176, (1986)

- Hartel, R.W. and Randolph, A.D., "Mechanisms and kinetic modeling of calcium oxalate crystal aggregation in a urinelike liquor. Part II: Kinetic modeling", *A.I.Ch.E. J.*, **32**, No. 7, 1186, (1986)
- Hess, B., Nakagawa, Y. and Coe, F.L., "New spectrophotometric method for measuring calcium-oxalate-monohydrate aggregation in the absence of supersaturation", in: *Urolithiasis*, Walker, V.A., Sutton, R.A.L., Cameron, E.C.B., Pak, C.Y.K. and Robertson W.G., (eds), 55, Plenum Press, New York, (1989)
- Hiemenz, P.C., *Principles of Colloid and Surface Chemistry*, 2nd ed., Marcel Dekker Inc., New York, 1986
- Hostomsky, J. and Jones, A.G., "Crystallization and agglomeration kinetics of calcium carbonate and barium sulphate in the MSMPR crystalliser", *Industrial Crystallization 91*, Rojkowski, Z.H., ed., **1**, 2-049, 1993
- Hounslow, M.J., Ryall, R.L., Marshall, V.R., 1988a, "A discretized population balance for nucleation, growth and aggregation", *A.I.Ch.E. J.*, **34**, No 11, 1821, (1988)
- Hounslow, M.J., Ryall, R.L., Marshall, V.R., 1988b, "Modelling the formation of urinary stones", *Proc. CHEMECA 88*, 1097, Sydney, 1988
- Hounslow, M.J., "A discretised population balance for simultaneous nucleation, growth and aggregation", *Ph.D. Thesis*, University of Adelaide, Australia, 1990
- Hounslow, M.J. and Wynn, E.J.W., "Short-cut models for particulate processes", *Comput. Chem. Eng.*, **17**, No.5-6, 505, (1993)
- Hulburt, H.M. and Katz, S., "Some problems in particle technology. A statistical mechanical formulation", *Chem. Eng. Sci.*, **19**, 555, (1964)
- Human, H.J., van Enckevork, W.J.P. and Bennema, P., "Spread in growth rates on the (111), (100) and (110) faces of potash alum growing from aqueous solutions", *Industrial Crystallization 81*, Jancić, S.J. and de Jong, E.J., (eds), North-Holland, Amsterdam, 387, 1982
- Ilievski, D., "Modelling $\text{Al}(\text{OH})_3$ agglomeration during batch and continuous precipitation in supersaturated caustic aluminate solution", *Ph.D. Thesis*, University of Queensland, Australia, 1991

- IMSL Inc., *IMSL Users Manual*, Version 1.0, 640, IMSL Inc., Houston, Texas, 1987
- Ito, H. and Coe, F.L., "Acidic peptide and polyribonucleotide crystal growth inhibitors in human urine", *Am. J. Physiol.*, **233**, F455-F463, (1977)
- Jordan, W.R., Finlayson, B. and Luxenberg, M., "Kinetics of early time calcium oxalate nephrolithiasis", *Invest. Urol.*, **15**, 465, (1978)
- Karel, S.F. and Robertson, C.R., "Autoradiographic determination of mass-transfer limitations in immobilized cell reactors", *Biotech. Bioeng.*, **34**, No. 3, 320, (1989)
- Kavanagh, J.P., "Methods for the study of calcium oxalate crystallisation and their application to urolithiasis research", *Scan. Microsc.*, **6**, No. 3, 685, (1992)
- Khan, S.R., Finlayson, B. and Hackett, R.L., "Histologic study of the early events in oxalate induced intranephronic calculosis", *Invest. Urol.*, **17**, 199, (1979)
- Kohri, K., Garside, J. and Blacklock, N.J., "The role of magnesium in calcium oxalate urolithiasis", *Br. J. Urol.*, **61**, 107, (1988)
- Kohri, K., Garside, J. and Blacklock, N.J., "The effect of glycosaminoglycans on the crystallisation of calcium oxalate", *Br. J. Urol.*, **63**, 584, (1989)
- Kok, D.J., Papapoulos, S.E. and Bijvoet, O.L.M., "Crystal aggregation is a major element in calcium oxalate urinary stone formation", *Kidney Int.*, **37**, 51, (1990)
- Koutsoukos, P.G., Lam-Erwin, C.Y. and Nancollas, G.H., "Epitaxial considerations in urinary stone formation I. The urate-oxalate-phosphat system", *Invest. Urol.*, **18**, 178, (1980)
- Kreyszig, E., *Advanced Engineering Mathematics*, 6th ed., Wiley, New York, 1993
- Larson, M.A., White, E.T., Ramarayanan, K.A. and Berglund, K.A., "Growth rate dispersion in MSMPR crystallizers", *75th Ann. Meet. of A.I.Ch.E.*, Los Angeles, (1982)
- Levenspiel, O., *Chemical Reaction Engineering*, 2nd ed., John Wiley and Sons, New York, 1972
- Li, M.K., Blacklock, N.J. and Garside, J., "Effects of magnesium on calcium oxalate crystallisation", *J. Urol.*, **133**, 123, (1985)

- Ligabue, A., Fini, M. and Robertson, W.G., "Influence of urine on *in vitro* crystallization rate of calcium oxalate: determination of inhibitory activity by [¹⁴C]oxalate technique". *Clin. Chim. Acta* 98, 39-46, (1979)
- Low, G.C., "Agglomeration effects in aluminium trihydroxide precipitation", *Ph.D. Thesis*, University of Queensland, Australia, 1975
- Marković, M. and Füredi-Milhofer, H., "Precipitation of calcium oxalates from high-ionic-strength solutions", *J. Chem. Soc., Faraday Trans. 1*, **84**, No.5, 1301, (1988)
- Marshall, V.R. and Ryall, R.L., "Investigation of urinary calculi", *Br. J. Hosp. Med.*, **26**, No. 4, 389, (1981)
- McCabe, W.L., "Crystal growth in aqueous solutions", *Ind. Eng. Chem.*, **21**, No. 1, 30, (1929)
- Meyer, J.L. and Smith, L.H., 1975a, "Growth of calcium oxalate crystals I. A model for urinary stone growth", *Invest. Urol.*, **13**, 31, (1975)
- Meyer, J.L. and Smith, L.H., 1975b, "Growth of calcium oxalate crystals II. Inhibition by natural urinary crystal growth inhibitors", *Invest. Urol.*, **13**, 36, (1975)
- Miller, G.H., Vermeulen, C.W. and Moore, J.D., "Calcium oxalate solubility in urine: Experimental Urolithiasis XIV", *J. Urol.*, **79**, 607, (1958)
- Miller, J.D., Randolph, A.D. and Drach, G.W., "Observations upon calcium oxalate crystallization kinetics in simulated urine", *J. Urol.*, **117**, 342, (1977)
- Muller, H., "Zur allgemeinen theorie der raschen koagulation", *Kolloidchemische Beihefte*, **27**, 223, (1928)
- Mullin, J.W., *Crystallization*, 3rd ed., Butterworth-Heinemann, Oxford, 1993
- Multisizer II Users Manual, Coulter Electronics Ltd, Luton, England, 1987
- Muralhidar, R. and Ramkrishna, D., "An inverse problem in agglomeration kinetics", *J. Colloid Interface Sci.*, **112**, 348, (1986)
- Nancollas, G.H., "Physical chemistry of crystal nucleation, growth and dissolution of stones", in: *Renal tract stone. Metabolic basis and clinical practice*, Wickham, J.E.A. and Buck, A.C., (eds), 71, Churchill Livingstone, London, 1990

- Nancollas, G.H. and Gardner, G.L., "Kinetics of crystal growth of calcium oxalate monohydrate", *J. Cryst. Growth*, **21**, 267, (1974)
- Nielsen, A.E., "The kinetics of calcium oxalate precipitation", *Acta Chem. Scand.*, **14**, 1654, (1960)
- Nielsen, A.E., "Electrolyte crystal growth mechanisms", *J. Cryst. Growth*, **67**, 289-310, (1984)
- Nielsen, A.E. and Toft, J.M., "Electrolyte crystal growth kinetics", *J. Cryst. Growth*, **67**, 278-288, (1984)
- Ouchiyama, N. and Tanaka, T., "Physical requisite to appropriate granule growth rate", *Ind. & Eng. Chem. Process Des. Dev.*, **21**, 35, (1982)
- Pak, C.Y.C., "Calcium urolithiasis: is it analogous to bone formation ?", *Calc. Tiss. Res.*, **26**, 195, (1978)
- Pangrle, B.J., Walsh, E.G., Moore, C.S. and DiBiasio, D., "Magnetic resonance imaging of laminar flow in porous tube and shell systems", *Chem. Eng Sci.*, **47**, No. 3. 517, (1992)
- Park, J.K. and Chang, H.N., "Flow distribution in the fiber lumen side of a hollow-fiber module", *A.I.Ch.E. J.*, **32**, No. 12, 1937, (1986)
- Perera, C.O., Hallett, I.C., Nguyen, T.T. and Charles, J.C., "Calcium oxalate crystals – The irritant factor in kiwifruit", *J. Food Sci.*, **55**, No.4, 1066, (1990)
- Pich, J., "Theory of gravitational deposition of particles from laminar flows in channels", *J. Aerosol Sci.*, **3**, 351, (1972)
- Prien, E.L. and Prien, E.L., Jr., "Composition and structure of urinary stones", *Am. J. Med.*, **45**, 654, (1968)
- Pulvermacher, B. and Ruckenstein, E., "Similarity solutions of population balances", *J. Colloid Interface Sci.*, **46**, No. 3, 428, (1974)
- Ramkrishna, D., "The status of population balances", *Revs. in Chem. Eng.*, **3**, No 1, 49, (1985)
- Randolph, A.D. and Drach, G.W., "Some measurements of calcium oxalate nucleation and growth rates in urine like liquors", *J. Cryst. Growth*, **53**, 195, (1981)

- Randolph, A.D. and Larson, M.A., *Theory of Particulate Processes*, 2nd ed., Academic Press, New York, 1988
- Robertson, W.G. and Nordin, B.E.C., "Physico-chemical factors governing stone formation", in: *Scientific foundations of urology*, Williams, D.I. and Chisholm, G.D., (eds), 254, Heinemann Medical, London, 1976
- Robertson, W.G. and Peacock, M., "Calcium oxalate crystalluria and inhibitors of crystallization in recurrent renal stone-formers", *Clin. Sci.*, **43**, 499, (1972)
- Robertson, W.G. and Peacock, M. and Nordin, B.E.C., "Calcium crystalluria in recurrent renal-stone-formers", *Lancet*, **2**, 21, (1969)
- Robertson, W.G. and Peacock, M. and Nordin, B.E.C., "Inhibitors of the growth and aggregation of calcium oxalate *in vitro*", *Clin. Chim. Acta*, **43**, 31, (1973)
- Robertson, W.G. and Scurr, D.S., "Modifiers of calcium oxalate crystallization found in urine. I. Studies with a continuous crystallizer using an artificial urine", *J. Urol.*, **135**, 1322, (1986)
- Rodgers, A.L. and Garside, J., "The nucleation and growth kinetics of calcium oxalate in the presence of some synthetic urine constituents", *Invest. Urol.*, **18**, 484, (1981)
- Rushton, H.G., Spector, M., Rodgers, A.L., Hughson, M. and Magura, C.E., "Developmental aspects of calcium oxalate tubular deposits and calculi induced in rat kidneys", *Invest. Urol.*, **19**, No. 3, 52, (1981)
- Ryall, R.L., "The formation and investigation of urinary calculi", *Clin. Biochem. Revs.*, **10**, 149, (1989)
- Ryall, R.L., Ryall, R.G. and Marshall, V.R., 1981a, "Interpretation of particle growth and aggregation patterns obtained from the Coulter Counter: a simple theoretical model", *Invest. Urol.*, **18**, 396, (1981)
- Ryall, R.L., Bagley, C.J. and Marshall, V.R., 1981b, "Independent assessment of the growth and aggregation of calcium oxalate crystals using the Coulter Counter", *Invest. Urol.*, **18**, 401, (1981)

- Ryall, R.L., Harnett, R.M. and Marshall, V.R., 1981c, "The effect of urine, pyrophosphate and glycosaminoglycans on the growth and aggregation of calcium oxalate crystals *in vitro*", *Clin. Chim. Acta*, **112**, 349, (1981)
- Ryall, R.G, Ryall, R.L. and Marshall, V.R., "A computer model for the determination of extents of growth and aggregation of crystals from changes in their size distribution", *J. Cryst. Growth*, **76**, 290, (1986)
- Sarig, S., Azoury, R., Lerner, E. and Kahana, F., "Assessment of aggregation of calcium oxalate-containing crystals", in: *Urolithiasis*, Walker, V.A., Sutton, R.A.L., Cameron, E.C.B., Pak, C.Y.K. and Robertson W.G., (eds), 151, Plenum Press, New York, (1989)
- Sastry, K.V.S. and Fuerstenau, D.W., "Size distribution of agglomerates in coalescing dispersed phase systems", *Ind. & Eng. Chem. Fundam.*, **9**, No. 1, 145, (1970)
- Sastry, K.V.S., "Similarity size distribution of agglomerates during their growth by coalescence in granulation or green pelletization", *Int. J. Miner. Process.*, **2**, 187, (1975)
- Schulz, E., "Studies on the influence of the flow field in the Pelvi-calyceal system (PCS) on the formation of urinary calculi", *Urol. Res.*, **15**, 281, (1987)
- Schulz, E. and Schneider, H.-J., "A new view of stone formation under the aspect of flow dynamics", in: *Urolithiasis: Clinical and basic research*, Smith, L.H., Robertson, W.G. and Finlayson, B., (eds), 533, Plenum Press, London, (1981)
- Schumann, T.E.W., "Theoretical aspects of the size distribution of fog particles", *Quart. J. Roy. Meteorol. Soc.*, **66**, 195, (1940)
- Seigneur, C., Hudischewskyj, A.B., Seinfeld, J.H., Whitby, K.T., Whitby, E.R., Brock, J.R. and Barnes H.M., "Simulation of aerosol dynamics: a comparative review of mathematical models", *Aerosol Sci. and Technol.*, **5**, 205, (1986)
- Shaw, D.J., *Introduction to Colloid and Surface Chemistry*, 3rd ed., Butterworths, London, 1980
- Sheehan, M.E. and Nancollas, G.H., "Calcium oxalate crystal growth: A new constant composition method for modelling urinary stone formation", *Invest. Urol.*, **17**, 446, (1980)
- Shinnar, R., "Use of residence and contact-time distributions in reactor design", in *Chemical reaction and reactor engineering*, Carberry, J.J. and Dekker, A.V., (eds), New York, 1987

- Shuster, J. and Schaeffer, R.L., "Economic impact of kidney stones in white male adults", *Urol.*, **14**, 327, (1984)
- Sierakowski, R., Finlayson, B., Landes, R.R., Finlayson, C.D. and Sierakowski, N., "The frequency of urolithiasis in hospital discharge diagnosis in the United States", *Invest. Urol.*, **15**, 438, (1978)
- Singh, R.P., Gaur, S.S., White, D.J. and Nancollas, G.H., "Surface effects in the crystal growth of calcium oxalate monohydrate", *J. Colloid Interface Sci.*, **118**, No. 2, 379, (1987)
- Škrtić, D., Marković, M., Komunjer, Lj. and Füredi-Milhofer, H., "Precipitation of calcium oxalates from high ionic strength solutions. I. Kinetics of spontaneous precipitation of calcium oxalate trihydrate", *J. Cryst. Growth*, **66**, 431, (1984)
- Škrtić, D., Füredi-Milhofer, H. and Marković, M., "Precipitation of calcium oxalates from high ionic strength solutions. V. The influence of precipitation conditions and some additives on the nucleating phase", *J. Cryst. Growth*, **80**, 113, (1987)
- Smit, D.J., Hounslow, M.J. and Paterson, W.R., "Aggregation and gelation – I. Analytical solutions for CST and batch operation", *Chem. Eng. Sci.*, **49**, No. 7, 1025, (1993)
- Smit, D.J., Paterson, W.R. and Hounslow, M.J., "Aggregation and gelation – II. Mixing effects in continuous flow vessels", *Chem. Eng. Sci.*, **49**, No. 18, pp.3147, (1994)
- Smith, J.M., *Chemical Engineering Kinetics*, 2nd ed., McGraw-Hill, London, 1970.
- Smoluchowski, M.V., "Drei Vorträge über Diffusion, Brownsche Bewegung und Koagulation von Kolloidteilchen", *Phys. Z.*, **17**, 557, (1916)
- Smoluchowski, M.V., "Mathematical theory of the kinetics of the coagulation of colloidal solutions", *Z. Phys. Chem.*, **92**, 129, (1917)
- Söhnel, O. and Garside, J., *Precipitation: Basic Principles and Industrial Applications*, Butterworth-Heinemann, Oxford, 1992
- Springmann, K.E., Drach, G.W., Gottung, B. and Randolph, A.D., "Effects of human urine on aggregation of calcium oxalate crystals", *J. Urol.*, **135**, 69, (1986)
- Stockmayer, W.H., "Theory of molecular size distributions and gel formation in polymerization", *J. Chem. Phys.*, **11**, 45, (1943)

- Tavare, N.S., "Mixing in continuous crystallizers", *A.I.Ch.E. J.*, **32**, No. 5, 705, (1986)
- Taylor, G., "Dispersion of soluble matter in solvent flowing slowly through a tube", *Proc. Roy. Soc.*, **A219**, 186, (1953)
- Thompson, P.D., "A transformation of the stochastic equation for droplet coalescence", *Proc. Int. Conf. Cloud Phys.*, Toronto, 115, (1968)
- Tomažič, B. and Nancollas, G.H., "The kinetics of dissolution of calcium oxalate hydrates", *J. Cryst. Growth*, **46**, 355, (1979)
- Tomson, M.B. and Nancollas, G.H., "Mineralisation kinetics: a constant composition approach", *Science*, **200**, 1059, (1978)
- van de Ven, T.G.M. and Mason, S.G., "The microrheology of colloidal dispersions VII. Orthokinetic doublet formation of spheres", *Colloid & Polymer Sci*, **255**, 468, (1977)
- Vermeulen, C.W. and Lyon, E.S., "Mechanisms of genesis and growth of calculii", *Am. J. Med.*, **45**, 648, (1968)
- Werness, P.G., Brown, C.M., Smith, L.H. and Finlayson, B., "EQUIL2: A BASIC computer program for the calculation of urinary supersaturation", *J. Urol.*, **134**, 1242, (1985)
- Westerterp, K.R., van Swaai, W.P.M. and Beenackers, A.A.C.M, *Chemical Reactor Design and Operation*, John Wiley and Sons, Chichester, 1984
- White, E.T. and Wright, P.G., "Magnitude of size dispersion effects in crystallization", *Chem. Eng. Prog. Symp. Ser.*, **67**, No. 110, 81, (1971)
- Will, E.J., Bijvoet, O.L.M., Blomen, L.J.M.J., and Van Der Linden, H., "Growth kinetics of calcium oxalate monohydrate. I. Method and validation", *J. Cryst. Growth*, **64**, 297, (1983)
- Yuan, S.W. and Finkelstein, A.B., "Laminar pipe flow with injection and suction through a porous wall", *Trans. A.S.M.E.*, **78**, 719, (1956)
- Zwietering, N. Th., "The degree of mixing in continuous flow systems", *Chem. Eng. Sci.*, **11**, No. 1, 1, (1959)

Appendix 3:

SOLUBILITY PRODUCT EXPERIMENTAL DATA

In Section 2.5.2 the results from batch crystallisation experiments were used to determine a value for the solubility product. In this appendix the data from these experiments are presented. Also the statistical method used to compare the experimental value of the solubility product with the one from EQUIL89d is explained.

A3.1 EXPERIMENTAL DATA

The experimental data are presented in Table A3.1.

Table A3.1 Crystal volume at equilibrium for solubility product experiments.

Experiment	Mean crystal volume ($\mu\text{m}^3/500\mu\text{l}$)	Standard deviation ($\mu\text{m}^3/500\mu\text{l}$)
25/6	8.95×10^6	1.97×10^5
28/6	8.42×10^6	1.30×10^5
29/6	8.55×10^6	3.25×10^5
30/6	8.62×10^6	1.79×10^5
1/7	8.55×10^6	1.57×10^5
11/7	8.76×10^6	1.66×10^5

The data reported are the mean total crystal volume from samples analysed using the Multisizer. There were a number of samples analysed from each flask in each experiment, however only the mean and standard deviation of all the samples are given. These were calculated using

$$\bar{x} = \sum_{i=1}^n \frac{x_i}{n}, \quad \sigma_x = \sqrt{\frac{1}{n-1} \sum_{i=1}^n (x_i - \bar{x})^2}$$

where x is the crystal volume in a sample and n is the number of samples analysed.

A3.2 CALCULATING THE SOLUBILITY PRODUCT

The solubility product as a function of the total calcium and oxalate concentrations is given by eq 2.33, re-produced here as

$$K_{sp} = \frac{\gamma_{\pm}^2 K_{CaOx} K_{NaOx} T_{Ca^{2+}} T_{Ox^{2-}}}{\gamma_{\pm}^2 K_{NaOx} (T_{Ca^{2+}} + T_{Ox^{2-}}) + K_{CaOx} (T_{Na^+} \gamma_{\pm} + K_{NaOx})} \quad (A3.1)$$

The computer package Microsoft Excel was used to produce a spreadsheet to calculate the values of the solubility product from eq A3.1. The total calcium and oxalate concentrations at equilibrium were determined by a mass balance. As described in Section 3.5.2, the total calcium and oxalate concentrations at any time are

$$T_{Ca^{2+}} = T_{Ca^{2+}}^0 - \Delta n \quad \text{and} \quad T_{Ox^{2-}} = T_{Ox^{2-}}^0 - \Delta n \quad (A3.2a \text{ and } b)$$

where the superscript, 0, refers to initial conditions and Δn is the number of moles of calcium oxalate deposited. The mass of the crystals in the samples at equilibrium can be calculated from the CSDs using eq 3.1. As the solids concentration of the seeds added at the start of the experiment is known (see Appendix 5) the mass of solid deposited can be determined, from which Δn can be evaluated.

A3.3 UNCERTAINTY IN THE SOLUBILITY PRODUCT

As the solubility product is not a product or a sum of the total concentrations, its standard deviation cannot be calculated using the methods outlined in Appendix 8. Instead an analysis based on a first order Taylor series for the solubility product was used.

The total concentrations may be written as

$$T_{Ca^{2+}} = \bar{T}_{Ca^{2+}} + \varepsilon \quad T_{Ox^{2-}} = \bar{T}_{Ox^{2-}} + \varepsilon \quad (A3.3a \text{ and } b)$$

where $\bar{T}_{Ca^{2+}}$ and $\bar{T}_{Ox^{2-}}$ are the mean total concentrations and ε is an uncertainty. For both concentrations the uncertainty may be expressed as a standard deviation. By the central limit theorem the standard deviation in estimates of the mean, $\sigma_{\bar{z}}$ and the population standard deviation, σ_z for a variable, Z , are related by

$$\sigma_{\bar{z}} = \frac{\sigma_z}{\sqrt{n}} \quad (A3.4)$$

where n is the population size. For the total concentrations

$$\varepsilon = \frac{\sigma_T C_a^{2+}}{\sqrt{n}} = \frac{\sigma_T O_x^{2-}}{\sqrt{n}} \quad (\text{A3.5})$$

Substituting eqs A3.3a and b into A3.1 gives K_{sp} as a function of the uncertainty in the total concentrations. The first order Taylor series for K_{sp} about $\varepsilon = 0$ is

$$K_{sp}(\varepsilon) = K_{sp}(0) + \left. \frac{\partial K_{sp}}{\partial \varepsilon} \right|_{\varepsilon=0} \varepsilon \quad (\text{A3.6})$$

Now $K_{sp}(0)$ is the value of K_{sp} from eq A3.1, evaluated with the mean total concentrations. The mean total concentrations can be evaluated from eqs A3.2a and b when $\varepsilon = 0$. Thus the uncertainty in K_{sp} is given by the second term on the right hand side of eq A3.6. As the uncertainty may be written as a standard deviation

$$\sigma_{K_{sp}} = \left. \frac{\partial K_{sp}}{\partial \varepsilon} \right|_{\varepsilon=0} \frac{\sigma_T C_a^{2+}}{\sqrt{n}} \quad (\text{A3.7})$$

A3.4 A STATISTICAL COMPARISON

The mean experimental value for the solubility product was compared with the value used by the program EQUIL89d. To test the mean, μ , of a normally distributed variable with an unknown variance, σ^2 , the t -distribution is used.

In this case the normally distributed variable is the experimental value of the solubility product. A two sided test at the 5% significance level was used to test the hypothesis that the experimental mean and the value from EQUIL89d, 2.24×10^{-9} , are the same against the alternative that they are different. If the hypothesis is true, the random variable, T , where

$$T = \left| \frac{\overline{K_{sp}} - 2.24 \times 10^{-9}}{\sigma_{K_{sp}}} \right|$$

has a t -distribution with $n - 1 = 5$ degrees of freedom (as there were six experiments). From Tables of the t -distribution, for example Kreyszig (1988), the critical value of T is 2.57.

From Table 2.2 the mean experimental value of K_{sp} is 2.01×10^{-9} . The standard deviation of K_{sp} is determined from eq A3.7. As the derivative of K_{sp} with respect to ε , at $\varepsilon = 0$, is quite complicated it was evaluated using the mathematical package, Mathematica. A value of

4.52×10^{-5} was obtained. From Table 2.2 the standard deviation in the total calcium concentration is 2.31×10^{-6} M. The value of $\sigma_{K_{sp}}$ is

$$\sigma_{K_{sp}} = \left. \frac{\partial K_{sp}}{\partial \epsilon} \right|_{\epsilon=0} \frac{\sigma_{T_{Ca^{2+}}}}{\sqrt{n}} = 4.52 \times 10^{-5} \times \frac{5.65 \times 10^{-6}}{\sqrt{6}} = 1.04 \times 10^{-10}$$

and the value of T is

$$T = \left| \frac{\overline{K_{sp}} - 2.24 \times 10^{-9}}{\sigma_{K_{sp}}} \right| = \left| \frac{2.01 \times 10^{-9} - 2.24 \times 10^{-9}}{1.04 \times 10^{-10}} \right| = 2.21$$

This value is less than the critical value and the hypothesis that the values of the solubility product are the same is accepted.

Appendix 4:

EXPERIMENTAL ANALYSIS PROCEDURES

A4.1 PARTICLE SIZE ANALYSIS

Nearly all the crystal size distributions (CSDs) reported in this thesis were obtained using a Coulter Multisizer II, the features that make this unit attractive are its high resolution, ability to determine the CSD by number and volume, and ease and speed of operation. Some CSDs reported in Chapter 5 were obtained using an Elzone 280 PC, however this unit works on the same principal as the Multisizer.

To obtain meaningful data from the Multisizer care must be taken to ensure it is operated correctly. For example, electrical noise, impure electrolyte, high levels of coincidence and many other factors may cause the Multisizer to give a CSD that is not representative of the sample analysed. Complete knowledge of the operation of the Multisizer comes only from experience, the purpose of this section is to outline some of the more important considerations.

Orifice tube selection and maintenance

An orifice tube can measure a size range from approximately 1 to 60% of the orifice diameter. The actual size range depends on the set-up chosen as outlined below. In the current work the size range of interest was 2 to 32 μm , which was easily covered by a single 70 μm orifice.

During operation the orifice must be kept very clean to obtain the most accurate results. After use the orifice and sampling system of the Multisizer were thoroughly rinsed with filtered (0.22 μm) 0.15 M saline. Periodically the orifice was cleaned by soaking in concentrated hydrochloric acid.

Size span

The number and progression type, arithmetic or geometric, of the channels and the size range spanned are determined by the set-up chosen. The size range spanned is determined by setting the aperture current and gain on the electrodes in the orifice. While various combinations of aperture current and gain will give a desired size range, it is recommended that the current should not be too high, as this can cause electrical noise.

Calibration

Each orifice must be calibrated before it can be used to determine CSDs. The calibration procedure is well documented in the Multisizer Users manual, and makes use of latex particles of a known size with a narrow distribution. Calibrations were checked using latex of a size different to that used for calibration.

Electrolyte

The main function of the electrolyte is to provide good electrical conductivity. The solutions used in the current work were all basically 0.15 M saline solutions. A saline solution of this ionic strength is a satisfactory electrolyte according to the Multisizer Users manual. The electrolyte was prepared using analytical grade chemicals and distilled water only. As previously mentioned the electrolyte was 0.22 μm filtered before use.

Noise

There are three main sources of noise in the Multisizer. The first is due to external factors, such as dust and other contaminants in the electrolyte, loose electrical connections, or the presence of air bubbles. The second source is due to the internal electronics, and the final is due to external electro-magnetic sources, such as other instruments. All these sources were negligible in the current work as verified from background counts. An electrolyte that has been filtered many times will still register counts on the Multisizer, which arise from contaminants and electrical noise. In the current work, background counts were regularly taken and were always low and reproducible.

Coincidence

If the concentration of particles in a sample is too high, two or more particles may pass through the sensing zone in the orifice at once and be counted as one large particle. The Multisizer has a coincidence correction feature, which can be used when the count is by sample volume. This feature was utilised, and all counts taken were of a volume of 500 μl . However, the Multisizer Users manual recommends that coincidence correction is only valid at low levels of coincidence. The level of coincidence in the samples analyzed in the current work were below the acceptable level.

A4.2 ATOMIC ABSORPTION SPECTROSCOPY

Calcium ion concentration was determined by atomic absorption spectroscopy, this technique utilises the characteristic absorption at 422.7 nm of calcium ions in a flame. All analysis were performed using a Varian AA-875 Atomic Absorption Spectrophotometer.

The samples were prepared for analysis as follows. A sample of approximately 5ml was 0.22 μm filtered, to remove an calcium oxalate crystals, and then acidified by the addition of one drop of concentrated (10 M) hydrochloric acid, to prevent any further precipitation.

Prior to analysis all samples must be diluted in a Lanthanum Chloride diluent, nominally a 1:100 dilution. The purpose of this is to ensure all calcium ions are present in their free state rather than being bound with other ions.

A4.3 SCANNING ELECTRON MICROSCOPY

The method used to prepare samples for examination under the electron microscope are as follows. A 5 ml aliquot of the solution was filtered (0.22 μm) and the filter paper rinsed with 2 ml of filtered (0.22 μm) distilled water. The filter paper was dried in air, mounted on an aluminium stub and coated with gold (200 s; SEM Autocoating Unit E5200, Polaron Equipment Ltd.). The stubs were examined using an ETEC Autoscan electron microscope (Siemens AG) at an operating voltage of 20 kV.

Appendix 5:

SEED SUSPENSION DATA

In this appendix the data and method used to determine the solids concentration of the seed suspension used in the batch crystallization experiments described in Chapter 3 are presented.

A5.1 EXPERIMENTAL DATA

As outlined in Section 3.3.2, before starting many of the batch experiments a small volume of the seed suspension was added to 0.15 M saline, saturated with respect to calcium oxalate, and samples analysed by the Multisizer. The values of the total crystal volume obtained from each experiment, as well as the mean and standard error in the mean are given in Table A5.1, on the following page.

A5.2 CALCULATING THE SOLIDS CONCENTRATION

The mass of crystals per unit volume of sample is given by,

$$M_T = \rho_s V_T \quad (\text{A5.1})$$

where the density of calcium oxalate monohydrate is 2200 kg/m^3 and V_T is the total crystal volume obtained from the Multisizer, which has units of $\mu\text{m}^3/500 \mu\text{l}$. Using the above value for the density of calcium oxalate it can be shown that multiplying V_T by 4.4×10^{-9} will give the solids concentration in units of g/litre. Further, as described in Section 3.3.2, in the experiments 4 ml of the seed suspension was added to 200 ml of saturated saline, thus the solids concentration of the seed suspension may be calculated from V_T as measured by the Multisizer using the following expression

$$M_T = V_T \times 4.4 \times 10^{-9} \times 204/4 \quad (\text{A5.2})$$

Table A5.1 Total crystal volume in samples of the seed suspension.

Experiment	Total crystal volume ($\mu\text{m}^3/500 \mu\text{l}$)
11/7	3.52×10^6
13/7	3.61×10^6
14/7	3.86×10^6
16/7	3.61×10^6
17/7	3.86×10^6
20/7	3.50×10^6
23/7a	3.74×10^6
23/7b	3.53×10^6
4/8a	3.73×10^6
4/8b	3.40×10^6
5/8a	3.82×10^6
5/8b	3.70×10^6
Mean	3.66×10^6
Standard deviation	4.4×10^4

Appendix 6:

CONVERSION OF SIZE DISTRIBUTIONS TO CSDs WITH A $\sqrt[3]{2}$ PROGRESSION

In this appendix the method used to convert the CSDs from Multisizer format to CSDs with a $\sqrt[3]{2}$ progression is described.

A6.1 CONVERTING THE CSDs

As outlined in Section 3.6 the method used to convert the CSDs from the Multisizer format to CSDs with a $\sqrt[3]{2}$ progression was to identify the channels which contained an exact value in the $\sqrt[3]{2}$ progression. The Multisizer was set-up such that the lower and upper limits of the size domain were 2 μm and 64.286 μm respectively and there were 256 channels. Table A6.1 gives the values of a $\sqrt[3]{2}$ progression, starting at 2 μm , and the Multisizer channels that span these values.

The upper and lower limits of each channel were calculated from eq 3.15 with L_{256} being 64.286 μm . For example for channel 25, $X = 25$, and from eq 3.16

$$U = 256 \left(\frac{X}{J} - 1 \right) = 256 \left(\frac{25}{256} - 1 \right) = -231$$

Then from eq 3.17 the upper size limit is

$$L_{25} = L_{256} i^U = 64.286 \times (2^{1/50})^{-231} = 2.533 \mu\text{m}$$

The lower limit of channel 25 is the upper limit of channel 24, from eq 3.14

$$L_{24} = \frac{L_{25}}{2^{1/50}} = \frac{2.533}{2^{1/50}} = 2.498 \mu\text{m}$$

To convert the Multisizer size distribution to a CSD with a $\sqrt[3]{2}$ progression, the data from channels 9 to 24 were summed. Channel 25 contains the exact value of the $\sqrt[3]{2}$ progression. Linear interpolation was used to allocate the particles in this channel between the first and second intervals in the $\sqrt[3]{2}$ progression. The size range of channel 25 is $3.5 \times 10^{-2} \mu\text{m}$. The

Table A6.1 Multisizer channels containing a value in a $\sqrt[3]{2}$ progression.

$\sqrt[3]{2}$ Progression	Channel spanning $\sqrt[3]{2}$	Lower size limit (μm)	Upper size limit (μm)
2.0	9	2.0	2.029
2.52	25	2.498	2.533
3.17	42	3.162	3.206
4.0	58	3.947	4.002
5.04	75	4.996	5.066
6.35	92	6.324	6.412
8.0	108	7.894	8.004
10.08	125	9.992	10.132
12.70	142	12.948	12.825
16.0	158	15.789	16.009
20.16	175	19.985	20.264
25.40	192	25.296	25.649
32	208	31.578	32.019

difference between the exact value for the $\sqrt[3]{2}$ progression, 2.52 μm and the lower limit of channel 25, 2.498 μm is 2.2×10^{-2} μm . Thus the fraction of crystals in the first channel of the $\sqrt[3]{2}$ progression is

$$f = \frac{2.2 \times 10^{-2}}{3.5 \times 10^{-2}} = 0.63$$

and the fraction in the second channel is 0.37. A similar calculation can be done for each of the channels that contains an exact value of the $\sqrt[3]{2}$ progression.

A7.2 CONVERSION ERRORS

The Multisizer reports CSDs by number and volume, the number distribution can be calculated from the volume distribution, or vice versa as the average size in each channel is known. It is possible to convert either the number or volume CSDs from the Multisizer format to a $\sqrt[3]{2}$ progression using the method described in the previous Section. The conversion of the CSDs from the Multisizer format to a $\sqrt[3]{2}$ progression conserves the parameter that the CSD describes. However, there will be a discretization error in other properties calculated from these converted CSDs as crystals from a large number of small

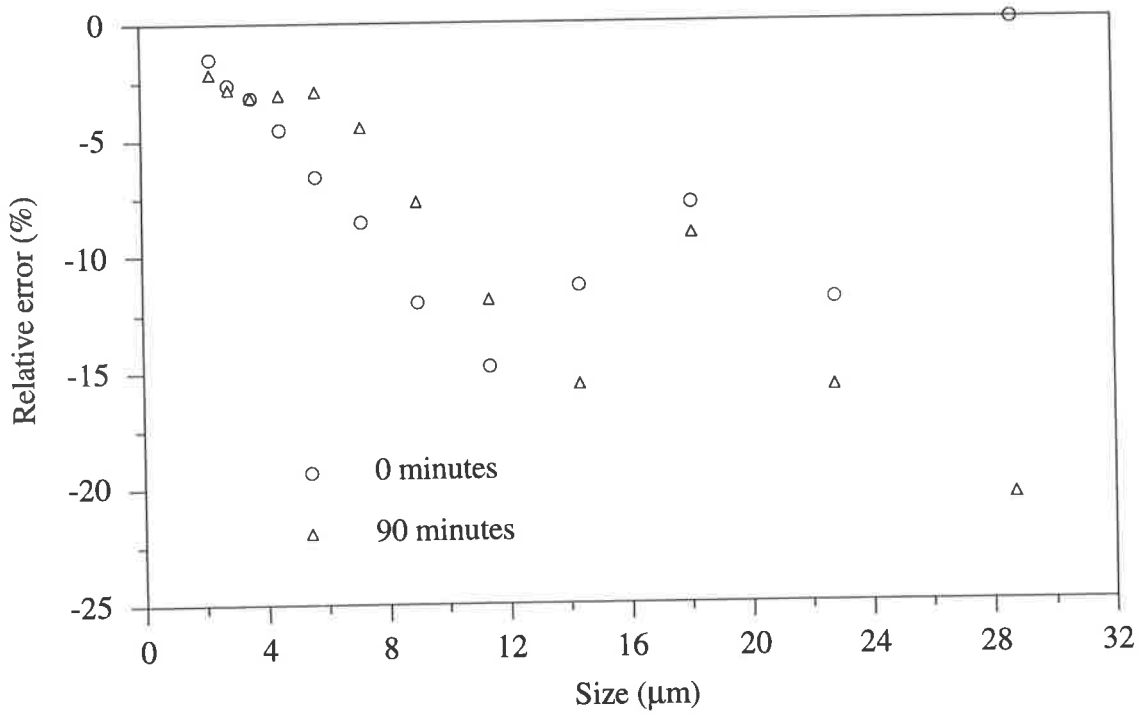
intervals, each with an average size, are allocated to one larger interval with one average size.

There is a discretization error in the volume distribution, with a $\sqrt[3]{2}$ progression, which is calculated from the Multisizer number distribution that has been converted to a $\sqrt[3]{2}$ progression. Similarly there is a discretization error in the number distribution, with a $\sqrt[3]{2}$ progression, which calculated from the Multisizer volume distribution that has been converted to a $\sqrt[3]{2}$ progression.

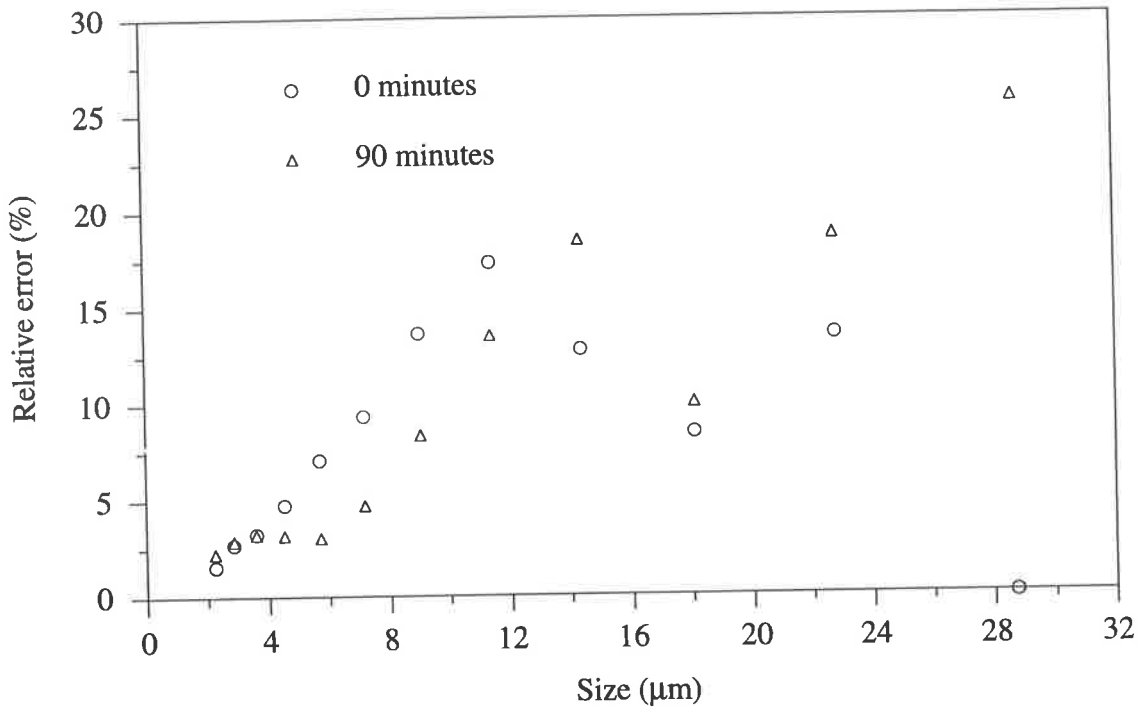
The relative error in the number CSD with a $\sqrt[3]{2}$ progression, is obtained by comparing the number CSD calculated from the volume distribution, which has been converted from Multisizer format to a $\sqrt[3]{2}$ progression, with the number distribution which has been converted from Multisizer format to a $\sqrt[3]{2}$ progression. The same argument can be used to calculate the relative error in the volume CSDs.

Figure A6.1(a) shows the relative error in each channel for the number distribution calculated from the volume distribution which was converted from Multisizer format to a $\sqrt[3]{2}$ progression. Figure A6.1(b) shows the relative error in each channel for the volume distribution calculated from the number distribution which was converted from Multisizer format to a $\sqrt[3]{2}$ progression. The data are from the batch experiment 11/7 at 0 and 90 minutes.

It can be seen that the errors are larger when the number distribution is used to calculate the volume distribution. Also the errors are greatest at the larger sizes, as there are fewer particles in these channels. As explained in Section 3.6, the number distributions were calculated from the volume distributions which had been converted from Multisizer format to a $\sqrt[3]{2}$ progression. There were two reasons for this, firstly the errors were lower using this method and secondly the ion concentrations and supersaturation were calculated from the crystal volume, so it is important to have as small an error as possible in the crystal volume.



(a)



(b)

Figure A6.1 The relative error in each channel for (a) a number CSD calculated from the converted Multisizer volume CSD and (b) a volume CSD calculated from the converted Multisizer number CSD

Appendix 7:

BATCH CRYSTALLISATION EXPERIMENTAL DATA

In this appendix the growth rates and aggregation rate constants calculated from the batch crystallisation experimental data are reported. The results are from the batch experiments described in Chapter 3 and analysed in Chapter 4.

The growth rates and aggregation rate constants were calculated from *Batch* as documented in Chapter 3. Details of the conditions in each experiment are given in Table 4.3.

The values of the relative supersaturation and oxalate ion concentrations were calculated from free ion concentrations using the method described in Chapter 2.

The units of the parameters reported are as follows: Time, minutes; growth rate, G , $\mu\text{m}/\text{min}$; β_0 , $\mu\text{l}/\text{min}$; $[\text{Ox}]$, M and the relative supersaturation, S is dimensionless.

Expt 11/7					Expt 13/7				
Time	G	β_0	$[\text{Ox}]$	S	Time	G	β_0	$[\text{Ox}]$	S
0	1.06E-01	7.75E-04	9.01E-05	1.93	0	9.23E-02	6.71E-04	8.83E-05	1.91
5	5.20E-02	3.86E-04	7.49E-05	1.74	5	4.34E-02	3.19E-04	7.45E-05	1.73
10	2.40E-02	2.32E-04	6.87E-05	1.65	10	2.20E-02	1.83E-04	6.97E-05	1.67
20	1.68E-02	1.91E-04	6.24E-05	1.57	20	1.74E-02	1.45E-04	5.98E-05	1.53
30	1.30E-02	1.37E-04	5.41E-05	1.45	30	1.07E-02	8.99E-05	5.35E-05	1.44
40	7.09E-03	9.45E-05	5.07E-05	1.40	40	8.14E-03	6.32E-05	4.96E-05	1.38
50	7.29E-03	6.85E-05	4.76E-05	1.35	50	8.41E-03	6.08E-05	4.57E-05	1.32
60	7.12E-03	4.15E-05	4.40E-05	1.29	60	6.83E-03	4.69E-05	4.13E-05	1.25
70	6.10E-03	2.27E-05	4.10E-05	1.24	70	5.00E-03	3.32E-05	3.88E-05	1.21
80	5.48E-03	3.38E-05	3.83E-05	1.20	80	4.56E-03	3.60E-05	3.63E-05	1.17
90	4.92E-03	5.36E-05	3.57E-05	1.16	90	3.73E-03	4.05E-05	3.42E-05	1.13

Expt 14/7				
Time	G	$\beta 0$	[Ox]	S
0	1.13E-01	6.71E-04	8.89E-05	1.92
5	4.96E-02	3.18E-04	7.21E-05	1.70
10	2.24E-02	1.93E-04	6.69E-05	1.63
20	1.93E-02	1.19E-04	5.70E-05	1.49
30	1.21E-02	7.41E-05	4.84E-05	1.36
40	7.73E-03	6.22E-05	4.49E-05	1.31
50	6.02E-03	4.44E-05	4.06E-05	1.24
60	3.51E-03	2.12E-05	3.87E-05	1.21
70	4.45E-03	2.85E-05	3.70E-05	1.18
80	3.63E-03	3.85E-05	3.40E-05	1.13
90	1.18E-04	2.87E-05	3.31E-05	1.11

Expt 16/7				
Time	G	$\beta 0$	[Ox]	S
0	7.67E-02	7.91E-04	9.07E-05	1.94
5	4.99E-02	4.70E-04	7.76E-05	1.77
10	3.10E-02	2.15E-04	6.94E-05	1.66
20	1.33E-02	9.15E-05	6.07E-05	1.54
30	8.22E-03	7.83E-05	5.70E-05	1.49
40	8.61E-03	5.22E-05	5.29E-05	1.43
50	7.72E-03	4.36E-05	4.87E-05	1.37
60	4.83E-03	4.44E-05	4.53E-05	1.31
70	3.20E-03	3.50E-05	4.38E-05	1.29
80	3.92E-03	2.57E-05	4.21E-05	1.26
90	4.87E-03	2.56E-05	3.99E-05	1.23

Expt 17/7				
Time	G	$\beta 0$	[Ox]	S
0	1.17E-01	8.74E-04	9.03E-05	1.93
5	5.04E-02	4.05E-04	7.26E-05	1.71
10	2.09E-02	1.79E-04	6.77E-05	1.64
20	1.45E-02	1.01E-04	5.85E-05	1.51
30	9.54E-03	7.03E-05	5.38E-05	1.44
40	9.32E-03	4.88E-05	4.91E-05	1.37
50	8.14E-03	5.20E-05	4.45E-05	1.30
60	6.55E-03	5.96E-05	4.08E-05	1.24
70	5.34E-03	4.71E-05	3.78E-05	1.19
80	4.06E-03	3.03E-05	3.52E-05	1.15
90	2.59E-03	8.35E-06	3.35E-05	1.12

Expt 20/7				
Time	G	$\beta 0$	[Ox]	S
0	1.06E-01	8.41E-04	9.07E-05	1.94
5	5.47E-02	4.31E-04	7.53E-05	1.74
10	2.73E-02	2.20E-04	6.83E-05	1.65
20	1.44E-02	1.16E-04	6.15E-05	1.55
30	1.13E-02	8.80E-05	5.55E-05	1.47
40	1.01E-02	8.44E-05	5.11E-05	1.40
50	8.56E-03	7.60E-05	4.61E-05	1.33
60	6.76E-03	6.87E-05	4.30E-05	1.28
70	6.17E-03	6.91E-05	3.96E-05	1.22
80	3.80E-03	4.84E-05	3.69E-05	1.18
90	7.70E-04	1.09E-05	3.58E-05	1.16

Expt 23/7a				
Time	G	$\beta 0$	[Ox]	S
0	9.14E-02	6.86E-04	8.84E-05	1.91
5	4.18E-02	3.05E-04	7.55E-05	1.75
10	1.95E-02	1.50E-04	7.13E-05	1.69
20	1.50E-02	9.61E-05	6.37E-05	1.59
30	1.40E-02	6.62E-05	5.81E-05	1.51
40	1.12E-02	4.33E-05	5.10E-05	1.40
50	7.63E-03	6.33E-05	4.75E-05	1.35
60	7.18E-03	6.65E-05	4.36E-05	1.29
70	4.94E-03	3.69E-05	4.05E-05	1.24
80	4.84E-03	4.47E-05	3.87E-05	1.21
90	7.17E-03	5.74E-05	3.57E-05	1.15

Expt 23/7b				
Time	G	$\beta 0$	[Ox]	S
0	7.08E-02	7.20E-04	8.76E-05	1.90
5	4.02E-02	3.65E-04	7.66E-05	1.76
10	2.59E-02	1.70E-04	7.11E-05	1.69
20	1.64E-02	1.02E-04	6.01E-05	1.54
30	1.03E-02	8.11E-05	5.62E-05	1.48
40	9.82E-03	7.11E-05	5.06E-05	1.40
50	5.68E-03	6.58E-05	4.68E-05	1.34
60	4.32E-03	4.86E-05	4.52E-05	1.31
70	5.37E-03	4.71E-05	4.27E-05	1.27
80	6.14E-03	4.22E-05	3.99E-05	1.23
90	7.21E-03	2.88E-05	3.65E-05	1.17

Expt 18/11				
Time	G	$\beta 0$	[Ox]	S
0	9.22E-02	7.39E-04	9.43E-05	1.98
5	5.00E-02	4.63E-04	8.04E-05	1.81
10	2.80E-02	2.98E-04	7.37E-05	1.72
20	1.64E-02	1.19E-04	6.49E-05	1.60
30	8.75E-03	4.71E-05	5.93E-05	1.52
40	6.38E-03	4.92E-05	5.69E-05	1.49
50	7.12E-03	4.71E-05	5.34E-05	1.44
60	7.91E-03	5.01E-05	5.02E-05	1.39
70	7.18E-03	5.67E-05	4.59E-05	1.32
80	5.57E-03	4.73E-05	4.32E-05	1.28
90	5.66E-03	2.31E-05	4.05E-05	1.24

Expt 19/11				
Time	G	$\beta 0$	[Ox]	S
0	5.74E-02	7.73E-04	8.91E-05	1.92
5	4.01E-02	4.59E-04	7.78E-05	1.78
10	2.50E-02	1.88E-04	7.06E-05	1.68
20	1.37E-02	1.10E-04	6.37E-05	1.59
30	1.15E-02	8.55E-05	5.73E-05	1.49
40	8.53E-03	7.40E-05	5.22E-05	1.42
50	7.60E-03	7.05E-05	4.86E-05	1.36
60	7.15E-03	5.73E-05	4.44E-05	1.30
70	4.74E-03	3.79E-05	4.11E-05	1.25
80	3.20E-03	2.53E-05	3.93E-05	1.22
90	3.00E-03	2.14E-05	3.77E-05	1.19

Expt 3/8a				
Time	G	$\beta 0$	[Ox]	S
0	1.90E-01	1.75E-03	1.40E-04	2.39
5	8.98E-02	1.08E-03	1.12E-04	2.08
10	4.43E-02	7.11E-04	1.01E-04	1.96
20	2.60E-02	3.46E-04	8.55E-05	1.77
30	1.83E-02	2.34E-04	7.64E-05	1.66
40	1.43E-02	1.85E-04	6.76E-05	1.55
50	1.01E-02	1.32E-04	6.20E-05	1.47
60	7.96E-03	8.29E-05	5.73E-05	1.41
70	7.40E-03	8.40E-05	5.37E-05	1.36
80	4.69E-03	6.31E-05	4.95E-05	1.30
90	1.63E-03	1.53E-05	4.87E-05	1.29

Expt 3/8b				
Time	G	$\beta 0$	[Ox]	S
0	1.63E-01	1.69E-03	1.37E-04	2.36
5	9.67E-02	1.25E-03	1.09E-04	2.05
10	5.73E-02	8.44E-04	9.30E-05	1.86
20	2.91E-02	4.22E-04	7.58E-05	1.65
30	2.11E-02	2.59E-04	6.40E-05	1.50
40	1.22E-02	1.42E-04	5.42E-05	1.37
50	7.11E-03	1.19E-04	5.10E-05	1.32
60	6.98E-03	9.40E-05	4.65E-05	1.26
70	4.71E-03	5.36E-05	4.34E-05	1.21
80	6.32E-03	3.47E-05	4.14E-05	1.18
90	1.13E-02	4.18E-05	3.65E-05	1.10

Expt 4/8a				
Time	G	$\beta 0$	[Ox]	S
0	1.95E-01	1.82E-03	1.42E-04	2.41
5	1.09E-01	1.32E-03	1.12E-04	2.08
10	6.10E-02	9.37E-04	9.48E-05	1.88
20	2.62E-02	4.03E-04	7.99E-05	1.70
30	1.72E-02	2.48E-04	7.01E-05	1.58
40	1.37E-02	1.76E-04	6.32E-05	1.49
50	9.26E-03	1.26E-04	5.65E-05	1.40
60	6.28E-03	1.12E-04	5.37E-05	1.36
70	6.51E-03	7.61E-05	5.01E-05	1.31
80	6.93E-03	2.36E-05	4.70E-05	1.26
90	8.79E-03	1.06E-05	4.29E-05	1.20

Expt 4/8b				
Time	G	$\beta 0$	[Ox]	S
0	1.65E-01	1.61E-03	1.38E-04	2.36
5	9.21E-02	1.04E-03	1.11E-04	2.07
10	5.32E-02	6.35E-04	9.65E-05	1.90
20	2.62E-02	3.60E-04	7.98E-05	1.70
30	1.36E-02	2.43E-04	7.05E-05	1.59
40	9.71E-03	1.57E-04	6.60E-05	1.53
50	1.36E-02	1.15E-04	6.06E-05	1.45
60	1.01E-02	8.56E-05	5.19E-05	1.33
70	2.30E-03	7.14E-05	4.97E-05	1.30
80	3.87E-03	4.13E-05	4.94E-05	1.30
90	1.04E-02	2.80E-05	4.55E-05	1.24

Expt 10/12				
Time	G	$\beta 0$	[Ox]	S
0	2.91E-01	2.16E-03	1.93E-04	2.79
5	1.47E-01	1.71E-03	1.44E-04	2.30
10	6.83E-02	1.53E-03	1.19E-04	2.04
15	4.99E-02	1.02E-03	1.09E-04	1.93
20	4.42E-02	7.00E-04	9.35E-05	1.76
30	1.70E-02	4.17E-04	8.45E-05	1.65
40	1.48E-02	2.40E-04	7.54E-05	1.54
50	1.35E-02	1.55E-04	6.84E-05	1.46
60	1.12E-02	1.31E-04	6.04E-05	1.36
70	8.88E-03	7.03E-05	5.57E-05	1.30
80	6.62E-03	4.00E-05	5.02E-05	1.22
90	1.05E-03	1.30E-04	4.79E-05	1.19

Expt 11/12				
Time	G	$\beta 0$	[Ox]	S
0	3.06E-01	2.18E-03	1.91E-04	2.77
5	1.39E-01	1.58E-03	1.40E-04	2.25
10	7.12E-02	1.43E-03	1.18E-04	2.02
15	5.58E-02	1.02E-03	1.02E-04	1.85
20	4.08E-02	6.55E-04	8.78E-05	1.69
30	1.87E-02	3.97E-04	7.58E-05	1.55
40	1.41E-02	2.24E-04	6.66E-05	1.44
50	1.19E-02	8.86E-05	5.95E-05	1.35
60	8.37E-03	6.59E-05	5.27E-05	1.26
70	5.84E-03	3.88E-05	4.95E-05	1.21
80	5.53E-03	3.61E-05	4.56E-05	1.16
90	4.06E-03	6.29E-05	4.27E-05	1.12

Expt 12/12				
Time	G	$\beta 0$	[Ox]	S
0	2.80E-01	2.10E-03	1.92E-04	2.78
5	1.44E-01	1.60E-03	1.44E-04	2.30
10	7.36E-02	1.49E-03	1.19E-04	2.03
15	5.22E-02	1.09E-03	1.06E-04	1.89
20	4.39E-02	7.71E-04	9.15E-05	1.73
30	2.05E-02	3.70E-04	7.74E-05	1.57
40	1.42E-02	2.03E-04	6.90E-05	1.47
50	1.22E-02	1.66E-04	6.15E-05	1.37

Expt 13/12				
Time	G	$\beta 0$	[Ox]	S
0	3.00E-01	2.26E-03	1.95E-04	2.81
5	1.46E-01	1.66E-03	1.45E-04	2.31
10	8.13E-02	1.55E-03	1.21E-04	2.06
15	5.42E-02	1.06E-03	1.03E-04	1.86
20	3.33E-02	7.16E-04	9.22E-05	1.74
30	1.80E-02	4.22E-04	8.19E-05	1.62
40	1.34E-02	2.43E-04	7.27E-05	1.51
50	1.15E-02	1.48E-04	6.71E-05	1.44
60	1.02E-02	9.43E-05	5.98E-05	1.35
70	8.21E-03	4.83E-05	5.54E-05	1.29
80	7.49E-03	1.19E-05	5.03E-05	1.22
90	4.97E-03	4.38E-05	4.66E-05	1.17

Expt 22/12a

Time	G	$\beta 0$	[Ox]	S
0	3.71E-01	2.18E-03	2.43E-04	3.10
5	1.78E-01	1.52E-03	1.77E-04	2.48
10	8.80E-02	2.09E-03	1.40E-04	2.11
15	5.15E-02	1.46E-03	1.26E-04	1.98
20	4.51E-02	1.23E-03	1.11E-04	1.82
30	2.63E-02	5.72E-04	9.52E-05	1.65
40	2.16E-02	4.07E-04	8.01E-05	1.49
50	1.38E-02	2.79E-04	6.94E-05	1.37
60	1.03E-02	1.78E-04	6.33E-05	1.29
70	8.63E-03	1.30E-04	5.67E-05	1.21

Expt 22/12b

Time	G	$\beta 0$	[Ox]	S
0	4.23E-01	2.69E-03	2.46E-04	3.13
5	1.75E-01	1.53E-03	1.73E-04	2.45
10	8.44E-02	1.87E-03	1.42E-04	2.14
15	5.59E-02	1.44E-03	1.23E-04	1.95
20	4.18E-02	9.46E-04	1.09E-04	1.80
30	2.29E-02	5.48E-04	9.11E-05	1.61
40	1.83E-02	2.86E-04	8.11E-05	1.50
50	2.18E-02	1.03E-04	6.85E-05	1.35

Expt 23/12

Time	G	$\beta 0$	[Ox]	S
0	3.97E-01	2.37E-03	2.47E-04	3.14
5	1.77E-01	1.41E-03	1.75E-04	2.47
10	8.56E-02	1.93E-03	1.39E-04	2.10
15	4.99E-02	1.40E-03	1.23E-04	1.95
20	4.23E-02	1.19E-03	1.09E-04	1.80
30	2.52E-02	4.60E-04	9.10E-05	1.61
40	1.80E-02	2.64E-04	7.78E-05	1.46
50	9.99E-03	1.66E-04	6.82E-05	1.35
60	5.39E-03	1.48E-04	6.48E-05	1.31
70	5.94E-03	2.28E-04	6.12E-05	1.27

Expt 24/12

Time	G	$\beta 0$	[Ox]	S
0	4.84E-01	3.12E-03	2.47E-04	3.14
5	1.79E-01	1.57E-03	1.65E-04	2.36
10	7.47E-02	1.68E-03	1.37E-04	2.08
15	5.07E-02	1.41E-03	1.19E-04	1.90
20	3.67E-02	1.04E-03	1.06E-04	1.77
30	2.85E-02	5.26E-04	9.11E-05	1.61
40	2.32E-02	2.87E-04	7.10E-05	1.38
50	1.07E-02	1.50E-04	6.11E-05	1.27
60	5.60E-03	1.02E-04	5.69E-05	1.21
70	4.18E-03	1.58E-04	5.36E-05	1.17

Expt 25/7

Time	G	$\beta 0$	[Ox]	S
0	1.04E-01	1.10E-03	1.45E-04	1.96
5	6.90E-02	7.80E-04	1.27E-04	1.79
10	4.43E-02	5.05E-04	1.14E-04	1.67
20	2.30E-02	2.80E-04	1.01E-04	1.54
30	1.61E-02	2.45E-04	9.19E-05	1.44
40	1.19E-02	1.86E-04	8.52E-05	1.38
50	1.16E-02	1.58E-04	7.98E-05	1.32
60	1.37E-02	1.42E-04	7.32E-05	1.25

Expt 26/7

Time	G	$\beta 0$	[Ox]	S
0	1.66E-01	1.60E-03	2.05E-04	1.99
5	8.31E-02	9.10E-04	1.79E-04	1.77
10	4.30E-02	4.64E-04	1.68E-04	1.67
20	3.03E-02	3.22E-04	1.52E-04	1.54
30	2.09E-02	2.39E-04	1.37E-04	1.41
40	1.08E-02	1.74E-04	1.30E-04	1.35
50	9.99E-03	1.55E-04	1.26E-04	1.31
60	1.39E-02	1.77E-04	1.19E-04	1.25

Expt 29/7

Time	G	$\beta 0$	[Ox]	S
0	1.01E-01	1.10E-03	9.09E-05	1.94
5	4.99E-02	5.94E-04	7.65E-05	1.76
10	2.59E-02	2.95E-04	7.11E-05	1.69
20	1.71E-02	1.64E-04	6.12E-05	1.55
30	1.04E-02	1.19E-04	5.65E-05	1.48
40	1.24E-02	1.22E-04	5.22E-05	1.42
50	1.15E-02	1.14E-04	4.55E-05	1.32
60	6.91E-03	9.05E-05	4.17E-05	1.26
70	4.29E-03	7.81E-05	3.91E-05	1.21
80	3.53E-03	7.41E-05	3.77E-05	1.19
90	4.79E-03	7.37E-05	3.58E-05	1.16

Expt 30/7

Time	G	$\beta 0$	[Ox]	S
0	9.34E-02	1.01E-03	9.29E-05	1.97
5	5.11E-02	5.79E-04	7.86E-05	1.79
10	2.76E-02	2.97E-04	7.19E-05	1.70
20	1.96E-02	1.82E-04	6.36E-05	1.58
30	1.63E-02	1.66E-04	5.47E-05	1.46
40	1.07E-02	1.28E-04	4.87E-05	1.37
50	6.45E-03	8.93E-05	4.47E-05	1.30
60	4.73E-03	6.95E-05	4.26E-05	1.27
70	5.38E-03	6.70E-05	4.02E-05	1.23
80	4.40E-03	7.03E-05	3.74E-05	1.19
90	1.83E-03	5.02E-05	3.59E-05	1.16

Expt 24/11a

Time	G	B0	[Ox]	S
0	9.67E-02	1.05E-03	9.47E-05	1.99
5	5.47E-02	6.46E-04	7.89E-05	1.79
10	2.99E-02	3.45E-04	7.13E-05	1.69
20	1.62E-02	2.03E-04	6.23E-05	1.57
30	1.09E-02	1.46E-04	5.67E-05	1.49
40	8.33E-03	1.32E-04	5.23E-05	1.42
50	7.36E-03	1.19E-04	4.89E-05	1.37
60	6.88E-03	9.70E-05	4.54E-05	1.32
70	5.14E-03	8.45E-05	4.25E-05	1.27
80	4.16E-03	7.27E-05	4.06E-05	1.24
90	4.22E-03	3.89E-06	3.86E-05	1.20

Expt 24/11b

Time	G	B0	[Ox]	S
0	7.88E-02	1.07E-03	9.27E-05	1.96
5	5.02E-02	7.39E-04	7.86E-05	1.79
10	2.93E-02	3.97E-04	7.09E-05	1.68
20	1.48E-02	2.72E-04	6.29E-05	1.57
30	1.22E-02	2.02E-04	5.77E-05	1.50
40	9.61E-03	1.80E-04	5.20E-05	1.42
50	6.59E-03	1.61E-04	4.91E-05	1.37
60	6.06E-03	1.13E-04	4.61E-05	1.33
70	6.36E-03	7.28E-05	4.36E-05	1.29
80	5.96E-03	6.78E-05	4.03E-05	1.23
90	3.48E-03	6.02E-05	3.82E-05	1.20

Expt 25/11

Time	G	B0	[Ox]	S
0	7.03E-02	7.93E-04	9.48E-05	1.99
5	4.91E-02	5.38E-04	8.19E-05	1.83
10	3.02E-02	3.22E-04	7.33E-05	1.72
20	1.40E-02	2.10E-04	6.69E-05	1.63
30	1.19E-02	1.39E-04	6.05E-05	1.54
40	1.00E-02	1.06E-04	5.59E-05	1.47
50	7.60E-03	1.13E-04	5.11E-05	1.40
60	5.18E-03	1.01E-04	4.86E-05	1.36
70	4.14E-03	7.93E-05	4.62E-05	1.33
80	4.35E-03	9.36E-05	4.46E-05	1.30
90	6.60E-03	8.56E-05	4.20E-05	1.26

Expt 31/7

Time	G	B0	[Ox]	S
0	1.05E-01	4.54E-04	9.20E-05	1.95
5	4.67E-02	1.95E-04	7.74E-05	1.77
10	2.18E-02	1.31E-04	7.24E-05	1.70
20	1.62E-02	6.78E-05	6.39E-05	1.59
30	1.17E-02	5.76E-05	5.74E-05	1.50
40	7.96E-03	4.18E-05	5.27E-05	1.43
50	5.55E-03	3.53E-05	4.96E-05	1.38
60	5.80E-03	4.16E-05	4.71E-05	1.34
70	6.61E-03	3.48E-05	4.38E-05	1.29
80	4.90E-03	2.58E-05	4.03E-05	1.23
90	1.55E-03	1.86E-05	3.86E-05	1.21

Expt 22/11a

Time	G	B0	[Ox]	S
0	6.85E-02	7.00E-04	9.27E-05	1.96
5	4.17E-02	3.45E-04	7.98E-05	1.80
10	2.35E-02	1.35E-04	7.31E-05	1.71
20	1.49E-02	9.25E-05	6.51E-05	1.60
30	1.16E-02	6.30E-05	5.80E-05	1.50
40	8.37E-03	5.28E-05	5.29E-05	1.43
50	6.44E-03	3.75E-05	4.90E-05	1.37
60	5.58E-03	2.31E-05	4.59E-05	1.32
70	4.55E-03	1.90E-05	4.29E-05	1.27
80	2.96E-03	2.22E-05	4.08E-05	1.24
90	1.59E-03	1.96E-05	3.95E-05	1.22

Expt 22/11b

Time	G	B0	[Ox]	S
0	6.40E-02	6.37E-04	9.02E-05	1.93
5	4.00E-02	3.47E-04	7.84E-05	1.78
10	2.48E-02	1.61E-04	7.18E-05	1.70
20	1.51E-02	9.55E-05	6.27E-05	1.57
30	1.03E-02	6.85E-05	5.67E-05	1.49
40	8.42E-03	4.44E-05	5.22E-05	1.42
50	7.39E-03	3.36E-05	4.79E-05	1.35
60	5.76E-03	2.45E-05	4.43E-05	1.30
70	5.19E-03	2.45E-05	4.16E-05	1.25
80	4.05E-03	2.49E-05	3.85E-05	1.20
90	1.08E-03	1.19E-05	3.71E-05	1.18

Expt 22/11c

Time	G	B0	[Ox]	S
0	8.49E-02	3.23E-04	9.28E-05	1.96
5	4.47E-02	1.39E-04	7.82E-05	1.78
10	2.34E-02	9.41E-05	7.11E-05	1.69
20	1.37E-02	5.37E-05	6.36E-05	1.58
30	1.11E-02	3.33E-05	5.65E-05	1.48
40	8.63E-03	3.50E-05	5.12E-05	1.40
50	6.19E-03	2.50E-05	4.65E-05	1.33
60	4.37E-03	1.10E-05	4.40E-05	1.29
70	4.01E-03	9.96E-06	4.13E-05	1.25
80	3.35E-03	8.16E-06	3.91E-05	1.21
90	2.90E-03	1.15E-05	3.72E-05	1.18

Expt 23/11a

Time	G	B0	[Ox]	S
0	8.78E-02	2.99E-04	9.36E-05	1.97
5	4.10E-02	1.16E-04	7.98E-05	1.80
10	1.98E-02	7.04E-05	7.47E-05	1.73
20	1.48E-02	4.49E-05	6.64E-05	1.62
30	1.16E-02	3.88E-05	5.95E-05	1.53
40	7.66E-03	3.07E-05	5.40E-05	1.45
50	4.95E-03	1.87E-05	5.11E-05	1.40
60	4.55E-03	1.51E-05	4.84E-05	1.36
70	5.04E-03	1.70E-05	4.59E-05	1.32
80	4.64E-03	1.48E-05	4.26E-05	1.27
90	2.68E-03	1.24E-05	4.04E-05	1.24

Expt 23/11b

Time	G	β_0	[Ox]	S
0	5.34E-02	3.68E-04	9.21E-05	1.96
5	4.50E-02	1.76E-04	8.12E-05	1.82
10	3.20E-02	7.48E-05	7.14E-05	1.69
20	1.36E-02	4.40E-05	6.27E-05	1.57
30	9.61E-03	3.86E-05	5.71E-05	1.49
40	7.81E-03	3.08E-05	5.22E-05	1.42
50	6.74E-03	2.43E-05	4.83E-05	1.36
60	5.68E-03	1.78E-05	4.45E-05	1.30
70	4.94E-03	1.13E-05	4.17E-05	1.26
80	3.65E-03	1.02E-05	3.86E-05	1.20
90	7.59E-04	1.57E-05	3.73E-05	1.18

Appendix 8:

ERROR ANALYSIS FOR GROWTH AND AGGREGATION RATES

In Chapter 4 growth rate and aggregation rate constants from batch crystallisation experiments are reported. As described in Section 3.3.3 CSDs were obtained from the four replicates of an experiment at regular time intervals. At each time interval, the CSDs from the replicates were averaged. The growth rate and aggregation rate constant were calculated from the averaged CSDs. In this appendix the errors associated with these parameters are calculated as is the error in the principal independent variables, the activity product and the oxalate ion concentration.

A8.1 ERROR ANALYSIS

Estimates of the uncertainty for a parameter Z which is a function of i different variables, X_i may be obtained using the propagation of error equation

$$\delta Z^2 = \sum_i \left(\frac{\partial Z}{\partial X_i} \right)^2 \delta X_i^2 \quad (\text{A8.1})$$

When the error, δX_i is equated to the standard deviation, σ_{X_i} then the methods of mathematical statistics can be used to obtain some useful results.

Let X and Y be un-correlated random variables and Z be dependent on X and Y . These variables take on values x , y and z , have mean values \bar{x} , \bar{y} and \bar{z} and have variances σ_x^2 , σ_y^2 and σ_z^2 . From eq A8.1 it follows that

$$\text{if } Z = XY \quad \text{then } \bar{z} = \bar{x}\bar{y} \quad (\text{A8.2a})$$

$$\text{and } \frac{\sigma_z^2}{\bar{z}^2} = \frac{\sigma_x^2}{\bar{x}^2} + \frac{\sigma_y^2}{\bar{y}^2} \quad (\text{A8.2b})$$

$$\text{if } Z = X^2 \quad \text{then } \bar{z} = \bar{x}^2 \quad (\text{A8.3a})$$

$$\text{and} \quad \frac{\sigma_z^2}{\bar{z}^2} = \frac{4\sigma_x^2}{\bar{x}^2} \quad (\text{A8.3b})$$

$$\text{if} \quad Z = kX \quad \text{then} \quad \bar{z} = k\bar{x} \quad (\text{A8.4a})$$

$$\text{and} \quad \sigma_z^2 = k^2\sigma_x^2 \quad (\text{A8.4b})$$

$$\text{if} \quad Z = X + Y \quad \text{then} \quad \bar{z} = \bar{x} + \bar{y} \quad (\text{A8.5a})$$

$$\text{and} \quad \sigma_z^2 = \sigma_x^2 + \sigma_y^2 \quad (\text{A8.5b})$$

In general the uncertainty in the best estimate of \bar{z} is required. By the central limit theorem the standard deviation in estimates of the mean, and the population mean are related by

$$\sigma_{\bar{z}} = \frac{\sigma_z}{\sqrt{n}} \quad (\text{A8.6})$$

where n is the sample size, in this case the number of replicates.

Growth rate analysis

From eq 1.22 the growth rate may be calculated from

$$G = \frac{1}{3m_2} \frac{dm_3}{dt} \quad (\text{A8.7})$$

Averaging over a set of replicates (i.e. at a constant time)

$$\bar{G} = \frac{1}{3m_2} \overline{\frac{dm_3}{dt}} \quad (\text{A8.8})$$

For two un-correlated variables from eq A8.2a

$$\bar{G} = \frac{1}{3m_2} \overline{\dot{m}_3} \quad (\text{A8.9})$$

Then from eq A8.2b

$$\left(\frac{\sigma_{\bar{G}}}{\bar{G}} \right)^2 = \left(\frac{\sigma_{m_2}}{m_2} \right)^2 + \left(\frac{\sigma_{\dot{m}_3}}{\dot{m}_3} \right)^2 \quad (\text{A8.10})$$

where the standard errors in the mean of the second moment, σ_{m_2} and the rate of change of the third moment, $\sigma_{\dot{m}_3}$ are calculated from eq A8.6.

The mean and variance in m_2 can be calculated directly from the experimental data. By rearranging eq A8.9, $\overline{\dot{m}_3}$ can be calculated from values of \overline{G} . The standard error, $\sigma_{\dot{m}_3}$, is more difficult to calculate and is determined as follows. An approximation for \dot{m}_3 is

$$\dot{m}_3 \approx \frac{\Delta m_3}{\Delta t} = \frac{m_3|_{t=t_{i+1}} - m_3|_{t=t_i}}{\Delta t} \quad (\text{A8.11})$$

From eq A8.4b

$$\sigma_{\dot{m}_3}^2 = \frac{1}{\Delta t^2} \sigma_{(m_3|_{t=t_{i+1}} - m_3|_{t=t_i})}^2 \quad (\text{A8.12})$$

Assuming the variance in m_3 is the same at each time interval

$$\sigma_{(m_3|_{t=t_{i+1}} - m_3|_{t=t_i})}^2 = \sigma_{m_3|_{t=t_{i+1}}}^2 + \sigma_{m_3|_{t=t_i}}^2 = 2\sigma_{m_3}^2 \quad (\text{A8.13})$$

Substituting into eq A8.11

$$\sigma_{\dot{m}_3}^2 = \frac{2\sigma_{m_3}^2}{\Delta t^2} \quad (\text{A8.14})$$

The variance in the rate of change of m_3 is now related to the variance in m_3 . The variance, $\sigma_{m_3}^2$ in this context is, in the language of analysis of variance, the *within group* variance, that would be seen by taking successive samples from a flask in which the CSD is not changing. This is denoted as $\sigma_{m_3,w}^2$.

Data from the experiments conducted to investigate the value of the solubility product reported in Section 2.5.2 were used to determine $\sigma_{m_3,w}^2$. In these experiments CSD's were obtained after 24 hours, when the system was at equilibrium. Under these conditions the CSD measured should be approximately constant as there is no growth or aggregation.

If a constant relative error is attributed to the samples collected with the Multisizer, the standard deviation in m_3 can be written in terms of its mean as

$$\sigma_{m_3,w} = \psi_{m_3} \overline{m_3} \quad (\text{A8.15})$$

where ψ_{m_3} is a constant. From the CSDs obtained from each long-time sample the mean and standard deviation in m_3 were calculated. The values from all the experiments were then averaged giving a value for ψ_{m_3} of 0.02. The data used are in Appendix 3.

Substituting eq A8.15, A8.14 and the expression for the standard errors in m_2 and $\overline{m_3}$ into eq A8.10 and re-arranging gives,

$$\sigma_{\overline{G}} = \overline{G} \sqrt{\frac{1}{n} \left(\frac{\sigma_{m_2}}{\overline{m_2}} \right)^2 + \frac{2}{n} \left(\frac{\psi_{m_3} \overline{m_3}}{3 \overline{m_2} \overline{G} \Delta t} \right)^2} \quad \text{A(8.16)}$$

Aggregation rate analysis

A similar analysis can be used for the aggregation rate constant. From eq 1.20 the mean value of the aggregation rate constant is

$$\overline{\beta_0} = \frac{-2}{m_0^2} \frac{dm_0}{dt} \quad \text{(A8.17)}$$

Uncertainty in m_0 arises largely from variation between replicates, the uncertainty in \dot{m}_0 arises from variations in consecutive measurements of m_0 from each replicate. Assuming these are not correlated

$$\overline{\beta_0} = \frac{-2}{m_0^2} \frac{dm_0}{dt} = \frac{-2}{m_0^2} \dot{m}_0 \quad \text{(A8.18)}$$

Using eqs A8.2b and A8.3b,

$$\left(\frac{\overline{\sigma_{\beta_0}}}{\overline{\beta_0}} \right)^2 = 4 \left(\frac{\overline{\sigma_{m_0}}}{\overline{m_0}} \right)^2 + \left(\frac{\overline{\sigma_{\dot{m}_0}}}{\overline{\dot{m}_0}} \right)^2 \quad \text{(A8.19)}$$

The mean and variance in m_0 are obtained from the experimental data. By re-arranging eq A8.18 $\overline{\dot{m}_0}$ can be calculated from $\overline{\beta_0}$. The standard errors, $\overline{\sigma_{m_0}}$ and $\overline{\sigma_{\dot{m}_0}}$ can be calculated from eq A76. Eqs A8.11 to A8.13 may also be written for m_0 rather than m_3 giving

$$\sigma_{\dot{m}_0}^2 = \frac{2 \sigma_{m_0,w}^2}{\Delta t^2} \quad \text{(A8.20)}$$

The standard deviation $\sigma_{m_0,w}$ was determined from the same data that were used to evaluate $\sigma_{m_3,w}$. Written in the same form as eq A8.15

$$\sigma_{m_0,w} = \psi_{m_0} \overline{m_0} \quad \text{(A8.21)}$$

From the experimental data the value of ψ_{m_0} is 0.033.

Substituting into eq A8.19 and re-arranging gives

$$\sigma_{\beta_0} = \bar{\beta}_0 \sqrt{\left(\frac{4}{n} \left(\frac{\sigma_{m_0}}{m_0} \right)^2 + \frac{2}{n} \left(\frac{-2 \psi_{m_0}}{\bar{\beta}_0 m_0 \Delta t} \right)^2 \right)} \quad (\text{A8.22})$$

Relative supersaturation analysis

The relative supersaturation depends on the value of the activity product, thus the error in the activity product must first be determined. From eq 2.1 the activity product is

$$AP = \gamma_{\pm}^2 [Ca^{2+}][Ox^{2-}] \quad (\text{A8.23})$$

In Section 2.6 it is shown that the fraction of both calcium and oxalate present as free ions was almost constant throughout an experiment, thus

$$AP \propto T_{Ca^{2+}} T_{Ox^{2-}} \quad (\text{A8.24})$$

The total calcium and oxalate concentrations can be related to the initial concentrations by a mass balance

$$\begin{aligned} AP &\propto (T_{Ca^{2+}}^0 - X)(T_{Ox^{2-}}^0 - X) \\ &= T_{Ca^{2+}}^0 T_{Ox^{2-}}^0 - (T_{Ca^{2+}}^0 + T_{Ox^{2-}}^0)X + X^2 \end{aligned} \quad (\text{A8.25})$$

where X is the change in the calcium and the oxalate ion concentrations. X can be calculated from the change in the third moment

$$X = \frac{\rho_s \pi k' (m_3 - m_3^0)}{6Mr} = k(m_3 - m_3^0) \quad (\text{A8.26})$$

where k is a constant that converts the third moment from $\mu\text{m}^3/500 \mu\text{l}$ to a concentration in mol/dm^3 . The value of k is 1.58×10^{-11} .

If $T_{Ca^{2+}}^0$ and $T_{Ox^{2-}}^0$ are denoted as C and O , then eqs A8.2a and b give

$$\begin{aligned}
\sigma_{AP}^2 &= \left(\frac{\sigma_C^2}{C^2} + \frac{\sigma_O^2}{O^2} \right) (\overline{CO})^2 \\
&+ \left(\frac{\sigma_X^2}{X^2} + \frac{\sigma_C^2}{C^2} \right) (\overline{XC})^2 + \left(\frac{\sigma_X^2}{X^2} + \frac{\sigma_O^2}{O^2} \right) (\overline{XO})^2 \\
&+ \sigma_{\overline{X}^2}^2
\end{aligned} \tag{A8.27}$$

From eq A8.26 it can be seen that X^2 is not an un-correlated variable, and thus eq A8.3b cannot be used for the variance of X^2 .

To evaluate the variance in AP, the mean and variance of X^2 , X , C and O are required. \overline{X} can be calculated directly from the experimental data. The values used for \overline{C} and \overline{O} were the initial concentrations, as the same metastable solution was used for all the replicates.

The standard error in the mean of X is calculated from eq A8.6 and the variance in X , using A8.4b and A8.5b, is

$$\sigma_X^2 = \sigma_{k(m_3 - m_3^0)}^2 = k^2 \left(\sigma_{m_3}^2 + \sigma_{m_3^0}^2 \right) \tag{A8.28}$$

Similarly the variance in X^2 , using eqs A8.2b, 3b and 5b, is given by

$$\begin{aligned}
\sigma_{X^2}^2 &= \sigma_{(k^2(m_3^2 - 2m_3m_3^0 + m_3^{02}))}^2 \\
&= k^4 \left(4\sigma_{m_3}^2 + 2 \left(\sigma_{m_3}^2 + \sigma_{m_3^0}^2 \right) + 4\sigma_{m_3^0}^2 \right) \\
&= 6k^4 \left(\sigma_{m_3}^2 + \sigma_{m_3^0}^2 \right)
\end{aligned} \tag{A8.29}$$

The value of σ_{m_3} , which is equivalent to the within group standard deviation, $\sigma_{m_{3,w}}$, can be calculated from eq A8.15. The value of $\sigma_{m_{3,w}^0}$ was determined from CSDs of the seed suspension used in the batch experiments. In the same form as eq A8.15

$$\sigma_{m_{3,w}^0} = \psi_{m_3^0} \overline{m_3^0} \tag{A8.30}$$

From the seed suspension data in Appendix 3 values for $\psi_{m_3^0}$ and $\overline{m_3^0}$ of 0.047 and $6.98 \times 10^6 \mu\text{m}^3/500 \mu\text{l}$ were obtained.

The variances $\sigma_{\overline{C}}$ and $\sigma_{\overline{O}}$ were estimated from the uncertainty associated with the addition of the correct volume of calcium and oxalate solutions to the metastable solution. The uncertainty was estimated at 2% and may be written in terms of the standard deviation and mean as

$$\psi_{\bar{C}} = \psi_{\bar{O}} = \frac{\sigma_{\bar{C}}}{\bar{C}} = \frac{\sigma_{\bar{O}}}{\bar{O}} = 0.02 \quad (\text{A8.31})$$

Now from eq 4.5,

$$AP = K_{sp} S^2 \quad (\text{A8.32})$$

Using eq A8.1,

$$\sigma_{\overline{AP}}^2 = 4 K_{sp}^2 \sigma_{\bar{S}}^2 \quad (\text{A8.33})$$

Re-arranging eq A8.33 implies

$$\sigma_{\bar{S}} = \frac{\sigma_{\overline{AP}}}{4 K_{sp}} \quad (\text{A8.34})$$

Oxalate ion concentration analysis

From Section 2.6, the fraction of oxalate present as a free ion is approximately constant, thus an analysis using total oxalate concentrations can be used to determine the error. The total oxalate ion concentration is given by

$$T_{Ox^{2-}} = T_{Ox^{2-}}^0 - X \quad (\text{A8.35})$$

where X is given by eq A8.26. Using eqs A8.28 for the error in the initial oxalate concentration, yields

$$\sigma_{\overline{T_{Ox^{2-}}}} = \sqrt{(0.02 \bar{O})^2 + \sigma_{\bar{X}}^2} \quad (\text{A8.36})$$

A8.2 SAMPLE CALCULATION

The values of m_0 , m_2 and m_3 from each flask for the samples collected after 5 minutes from the batch experiment 11/7 are given in Table A8.1. The values of the mean and standard deviation of the variables in Table A8.1 were calculated using

$$\bar{x} = \sum_{i=1}^n \frac{x_i}{n} \quad \text{and} \quad \sigma_x = \sqrt{\frac{1}{n-1} \sum_{i=1}^n (x_i - \bar{x})^2}$$

Table A8.1 Data from batch experiment 11/7 5 at $t = 5$ minutes.

Replicate	m_0 (Number/500 μ l)	m_2 (μm^2 /500 μ l)	m_3 (μm^3 /500 μ l)
1	64320	1.59×10^6	1.01×10^8
2	61549	1.61×10^6	1.04×10^8
3	63856	1.61×10^6	1.01×10^8
4	65016	1.67×10^6	1.07×10^8
mean	63685	1.62×10^6	1.03×10^8
standard deviation, σ	1502	3.29×10^4	2.81×10^5

From the data in Appendix 7 the growth rate obtained from the program *Batch* at 5 minutes is 0.052 $\mu\text{m}/\text{min}$. The standard error in the growth rate is calculated from eq A8.16

$$\begin{aligned}\sigma_{\bar{G}} &= \bar{G} \sqrt{\frac{1}{n} \left(\frac{\sigma_{m_2}}{\bar{m}_2} \right)^2 + \frac{2}{n} \left(\frac{\Psi_{m_3} \bar{m}_3}{3 \bar{m}_2 \bar{G} \Delta t} \right)^2} \\ &= 0.052 \times \sqrt{\frac{1}{4} \left(\frac{3.29 \times 10^3}{1.62 \times 10^6} \right)^2 + \frac{2}{4} \left(\frac{0.02 \times 1.03 \times 10^7}{3 \times 1.62 \times 10^6 \times 0.052 \times 5} \right)^2} \\ &= 0.006 \mu\text{m}/\text{min}\end{aligned}$$

The standard error is approximately 11% of the growth rate.

From the data in Appendix 7 the value of β_0 obtained from the program *Batch* is 3.86×10^{-4} $\mu\text{l}/\text{min}$. From eq A8.22 the standard error in β_0 is

$$\begin{aligned}\sigma_{\bar{\beta}_0} &= \bar{\beta}_0 \sqrt{\frac{4}{n} \left(\frac{\sigma_{m_0}}{\bar{m}_0} \right)^2 + \frac{2}{n} \left(\frac{-2 \Psi_{m_0}}{\bar{\beta}_0 \bar{m}_0 \Delta t} \right)^2} \\ &= 3.86 \times 10^{-4} \times \sqrt{\frac{4}{4} \left(\frac{1502}{63685} \right)^2 + \frac{2}{4} \left(\frac{-2 \times 0.033}{3.86 \times 10^{-4} \times 63685 \times 5} \right)^2} \\ &= 9.11 \times 10^{-6} \mu\text{l}/\text{min}\end{aligned}$$

The standard error is approximately 2.4% of the value of β_0 .

For the activity product, eq A8.27 is used together with eqs A8.28 to A8.31. Firstly, \bar{X}^2 is calculated from eq A8.26

$$\begin{aligned}\bar{X}^2 &= k^2 \left(\bar{m}_3 - \bar{m}_3^0 \right)^2 \\ &= (1.58 \times 10^{-11})^2 \times (1.03 \times 10^7 - 6.98 \times 10^6)^2 \\ &= 2.75 \times 10^{-9} (\text{mol/dm}^3)^2\end{aligned}$$

Substituting eqs A8.15, A8.28 and A8.30, into eq A8.6,

$$\begin{aligned}\sigma_{\bar{X}}^2 &= \frac{k^2 \left(\left(\psi_{m_3} \bar{m}_3 \right)^2 + \left(\psi_{m_3^0} \bar{m}_3^0 \right)^2 \right)}{n} \\ &= \frac{(1.58 \times 10^{-11})^2 \times \left((0.02 \times 1.03 \times 10^7)^2 + (0.047 \times 6.98 \times 10^6)^2 \right)}{4} \\ &= 9.33 \times 10^{-12} (\text{mol/dm}^3)^2\end{aligned}$$

Substituting eqs A8.15, A8.29 and A8.30 into eq A8.6 gives

$$\begin{aligned}\sigma_{\bar{X}^2}^2 &= \frac{6k^4 \left(\left(\psi_{m_3} \bar{m}_3 \right)^2 + \left(\psi_{m_3^0} \bar{m}_3^0 \right)^2 \right)}{n} \\ &= \frac{6 \times (1.58 \times 10^{-11})^4 \left((0.02 \times 1.03 \times 10^7)^2 + (0.047 \times 6.98 \times 10^6)^2 \right)}{4} \\ &= 1.39 \times 10^{-32} (\text{mol / dm}^3)^4\end{aligned}$$

As a standard metastable solution was used in experiment 11/7 from Table 3.2 the values of the initial calcium and oxalate concentrations are 9.81×10^{-4} and 9.81×10^{-4} M. Then from eq A8.27

$$\begin{aligned}\sigma_{AP}^2 &= (2\psi_C^2)(\bar{C}\bar{O})^2 + \left(\frac{\sigma_{\bar{X}}^2}{\bar{X}^2} + \psi_C^2 \right) (\bar{X}\bar{C})^2 + \left(\frac{\sigma_{\bar{X}}^2}{\bar{X}^2} + \psi_O^2 \right) (\bar{X}\bar{O})^2 + \sigma_{\bar{X}^2}^2 \\ &= (2 \times 0.02^2) \times (9.81 \times 10^{-4} \times 1.96 \times 10^{-4})^2 \\ &\quad + \left(\frac{9.33 \times 10^{-12}}{2.75 \times 10^{-9}} + 0.02^2 \right) \times (9.33 \times 10^{-12} \times 9.81 \times 10^{-4})^2 \\ &\quad + \left(\frac{9.33 \times 10^{-12}}{2.75 \times 10^{-9}} + 0.02^2 \right) \times (9.33 \times 10^{-12} \times 1.96 \times 10^{-4})^2 \\ &\quad + 1.39 \times 10^{-32} \\ &= 4.0 \times 10^{-17} (\text{mol/dm}^3)^4\end{aligned}$$

Taking the square root of this result

$$\sigma_{AP} = 6.33 \times 10^{-9} (\text{mol/dm}^3)^2$$

From eq A8.34, and using the value of K_{sp} for total ion concentrations (see eq 5.41),

$$\sigma_S = \frac{\sigma_{AP}}{4 K_{sp}} = \frac{6.33 \times 10^{-9}}{4 \times 4.39 \times 10^{-8}} = 0.036$$

which is approximately 2.1% of the value of S , which from Appendix 7 is, 1.74.

Finally, from eq A8.36

$$\begin{aligned}\sigma_{T_{Ox^{2-}}} &= \sqrt{(0.02\bar{O})^2 + \sigma_X^2} \\ &= \sqrt{(0.02 \times 1.96 \times 10^{-4})^2 + 9.33 \times 10^{-12}} \\ &= 4.97 \times 10^{-6} \text{ M}\end{aligned}$$

which is approximately 3.5% of the value of the oxalate ion concentration.

Appendix 9:

CONTINUOUS CRYSTALLISATION EXPERIMENTAL DATA

In this appendix the experimental data from the continuous crystallisation experiments described in Chapter 9 are reported. The data given are the moments of the CSDs measured by the Multisizer as calculated from eq 9.20. The conditions in each of the experiments are given in Tables 9.1 and 9.2.

The values of the rate constants and independent variables were calculated from the experimental moments using the methods described in Chapter 9. The units and abbreviations used for the rate constants in the data are:

α , dilution factor

m_j , j th moment, $\mu\text{m}^{3j}/500 \mu\text{l}$

t_{bar} , mean residence time, seconds

k_B , breakage rate constant, s^{-1}

γ_B , shear rate for breakage, s^{-1}

k_S , sticking rate constant, s^{-1}

γ_S , shear rate for sticking, s^{-1}

S , relative supersaturation

G , growth rate ($\mu\text{m}/\text{s}$)

β_0 , aggregation rate constant, m^3/s

Expt 20/7, QL=4ml/min

Feed

α	m-1	m-2/3	m-1/3	m0	m1/3	m2/3	m1	m4/3	m5/3	m2
1	1.54E+03	5.03E+03	1.89E+04	8.16E+04	4.00E+05	2.17E+06	1.28E+07	8.15E+07	5.55E+08	4.05E+09

Saturated saline

α	m-1	m-2/3	m-1/3	m0	m1/3	m2/3	m1	m4/3	m5/3	m2
1	1.20E+03	3.60E+03	1.21E+04	4.59E+04	1.99E+05	9.71E+05	5.23E+06	3.07E+07	1.95E+08	1.34E+09
2	1.68E+03	5.14E+03	1.76E+04	6.89E+04	3.06E+05	1.52E+06	8.34E+06	4.97E+07	3.22E+08	2.26E+09
3	1.93E+03	5.92E+03	2.05E+04	8.08E+04	3.63E+05	1.83E+06	1.01E+07	6.13E+07	4.01E+08	2.85E+09
4	2.05E+03	6.26E+03	2.16E+04	8.54E+04	3.85E+05	1.94E+06	1.08E+07	6.56E+07	4.30E+08	3.06E+09
5	2.11E+03	6.47E+03	2.24E+04	8.85E+04	3.99E+05	2.01E+06	1.12E+07	6.77E+07	4.43E+08	3.14E+09
6	2.26E+03	6.87E+03	2.36E+04	9.29E+04	4.16E+05	2.09E+06	1.15E+07	6.96E+07	4.54E+08	3.23E+09

α	tbar	gammaB	kB	gammaS	kS
1	2.26E+02	2.08E+01	2.25E-03	3.76E+01	4.01E-03
2	1.60E+02	2.96E+01	2.47E-03	5.36E+01	2.73E-03
3	1.28E+02	3.71E+01	2.62E-03	6.72E+01	1.83E-03
4	1.09E+02	4.40E+01	2.98E-03	7.97E+01	1.55E-03
5	9.60E+01	5.04E+01	3.42E-03	9.13E+01	1.43E-03
6	8.63E+01	5.66E+01	4.10E-03	1.02E+02	1.21E-03

Metastable solution, S=1.61

α	m-1	m-2/3	m-1/3	m0	m2/3	m1	m4/3	m5/3
1	1.18E+03	3.54E+03	1.19E+04	4.58E+04	1.01E+06	5.59E+06	3.38E+07	2.22E+08
2	1.71E+03	5.10E+03	1.72E+04	6.60E+04	1.44E+06	7.89E+06	4.72E+07	3.06E+08
3	1.87E+03	5.66E+03	1.95E+04	7.79E+04	1.85E+06	1.05E+07	6.48E+07	4.30E+08
4	1.94E+03	5.90E+03	2.05E+04	8.22E+04	1.96E+06	1.12E+07	6.97E+07	4.66E+08
5	1.92E+03	5.84E+03	2.03E+04	8.20E+04	2.01E+06	1.17E+07	7.36E+07	5.02E+08
6	1.85E+03	5.60E+03	1.95E+04	7.94E+04	2.00E+06	1.18E+07	7.51E+07	5.12E+08

α	S	tbar	G	kB	kS	β_0	gammaB
1	1.61	2.26E+02	5.33E-04	2.25E-03	3.94E-03	4.15E-15	2.08E+01
2	1.62	1.60E+02	5.49E-04	2.47E-03	3.32E-03	3.82E-15	2.96E+01
3	1.62	1.28E+02	5.55E-04	2.62E-03	1.83E-03	3.82E-15	3.71E+01
4	1.62	1.09E+02	5.58E-04	2.98E-03	1.49E-03	5.29E-15	4.40E+01
5	1.62	9.60E+01	5.60E-04	3.42E-03	1.25E-03	1.18E-14	5.04E+01
6	1.62	8.63E+01	5.62E-04	4.10E-03	1.23E-03	2.25E-14	5.66E+01

Expt 21/7, QL=6ml/min

Feed

α	m-1	m-2/3	m-1/3	m0	m1/3	m2/3	m1	m4/3	m5/3	m2
1	1.29E+03	4.10E+03	1.49E+04	6.17E+04	2.91E+05	1.52E+06	8.72E+06	5.38E+07	3.58E+08	2.56E+09

Saturated saline

α	m-1	m-2/3	m-1/3	m0	m1/3	m2/3	m1	m4/3	m5/3	m2
1	1.05E+03	3.15E+03	1.05E+04	3.93E+04	1.66E+05	7.80E+05	4.05E+06	2.30E+07	1.42E+08	9.55E+08
1.67	1.52E+03	4.58E+03	1.54E+04	5.83E+04	2.49E+05	1.19E+06	6.26E+06	3.60E+07	2.25E+08	1.54E+09
2.33	1.59E+03	4.83E+03	1.65E+04	6.34E+04	2.76E+05	1.34E+06	7.16E+06	4.17E+07	2.64E+08	1.83E+09
3	1.82E+03	5.46E+03	1.82E+04	6.87E+04	2.93E+05	1.40E+06	7.36E+06	4.24E+07	2.67E+08	1.83E+09
3.67	1.94E+03	5.81E+03	1.93E+04	7.23E+04	3.05E+05	1.44E+06	7.52E+06	4.31E+07	2.69E+08	1.85E+09
4.33	1.96E+03	5.87E+03	1.95E+04	7.31E+04	3.09E+05	1.47E+06	7.70E+06	4.44E+07	2.81E+08	1.96E+09

α	tbar	gammaB	kB	gammaS	kS
1	1.53E+02	3.12E+01	3.26E-03	5.64E+01	5.10E-03
1.67	1.18E+02	4.04E+01	3.60E-03	7.31E+01	2.87E-03
2.33	9.90E+01	4.85E+01	3.46E-03	8.79E+01	2.05E-03
3	8.62E+01	5.60E+01	5.03E-03	1.01E+02	2.01E-03
3.67	7.71E+01	6.31E+01	6.15E-03	1.14E+02	1.94E-03
4.33	7.01E+01	6.98E+01	6.37E-03	1.26E+02	1.69E-03

Metastable solution, S=1.61

α	m-1	m-2/3	m-1/3	m0	m2/3	m1	m4/3	m5/3
1	1.23E+03	3.70E+03	1.24E+04	4.74E+04	9.94E+05	5.35E+06	3.15E+07	2.02E+08
1.67	1.41E+03	4.29E+03	1.46E+04	5.65E+04	1.22E+06	6.59E+06	3.90E+07	2.51E+08
2.33	1.41E+03	4.33E+03	1.50E+04	5.98E+04	1.38E+06	7.77E+06	4.76E+07	3.16E+08
3	1.52E+03	4.59E+03	1.57E+04	6.20E+04	1.42E+06	7.91E+06	4.79E+07	3.13E+08
3.67	1.59E+03	4.80E+03	1.65E+04	6.50E+04	1.49E+06	8.34E+06	5.10E+07	3.40E+08
4.33	1.45E+03	4.42E+03	1.53E+04	6.07E+04	1.41E+06	7.93E+06	4.85E+07	3.22E+08

α	S	tbar	G	kB	kS	β_0	gammaB
1	1.61	1.53E+02	5.44E-04	3.26E-03	3.46E-03	8.38E-15	3.12E+01
1.67	1.62	1.18E+02	5.53E-04	3.60E-03	2.63E-03	7.65E-15	4.04E+01
2.33	1.62	9.90E+01	5.57E-04	3.46E-03	1.43E-03	1.94E-14	4.85E+01
3	1.62	8.62E+01	5.59E-04	5.03E-03	1.38E-03	2.84E-14	5.60E+01
3.67	1.62	7.71E+01	5.61E-04	6.15E-03	8.09E-04	3.97E-14	6.31E+01
4.33	1.62	7.01E+01	5.62E-04	6.37E-03	1.58E-03	4.48E-14	6.98E+01

Expt 18/7, QL=8ml/min

Feed

α	m-1	m-2/3	m-1/3	m0	m1/3	m2/3	m1	m4/3	m5/3	m2
1	1.36E+03	4.36E+03	1.59E+04	6.66E+04	3.16E+05	1.68E+06	9.72E+06	6.10E+07	4.12E+08	3.00E+09

Saturated saline

α	m-1	m-2/3	m-1/3	m0	m1/3	m2/3	m1	m4/3	m5/3	m2
1	1.24E+03	3.78E+03	1.29E+04	5.00E+04	2.19E+05	1.07E+06	5.79E+06	3.42E+07	2.20E+08	1.55E+09
1.5	1.58E+03	4.82E+03	1.64E+04	6.28E+04	2.73E+05	1.33E+06	7.13E+06	4.20E+07	2.69E+08	1.89E+09
2	1.67E+03	5.11E+03	1.74E+04	6.70E+04	2.91E+05	1.42E+06	7.63E+06	4.50E+07	2.90E+08	2.05E+09
2.5	1.75E+03	5.36E+03	1.83E+04	7.09E+04	3.10E+05	1.52E+06	8.18E+06	4.83E+07	3.11E+08	2.19E+09
3	1.84E+03	5.60E+03	1.90E+04	7.32E+04	3.18E+05	1.55E+06	8.33E+06	4.93E+07	3.20E+08	2.29E+09
3.5	1.81E+03	5.54E+03	1.90E+04	7.36E+04	3.23E+05	1.58E+06	8.59E+06	5.11E+07	3.32E+08	2.36E+09

α	tbar	gammaB	kB	gammaS	kS
1	1.15E+02	4.15E+01	3.05E-03	7.52E+01	4.57E-03
1.5	9.38E+01	5.10E+01	4.07E-03	9.22E+01	3.36E-03
2	8.07E+01	5.94E+01	4.57E-03	1.08E+02	3.02E-03
2.5	7.15E+01	6.73E+01	4.92E-03	1.22E+02	2.48E-03
3	6.47E+01	7.47E+01	5.60E-03	1.35E+02	2.31E-03
3.5	5.93E+01	8.18E+01	5.51E-03	1.48E+02	2.06E-03

Metastable solution, S=1.61

α	m-1	m-2/3	m-1/3	m0	m2/3	m1	m4/3	m5/3
1	1.19E+03	3.63E+03	1.25E+04	4.97E+04	1.15E+06	6.49E+06	3.98E+07	2.64E+08
1.5	1.42E+03	4.38E+03	1.53E+04	6.07E+04	1.40E+06	7.90E+06	4.84E+07	3.22E+08
2	1.39E+03	4.31E+03	1.52E+04	6.15E+04	1.47E+06	8.34E+06	5.16E+07	3.44E+08
2.5	1.48E+03	4.58E+03	1.61E+04	6.48E+04	1.54E+06	8.74E+06	5.39E+07	3.58E+08
3	1.31E+03	4.11E+03	1.47E+04	6.12E+04	1.55E+06	9.06E+06	5.72E+07	3.89E+08
3.5	1.18E+03	3.76E+03	1.38E+04	5.87E+04	1.55E+06	9.17E+06	5.86E+07	4.01E+08

Metastable solution, S=2.20

α	m-1	m-2/3	m-1/3	m0	m2/3	m1	m4/3	m5/3
2	9.88E+02	3.04E+03	1.08E+04	4.54E+04	1.27E+06	7.94E+06	5.42E+07	3.98E+08
3.5	1.25E+03	3.78E+03	1.31E+04	5.37E+04	1.45E+06	9.04E+06	6.18E+07	4.57E+08

Metastable solution, S=1.93

α	m-1	m-2/3	m-1/3	m0	m2/3	m1	m4/3	m5/3
2	8.51E+02	2.63E+03	9.43E+03	4.02E+04	1.17E+06	7.62E+06	5.42E+07	4.17E+08
3.5	1.02E+03	3.13E+03	1.12E+04	4.77E+04	1.40E+06	9.06E+06	6.45E+07	4.99E+08

Metastable solution, S=2.20

α	m-1	m-2/3	m-1/3	m0	m2/3	m1	m4/3	m5/3
2	8.62E+02	2.60E+03	9.10E+03	3.82E+04	1.15E+06	7.87E+06	6.04E+07	5.15E+08
3.5	9.35E+02	2.89E+03	1.04E+04	4.50E+04	1.37E+06	9.07E+06	6.55E+07	5.11E+08

Metastable solution, S=1.21

α	m-1	m-2/3	m-1/3	m0	m2/3	m1	m4/3	m5/3
2	1.48E+03	4.56E+03	1.59E+04	6.33E+04	1.46E+06	8.18E+06	4.99E+07	3.30E+08
3.5	1.42E+03	4.42E+03	1.57E+04	6.42E+04	1.56E+06	8.94E+06	5.55E+07	3.71E+08

Metastable solution, S=2.21

α	m-1	m-2/3	m-1/3	m0	m2/3	m1	m4/3	m5/3
2	8.14E+02	2.50E+03	8.94E+03	3.83E+04	1.17E+06	7.91E+06	5.88E+07	4.76E+08
3.5	1.06E+03	3.25E+03	1.15E+04	4.84E+04	1.39E+06	8.95E+06	6.31E+07	4.82E+08

Expt 18/7, QL=8ml/min

Metastable solution, S=1.61

α	S	tbar	G	kB	kS	β_0	gammaB
1	1.61	1.15E+02	5.44E-04	3.05E-03	3.77E-03	1.57E-14	4.15E+01
1.5	1.62	9.38E+01	5.51E-04	4.07E-03	2.46E-03	1.95E-14	5.10E+01
2	1.62	8.07E+01	5.55E-04	4.57E-03	2.14E-03	3.03E-14	5.94E+01
2.5	1.62	7.15E+01	5.57E-04	4.92E-03	1.73E-03	2.91E-14	6.73E+01
3	1.62	6.47E+01	5.59E-04	5.60E-03	1.32E-03	6.02E-14	7.47E+01
3.5	1.62	5.93E+01	5.60E-04	5.51E-03	1.22E-03	7.74E-14	8.18E+01

Metastable solution, S=2.20

α	S	tbar	G	kB	kS	β_0	gammaB
2	2.19	8.07E+01	2.04E-03	4.57E-03	3.50E-03	8.84E-14	4.57E-03
3.5	2.20	5.93E+01	2.07E-03	5.51E-03	2.22E-03	9.23E-14	5.51E-03

Metastable solution, S=1.93

α	S	tbar	G	kB	kS	β_0	gammaB
2	1.93	8.07E+01	1.26E-03	4.57E-03	3.60E-03	1.21E-13	4.57E-03
3.5	1.93	5.93E+01	1.27E-03	5.51E-03	1.77E-03	1.43E-13	5.51E-03

Metastable solution, S=2.20

α	S	tbar	G	kB	kS	β_0	gammaB
2	2.20	8.07E+01	2.08E-03	4.57E-03	3.59E-03	1.40E-13	4.57E-03
3.5	2.20	5.93E+01	2.08E-03	5.51E-03	2.14E-03	1.62E-13	5.51E-03

Metastable solution, S=1.21

α	S	tbar	G	kB	kS	β_0	gammaB
2	1.21	8.07E+01	6.69E-05	4.57E-03	2.13E-03	2.19E-14	4.57E-03
3.5	1.22	5.93E+01	6.99E-05	5.51E-03	1.40E-03	4.34E-14	5.51E-03

Metastable solution, S=2.21

α	S	tbar	G	kB	kS	β_0	gammaB
2	2.21	8.07E+01	2.11E-03	4.57E-03	3.55E-03	1.40E-13	4.57E-03
3.5	2.21	5.93E+01	2.12E-03	5.51E-03	2.40E-03	1.28E-13	5.51E-03

Expt 22/7, QL=10ml/min

Feed

α	m-1	m-2/3	m-1/3	m0	m1/3	m2/3	m1	m4/3	m5/3	m2
1	1.34E+03	4.14E+03	1.45E+04	5.76E+04	2.61E+05	1.32E+06	7.35E+06	4.45E+07	2.92E+08	2.08E+09

Saturated saline

α	m-1	m-2/3	m-1/3	m0	m1/3	m2/3	m1	m4/3	m5/3	m2
1	1.26E+03	3.78E+03	1.26E+04	4.73E+04	2.00E+05	9.45E+05	4.94E+06	2.83E+07	1.78E+08	1.23E+09
1.4	1.38E+03	4.16E+03	1.40E+04	5.34E+04	2.29E+05	1.10E+06	5.79E+06	3.36E+07	2.13E+08	1.50E+09
1.8	1.54E+03	4.63E+03	1.55E+04	5.83E+04	2.48E+05	1.18E+06	6.23E+06	3.60E+07	2.27E+08	1.58E+09
2.2	1.56E+03	4.71E+03	1.59E+04	6.01E+04	2.57E+05	1.22E+06	6.41E+06	3.67E+07	2.30E+08	1.58E+09
2.6	1.56E+03	4.75E+03	1.61E+04	6.12E+04	2.62E+05	1.26E+06	6.62E+06	3.81E+07	2.40E+08	1.65E+09
3	1.62E+03	4.87E+03	1.64E+04	6.21E+04	2.66E+05	1.28E+06	6.79E+06	3.96E+07	2.55E+08	1.82E+09

α	tbar	gammaB	kB	gammaS	kS
1	9.24E+01	5.19E+01	3.43E-03	9.40E+01	4.36E-03
1.4	7.81E+01	6.15E+01	3.16E-03	1.11E+02	3.06E-03
1.8	6.86E+01	7.03E+01	4.11E-03	1.27E+02	2.45E-03
2.2	6.16E+01	7.84E+01	4.70E-03	1.42E+02	2.43E-03
2.6	5.62E+01	8.62E+01	4.67E-03	1.56E+02	2.07E-03
3	5.20E+01	9.36E+01	4.38E-03	1.70E+02	1.37E-03

Metastable solution, S=1.61

α	m-1	m-2/3	m-1/3	m0	m2/3	m1	m4/3	m5/3
1	1.12E+03	3.40E+03	1.16E+04	4.51E+04	9.98E+05	5.50E+06	3.31E+07	2.16E+08
1.4	1.28E+03	3.91E+03	1.35E+04	5.30E+04	1.20E+06	6.68E+06	4.06E+07	2.68E+08
1.8	1.41E+03	4.27E+03	1.45E+04	5.63E+04	1.24E+06	6.79E+06	4.06E+07	2.64E+08
2.2	1.36E+03	4.16E+03	1.44E+04	5.66E+04	1.28E+06	7.09E+06	4.30E+07	2.84E+08
2.6	1.24E+03	3.81E+03	1.33E+04	5.33E+04	1.24E+06	6.97E+06	4.26E+07	2.83E+08
3	1.25E+03	3.86E+03	1.35E+04	5.41E+04	1.26E+06	7.08E+06	4.33E+07	2.89E+08

α	S	tbar	G	kB	kS	β_0	gammaB
1	1.61	9.24E+01	5.48E-04	3.43E-03	3.40E-03	3.12E-14	5.19E+01
1.4	1.62	7.81E+01	5.53E-04	3.16E-03	1.50E-03	3.05E-14	6.15E+01
1.8	1.62	6.86E+01	5.56E-04	4.11E-03	1.42E-03	2.67E-14	7.03E+01
2.2	1.62	6.16E+01	5.58E-04	4.70E-03	8.35E-04	4.36E-14	7.84E+01
2.6	1.62	5.62E+01	5.59E-04	4.67E-03	1.21E-03	5.97E-14	8.62E+01
3	1.62	5.20E+01	5.60E-04	4.38E-03	9.84E-04	5.66E-14	9.36E+01